Eighth International Conference on

Local Mechanical Properties LMP 2011

Olomouc, Czech Republic

9–11 November 2011

Organized by

Joint Laboratory of Optics

Palacky University and Institute of Physics

Academy of Sciences of the Czech Republic

2011

s367

SPONSORS OF THE CONFERENCE

Preface

The Eighth International Conference on Local Mechanical Properties LMP 2011 was held in Olomouc, The Czech Republic, on November 9-11, 2011. The LMP 2011 conference was organized by the Joint Laboratory of Optics of Palacky University and Institute of Physics of the Academy of Sciences of the Czech Republic.

Continuing in the tradition of the LMV (Lokální mechanické vlastnosti) conference series started in 2004, the LMP 2011 brought together material specialists, researchers and scientists from universities, research institutes and also the private companies representatives. It was again a really open forum for the intensive discussion and exchange of knowledge and experience.

The meeting that becomes a well established forum in the field of local mechanical testing provided an opportunity to highlight recent results of research and development in the field of materials engineering, experimental methods, modeling, etc., with the aim to characterize mechanical properties of broad range of materials from nano to micro/meso-scale. Especially nanoindentation and other methods of hardness assessment, measurement of local stresses and deformations and related microstructure analyses were discussed.

Over 90 participants from 11 countries around the world attended this conference. The conference program covered 35 oral presentations in 8 sections and 53 posters on recent progress in research, development and applications of measurement of mechanical properties at small scale.

The LMP 2011 conference organizers would like to thank all the speakers, session chairpersons, invited speakers and participants for making this conference successful. The support of the conference sponsors is also greatly appreciated. It is our hope that LMP 2011 conference has been fruitful and presented works will provide valuable information and guidance on the latest trends and future advances in local mechanical testing. This issue contains 68 peer reviewed papers.

Declaration

All contributions included in the special issue of this journal have been reviewed prior to publication by the members of the Scientific Board. Linguistic usage in the articles has not been modified by the editors.

CELLS ON SURFACES: AN INDENTATION APPROACH

MICHAEL V. SWAIN[a,b], S. SCHULZ[a], T. STEINBERG[a], and P. TOMAKIDI[a]

[a] *Department of Prosthodontics, School of Dentistry, Albert-Ludwigs University, Freiburg, Germany,* [b] *Biomaterials, Faculties of Dentistry, The University of Sydney, Australia and Otago University, Dunedin, New Zealand*
michael.swain@uniklinik-freiburg.de

Keywords: cells, surface interaction, pillars, indentation

1. Introduction

Recent studies have established the critical role for cells of the mechanical properties of the extra-cellular matrix on which they are supported. It has been shown that mysenchyme stem cells can differentiation into specific cells ranging from nerve to bone. In addition it is known that cells in attachment with a substrate generate traction forces which contribute to their movement and reorientation.

The mechanical properties, dimensions and structural form of the filamentous components of calls are also well investigated. In addition, the basic cell membrane properties have been investigated by many authors using a variety of techniques including; micro pipette, optical tweezers, shear flow and magnetic particle interaction and nano-indentation being the most common[1]. The basis for interpretation of the force-displacement data is very different from the analysis of indentation of elastic-plastic materials.

Various techniques based upon those developed for semiconductor production to develop surfaces that enable the micromechanical responses of cells to be explored. Micro-grooving, dimples and micro-pillars enable a number of variables of surfaces to be investigated in a systematic manner. For pillars these include the roles of elastic modulus, height, spacing and diameter as a means to influence cell response. The majority of these studies focussed on the role of the surface on the subsequent cell morphology along with incorporation of various fluorescent dyes to enable the various filament structures to be visualised.

A critical review of this area by Flemming et al.[2] identified the effect of features, primarily that of micro grooving and the resulting cell morphology and growth. They noted that cells tended to align parallel to grooves and the cytoskeleton components formed parallel to the grooves. The work of Wojciak-Stothard et al.[3] noted that actin filament condensation appeared at topographic discontinuities. Flemming et al.[2] indicated the depth of grooves were more important than width in determining cell orientation. More recently Martinez et al.[4] used cryo and subsequent focussed ion beam (FIB) sectioning to investigate the role of pattern spacing and height on the basal response of cells to surfaces. They observed with line patterns that it was the ratio of pattern height to width that was critical.

Recent work has placed considerable focus on biochemical, gene expression responses and the traction forces developed on various surfaces. Again the feature that is persistently remarked upon in these studies is the location of the various cells investigated as a function of pillar height, diameter and spacing. At relatively close pillar spacing the cells sit on top of the pillar arrays whereas at larger pillar spacing they lie between the pillars.

Steinberg et al.[5] investigated PDMS pillars with E moduli of 0.5 to 3.5 MPa and 8 to 14 μm spacing on keratinocyte cell differentiation. They observed that with a decrease in pillar spacing an increase in the cell differentiation. Mussig et al.[6,7] investigated 3 periodontal type cells on cell morphology and gene expression. Pillar spacing of 5 μm enabled regular cellular response for all cells, increasing pillar spacing resulted in reduced cell numbers. Cell observations with the osteoblasts indicated the cells were only slightly indented when pillars were 5μm apart but more substantially indented and almost resting on the space between the pillars at 11 μm spacing. A recent study by Papenberg et al.[8] investigated wetability of micro-pillars of three materials (PDMS, PEOT/PBT and PLLA) with E modulus (2 MPa, 30–70 MPa to 2 GPa) with pre-myoblasts cells. For pillar spacing of 2 μm all cells grew on top of the pillars while at 5 μm spacing there was a transition from growing on top of the pillars to between the pillars especially for the 5 μm high pillars. The authors state surface topography rather than pillar elastic modulus influenced cell attachment, proliferation and morphology.

The aim of the present paper is to more closely investigate the interaction mechanics between various cells and the micro pillars they are supported on. A simple generalised contact analysis of the cell pillar interaction is developed that is used to compare with the experimental observations. The simple contact mechanics and cell membrane deformation concepts are then applied to a number of cell systems published in the literature

2. Materials and methods

As stated above, many authors have used micro pillars to support cells in order to study the morph-ological, detailed microbiological and gene expression responses. These pillars are generally fabricated using photolithography based procedures with tailored diameter, pillar height and spacing. Details regarding the development of such

materials are given in the studies by Steinberg et al.[5]. A typical SEM observation of such pillars is shown in Fig. 1.

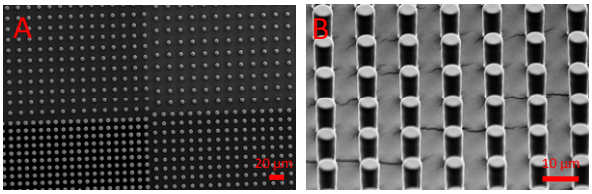

Fig. 1. **SEM images of a PDMS pillar array with pillar heights of 15 μm, pillar diameters of 5 μm and spacing between the pillars varying between 5 to 11 μm. Note that four pillar spacing distances have been created simultaneously. A normal and B inclined view**

Various approaches have been used to visualise cells including confocal and optical microscopy, SEM as well as an array of staining and visualisation approaches. SEM often results in dehydration induced shrinkage of the cells during preparation. In this study details of micro-biology or gene expression outcomes will not be addressed directly.

3. Contact and deformation mechanics

In this section only the initial phase of cell deformation that is, the contact pressure between the pillars and the cell membrane is considered.

3.1. Contact mechanics

Consider a cell as a spherical entity with a plasma membrane having a constant volume, *V*, and density, ρ. It is suspended in a fluid culture medium that has a density of $\rho_o \sim 1$ gm/cc. When the cell rests on the pillars then contact stresses are developed between the pillar and cell membrane. Consider a square array of cylindrical pillars with diameter *D* that have a centre to centre spacing of *L*, Fig. 2.

Consider the cell upon contacting the pillars to form into a hemispherical shaped body then the relationship between the volume, *V*, of the cell and its radius, *R*, is:

$$V = \frac{2}{3}\pi R^3 \qquad (1)$$

The support area of an individual pillar is given by $A_p = \pi D2/4$. For a square array of pillars with spacing *L* between the pillar centres, each pillar contributes one quarter to the unit cell area of the pillar array, and is given by, Pillar area per unit cell

$$= \frac{\pi D^2}{4L^2} \qquad (2)$$

For a cell of volume *V* that forms into a hemispherical body upon contact with the array, the diameter of the cell is 2*R* (Fig. 3). The contact area assuming the pillar array a continuous flat surface is given by πR^2. Thus the supporting area provided by the pillars beneath the cell is given with eq (*2*) by,

$$A_p = \left(\frac{\pi D^2}{4L^2}\right)(\pi R^2) = \left(\frac{\pi DR}{2L}\right)^2 \qquad (3)$$

The force exerted by the cell on the supporting contact area in the liquid media is given by;

$$F = V\Delta\rho g \qquad (4)$$

where *V* is the cell volume, $\Delta\rho$, that is $(\rho - \rho_o)$ is the density difference between the cell and supporting liquid medium and *g* is the gravitation constant. The average contact pressure between the cell and the pillars is then given from eqs (*3*) and (*4*), namely;

$$P_c = \frac{F}{A_p} = \frac{V\Delta\rho g}{(\pi DR/2L)^2} = \frac{8RL^2\Delta\rho g}{3\pi D^2} \qquad (5)$$

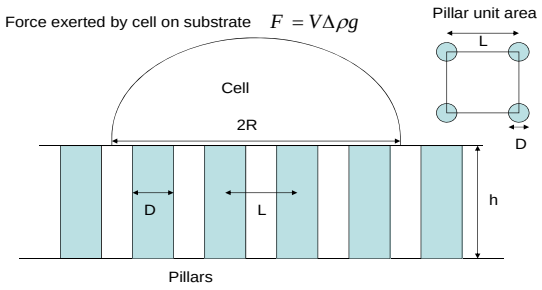

Fig. 2. **Schematic illustration of a cell on an array of pillars with dimensions and spacing defined**

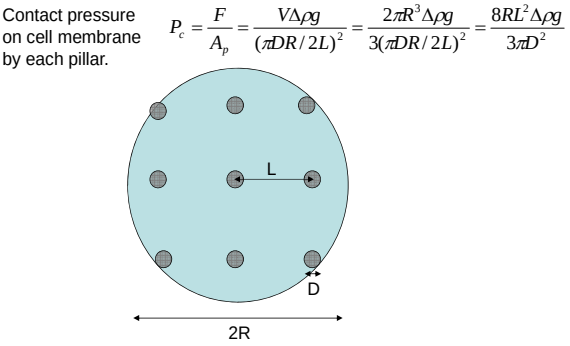

Fig. 3. **Schematic diagram of projected cell supported on an array of pillars**

For a specific cell with similar volume and for pillars of constant diameter the contact pressure is directly related to L^2. For the pillar spacings considered there is almost a 4 fold increase in the contact pressure as L changes from 10 to 19 μm. The relationship between centre to centre pillar spacing L with diameter D and often stated edge to edge spacing X is $L = D + X$.

Fig. 4 is plotted, from eq (*5*), the dependence of the contact pressure as a function of pillar spacing L pillar diameter D for cell where $\Delta\rho$ is 0.3 kg m^{-3}.

3.2. Stresses and axial deflection of pillars

The force on the pillar due to the loading by the cell is given by

$$F_p = \frac{V\Delta\rho g}{n} \qquad (6)$$

where n is the number of pillars supporting the cell, which is given by the ratio of the area of the cell divided by the pillar array unit cell area, namely;

$$n = \frac{\pi R^2}{L^2} \qquad (7)$$

Substituting into eq (*7*) for n and V from eq (*1*), results in

$$F_p = \frac{2\Delta\rho g R L^2}{3} \qquad (8)$$

The resultant axial compressive stress on the pillars is then given by the pillar force divided the cross sectional area of the pillar, namely

$$\sigma_p = \frac{8\Delta\rho g R L^2}{3\pi D^2} \qquad (9)$$

and the resultant displacement, ς_p, of a pillar of height, h, and elastic modulus, E, due to this stress is given by

$$\zeta_p = \frac{8\Delta\rho g R L^2 h}{3\pi D^2 E} \qquad (10)$$

The maximum displacement experienced by a pillar for a value of L of 20 μm, R of 25 μm, h of 15 μm, D of 5 μm on a PDMS pillar of 0.6 MPa E modulus is only ~ 25 pm. That is axial displacement or deformation of the pillars by cells on even the softest pillars is negligible. For line contact the stresses and deflections would be even lower.

4. Results

4.1. SEM and Optical images

Typical SEM image of successfully achieved keratinocyte adhesion and viability on the micro-pillar

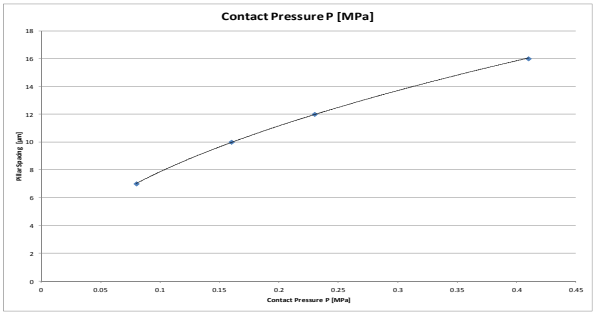

Fig. 4. **Contact pressure (from Eq (*5*)) between pillar and cell as a function of pillar spacing, L. Pillar diameter 5 μm and cell radius R of 15 μm**

interfaces, the interpillar distances are shown in Fig. 5. While keratinocytes, cultured on FN coated pillars with interpillar distances of 8 μm and 5 μm (the later shown in Fig. 5a), covered the pillar tops and were quite round-shaped, the cells clearly penetrated into the micropillar field on substrates with distances of 11 μm and greater (Fig. 5b).

The shape of the latter cells had a more linear or triangular shape depending on how many pillars they covered. To exclude drying artefacts from the sample preparation for the electron microscopy and to ensure successful adhesion of the keratinocytes, they were stained by IIF for the focal adhesion kinase (FAK), see Steinberg et al.[5] paper for typical images. The results obtained optically confirmed the morphological differences observed in the SEM.

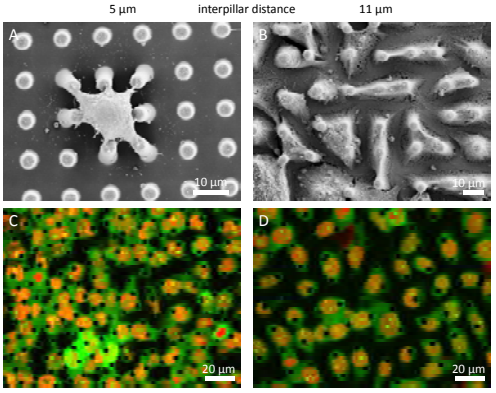

Fig. 5. **Morphology differences of keratinocyte on pillar fields with pillar spacing of 5 μm (A, C) and 11 μm ((B), (D)): SEM of (A) a keratinocyte spread on a FN-coated pillar field. The cell adheres to the pillar top while in (B) it sinks into the substrate. Fluorescent images of the cells stained for FAK (green) ((C), (D)) reveal the same morphological differences**

4.2. Confocal images

Typical examples are shown in Fig. 6a and 6b. On the substrate with pillar spacing of 5 μm the keratinocytes were round shaped, covered pillar tops (Fig. 6a) and penetrated slightly into the micro-pillar field. The FAK was stained green with a counter stain of the cell nuclei in red. 3D reconstructions enabled visualisation of the pillar protrusion into the cells.

A different morphology was observed for cells cultured on substrates with pillar spacing of 11 μm (Fig. 6b). The cells were more linear shaped and penetrated almost completely into the micropillar field. The 3D images confirmed the extent of penetration of the pillars into the cells. A more extensive study showed that keratinocyte differentiation varies with respect to different interpillar distances.

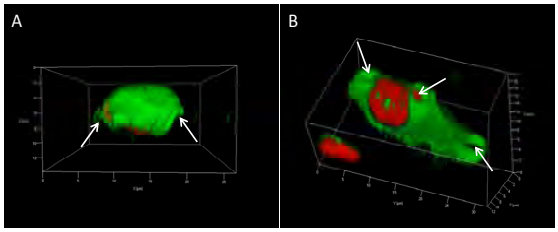

Fig. 6. **Confocal images of cells sitting on pillars spaced A) 5μm and B) 11 μm apart. Arrows point to where pillars were acting on the cells. The green fluoresence arises from focal adhesion kinease (FAK) while the red stain shows the cell nuclei**

4.3. Indentation depth

Confocal images (Fig. 6) indicate that the depth of penetration of the keratinocyte cells when the pillar spacing 5 μm apart is only 1 to 2 μm whereas for the 11 μm spacing the pillars protruded the entire height.

5. Discussion

The observations shown in Fig. 6 indicate that contact stresses generated by the pillars on the keratinocyte cell membrane under the gravitational force acting on the cells in the culture medium are sufficient to cause significant deformation of the membrane. These observations are similar to those by Mussig et al.[6,7] for osteoblast cells. Considering the observed indentation protrusion of the pillars into the cells as sown in Fig. 6 there is a clear influence of pillar spacing and as such contact pressure between the membrane and the pillars. From the analysis above the contact pressure for the two conditions shown in Fig. 6, namely eq (*5*), can be estimated. In the case of the edge spacings shown (5 and 11 μm) the values of L in eq (*5*) are X + D, namely 10 and 16 μm respectively. The calculated mean contact pressures between the pillars and these keratinocyte cells are 0.16 and 0.41 MPa respectively with the radius of the keratinocyte cell as 15 μm. The confocal observations suggest that the protrusion depth does not scale linearly with the contact pressure as a 2.5 fold increase in contact pressure changes the depth of protrusion of the pillars into the cells by greater than a factor of 5. These conclusions are in agreement with the response of Mussig et al.[6,7] and also Papenberg et al.[8] who considered different cell types. The latter study also considered pillars of different elastic rigidity and changed the wetability of the pillars and minimal change was observed in terms of the cell deformation by the pillars. The simple analysis above also indicates that for the range of pillar materials considered by Papenberg et al.[8] the extent of axial displacement of the pillars by the cells is negligible. There would be greater horizontal deflection of the softer material for the longer pillars as a consequence of the actin myosin motor development. Direct nano-indentation studies of various shaped indenters into cells by Evans et al.[9] and Hartegan et al.[10] indicate very extensive cell membrane deflection of many μms at nN forces. However a major difference between the present observations and those of direct nano-indentation testing of cells is the time scale of the experiments. In the nanoindentation tests typically a minute or two is the test duration whereas the current observations were made after 24 hours contact between the cells and pillars. This time difference for the two approaches raises two important issues namely the role of visco-elastic response of the cell membrane under stress and also the response of the cytoskeleton machinery within the cell. Here the former will not be discussed but rather more a focus placed upon the latter effects.

At the contact sites between cells and pillars the local stress initiates actin filament nucleation and growth. The stress state in the membrane about the pillars is complex but the areas of highest tensile stress are at the boundaries that become more uniform between the pillars. The rate of filament growth is relatively rapid and dependent upon the stress level. According to Fletcher and Mullins[11] the form of the network of actin filaments is highly dependent upon the stress. Considering first the top of the pillars, this would experience compression and result in assemblage into a type a mesh structure. Whereas at the edge of the pillars tensile stresses develop, resulting in a more randomised type of mesh formation. In both instances as well continuous filament formation nucleation sites develop on these for growth of cross hatching filaments. Such 3D meshes provide additional rigidity of the cell against local stress and penetration of the pillars. These mesh structures will continue to grow depending upon the extent of the actin precursor concentration in the cell.

In addition the observations in Fig. 6 show that focal adhesion kinease (FAK), which is an indicator of intermediate filament development, has also occurred and is concentrated at the base of the cells and appears to act to support the cell membrane. It would also be expected that the microtubular filaments within the cell, which are of more radial formation, would also respond to the stresses imposed on the cell by the pillars. In addition there are linkages between the three filamentous structures that could further enhance the effective rigidity of the cell. However

as all these filamentous components are essentially polymers they take time to grow and hence the associated effective rigidity of the cell membrane takes time. For the confocal observations shown above it appears that for the closely placed pillars there has been sufficient time for the cytoskeleton machinery to respond and reinforce the membrane rigidity thereby limiting the extent of pillar protrusion into the membrane. Whereas for the 11 μm spaced pillars there is a comparable development of the FAK and presumably other filamentous structure, but not before the pillars have extensively protruded into the cells.

REFERENCES

1. Bao G. & Suresh S.: Nature Mat. *2*, 715 (2003).
2. Flemming R. G., et al.: Biomater. *20*, 573 (1999).
3. Wojciak-Stothard B., et al.: Exp. Cell Res. *223*, 426 (1996).
4. Martinez E., et al. : Micron *39*, 111 (2008).
5. Steinberg T., et al.: Nano Lett. *7*, 287 (2007).
6. Mussig E., et al.: Eur. J. Cell Biol. *89*, 315 (2010).
7. Mussig E., et al.: Adv. Funct. Mat. *18*, 2919 (2008).
8. Papenberg B., et al.: Soft Mater. *6*, 4377 (2010).
9. Evans E.: Biophys. J. *68*, 2580 (1995).
10. Hategan A., et al.: Biophys. J. *85*, 2746 (2003).
11. Fletcher D. A., Mullins R. D.: Nature *463(7280)*, 485 (2010).

M. V. Swain[a,b], S. Schulz[a], T. Steinberg[a], and P. Tomakidi[a] *([a] Department of Prosthodontics, School of Dentistry, Albert-Ludwigs University, Freiburg, Germany, [b] Biomaterials, Faculties of Dentistry, The University of Sydney, Australia and Otago University, Dunedin, New Zealand):* **Cells on Surfaces: an Indentation Approach**

A simple contact mechanics approach is developed to investigate the initial response of biological cells resting on patterned pillar surfaces. The results are compared with recent cell morphology observations by a number of groups. It is evident that the changing internal cytoskeleton of the cell and its time dependence plays an important role in determining the developing cell morphology.

GEOMETRICAL AND MICROHARDNESS ASPECTS OF ALUMINIUM PM ALLOYS AS FUNCTION OF LOCAL PLASTIC DEFORMATION

RÓBERT BIDULSKÝ[a], JANA BIDULSKÁ[b], and MARCO ACTIS GRANDE[a]

[a] *Politecnico di Torino, Department of Applied Science and Technology, 15121, Alessandria, Italy,* [b] *TU of Kosice, Faculty of Metallurgy, Dpt. of Metals Forming, 042 00, Košice, Slovakia*
robert.bidulsky@polito.it, marco.actis@polito.it, jana.bidulska@tuke.sk

Keywords: aluminium alloys, compaction, compressibility, porosity, microhardness, FEM

1. Introduction

In terms of cost effectivity, the traditional uniaxial powder consolidation process is still widely employed for the production of powder metallurgy (PM) parts, especially for the automotive industry. PM is a well established technology for manufacturing parts to net or near net shape and in the present time, the growing demand for weight reductions in automotive applications has pushed the PM industry to develop components on the basis of light material[1–3].

2. Material and experimental conditions

Commercial ready-to-press aluminium based powders, ECKA Alumix 321 (Al-0.95Mg-0.49Si-0.21Cu-0.07Fe-1.5lub) and ECKA Alumix 431 (Al-5.8Zn-2.6Mg-1.7Cu-0.23Sn-1.5lub), were used as materials to be investigated. Particles size distribution was carried out by sieve analyzer according to ISO 4497. Test specimens 55×10×10 mm^3 were uniaxially pressed in a hardened floating steel die. The green compacts were weighed with an accuracy of ±0.001 g. The dimensions were measured with a micrometer calliper (±0.01 mm). Microhardness was recorded by Duramin-5 Tester on minimum 15 points. For the identification of the compressibility behaviour different compacting pressures were applied (50, 100, 200, 300, 400, 500, 600 and 700 MPa) and the following compressibility equation[4] was used:

$$P = P_0 \cdot \exp\left(-K \cdot p^n\right) \text{ , [\%]} \qquad (1)$$

Where: P – porosity achieved at an applied pressure p, [%]; p – applied pressure, [MPa]; K – parameter related to particle morphology, [–]; n – parameter related to activity of powders to densification by the plastic deformation, [–]; P_0 – apparent porosity calculated from the value of experimentally estimated apparent density, [%]:

$$P_0 = \left[1 - \frac{\rho_a}{\rho_{th}} \cdot 100\right] \text{ , [\%]} \qquad (2)$$

where: ρ_a – apparent density, [g cm^{-3}]; ρ_{th} – theoretical density, [g cm^{-3}].

3. Results and discussion

Tab. I shows data for the calculated compressibility parameters K, n and correlation coefficient r. According to data listed in Tab. I, the compressibility parameter n is related to activity of powders to densification by the plastic deformation. In case of powders with high plasticity, n is close to 0.5; in case of low plasticity, n is close to 1. System A (n = 0.5175) shows a higher ability to plastically deform than system B (n = 0.6181).

The effect of powder morphology is reflected in the values of compressibility parameter K, which is lower for powder B ($K = 0.479 \cdot 10^{-2}$) than for powder A ($K = 1.161 \cdot 10^{-2}$). The difference between powder A and B is connected with the effect of particle geometry. Particle geometry is linked to the morphological properties as well as particle size distribution (A: d_{50}=100 μm, B: d_{50}=63 μm). Morphological aspect of powder shape is controlled by manufacturing process. Tab. I shows that the fitting experimental data and calculated data are higher than 0.96 (last column). The compressibility equations for the studied systems are reported as follows:

Table I
Theoretical density values, apparent porosity, compressibility parameters and correlation parameters

No.	ρ_{th} [g.cm^{-3}]	P_0 [%]	K [–]	n [–]	r [–]
A	2.6229	58.44	$1.161 \cdot 10^{-2}$	0.5175	0.9675
B	2.7213	59.58	$0.479 \cdot 10^{-2}$	0.6181	0.9899

A: $P = 58.44 \cdot \exp\left(-0.1161 \cdot p^{0.5175}\right)$ *(3)*

B: $P = 59.58 \cdot \exp\left(-0.0479 \cdot p^{0.6181}\right)$ *(4)*

Table II
Microhardness values of studied PM aluminium alloys at various pressing pressures

No. / p [MPa]	50	100	200	400	500	600	700
A	17.8±4.2	21.4±4.3	25.4±5.9	29.4±4.2	32.2±2.6	34.6±3.5	35±3.6
B	19.3±3.0	24.8±2.9	31.9±5.1	33.3±2.3	36.3±2.5	40.6±5.7	39.2±4.7

Geometrical rearrangement plays an important role during the densification process (as well as plastic deformation). Moreover, also the compressibility parameter *K* has to be considered as an indicator of the physical-metallurgical characteristics including the geometrical and morphological characteristics of metal powder particles. Authors[4,5] underline that parameter K depends, mainly, on the microhardness values, Tab. II. Microhardness (strongly impacted by yield stresses) as well strengthening coefficient represents essential parameters of metal powder plasticity.

Tab. II shows that microhardness values increase with increasing pressing pressure. At higher pressing pressure, 600 MPa, previous investigations[1,3] show that the final stages of densification of powder particles are achieved. Therefore, the higher applied pressure at 700 MPa shows lower microhardness value due to the spring back effect as results of work hardening and exhaustion of plasticity in some local volume and relaxation.

During PM production, the employed compaction conditions dictate the stress and density distribution in the green compact prior to sintering, these parameters having a profound influence on the overall strength of the final component. The distribution of stress and strain during pressing can be predicted by means of finite element method (FEM). FEM analysis helps understanding the complexity of stress-strain processes[6,7]. Compressibility parameters *K* and *n* cover the plastic deformation processes performed during pressing as well as those defined by the physical significance. Moreover, they enable to quantify the intensity of the development of compaction facets. The dimensions of particle contact areas depend primarily on particle shape and the localization of plastic deformation depends on surface geometry and pressure level. This means that the compaction facets, as results of overall compressibility effect, depend on granulometry, compaction pressure, and particle surface roughness form discontinuous adhesive and mechanical particle contacts.

4. Conclusion

The results show that the development of compressibility values with pressing pressure enables to characterize the effect of particles geometry and matrix plasticity on the processes performed during pressing. The compressibility results exhibit a high value of plasticity, as a property related to compressibility parameters *K* and *n*.

R. Bidulský thanks the Politecnico di Torino, the Regione Piemonte, and the CRT Foundation for co-funding the fellowship. J. Bidulská thanks Slovak national project VEGA 1/0385/11.

REFERENCES

1. Bidulská J. et al.: Chem. Listy *105*, s471 (2011).
2. Lefebvre L.P., Thomas Y., White B.: J. Light Met. *2*, 239 (2002).
3. Kvačkaj T., Bidulský R. (ed.): *Aluminium Alloys, Theory and Applications*. InTech, Rijeka 2011.
4. Dudrová E. et al.: *Powder Metallurgy in ČSSR*, Part 1, p. 73. Brno, Žilina: DT ČSVTS, 1982 (Lecture).
5. Šlesár M. et al.: Pokroky Praskove Metal. VUPM *18*, 3 (1980).
6. Kvačkaj T. et al.: Kovove Mater. *45*, 249 (2007).
7. Kvačkaj M., Kvačkaj T., Kováčová A., Kočiško R., Bacsó J.: Acta Metall. Slovaca *16*, 84 (2010).

R. Bidulský[a], J. Bidulská[b] and M. Actis Grande[a]
([a] Politecnico di Torino, Department of Applied Science and Technology, Alessandria, Italy, [b]TU of Kosice, Faculty of Metallurgy, Dpt. of Metals Forming, Slovakia): **Geometrical and Microhardness Aspects of Aluminium PM Alloys as Function of Local Plastic Deformation**

The paper deals with the compressibility analysis of PM aluminium alloys Al-Mg-Si-Cu-Fe and Al-Zn-Mg-Cu-Sn. Compaction pressures ranged from 50 MPa up to 700 MPa. Considering the densification of metal powders in uniaxial compaction, quantification of aluminium compaction behaviour was performed using the linear regression analysis. The compressibility behaviour was evaluated in relation to geometry and mechanical properties of powder particles on pressing pressure as well as microhardness values. The development of compressibility values with pressing pressure enables to characterize the effect of particles geometry and matrix plasticity on the compaction process.

NUMERICAL MODELLING OF THE NANOCOMPOSITES IN STEEL/Ti-B-C SYSTEM

ANNA BIEDUNKIEWICZ, WITOLD BIEDUNKIEWICZ, PAWEŁ FIGIEL, and DARIUSZ GRZESIAK

West Pomeranian University of Technology Szczecin, Piastow Ave. 17; 70-310 Szczecin, Poland
Anna.Biedunkiewicz@zut.edu.pl

Keywords: nanocomposite, FEM, SLS/M, 316L steel, TiC, TiB_2, B_4C

1. Introduction

Metal matrix composites (MMCs) are the focus of intense research and development world wide for many industrial branches. B_4C ceramics have some excellent physical and chemical properties. Its ultrahigh hardness, high wear and impact resistance, low specific weight and good chemical stability makes it suitable for application in ball mills, blasting nozzles, wheel dressing tools, wire drawing dies, rocket propellant light weight armour plates and mechanical seal faces, etc[1,2]. TiB_2 and TiC have attracted great interest in their excellent mechanical properties, chemical resistance and good thermal and electrical conductivities. The composites containing the TiC and TiB_2 phases are characterized by good fracture and wear resistance and the increase in their hardness along with the increase in temperature[4,5].

Our work presents the comparison of the results of investigations on 316L steel and nanocomposites manufactured by SLS/M method. The differences in mechanical properties between steel, 316L steel/TiC and 316L steel/Ti-B-C composites based on the results of modelling by numerical method are presented.

2. Experimental details and results

The technology of the production of nanocomposite structures based on the Selective Laser Sintering/Melting technology has been worked out[6–8]. The stainless steel 316L was used as a matrix and as the filler nc-TiC and nc-Ti-B-C powders were used. Before the SLS/M the powders were prepared by ball-milling method. In the SLS/M process the following parameters were used: the laser power: 5000 mA; the exposure time: 200 μs, s layer thickness: 50 μm. Samples were subjected to hardness tests for quick estimation of the mechanical parameters. Hardness and modulus measurements were performed on MTS Nano Indenter XP using Brekovich tip (Tab. I).

Table I
Hardness (H) and elastic modulus (E) values of the samples

	H [GPa]	E [GPa]
Steel 316L	4,77	201
60% vol TiC	9,93	230
20% vol Ti-B-C	17,75	263

2.1. FEM model

For prediction of the result of introducing additional phases into the composite, two-variant FEM model of the structure has been prepared. The Representative Volume Element (RVE) with dimensions 1×0.5×0.5μm (X,Y,Z) has been taken instead of the bulk structure for making calculation time reasonable. The amount of all three filler phases was equal and together it came up to 15% of whole volume. The rest of the volume was the steel matrix. The fillers particles were mixed and randomly distributed in the whole RVE.

Material models of the filler particles were taken as perfectly elastic with the following parameters: TiC: E = 460 GPa, d = 4800 kg m^{-3}; TiB_2: E = 560 GPa, d = 4500 kg m^{-3}; B_4C: E = 660 GPa, d = 2520 kg m^{-3}. The matrix was modeled as elastic-plastic material with the following parameters: E = 193 GPa, d = 8000 kg m^{-3}, yield stress = 250 MPa.

To simulate the bulk structure, periodic boundary was applied to the whole RVE and to estimate the mechanical properties of composites, simulation of the tension was used in which uniaxial monotonic displacement in X direction was applied to the opposite sides of the RVE. Value of the displacement was increased up to the value of 2% of the RVE size and then decreased to the value of zero.

The structure was meshed with C3D4 elements (a 4-node linear tetrahedron). To avoid any mesh changes, there were no remeshing rules used. After all preparing operations were finished and before the calculation stage, the model was copied and in the newly created version only the material parameters of B_4C and TiB_2 phases were replaced with the values equal to the TiC. Such prepared models were identical in every case (including geometrical shape of the mesh), except of the material properties of the particles representing filler phase of the composite. Additionally the model made of pure steel was prepared with the same technique to compare it to both composites types. As comprised parameter the reaction force measured in reference point in which the tension was applied was taken. The resulting plots of force courses for all three models are presented in Fig. 1.

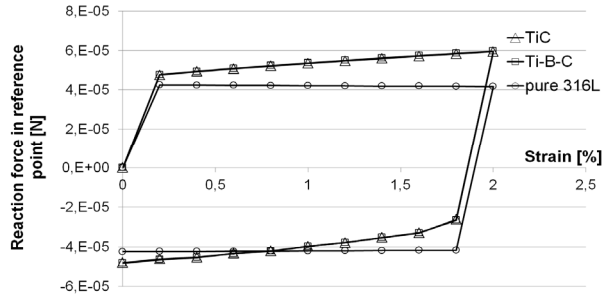

Fig. 1. **Values of the reaction forces during the load and unload of the samples**

In the Fig. 2 the result of the subtraction of the forces values obtained from the steel/TiC composites from the forces values obtained from the steel/(TiC+TiB_2+B_4C) composite are presented.

As can be seen, the differences between both composites are very small and the significant difference is observed in the case of pure steel. Because of using periodic boundary conditions, the resulted values representing mechanical properties of the pure steel model are equal in whole RVE, which proves ideal representation of bulk structure. In the case of composite, inclusions are generating variable values of the same parameter (plastic strain for example), which apparently can cause the composite stiffness increase and because of big amount of small particles in nanocomposites, it can be one of the reasons of superhardness effect.

The presented approach for the FEM modelling of the nanocomposite structures allows to predict mechanical properties of its different variants before the real material will be created, what can significantly increase the efficiency of the new materials designing[9,10].

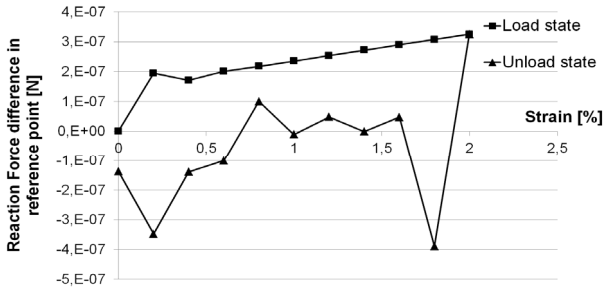

Fig. 2. **Values of differences of the reaction forces between TiC-steel and TiC+TiB_2+B_4C-steel composites**

3. Conclusion

Nanoindentation tests have shown that the hardness and elastic modulus increase in following order: 316L steel, TiC/steel and (Ti-B-C)/steel nanocomposites respectively.

The numerical analysis showed that the composites stiffness is noticeably higher in comparison to the steel. The mechanical properties (stiffness) of the composite with boron presence are better (higher stiffness) in comparison to the steel and composite with TiC. The presented differences in values of reaction force are small. This results from the small sizes of analysed structures.

Financial support of the work by the Ministry of Science and Higher Education within the project No. NR15-0067-10/2010-2013, is gratefully acknowledged.

REFERENCES

1. Alizadeh A., Nassaj E. T., Ehsani N.: J. Eur. Ceram. Soc. *24*, 3277 (2004).
2. Sinha A., Mahata T., Sharma B. P.: J. Nucl. Mater. *301*, 165 (2002).
3. Gursoy A., Ferhat K., Servet T.: J. Eur. Ceram. Soc. *23*, 1243 (2003).
4. Matkovich V. I., Samsonov G. V., Hagenmuller P., Lundstrom T.: *Boron and Refractory Borides*, Springer-Verlag, New York 1977.
5. Vallauri D., Atias Adrian I. C., Chrysanthou A.: J. Eur. Ceram. Soc. *28*, 1697 (2008).
6. Biedunkiewicz A., Biedunkiewicz W., Figiel P., Grzesiak D.: Chem. Listy *105*, s767 (2011).
7. Biedunkiewicz A., Wysiecki M., Noworol P.: Polish Patent: *Organotitanium precursor and method of producing and processing of organotitanium precursor* P200978 (2008).
8. Biedunkiewicz A., Figiel P., Gabriel U., Sabara M., Lenart S.: Cent. Eur. J. Phys. *9*, 417 (2011).
9. Zubko P., Pesek L., Bláhová O.: Chem. Listy *105*, s664 (2011).
10. Hausild P., Nohava J., Materna A.: Chem. Listy *105*, s676 (2011).

A. Biedunkiewicz, W. Biedunkiewicz, P. Figiel, and D. Grzesiak, *(West Pomeranian University of Technology, Szczecin, Poland):* **Numerical Modelling of the Nanocomposites in Steel/Ti-B-C System**

The Selective Laser Sintering/Melting process was used to prepare Ti-B-C/316L stainless steel nanocomposite materials. Hardness and elastic modulus measurements were performed on MTS Nano Indenter XP. The differences in mechanical properties between steel, 316L steel/TiC and 316L steel/Ti-B-C composites based on the results of modelling by numerical method have been presented.

ASSESSMENT OF THE CRITICAL PLACES IN THE CASTED PISTON BASED ON A LOCAL STRENGTH – MICROSTRUCTURE MODEL

PETER BIGOŠ[a], MICHAL PUŠKÁR[a], and LADISLAV PEŠEK[b]

[a] *Department of Machine Design, Transport and Logistics, Faculty of Mechanical Engineering,*
[b] *Department of Material Science, Faculty of Metallurgy, TU in Košice, Letná 9, 040 01 Košice, Slovak Republic*
michal.puskar@tuke.sk

Keywords: local strength, secondary dendrite arm spacing – SDAS, FEM

1. Introduction

A failure of construction elements depends on the position of a critical place and its local mechanical properties which are related to processing technology of the given machine part. In the case of a casted piston of two-stroke combustion engine, the local mechanical properties are affected predominately by the casting technology[1,2]. The decisive factors are especially: tension strength, critical deformation, modulus of elasticity, fatigue strength. These factors are influenced greatly by the casting method[3]. A cooling rate during casting is the most important factor with regard to material microstructure and its mechanical characteristics. An ultimate tensile strength (UTS) correlates well with the secondary dendrite arm spacing (SDAS)[4]. During the evaluation of reliability an assumption that the mechanical properties of material are homogenous is usually taken into consideration. However, the real differences in microstructure cause a variability of mechanical characteristics in individual localities of the same material.

Pistons of combustion engines are usually made of the near eutectic aluminium-silicon alloys. Since the microstructure of a cast differs in its various areas, there are also different values of mechanical properties and it is insufficient to take into consideration the mechanical characteristics of the global cast material.

One of the possibilities how to determine the ultimate tensile strength is based on the secondary dendrite arm spacing (SDAS). There are well-known relations between the tensile strength and microstructure of silumins[5]:

$$UTS = 270 - 1.4399\ SDAS \qquad (1)$$

where: UTS – ultimate tensile strength [MPa], SDAS – secondary dendrite arm spacing [μm].

The main purpose of this work is to determine the local values of the strength by means of metallographic analysis, as well as to define the critical areas of the piston using a finite element analysis.

2. Experiments

The gravity casted piston of the company Vertex made from near eutectic aluminium-silicon alloy was provided for this study. The piston was cut into two cross-section parts. The samples were prepared from its various areas in order to apply metallographic light microscopy which enables a statistical analysis of microstructure. The secondary dendrite arm spacing (SDAS) was measured in specific parts of the piston by identifying and measuring small groups of well-defined secondary dendrite arms on the screen of the image analyzer.

$$SDAS = d/n \qquad (2)$$

where: d – length of the line drawn from edge to edge of measured arms, n – number of dendrite arms.

The volume fractions of the constituents were quantified with the image analysis (Fig. 1) of the microstructure.

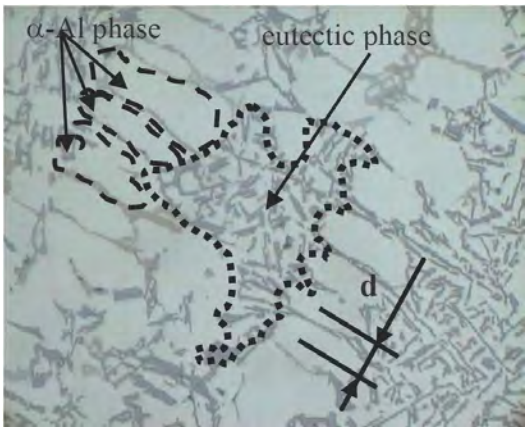

Fig. 1. **Microstructure of silumin**

The values of von Mises stress, σ_{vM}, were determined in the next step in the selected areas of the piston by means of the FEM using the Cosmos software. The material was considered to be elastic and the dimensions of analysed positions (Fig. 2) were from several hundreds μm to 1 mm in the size.

3. Results of measurement

The values of the secondary dendrites arm spacing in individual areas of the microstructure are presented on Fig. 3. The difference between the minimal value (24 μm) and the maximal value (47 μm) is 96 %. From a quantification of the constituent phases, Fig. 4, results that the volumetric share of eutectics increases from the position 1 (upper position) to the position 5 gradually (position of

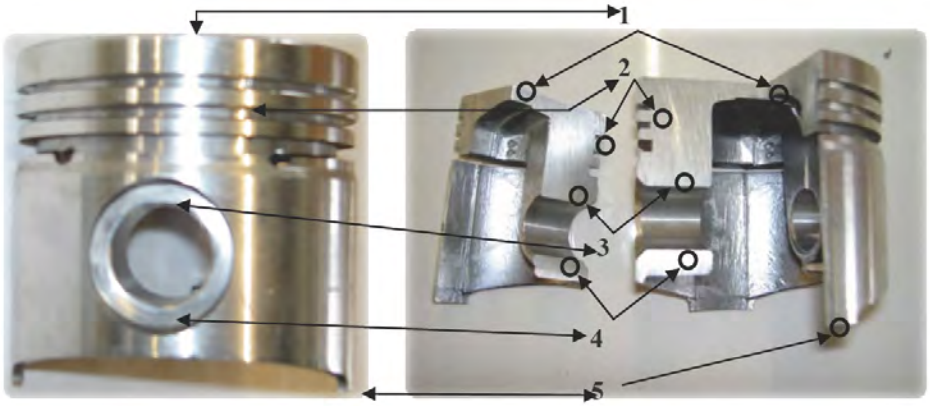

Fig. 2. **Analysed positions in the piston:** 1. upper surface (US), 2. piston rings (PR), 3. pin (P), 4. Seeger ring (SR), 5. sealing flap (SF)

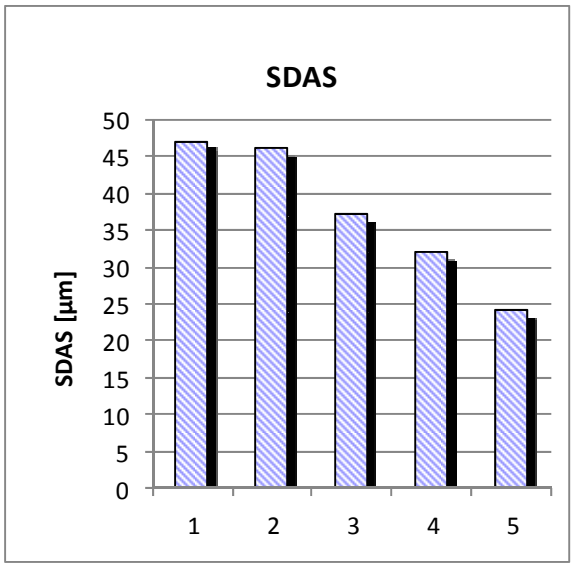

Fig. 3. **SDAS values for specific individual analysed positions**

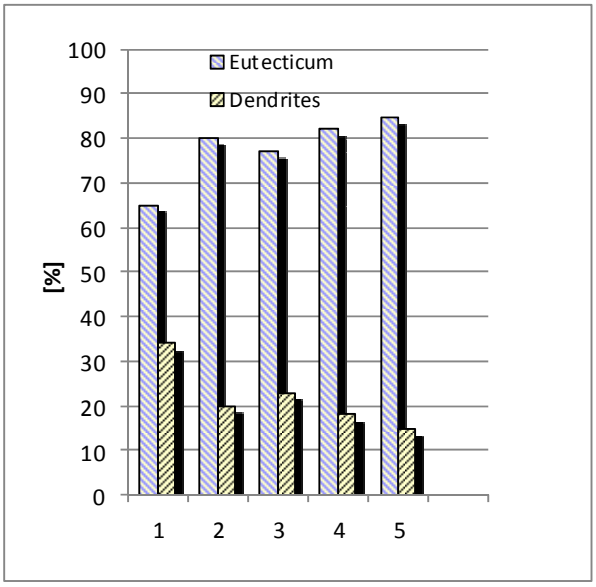

Fig. 4. **Quantification of constituent phases**

sealing flap). A supplement to the 100 % of the whole creates the dendrite α-phase. Analysing together the volume fraction of the eutectic phase with the SDAS results it is interesting to highlight the fact that a relation exists between them: the region with higher values of the SDAS has got a small amount of eutectic phase and reverse the region with the smaller values of the SDAS has got higher values of the eutectic phase.

4. Discussion

The critical positions are such places where the ratio between the local loading stress and the local strength is the highest.

Thus, estimative prediction of the cast aluminium component properties should be made based on local material mechanical properties, which enables to calculate the ratio of stress vs. ultimate tensile strength. Local mechanical properties may be obtained by local metallographic analysis.

The ultimate tensile strength UTS_{SDAS} was then calculated from experimentally determined values of SDAS according relation (1) in all specific positions 1–5. The results of microstructure evaluation (SDAS) and local strength value UTS_{SDAS} are presented in the Tab. I. It can be seen that there is a change in SDAS of about 100%, as occurs between positions 5 and 1, and that it is equivalent

Table I
Measured and calculated values of SDAS and load for different positions in the piston

Position	SDAS [μm]	UTS_{SDAS} [MPa]	σ_{FEM} [MPa]	σ_{FEM} / $UTS_{SDAS,max}$ global	σ_{FEM} / UTS_{SDAS} local	local-global [%]
1 upper surface	47.0	202	56	0.237	0.277	16.7
2 piston rings	45.6	204	78.4	0.332	0.384	15.6
3 pin	37.9	215	96	0.407	0.446	9.6
4 Seeger ring	31.5	225	44	0.186	0.196	5.1
5 sealing flap	23.6	236	21.2	0.080	0.090	0.1

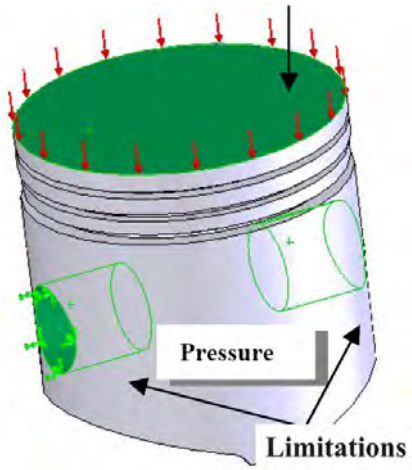

Fig. 5. **Pressures and limitations applied on piston surfaces**

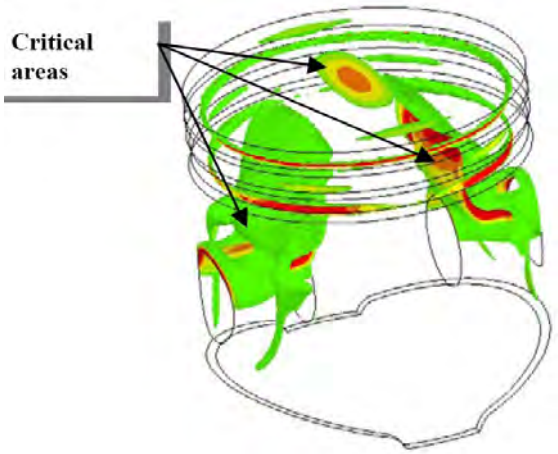

Fig. 6. **Stress distribution in critical positions**

to significant changes in UTS, e.g. the stress level changes from about 236 to 202 MPa (about 17 %).

The FEM stress analysis[6] of the loaded piston, Fig. 5, proved that there are predominately two important critical areas with high stress: the upper holes of the piston pin (3) and the piston head (1) with the piston rings (2), Fig. 6. The stress values σ_{FEM} for each of the piston position (Fig. 2) obtained by means of the FEM are in Tab. I.

A global design uses only one material value for the whole component, e.g the UTS=236 MPa for the microstructure with the highest strength. The corresponding relative load σ_{FEM} / $UTS_{SDAS,max}$ is in the 4rd column in the Tab. I. These values are different from those obtained by means of a local approach which are the values of the stress σ_{FEM} related to the real ultimate tensile stress values UTS_{SDAS} obtained by the metallographic way based on the SDAS in different positions of the component, σ_{FEM}/ UTS_{SDAS}, Tab. I, 5th column. The difference between local and global approach can reach up to 16.7 %.

These differences can be relevant mainly in the case of fatigue loading, in this case also changes of positions of the critical areas can be expected[7].

5. Conclusions

The values of local strength were determined in selected specific positions of piston casted from the silumin alloy based on relation between UTS and microstructure parameter SDAS. The difference between local and global approach reach up to 17 % for selected positions of the whole component. Ignoring the real local load can cause an early failure of component.

This study was supported by the grant tasks „VEGA 1/0356/11 Innovative Processes in Design of Driving Units for Transport Machines and Optimisation of Material Flows and Logistics in Order to Save Energy and to Increase Reliability for Application Purposes in Practice“ and „Research Centrum for Control of Technical, Environmental and Human Risks for Sustainable Development of Production and Products in Engineering“.

REFERENCES

1. Bigoš P., Puškár M.: Strojarstvo *50*, 2 (2008).
2. Kovařík L., Ferencey V., Skalský R., Částek L.: *Konstrukce vozidlových spalovacích motorů*. Naše vojsko,

Praha 1992.
3. Juliš M. et al.: Chem. Listy *105*, 812 (2011).
4. Lim C. S., Clegg A. J., Loh N. L.: J. Mater. Proces. Technol. *70*, 99 (1997).
5. Takahashi T., Sugimura Y., Sasaki K.: J. Manuf. Sci. Eng. *126*, 25 (2004).
6. Puškár M., Bigoš P.: Strojarstvo *52*, 5 (2010).
7. Stroppe H.: Materialwissenschaft und Werkstofftechnik *40*, 738 (2009).

P. Bigoš, M. Puškár, and L. Pešek *(Technical university of Košice, Košice, Slovak Republic)*: **Assessment of the Critical Places in the Casted Piston Based on a Local Strength – Microstructure Model**

The study analyses the critical positions in the combustion engine pistons produced by gravity casting of near eutectic aluminium-silicon alloys. The local strength in various positions was calculated from secondary dendrite arm spacing in the microstructure, the real local load was calculated via finite element analysis. The global strength approach uses one strength value for the whole component, while the local approach uses the local strength values depending on local microstructure. The difference between both local and global strength approach can reach up to 17 %.

CHANGE IN PROPERTIES OF HVOF COATINGS UNDER CONDITIONS OF THERMAL CYCLIC LOADING

JANETTE BREZINOVÁ, ANNA GUZANOVÁ, and MARIÁN EGRI

Technical University of Košice, Faculty of Mechanical Engineering, Mäsiarska 74, 040 01 Košice, Slovak Republic
janette.brezinova@tuke.sk

Keywords: HVOF coatings, high temperature cyclic loading, microhardness

1. Introduction

Thermally-sprayed coatings belong to the dynamically developing field of surface engineering[1,2]. These high -quality functional coatings are applied in the basic industry, as well as in renovations[3], mainly due to their excellent properties, which are characterized by high wear resistance[4–8], corrosion resistance and resistance against high temperatures[9,10]. Thanks to a wide range of different combinations of coating–substrate materials, thermal spraying offers as many possibilities as no other technology of coatings deposition. HVOF (High Velocity Oxygen Fuel) is one of the technologies, which form coatings with very low porosity (<1 %) compared with the basic material and with high adhesion strength (> 80 MPa). The substrate undergoes minimal thermal changes during spraying. The roughness of the resulting coating surface is low.

Thanks wide variety of suitable materials and their combinations, the area of utilization thermally sprayed coatings is very broad. It is possible to deposit coatings of various materials from pure metals to special alloys. Properties of cermet-based coatings are given by the type, morphology and size of hard particles and their volume fraction in tough matrix.

This paper presents results of assessesment of HVOF coatings. The coatings were subjected to cyclic thermal stress. Their tribological properties were evaluated under conditions of erosive wear. The quality of coatings was mearsured by pull-off testing, microhardness testing, and by EDX analysis. The experimental conditions were set to simulate the operating conditions of iron manufacturing in a basic oxygen furnace (BOF).

2. Materials and methods

The substrate for application of the coatings was C15E carbon steel (STN 41 2020, 12 020, 1.1141). Chemical composition of the steel is listed in Tab. I.

Table I
Chemical composition of the steel substrate (mass %)

C	Mn	Si	P	S
0.12–0.18	0.30–0.60	0.15–0.40	max 0.035	max 0.035

Mechanical properties of the steel substrate: tensile strength 740–880 MPa, yield strength ≥ 440 MPa. The test samples were made from Ø 50 mm round bar with a length of 15 mm.

Substrate pre-treatment: test samples were pre-treated by air grit blasting at air pressure of 0.5 MPa with brown corundum with a grain size of 1.00 mm.

Three types of coatings were deposited by HVOF technology on pretreated samples: WC-729-1/1343 VM (WC-17Co), WC-731-1/1350 VM (WC-Co-Cr) and CRC-300-1/1375 VM (Cr_3C_2-25NiCr). Materials were supplied in the form of powder, agglomerated and sintered, produced by Praxair, Inc., USA. Tab. II shows chemical compositions of the powders.

Table II
Chemical compositions of the powders sprayed

Coating	C	Co	Fe	W	Cr	Ni
C-17Co 1343	5.5	16.2	0.036	78.4	–	–
WC-Co-Cr 1350	5.5	9.9	0.02	80.58	3.9	–
Cr_3C_2-25NiCr 1375	10	–	–	–	68.5	21

The equipment JP-5000, Praxair TA employed in the experiment uses the HP/HVOF (High Pressure / High Velocity Oxygen Fuel) process with System Powder Feeder 1264. The surface of deposited coatings was not conditioned after spraying. Spraying parameters are listed in Tab. III.

The thickness of coatings was determined by a magnetic thickness gauge. Adhesion of coatings was evaluated by the pull-off test according to STN EN 582 using a tensile machine ZDM 10/91.

After the pull-off adhesion test, the tensile stress required to sever the weakest inter-phase bond (adhesive fracture) or to rupture the weakest structure component (cohesive fracture) was determined and fractographic assessment was performed.

Table III
Parameters of spraying

Particle velocity	Adhesion	Oxide content	Porosity	Deposition power	Typical coating thickness
[m/s]	[MPa]	[%]	[%]	[kg/h]	[mm]
600 - 1000	< 70	1 - 2	1 - 2	3 - 6	0.2 - 2

Microhardness was measured according to STN ISO 4516 on Shimadzu HMV-2E test equipment, with the load of 980.7 mN (100 g) and a dwell time of 15 s. Samples were subjected to cyclic thermal load in an electric chamber furnace according to the following schedule:

1. heating to 900 °C,
2. dwell in the furnace for 20 minutes,
3. cooling of samples in still air to ambient temperature.

Samples were subjected to 10 thermal cycles. After the 3rd, 5th, 8th and 10th thermal cycle, samples were collected to evaluate the adhesion of coatings. Structure and chemical composition of coatings were studied using the scanning electron microscope (SEM) JEOL JSM – 7000 F with INCA EDX analyzer for local chemical analysis.

To simulate the process conditions in BOF (impact and flow of oxides in BOF gas), the coatings were subjected to erosion wear at abrasive impact angles of 45° and 75°. To simulate the process of oxide impact, a laboratory mechanical blasting device KP-1 was used that allows the circulation of abrasive to be monitored. The abrasive used – brown corundum (Al_2O_3) had a grain size of 1 mm. The intensity of coatings´ wear was evaluated using gravimetry (mass loss of the coating). Peripheral speed of the blasting wheel was 5.0 m s^{-1} and the exit speed of abrasive was 70.98 m s^{-1}.

3. Results and discussion

Thicknesses of the as-sprayed coatings were as follows: 1343–234 μm, 1350–356 μm and 1375–393 μm. The highest microhardness values (Fig. 1) was found in the coating 1350 (1447 HV 0.1). It was due to a high content of tungsten and an addition of cobalt. In comparison, the coating 1343 contains tungsten at lower concentration and showed a lower value of microhardness (1010 HV 0.1). The lowest microhardness values were found in the coating 1375, which has a high content of chromium and is tungsten-free (975 HV 0.1).

Thermal cycles caused changes in microhardness of specimens. The most significant change occurred in the coating 1343. The hardness of the coating 1375 decreased, whereas that of the coating 1350 slightly increased. These values are related to structural changes in the coatings.

Fig. 2 shows fracture surfaces and the appearance of surfaces of the coatings upon thermal cycles.

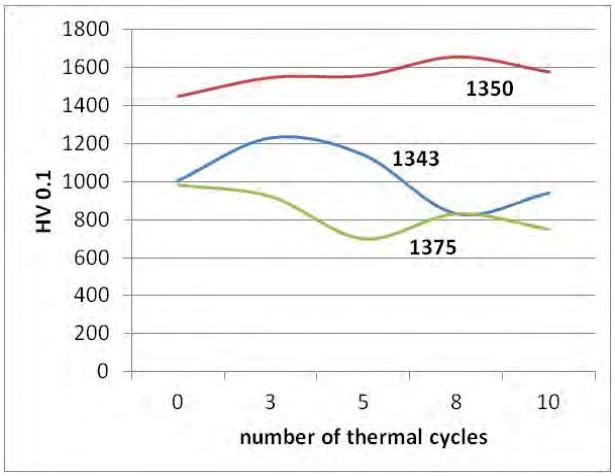

Fig. 1. **Trend in microhardness in coatings**

EDX spectral analysis of the coating 1343 revealed the presence of two basic phases – solid WC particles and cobalt, which is in line with the chemical composition of the powder. EDX spectral analysis of the coating 1350 showed the presence of WC particles, chrome and cobalt matrix, in which WC particles were embedded. EDX spectral analysis of the coating 1375 confirmed the presence of large particles of Cr_3C_2 and the prevailing component of the coating 1375: nickel-chromium matrix. The matrix and hard particles of WC and Cr_3C_2 are well visible on fractures of the coatings, Fig. 2.

Despite its high hardness, the coating 1350 suffered thermal cracking after 3 thermal cycles, as seen in Fig. 2 – showing the surface after thermal cycles. The surface of coating 1343 covered with a layer of blue oxides and showed strong chalking during the thermal cyclic loading. The coating 1375 retained its aesthetic and tactile qualities after thermal cycles. The appearance of surfaces of coatings during thermal cyclic loading and the character of their fractures are also shown in Fig. 2. Results of the evaluation of coatings adhesion are shown in Fig. 3.

The adhesion of coatings already decreased after three thermal cycles but then it remained almost constant during subsequent thermal loading.

The coating 1375 did not fracture in the pull-off test. Its adhesion may therefore be considered to be higher than the value listed.

Fig. 4 depicts the dependence of erosive wear on impact angles of abrasive. For all types of coatings, very similar dependences were observed. Higher weight losses were recorded at an impact angle of 75° in all types of coatings. Literature data suggest that hard materials, such as the coatings suffer heavier wear at larger impact angles. This was confirmed by the experiment.

The intensity of erosive wear is influenced by the ratio of the coating – abrasive hardnesses and by the structural characteristics of the coating. Wear intensities in all coatings were almost identical, being higher at the impact angle of 75°. More complex surface states were reached at

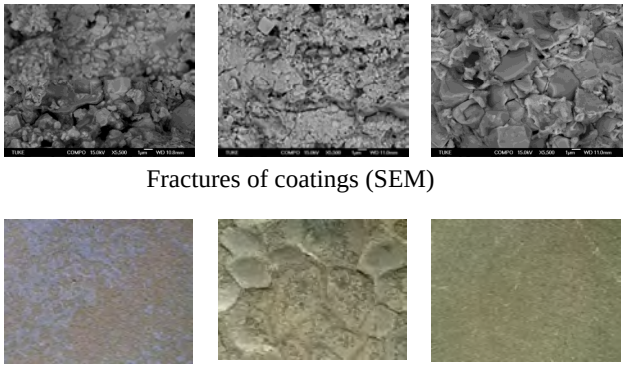

Fig. 2. F**ractures and appearance of surfaces of coatings after thermal cycles**

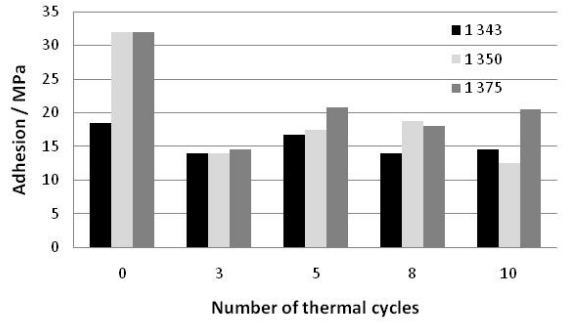

Fig. 3. **Adhesion of coatings after thermal cycles**

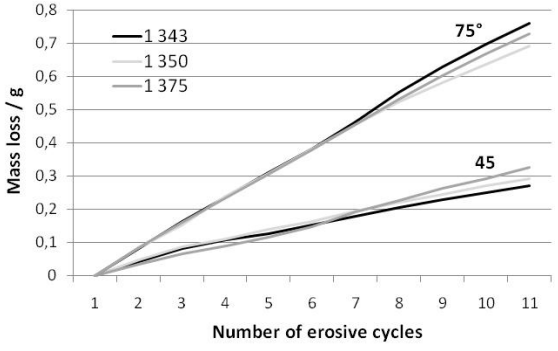

Fig. 4. **Erosive wear of coatings**

75° impact angle, material was removed and new surface configuration followed the direction and shape of the incident abrasive.

At larger impact angles, the forging effect of the abrasive prevails, whereas at smaller impact angles, the grooving effect dominates.

4. Conclusion

The coating 1350 (1447 HV 0.1) showed the highest hardness, whereas the coating 1375 (975 HV 0.1) showed the lowest hardness value. The coating 1350 cannot be used in the environment of BOF with high and fluctuating temperatures because of it cracks after a few thermal cycles. This would disrupt its protective function and allow high temperature corrosion of the substrate. At high temperatures, the coating 1343 showed strong chalking. This may cause significant losses in weight (and consequently in thickness) of the coating and reduce its durability. The coating 1375 showed lower hardness than others, retained its integrity and adhesion during thermal cyclic loading. No other qualitative changes occurred in this material. Its resistance to erosive wear was equal to that of the other coatings.

Based on the experimental results obtained the recommend for renovation of components operating under extremely high and cyclic temperatures and erosion wear condition would be the coating 1 375 (Cr_3C_2-25NiCr).

This paper is a result of the project: "Unique equipment for evaluation of tribocorrosion properties of the mechanical parts surfaces" (ITMS: 26220220048) supported by the Research & Development Operational Programme funded by the ERDF and Grant Scientific Project KEGA No. 059TUKE-4/2012.

REFERENCES

1. Sololenko O. P.: *Thermal Plasma Torches and Technologies*. Cambridge international science publishing, Cambridge 2000.
2. Suryanarayanan R.: *Plasma Spraying: Theory and Aplicattions*. CNRS, London 1993.
3. Tan J. C. L., Looney M. S. J., Hashmi: J. Mater. Proces. Technol. *92-93*, 203 (1999).
4. Kašparová M., Zahálka F., Houdková Š.: *Proceedings from conference METAL*, Hradec nad Moravicí, pp.1-4 (2009).
5. Kupková M., Jakubéczyová D., Hagarová M.: Metalurgija *49*, 203 (2010).
6. Bidulský R., Actis Grande M., Bidulská J., Vlado M., Kvačkaj T.: High Temperature Materials and Processes *28*, 175 (2009).
7. Guilemany J. M., Miguel J. M., Vizcaíno S., Lorenzana C., Delgado J., Sánchez J.: Surf. Coat. Technol. *157*, 207 (2002).
8. Ábel M.: Transfer inovácií *10*, 157 (2007).
9. Matthews S., James B., Hyland M.: Surf. Coat. Tech-

nol. *203*, 1086 (2009).
10. Li J. F. Li, Ding L. C. X.: Mater. Sci. Eng. A *394*, 229 (2005).

J. Brezinová, A. Guzanová, and M. Egri *(Technical University of Košice, Faculty of Mechanical Engineering, Department of Technology and Materials, Slovakia):*
Change in Properties of HVOF Coatings under Conditions of Thermal Cyclic Loading

This contribution presents interim results of evaluation of changes in local mechanical properties of HVOF coatings. The research was aimed at changes in microhardness of composite coatings deposited by the high velocity oxygen fuel process. The evaluated coatings were subjected to high-temperature cyclic loading. Microhardness of the coatings was measured on cross-sections of samples. Three types of coatings based on WC-Co, WC-Co-Cr and Cr_3C_2-25NiCr were examined. Their microstructure was studied using SEM-EDX techniques.

EFFECT OF WORKING TEMPERATURES ON PROPERTIES OF CONTINUOUS STEEL CASTING ROLLS CLADDING LAYERS

JANETTE BREZINOVÁ, JÁN VIŇÁŠ, and DENISA LORINCOVÁ

Technical University of Košice, Faculty of Mechanical Engineering, Mäsiarska 74, 040 01 Košice, Slovak Republic
janette.brezinova@tuke.sk

Keywords: cladding, renovation, continous casting rolls, layer structure, microhardness, thermal loading

Introduction

Continuous casting rolls provide of slab movement in the line and are therefore the key equipment of a line for continuous casting of steel. Their reliable operation is closely associated with their lifetime, which can be extended by renovation[1–4].

Wear affecting rolls in continuous casting of steel is illustrated in Fig. 1 and Fig. 2 depends on the location of the rolls in the continuous casting line, on the temperature of cast slabs, surface temperature of the rolls, method of cooling, cooling water quality and other factors.

The paper explores the impact of heating cycles on micro-hardness of cladding layers.

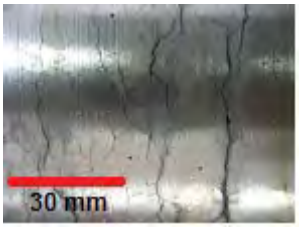

Fig. 1. **Surface of the roll: the crack caused by thermal fatigue**

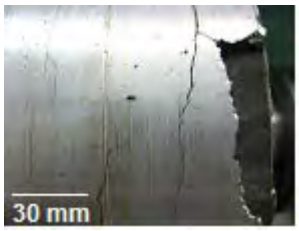

Fig. 2. **Exfoliation of cladding layers caused by combined loads**

Experimental

The continuous casting roll of 180 mm in diameter examined in this study was renovated by welding. The roll was part of the curvilinear section of the continuous casting line shown in Fig. 3. It was made from forged steel 41CrMo4 EN 10083-1-91 with chemical composition given in Table I.

Table I
Chemical composition of steel 41CrMo4 roll EN 10083-1-91 (in wt. %), balance of Fe

C	Mn	Si	Cr	Ni	Mo	P	S	Fe
0.41	0.63	0.26	1.12	0.27	0.18	0.017	0.015	bal.

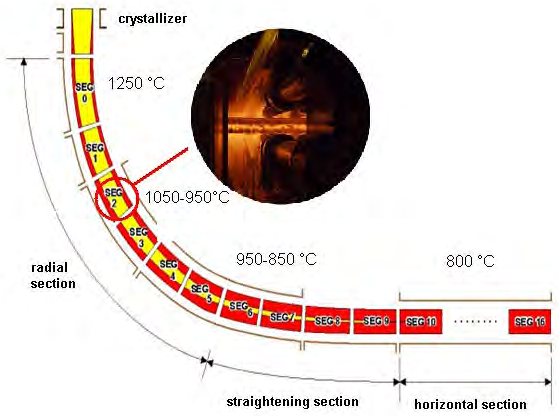

Fig. 3. **Continuous casting line**

The three-layer weld cladding was created on the surface of the roll by submerged arc welding technology (SAW) according to EN ISO 121 4063. The clad was created without an interlayer, using Weldclad GU125LZ – COREWIRE equipment. This device allows welding

Table II
Chemical composition of weld wires (in wt. %), Fe bal.

Element	Wire		
	A	B	C
C	0.1	0.25	0.3
Si	0.6	0.6	0.6
Mn	1.0	1.0	1.0
Ni	2.5	0.25	–
Cr	12.2	9.0	12.2
Mo	0.8	2.0	0.75
Nb	0.15	–	–
Cu	–	–	–
V	0,15	–	0,15

Table III
Chemical composition of the universal flux (in wt. %)

(SiO_2 + TiO_2)	(Al_2O_3 + MnO)	(CaO+MgO)	(CaF_2)
20	17	38	19

parameters to be changed in the course of rotation of the roll during the renovation.

Weld wires W3-WLDC3 (A), W5HT-WLDC 5Mod (B) and W8-WLDC8 (C) with a diameter 3.2 mm from COREWIRE, Ltd., UK were used for making the claddings. Chemical compositions of the wires (as declared by the manufacturer) are given in Table II.

Universal flux suitable for weld wires with iron content of up to 50 % was used. Its chemical composition is given in Table III.

Prior to cladding, the roll was preheated to 400 °C. After cladding, it was wrapped and cooled to room temperature. Then it was pre-heated in furnace at 500 °C and held for 8 hours, then slowly cooled in the furnace. Welding parameters are listed in Table IV.

The samples for metallographic analysis, thermal cycles and microhardnesss testing were taken from the renovated roll´s surface.

Microhardness was measured by Vickers method, described in the standard STN EN 1043-2, on SHIMADZU HMV-2 on polished transverse metallographic sections. The work load was 980.7 mN (HV 0.1). Test samples were exposed to thermal cycles at 900 °C for 120 s.

Table IV
Cladding parameters

Wire	Voltage [V]	Current [A]	Oscillation [mm]
A	28	450	45
B	26	600	47
C	26	450	50

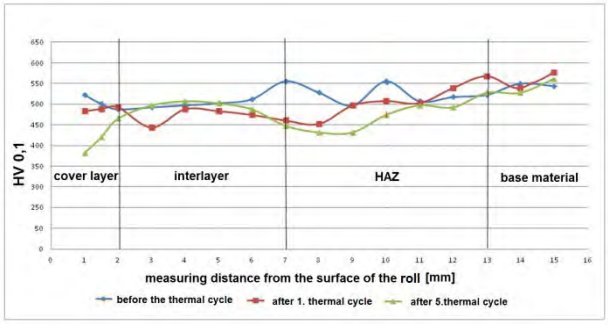

Fig. 4. **Microhardness before and during thermal load measured on cladding made by weld wire A**

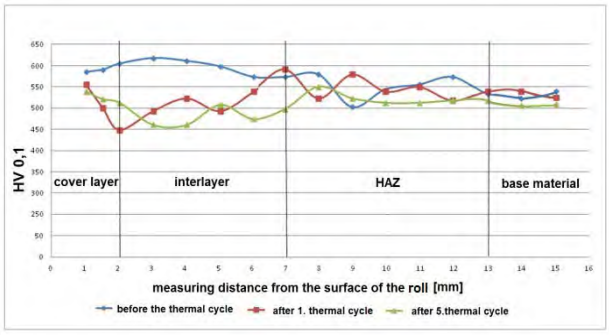

Fig. 5. **Microhardness before and during thermal load measured on cladding made by weld wire B**

Subsequently, the samples were cooled in water at 18 °C.

Fig. 4, 5 and 6 document cladding microhardness before the thermal load and upon the first and the fifth thermal cycle.

The highest values of microhardness during thermal cycles were measured in the cladding made of welding wire C – 600 HV 0.1. Microhardness value is consistent with the chemical composition of the welding wire, especially with the highest carbon content and also high chromium content among the evaluated additional materials.

Due to thermal cycles, microhardness values of all weld deposits decreased. The cladding made of weld wire A decreased about 150 HV 0.1, the cladding made of weld wire B to 60 HV 0.1 and cladding made of weld wire C there was found the decrease of microhardness of 130 HV 0.1 in comparison with measured values before thermal cycles. The decline of microhardness values continued depending on the number of thermal cycles in all tested weld deposits. As for the microhardness values measured in the interlayer of cladding A, thermal cycles had not a major impact, but the microhardness of B and C weld deposits decreased compared to microhardness values measured before the thermal stress.

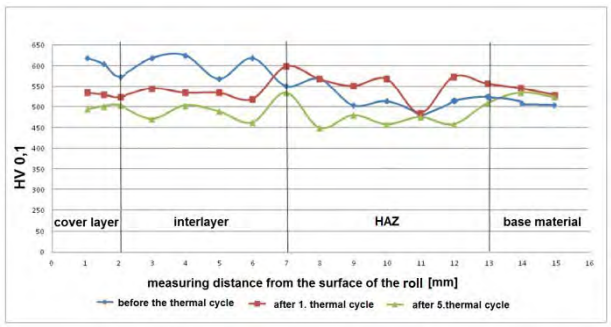

Fig. 6. **Microhardness before and during thermal load measured on cladding made by weld wire C**

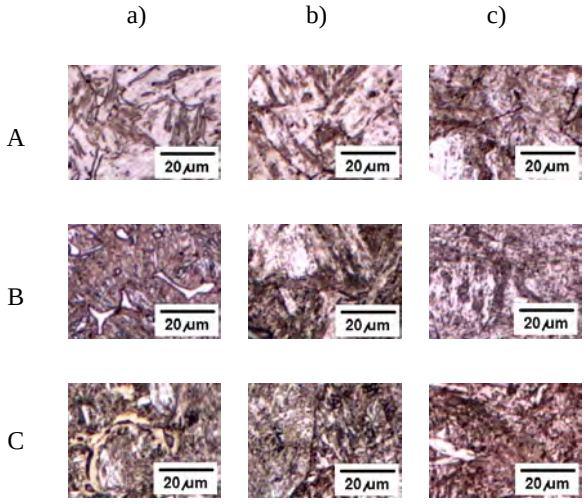

Fig. 7. **Structures of weld clad A, B, C before the thermal stress**

The microhardness values measured in HAZ are in the range of 500 to 600 HV 0.1, which correspond to the chemical composition and used cladding parameters. The higher hardness was found in HAZ of cladding B.

The microscopic analysis of each layer in renovated rolls was performed using light microscopy.

The structure of the base material of the roll is formed by coarse-grained martensite. Results of microscopic analysis are presented in Fig. 7.

Fig. 7b presents the structural analyse of interlayer weld clad A, B, C, which is fine-grained martensite. The structure of heat affected zone (HAZ) is documented in Fig. 7c and consists of low-carbon martensite.

Identified microstructure corresponds to the chemical composition of additional materials. Cover layer of weld A is formed by a low-carbon martensite-ferrite structure. Cover layer of weld B and C also has a ferrite-martensite structure, with less distinct grain boundaries. In the structure the presence of carbide precipitates has been reported. Based on the chemical composition of additional materials, especially Cr and Ni, content of the precipitates is of the type M_3C and M_7C_3 (ref.[4,5]). Molybdenum and other alloying elements, such as tungsten, vanadium and niobium precipitate in the M_7C_3, $M_{23}C_6$ and M_6C eutectic carbides and also carbides (e.g. Mo_2C, VC), which is consistent with the ref.[6–10]. The microstructure of the interlayer is formed martensite – ferrite structure as well. The HAZ has documented martensite of coarse texture.

3. Conclusion

Based on experiments realized by the evaluation of local mechanical properties of cladding metal parts and the HAZ can be concluded that the weld made by additional material B (W5HT-5Mod WLDC) resisted thermal cyclic stresses the best. The cover layer which is in practice subjected to the most intense tribodegradation effects decreased its microhardness of 60 HV 0.1, while the additional material A decreased of 150 HV 0.1 and C decreased of 130 HV 0.1. The measured values correspond to the martensite structure of precipitation hardened ferritic carbides of M_3C and M_7C_3 type.

The contribution was elaborated within the Research Project KEGA No. 059TUKE-4/2012 and within the Research Project ITMS 26220120060 – Management Research Centre for technical, environmental and human risks to continuous development and production of products in engineering.

REFERENCES

1. Čomaj M., Šefčík D.: *Proceedings from conference Welding 99*, Tatranská Lomnica, 68–71 (1999).
2. Kamenský M.: *Zváranie XIX*, *9-10*, 315–316 (1970).
3. Viňáš J., Kaščák Ľ: Bull. Mat. Sci. *31*, 125 (2008).
4. Viňáš J.: *Dissertation*. Technical University of Košice, Košice 2003.
5. Durand-Charre M.: *Microstructure of steels and Cast Irons*. Springer-Verlag, Berlin 2003.
6. Kovaříková I., Szewczyková B., Blaškovitš P., Hodúlová E., Lechovič E.: Mater. Sci. Technol. *9*, 1 (2009).
7. Knoško P., Kovaříková I., Hodúlová E.: Science work MtF STU *25*, 83 (2008).
8. Knoško P., Blaškovitš P., Kovaříková I.: *Proceedings from conference Zváranie 2007*,196-199 (2007).
9. Čabelka J.: 'Weldability of metals and alloys' VEDA, 1977.
10. Kotus M., Andrássyová Z., Čičo P., Fries J., Hrabě P.: Res. Agr. Eng. *57*, 74 (2011).

J. Brezinová, J. Viňáš, and D. Lorincová *(Technical University of Košice, Faculty of Mechanical Engineering, Department of Technology and Materials, Slovakia):* **Effect of Working Temperatures on Properties of Continuous Steel Casting Rolls Cladding Layers**

This contribution deals with properties evaluation of cladding layers realized by SAW - submerged arc welding 121 STN EN ISO 4063. Worn roll comes from curved sector of continual steel casting line and was made of material 41CrMo4 EN 10083-1-91 by forging. There were three cladding layers deposited on the roll surface. For the renovation of the roll following welding wires were used W3-WLDC3, W5HT-WLDC 5Mod a W8-WLDC8, diameter Ø 3.2 mm. Mixing of cladding layers and their microstructure using light microscopy were evaluated. On the created welds microhardness of the base material, heat-affected area and cover area of the weld in the initial state and after the exploitation in simulated work environment was assessed. Heat cycles corresponded to work conditions of continous casting rolls.

MECHANICAL PROPERTIES AND MICROSTRUCTURE OF MODEL LEAD-FREE JOINTS FOR ELECTRONICS MADE WITH USE OF NANOPOWDERS

JIŘÍ BURŠÍK[a], VILMA BURŠÍKOVÁ[b,c], ZBYNĚK PEŠINA[d], and JIŘÍ SOPOUŠEK[e]

[a] *Institute of Physics of Materials, Academy of Sciences of the Czech Republic, Žižkova 22, 616 62 Brno,* [b] *Masaryk University, Faculty of Science, Regional R&D center for low-cost plasma and nanotechnology surface modifications, Kotlářská 2, 611 37 Brno,* [c] *Masaryk University, CEITEC, Kotlářská 2, 611 37 Brno,* [d] *Brno University of Technology, Faculty of Mechanical Engineering, Technická 2, 616 69 Brno,* [e] *Masaryk University, Faculty of Science, Department of Chemistry, Kotlářská 2, 611 37 Brno, Czech Republic*
bursik@ipm.cz

Keywords: solder, silver nanopowder, nanoindentation

1. Introduction

Based on EU legislative, classical solders based on lead and tin are being replaced by their lead-free alternatives with the obvious aim to reduce health risks and environmental problems. The search for a replacement solder material has been underway for some time and a number of formulations are already in use[1]. However, solutions presently used have often reliability problems caused by worse mechanical properties, higher tendency to oxidation and higher melting temperature. After a decade of research it is now an accepted fact that there is no universal replacement for the traditional lead-tin solder.

Nanoparticles of pure metals and alloys exhibit the depression of melting point compared to bulk materials[2], hence they are able to aggregate and to form firm interlayer joints at low temperatures. Exploiting this effect in soldering industry can save energy, work and materials, and in particular it may subscribe to the solution of the above last mentioned problem[3].

In this work, Ag nanopowders were prepared as potential low-toxic constituents of novel solders by a chemical wet synthesis with the aim to study the effect of melting temperature depression and to evaluate the mechanical properties of sintered layers prepared in various annealing regimes.

2. Experimental

Chemical wet synthesis of Ag nanoparticles proceeded in two steps. At first the complex of $AgNO_3$ with dodecylamine was prepared in acetonnitrile and subsequently it was broken down at elevated temperature (170 °C):

$$AgNO_3 + 2NH_2C_{12}H_{25} \xrightarrow{CH_3CN} \xrightarrow{CH_3CN} \left[Ag\left(NH_2C_{12}H_{25}\right)_2\right]NO_3 \quad (1)$$

$$\left[Ag\left(NH_2C_{12}H_{25}\right)_2\right]NO_3 \xrightarrow{170\ °C,\ 15\text{min}} \xrightarrow{170\ °C,\ 15\text{min}} Ag^0(nano) + NO_x + 2NH_2C_{12}H_{25} \quad (2)$$

Resulting nanoparticles were separated as a solid product and stored in a toluene bath. They were characterized using a Philips CM12 STEM transmission electron microscope (TEM). Model joints, i.e. sandwiches consisting of thin copper plates with Ag nanopowder interlayer were prepared and annealed at various temperatures (see Table I). Samples 3, 4 and 5 were heated up inside the furnace from the room temperature at 15 K min^{-1} rate (marked as "ramp" in the Table; heating time is not included in the annealing time in the Table); the other samples were placed in the furnace already at the declared temperature (marked as "flash"). After annealing the samples were let in the furnace to cool down. Metallographic cross-sections were prepared from annealed samples and studied using a TESCAN LYRA 3 XMU FEG/SEM×FIB scanning electron microscope (SEM) and a JEOL JSM6460 SEM with an Oxford Instruments energy dispersive X-ray (EDX) analyser.

Table I
Thermal treatment of the samples

Sample	T [°C]	t [min]	Regime
1	250	25	flash
2	300	25	flash
3	200	30	ramp
4	250	30	ramp
5	300	30	ramp
6	350	25	flash

The main emphasis was placed on the characterization of sintered Ag layers by means of nanoindentation experiments. Microhardness and other mechanical properties of sintered Ag layers were measured by instrumented indentation technique using a Fischerscope H100 depth sensing indentation tester equipped with Berkovich indenter.

3. Results and discussion

Fig. 1 shows TEM micrographs of Ag nanoparticles on a holey carbon film. The majority of particles have diameter below 10 nm (Fig. 1a), with a narrow size distribution. Only sporadic clusters of larger particles were found (Fig. 1b). Overall quality of this in-house prepared nanopowder was better and the particle size smaller than the one of the commercial nanopowder (Fig. 1c) and the one of the nanopowder prepared in our laboratory a year ago using a slightly different method of wet chemical analysis (Fig. 1d), both reported in our similar previous studies[4,5].

Fig. 2 shows SEM micrographs of cross sections of interfacial regions of a selected subset of studied samples. All samples showed well sintered Ag layers with a small volume fraction of pores. Only the microstructure of Ag layer annealed at the lowest temperature of 200 °C reveals signs of the original powder-like constitution of the layer (Fig. 2c). Furthermore, the characteristic size of fuzzy objects in Fig. 2c is substantially larger than the average nanoparticle size, meaning that we captured an intermediate stage of sintering with individual nanoparticles fully sintered in compact clusters but the clusters incompletely sintered in the macroscopic bulk material.

An increasing thickness of interface layer was observed with increasing temperature of annealing. Series of EDX analyses across the interface detected high oxygen content, which corresponds to formation of Cu_2O interlayer. Comparing pairs of micrographs **a** *vs.* **d** and **b** vs. **e** in Fig. 2, it is seen that "flash" temperature setup produces (even in a slightly shorter time) more compact and homogeneous oxide layers with sharper interfaces and higher peak values of oxygen content.

The look of cross sections of sintered layers observed in the SEM does not reveal any substantial differences compared to previously studied materials after similar heat treatment[4,5]. However the local mechanical testing of the layers turned out to be more conclusive. Results of depth sensing indentation tests are summarized in Table II. Each value is the average of at least 40 measurements. Martens hardness HM, indentation hardness H_{IT}, elastic modulus $E_{IT}=E/(1-\nu^2)$, where E is Young's modulus and ν is Poisson's ratio, and creep CR values were obtained at testing load of 5 mN. The creep values after 5 s dwell time are expressed as the percentage of the maximum indentation depth.

The results show that the „flash" annealing regime (samples 1 and 2) leads to slightly better mechanical properties than the „ramp" annealing regime at the same temperatures (samples 4 and 5). An explanation of this difference may lie in the time dependence of the intensity of sintering proces. We suppose that during the slow heating

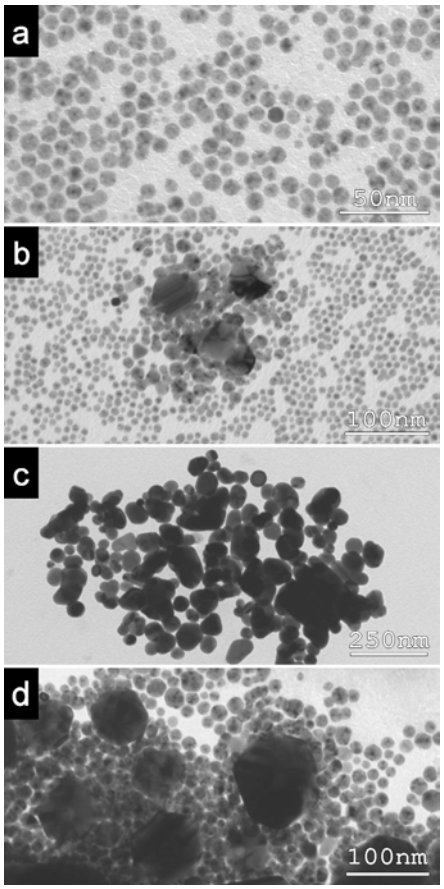

Fig. 1. **TEM micrographs of in-house prepared Ag nanoparticles (a,b), a commercial product (c) and an older variant of in-house prepared Ag nanoparticles (d)**

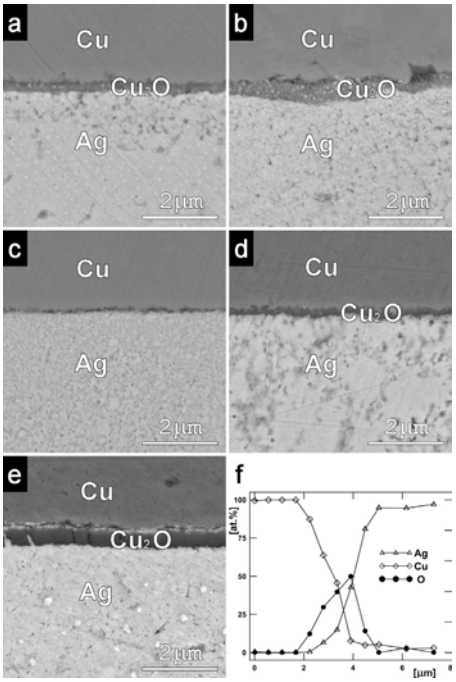

Fig. 2. **SEM micrographs (signal of backscattered electrons) of Cu/Ag interface in samples 1 (a), 2 (b), 3 (c), 4 (d) and 5 (e), together with the results of EDX analyses across the interface in sample 5 (f)**

Table II
Results of depth sensing indentation tests

Sample	HM [GPa]	H_{IT} [GPa]	E_{IT} [GPa]	CR [%]
1	0.90±0.10	1.15±0.07	20±2	3.3±0.9
2	1.08±0.25	1.82±0.15	37±3	1.3±0.4
3	0.72±0.12	1.10±0.25	17±4	4.2±1.5
4	0.87±0.14	1.20±0.18	18±4	3.5±1.2
5	1.00±0.46	1.43±0.44	32±4	3.0±1.1
6	0.85±0.06	1.07±0.09	35±2	3.0±1.0

up (the „ramp“ regime) individual nanoparticles at some temperature sinter to bigger clusters and in this stage they loose all the driving force for easy melting given by their small size. Further sintering of clusters is more dificult, resulting in pores (observed best in Fig. 2c) and worse mechanical properties.

The effect of annealing temperature is stronger than that of annealing regime. The values in Tab. II show a substantial improvement during the annealing temperature increase from 250 to 300 °C (samples 1 and 4 *vs.* samples 2 and 5). The results of indentation tests enabled us to settle the optimum thermal treatment. The mechanical parameters of samples 1, 2 and 6 treated in „flash“ regime showed less scatter than those of samples treated in „ramp“ regime. The highest hardness and elastic modulus [H_{IT}=(1.82±0.15) GPa and E_{IT}=(37±3) GPa] were achieved for sample treated at 300 °C in „flash“ regime.

The comparison of the values shown in Tab. II with the results obtained previously on sandwiches prepared using a commercial Ag nanopowder[4] [H_{IT}=(0.6±0.2) GPa and E_{IT}=(35±15) GPa] shows much better mechanical properties of recently presented Ag layers. The results of indentation tests of sintered Ag layers of an in-house Ag nanopowder prepared previously by different procedure[5] [H_{IT}=(1.25±0.5) GPa and E_{IT}=(35±7) GPa] showed a very large scatter of measured values because of the heterogeneous nanoAg grain size and sample porosity. The decrease in particle size to 10 nm and improvement in particle size uniformity led to well sintered nanoAg layers with low porosity. Consequently the scatter in mechanical parameters substantially decreased.

4. Summary

Mechanical properties of sintered layers of Ag nanopowder prepared in various annealing regimes were studied. Comparison between the in-house prepared Ag nanopowder and a commercial product shows smaller average particle size and more uniform particle size of the former. This leads to well sintered nanoAg layers with low porosity. Consequently the scatter in mechanical parameters substantially decreases. For Ag nanopowder the annealing temperature as low as 200 °C is sufficient to produce a continuous Ag layer and to form a firm junction between copper plates. A Cu_2O transition layer of increasing thickness is observed at the Cu-Ag interfaces annealed at 200 to 350 °C. Mechanical properties of the sintered Ag nanopowder layer reflect obviously the choice of annealing temperature. Moreover also other details play important role, namely the heating rate. The results of indentation tests enabled us to settle the optimum thermal treatment. The highest hardness and elastic modulus [H_{IT}=(1.82±0.15) GPa and E_{IT}=(37±3) GPa] were achieved for sample treated at 300 °C in fast heating regime.

The financial support was provided by the Czech Science Foundation (Project 106/09/0700).

REFERENCES

1. Dinsdale A., Watson A., Kroupa A., Vrestal J., Zemanova A., Vizdal J.: COST *Action 531 - Atlas of Phase Diagrams for Lead-Free Soldering*. COST office, Brno 2008.
2. Pawlow P.: Z. Phys. Chem. *65*, 545 (1909).
3. Youn J. I., Ha W., Kim Y.: J. Adv. Mater. Res. *15-17*, 995 (2007).
4. Sopoušek J., Buršík J., Zálešák J., Buršíková V., Brož P.: Science of Sintering *43*, 33 (2011).
5. Buršík J., Sopoušek J., Buršíková V., Stýskalík A., Škoda D.: Chem. Listy *105*, s777 (2011).

J. Buršík[a], V. Buršíková[b,c], Z. Pešina[d], and J. Sopoušek[e] *([a] Institute of Physics of Materials, ASCR, Brno, [b] Masaryk University, Faculty of Science, Regional R&D center for low-cost plasma and nanotechnology surface modifications, Brno, [c] Masaryk University, CEITEC, Brno, [d] Brno University of Technology, Faculty of Mechanical Engineering, Brno, [e] Masaryk University, Faculty of Science, Department of Chemistry, Brno, Czech Republic):* **Mechanical Properties and Microstructure of Model Lead-Free Joints for Electronics Made with Use of Nanopowders**

Ag nanopowders were prepared as potential low-toxic constituents of novel solders by a chemical wet synthesis. Resulting nanoparticles were characterized using a transmission electron microscope. Model joints, i.e. sandwiches consisting of thin copper plates with Ag nanopowder interlayer were prepared and annealed at various temperatures. Metallographic cross-sections were studied using a scanning electron microscope. The main emphasis was placed on the characterization of sintered Ag layers on cross-sections by means of nanoindentation experiments. Microhardness and other mechanical properties of sintered Ag layers were measured by instrumented indentation with Berkovich indenter. Both the mechanical properties and the observed microstructure were compared with our previous results obtained on similar materials.

MICROSTRUCTURE AND PROPERTIES OF nc-WC/a-C COATING DEPOSITED ON HIGH SPEED STEEL BY MAGNETRON SPUTTERING

GRZEGORZ CEMPURA[a], TOMASZ MOSKALEWICZ[a], BOGDAN WENDLER[b], FRANTIŠEK LOFAJ[c], and ALEKSANDRA CZYRSKA-FILEMONOWICZ[a]

[a] AGH University of Science and Technology, Al. Mickiewicza 30, 30-059 Krakow, Poland, [b] Technical University of Łódź, ul. Stefanowskiego 1/15, 90-924 Łódź, Poland, [c] Institute of Materials Research of SAS, Watsonova 47, 040 01 Košice, Slovakia
cempura@agh.edu.pl

Keywords: microstructure, nc-WC/a-C coating, magnetron sputtering, nanocomposites, mechanical properties

1. Introduction

Coefficient of friction (COF) of engineering materials may be decreased by application of low-friction nanocomposite nc-WC/a-C coating[1,2].

The aim of the present investigation was a microstructure characterization as well as determination of selected micro-mechanical and tribological properties (COF, hardness, Young's modulus, coating's adhesion to the substrate) of the nc-WC/a-C coating deposited on high speed steel by magnetron sputtering.

2. Experimental details

Prior to the coating deposition, the HS6-5-2 high speed steel (chemical composition is given in Table I) was heat treated as follows: heating to 1150 °C with two 5 minutes' steps (at 550 °C and 850 °C), annealed at 1150 °C for 15 minutes and quenched in oil. In the last step steel was hold at 550 °C for one hour and cooled down with the furnace. The nc-WC/a-C coating was deposited by magnetron sputtering. The details of coating deposition are given in ref.[3]. An intermediate layer was deposited in order to improve the adhesion of the nanocomposite coating to steel substrate.

Microstructural investigation was carried out by light microscopy (LM), scanning- and analytical transmission electron microscopy (SEM, TEM). The SEM investigation was performed by Zeiss NEON 1540EsB microscope equipped in Quantax 200 X-ray Energy Dispersive Spectrometer of Brucker. The TEM investigation was performed by JEOL JEM-2010 ARP and FEI Tecnai G2 microscopes. Specimens for TEM were prepared as cross-section lamellas by Focused Ion Beam (FIB) technique using Zeiss NEON 1540EsB. Phase identification of the coated steel was performed by Selected Area Electron Diffraction (SAED) technique and by X-Ray diffraction (XRD). XRD investigation was carried out using Siemens D500 diffractometer (λ=1.54 Å) on plan view specimens. The analysis of SAED patterns was supported by JEMS software[4]. Surface topography was studied with Atomic Force Microscope (AFM) Dimension 3000 of Digital Instruments (using Veeco SNL-10 indenters).

Adhesion of the coating to the substrate was measured by micro-scratch technique using Rockwell stylus. Scratch-tests were performed under increasing load (0.03–30 N) and scratch length of 3 mm. The COF of the substrate-coating system were measured on with a ball-on-disc apparatus using Al_2O_3 ball with diameter of 1 mm. Indentation hardness and reduced elastic modulus were determined with the CSM Micro Combi Tester (Vickers diamond indenter and load in the range of 10 mN–50 mN). Indentation data were analyzed by Oliver & Pharr method[5], (9 indentation tests were performed).

3. Results and Discussion

Microstructure

Investigation of the coating's microstructure by SAED and XRD revealed a presence of the W_3C phase (cubic primitive, cp) within the coating. Ferrite and Fe_3W_3C (face centered cubic, fcc) were found in the steel substrate using Bragg-Brentano (B-B) and Grazing Incidence X-ray Diffraction (GIXRD), incidence angle α_p=5°. The thickness of the coating was measured on SEM micrographs (Fig. 1) as 1.8 μm.

The SEM-EDS investigation showed enrichment of tungsten in an intermediate layer. The TEM micrograph of the coating is presented in Fig. 2.

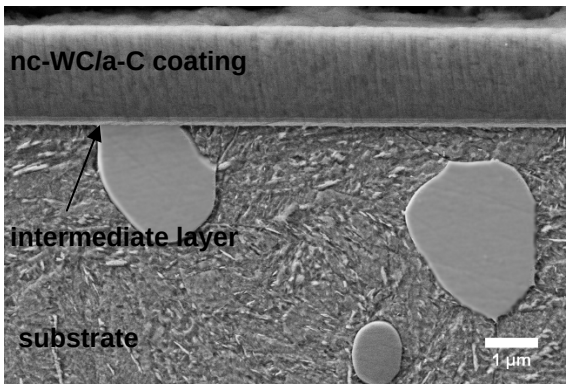

Fig. 1. **Microstructure of nc-WC/a-C coating on HS6-5-2 steel, SEM - cross section**

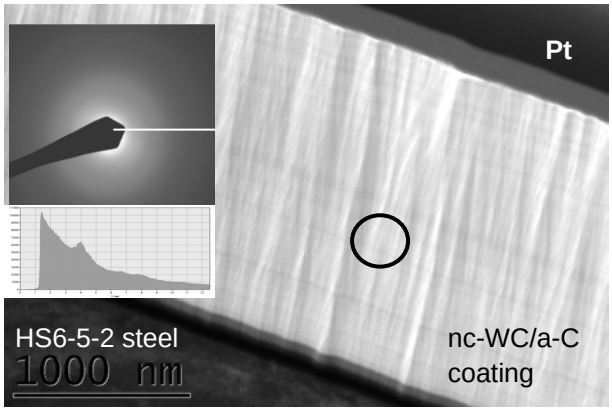

Fig. 2. **Microstructure of nc-WC/a-C coating on HS6-5-2 steel and SAED pattern from marked area within the coating as well as intensity profile from marked line of SAED pattern**

The SAED patterns from the coating area exhibited high blur of diffraction rings due to amorphous structure, however based on an intensity profile analysis it was possible to identify W_3C phase (a peak 111 ring is clearly visible).

The nc-WC/a-C coating had a columnar structure which was observed on FIB prepared lamellas as well as on cross section thin foils prepared by Precision Ion Polishing System (PIPS). HRTEM investigation of similar coating deposited on titanium alloy revealed that microstructure consisted of different nanocrystaline tungsten carbides (size of 2–5 nm) embedded in an amorphous matrix[6].

The thickness of the intermediate layer present between the coating and substrate was measured on TEM foils as 50 nm.

The surface topography analysis was carried by AFM in areas of 50 μm × 50 μm. The results indicated high surface development: surface area factor, SAF=1.0577, root mean square R_q=14.7 nm and center line average height R_a=10.5 nm.

Mechanical properties

Coating hardness measured at 10 mN and 50 mN loading was similar and equal to about 12.5 GPa, reduced Young modulus was about 199 GPa.

The investigated coating had a relatively good adhesion to the substrate. First cohesive cracks appeared at relatively low load of 4 N during scratch test. However the adhesive cracks were formed at load of 24 N. It was found that the nanocomposite nc-WC/aC coating significantly decreased COF from 0.7 for an uncoated steel to 0.1 for the coated one.

4. Summary

The nc-WC/a-C coating was deposited on HS-6-5-2 high speed steel by magnetron sputtering. Thickness of the coating was measured as 1.8 μm. The coating consisted of nanocrystalline W_3C carbides embedded in an amorphous C matrix. The coating had a good adhesion to the steel substrate. The coating decreases COF and improves wear resistance properties of the steel.

The authors acknowledge financial support from the National Centre for Research and Development (NCBiR) under MNT ERA-NET HANCOC project (no 402/ERA-NET/2009).

REFERENCES

1. Carvalho N. J. M, DeHosson J. Th. M.: Thin Solid Films *150-159*, 388 (2001).
2. Liu Y., Erdemir A., Meleti E. I.: Surf. Coat. Technol. *48-56*, 82 (1996).
3. Wendler B. G., Pawlak W.: J. Ach. Mater. Manuf. Eng. *26*, 207 (2008).
4. Stadelmann P.: JEMS: Java Electron Microscopy Software, Available from: http://cime.epfl.ch/.
5. Oliver W. C., Pharr G. M.: J. Mater. Res. *7*, 1564 (1992).
6. Moskalewicz T., Wendler B., Czyrska-Filemonowicz A.: Mater. Char. *61*, 959 (2010).

G. Cempura[a], T. Moskalewicz[a], B. Wendler[b], F. Lofaj[c], and A. Czyrska-Filemonowicz[a] *([a] AGH University of Science and Technology, Krakow, Poland, [b] Technical University of Łódź, Poland, [c] Institute of Materials Research of SAS, Košice, Slovakia):* **Microstructure and Properties of nc-WC/a-C Coating Deposited on High Speed Steel by Magnetron Sputtering**

One possibility to improve friction properties of steel is deposition of nanocomposite coating. In this work the nanocomposite nc-WC/a-C coating was deposited on high speed H6-5-2 steel by magnetron sputtering. Microstructure investigation of the coating and the substrate were performed by means of scanning- and transmission electron microscopy (SEM, TEM) as well as X-ray diffractometry (XRD). It was found that the coating, 1.8 μm thick, was consisted of the W_3C phase (cubic primitive) embedded in an amorphous matrix. Selected properties (coating adhesion to the underlying substrate, reduced Young modulus, microhardness, coefficient of friction and wear resistance) were determined. The hardness of the coating was much higher than steel hardness. The nc-WC/a-C coated steel exhibited and lower coefficient of friction then the uncoated steel.

EFFECT OF DEPOSITION CONDITIONS ON MECHANICAL PROPERTIES OF MAGNETRON SPUTTERED SiC THIN FILMS

RADIM ČTVRTLÍK[a], VALERIY KULIKOVSKY[b], PETR BOHÁČ[b], and OLGA BLÁHOVÁ[c]

[a] Palacky University, Faculty of Science, Regional Centre of Advanced Technologies and Materials, Joint Laboratory of Optics of Palacky University and Institute of Physics of Academy of Sciences of the Czech Republic, 17. listopadu 50A, 779 00 Olomouc, [b] Institute of Physics, Academy of Sciences of the Czech Republic, v.v.i., Na Slovance 2, 182 21 Praha, [c] New Technologies-Research Centre, University of West Bohemia, Univerzitní 8, 306 14 Plzeň, Czech Republic
ctvrtlik@fzu.cz

Keywords: silicon carbide, thin films, nanoindentation, mechanical properties, coefficient of friction

1. Introduction

Silicon carbide (SiC) is a promising material for a variety of mechanical and high temperature applications as well as for use in microelectromechanical systems (MEMS) due to its excellent physical, chemical and mechanical properties.

SiC films and coatings are one of the most commonly used forms of SiC as a functional material, especially due to low costs and relatively simple preparation.

Amorphous hydrogen-free silicon carbide coatings (a-SiC) exhibit a variety of attractive properties, such as high hardness and wear resistance, low intrinsic stress, good thermal stability and adhesion to steel substrates. Furthermore, their high hardness can be reached by performing deposition at room temperature that is technologically beneficial. On the other hand, they possess high coefficient of friction, especially in comparison with carbon-based coatings[1–3].

Various practical applications of thin films and coatings require specific combinations of their mechanical properties like hardness, toughness, wear resistance, coefficient of friction and others that can often be hardly compatible. In this respect the interrelationship between deposition conditions, composition, structure and mechanical properties is a key issue.

The aim of this paper is to outline how the deposition conditions of DC magnetron sputtering affect mechanical properties (hardness, modulus of elasticity and coefficient of friction) of amorphous and nanocrystalline SiC thin films and how to prepare SiC films with specific combinations of mechanical and tribological properties. The first part deals with the effect of substrate bias and temperature whilst the second part with carbon concentration. The hardness of the films is also compared with the corresponding single crystal.

2. Experimental details

Amorphous and nanocrystalline SiC films were deposited by DC magnetron sputtering using the Leybold-Heraeus Z 550M sputtering plant. The target-substrate distance was 50 mm and the discharge power was typically 300 W. All the films were prepared on the Si(111) substrates except the films for tribological tests that were deposited on steel substrates.

In the first case DC sputtering of hot pressed conductive $SiC_{1.1}$ target in argon at pressure of 0.5 Pa was used. Hydrogen-free a-SiC films were deposited on grounded or biased substrates. A bias voltage ranging from 0 to –160 V was applied at deposition to unheated substrates using 13.56 MHz power source. Some films were deposited on substrates preheated to temperatures of 200, 400, 600 and 750 °C.

In the second case amorphous hydrogenated silicon carbide films (a-SiC:H) were sputtered from $SiC_{1.1}$ target in the gas mixture of argon and CH_4. Flow rate of CH_4 was changed from 0 to 12 sccm in order to prepare films with various carbon concentrations, corresponding CH_4/Ar ratio varied in the range of 0–48 %. Bias voltage of –55 V was applied on the unheated substrates.

The film structure was studied by micro-Raman spectroscopy. Composition was investigated using electron probe X-ray microanalysis (EPMA). Internal stress was estimated according to the Stoney's classical formula[4].

Nanoindentation was performed using the Nano-Test™ NTX system in a load controlled mode with a calibrated Berkovich tip. Indentation Hardness and reduced modulus were determined from nanoindentation curves using the analysis by Oliver and Pharr[5]. The peak load of 20 mN was chosen in order to ensure fully plasticity and minimize the influence of surface roughness and other effects related to the shallow indents, whilst ensuring that the maximum depth did not exceed ~13 % of the film thickness. So the presented hardness and elastic modulus values can be considered as film-dominated. The average values of hardness and reduced elastic modulus were calculated from 5 independent measurements. The reduced indentation modulus E_r that takes into account also the elastic deformation of the indenter is defined as

$$\frac{1}{E_r} = \frac{1-\nu^2}{E} + \frac{1-\nu_i^2}{E_i} \qquad (1)$$

where E and ν, and E_i = 1141 GPa and ν_i = 0.07, describe

the elastic modulus and Poisson's ratio of the sample and the indenter, respectively.

Pin-on-disc tribometer with alumina ball with diameter of 6 mm was used for investigation of coefficient of friction. Samples were tested at normal load of 5 N and sliding velocity of 1 cm s^{-1} for a sliding radius of 5 mm. Each test consisted of 2000 cycles.

3. Results and discussion

3.1. Hydrogen-free amorphous SiC films

Thickness of the hydrogen-free SiC films deposited in pure argon varied in dependence on deposition conditions in the range of 3.2–4.4 μm. The carbon concentration changed only slightly with the changing substrate bias or temperature and was approx. 52 at.% for all of the films. That means that the change of mechanical properties is linked with the change of the film structure.

Raman spectroscopy pointed out that all of the investigated films are amorphous except the film deposited at 750 °C, where traces of crystalline phase were revealed.

Indentation hardness and reduced modulus of a-SiC films deposited on unheated substrates as a function of negative substrate bias are shown in Fig. 1. As can be seen hardness and reduced modulus decrease with increasing bias voltage. Compressive stress of these films initially increases to 1.4 GPa along with increasing bias voltage up to –100 V and then decreases.

These effects are connected with the creation of numerous point defects and reduction of the short-range order and strength of interatomic bonding due to the ion bombardment. The influence of increasing Ar concentration in the films is also probably involved[6].

Increase of substrate temperature during deposition results in gradual increase of indentation hardness as well as reduced modulus as can bee seen from Fig. 2. This positive correlation between hardness and modulus is well known for hard coatings and has been frequently reported in the literature[7,8]. Increase of deposition temperature

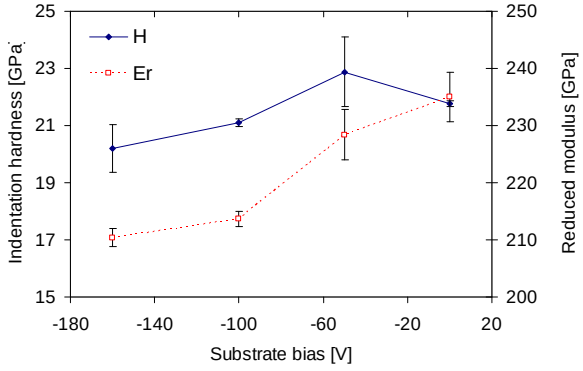

Fig. 1. **Indentation hardness and reduced modulus of SiC films as a function of substrate bias**

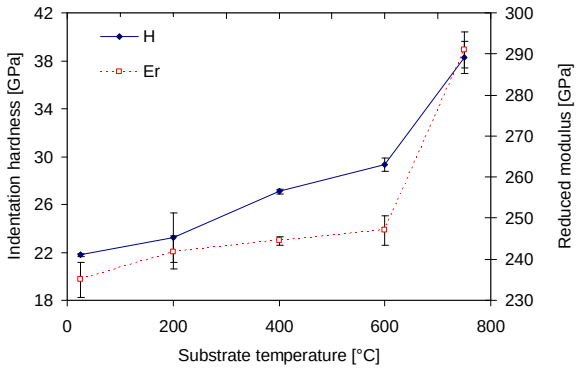

Fig. 2. **Indentation hardness and reduced modulus of SiC films as a function of substrate temperature**

simultaneously leads to the monotonous decrease of compressive stress in the films and improvement of the atomic short-range order and the bonding between the clusters[9]. It should be noted that the film deposited at 750 °C, where the partial crystallization of SiC takes place inside the amorphous matrix, posses hardness of 40 GPa that is significantly higher in comparison with approx. 36 GPa of α-SiC(001). The details are given in ref.[10].

3.2. Hydrogenated amorphous SiC films

Although the amorphous $Si_{48}C_{52}$ films possess high hardness, they also exhibit very high coefficient of friction of approx. 0.7.

It is well known that for good tribological performance the weak bonding between contacting surfaces and low surface roughness are required. In the case of amorphous carbon based films the former is fulfilled due to the layered structure with weak van der Vaals bonding between layers[9]. The surface roughness of amorphous films is generally lower than for crystalline ones.

The a-SiC films with various excess of carbon were deposited by adding CH_4 to Ar during deposition at bias voltage of –55 V in order to investigate the possibilities of reduction of coefficient friction. Such approach allowed to limit a content of hydrogen in the films in comparison to other deposition methods[11].

Fig. 3 describes the indentation hardness and reduced modulus of a-SiC:H films with thickness of 1.9–2.5 μm as a function of carbon concentration. As the carbon content increases from 52 at.% to 92 at.% the hardness and modulus decreases from 23 to 10 GPa and from 222 to 97 GPa, respectively. Increase of carbon concentration also leads to reduction of compressive stress from 1.1 to 0.3 GPa. It is a result of atomic bonds termination by hydrogen that decreases the number of eventual cross-links in the atomic network[9].

The hydrogen concentration in the investigated films was estimated from the analysis of the Raman spectra using empirical relation originally presented for hydrogenated amorphous carbon[12]. It revealed that hydrogen

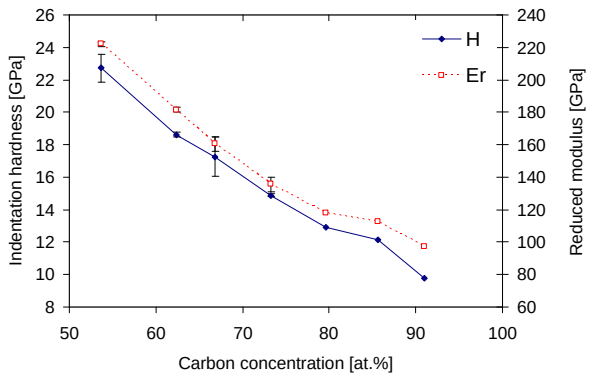

Fig. 3. **Indentation hardness and reduced modulus of a-SiC:H films as a function of carbon concentration**

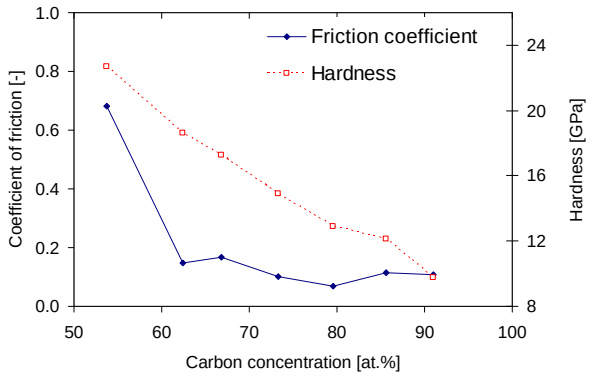

Fig. 4. **Coefficient of friction and indentation hardness of a-SiC:H films as a function of carbon concentration**

concentration is approx. 26–28 at.% for the films with carbon concentration above 67 at.%, i.e. for films deposited at higher CH_4 flow rates.

Results of Pin-on-disc experiments are summarized in Fig. 4. One can see an initial dramatic decrease of coefficient of friction from 0.7 to 0.15 with increase of carbon concentration in the films from 52 to 62 at.%. Further increase of carbon content results only in moderate reduction of friction coefficient. This decrease of friction is probably connected with the raising number of a-C:H clusters and passivation of dangling bonds in the a-SiC:H clusters by hydrogen or its radical groups.

4. Conclusion

The paper demonstrated how appropriate choice of deposition parameters (substrate bias and temperature) can lead to the production of a-SiC films with various mechanical or tribological properties.

It has been presented that indentation hardness and reduced modulus of hydrogen-free a-SiC decrease with increasing bias voltage, whilst they grow with increasing temperature.

First traces of crystallization were observed for the film sputtered at 750 °C with hardness of 40 GPa. Such high hardness exceeding the a-SiC single-crystal is linked to the nanocrystalline structure of the film.

Friction coefficient of a-SiC:H films was optimized by changing the carbon concentration. The film deposited in pure Ar (52 at.% of C) exhibits value of 0.7. Increase of carbon concentration leads to gradual decrease of hardness in the whole range from 52 to 91 at.%, whilst friction coefficient drops dramatically already at small addition of excess carbon (62 at.%) and then decrease slightly.

Thus using appropriate deposition conditions it is possible to prepare a-SiC:H films with sufficiently high hardness of approx. 19 GPa and a low coefficient of friction of approx. 0.15.

This work has been supported by the Operational Program Research and Development for Innovations - European Regional Development Fund (CZ.1.05/2.1.00/03.0058) and co-financed from the Operational Program Education for Competitiveness - European Social Fund (project CZ.1.07/2.3.00/20.0017) of the Ministry of Education, Youth and Sports of the Czech Republic and by the Technology Agency of the Czech Republic (TA01010517).

REFERENCES

1. Kulikovsky V., Vorlíček V., Bohac P., Kurdyumov A., Jastrabik L.: Diamond Relat. Mater. *13*, 1350 (2004).
2. Ctvrtlik R., Stranyanek M., Bohac P., Kulikovsky V., Suchanek J.: Int. J. Mater. Res. *8*, 871 (2008).
3. Sobota J., Grossman J., Vyskočil J., Novák R., Fořt T., Vítů T., Dupák L.: Chem. Listy *104*, 375 (2010).
4. Stoney G. G.: Proc. R. Soc. London A *82*, 172 (1909).
5. Oliver W. C., Pharr G. M.: J. Mat. Res. *7*, 1564 (1992).
6. Ohring M., v knize: *Materials Science of Thin Films. 2nd. ed.*, Academic Press, London 2002.
7. Han Z. H., Li G. Y.: Mater. Lett. *57*, 899 (2002).
8. Jacobsohn L. G., Nastasi M.: Surf. Coat. Technol. *200*, 1472 (2005).
9. Kulikovsky V., Vorlicek V., Ctvrtlik R., Bohac P., Suchanek J., Blahova O., Jastrabik L.: Surf. Coat. Technol. *205*, 3372 (2011).
10. Kulikovsky V., Vorlicek V., Bohac P., Stranyanek M., Ctvrtlik R., Kurdyumov A., Jastrabik L.: Surf. Coat. Technol. *202*, 1738 (2008).
11. Precht W., Czyzniewski A.: Surf. Coat. Technol. *174–175*, 979 (2003).
12. Casiraghi C., Ferrari A. C., Robertson J.: Phys. Rev. B *72*, 085401 (2005).

R. Čtvrtlík[a], V. Kulikovsky[b], P. Boháč[b], and O. Bláhová[c] *([a] Palacky University, Faculty of Science, Regional Centre of Advanced Technologies and Materials, Joint Laboratory of Optics of Palacky University and Institute of Physics of Academy of Sciences of the Czech Republic, Olomouc, [b] Institute of Physics, Academy of Sciences of the Czech Republic, Praha, [c] New Technologies-Research Centre, University of West Bohemia, Plzeň, Czech Republic)*: **Effect of Deposition Conditions on Mechanical Properties of Magnetron Sputtered SiC Thin Films**

The interdependence of mechanical properties (hardness, elastic modulus, internal stress, coefficient of friction), structure and composition of various amorphous and nanocrystalline DC magnetron and DC reactive magnetron sputtered SiC a SiC:H films was studied.

Composition was determined by electron micro analyses and structure was investigated using Raman spectroscopy. Indentation hardness and reduced modulus were measured by instrumented nanoindentation, the coefficient of friction was evaluated using pin-on-disc method.

It has been shoved that mechanical and tribological properties of a-SiC are strongly influenced by conditions of deposition process. Using appropriate deposition setup it is possible to obtain superhard nanocrystalline films with hardness of 40 GPa (higher than α-SiC) as well as films compromising high hardness (approx. 19 GPa) and relatively low friction (approx. 0.15).

ANALYSIS OF CROSS-SECTION SURFACE ROUGHNESS EVOLUTION OF CARBON FIBRE REINFORCED POLYMER UNDER FATIGUE LOADING

TOMÁŠ DOKTOR[a], JAROSLAV VALACH[b], DANIEL KYTÝŘ[b], TOMÁŠ FÍLA[b], JIŘÍ MINSTER[b], and MICHAELA KOSTELECKÁ[c]

[a] Czech Technical University in Prague, Faculty of Transportation Sciences, Department of Mechanics and Materials, Na Florenci 25, 110 00 Prague 1, [b] Academy of Sciences of the Czech Republic, Institute of Theoretical and Applied Mechanics v.v.i., Prosecká 76, 190 00, Prague 9, [c] Czech Technical University in Prague, Klokner Institute, Šolínova 7, 166 08, Prague 6, Czech republic
xdoktor@fd.cvut.cz

Keywords: surface roughness, degradation monitoring, SEM, LSCM

1. Introduction

The article deals with monitoring of degradation of fibre reinforced thermoplastic matrix composite under cyclic loading. The investigated material is composed of polyphenylensulfid matrix and carbon fibres arranged symmetrically in 8 plies with three different fibre orientation (0, 45 and 90 degrees). The material is widely used for secondary, i.e. non-structural elements in aircraft industry. The main aim of the presented work is to correlate observed microstructural changes to measurable morphometric properties and the number of applied load cycles.

2. Materials and methods

Fatigue loading

Four specimens of carbon fibre reinforced polymer[1] (CFRP) were subjected to cyclic loading. The investigated specimens were prismatic, with rectangular cross section (dimensions 12.5×2.5 mm) and length 125 mm. The dimensions were chosen due to limited dimensions of working chambers of used microscopes. The cyclic loading was carried out using loading device Instron 1293 (Instron, Nordwood, US) in three-point bending arrangement[2,3]. For the cyclic loading sinusoidal run of the loading force was used. The upper limit of deflection was 5 mm. Frequency 5 Hz was chosen for the cyclic loading to avoid heat accumulation[4,5] in the tested specimens. After selected numbers of loading cycles the surface of the specimens was observed by scanning electron microscope (SEM) and laser scanning confocal microscope (LSCM).

Surface analysis

Using confocal microscope LEXT OLS 3000 (Olympus Corporation, Tokyo, Japan) surface profile was scanned and images (dimensions 2250×9150 μm) were obtained (1 px in the images corresponds to 9 μm). Information about the surface was obtained in form of two-dimensional matrix containing ascertained heights. Each image was divided into several regions of interest[6] (dimensions 500×500 μm) and in these regions roughness characteristics were estimated (described in detail by Dudíková[7]).

A scanning electron microscope MIRA LMU (TESCAN, a.s., Brno, Czech Republic) was used for observation of degradation processes on the surface of investigated specimens. The images were acquired in high vacuum mode using secondary electron detector. Images with magnification 1000× were used to assess of changes on the samples‘ surface.

3. Results

Roughness evolution

Surface characteristics were estimated in 4 states during the test process. Evolution of the average roughness is depicted in Fig. 1 and in Fig. 2. Increasing indicators of the surface roughness were observed with increasing number of loading cycles.

SEM inspection

SEM was employed to observe changes on the specimens' surface. Free edge of the specimen in four steps of the fatigue loading is depicted in Fig. 3. The images were acquired with magnification 1000× (white bars correspond to 100 μm).

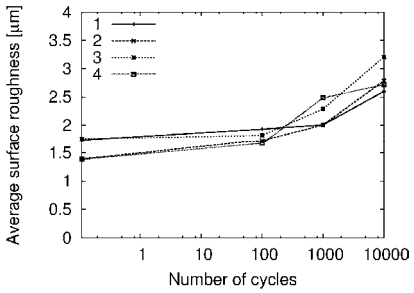

Fig. 1. **Average surface roughness (R_a)**

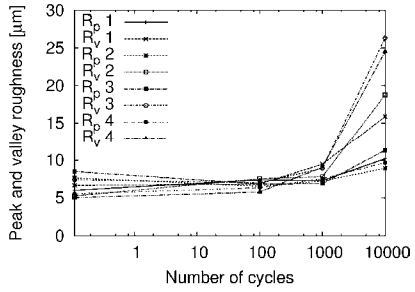

Fig. 2. **Peak and valley roughness (R_p, R_v)**

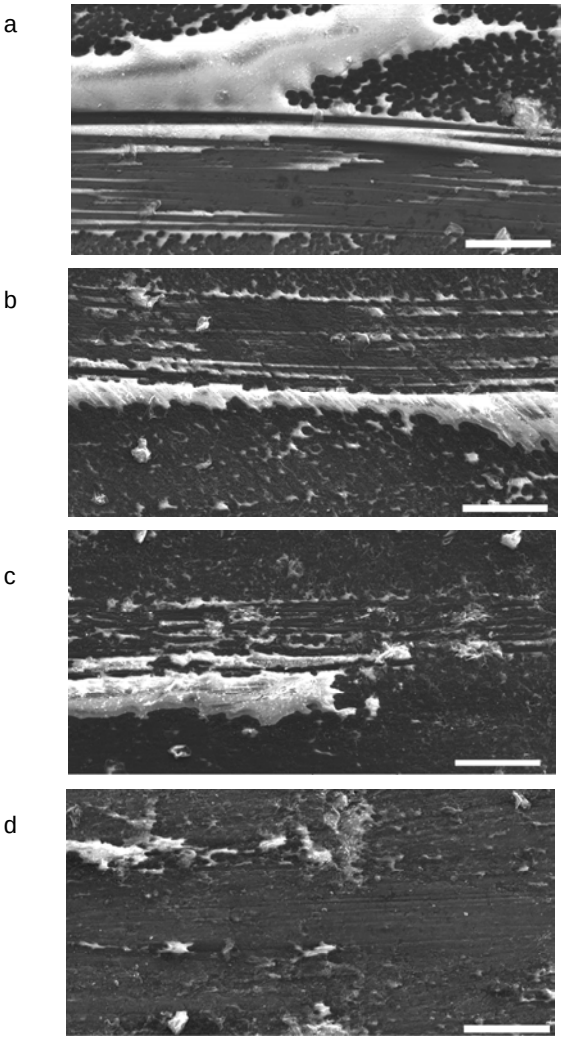

Fig. 3. **Free edge of specimen: intact (a) and 10^2 (b), 10^3 (c) and 10^4 (d) cycles**

4. Conclusions

In this preliminary analysis degradation monitoring of CFRP composite using surface roughness measurements was performed. The increase of surface roughness observed with increasing number of loading cycles indicates at the level of micromechanics changes in fibre-matrix interface and also changes in the matrix structure itself. Increasing values of R_p are connected with detachment of matrix from the fibers and increasing values of R_v show degradation of the matrix. Obtained results of surface analysis correspond with result of SEM inspection performed after distinct steps of the fatigue loading. The SEM images show decreasing surface quality with higher number of loading cycles (both in detachment of fibres and changes in the matrix).

The research has been supported by Grant Agency of the Czech Technical University in Prague (grants No. SGS12/205/OHK2/3T/16 and SGS10/227/OHK1/2T/31), research plan of the Academy of Sciences of the Czech republic AV0Z0710524 and research plan of the Ministry of Education, Youth and Sports MSM6840770043.

REFERENCES

1. Airbus: *AIMS – Airbus Material Specification, Airbus S.A.S* (2007).
2. De Baere, I. et al.: Int. J. Fatigue *31*, 1095 (2006).
3. Van Paepegem W., et al.: Int. J. Fatigue *72*, 212 (2006).
4 Steinberger R., et al.: Int. J. Fatigue *28*, 1340 (2006).
5. Toubal L.: Int. J. Fatigue *28*, 1867 (2006).
6. Al-Shammery H. D. O., et al.: Dent. Mater. *23*, 736 (2007).
7. Dudíková M., et al.: Chem. Listy *105*, s790 (2011).

T. Doktor[a], J. Valach[b], D. Kytýř[b], T. Fíla[b], J. Minster[b], and M. Kostelecká[c] *([a] Czech Technical University in Prague, Faculty of Transportation Sciences, Department of Mechanics and Materials [b] Academy of Sciences of the Czech Republic, Institute of Theoretical and Applied Mechanics v.v.i., [c] Czech Technical University in Prague, Klokner Institute):* **Analysis of Cross-Section Surface Roughness Evolution of Carbon Fibre Reinforced Polymer under Fatigue Loading**

The article deals with monitoring of degradation of carbon fibre reinforced polymer (CFRP) under cyclic loading. The investigated material is composed of polyphenylensulfid matrix and carbon fibres. Four specimens were subjected to repeated cyclic loading. During the fatigue loading surface of tested specimens was observed by scanning electron microscopy (SEM) and laser scanning confocal microscopy (LSCM) to obtain surface roughness characteristics and micrographs of surface morphology. With increasing number of cycles the measured surface characteristics showed increasing surface roughness indicating at the level of micromechanics detachment of matrix from the fibers and also changes in the matrix structure itself.

PREDICTION OF LOCAL LIMIT DEFORMATIONS OF STEEL SHEETS DEPENDING ON DEFORMATION SCHEME

EMIL EVIN, MIROSLAV TOMÁŠ, and JOZEF VÝBOCH

Department of Technologies and Materials, Faculty of Mechanical Engineering, Technical University of Kosice, Mäsiarska 74, 040 01 Košice, Slovak Republic
Emil.Evin@tuke.sk
Miroslav.Tomas@tuke.sk

Keywords: local limit deformation, stress-strain state, forming limit diagram, CCD camera, FEM simulation

1. Introduction

Regarding economic and ecological requests the main appeal for design, material science and production technology engineers is car's body parts weight decreasing. Car's body components design strategies are fixed to optimisation of material selection from aspects of both weight minimisation at first and preservation or improvement of functional properties (safety, power, fuel consumption, comfort, etc.)[1–3]. ULSAB studies show weight decreasing potential of steel sheets components consists in lower thickness steel sheets application with higher strength properties and combined laser welded tailored blanks from these steel sheets (Table I).

Application of steel sheets with lower thickness and higher strength properties leads to technological characteristics of formability downgrading. Formability, or reached deformation degree (limit value) in sheet plane, respectively necking of cup wall thickness depends on material properties, stress-strain state, initial blank thickness and strain rate – Fig. 1 (ref.[1,2,4]).

Stress state in sheet plane can be expressed by main stresses ratio $\alpha = \sigma_2/\sigma_1$ and strain state by main deformations ratio $\beta = \varepsilon_2/\varepsilon_1$ (Fig. 2), where first main (major) deformation $\varepsilon_1 > 0$, second main (minor) deformation $\varepsilon_2 < 0$ or $\varepsilon_2 > 0$.

Table I
Comparison of car's body parameters produced form different steel sheets

	Weight [kg]	Torsional stiffness [°/Nm]
Car's body based on typical high strength steels	300	>15 000
ULSAB	210	> 19 000
Car's body skeleton based on austenitic steel sheets	160	> 25 000

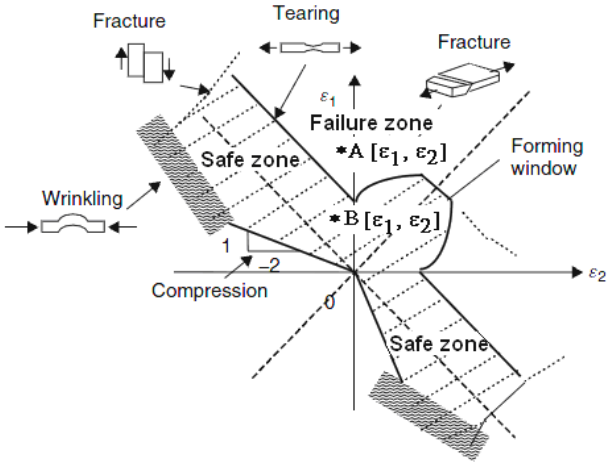

Fig. 1. **Sheets formability window**[4]

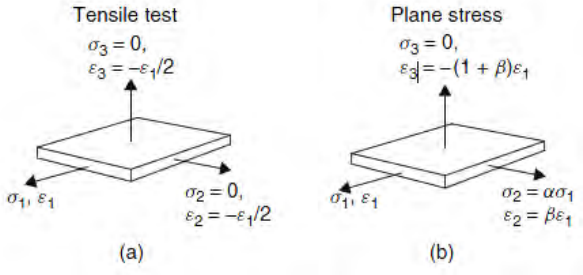

Fig. 2. **Stress-strain states at stamping**

At certain combination of major and minor deformations ε_1 and ε_2 in sheet plane localised deformation in critical area occurs, i.e. local narrow area occurs (neck), followed by fracture. Level of combination of major and minor deformations in sheet plane before localised deformation (before local narrowing) creates limit between good drawn parts – B point and failure drawn parts – A point. This dependence of limit deformations ε_{1c} and ε_{2c} in sheet plane is known as Keeler-Goodwin forming limiting diagram – FLD. Nowadays forming limiting curves (FLC) are considered as inseparable formability characteristic of steel sheets, because they quote development of deformation depending on time and also allows identifying deformation mechanism depending on strain state.

Position of FLC curve in FLD diagram depends not only on material properties, stress-strain state, but also on initial blank thickness, strain rate and friction between blank-die contact surfaces. As it is shown in Fig. 1, maxi-

mal major deformation ε_{1c} is located at areas near to $\varepsilon_{1c} = \pm \varepsilon_2$. When $\varepsilon_{1c} = -\varepsilon_2$ wrinkling occurs at pressings production. At crash situations wrinkling occurs first followed by fracture after overloading of limit fracture deformation. The lowest values of major deformation ε_{1c} are reached in areas where minor deformation $\varepsilon_2 = 0$. In area from $\varepsilon_{1c} = -2\varepsilon_2$ to $\varepsilon_{1c} = \varepsilon_2$ fracture occurs after local necking due to tensile stresses acting.

2. Methods of experimental research

Within last 50 years there was a lot of experimental work done and big effort invested in analytic and experimental creation of forming limit curves[1,2,5,6]. In this contribution there are presented results of limit deformation research by application CCD video camera recording and by numerical simulation.

As experimental materials were used austenitic stainless steel sheet DIN 1.4301 and deep drawing quality steel sheet DX54D. Their chemical composition and mechanical properties are shown in Table II and Table III.

Localised plastic deformations were researched at deformation states within interval $\beta = (-1/2;0)$. Deformation schemes were modelled on tensile test specimens with different notch radii – R5, R10, R17.5 and R25. Local limit deformations at experiments were researched using circle deformation grid ($l_0 = 2$ mm) etched on test specimens.

Testing machine TiraTEST 2300 was used and load velocity was set to 10 mm/min. Change of specimen's dimensions and grid's shape in notch area was contuinuously recorded by CCD camera. Local limit deformations $\varepsilon_1 = l_1/l_0$, $\varepsilon_2 = l_2/l_0$ were calculated and evaluated by software Matlab's Image Processing Toolbox[1,5]. Used video-recording method also allows research all deformation history from test start to specimen fracture.

Deformation net dimensions were evaluated before deformation (initial state), before crack occurred (limit state) and after crack occurred (specimen fracture) – see Fig. 3. Following assumptions were considered to define limit state of deformations based on deformation history:

– homogeneous deformation occurs in the first phase, deformation history is linear $\varepsilon_{1i} = \beta_i.(-\varepsilon_{2i}) \cap \beta_{i-1} \approx \beta_i$,
– localised deformation (diffuse necking) occurs at the second phase under constant loading, deformation history isn't linear $\varepsilon_{1i} = \beta_i.(-\varepsilon_{2i}) \cap \beta_{n-2} > \beta_{1n-1}$,
– at the third phase localised neck (local necking) occurs of width $2.a_0$ and sudden drop of loading force is recorded, followed by fracture, where $\varepsilon_{1n-1} < \varepsilon_{1n} \cap \varepsilon_{2n-1} = \varepsilon_{2n} \cap \beta_{n-1} \approx< \beta_n$.

Deformations evaluated from net dimensions at the end of the second phase were defined as limit deformations; deformations evaluated in the third phase aren't useful for application at stamping processes, because fracture occurs – Fig. 3b.

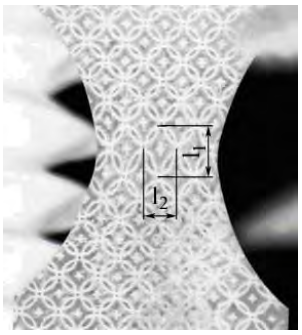

Fig. 3a. **Etched deformation net before specimen cracking**

Fig. 3b. **Deformation net after specimen cracking**

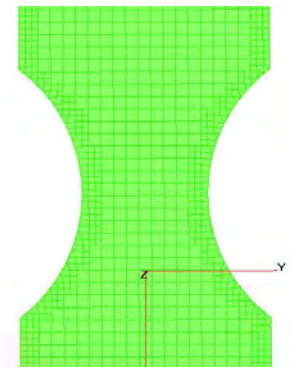

Fig. 4a. **Meshed specimen in numerical simulation**

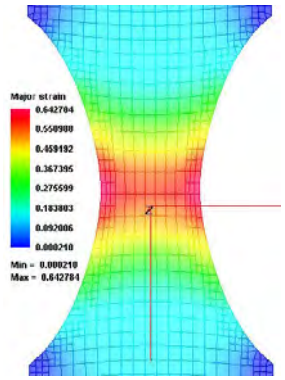

Fig. 4b. **Limit state of major strain in numerical simulation**

Numerical simulation of necked specimens was done using Pam Stamp 2G simulation software. Specimen's models were defined and simulation set-up was done in pre-processing.

Specimen's models were created using 3D CAD/CAM software Pro/Engineer and exported into simulation software in neutral format igs. In Pam Stamp 2G meshing module specimens were meshed to square finite elements with dimension 2 mm – Fig. 4a. Following input data were

Table II
Chemical composition of experimental materials [%]

Material	C	Mn	Si	P	S	Al	N
DX54D	0.05	0.2	0.02	0.009	0.01	0.049	0.006
DIN 1.4301	0.07	2.0	1.0	0.045	0.03	Cr 19	Ni 10

Table III
Mechanical properties in 90° of rolling direction

Material	0.2% YS [MPa]	UTS [MPa]	K [MPa]	n_{90} [-]	r_{90} [-]
DX54D	184	311	487	0.215	1.59
DIN 1.4301	273	621	1491	0.515	0.99

set up in Pam Stamp 2G preprocessor:

– basic material data (density, Young's modulus, Poisson's constant,
– blank thickness,
– strain-hardening curve defined by Hollomon's law according to data shown in Table III,
– Lankford's coefficients in directions 0°, 45° and 90° to rolling direction, as definition of sheet normal anisotropy,
– rolling direction 0° in longitudinal axis of specimens,
– Yield law defined by Hill 48 model.[1,7]

Visualisation of computed data (post processing) allows displaying major σ_1 and minor σ_2 stress distribution, major ε_1 and minor ε_2 strain distribution, wall thickening, variation of forces, deformation energy etc. Localised deformation was researched in postprocessor by visualisation

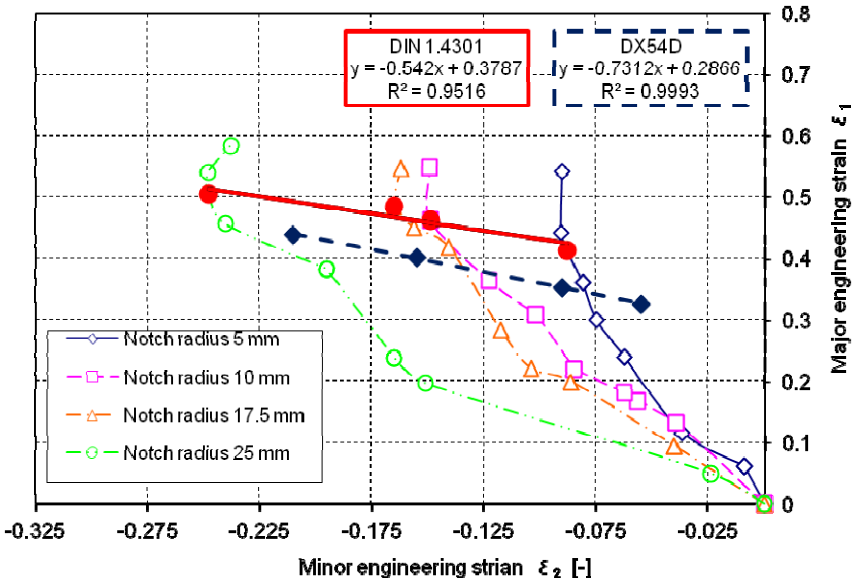

Fig. 5. **Experimentaly acquired forming limit curves**

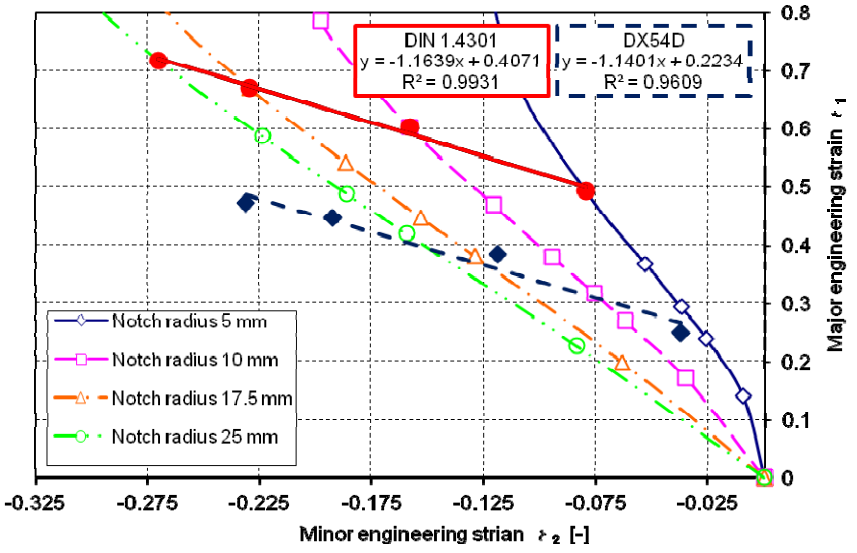

Fig. 6. **Forming limit curves acquired from numerical simulation**

of major ε_1 and minor ε_2 engineering deformations – Fig. 4b. Fig . 5 shows deformation paths of selected deformation net element with computed limit forming limit curves FLC for both materials.

A comparison of Fig. 5 and Fig. 6 shows there is good agreement between experimentally measured FLC and FLC computed by numerical simulation.

3. Reached results and discussion

The measured results of plastic deformation distribution from tensile test of necked specimens shows the deformation history is linear to the limit values described by FLC (Fig. 5). To define the limit formability conditions are important limit deformations in the sheet plane or limit values of material thinning before the plastic deformation localization – neck creation. If we put a curve through the points where there is a significant change of line slope (the critical value of deformation), we get the left part of the FLC. Comparing the FLC defined for austenitic steel sheet (material DIN 1.4301 – Fig. 5) and ferrite steel sheet (material DX54D) the FLC is situated higher the higher values of elongation and strain hardening exponent are. The values of these material characteristics are in the austenitic steel sheets larger than the values in low carbon steel sheets – material DX54D / Table II. The measured results show that the position of the FLC isn't affected by normal anisotropy ratio (austenitic steel sheet r = 1, low carbon steel sheet r = 1.8). Reached FLC comply with present knowledge[1,8,9]. The finding that the position of FLC depends largely on the elongation and strain hardening exponent confirmed the results obtained with strain rate $\dot{\varphi}$ = 0.0083 s^{-1}. When changing the strain rate from 0.0007 s^{-1} to 0.0083 s^{-1} approximately 1 % shift for the material DIN1.4301 as well as for the material DX54D was reached. When changing the strain rate from 0.0007 s^{-1} to 0.0083 s^{-1}, the decrease in elongation of about 3 % for austenitic steel sheet as well as the slight decrease in elongation of about 2 % for drawing quality low carbon steel sheets was also recorded[1].

As it was mentioned FLC reached by experimental measurement and by numerical simulation shows good agreement. Further research should be focused on the analysis of material models in relation to the FLC.

4. Conclusion

New materials bring to vehicles construction new ways to improve their performance – passenger's safety at crash situations, weight loss, etc. Achieved results show the austenitic steel sheets should be included in these materials.

The virtual simulation is commonly used in the design of different variants of design solutions for vehicles and their components as well as in the design of production. In the simulation is necessary to respect the requirements of functionality and manufacturability, which are defined by material properties and used simulation software. Functionality requirements are defined by material properties in elastic-plastic area. In crash situations and manufacture of car components by stamping is necessary to supplement this data with data allowing to predict the localization of plastic deformation followed by fracture. Localised plastic deformation for different stress-strain states can be described by FLC. This paper presents a procedure for determining the FLC by video-camera recording and by numerical simulation. Comparing the FLC at different stress-strain states follows that FLC for austenitic steel sheet is situated higher than FLC for low carbon steel sheet. It means austenitic steel sheet shows better formability and ability to absorb impact energy.

This contribution was working out with the support of the grant project VEGA 1/0824/12.

REFERENCES

1. Hrivňák A., Evin E.: *Lisovateľnosť plechov*. Elfa, Košice 2004.
2. Čada R.: *Tvařitelnost ocelových plechu*. Repronis, Ostrava 2001.
3. Rosenberg G., Gaško M., Sinaiova I., Halama M.: Chem. Listy *105*, s568 (2011).
4. Ramaekers J. A. H.: A Criterion for Local Necking. In.: *6th Shemet*. 2, (1998).
5. Mihalíková M., Ambriško, Ľ., Pešek, L.: Chem. Listy *104*, s350 (2010).
6. Ganesh Narayanan R., Narasimhan K.: J. Strain Analysis. 43, (2008).
7. Kováč P., Tittel V.: Mater. Sci. Technol. *5*, 5 (2010).
8. Chow L. C., Yang X. J., Chu E.: J. Eng. Mater. Technol. 124 (2002).
9. Mishra S. K., et all: Int. J. Mater. Forming *2*, 59 (2009).

E. Evin, M. Tomáš, and J. Výboch *(Department of Technologies and Materials, Faculty of Mechanical Engineering, Technical University of Kosice):* **Prediction of Local Limit Deformations of Steel Sheets Depending on Deformation Scheme**

Paper presents study results of localised deformation, described by FLC, at different deformation schemes. FLC are used for fracture prediction at crash and formability tests in automotive industry. In experiments were used two types of steel sheets: hot deep galvanized steel sheet DX54D and austenitic stainless steel DIN 1.4301. Limit localised deformations were researched by experimental tests (CCD video camera recording) and numerical simulation. Deformation schemes were modelled on tensile test specimens by different notch radii (R5, R10, R17.5, R25). Reached forming limit curves from experiment and simulation were compared. There was shown good agreement of FLC experimentally measured and computed by numerical simulation.

THE INFLUENCE OF ISOTHERMAL ANNEALING ON DEGRADATION OF MECHANICAL PROPERTIES OF HOMOGENEOUS WELDMENT OF THE 9Cr-Mo STEEL

LADISLAV FALAT, ANNA VÝROSTKOVÁ, JÁN KEPIČ, and LUCIA ČIRIPOVÁ

Institute of Materials Research, Slovak Academy of Sciences, Watsonova 47, 040 01 Košice, Slovak Republic
jkepic@imr.saske.sk

Keywords: 9Cr-Mo creep-resistant steel, homogeneous weldment, hardness, impact toughness, fracture mode

1. Introduction

The weldments of 9Cr-Mo martensitic/ferritic creep-resistant steels are commonly used in construction of steam boilers of power generating plants[1,2]. It is well-known that the microstructure of individual regions of welments, namely weld metal (WM), fusion zone (FZ) and heat-affected zone (HAZ), depends on location (distance from weld center-line) and reached peak temperature during welding. The thickness of HAZ basically depends on heat input and thermal conductivity of base material (BM). The weldments of 9Cr-Mo steels require the application of post-weld heat treatment (PWHT), typically in the range from 720 to 760 °C. Requirements on the weldments of creep-resistant steels include besides their high creep-strength also suitable hardness and sufficient toughness[3].

The aim of present work is to study the influence of isothermal annealing on the mechanical properties and fracture behaviour in the individual locations of homogeneous weldment of the 9Cr-Mo „CB2“ steel.

2. Experimental material and procedure

Two bulk pieces (wall thickness 92 mm) of the weldment of CB2 steel were obtained in the Post Weld Heat Treatment (PWHT) state (730 °C / 24 h / furnace cool) within the framework of *COST Action 536* project. The chemical composition of CB2 steel BM and WM is shown in Tab. I. The weldments were annealed at 625 °C for 10´000 and 30´000 h, respectively. Afterwards the weldments were cut into smaller pieces for metallographic analysis and mechanical testing. Vickers hardness (HV10) and Charpy V-notch impact toughness (CVN) were measured at room temperature (RT) in WM, HAZ and BM for the as-received (AR) state and both annealed states. The CVN tests of the samples after 30 kh annealing were performed also at 100 °C. Fracture surfaces of the samples after impact testing were analysed by scanning electron microscopy (SEM).

Table I
Chemical composition [wt.%] of CB2 steel BM and WM

	C	Si	Mn	Cr	Ni	Mo	V
BM	0.12	0.29	0.86	9.14	0.22	1.5	0.19
WM	0.11	0.45	0.65	9.1	0.7	1.3	0.24
	Ti	Al	Co	Nb	B	N	Fe
BM	0.002	0.006	0.95	0.06	0.012	0.020	Balance
WM	0.01	0.01	1.09	0.06	0.003	0.028	Balance

3. Results and discussion

Typical microstructural gradient of the studied weldment is shown in Fig. 1.

With respect to the existence of microstructural gradient, the hardness profiles were determined to characterize the individual regions in all experimental states (see Fig. 2).

The highest hardness in the coarse-grained HAZ region next to WM can be attributed to the presence of „fresh”, carbon-enriched martensite, formed during the

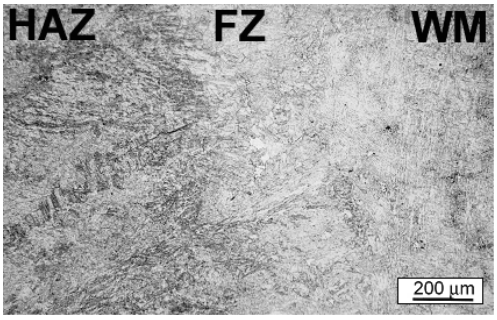

Fig. 1. **Microstructural gradient of CB2 weldment**

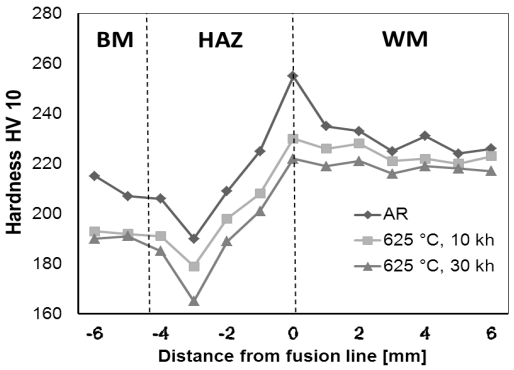

Fig. 2. **Cross-weld hardness of the CB2 weldment**

welding. The lowest hardness was measured in the inter-critical HAZ close to BM as a result of „double-tempering effect" of original martensite and back transformation of unsaturated austenite to the fine-grained ferrite[4]. Apart from hardness tests, Charpy V-notch impact toughness tests (CVN) were carried out (see Tab. II).

Table II
Results of CVN impact toughness tests

Notch location	Average CVN [J.cm^{-2}] (material state / testing condition)			
	(AR /RT)	(10 kh / RT)	(30 kh /RT)	(30 kh /100 °C)
BM	48	18	24	57
HAZ	40	18	18	30
WM	67	22	24	56

The coarse-grained HAZ region exhibits the lowest CVN values in all experimental states which can be ascribed to the presence of coarse prior austenite grains in this location. In contrast, the highest CVN values were measured in WM due to the presence of oxide inclusions which promote the formation of dimples during deformation. Compared to the AR state, CVN values rapidly decrease after the long-term annealing which can be attributed to the thermal degradation of microstructure[5]. However, the small differences in CVN values between the annealed states are caused by the similar level of their microstructure degradation.

Fig. 3 compares the fracture characteristics of CVN samples with notch in WM after RT impact test, in the AR state (Fig. 3a) and after the annealing (Fig. 3b).

The fracture in Fig. 3a can be characterized by a presence of cleavage facets and ductile dimples. In contrast, the fracture in Fig. 3b is almost fully formed of trans-granular cleavage.

Fig. 4 compares the fracture characteristics of CVN samples in the annealed state after the impact test at 100 °C with notch location in WM (Fig. 4a) and in coarse-grained HAZ (Fig. 4b). The fracture mode in Fig. 4a is characterized by ductile dimple tearing. Such manifestation of fracture behaviour at increased temperature can be generally related to the thermally enhanced plasticity via increasing mobility of free dislocations in the lattice. The appearance of fracture surface of the CVN sample

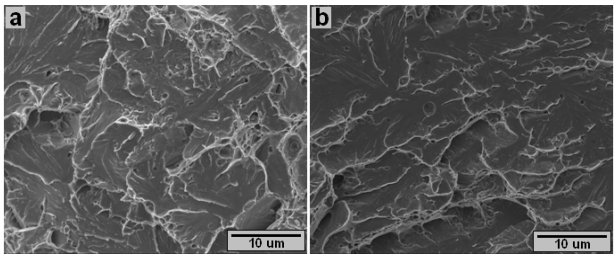

Fig. 3 **Fracture surface of CVN sample with notch in WM after RT impact test in the AR state (a) and after annealing at 625 °C for 30 kh (b)**

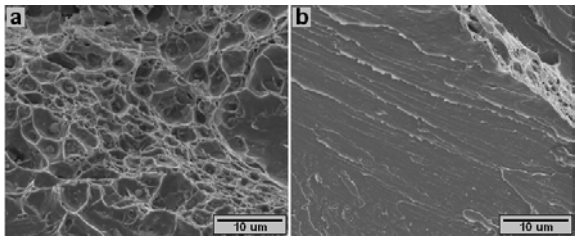

Fig. 4. **Fracture surface of CVN sample in the annealed state (30 kh at 625 °C) after the impact test at 100 °C with notch location in WM (a) and in coarse-grained HAZ (b)**

tested at 100 °C indicates that the impact test was carried out above the brittle-to-ductile transition temperature (BDTT). However, the brittle character of fracture from the HAZ region (Fig. 4b) tested also at 100 °C indicates the strong influence of local thermal degradation on the resulting mechanical behaviour.

4. Conclusion

The determination of local mechanical properties such as hardness and impact toughness of the studied welded joint of CB2 steel revealed significant differences in the individual locations in different experimental states after thermal exposure.

The present work was supported by the European international collaborative project COST Action 536 and the Slovak national project VEGA 2/0128/10.

REFERENCES

1. Jandová D., Kasl J.: Mater. High Temp. *27*, 135 (2010).
2. Sklenička V., Kuchařová K., Kudrman J., Svoboda M., Kloc L.: Kovove Mater. *43*, 20 (2005).
3. Brziak P., Holý A., Bernasovský P.: Zváranie – Svařování *3*, 74 (2007).
4. Wang X., Shi Z., Pan Q., Wu H.: Trans. Nonferrous Met. Soc. China *19*, 772 (2009).
5. Buršák M., Micheľ J., Janek J., Vojtko M.: Chem. Listy *105*, s622 (2011).

L. Falat, A. Výrostková, J. Kepič, and L. Čiripová *(Institute of Materials Research, Slovak Academy of Sciences, Košice, Slovakia):* **The Influence of Isothermal Annealing on Degradation of Mechanical Properties of Homogeneous Weldment of the 9Cr-Mo Steel**

This paper deals with characterization of hardness (HV10), impact toughness (CVN) and fracture behavior in the individual locations of thermally exposed weldment of 9Cr-Mo creep-resistant steel. The variation of mechanical properties strongly depends on the duration of thermal exposure and testing temperature. The observed differences in fracture characteristics of the individual regions and material states correspond well with their different local mechanical properties.

INDENTATION TOUGHNESS OF Si_3N_4 REINFORCED WITH GRAPHENE PLATELETS

LENKA FORRAIOVÁ - KVETKOVÁ[a], FRANTIŠKA DORČÁKOVÁ[a], MARTIN NOSKO[b], JÁN DUSZA[a], PÉTER KUN[c], and CSABA BALÁZSI[c]

[a] Institute of Material Research, Slovak Academy of Science, Kosice, Slovakia, [b] Institute of Materials & Machine Mechanics SAS, Bratislava 3, Slovakia, [c] Research Institute for Technical Physics and Materials Science, Ceramics and Nanocomposites Department, Budapest, 49, H-1525, Hungary
lforraiova@imr.saske.sk

Keywords: ceramic composites, GPLs, toughness

1. Introduction

Recently graphene, a monolayer of sp2-hybridized carbon atoms arranged in a two-dimensional lattice, with exceptional thermal, mechanical, and electrical properties has attracted tremendous attention. This material exhibits exceptional electrical, mechanical and thermal properties[1]. Recently a new cost effective, high quality carbon based filamentous was developed in the form of graphene platelets (GPL) also called graphene nanoplatelets (GNP) or multilayer graphene nanosheets (MGN), which is an alternative to the more expensive nanotubes and monolayer graphene. Walker et al[2]applied graphene to enhance the toughness of bulk silicon nitride ceramics. They found that the ceramics fracture toughness with 1.5% graphene increases from 2.8 MPa $m^{0.5}$ to 6.6 MPa $m^{0.5}$. The aim of this contribution is to investigate the influence of the addition of various kinds of graphene platelets on the fracture toughness and toughening mechanism of Si_3N_4 – GPLs composites.

2. Experimental part

Different types of GPLs/multilayer or few-layer graphene were used as reinforcement material for Si_3N_4 matrix as multilayer graphene (MLG) nanosheets prepared by mechanical milling methode, commercial exfoliated graphite nanoplatelets (xGnP-M-5 and xGnP-M-25)[3] and nano graphene platelets (Angstron N006-010-P)[4]. The specimens were processed by hot isostatic pressing (HIP) performed at 1700 °C by a two-step sinter-HIP method at 20 MPa, with 3 h holding time.

The tests of the microhardness (Leco Instruments) and hardness were performed by the Vickers indentation method at loads from 9.81 N to 150 N. The small specimen size did not allowed to use standard fracture toughness test, therefore indentation fracture toughness testing was performed at loads of 147 N using a Vickers indenter, and the K_{IC} was calculated using the Shetty equation[5]:

$$K_{ICInd} = 0.0899\ (H.P/4l)^{0.5} \qquad (1)$$

where H is the hardness, P is the indentation load, l = c-a is the length of the indentation crack.

Serial sectioning has been used for the characterization of indented crack systems. Microfractography was used to study the fracture lines and surfaces of the specimens and to identify the fracture micromechanisms in the monolithic material and in the composites. This study was realised by SEM analysis (Jeol JSM 700).

3. Results

Fractography study showed that in the present Si_3N_4 – GPLs composites no clusters were found with globular shape and the GPLs are relatively homogenously distributed in all systems, Fig. 1a. Beside separated platelets there are often two or more platelets stuck closely together on the plane parallel with the plane of the graphene sheets, Fig. 1b.

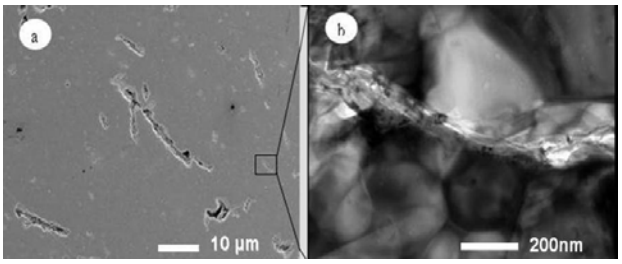

Fig. 1. **Distribution of the multilayer graphene nanosheets in the Si_3N_4 matrix – a, stuck nanosheets – b**

The hardness and indentation fracture toughness of the investigated materials are illustrated in Tab. I.

According to the results beside the system reinforced by multilayer graphene nanosheets all composites exhibit lower hardness in comparison to the hardness of monolith. The lower hardness of these composites compared to the monolithic material is mainly dependent on the residual porosity that remains in the material after the sintering, similar to that observed in other investigations[6]. The highest hardness for the mentioned system can be explained by the lowest porosity and lower grain size of the matrix in comparison to the other composites and to the monolith.

All composites exhibit higher indentation fracture toughness compared to the monolith, thanks to the more frequently occurred toughening mechanisms during the crack propagation. These are very similar for all systems reinforced by different GPLs, only the frequency of their

Table I
Composition, toughness and hardness of investigated materials

Composition of investigated materials [wt%]			Type of GPL additives	Hardness HV1 [GPa]	Toughness K_{Ic} [MPa $m^{0,5}$]
Si_3N_4	Al_2O_3	Y_2O_3			
90	4	6	-	15.4 $^{+}$/- 0.5	6.9 $^{+}$/- 0.4
90	4	6	xGnP-M-5	14.6 $^{+}$/- 0.2	7.8 $^{+}$/- 0.4
90	4	6	xGnP-M-25	15.1 $^{+}$/- 0.3	8.6 $^{+}$/- 0.1
90	4	6	Angstron N006-010-P	14.6 $^{+}$/- 0.4	8.8 $^{+}$/- 0.3
90	4	6	Multilayer graphene	16.4 $^{+}$/- 0.4	9.9 $^{+}$/- 0.3

occurrence during the crack propagation or their effectiveness in toughening process is different.

The main toughening mechanisms are; crack branching Fig. 2, crack deflection Fig. 3a,b and crack bridging Fig. 3c,d.

The origin of this mechanism is the interaction of the propagating crack and GPLs with smaller size. The length of the secondary cracks is several micron and the frequency of occurrence of this mechanism is very high.

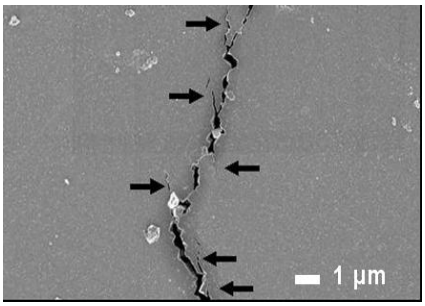

Fig. 2. **Crack branching during the propagation of crack in nanographene platelets reinforced composite**

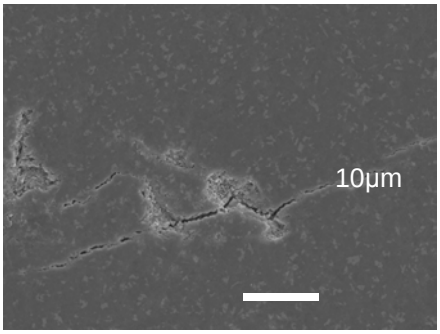

Fig. 3. **Toughening mechanisms in the form of crack bridging and branching on the fracture line**

4. Conclusion

The GPLs are relatively well distributed in the Si_3N_4 matrix of all systems however we often found that two or more platelets are stuck closely together. These single or multi platelets are located at the Si_3N_4/Si_3N_4 grain boundaries and are often connected with a presence of pores. The indentation fracture toughness of the composites is significantly higher compared to the monolithic silicon nitride with the highest value of 9.92 MPa $m^{0.5}$ in the case of composite reinforced by multilayer graphene nanosheets. The toughening mechanisms were similar in all composites in the form of crack deflection, crack branching and crack bridging.

Would like to thank Ľubomír Čaplovič, Karol Iždinský and Jerzy Morgiel for the help with SEM and TEM measurement. The work was supported by NANOSMART, Centre of Excellence, SAS, by the Slovak Grant Agency for Science, grant No. 2/7914/27 by the APVV 0171-06 and LPP 0203-07 and by the KMM-NoE EU 6FP Project.

REFERENCES

1. Soldano C., Mahmood A., Dujardin E.: Carbon *48*, 2127 (2010).
2. Walker L. S., Marotto V. R., Rafiee M. A., Koratkar N., Corral E. L.: ACS Nano *5*, 3182 (2011).
3. http://www.xgsciences.com
4. http://angstronmaterials.com
5. Shetty D. K., Wright I. G, Mincer P. N., Clauser A. H.: J. Mater. Sci. *20*, 1873 (1985).
6. Sun J., Gao L., Iwasa M., Nakayama T., Niihara K.: Ceram. Int. *31*, 1131 (2005).

L. Forraiová-Kvetková[a], F. Dorčáková[a], M. Nosko[b], J. Dusza[a], P. Kun[c], and Cs. Balázsi[c] *([a] Institute of Materials Research of SAS, Kosice, Slovakia, [b] Institute of Materials & Machine Mechanics SAS Bratislava, Slovakia, [c] Research Institute for Technical Physics and Materials Science, Ceramics and Nanocomposites Department, Budapest, Hungary):* **Indentation Toughness of Si_3N_4 Reinforced with Graphene Platelets**

The aim of the present contribution is to study the influence of graphene platelets addives on the fracture toughness of Si_3N_4-graphene system. The experimental materials were silicon nitride with various types of graphene additives, multilayer graphene, exfoliated graphene nanoplatelets and nano graphene platelets. The indentation toughness was measured using indentation fracture method and was calculated using the Shetty's equation. According to the result the composites exhibit higher fracture toughness in comparison to the monolithic material. The highest fracture toughness was found in the case of composite with multilayer graphene platelets. Scanning electron microscope was used for the characterization of toughening mechanisms.

NANOINDENTATION PROPERTIES OF PHASE PARTICLES IN AUSTENITIC CAST STEEL

MAŁGORZATA GARBIAK and BOGDAN PIEKARSKI

West Pomeranian University of Technology, Al. Piastów 17 70-310 Szczecin, Poland
Malgorzata.Garbiak@zut.edu.pl

Keywords: nanoindentation, microstructure, mechanical properties

1. Introduction

Austenitic cast steels assigned for operation at high temperatures are enriched with titanium or niobium mainly to improve the creep resistance or to reduce the carburising effect[1]. Introducing niobium or titanium to 0.3%C-30%Ni-18%Cr cast steel causes the formation in the as-cast structure of niobium or titanium MC carbides instead of chromium carbides of $M_{23}C_6$ type. During annealing at 900 °C the MC carbides undergo transformation into an intermetallic G phase of formula $Ni_{16}(Nb,Ti)_6Si_7$. This transformation is accompanied by the precipitation of chromium carbides of the $M_{23}C_6$ type, due to carbon being liberated from the MC carbides. As a result of changes caused by partial or total replacement of the chromium $M_{23}C_6$ carbides with simple MC carbides, the tansformation of MC carbides into the G phase and secondary precipitation processes due to annealing, the complex precipitates composed of several phases appear in the alloy structure[2]. Each of the phases has its own hardness which makes their differentiation possible by the use of microhardness[3] or nanoindentation method[4].

In the recent years the nanoindentation method has become a valuable tool for the evaluation of materials mechanical properties. The method allows to determine the hardness and the Young´s modulus from the nanoindentation load displacement data. The main advantage of this method is that the load applied can be very small and therefore the dimensions of measured microstructure elements (phase, particles) can be small and it is possible to determine their individual contributions in multiphase alloys.

In the present work the changes of the microstructure 0.3C-30Ni-18Cr cast steel due to titanium and niobium additions were investigated in relation to mechanical properties of microstructure phase constituents. Nanoindentation experiments were carried out to determine the hardness and Young´s modulus of matrix and phase particles of cast steel with and without additions of Ti or Nb.

2. Material and tests

The austenitic 0.3C-30Ni-18Cr cast steel was used for investigations. The content of individual elements was varying within the chemical composition of the tested alloys and is shown in Tab. I. The investigated alloys were in the same heat treatment condition – after annealing in air at 900 °C for 500 hrs and then cooling down together with furnace.

Table I
The content of Ti and Nb in 0.3C-18Cr-30Ni cast steel [wt.%]

Alloy no	Ti	Nb
1	0.03	0.03
2	1.00	0.03
3	0.05	1.84

The phase composition was investigated by X-ray diffraction method. Detailed analysis of XRD diffraction patterns is presented in work[5]. The microstructure investigations were carried out with use of optical microscope, SEM and AFM microscopy.

Nanoindentation tests were performed using Nanoindenter XP with a diamond pyramidal-shaped Berkovich type indenter. The experiments were carried out by the CSM method at a constant depth of 300 nm. For each alloy a set of 100 indentations was performed. The measurements were taken on polished metallographic cross-sections of etched specimens.

3. Results and discussion

Microstructure

Austenite matrix and phase precipitates compose the microstructure of tested alloys. Titanium and niobium

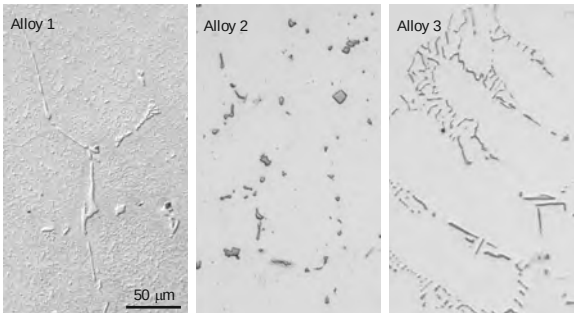

Fig. 1. **Microstructure of tested alloys**

(alloy 2 and 3 respectively) induce the refinement of microstructure of the base cast steel (alloy 1) – Fig. 1. Parameter SDAS (secondary dendrite arm spacing) is lower in cast steels with Nb or Ti additions[6].

By changing the type of solidified carbides both the elements Ti and Nb change the morphology of primary precipitates. The shape and distribution of carbides in the alloy varies depending on kind of element, as in Fig. 1. Annealing of cast steel causes the secondary precipitation processes. The small secondary precipitates are visible in the matrix of alloy 1, as in Fig. 1.

Chromium carbides of $M_{23}C_6$ type are the only precipitates in alloy 1. They form almost continuous network at boundaries of dendrites. Chromium carbides $M_{23}C_6$ are present in alloys 2 and 3 as well. Mostly they appear at the precipitate-matrix boundary, but the small precipitates of chromium carbides can also be seen in the matrix, as in Fig. 2.

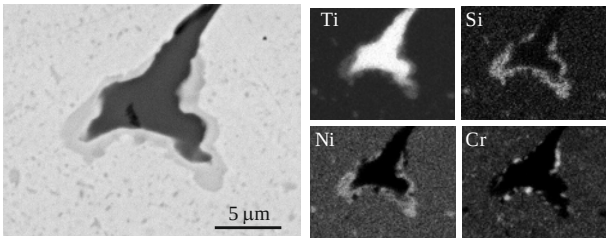

Fig. 2. **Microstructure and mapping of elements in alloy 2, SEM**

The main phase constituents in alloy 2 are titanium carbides TiC and in alloy 3 niobium carbides NbC. Additionally carbonitride TiN which forms the center of TiC precipitates was found in very small quantities in alloy 2. In both alloys 2 and 3 the phase G of formula $Ni_{16}Ti_6Si_7$ and $Ni_{16}Nb_6Si_7$ respectively was also indentified. Phase G rich in silicon and nickel was found surrounding the primary precipitates of MC carbides, as in Fig. 2.

Nanoindentation

The indentations were done in the vicinity of interdendritic boundaries. The aim was to encompass the region of both the austenite matrix and eutectic carbides precipitates. Indentations of 100 points were performed with a step of 7.5 μm what gave 90 × 55 μm of measured area. Indentations were mostly located in the matrix. The indentations grid in alloy 3 is shown in Fig. 3.

The obtained load – displacement curves for alloys 1, 2 and 3 are shown in Fig. 4. The minimal load was 7 mN.

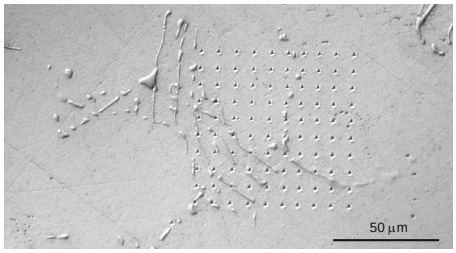

Fig. 3. **Indentation grid on the cross section of alloy 3**

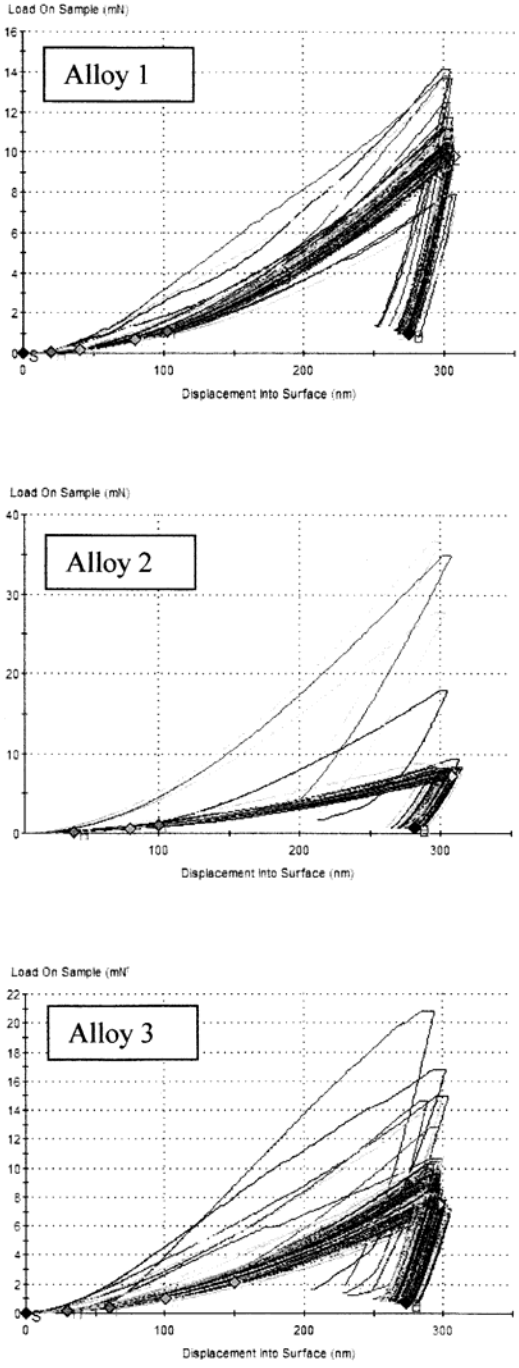

Fig. 4. **Load-displacement curves in alloys 1, 2 and 3**

To reach the indentation depth of 300 nm the maximal load increased to about 14, 38 and 21 mN in alloys 1, 2 and 3 respectively.

The hardness value is known to be strongly dependent on the indentation depth[7]. To enable the values of hardness and Young´s modulus to be comparable between the alloys the constant maximal depth equal to 300 nm was chosen for nanoindentation measurements. According to ISO 14577-1 the nano range is limited to the maximum nanoindentation depth h_{max} less/equal to 200 nm (ref.[4,7]). It means that the measurements in terms of depth were done on nano-micro scale. However, the maximal load of the indentations was below the value of 100 mN, which is considered as the nano force limit.

Fig. 5 shows the images of the single indentations performed in matrix and precipitates of alloys 2 and 3.

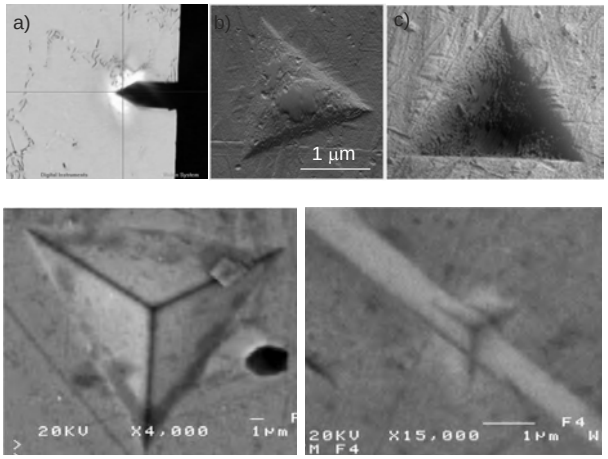

Fig. 5. **AFM and SEM images of indentations: a) alloy 3, screenshot from the optical alignment microscope of the AFM, b) alloy 2, AFM amplitude image, c) 3D surface plot of indentation in b), d) alloy 3, indentation in austenite matrix, SEM e) alloy 3, indentation in NbC carbide, SEM**

The curves of Young´s modulus and hardness versus displacement into surface are presented in Fig. 6–8.

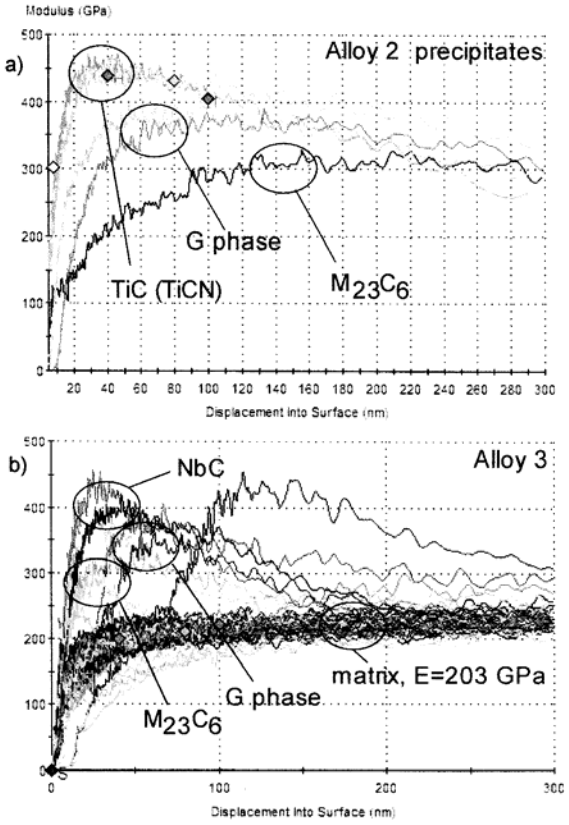

Fig . 7. **Modulus *vs.* indentation depth curves: a) for precipitates in alloy 2, b) for matrix and precipitates in alloy 3**

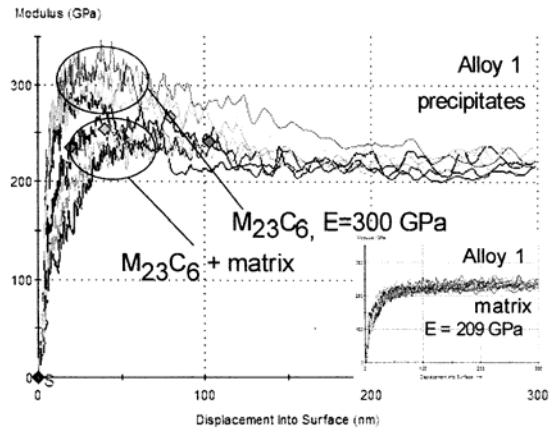

Fig. 6. **Modulus as a function of indentation depth. Curves for precipitates and matrix in alloy 1**

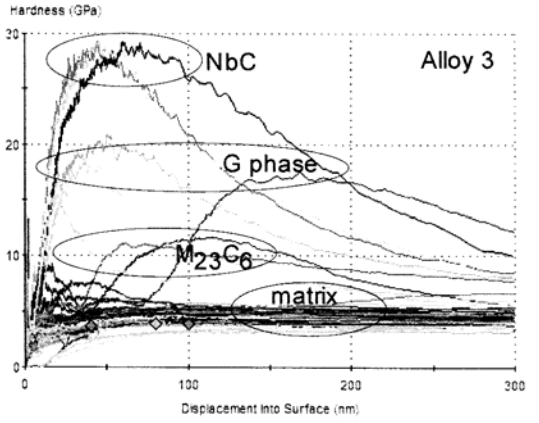

Fig. 8. **Hardness curves as a function of indentation depth, alloy 3**

Alloy 1, in which only two phase constituents were identified in the microstructure, was the first alloy analysed on the basis of the parameters obtained from nanoindentation test for individual precipitates in alloys. Taking into account the fact that the number of indentations performed in the matrix was several times higher than the number of indentations in precipitates, the modulus (E) and hardness (H) of the matrix were the first parameters, which were determined, Fig. 6, Tab. II. The highest values of E and H were attributed to chromium carbides. As the number of indentations was small, only the approximate values of E=300 GPa and H=10 GPa were determined. The values of modulus and hardness between the matrix and carbides were attributed to indentations taken partly from the matrix and partly from the carbides, Fig. 6.

The values of E and H for the matrix of the investigated alloys are shown in Tab. II. The differences among alloys are minor and, taking into account the standard deviation value, they are practically irrelevant.

The modulus and hardness for phase precipitates are given in Tab. III. As the number of indentations responding to individual precipitates was small, the standard deviation from the mean value was not evaluated and only approximate values are presented.

4. Conclusions

On the basis of nanoindentation measurements of alloys based on austenitic cast steel 0.3C-30Ni-18Cr with different content of niobium and titanium, the values of Young´s modulus E and hardness H of phase constituents identified in alloys were evaluated.

The value of modulus (E ~ 200 GPa) and hardness (H ~ 4.5 GPa) of the matrix were similar for all three alloys. So, the conclusion can be drawn that the additions of niobium 1,84 wt.% and titanium 1wt.% do not influence precipitation processes occurring in the matrix of austenitic cast steel during annealing in air at 900 °C for 500 hrs. However, the big difference in properties of other phase constituents (E=300÷450 GPa, H=10÷38 GPa) having diverse morphology can suggest that in macro scale the investigated alloys will exhibit different mechanical properties. In presented investigations the quantitative contribution of individual phases was not analysed. However, taking into account a good repeatability of results for individual phases (E and H for the matrix), the quantitative contribution seems to give a possibility of investigation of the kinetics of phase transformations taking place in investigated alloys.

Nevertheless, in order to use the nanoindentation measurements to statistic analysis of phase contribution, the number of indentations should be increased. Moreover, it is not only important to carry out the representative quantitative test for individual phases, but first of all to increase an area subjected to measurements, what is essential for dendritic structures.

Table II
Mean values of E and H for matrix, GPa

Alloy no	E	Std dev	H	Std dev.
1	209	10	4.2	0.45
2	197	16	4.8	0.62
3	203	10	4.3	0.56

Table III
Approximated values of E and H for precipitates indentified in alloys, GPa

	TiC (TiCN)	NbC	G phase	$M_{23}C_6$
E	450	400	350	300
H	38	28	18	10

This work was supported by the SK-PL-0019-09 project.

REFERENCES

1. Piekarski B.: Prace Nauk. PS, nr 573, Szczecin 2003.
2. Piekarski B., Garbiak M.: Metalurgija *41*, 77(2002).
3. Garbiak M., Chylińska R.: Chem. Listy *105*, 187 (2011).
4. Lucca D. A., Hermann K., Klopfstein M. J.: Manuf. Techn. *59*, 803 (2010).
5. Chylińska R., Garbiak M., Piekarski B.: Mater. Sci. *11*, 348 (2005).
6. Garbiak M., Piekarski B.: Inż. Mater. *1*, 12 (2010).
7. Rodrigues R., Gutierrez I.: Mater. Sci. Eng. *A361*, 377 (2003).

M. Garbiak and B. Piekarski *(West Pomeranian University of Technology, Szczecin, Poland):* **Nanoindentation Properties of Phase Particles in Austenitic Cast Steel**

The nanoindentation measurements performed on three cast steels of 0.3C-30Ni-18Cr type with different content of niobium and titanium were presented and results compared between the tested alloys annealed at 900 °C/500 hrs. The phase constituents (austenite, NbC, TiC, $M_{23}C_6$, G phase) were indentified with X-ray and SEM analysis and distinguished by nanoindentation measurements. It was found that the additions of 1.84 Nb or 1 Ti wt% did not change the precipitation processes occurring in austenite matrix. The value of hardness and Young´s modulus for the matrix were similar within the alloys. Essential differences (E=300–450 GPa, H=10–38 GPa) were found between the phase constituents of alloy.

DEPENDENCE OF INDENTATION PROPERTIES OF ELECTROTECHNICAL STEEL ON TEMPERATURE AND GRAIN ORIENTATION

PETRA GAVENDOVÁ[a], RADIM ČTVRTLÍK[b], FRANTIŠEK KOVÁČ[a], LADISLAV PEŠEK[c], and IVAN PETRYSHYNETS[a]

[a] *Institute of Materials Research, Slovak Academy of Sciences, 040 01 Košice, Slovakia,* [b] *Palacky University, Faculty of Science, Regional Centre of Advanced Technologies and Materials, Joint Laboratory of Optics of Palacky University and Institute of Physics of Academy of Sciences of the Czech Republic, 17. listopadu 12, 771 46 Olomouc, Czech Republic,* [c] *Department of Materials Science, Technical University of Košice, Faculty of Metallurgy, 042 00 Košice, Slovakia*
pgavendova@imr.saske.sk

Keywords: non-oriented electrotechnical steel, high-temperature nanoindentation, nanohardness measurement

1. Introduction

Electrical steels are soft magnetic materials[1,2]. Electrical engines use a variable magnetic filed, parallel to the sheet surface. For this kind, the ideal steel would be the non-oriented grain electrical steels (NO steels)[3]. The highest quality of these steels is achieved using the advanced technology of the very clean steels production with precise control of both the chemical composition and the microstructure of the steels.

Taking into account the directional anisotropy of physical properties in crystallographic lattice of ferrite (bcc) and fact that NO steels are mainly used in circuit electromagnetic field, particularly in electrical motors as a core material, it is necessary to provide crystallographic isotropy in the plane of the sheet in order to achieve good final magnetic properties. The „rotating" cube or {100} <0vw> crystallographic orientation in the sheet plane is ideal for the NO steels. However this texture is not achieved in the practise so far[4].

Nanoindentation has proven to be an effective and convenient technique of determining the mechanical properties of solids, especially Young´s modulus and hardness. The most popular metod of extraction of hardness and modulus from experimental load-displacement response relies on an analysis of the unloading part which is assumed to be elastic, even if the contact is elastic-plastic[5,6].

High-temperature or elevated-temperature nanoindentation testing represents an additional capability in nanoindentation techniques, which have demonstrated tremendous potential in the study of nanoscale mechanical behaviour. The use of the elevated–temperature nanoindentation enhances our ability to study nanoscale behaviour of microstructure since by using temperature as a variable the observation of additional and/or new mechanisms is expected[7].

In this study, nanoindentation tests were conducted to determine the diference in hardness and Young´s modulus between the grains possessing three predefined orientations (with (100); (110); and (111) planes perpedicular to the loading) in dependence on temperature up to 250 °C.

2. Experimental material and procedure

The investigated sample of NO electrical steel with dimensions of 2×4 mm was taken from industrial line after hot rolling. The chemical composition of studied material is presented in Tab. I and the microstructure of the investigated steel is presented in Fig. 1. It is apparent that the average grain size is about 150–250 μm.

Crystallographic orientation of single grains was examined using Electron Backscatter Diffraction commonly used for microstructural-crystallographic analysis.

Nanoindentation experiments were performed using NanoTest NT600 instrument equipped with the calibrated Berkovich indenter at the maximum force of 25 mN. Loading as well as unloading lasted 20 s and the hold period was 10 s. The indentation experiments were performed at room temperature (RT) and at elevated temperatures of 100, 200, 250 °C using load control system.

The NanoTest system was equipped with a computer-control heating stage for measurement at elevated temperatures. Heating was applied to both indenter and the sample utilizing separate temperature control. This isothermal contact ensures that there is no heat flow during indentation process. The sample was fixed to the heated holder using a special cement paste.

Hardness H_{IT} and indentation modulus E_{IT} were determined from load-displacement curves using Oliver-Pharr method[8]. The presented data here were acquired during a single continuous heating sequence. Each grain was measured at target temperature after stabilization (typically 2 hours). When all grains were measured at specific temperature the sample was heated to the next

Table I
Chemical composition of investigated NO steel

Element	C	Mn	Si	P	S	Al	N
%wt	0.004	0.23	2.8	0.008	0.005	0.48	0.004

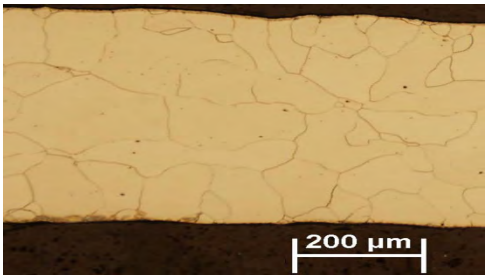

Fig. 1. **Microstructure of NO steel**

temperature, without intermediate cooling. When all of the experiments were completed, the specime was cooled down to room temperature. Heating as well as cooling rate was 1.6 °C min^{-1}.

3. Results and discussion

Investigated grains of the examined material are characterized by single crystal orientation in space with low defects (dislocation) density.

The map describing the spatial orientation of single grains (Inverse Pole Figure – IPF) is in Fig. 2.

In order to study the effect of crystallographic orientation on indentation properties three grains with different crystallographic orientation were choosen; G1 (111), G2 (001), G3 (011). These grains were subjected to the nanoindentation measurements. 20 indentations have been carried out for each grain at each temperature in array of 2 ×10 with spacing of 25 µm. Fig. 3 shows the residual indents in the grain G2 with (001) crystallographic orientation.

Typical nanoindentation results from NO steel are illustrated in Fig. 4. Since we are interested primarily in the presence or absence of serated flow at elevated temperature in the present work, the loading portion of the F-h curve was analysed and two important observations apparent from Fig. 4 were found.

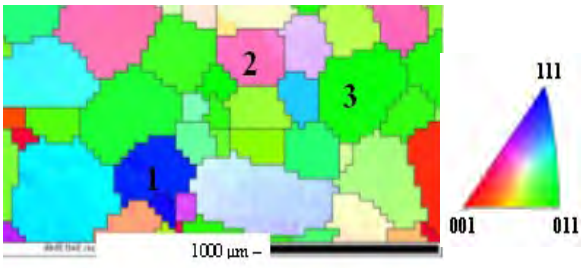

Fig. 2. **IPF map representig the grains of NO steel**

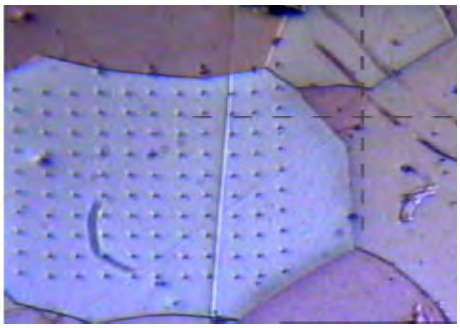

Fig. 3. **The indentation array at G2 after room and elevated temperatures measurements**

First, we observed that the maximum depth of the indentations does not change very much as temperature increases up to 100 °C. Further increase to 200–250 °C leads to a sudden increase in the indentation depth. Second, one can see that as the temperature increases, there is a clear accentuation of serrated flow due to a thermal activation of dislocations. This phenomenon becomes pronounced especially at higher temperature 200 and 250 °C.

This effect with the load drops/serrated flows at elevated temperature was observed in all three grains. Schuh et al.[9] observed a similar trend during the elevated temperature Berkovich indentation of metallic glasses, or Leipner et al.[10] observed the „pop-in“ effect as homogenenous nucleation of dislocations during nanoindentation. This process is related to a sudden displacement shift in the load-depth curve (F-h curve).

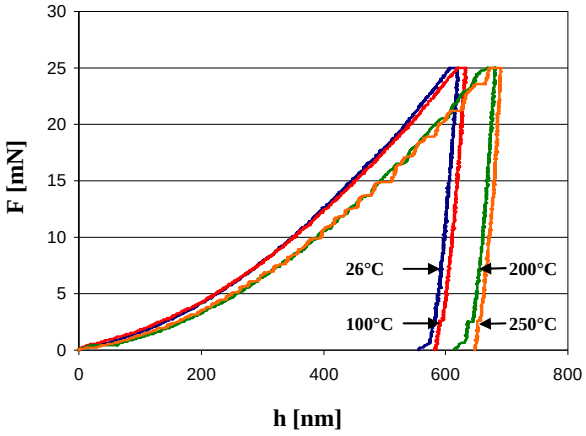

Fig. 4. **Individual load-displacement (F-h) curves obtained by nanoindentation of NO steel**

Hardness and modulus analysis

Indentation hardness H_{IT} slightly decreases with increasing temperature for grains G1, G2 and G3 from RT up to 250 °C from 2.7 to 2.3 GPa, from 2.7 to 2.1 GPa and from 2.8 to 2.1 GPa, respectively, Fig. 5.

As one can see in Fig. 5 there are some diferences in hardness values between particular grain orientations. Decrease of hardness with increasing temeprature for grains G1, G2 and G3 was about 15, 22 and 26 %, respectively. This differences between individual grains can be related to various number of active slip systems in grains[11].

Similarly to hardness, the differences in indentation modulus of particular grains are also observed, E_{IT} decreases with increasing temperature as illustrates Fig. 6, however, not so pronounced as for H_{IT}.

The average value of indentation modulus for grains G1, G2 and G3 decreases by the temperature change from RT up to 250 °C from 198 to 185 GPa, from 193 to 171 GPa and from 204 to 201 GPa, which expressed in % is 6.7, 11.2 and 1.5 %, respectively.

These results, when the values of both hardness and indentation modulus decreases with increasing temperature are in agreement with other research paper[12].

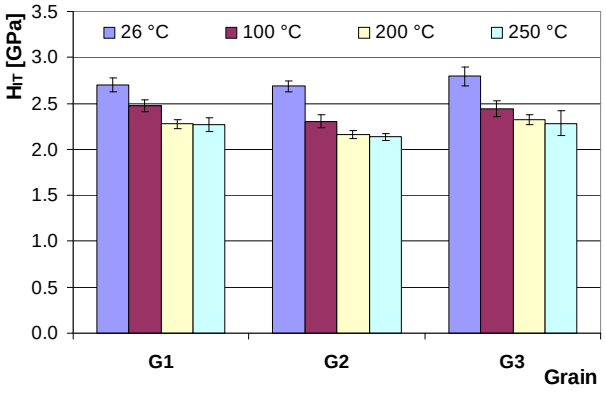

Fig. 5. **Dependence of hardness on temperatures in each of grain orientations**

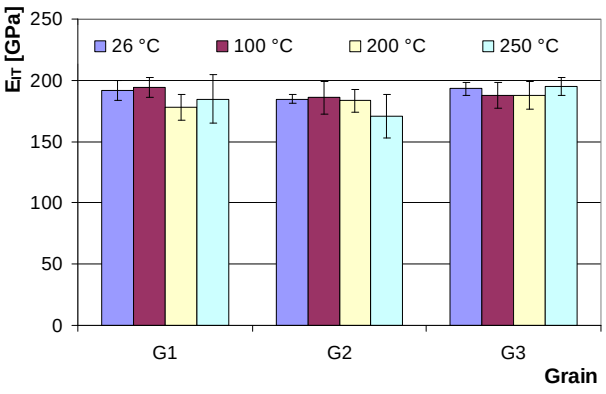

Fig. 6. **Dependence of indentation modulus on temperatures in each of grain orientations**

Conclusions

In situ high temperature nanoindentation experiments were performed in order to study the influence of temperature on indentation properties of grains with different crystallographic orientation.

On the basis of results from elevated temperature nanoindentation measurements in each of particular grain orientations it was observed following:

– Analysis of the load drops/ serrations in the load – displacement curves allowed for the identification of onset of serrated flow during elevated temperature nanoindentation. This pop-in effect or the transitions from smooth to serrated flow were observed at 200–250 °C. The pop-in effect could be related to homogeneous nucleation of dislocation during nanoindentation or with increasing temperature so that the transition is tempereture-dependent.
– Hardness was found decrease for all investigated grain orientations G1 (111), G2 (001) and G3 (011) with increasing temperature from room temperature up to 250 °C. The differences of hardness values were observed also between particular grain orientations. This can be explained with various number of active slip systems in the individual grains.
– The values of indentation modulus are slightly decreasing with increasing temperature. These results are in agreement with other research papers. The presented results proved that high temperature indentation is a promising technique which extends the possibilities of studying of local mechanical properties.

This work was realized within the frame of the project „New Materials and Technologies for Energetics“, ITMS: 26220220037, which supported by the operational Program „Research and Development financed through European Regional Development Fund.

REFERENCES

1. Zhaosuo X., Yonglin K., Quanli W.: J. Magn. Mater. *320*, 3229 (2008).
2. Castro S. F., Gallego J., Landgraf F. J. G., Kestenbach H.: Mater. Sci. Eng. A *427*, 301 (2006).
3. Cardoso R. F., Brandao L., Cunha M. A.: Mater. Res., *11*, 51 (2008).
4. Kováč F., Stoyka V., Petryshynets I.: J. Magn. Magn. Mater. *320*, 627 (2008).
5. Fisher-Cripps A. C.: *Nanoindentation*, second ed., Springer LLC, New York 2004.
6. Němeček J., Lukeš J.: Chem. Listy *104*, 267 (2010).
7. Duan Z. C., Hodge A. M.: Nanomechanical Testing – Overview *61*(12), 32 (2009).

8. Oliver W. C., Pharr G. M.: J. Mater. Res. *19*, 3 (2004).
9. Schuh C. A., Lund A. C., Nieh T. G.: Acta Materialia *52*, 5879 (2004).
10. Leipner H. S., Johansen H., et al.: Physical Review B *67*, 172101 (2003).
11. Lloyd G. E., Farmer A. B., Mainprice D: Tectonophysics *279*, 55 (1977).
12. Latella B. A., Humphries S. R.: Scripta Materialia *51*, 635 (2004).

P. Gavendová[a], R. Čtvrtlík[b], F. Kováč[a], L. Pešek[c], and I. Petryshynets[a] *([a] Institute of Materials Research, Slovak Academy of Sciences, Košice, Slovakia, [b] Palacky University, Faculty of Science, Regional Centre of Advanced Technologies and Materials, Joint laboratory of Optics of Palacky University and Institute of Physics of Academy of Sciences of the Czech Republic, Olomouc, Czech Republic, [c] Department of Materials Science, Technical University of Košice, Faculty of Metallurgy, Košice, Slovakia):* **Dependence of Indentation Properties of Electrotechnical Steel on Temperature and Grain Orientation**

The elevated temperature response of NO electrical steel was examined using a nanoindenter Nano Test NT 600 with tip and sample heating. Hardness was faound to decrease with increasing temperature in each of tested grain orientation. The similar situation occured in the case of elastic modulus. It was shown some diferences in values of hardness and indentation modulus between particular grain orientations. Conversely, the magnitude of the load drops/ serrated flow in the load displacement curve was found to increase with temperature.

INDENTATION TESTING OF HUMAN ENAMEL

RADOSLAV HALGAŠ[a,b], JÁN DUSZA[b], LUCIA KOVÁCSOVÁ[c], JANA KAIFEROVÁ[c], and NEDA MARKOVSKÁ[c]

[a] *Faculty of Material Science and Technology of STU, Paulínska 16, 917 24 Trnava,* [b] *Institute of Materials Research of SAS, Watsonova 47, 040 01 Košice,* [c] *1st Department of Stomatology of UPJS, Trieda SNP 1, 041 66 Košice, Slovakia*
radoslav.halgas@stuba.sk

Keywords: human enamel, nanoindentation, AFM

1. Introduction

As the hardest and one of the most durable load bearing tissues of the body, enamel has attracted considerable interest during the last decade from both material scientists and clinical practitioners due to its excellent mechanical properties[1,2]. Knowledge of the mechanical and wear properties of human teeth is of importance as they act as a mechanical device during masticatory processes such as cutting, tearing and grinding of food particles. In the last years, depth-sensing indentation has become a useful technique for mechanical characterization of mineralized biological tissues, including enamel and dentin[3,4]. Due to its small probe size, nanoindentation is suited to measure local material properties in small, thin samples and allows characterizing the properties of individual constituents within composite tissues, such as enamel and dentin, or mapping their mechanical properties across a sample surface[5].

The aim of this investigation is to characterize the hardness and elastic modulus of human teeth using instrumented indentation.

2. Experimental materials and methods

2.1. Sample preparation

The used samples were fresh intact human premolars extracted due to orthodontic reasons. The samples were collected with the patients' informed consent with professional dentist (team of dentists from UPJŠ Košice). Teeth were stored in salt solution after removal and before testing, were embedded in EpoFix20 epoxy cold-mounting compound (Buehler Ltd., Lake Bluff, IL). Samples were cut with a precise diamond saw so that the teeth were divided into two halves. Cutting parameters were: low speed rotation (150 rt./min) and cooling with water to protect dehydration and heating.

The sample surface was polished sequentially with 6-, 3-, 1- μm diamond paste and 0.25 – μm alumina suspension. Between polishing steps, the sample was ultrasonically cleaned in de-ionized water to remove any polishing debris and stored in a saline solution at 4 °C. Effect of the epoxy compound on the measured hardness is minimal, due to the used low indentation load.

2.2. Nanoindentation

The nanoindentation experiments were performed using instrumental hardness tester (TTX/NHT by CSM Instruments) equipped with Berkovich indenter using the indentation load of 5 mN. The indents have been applied to the area of enamel, dentin and dentin-enamel junction (DEJ). The number of indents was 20 in three rows. The first indents were located near the occlusal surface, followed by indents toward dentin across DEJ, with the distance of 0.25 mm between the indents. The indentation hardness, H_{IT}, and reduced modulus, E_{IT}, were calculated by Oliver-Pharr method[6]. The average values of hardness and reduced elastic modulus were calculated at least from three independent measurements. Light microscopy (LM) and atomic force microscopy (AFM) was used for the characterization of indents.

3. Results and discussion

In Fig. 1 characteristic indents are illustrated located in different parts of human tooth. The hardness of enamel is significantly higher (Fig. 2a) than that of the dentin with values different for the area close to the surface ~ 5 GPa and area close to the DEJ (~ 3 GPa). The hardness of dentin is significantly lower in comparison to the enamel with the average value of ~ 0.4 GPa. Similar behaviour was found in the case of reduced modulus (Fig.2b), however the decrease in its value from the enamel surface (~ 88 GPa) to DEJ (~ 81 GPa) is not so visible as in the case of hardness. There is a significant change in reduced modulus at the DEJ from ~ 81 GPa to ~ 20 GPa. Cuy et al.[4] used nanoindentation for mapping mechanical properties of human molar teeth enamel. They found the enamel surface hardness, $H_{IT} > 6$ GPa and reduced modulus, $E_{IT} > 115$ GPa, while at the enamel–dentine junction $H_{IT} < 3$ GPa and $E_{IT} < 70$ GPa. He and Swain[2] also used nanoindentation for characterisation of hardness of enamel. Their results are similar as the results of Cuy et al., but with slightly lower values of hardness and reduced modulus, which can be explain with the higher applied indentation load. Our results are in good agreement with these findings and can contribute to the design and development of functionally graded coatings.

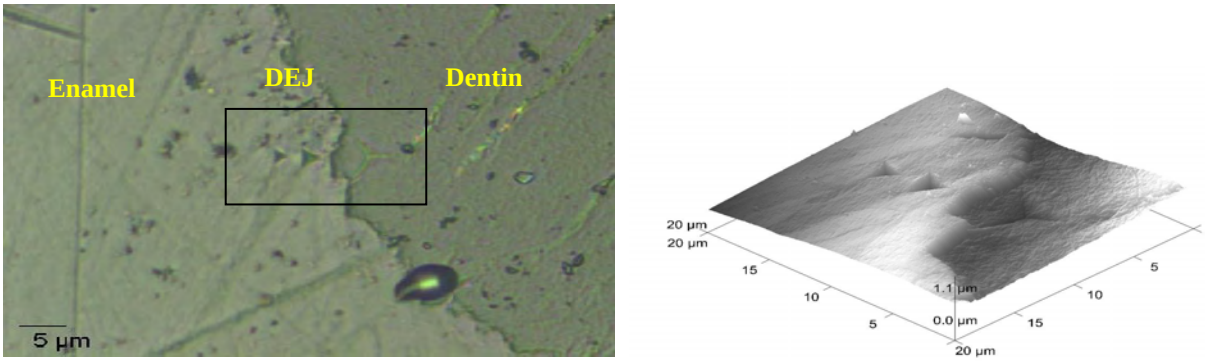

a b

Fig. 1. **Light microscopy observations of Berkovich indents in enamel and dentin, near to DEJ, (a), AFM observation of the same area, (b)**

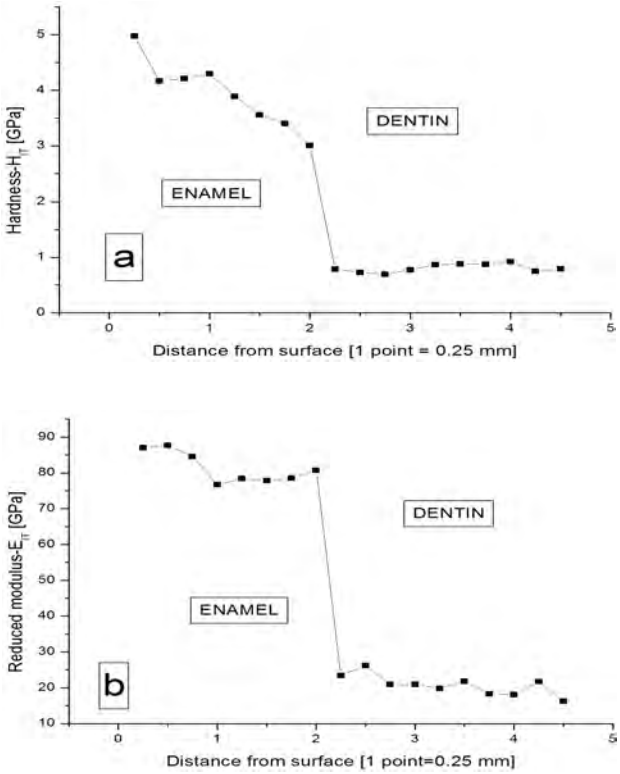

Fig. 2. **Profiles of the hardness (a) and reduced modulus (b) across the enamel – dentin cross section**

4. Conclusion

The values of indentation hardness and reduced modulus of human teeth were characterized as a function of position on the cross-section of enamel/DEJ/dentin areas. The H_{IT} and E_{IT} of enamel exhibits a distinct decrease on traversing from the outer surface of enamel to the DEJ. According to the results at the enamel surface, H_{IT} > 5.0 GPa and E_{IT} > 90 GPa, while at the enamel – dentin – junction H_{IT} < 3.0 GPa and E_{IT} < 80 GPa. The indentation hardness and reduced modulus of dentin, H_{IT} ~ 0.6 GPa and E_{IT} ~ 20 GPa.

REFERENCES

1. He Li Hong, Swain M. V.: J. Mech. Behav. Biomed. Mater. *1*, 18 (2008).
2. He Li Hong, Swain M. V.: J. Dent. *35*, 431 (2007).
3. Giráldez de Luis I., Garrido M.A., Gómez-del Río T., Ceballos L., Rodríguez J.: Bol. Soc. Esp. Ceram. *49*, 177 (2010).
4. Cuy J. L., Mann A. B., Livi K. J., Teaford M. F., Weihs T. P.: Arch. Oral Biol. *47*, 281 (2002).
5. He Li Hong, Swain M. V.: J. Dent. *37*, 596 (2009).
6. Oliver W., Pharr G.: J. Mater. Res. *19*, 3 (2004).

R. Halgaš[a,b], J. Dusza[b], L. Kovácsová[c], J. Kaiferová[c], and N. Markovská[c] (*[a] Faculty of Material Science and Technology of STU, Trnava, Slovakia, [b] Institute of Materials Research of SAS, Košice, Slovakia, [c] 1st Department of Stomatology of UPJS, Košice, Slovakia):* **Indentation Testing of Human Enamel**

The aim of the present contribution was to investigate the local mechanical properties on cross-section of fresh extracted human molar teeth using nanoindentation method and Berkovich diamond indenter. The indentation hardness, H_{IT} and reduced modulus, E_{IT} in enamel decreased on traversing from the outer surface of enamel to the DEJ from H_{IT} > 5.0 GPa and E_{IT} > 90 GPa to H_{IT} < 3.0 GPa and E_{IT} < 80 GPa, respectively. The characteristics of dentin are; H_{IT} ~ 0.6 GPa and E_{IT} ~ 20 GPa.

CHARACTERIZATION OF INDENTATION INDUCED MARTENSITIC TRANSFORMATION BY SCANNING ELECTRON MICROSCOPY AND ELECTRON BACK-SCATTERED DIFFRACTION

PETR HAUŠILD[a] and JIŘÍ NOHAVA[b]

[a] *Czech Technical University in Prague, Faculty of Nuclear Sciences and Physical Engineering, Department of Materials, Trojanova 13, 120 00 Praha, Czech Republic,* [b] *CSM Instruments, Rue de la Gare 4, CH-2034 Peseux, Switzerland*
hausild@fjfi.cvut.cz

Keywords: nanoindentation; stainless steel; martensitic transformation

1. Introduction

Instrumented indentation with spherical indenter is widely used for characterization of local mechanical properties of various materials including metals, ceramics or polymers and offers several advantages comparing to the indentation with sharp indenters. Using spherical indenter, plastic deformation under the indenter is gradually changed as the indentation depth increases[1–3]. This can appropriately be utilized for characterization of the deformation-induced phase transformation during indentation[4]. On the other hand, the triaxial stress-strain field under the indenter differs substantially from tensile stress-strain field.

2. Experimental details

Recrystalized metastable austenitic stainless steel (AISI 301) was chosen as an experimental material. The chemical composition is given in Tab. I. Surface of samples was electro-polished to avoid the subsurface layer affected by mechanical grinding and polishing.

Nanoindentation measurements were performed on CSM Instruments NHT Nanoindentation Tester with spherical indenter (with radius of 50 μm) using instrumented indentation technique[5–7]. Increasing load was applied up to maximum load of 400 mN. The indents were subsequently characterized by light microscopy using differential interference (Nomarski) contrast, scanning electron microscope (SEM) JEOL JSM5510LV using back-scattered electron channeling contrast and by three-dimensional reconstruction (Alicona™) using stereopair technique.

Local analysis of martensite transformed in the vicinity of the indents was carried out by electron back-scattered diffraction (EBSD) HKL™ system mounted on scanning electron microscope JEOL JSM 7600F equipped with field emission gun (FEG).

Table I
Chemical composition of AISI 301 steel (in wt.%)

	C	Cr	Ni	Si	Mn	Mo
Nominal	max 0.12	16-18	6.5-9	<1.5	<2	<0.8
Analyzed	0.05	17	7	0.5	1.5	0.1

3. Results and discussion

Light and SEM micrographs are shown in Fig. 1. It can be seen that AISI 301 steel undergoes at room temperature deformation-induced phase transformation of face-centered cubic γ austenite to body-centered cubic α'-martensite[8–10].

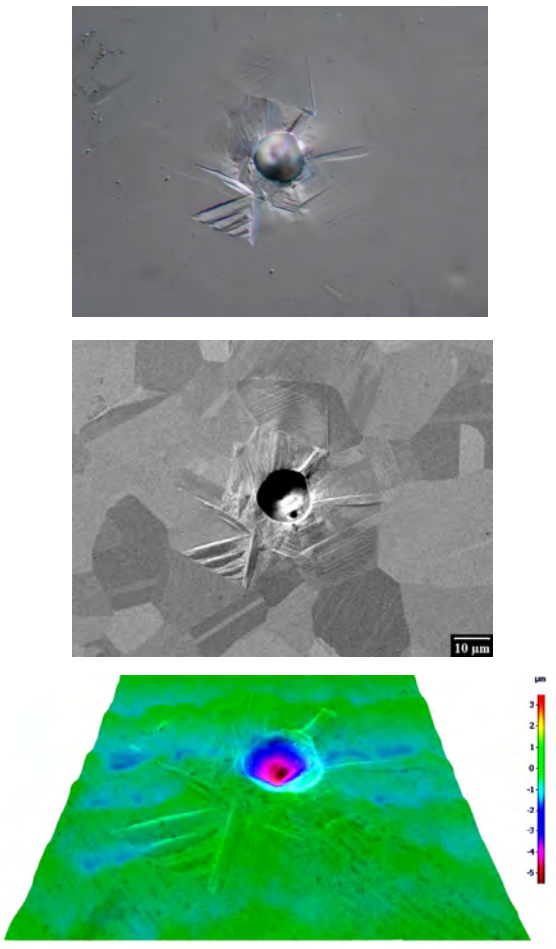

Fig. 1. **Deformation-induced martensite in the vicinity of spherical indent - light microscopy (Nomarski contrast), SEM back-scattered electron channeling contrast and 3D stereopair reconstruction**

Martensitic transformation is accompanied by volume change which results in a significant relief on the surface sample in the vicinity of indent (see Fig. 1).

Non-transformed austenite and deformation-induced martensite in the vicinity of spherical indents were characterized by EBSD. The crystallographic orientation of the transformed martensite is in the relation to the parent austenite grain according to the Kurdjumov-Sachs (K-S) orientation relations (see Fig. 2). The transformation is significantly influenced by the stress state. The transformation texture arises because not all possible martensite crystallographic variants grow when the austenite is subjected to external stress; i.e. the total number of selected martensite variants within a γ-grain is much lower than 24 theoretically allowed by K-S orientation relation.

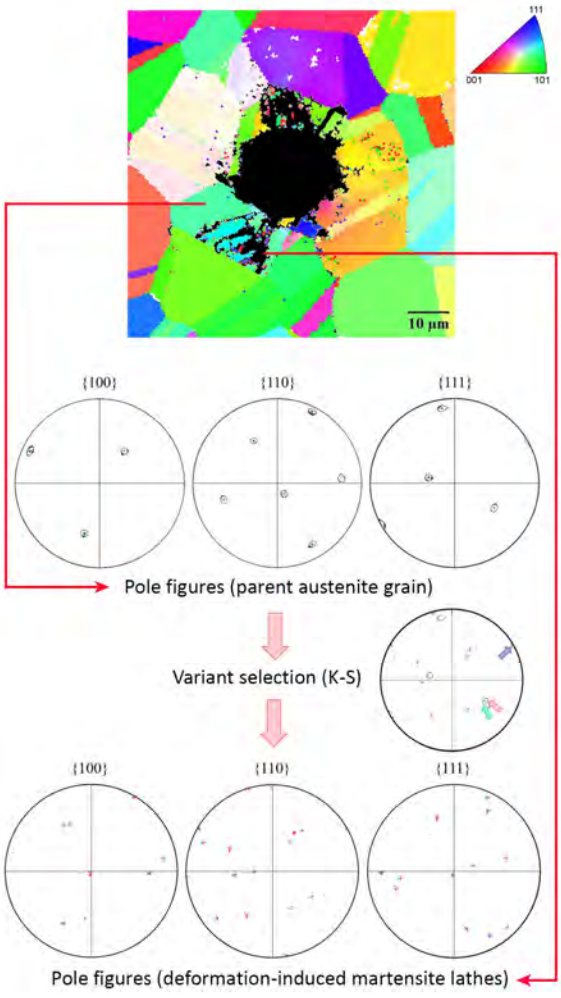

Fig. 2. **Electron back-scattered diffraction in the vicinity of spherical indent – inverse pole figure of austenite with orientation triangle (top-right). Variant selection of the deformation-induced martensite – pole figures of parent austenite grain and transformed martensite (bottom)**

4. Conclusions

The results of the study can be summarized as follows:

High internal stresses are generated due to an incompatible transformation strain accompanying the γ → α' transformation.

Multiaxial stress-strain field under the indent has a significant effect on the orientation of the martensite variants.

Combining nanoindentation with scanning techniques such as SEM and EBSD brings more insight into the whole indentation process.

This work was carried out in the frame of research project GACR 101/09/0702.

REFERENCES

1. Tabor D.: *The Hardness of Metals*, Clarendon Press, Oxford 1951.
2. Johnson K. L.: *Contact Mechanics*. Cambridge University Press, 1985.
3. Menčík J.: Chem. Listy *105*, s680 (2011).
4. Haušild P., Nohava J., Materna A.: Chem. Listy *105*, s676 (2011).
5. Oliver W. C., Pharr G. M.: J. Mater. Res. *7*, 1564 (1992).
6. Oliver W. C., Pharr G. M.: J. Mater. Res. *19*, 3 (2004).
7. Menčík J.: Chem. Listy *105*, s115 (2011).
8. Mangonon Jr., L., Thomas G.: Metall. Trans. *1*, 1577 (1970).
9. Haušild P., Davydov V., Drahokoupil J., Landa M., Pilvin P.: Mater. Design *31*, 1821 (2010).
10. Nohava J., Haušild P.: Chem. Listy *104*, s360 (2011).

P. Haušild[a] and J. Nohava[b] (*[a]Faculty of Nuclear Sciences and Physical Engineering, Czech Technical University in Prague, Czech Republic, [b]CSM Instruments, Switzerland):* **Characterization of Indentation Induced Martensitic Transformation by Scanning Electron Microscopy and Electron Back-Scattered Diffraction**

Local analysis of martensite transformed in the vicinity of the spherical indents was carried out by light and scanning electron microscopy, 3D stereopair reconstruction and electron back-scattered diffraction. Multiaxial stress-strain field under the indent has a significant effect on the orientation of the martensite variants. Combining nanoindentation with scanning techniques such as SEM and EBSD brings more insight into the whole indentation process.

CAUSES OF INCONEL 622 WELD CRACKING

JAKUB HORNÍK, PAVLÍNA HÁJKOVÁ, EVGENIY ANISIMOV, and JAN RYBNÍČEK

CTU in Prague, Faculty of Mechanical Engineering, Department of Materials Engineering, ICDAM, Karlovo nám. 13, 121 35 Praha 2
jakub.hornik@fs.cvut.cz

Keywords: inconel, weld, fractography, nanohardness, impact test

Introduction

This paper is dealt with the topic of welding of duplex steel with Ni alloy Inconel 622 being used e.g. in aerospace, offshore and chemical industry. The welding procedure for Ni based alloys typically requires a cautious control over parameters outlined by the Welding Procedure Specifications (WPS) and using high quality filler metals. Even if the welding procedure matches the WPS requirements, the random occurrence of weld defects may cause the failure initiation.

Experimental

By evaluating the weldment, a tendency to cracking was indicated in the SMAW region of the weld metal and at a fusion zone during the bend test. In order to estimate causes of undesired behaviors of the weld metal, a metallographic evaluation was applied. Light and electron microscopy have been used for a structural analysis of the weld. Furthermore, the Charpy impact testing and fractographic analysis of the fracture surface was used. For the mechanical properties of discrete material areas, the nanoindentation method was applied. Carl Zeiss Neophot 32 metallographic microscope, Jeol 7600F High Resolution Scanning Electron Microscope with EDS analyzer (Oxford) and Nanohardness Tester was used.

Results and discussion

The welding procedure used for the joining of thicker plates had two steps. The root of the joint was prepared using the Gas Tungsten Arc Welding (GTAW) method. In next, filing passes were made by Shielded Metal Arc Welding (SMAW). Tab. I shows the typical chemical composition of Inconel 622.

Metallographic evaluation carried out on polished samples showed a significant disproportion in micropurity in different weld regions. The root of the weld, produced by the TIG method (GTAW), had a relatively low content of inclusions (Fig. 1a). The SMAW region shown in Fig. 1b exhibited a large number of spherical inclusions of various dimensions.

Table I
Chemical composition of Inconel 622 [wt.%]

C	S	P	Mn
0.01	0.015	0.03	1.0
Si	Cr	Mo	W
0.2	20.0 – 22.5	12.5 – 14.5	2.5 – 3.5
Cu	Co	Fe	V
0.5	2.5	2.0 – 6.0	0.35

The microstructure of both weld regions was similar. The weld metal had a typical dendritic form (Fig. 2 and Fig. 4). Fig. 3 shows that the microstructure of the filler metal rod was oxide-less. On the other hand, Fig. 4 shows the SEM image demonstrating that the presence of inclusions was significantly higher in SMAW region. Table II displays the example of a chemical composition measured by EDS on large spherical inclusions.

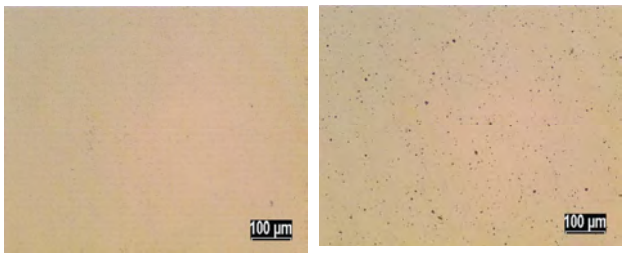

a) GTAW b) SMAW

Fig. 1. **Microstructure of weld metal, unetched**

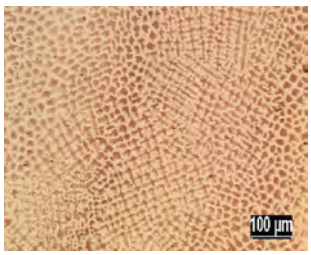

Fig. 2. **GTAW region, Beraha III etched**

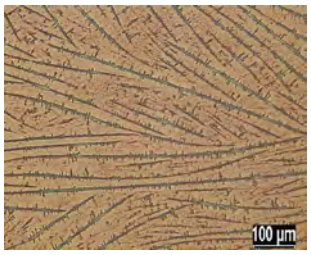

Fig. 3. **Filler metal rod, Beraha III etched**

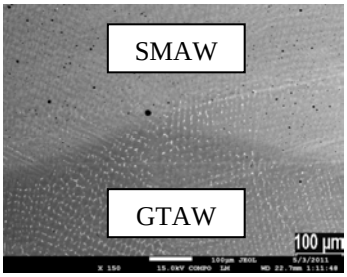

Fig. 4. **SEM micrograph of SMAW / GTAW regions**

Table II
Chemical composition of large inclusion, [wt. %]

O	Al	Ti	Cr	Mn
45.5	32.2	3.5	12.1	2.2

The Charpy impact test was conducted on samples from different areas of the weld. The 2 mm V notches of samples were positioned to the weld metal, fusion edge and root. The orientations of the notch in the root area permitted a simultaneous fracture analysis in both weld regions (GTAW and SMAW).

The average impact energy KV, measured at room temperature on samples with different positions in the weld region, was 55 ± 4 J. This value was lower than the material standard value declared by the weld wire supplier.

Following the Charpy impact test, fracture surfaces were analyzed. The priority was given to a sample specially oriented to the weld notch region. The fracture surface typical for GTAW and SMAW regions is documented in Fig. 5. Fractographic analyses revealed an increased number of oxide particles in GTAW region in accordance to the microstructural evaluation.

The surface morphology of both weld regions indicated a predominantly ductile fracture. The dendritic arrangement of microstructure was evident. Sporadically, a brittle transgranular fracture was observed in small isolated areas. In SMAW region a large amount of particles was monitored. Predominantly, spherical inclusions with various diameters were observed. Approximately 5 % of the present particles were fine angular shaped.

Fig. 6 shows the distribution of selected chemical elements in the fracture surface. The inclusions had an oxide origin of varied chemical composition. The predominantly detected elements were Al, Mn and Ti.

The increased number of the oxide particles had negative influence on toughness[1]. The crack initiation and propagation was easier due to the presence of the described particles[2].

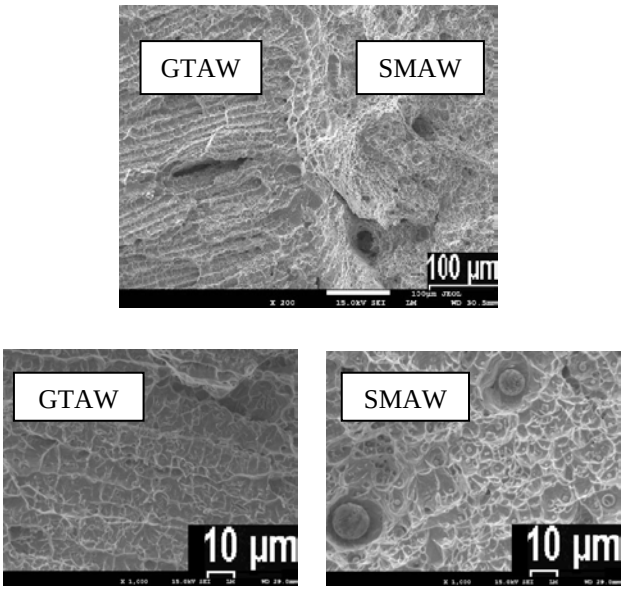

Fig. 5. **Fracture surface after Charpy impact test**

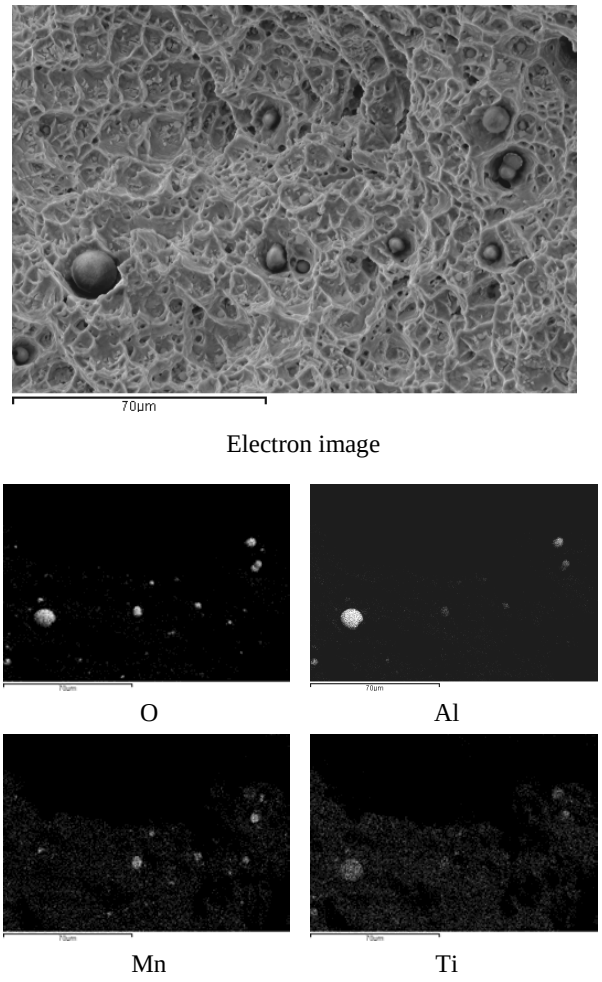

Fig. 6. **SMAW region – oxide particles, distribution of selected chemical elements**

Table III
Experiment details

Maximal load	Indentation times		
[mN]	Load [s]	Dwell [s]	Unload [s]
200	10	5	10

The standard methods for testing of mechanical properties as the Charpy impact test, hardness and microhardness measurements have not been sufficiently sensitive to indicate the difference between both monitored weld regions (GTAW and SMAW). The nanoindentation method was then used for the evaluation.

Indentation was performed in line and in grid form in both evaluated regions[3]. Parameters applied were summarized in Tab. III. Indents map of line profile measurements and corresponding indentation curves were documented in Fig. 7 (GTAW region) and Fig. 8 (SMAW region).

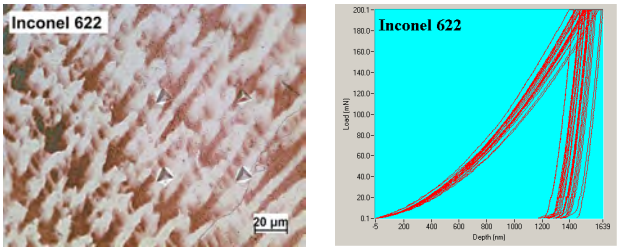

Fig. 7. **GTAW region indents and indentation curves**

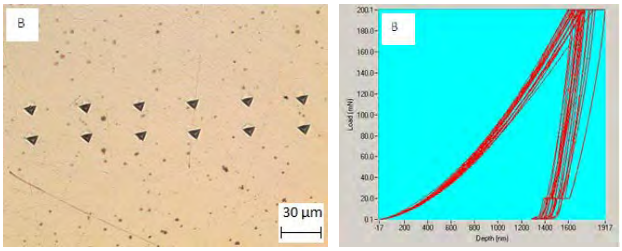

Fig. 8. **SMAW region indents and indentation curves**

Tab. IV compares the hardness of GTAW and SMAW regions. The measurement conditions have been identical (Tab. III). The hardness and reduced modulus of GTAW were lower than that of SMAW region. It was evident that the indentation plastic work of GTAW region was higher by about 12 %. It could be assumed that the GTAW matrix was more ductile than that of SMAW.

However, certain interaction has been indicated between the indenter and the particles dispersed in the matrix (see the indents map in Fig. 7 and related indentation diagrams in Fig. 8). The deviation was affected by the heterogeneity in chemical composition of the dendritic structure. As expected, interdendritic regions had slightly higher hardness values then the dendrite axis. The presence of oxide particles was observed only in the interdendritic spaces.

Table IV
Results of nanohardness measurement

Region	Hardness	Reduced modulus	Elastic work
	[GPa]	[GPa]	[nJ]
GTAW	3.46 ± 0.23	124.36 ± 16.05	24.49 ± 3.27
SMAW	4.18 ± 0.30	201 ± 7	16.32 ± 0.55
Region	Plastic work	Maximal depth	Contact depth
	[nJ]	[nm]	[nm]
GTAW	114.01 ± 6.06	1730 ± 67	1587 ± 58
SMAW	100.17 ± 4.04	1533 ± 53	1438 ± 54

4. Conclusions

It was demonstrated that the weld microstructure contained hard particles, mostly of an oxide origin. The volume fraction of these particles was significantly higher in the SMAW than in GTAW region of the weld. Nanoindentation proved a high hardness of oxide particles and the proper toughness of the matrix. As expected, the plasticity of the GTAW region was higher. An increased volume fraction of oxide particles caused a decrease of the toughness of the weld metal in SMAW region. Oxides played the role of the crack initiators and facilitated the crack propagation.

The oxide presence was probably caused by a technological discrepancy.

This paper has been supported by the CTU project: SGS number SGS10/258/OHK2/3T/12, MEYS project FRVŠ number 2610/2011, OPPA project number CZ.2.17/1.1.00/32213 and OPPK project number CZ.2.16/3.1.00/21037.

REFERENCES

1. *ASM Handbook: Volume 6: Welding, Brazing, and Soldering*, pp. 740–751, ASM International® 2004.
2. *ASM Handbook: Volume 12: Fractography*, pp. 678–692, ASM International® 2004.
3. Nohava J., Haušild P.: Chem. Listy. *104*, 360 (2010).

J. Horník, P. Hájková, E. Anisimov, and J. Rybníček *(CTU in Prague, Faculty of Mechanical Engineering, Department of Materials Engineering, ICDAM, Prague, Czech Republic):* **Causes of Inconel 622 Weld Cracking**

Problems related to the welding of duplex steel with Ni alloy Inconel 622 are described. The GTAW welding procedure was used for the root and SMAW of the main weld. The weldment was characterized by a tendency of the weld metal to cracking in the SMAW region during the bend test. Microstructural analysis of the weld was performed and supplemented by nanohardness measurements. The Charpy impact test and fractographic analysis were carried out. Microstructure of the weld exhibited the presence of hard particles, mostly of an oxide region in SMAW region. Their presence had a negative effect on the ductility of the weld. The oxide presence was probably caused by a technological discrepancy.

AN OPTICAL SENSOR FOR LOCAL STRAIN MEASURING OF AN OBJECT BY MEANS OF A SPECKLE CORRELATION METHOD

PAVEL HORVÁTH[a], PETR ŠMÍD[b], MIROSLAV HRABOVSKÝ[a], and IVANA HAMAROVÁ[b]

[a] *Palacky University, Faculty of Science, Regional Centre of Advanced Technologies and Materials, Joint Laboratory of Optics of Palacky University and Institute of Physics of the Academy of Sciences of the Czech Republic, 17. listopadu 12, Olomouc, 771 46,* [b] *Institute of Physics of the Academy of Sciences of the Czech Republic, Joint Laboratory of Optics of Palacky University and Institute of Physics of the Academy of Sciences of the Czech Republic, 17. listopadu 12, Olomouc, 771 46, Czech Republic*
pavel.horvath@upol.cz

Keywords: non-contact measurement, strain, speckle, speckle correlation

1. Introduction

Measuring of object deformation is a frequent measurement used in mechanics. There are several methods allowing to obtain the needed information as strain or stress. However, most of them are based on close contact of a measuring tool with a measured object what often leads into destructive effect. Optical methods offer one of suitable solutions since light in optical region can serve as a non-destructive agent.

Speckle interferometry[1] forms an important group of the optical methods. Speckle is the peculiar appearance, which is generated, if an object with a rough surface is illuminated by a coherent beam. The speckle interferometry utilizes optical interferometers for the coherent addition of speckle fields diffracted by object and reference fields. This method have achieved intense progress during last decades in consequence of development of modern optoelectronic components and converted to their electronic or digital modification[2–4].

Currently correlation methods[5–11] join the speckle interferometry in the speckle metrology. In these methods linear or matrix detectors detect the speckle field generated by the object under investigation during its deformation. Their output signals are then mutually correlated by means of computer or hardware correlators. The results of correlation enable to get the information about behaviour of deformation of the object.

The measurement method presented in this paper uses the same principle as aforementioned correlation methods. Deformation of an elementary area of rough surface of an object responsible for the speckle character of reflected coherent light in a general way results in shift of the corresponding speckle pattern in the detection plane and partial modification of its chaotic structure. The position of the global maximum of a cross-correlation function of two intensity sets (speckle patterns) recorded before and after the surface deformation determine the speckle pattern displacement. The displacement is then used for evaluation of small deformation tensor components describing the deformation state of the elementary area of object's surface. The theoretical study of speckle displacement and decorrelation in the diffraction and image fields was made by Yamaguchi[12].

The aim of this paper is to present a design of an optical sensor and its experimental verification in non-contact detection and quantitative evaluations of a local strain of a rubber specimen used in tire manufacturing by a speckle correlation method.

2. Theory

For measurement of strain ε_{xx} of a surface element of an object it is convenient to use an optical set-up with the symmetrical arrangement of two detection planes and one illumination source (see Fig. 1). Observation directions form the angles $-\theta_o$ and θ_o with illumination direction. There are placed thin lenses with identical focal lengths f' between the object and detectors to magnify the speckle field.

The equation[13, 14] for evaluation of ε_{xx} is valid for this case of the sensor arrangement

$$\Delta A_X = A_X(\theta_s, \theta_o) - A_X(\theta_s, -\theta_o) = 2\varepsilon_{xx} \tan\theta_o \left(-L_c \frac{L'_p - f'}{f'} + L'_p \right), \quad (1)$$

where ΔA_X represents the difference between the displacements of speckle fields detected in the planes (X_1,Y_1) and (X_2,Y_2), L_c and L'_p are the distances of the thin lens from the object plane and detection plane, respectively.

Knowledge of strain ε_{xx} enables to state local stress σ_{xx} according to the known relation $\sigma_{xx} = E\varepsilon_{xx}$ valid in the case of one axis elastic tension of the object, where E is modulus of elasticity of isotropic material of the object.

In general case of study of object's surface stress state it is necessary to carry out the measurement of specific elongation in three different directions in the plane of object's surface. There is a direct analogy with the usage of resistance strain gauges and the term of an optical speckle strain gauge appears[14].

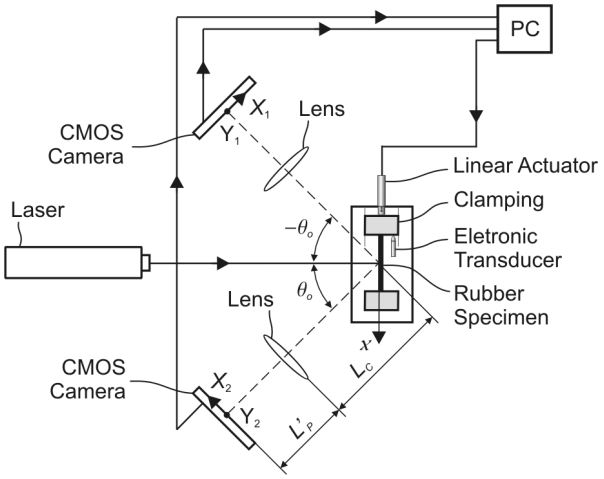

Fig. 1. **Designed optical sensor for measuring of the object´s strain ε_{xx} (or local strain)**

3. Description of an optical sensor

There is a designed optical sensor for measuring of strain ε_{xx} in *x*-axis outlined in Fig. 1 and Fig. 2.

A He-Ne laser is chosen as a source of coherent light. Its beam is directed perpendicularly on the surface of a measured object. The investigated object is represented by a rubber specimen. It is a specific type of black rubber that is convenient for tire manufacturing. The specimen has form of a thin tape that is 118.3 mm long and 6.6 mm wide. Its thickness is 2.1 mm. The specimen is firmly fastened at its both ends into two clamping jaws. One is static and the other movable. The position of the adjustable clamping jaw is actuated by means of an electronic linear actuator. Therefore specimen loading or unloading can be controlled very exactly. Besides an electronic transducer touching the movable jaw supervises the jaw displacement.

The reflected speckle field is captured with a pair of monochrome cameras containing matrix CMOS image. The sensors have resolution of 1288 × 1032 pixels with pixel size of 7.5 × 7.5 μm^2 and bit depth of 8 bits per pixel. Since for the measurement by the speckle correlation method only linear detectors are sufficient the scanning area of the CMOS detectors is reduced in order to obtain only one row from the whole matrix.

Geometrical and optical parameters of the designed sensor are $L'_p = 181$ mm, $L_c = 111$ mm, $\theta_o = 45^o$, $f' = 19.96$ mm.

4. Measurement process

The measurement process is divided into two stages. First the electronic linear actuator elongates the rubber specimen with required constant loading rate and accuracy of 0.1 μm. The maximum deformation is $2100 \cdot 10^{-6}$. This value corresponds to linear expansion of 200 μm while the initial pitch of the jaws is 95 300 μm. In the second stage the linear actuator unloads the rubber specimen into the reference state. The initial pitch of the jaws is 95 500 μm and the unloading actuator displacement is 200 μm. The unloading rate is the same as the one used in the first stage.

During each stage of the measurement process both cameras capture $N + 1$ times the developed speckle field with defined capturing frequency. So that N measurement steps are obtained in each stage of the measurement process. The selection of the constant rate of the specimen loading/unloading and the capturing frequency defines value of strain ε_{xx} for each measurement step. Then the maximum deformation in the corresponding stage of the measurement process is given as $N\varepsilon_{xx}$.

In our case of measurement both the loading and unloading rate is 7.6 μm/s and the capturing frequency is 4 Hz. Exposure time is 40 ms. With these conditions the strain $\varepsilon_{xx} = 20 \cdot 10^{-6}$ is achieved for each of 105 measurement steps in every stage of the measurement process over the maximum deformation $2100 \cdot 10^{-6}$.

Each capture of the developed speckle field is represented by a set of 8-bit numbers. The 8-bit number represents an intensity level of light detected by the corresponding pixel of the row of the CMOS matrix. Obtained sets are numerically processed in the PC by a program that determines the maximum position of the normalized cross-correlation function and next the deformation components ε_{xx} are evaluated using Eq. (*1*).

5. Experimental results

The example of reached results of measurement is plotted into a graph shown in Fig. 3. Since the measurement process consists of two stages there are two lines in the graph. A straight line corresponds to the

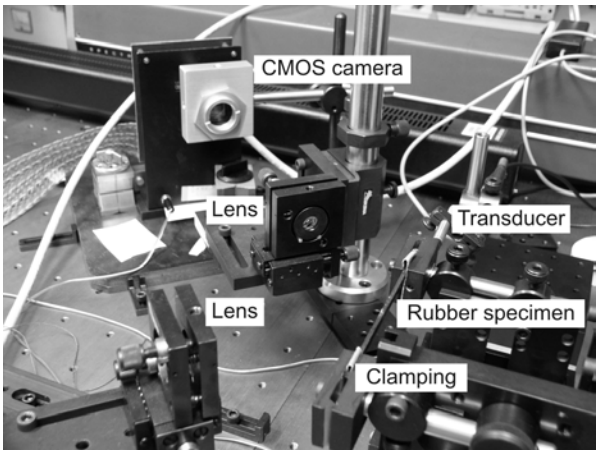

Fig. 2. **Close view on a part of the measuring sensor (clamping jaws with rubber specimen, pair of lenses and a camera)**

specimen elongation. A dashed line represents the results of the following specimen unloading. On the horizontal axis there is strain $\Delta l / l$ measured by means of the electronic transducer where Δl is longitudinal increment to the initial specimen length l determined by the jaws pitch. On the vertical axis there are results of strain ε_{xx} obtained by means of the presented speckle correlation method.

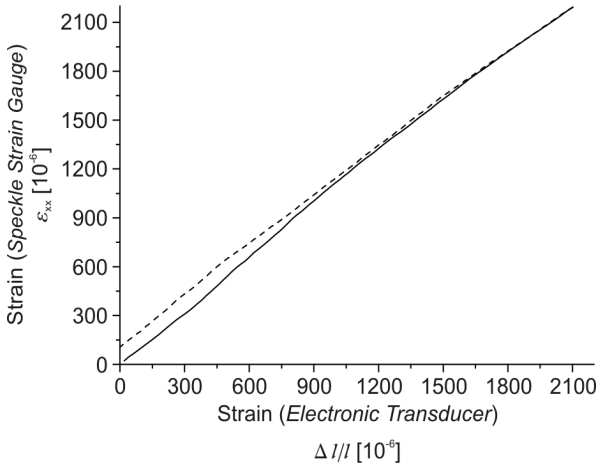

Fig. 3. **Strain ε_{xx} of the rubber specimen obtained by means of the presented speckle strain gauge plotted as a function of strain $\Delta l / l$ determined by means of the electronic transducer. A straight line corresponds to elongation of the rubber specimen under investigation. A dashed line represents the results of the displacement during unloading**

6. Conclusion and discussion

The paper shows good agreement of results obtained with the electromechanical and optical measurement instruments. In the ideal case the results should be the same and both lines in Fig. 3 (the solid line and the dashed one) should merge into one line with the slope equaled to unity. However presented real case shows small difference from the ideal case. The results obtained using the speckle strain gauge differ from those obtained with electronic transducer no more than 5 %. Hysteresis in the results can be related to the measurement in real time and to the expected inertia of the rubber specimen during its unloading.

The sensor has advantages: measurement is non-contact and non-destructive, sensitivity and accuracy of measurement is defined through geometrical and optical parameters of the sensor and measurement runs in quasi-real time. On the contrary there are limiting factors of the sensor: source of coherent light needs to be used and low level of background light has to be secured because of the reason of use of CMOS (CCD) cameras.

The supports of the grant of the Academy of Sciences of the Czech Republic (No. KAN301370701) and the grant of the Ministry of Education, Youth and Sports of the Czech Republic (No. LG11044) are acknowledged.

REFERENCES

1. Jones R., Wykes C.: *Holographic and speckle interferometry*, 2nd ed. Cambridge University Press, Bristol 1989.
2. Rastogi P. K. (ed.): *Digital Speckle Pattern Interferometry and Related Techniques*. J. Wiley, Chichester 2001.
3. Sjödahl M.: Opt. Lasers Eng. *29*,125 (1998).
4. Lanza di Scalea F., Hong S. S., Cloud G. L.: Exp. Mech. *38*, 55 (1998).
5. Peters W. H., Ranson W. F.: Opt. Eng. *21*, 427 (1982).
6. Cheng P., Sutton M. A., Schreier H. W., McNeill S. R.: Exp. Mech. *42*, 344 (2002).
7. Zhang D., Zhang X., Cheng G.: Exp. Mech. *39*, 62 (1999).
8. Anwander M., Zagar B. G., Weis B., Weiss H.: Exp. Mech *40*, 98 (2000).
9. Amodio D., Broggiato G. B., Campana F., Newaz G. M.: Exp. Mech. *43*, 396 (2003).
10. Chen D. J., Chiang F. P.: Exp. Mech. *32*, 145 (1992).
11. Milosevic M., et al.: Chem. Listy *105*, s751 (2011).
12. Yamaguchi I.: Optica Acta *28*, 1359 (1981).
13. Horváth P., Hrabovský M., Šmíd P.: J. Mod. Opt. *51*, 725 (2004).
14. Horváth P., Šmíd P., Hrabovský M., Neumannová P.: Exp. Mech. *46*, 713 (2006).

P. Horváth[a], P. Šmíd[b], M. Hrabovský[a], and I. Hamarová[b] *([a] Palacky University, Faculty of Science, RCPTM, Joint Lab. of Optics, Olomouc, [b] Institute of Physics of the Academy of Sciences of the Czech Republic, Joint Lab. of Optics, Olomouc, Czech Republic):* **An Optical Sensor for Local Strain Measuring of an Object by Means of a Speckle Correlation Method**

The paper presents design of an optical sensor and its experimental verification for non-contact detection and quantitative evaluations of a local strain of a rubber specimen by a speckle correlation method. The presented optical method gives results comparable with the ones obtained by means of electromechanical method using electronic position transducer. Non-contact and non-destructive measuring is one of the sensor's advanteges. Next sensitivity and accuracy of measurement is defined through geometrical and optical parameters of the designed sensor and measurement runs in quasi-real time.

THE MECHANICAL PROPERTIES OF HVOF SPRAYED Cr_3C_2-25%CoNiCrAlY COATING DETERMINED BY INDENTATION

ŠÁRKA HOUDKOVÁ[a], OLGA BLÁHOVÁ[a], and MICHAELA KAŠPAROVÁ[b]

[a] University of West Bohemia, New Technologies Research Centre, Univerzitní 8, 306 14 Plzeň, [b] University of West Bohemia, Department of Material Science and Technology, Univerzitní 22, 306 14 Plzeň, Czech Republic
houdkov@ntc.zcu.cz

Keywords: HVOF, coating, CrC-based, depth sensing indentation, indentation fracture toughness

1. Introduction

The Cr_3C_2-25%CoNiCrAlY HVOF (High Velocity Oxy-Fuel) sprayed coating belongs to the group of hard-metal coatings intended for wear protection of highly mechanically and thermally stressed components. The hard-metal based HVOF coatings benefit from the combination of hard particles, embedded in tough matrix. While the hard particles ensure the high hardness, the tough matrix is responsible for lowering the brittleness, usual for hard materials. Compared to WC-based, the CrC-based coatings have lower inner cohesion, thanks to the lower bonding of Cr_3C_2 grains into the metallic matrix, typically found in coatings of this composition[1]. On the other hand, they offer the resistance to high temperatures due to the content of Cr in the carbides and matrix. Two CrC-based types of cermets are commercially available: CrC in NiCr matrix and CrC in CoNiCrAlY matrix. The used CoNiCrAlY matrix offers better sliding properties and thermal resistance.

In the case of thermally sprayed coatings, the quality and properties of coatings are strongly influenced by spraying parameters. The not optimal choice of parameters can significantly deteriorate the qualities of sprayed materials.

The most common way of coatings evaluation is the microstructure analyses (presence of tensile or adhesion cracks, amount of porosity, oxides, shape of individual splats), surface hardness (HR15N) measurements and microhardnes (HV0.3) measurements. It is usually sufficient for confirmation of coatings quality.

In the paper, the results of measurement of coating hardness and elastic modulus by continuous stiffness measurement (CSM) method and Vickers indentation fracture toughness (IFT) of Cr_3C_2-25%CoNiCrAlY are presented. The results are compared with the results of previously measured Cr_3C_2-25%NiCr coating. From the comparison, the deterioration of Cr_3C_2-25%CoNiCrAlY coating cohesive strength due to used parameters are apparent, even if the coating microstructure and surface hardness measurement does not show any imperfections. The lower coatings cohesion became evident analyzing the results of corrosion and abrasion wear tests.

2. Experimental

The HVOF coatings were sprayed by the HVOF TAFA JP5000 spraying equipment onto a grid blasted steel surface in Výzkumný a zkušební ústav Pzeň, s.r.o., using the standard spraying procedure. While the spraying parameters for Cr_3C_2-25%NiCr were previously optimized[2], the Cr_3C_2-25%CoNiCrAlY coating was sprayed by the same spraying parameters. The thickness of the coatings varied from 350 to 400 μm. The cross sections of the samples, embedded in an epoxy resin, were mechanically grinded and polished using the Struers automatic polishing machine.

The instrumented microhardness and Young's elastic modulus in dependence on the depth of indentation was measured by the MTS Nanoindentor. For each coating, more than 50 measurements were done. The methodology, described in ref.[3] was used for determination of properties of carbides, matrix and coatings.

The superficial coating's hardness was measured on the as-sprayed coating surface by HR15N method to avoid the influence of the substrate. For the IFT measurements, the CSEM Scratch Tester, equipped with the Vickers indenter, was used. The indentations in to the coatings cross sections were done using 25, 50, 75, 100, 125, 150, 175 and 200 N loads, for each load 16–20 indents were made in dependence on their size. The space between the individual indents equaled at least 3 indents diagonal to avoid their mutual affecting. The methodology, recommended by Chicot[4] was used to determine the value of K_{Ic}. The equation of Chicot[4] enables to incorporate the Meyer's index, characterizing the Indentation Size Effect, in to the equation for K_{Ic}, and exclude the Indentation size effect from the IFT evaluation.

The lengths of indents diagonals, as well as the lengths of cracks (Fig. 1), were measured by NICON EPIPHOT 200 microscope with software LUCIA. For the K_{Ic} calculations, the equation proposed by Chicot[4] was used:

The E/H ratio used in in the Eq. (*1*) was determined

$$K_{Ic(M-M)} = (0{,}0074 - 0{,}0043q) f\left(\frac{E}{H_v}\right) \frac{L}{a^q c^{1,5-q}} \qquad (1)$$

as an average value of the E/H ratio in the range defined from the depth of indentation 2–8.5 μm.

The wear tests were realized according to ASTM G-65 – Dry sand rubber wheel test (DSRW)[5]. The wear rate K_{abr} [mm^3/m] was calculated from measured volume loss

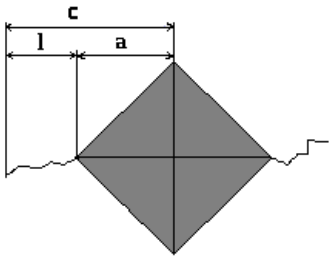

Fig. 1. **Schematic picture of the Vickers indent**

of the coatings material and the length of abrasive distance.

2. Results and discussion

The results of instrumented hardness and Young's elastic modulus of the hard particles, matrix and coatings is shown in the Fig. 2 and Fig. 3 and summarized in the Table I.

The H and E values of Cr-based carbides, embedded

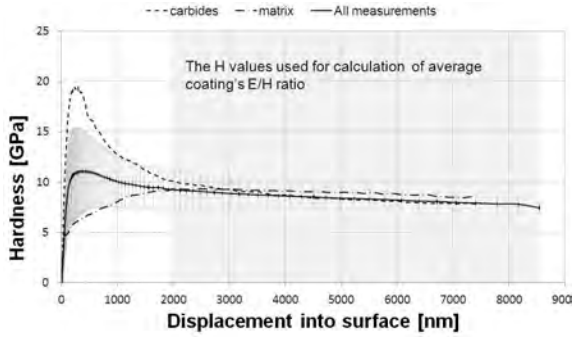

Fig. 2. **Cr_3C_2-25%CoNiCrAlY hardness values in dependence on indentation depth**

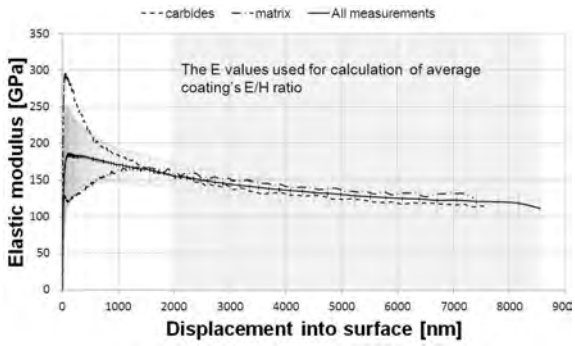

Fig. 3. **Cr_3C_2-25%CoNiCrAlY Young's elastic modulus values in dependance on indentation depth**

Table I
Hardness and Young's elastic modulus of the CrC-based coatings

	CrC-25% CoNiCrAlY	CrC- 25% NiCr[3]
H carbides [GPa]	19.5 ± 1.7	30.2 ± 0.8
E carbides [GPa]	293 ± 58	398 ± 7
H matrix [GPa]	9.3 ±1.1	10.7 ± 1.2
E matrix [GPa]	167 ± 13	280 ± 47
H coating [GPa]	8.5 ± 0.4	15.1 ± 1.2
E coating [GPa]	135 ± 12	259 ± 26

in 25%CoNiCrAlY matrix is significantly lower compare to the values, measured for CrC-based carbides in 25% NiCr matrix (published elsewhere[3,6]).

This effect can be caused by not sufficient amount of measurement in the case of Cr_3C_2-25%CoNiCrAlY coating. But with respect to the previous experiences with measurements of coatings with comparable hard particles size the set of 60 measurements is sufficient to hit several of them.

The other explanation can be found in coating worse inner cohesion, indicated in particular by the IFT measurements.

The results of the IFT measurements are shown in the Fig. 4 and Fig. 5.

In the Fig. 4, the K_{Ic} values calculated according to formula Chicot[4] for Palmqvist cracks mode (P), Radian-median cracks mode (R-M) and mixed cracks mode are shown in dependence on used indentation load. It can be seen, that while for Palmqvist cracks mode and Radian-median cracks mode formulas the indentation size effect (ISE) is significant, it is successfully excluded using the formula for mixed cracks mode proposed by Chicot[4].

In the Fig. 5 the comparison between K_{Ic} of Cr_3C_2-25%CoNiCrAlY and Cr_3C_2-25%NiCr coating is displayed. The average value of K_{Ic} was calculated to be 0.395 ± 0.045 for Cr_3C_2-25%CoNiCrAlY, while for Cr_3C_2-25% NiCr it was 0.763 ± 0.059.

The difference in the toughness of two coatings can be seen also from the measured length of cracs. In Fig. 6 and 7, the dependence of cracks length on the indentation load is demonstrated for Cr_3C_2-25%CoNiCrAlY and Cr_3C_2 -25%NiCr resp. In the Ponton-Rowlings work[7], the Palmqvist and Radial-median cracking mode was recognized according to ratio c/a (c/a < 2.8 for Palmqvist cracks and c/a > 2.8 for Radial-median cracks). The slopes of the length of the crack – load of indentation dependencies measured in this work confirm the Ponton – Rowling rule. The tougher Cr_3C_2-25%NiCr coating reached the transition between the Palmqvist and Radial-median cracks mode at higher load, than the coating with lower inner cohesion. The transition between the two cracks mode in the material in dependence on used load was described by Rios[8]. For thermally sprayed coatings it was observed in Lima's

work[9]. The WC-12%Co coating was found to have the transition load between Palmqvist and Radian-median cracks load about 150 N.

The transition between the Palmqvist and Radial-median crack mode is characterized by a significant increase of cracks length. The sudden decrease of K_{Ic} value calculated according to the formula for Palmqvist crack mode is induced by the increase of cracks length. For the K_{Ic} value calculated according to the formula for Radial-median crack mode the decrease is less pronounced, while it has no influence on the K_{Ic} value calculated according to the Chicot formula for the mixed crack mode.

The Dry sand rubber wheel wear test according to

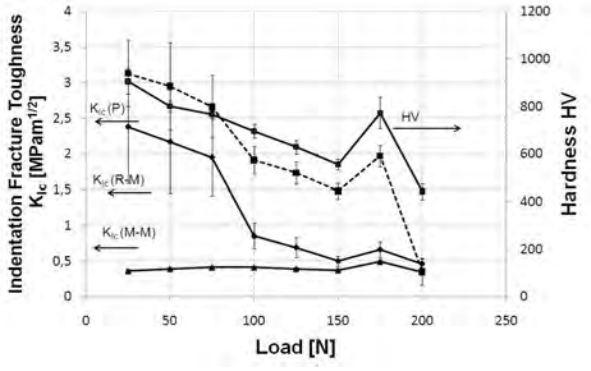

Fig. 4. **The dependence of HV and K_{Ic} on the indentation load for Cr_3C_2-25%NiCr coating**

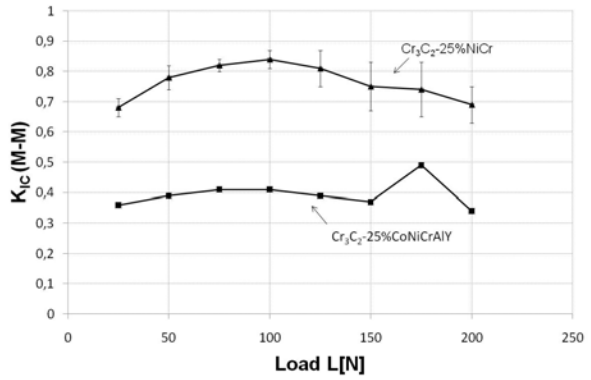

Fig. 5. **The dependence of K_{Ic} on the indentation load for Cr_3C_2-25%CoNiCrAlY and for Cr_3C_2-25%NiCr coating**

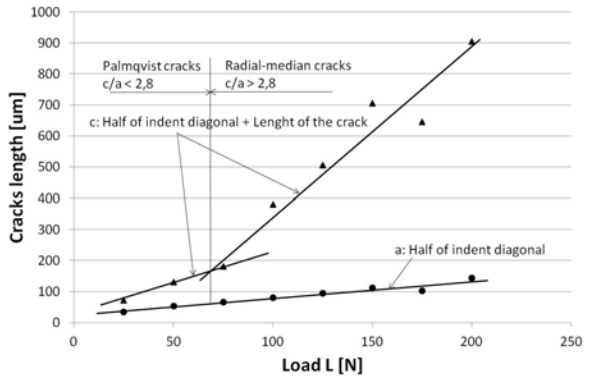

Fig. 6. **The transition between Palmqvist and radial-median cracking mode for Cr_3C_2-25%CoNiCrAlY coating**

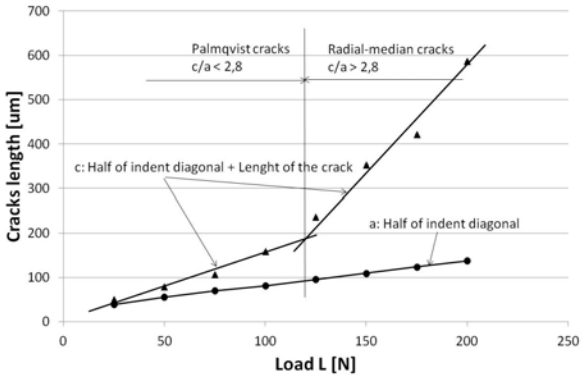

Fig. 7. **The transition between Palmqvist and radial-median cracking mode for Cr_3C_2-25%NiCr coating**

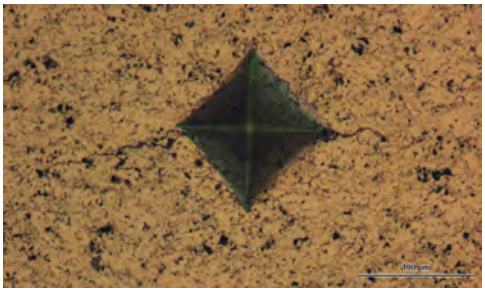

Fig. 8. **The Vickers indent in Cr_3C_2-25%CoNiCrAlY coating made at 75 N**

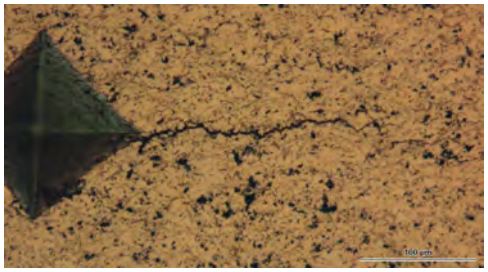

Fig. 9. **The Vickers indent in Cr_3C_2-25%CoNiCrAlY coating made at 100 N**

ASTM G-65 showed the wear rate 0.01 mm^3/m for Cr_3C_2-25%CoNiCrAlY and 0.08 mm^3/m for Cr_3C_2-25%NiCr. For the abrasive wear, the hardness and microhardness of material is the crucial property. The fracture toughness does not play such a significant role in the case of abrasive wear, but is essential in erosive and cavitation conditions[10].

In our case, the superficial hardness HR15N was measured to be 85.3 ± 0.9 for Cr_3C_2-25%CoNiCrAlY and 84.0 ± 0.5 for Cr_3C_2-25%NiCr resp. In contradiction to that, the measured microhardness HV0.3 was 848 ± 30 for Cr_3C_2-25%CoNiCrAlY and 1030 ± 114 for Cr_3C_2-25% NiCr resp.

The higher microhardness and fracture toughness of Cr_3C_2-25%NiCr coating is responsible for its better abrasive wear resistance.

In the Fig. 10, the appearance of the Cr_3C_2-25% CoNiCrAlY and Cr_3C_2-25%NiCr after the 150 h exposition to the steam environment (550°C, 245 bar) can be seen.

It is obvious, that the corrosion of Cr_3C_2-25% CoNiCrAlY is much more pronounced compare to Cr_3C_2-25%NiCr coating, although the CoNiCrAlY was expected to increase the corrosion resistance of CrC-based coating. The poor corrosion resistance is believed to be caused by coatings low intersplat cohesion.

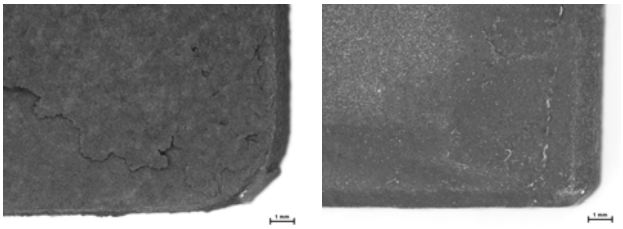

a b

Fig. 10. **The corroded a)Cr_3C_2-25%CoNiCrAlY and b)Cr_3C_2-25%NiCr coating**

3. Conclusions

The indentation test measurements pointed to the necessity of optimization process of spraying parameters for Cr_3C_2-25%CoNiCrAlY. The parameters, successfully used for Cr_3C_2-25%NiCr, have to be modified for using CoNiCrAlY matrix to reach coating's expected mechanical properties. The lower microhardness of coatings components as well as coating's itself and significantly lower fracture toughness lead to the deterioration of coating's wear and corrosion resistance.

The methodology of fracture toughness determination according to Chicot's mixed cracks mode excludes the indentation size effect, and enables to compare the values measured at different load. More to that, it enables do determine the load, representing the transition between the Palmqvist and Radial-median cracks mode.On the other hand, it requires creating and measuring a big amount of indents, which although it's not experimentally demanding, is time-consuming. This fact is limiting for its common, routine use in parameters optimization process.

The paper was prepared thanks to the project of Ministry of Industry and Trade of Czech Republic no. FR-TI1/273.

REFERENCES

1. Berger L.-M.: Powder Metallurgy *50*, 205 (2007).
2. Fiala P.: *PhD Thesis*, UWB, Plzen (2000).
3. Houdkova S., Blahova O., Zahalka F., Kasparova M.: J. Therm. Spray Technol., in press.
4. Chicot D., Duarte G., Tricoteaux A., Jorgowski B., Leriche A., Lasage J.: Mater. Sci. Eng. A *257*, 65 (2009).
5. ASTM G 65-00, Standard Test Method for Measuring Abrasion Using the Dry Sand/Rubber Wheel Apparatus, ASTM International, USA (2000).
6. Houdková Š., Bláhová O., Zahálka F.: Chem. Listy *103*, 318 (2009).
7. Ponton C. B., Rawlings R. D.: Mater. Sci. Technol. *5*, 865 (1989).
8. Rios C. T., Coelho A. A., Batista M. C., Caram R.: J. Alloys Compd. *479*, 229 (2009).
9. Lima M. M., Godoy C., Avelar-Balista J. C., Modenesi P. J.: Mater. Sci. Eng. A *337*, 337 (2003).
10. Lima M. M., Godoy C., Modenesi P. J., Avelar-Balista, J. C., Davison A., Mattews A.: Surf. Coat. Technol. *177-178*, 489 (2004).

Š. Houdková, O. Bláhová, and M. Kašparová *(University of West Bohemia):* **The Mechanical Properties of HVOF Sprayed Cr_3C_2-25%CoNiCrAlY Coating Determined by Indentation**

In the paper, the experimental evaluation of basic mechanical properties such as hardness, Young elastic modulus and fracture toughness of HVOF sprayed Cr_3C_2-25% CoNiCrAlY coating are presented. The continuous stiffness measurement method was used to determine the coatings hardness and Young elastic modulus of single microstructure phases as well as the composite properties. The Vickers indentation with high loads was then used to evaluate the coatings indentation fracture toughness. The methodology of Chicot was used to calculate the indentation fracture toughness independently on used load, excluding the ISE effect.

The measured results are compared with previously determined behavior of other CrC-based coating. Compared to them, the Cr_3C_2-25%CoNiCrAlY coating shown poor results considering the coating microstructure, cohesion strength and hard particle instrumented indentation hardness, but not the superficial hardness and overall coating microhardness. The not optimal spraying parameters were indentified to be responsible for the deteriorated coating properties.

EFFECT OF FINE CLAY FRACTION ON FUNCTIONAL PROPERTIES OF VITREOUS ENAMEL COATINGS

KAMILA HRABOVSKÁ[a,c], JITKA PODJUKLOVÁ[b], KARLA BARČOVÁ[a], ONDŘEJ ŽIVOTSKÝ[a], IVO ŠTĚPÁNEK[d], VRATISLAV BÁRTEK[b], TOMÁŠ LANÍK[b], PETR ŠRUBAŘ[b], SYLVIE KOPAŇÁKOVÁ[b], and KATEŘINA SUCHÁNKOVÁ[b]

[a] Institute of Physics, [b] Faculty of mechanical Engineering [c] RMTVC-606, VŠB -Technical University of Ostrava, 17. listopadu 15, 708 33 Ostrava Poruba, [d] Faculty of mechanical Engineering , University of West Bohemia in Pilsen, Univerzitní 8, 306 14 Plzen, Czech Republic kamila.hrabovska@vsb.cz

Keywords: coating, clay, glass, nano indentation test

1. Introduction

Vitreous enamels are glazes formed on a metallic undercoat by burning at temperature exceeding 800 °C (ref.[1–4]). Final brittle-fracture properties of the coatings are dependent on the structure, texture and chemical composition. Clay is one of the most important inorganic components of enamel slurry used in the technique of wet enamel coating. The addition of clay in suspension prevents sedimentation of particles milled glassy frit. The resulting quality of the coating is influenced by the use of components with different particle size. The main goal of this paper is to compare brittle-fracture properties of vitreous enamel coatings made by using commonly-dimensioned and nano-dimensioned inorganic particles.

2. Sample preparation

For experimental testing, as a substrate was used steel plate Kosmalt E 300T (produced by U.S. Steel Košice), thickness 3 mm, with the following chemical composition (wt.%): C: 0.041; Si: 0.02; S: 0.007; N: 0.006; Mn: 0.241; P: 0.010; Al: 0.052; Ti: 0.067; Cr: 0.023; Mo: 0.005; V: 0.005). The surface of hot-rolled steel plate was treated by mechanical shot blasting to obtain the surface cleanliness of Sa 2.5 (ČSN EN ISO 12944-4 Paints and varnishes – Corrosion protection of steel structures by protective paint systems – Part 4: Types of surface and surface preparation) and degreased for 5 minutes in the degreasing alkali liquid Simple Green (pH 9.4) with the concentration 1:10. The 24 hours-old enamel slurry was applied on degreased steel substrate by pneumatic spraying, dried at the temperature 100 °C for 5 minutes, and subsequently burned at the temperature 820 °C for 8 minutes. Finally the samples were cooled in air at room temperature. In accordance to the colour of enamel slurry two types of enamels were distinguished: the grey under-coat and the green top-coat. Density of both enamels is 1400 kg m^{-3} and main chemical composition (wt.%): quartz ground: 25; clay MIC: 8; boric acid: 0.4; Sb_2O_3: 0.3; K_2CO_3: 0.05; $NaNO_2$: 0.15; colouring pingments:10,1 and water: 56. Undercoat enamel layer forms the function interlayer in enamel-metal system. Increasing content of elements (Si, Ni, Ca, K …) causes improving adhesion of glassy phase to the substrate and strongly influences a surface design of final product. MIC clay is a valuable kind of clay and has a quite favourable plasticity and it is suitable for the enameller's purposes. Chemical composition of the MIC Clay (wt.%): mineralogical pure clay: 83.5; admixtures: feldspar: 8; silica from feldspar 8.5 (of which SiO_2: 60; Al_2O_3: min 30; Fe_2O_3: max 3; TiO_2 : max 1.5, CaO: max. 0.2; MgO: max. 0.4). MIC clays used for surface enamel coatings: MIC coarse clay fractions – average size of particles 15 μm, MIC fine clay fraction – average size of particles 1.85 μm with a 1D dimension of 400 nm. Fine clay had been prepared using jet vertical mill STURTEVANT. The enamel slurry was applied on steel substrate after mechanical shot blasting and degreasing processes. The thickness of both layers of enamel coatings (under-coat and top-coat) is 200 μm. Sample 1 is the substrate covering by grey undercoat with MIC coarse clay fractions. Sample 2 is the substrate covering by grey under-coat with MIC fine clay fractions. Sample 3 is the substrate covering by grey undercoat and green top-coat enamel layers with MIC coarse clay fractions. Sample 4 is the substrate covering by grey under-coat and green top-coat enamel layers with MIC fine clay fractions.

3. Results and discussions

To realize these experiments number of modern experimental methods were applied kinematic viscosity (ČSN EN ISO 2431– Paints and varnishes – Determination of flow time by use of flow cups), microhardness measurements and fracture toughness, resistance to shot (shot firing test), surface roughness – (ČSN ISO 4287 Geometrical product specifications – Surface texture: Profile method – Terms, definitions and surface texture parameters), scratch, static and nano-indentation test.

On the basis of the kinematic viscosity measurements: enamel slurry with fine clay showed higher viscosity than enamel slurry with classic coarse clay (usage of fine clay at the same weight content as coarse clay), and therefore its rheological properties are different. Finally milled clay (with average size of particles 1.85 μm) shows more uniform structure and the fraction. By measuring the

brittle-fracture properties was proved a significant positive effect of fine clay fraction in enamel slurry.

For sample 2 can be observed increasing the parameter Hv and analogue fracture toughness in comparison with sample 1. Higher microhardness comparable to the fracture toughness is obvious for sample 3 (in comparison with the sample 4). Increased levels of bursting force Fp for fine-clay coatings represent an increase in enamel adhesion to the steel substrate. The most significant damage at minimal perpendicular force arises to the sample 2. There is rapid penetration of the indenter to the volume of coating. On the edges a large expansion of the cohesive crack is visible. Significant damage of coating is also evident on sample 1. Similar to sample 2 there is a great damage on the incision edges. These results correspond with the lowest values of the parameter Hv (see Table I). For samples 3 and 4 there is a distinct shift in the beginning of damage to higher loading forces. At the scratch edges the expansion and cohesion damage is lower. Sample 4 also shows significant wear of surface on the bottom of the scratch. Set of nano-indentation curves with the maximal normal loading of 200 g displays the highest nano-hardness for sample 1–610 DHV, which is related to damage during scratch indentation test. Significantly lower value of nanohardness is recognized for the sample 2–480 DHV, but in total it achieves the lowest value for sample 3–460 DHV. The higher hardness due to brittle cracking is apparent for the fourth sample. Decreasing acoustic emissivity at high perpendicular forces can be seen for sample 1. This corresponds to deeper penetration into the enamel volume. The significant stress generation occurs deep in the volume of the coating, which corresponds to the morphology of the crack. Increase of acoustic emission (at high perpendicular forces) for sample 3 corresponds to a slower rate of damage in the morphology of the rift.

Table I
Average values of kinematic viscosity, microhardness, fracture toughness, bursting force by the shot firing test, nanohardness and surface roughness of the vitreous enamel (Ra, Rq, Rt parameters from CSN ISO 4287)

	Sample 1	Sample 2	Sample 3	Sample 4
Kinematic viscosity [m^2s^{-1}]	5.10^{-6}	60.10^{-6}	10.10^{-6}	$80.\ 10^{-6}$
$HV_{0.1}$ [MPa]	4042	4227	5136	4376
K_{IC} [MPa $m^{1/2}$]	0.88	0.87	1.01	1.04
Bursting force Fp [N]	50	55	50	70
Nanohardness	610 DHV	480 DHV	460 DHV	530 DHV
Surface Roughness [μm]	Ra =1.02	Ra = 0.87	Ra =0.56	Ra = 0.52
	Rq = 1.31	Rq = 1.08	Rq=0.71	Rq= 0.67
	Rt =25.75	Rt =13.64	Rt =15.21	Rt =16.42

4. Conclusion

The use of clay with different particle size affects the cohesive and adhesive degradation of metal – vitreous enamel coating, leading to significant changes in the deformation processes as well as the initiation of damage of the surface enamel layer. On the basis of experimental tests positive affect of fine clay onto the brittle-fracture and functional properties of the coat have been shown. Tendency to defect formation is also substantially reduced. These benefits can be used in practice especially in assembling of enameled segments.

Acknowledgments – MŠMT ME 08083, MSM6198910016, SP2012/78, CZ.1.05/2.1.00/01.0040.

REFERENCES

1. Barcova K., Mashlan M., Zboril R., Filip J., Podjuklova J., Hrabovska K., Schaaf P.: Surf. Coat. Technol. *201*, 1836 (2006).
2. Barcova K., Zboril R., Mashlan M., Jiraskova Y., Filip J., Lunacek J., Hrabovska K.: Surf. Interface Anal. *38*, 413 (2006).
3. Hrabovská K., Podjuklová J., Barčová K., Dobrovodská L., Pelikánová K.: Solid State Phenom. *147-149*, 856 (2009).
4. Hrabovská K., Podjuklová J., Životský O., Barčová K., Štěpánek I., Bártek V., Laník T.: Chem. Listy *105*, s739 (2011).

K. Hrabovská[a,c], J. Podjuklová[b], K. Barčová[a], O. Životský[a], I. Štěpánek[d], V. Bártek[b], T. Laník[b], P. Šrubař[b], S. Kopaňáková[b], and K. Suchánková[b]
([a] Institute of Physics, [b] Faculty of mechanical Engineering, [c] RMTVC-606, VŠB - Technical University of Ostrava, [d] Faculty of mechanical Engineering , University of West Bohemia in Pilsen, Czech Republic): **Effect of Fine Clay Fraction on Functional Properties of Vitreous Enamel Coatings**

Final brittle-fracture properties of vitreous enamel coating are dependent on its structure, texture and chemical composition. The most important inorganic components during production of this coating are clay and fritted glass. Usage of various sizes of these components influences final quality of the coating. The main goal of this thesis was to compare functional properties of vitreous enamel coatings made by using commonly-dimensioned and nano-dimensioned particles.

PARTICLE SWARM OPTIMIZATION FOR AUTOMATIC HARDNESS MEASUREMENT

MAREK HRÚZ[a], JAN ŠIROKÝ[a], and DAVID MAŇAS[b]

[a] University of West Bohemia, Faculty of Applied Sciences, Department of Cybernetics, [b] Tomas Bata University in Zlin, Faculty of Technology, Department of Production Engineering, Czech Republic
mhruz@kky.zcu.cz

Keywords: particle swarm optimization, hardness measurement, image processing

1. Introduction

Hardness measurement enables fast and reliable identification of low quality material and helps to prevent its use in the production process. Automatic hardness measurement can speed up the measurement process and provides repeatable results in contrast to manual measurement that is time consuming and always affected by a human factor. On the other hand, the automatic measurement often fails, when the specimen surface is not well prepared. This article introduces an algorithm that enables measurement of rough polished specimens and minimizes the effect of specimen surface properties.

2. Hardness measurement

Hardness is one of the important mechanical properties of construction materials and therefore it is very often measured in the technical practice. The main advantage of hardness tests is their easiness, repeatability and also the fact that in many cases the measurement can be performed directly on a product or on samples produced and designed for other types of mechanical tests.

Hardness can be defined as the resistance of material (surface of the material in the measured spot) against local deformation caused by pressing indenter of a specific geometrical shape at a defined load. The degree of hardness is determined by the size of the permanent plastic deformation.

Hardness tests can be divided according to different criteria: In terms of principle, we can recognize a scratch test, indentation test, impact test and rebound test. In terms of the loading force we can recognize static and dynamic tests for hardness.

The most frequent methods of measuring microhardness are static methods of Brinell (ČSN EN ISO 6506), Rockwell (ČSN EN ISO 6508), Vickers (ČSN EN ISO 6507) and Knoop (ČSN EN ISO 4545). The article focuses on Vickers test.

Table I
Hardness according to Vickers – areas of testing load for metals

Ranges of testing load F [N]	Symbol of hardness	Previous marking (ISO 6507-1:1982)
$F \geq 49.03$	$HV \geq 5$	Test of hardness according to Vickers
$1.961 \leq F < 49.03$	$0.2 < HV < 5$	Test of hardness according to Vickers with low load
$0.0980 \leq F < 1.961$	$0.01<HV< 0.2$	Test of micro-hardness according to Vickers

Test of hardness according to Vickers is prescribed by European standard, for three different ranges of testing load (Tab. I).

The penetrating body – made of diamond shaped as a regular tetragonal pyramid with the square base and with preset vertex angle (136°) between opposite walls – is pushed against the surface of testing body. Then, the diagonal size of the indent left after load removal is measured (Fig. 1).

Vickers´ hardness is then expressed as the ratio of the testing load applied to indent area in form of regular tetragonal pyramid with square base and the vertex angle equal to the angle of penetrating body (136°) as:

$$HV = 0.1891 \cdot \frac{F}{d^2} \qquad (1)$$

Where HV – Hardness according to Vickers, F – Testing load in N, d – Arithmetic average of two diagonals d_1, d_2 in mm.

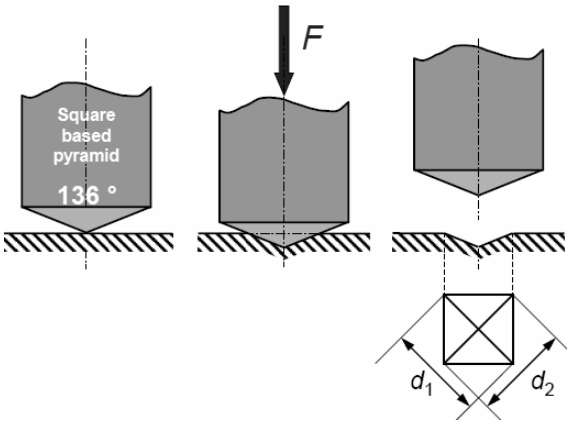

Fig. 1. **The basic principle of hardness testing according to Vickers**

Evaluated sample has to have smooth and even surface, without flakes, lubricants and foreign particles. The sample is thus prepared as a metallographic scratch pattern. Generally, the preparation is done by wet grinding and then by polishing on diamond pastes or by electropolishing. Exact method of sample preparation is chosen according to respective materials. Thickness of testing body or layer has to be at least 1.5-6 times longer than the diagonal length of the indent.

3. Automatic hardness measurement

Several different approaches to automatic hardness measurement were presented in the past. Straightforward technique of indentation vertex calculation is presented in ref[1]. It uses the least square method for the average diagonal length calculation. Key issue of the threshold determination is discussed there as well. Region growing technique is presented in ref[2]. More sophisticated method that utilizes thick line Hough transform is discussed in ref[3]. In ref[4], the hardness measurement process is divided in three steps: image preprocessing, indentation recognition and indentation measurement. Different techniques for each stage are briefly introduced. Another advanced approach that utilizes wavelet functions is discussed in ref[5,6].

The proposed algorithm is based on a parametric description of indentation. The indentation is described by the following parameters: centre of horizontal and vertical axes, horizontal and vertical diagonal length and rotation of the axes with respect to the image axes

$$\Theta = \{x, y, a, b, \varphi\} \in R^5. \qquad (2)$$

Using these parameters we are able to compute vertexes of the indentation in the frame of the image. The final edge is constructed by connecting the vertexes with lines in the proper order. In digital images the lines are composed of pixels and we will denote the set of the pixels that form the edges as E_k. The goal is to find such values of the parameters that match a processed camera image of indentation the best. Testing of all combinations of values is numerically overwhelming and therefore some of the global optimization techniques can be employed. Our article describes the usage of the particle swarm optimization.

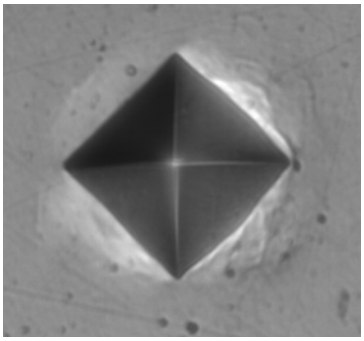

Fig. 2. **Original image of an indentation**

The first step of the algorithm is filtering of the original image that is depicted in Fig. 2. The goal is to highligth important objects in the image. In the case of hardenss measurement, we focus on filtration of indentation edges. To process the image we use a bank of filters for gradient estimation. General form of the filters' kernels which respect the diagonal direction of the indentation edges is the following

$$F_1 = \begin{bmatrix} 0 & -1 & 0 \\ -1 & 0 & 1 \\ 0 & 1 & 0 \end{bmatrix} \quad F_2 = \begin{bmatrix} 0 & -1 & 0 \\ 1 & 0 & -1 \\ 0 & 1 & 0 \end{bmatrix} \qquad (3)$$

$$F_3 = \begin{bmatrix} 0 & 1 & 0 \\ 1 & 0 & -1 \\ 0 & -1 & 0 \end{bmatrix} \quad F_4 = \begin{bmatrix} 0 & 1 & 0 \\ -1 & 0 & 1 \\ 0 & -1 & 0 \end{bmatrix}$$

The image I is filtered four times. Each time we use a different kernel F_i

$$IF_i(x, y) = (I * F\ )(x, y) = \qquad (4)$$
$$\sum_{m=-1}^{1} \sum_{n=-1}^{1} I(x-m, y-n) \cdot IF_i(m+2, n+2),$$

where $IF_i(x,y)$ can be seen as an indication of a match between the filter F_i and the image I at position (x,y). Thus, for each pixel we obtain four responses from four filters. For each pixel we choose the largest response as the approximation of the gradient magnitude (Eq. (5)). The filtered gradient image is denoted as I_g

$$I_g(x, y) = \max_i IF_i(x, y). \qquad (5)$$

In our calculations we use wider kernels which respect the character of the visual data. The result can be seen in Fig. 3. Since the image is too noisy we do not use any post processing of the gradient image to obtain thin edges. We are interested in the magnitude of the gradient. The larger the magnitude is for a pixel the larger is the certainty of the edge in the position of the pixel.

When the gradient magnitude in the image is estimated we can begin to search for the best set of the model parameters. One set of the model parameters is called a particle. We consider a constant number of particles during iterations of the algorithm. The set of particles is defined as

$$\Pi = \{x_k \in \Theta : k = 1..N\}, \qquad (6)$$

where N is the number of particles. At first, the set of particles is initialized by values that cover the parametric space reasonably, as in Fig. 4. Each particle generates an edge model of the indentation. We fit each edge model to the gradient image and we compute the sum of the magnitude of the gradient field in positions defined by the model

$$s_k = \sum_{(x,y)\in E_k} I_g(x,y). \quad (7)$$

This sum is the score s_k for the given particle. E_k is the set of coordinates of the edge defined by the particle x_k. In the next step we do the re-sampling. This means that the particles that achieved the highest score have the highest probability of being re-sampled (used in the next iteration of the algorithm). Since we use a constant number of particles we draw each particle independently from the distribution given by the particles' scores. All particles that are passed to the next iteration are shifted towards the particle that achieved the best score in the current iteration

$$x^* = \arg\max_{x_k \in \Pi} s_k \quad (8)$$

The shifting of the particle means that we compute a vector

$$v_k = x^* - x_k \quad (9)$$

and the particle in the next iteration (denoted as x_k^+) is given as

$$x_k^+ = x_k + c \cdot v_k + \sigma, \quad (10)$$

where the $c \in \langle 0;1 \rangle$ constant defines the extent of the shifting towards the best particle. A small Gaussian noise σ is added to the shift, so that the particles cover larger volumes in the parametric space.

Correspondence of particle set is evaluated by the weighted average based on the score of all particles

$$E_{weighted} = \sum_{k=1}^{N} s_k \cdot x_k. \quad (11)$$

$$S = \sum_{(x,y)\in E_{weighted}} I_g(x,y). \quad (12)$$

If the score is the highest achieved so far it is remembered as the best result. The algorithm iterates until the score of the weighted particle decreaces below a given value or the maximum number of iterations was achieved. Then the intermediate result with the highest achieved score *S* is chosen as the final result. In Fig. 5 and Fig. 6 we show specific iterations of the algorithm. The final result is shown over the original image in Fig. 7.

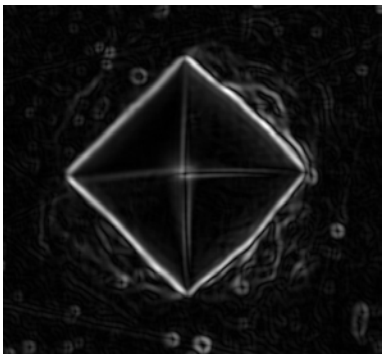

Fig. 3. **Filtered image**

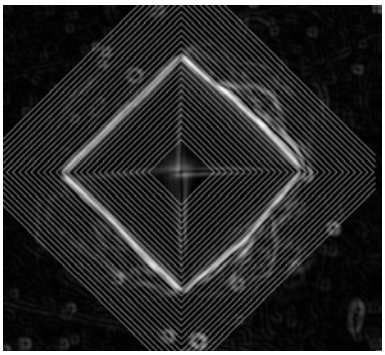

Fig. 4. **First iteration**

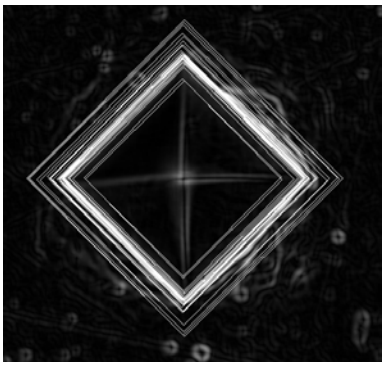

Fig. 5. **Second iteration**

4. Conclusion

A novel technique of automatic hardness measurement was described in the paper. The goal was to automatically measure the length of indentation diagonals. The algorithm is based on the particle swarm optimization. It enables to measure hardness even if the specimen is etched or rough polished. Emloyment of the automatic algorithm speeds up hardness measurement process and increases measurement repeatability.

On a standart PC (Intel® Core™ 2 Quad @ 2.83 GHz) with four CPU cores the algorithm runs ~ 0.3 sec. The algorithm is optimized for multi-core CPU.

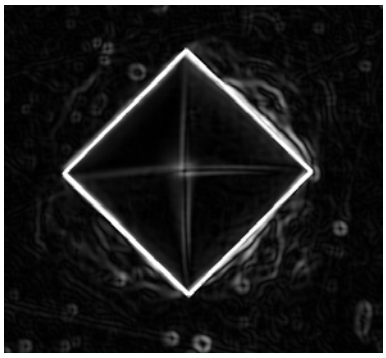

Fig. 6. **Fifth iteration**

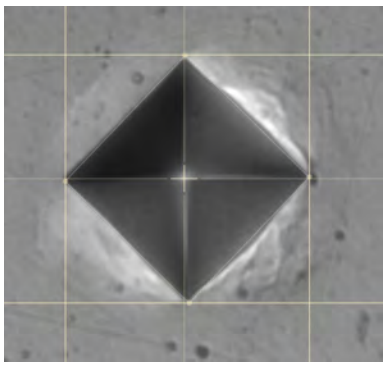

Fig. 7. **Detected indentation**

This work was supported by the grant MPO No. FR TI1/487 Development of the hardness measurement system with focus on research of the new possibilities in the area of polymer properties analysis and its application in the market.

REFERENCES

1. Sugimoto T., Kawaguchi T.: IEEE Trans. Ind. Electron. *44*, 696 (1997).
2. Filho P. P. R., Cavalcante T., de Albuquerque V. H. C., Tavares J. M. R. S.: J. Test. Eval. *38* (2010).
3. Ji Y., Xu A. W.: *2nd International Congress on Image and Signal Processing, CISP '09*, (Qiu, P. ed.), pp 1–4, (2009).
4. Mendes V. B., Leta F. R.: *Proceedings, XVII IMEKO World Congress*, pp 992–995, (2003).
5. Qu Z., Guo-Zheng, YAN, Yi Z.: Acta Metrologica Sinica, issue 3, (2005).
6. Amitay-Sadovsky E., Wagner H. D.: Polymer *39*, 2387 (1998).

M. Hrúz[a], J. Široký[a], and D. Maňas[b] ([a] *University of West Bohemia, Faculty of Applied Sciences, Department of Cybernetics,* [b] *Tomas Bata University in Zlin, Faculty of Technology, Department of Production Engineering, Czech Republic):* **Particle Swarm Optimization for Automatic Hardness Measurement**

Hardness measurement enables fast and reliable identification of low quality material and helps to prevent its use in the production process. Automatic hardness measurement can speed up the measurement process and provides repeatable results in contrast to manual measurement that is time consuming and always affected by a human factor. On the other hand, the automatic measurement often fails, when the specimen surface is not well prepared. This article introduces an algorithm that enables measurement of rough polished specimens and minimizes the effect of specimen surface properties.

MEASURING OF MECHANICAL PROPERTIES OF ELECTROCHEMICALLY DEPOSITED ZrO_2, Ce_2O_3-CeO_2 AND La_2O_3 FILMS BY NANOINDENTATION

SABINA CHERNEVA[a], DIMITAR STOYCHEV[b], and ROUMEN IANKOV[a]

[a] *Institute of Mechanics – Bulgarian Academy of Sciences, Acad. G. Bonchev str., Bl.4, 1113 Sofia, Bulgaria,*
[b] *Institute of Physical Chemistry – Bulgarian Academy of Sciences, Acad.G.Bonchev str., Bl.11, 1113 Sofia, Bulgaria*
sabina_cherneva@yahoo.com

Keywords: thin films, cerium oxide, zirconium oxide, lanthanum oxide, mechanical properties, nanoindentation

1. Introduction

Zirconia is proving an exciting novel material which is gaining in popularity due to its specific key advantages over other more traditional ceramics. It does not have the malleability of metals but does have significantly high fracture toughness. Zirconia is wear resistant and inert and can therefore be utilised in areas where traditional metallic systems would not be able to function. That's why zirconia is widely used in the oil and gas industry. In sub-sea systems where metallic systems would corrode, zirconia excels. Zirconia has great wear resistance, which, combined with its high fracture toughness makes it an ideal material for pumps and turbines. As zirconia is so hard, it is the perfect material from which to manufacture knives and blades – cutting edges remain sharp for much longer. Zirconia is also used for femoral head components in hip implants. Now it is successfully applied in dental medicine too. Zirconium dioxide is used for making single crowns and bridges with 4 elements, veneers and laboratory-made fillings. These have high aesthetic qualities because they do not have the grey metallic color that is often shown through the porcelain in metal-porcelain constructions. Zirconium constructions are distinguished by unique resistance to breakage, perfect biocompatibility, good transmittance, low heat conductivity by showing no darkish borders of the crown towards the gum; and by color stability over time.

Zirconium oxide thin films are excellent candidates for hard and protective coating applications where transparency is required. They may be used as diffusion barrier coatings in nuclear energy reactors, as protective layers on metal cutting tools[1], as insulating layers in microelectronics and in optical filters[2].

Excellent chemical stability, mechanical strength, wear resistance as well as some peculiarities of electron conductance allow zirconia layers to be used as catalysts or catalyst supports[3] in exhaust-gas purifying devices where high thermal, mechanical and corrosion stability are required.

Cerium oxide is a technologically important material with remarkable properties that is used in a number of applications such as oxygen storage – in automobile exhaust catalytic converters thanks to its ability to uptake and release oxygen under oxidizing and reducing conditions. The cause of this effect is the continuous transformation between two Ce oxides: the oxygen-rich CeO_2 and the oxygen-deficient Ce_2O_3 depending on the external oxygen concentration. Other important properties such as high dielectric constant and good epitaxy on Si, make Ce oxide a promising material for future microelectronic applications. In particular, CeO_2 is considered candidate for replacing silicon dioxide in electronic appliances[4]. Cerium oxide layers deposited on metals and alloys offer also excellent corrosion-protection against various aggressive media[5,6]. This explains the present intensive attention that is drawn to this oxide and its properties[7].

La_2O_3 is used to make optical glasses, to which it provides increased density, refractive index, and hardness. Together with oxides of tungsten, tantalum, and thorium, La_2O_3 improves the resistance of the glass to attack by alkali. La_2O_3 is an ingredient for the manufacture of piezoelectric and thermoelectric materials. Automobile exhaust-gas catalytic converters contain La_2O_3 (ref.[8]). La_2O_3 is also used in X-ray imaging intensifying screens, phosphors as well as dielectric and conductive ceramics. La_2O_3 has been examined for the oxidative coupling of methane[9].

The broad spectrum of applications of zirconium, cerium and lanthanum oxides and the fact that properties of thin films are typically very different from the properties of bulk material make investigation of properties of ZrO_2, Ce_2O_3-CeO_2 and La_2O_3 films very important.

There are many studies of their electrochemical properties, numerours SEM and XPS studies of these films[10–13], but little information is available on their mechanical properties. That's why the aim of the present work is to investigate mechanical properties of these films by means of instrumented indentation testing.

2. Theoretical

Instrumented-indentation testing (IIT) has been developed over the last decade for the purpose of probing mechanical properties of very small volumes of material. IIT is ideal for exploring mechanical properties of thin films, coatings, and surface layers. Because indents can be positioned to within about 1 micron, IIT also enables one to map the spatial distribution of surface mechanical properties with a good resolution. For example, one could map the mechanical properties within and around a weld. Even if a sample is spatial-large enough to be tested by other means, IIT often remains the method of choice because it requires little sample preparation. At its most basic

level, IIT employs a high-resolution actuator to force an indenter into the tested surface and a high-resolution sensor to continuously measure the penetration. One of the great advantages of this technique is that the contact area under load can often be inferred from the continuous load-displacement data alone. In other words, the residual hardness impression does not have to be directly imaged, thus facilitating property measurement at the sub-micron scale. Hardness (H_{IT}) and indentation elastic modulus (E_{IT}) are the properties most frequently measured by IIT using Oliver& Pharr approximation method[14].

The fundamental relationships, from which H_{IT} and E are determined, are:

$$H_{IT} = P / A \qquad (1)$$

where P is the load and A is the projected contact area at that load, and:

$$E_r = \frac{\sqrt{\pi}}{2\beta}\frac{S}{\sqrt{A}} \qquad (2)$$

where E_r is the reduced elastic modulus, S is the slope of the upper portion of the unloading curve ($S = dP / dh$) and β is a constant that depends on the geometry of the indenter. For indenters with triangular cross section like the Berkovich one $\beta = 1.034$.

A reduced modulus, E_r, is used in Eq. (*2*) to account for the fact that elastic displacements occur in both the indenter and the sample. The elastic modulus of the test material, E_{IT} , is calculated from E_r using:

$$\frac{1}{E_r} = \frac{1-\nu^2}{E_{IT}} + \frac{1-\nu_i^2}{E_i} \qquad (3)$$

where ν is the Poisson's ratio for the test material, and E_i and ν_i are the elastic modulus and Poisson's ratio, respectively, of the indenter. For diamond, elastic constants E_i = 1141 GPa and $\nu_i = 0.07$ are often used. While it may seem counterintuitive that one must know the Poisson's ratio of the material in order to compute its modulus, even a rough estimate, say $\nu = 0.25 \pm 0.1$, produces only about a 5% uncertainty in the calculated value of E for most materials[15].

3. Experiment

3.1. Deposition of films

The samples/substrates from stainless steel (SS) (SS OC 404, containing 20 % Cr, 5 % Al, 0.02 % C and up to 100 % Fe) were plates with sizes 20×20 mm, which were cut from a steel foil with a thickness of 50 μm. Films of ZrO_2 , Ce_2O_3-CeO_2 and La_2O_3 with thickness 0.5 μm were electrodeposited from non-aqueous electrolytes using the compositions and schedules, described in ref.[10–13].

3.2. Nanoindentation experiments

Mechanical properties of ZrO_2, Ce_2O_3-CeO_2 and La_2O_3 films were investigated by nanoindentation experiments, using Nano Indenter G200 (Agilent Technologies). These films were electrochemically deposited on stainless steel substrate (SS OC 404) with a thickness of 50 μm. The nanoindenter is equipped with a Berkovich three-sided diamond pyramid with centerline-to-face angle 65.3º and a 20 nm radius at the tip of the indenter. The minimum allowed load is 10 mN, and the maximum load is 500 mN. Displacement recording resolution is 0.01 nm and the load recording resolution is 50 nN. The device is equipped with an optical microscope with 2 objectives with magnifications of 250× and 1000×. We made series of 25 indentations on each sample probe in order to have better statistics. We used an indentation method which prescribes series of 10 loading/unloading cycles in a single indentation experiment. Hardness and modulus are determined using stiffness calculated from the slope of the load-displacement curve during each unloading cycle. Basic input parameters used in this indentation method are given in Tab. I.

Table I
Input parameters for nanoindentation experiments

Parameter	Unit	Values
Percent To Unload	[%]	90
Surface Approach Velocity	[nm/s]	10
Delta X For Finding Surface	[μm]	-50
Delta Y For Finding Surface	[μm]	-50
Maximum Load	[gf]	50
Load Rate Multiple For Unload Rate	[-]	1
Number Of Times To Load	[-]	10
Allowable Drift Rate	[nm/s]	0.05
Approach Distance To Store	[nm]	1000
Peak Hold Time	[s]	20
Time To Load	[s]	15
Surface Approach Distance	[nm]	5000
Surface Approach Sensitivity	[%]	40
Poisson Ratio	[-]	0.3

4. Results and discussion

As a result of nanoindentation experiments, load-displacement curves were obtained and two mechanical characteristics of substrate and investigated films – indentation hardness (H_{IT}) and indentation modulus (E_{IT}) were calculated using Oliver&Pharr approximation method[16]. Dependence of indentation modulus and inden-

tation hardness on depth of indentation was investigated as well.

Dependences of indentation modulus E_{IT} and indentation hardness H_{IT} on depth of indentation for the stainless steel substrate are shown on Fig. 1 and Fig. 2.

Fig. 1 and Fig. 2 clearly show that with increasing depth of indentation the indentation hardness and indentation modulus of the substrate decrease. In our opinion, this effect is associated with the presence of a thin natural passive film on the surface of the stainless steel. The chemical and phase composition of the film are quite different from those of the bulk steel. XPS investigations showed that the film's thickness is about 1.5 nm and that consists of Fe^0, FeO, Fe_2O_3, FeOOH, Cr^0, Cr_2O_3, Al^0 and Al_2O_3. At the same time, the concentrations of the metallic Cr and Al, their oxides respectively, in it are higher than concentrations of metallic Fe and its oxides, when compared with the ratio of metallic Fe, Cr and Al in the bulk steel[17,18]. Results for stainless steels presented in ref.[19] suggest that in this case, a passive film may form that will contain Fe^{3+}, Cr^{3+} and Al^{3+}; most probably an Al^{3+}-containig spinel of the type of $Fe^{2+}(Fe^{3+},Cr^{3+})O_4$. In this case, a Cr^{3+}:Fe^{3+} ratio of about 3 is attained. Obviously, the surface passive film consist vastly highest concentration of metallic Cr, Cr oxides and Al oxides will determine measuring of considerably highest indentation hardness and indentation modulus in beginning stages of nanoindentation. The average values of indentation hardness and indentation modulus of the substrate obtained are H_{IT} = 2.67 GPa, E_{IT} = 119.13 GPa.

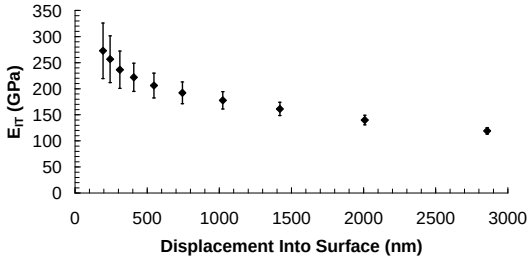

Fig. 1. **Dependence of indentation modulus on depth of indentation for stainless steel substrate**

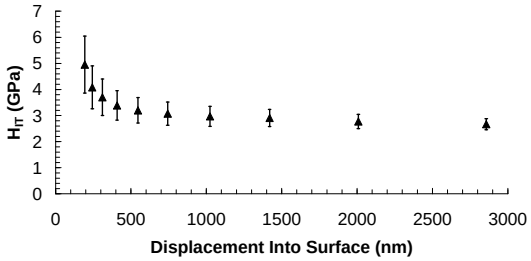

Fig. 2. **Dependence of indentation hardness on depth of indentation for stainless steel substrate**

They were calculated using Eq. (*4*) and Eq. (*5*), where H_{IT_i} and E_{IT_i} are measured hardnesses and modulus at 10 different depths of indentations, shown on Fig. 1 and Fig. 2.

$$H_{IT} = \frac{\sum_{i=1}^{10} H_{IT_i}}{10} \qquad (4)$$

$$E_{IT} = \frac{\sum_{i=1}^{10} E_{IT_i}}{10} \qquad (5)$$

The dependences of indentation modulus E_{IT} and indentation hardness H_{IT} on depth of indentation for investigated films are shown in Fig. 3 and Fig. 4. It's evident from Fig. 4 that the hardness of zirconium and lanthanum films decreases with increasing depth of indentation, due to the influence of the soft substrate. At one point, it becomes close to the hardness of the substrate. The reason is that below the depth of indentation of 500 nm, the substrate is reached. This boundary is marked with a vertical dashed line in Fig. 4. The hardness of the the cerium film increases with increasing of depth of indentation, due to the influence of the substrate. The substrate shows higher hardness (2.67 GPa). Below the depth of indentation of 500 nm hardness becomes equal to the hardness of the substrate. Moreover, the lanthanum film has the highest hardness (3.09 GPa). Hardnesses of zirconium (2.69 GPa) and cerium films (1.11 GPa) follow. Fig. 3 shows that the lanthanum film has the highest elastic modulus (185.28 GPa), followed by the modulus of zirconium (162.09 GPa) and cerium films (158.52 GPa). They were calculated using Eq. (*6*) and Eq. (*7*), where H_{IT_j} and E_{IT_j} are measured hardnesses and modulus at first 5 depths of indentations (only inside the films), shown on Fig. 3 and Fig. 4.

$$H_{IT} = \frac{\sum_{j=1}^{5} H_{IT_j}}{5} \qquad (6)$$

$$E_{IT} = \frac{\sum_{j=1}^{5} E_{IT_j}}{5} \qquad (7)$$

Authors gratefully acknowledge the financial support of Bulgarian National Science Fund under grant No. TK01/0185.

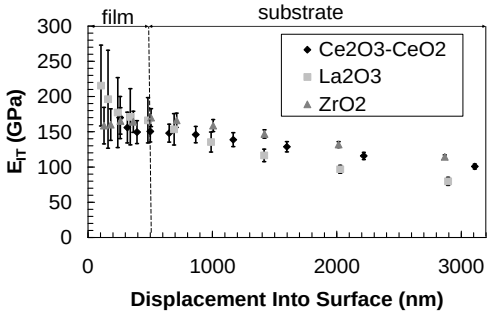

Fig. 3. **Dependence of indentation modulus on depth of indentation**

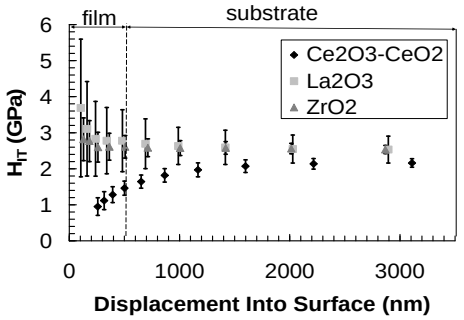

Fig. 4. **Dependence of indentation hardness on depth of indentation**

REFERENCES

1. Von Stebut J., Febvay S., Stauder B., Lepage J., Brion J., Sander B., Pierson G.: Surf. Coat. Technol. *60*, 458 (1993).
2. Koski K., Hölsä J., Juliet P.: Surf. Coat. Technol. *120-121*, 303 (1999).
3. Yamaguchi T.: Catal.Today *20*, 199 (1994).
4. Nakazawa T., Inoue T., Satoh M., Yamamoto Y.: Jpn. J. Appl. Phys. *34*, 548 (1995).
5. Stoyanova E., Nikolova D., Stoychev D., Stefanov P., Marinova T.: Corrosion Sci. *48*, 4037 (2006).
6. Stoyanova E., Nikolova D., Stoychev D., Avramova I., Stefanov P.: Electrochem. Acta *55*, 1725 (2010).
7. Skorodumova N., Ahuja R., Simak S., Abrikosov I., Johansson B., Lundqvist B.: Phys. Rev. B *64*, 115108 (2001).
8. Cao J., Ji H., Liu J., Zheng M., Chang X., Ma X., Zhang A., Xu Q.: Mater. Lett. *59*, 408 (2005).
9. Manoilova O., Podkolzin S., Tope B., Lercher J., Stangland E., Goupil J., Weckhuysen B.: J. Phys. Chem. B *108*, 15770 (2004).
10. Valov I., Stoychev D., Marinova T.: Electrochim. Acta *47*, 4419 (2002).
11. Valov I., Guergova D., Stoychev D., in book: *Nanotechnological Bases for Advanced Sensors, NATO Science for Peace and Security Series-B: Physics and Biophysics*, Chap. 17, p. 167, Springer, The Netherlands 2010.
12. Stoychev D., Valov I., Stefanov P., Atanasova G., Stoycheva M., Marinova Ts.: Mater. Sci. Eng. C *23*, 123 (2003).
13. Kale S., Jadhav K., Patil P., Gujar T., Lokhande C.: Mater. Lett. *59*, 3007 (2005).
14. Agilent Technologies G200 Nano Indenter User's Guide, Agilent Technologies Inc., Part Number G2A-13192-1, USA (2009).
15. Pharr G., Hay J.: *ASM Handbook Volume 08: Mechanical Testing and Evaluation*, ASM International. 2008, 231.
16. Oliver W., Pharr G.: J. Mater. Res. *19*, 3 (2004).
17. Stoychev D., Stefanov P., Stoycheva M., Nikolova D., Marinova T.: Trans IMF *78*, 67 (2000).
18. Gergova D., Stoyanova E., Stoychev D., Avramova I., Stefanov P.: Bulg. Chem. Commun. *40*, 227 (2008).
19. Evans U.: *The Corrosion and Oxidation of Metals: Scientific Principles and Practical Applications*, Edward Arnold Ltd., London 1962.

S. Cherneva[a], D. Stoychev[b], and R. Iankov[a]
([a] Institute of Mechanics, Bulgarian Academy of Sciences, Sofia, [b] Institute of Physical Chemistry, Bulgarian Academy of Sciences, Sofia, Bulgaria): **Measuring of Mechanical Properties of Electrochemically Deposited ZrO_2 , Ce_2O_3-CeO_2 and La_2O_3 Films by Nanoindentation**

Mechanical properties of ZrO_2, Ce_2O_3-CeO_2 and La_2O_3 films with thickness of 0.5 μm were investigated by means of nanoindentation using Nanoindenter G200 (Agilent Technologies), equipped with Berkovich diamond indenter. These films were electrochemically deposited on stainless steel substrate – SS OC 404 with a thickness of 50 μm. Two mechanical characteristics of investigated films: indentation hardness (H_{IT}) and indentation modulus (E_{IT}), were determined by means of instrumented indentation and Oliver&Pharr approximation method. We used an indentation method that prescribes series of 10 loading/unloading cycles in a single indentation experiment. Hardness and modulus are determined using stiffness calculated from the slope of the load-displacement curve during each unloading cycle. The dependences of indentation modulus and indentation hardness on depth of indentation were also investigated.

USE OF MODULUS MAPPING TECHNIQUE TO INVESTIGATE CROSS-SECTIONAL MATERIAL PROPERTIES OF EXTRACTED SINGLE HUMAN TRABECULAE

ONDŘEJ JIROUŠEK[a], DANIEL KYTÝŘ[a], PETR ZLÁMAL[a], TOMÁŠ DOKTOR[a], JOSEF ŠEPITKA[b], and JAROSLAV LUKEŠ[b]

[a] *Academy of Sciences of the Czech Republic, Institute of Theoretical and Applied Mechanics, v.v.i., Prosecká 76, 190 00, Prague 6,* [b] *Czech Technical University in Prague, Faculty of Mechanical Engineering, Technická 4, 166 07 Prague 6, Czech Republic*
jirousek@itam.cas.cz

Keywords: modulus mapping, trabecular bone, nanoindentation, micromechanical testing

1. Introduction

Overall material properties of trabecular bone are function not only of bone density and architecture, but they are strongly dependent on the tissue properties. These properties at level of individual trabeculae can be obtained using nanoindentation of polished larger blocks of trabecular bone, however, one cannot distinguish between superficial layers and core of the trabecula where the properties are expected to differ[1].

The only study that uses nanoindentation of individual trabeculae in their cross-sections is the study by Brennan el al.[1], however, the properties were measured only in three distinct areas (core, middle, outer) and the authors used quasi-static nanoindentation. To our knowledge, modulus mapping (MM) has not been applied to measure properties of trabecular bone.

In their pioneering work[2], Asif et al. used modulus mapping to measure elastic properties of a carbon fiber epoxy composite. MM has been used to measure the nanoscale elastic properties of the collagen fibers, fibrils and mineral deposits in extrafibrillar space[3] in order to evaluate properties of nanocomposite films to mimic the hierarchy of natural bone. Recently the technique was used to measure the local variations in dentin and enamel in human teeth[4] but no verification with other experimental method has been done.

This study aims for the first time to investigate the local variations in material properties of single human trabecula in its cross-section. Average material properties obtained using MM technique are compared to elastic modulae measured by micromechanical testing.

2. Materials and methods

Thin and straight trabeculae (n=5, n – number of specimens) were located in a thin slice of trabecular bone extracted from proximal femur under magnification glass (4×). First, the samples were subjected to micromechanical testing and then modulus mapping procedure was performed.

Micromechanical tests

The trabeculae were tested in tension (n=3) and in three-point bending (n=2) to determine elastic modulae, yield strains and yield stresses. For tensile experiments, ends of the extracted trabeculae were embedded in epoxy resin. Samples were glued in custom tension-compression loading device, specially designed for these deliberate mechanical tests. For the three-point bending tests, no gluing was necessary and the samples were carefully placed on supports made of thin metal sheets.

Positioning of the samples as well as loading was provided by means of stepper motors and precision linear stages (UMR-3.5, Newport Corp, Irvine, CA). Deforming samples were recorded using a high-resolution CCD camera (CCD-1300F, Vosskuhler GmbH, Germany). Magnification was provided by an optical microscope (Navitar Imaging Inc., USA). Design of the experimental setup is shown in Fig. 1.

The samples were tested until complete fracture occurred. From the recorded images, displacements were evaluated using Lukas-Kanade tracking algorithm[5,6]. From the displacements, strains were calculated and complete stress-strain diagram was ascertained for each tested sample.

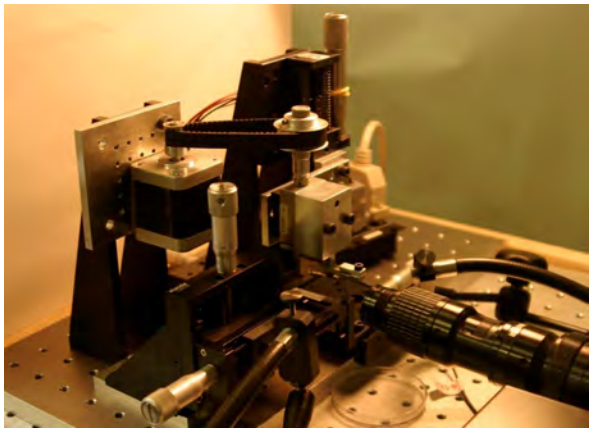

Fig. 1. **Experimental setup for micromechanical testing of isolated trabeculae (three point bending)**

The broken samples were then scanned in scanning electron microscope to quantify the damaged volume and later embedded in a low shrinkage epoxy resin, polished with diamond discs with decreasing grain sizes to reach the surface roughness of 20 nm to reveal the cross-section in undamaged part of trabecula. Detailed description of the sample preparation process can be found in a paper by Dudíková et al[7]. Example of cross-sectional image of the polished sample is depicted in Fig. 2.

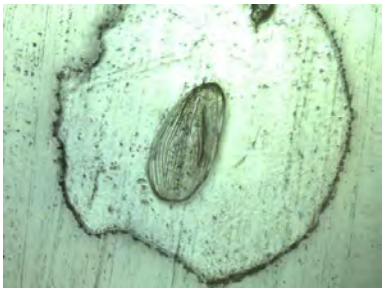

Fig. 2. **Cross-section of trabecula embedded in epoxy resin. Image acquired by optical microscopy**

Modulus mapping procedure

To measure elastic properties in a larger area (35×35 μm) of trabecula's cross-section, modulus mapping technique (combination of dynamic mechanical analysis – nanoDMA and *in-situ* scanning probe microscopy – SPM) was applied in samples' undamaged parts. In this process, the probe is sinusoidally oscillating over the polished surface with a given frequency and load. From the recorded displacement amplitude and phase lag storage and loss modulae are determined.

During MM a small sinusoidal force is superimposed on top of a larger quasi-static force. Motion of the vibrating system of indenter and the surface sample can be described by equation of motion for one degree of freedom. Harmonic equation describing the motion is:

$$F_0 \sin(\omega t) = m\ddot{x} + c\dot{x} + kx \qquad (1)$$

in which F_0 is the magnitude of the harmonic force, ω is the circular frequency of the system, c is the damping coefficient and k is the stiffness of the system. The system is assumed to be linear viscoelastic.

Denoting C_i stiffness of the indenter, C_s stiffness of the sample and A_0 amplitude of the system's response, we can write following equation for the time evolution of the dynamic response:

$$A_0 = \frac{F_0}{\sqrt{\left(k - m\omega^2\right)^2 + \left[\left(C_i + C_s\right)\omega\right]^2}} \qquad (2)$$

Denoting $k=k_s+k_i$ (k_s is stiffness of the sample, k_i is stiffness of the indenter and k is the total spring stiffness) we can calculate the phase difference φ between the force and displacement from:

$$\tan\varphi = \frac{\left(C_i + C_s\right)\omega}{k - m\omega^2} \qquad (3)$$

Prior the measurement, a dynamic calibration of the system is performed to establish three parameters of the system (indenter mass m, damping coefficient of the capacitive displacement sensor C_i, stiffness of the indenter k_i), leaving only stiffness k_s and damping coefficient C_s of the sample as unknown values.

In indentation, the contact stiffness k_s is proportional to the projected contact area A_c:

$$k_s = 2E^*\sqrt{\frac{A_c}{\pi}} \qquad (4)$$

Using this, storage modulus *E'*, loss modulus *E''* and phase shift between the force and displacement δ can be calculated using following equations:

$$E' = \frac{k_s\sqrt{\pi}}{2\sqrt{A_c}},\ E'' = \frac{\omega C_s\sqrt{\pi}}{2\sqrt{A_c}},\ \tan\delta = \frac{\omega C_s}{k_s} \qquad (5)$$

From the storage and loss modulae, complex modulus *E** can be computed using:

$$E^* = E' + iE'' \qquad (6)$$

Comparison with quasi-static nanoindentation

Modulus mapping provides information about storage and loss modulae in a 256×256 square matrix. In our experiments, this matrix represented physical area 35×35 μm). To compare results from MM technique with quasi-static indentation, each sample was indented with a set of 9 indents in the center of the area used for MM.

In quasi-static indentation, maximal force 1000 μN was applied in 5 s loading part, which was followed by 5 s holding part, finally finished with 5 s unloading part. Nanoindentation curves, i.e. plots of force to depth for sample No. 4 are depicted in Fig. 3.

3. Results

Five samples have been successfully tested using micromechanical tests, modulus mapping and quasi-static nanoindentation. For nanoindentation, Poisson's number equal to 0.32 (ref.[8]) was considered.

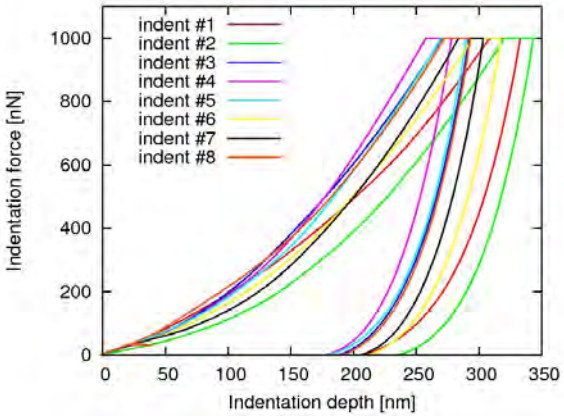

Fig. 3. **Example of the indentation curves from quasi-static indentation of sample No. 4**

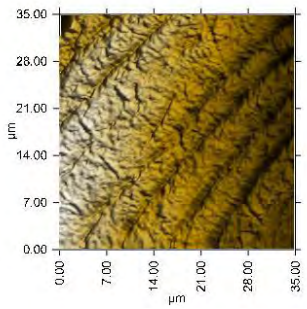

Fig. 5. **Typical topography of the surface sample acquired by in-situ SPM (dimensions of scanned area 35×35 µm; sample No. 4)**

Young's modulae obtained from quasi-static indentation were in good correlation with results from micromechanical testing.

In every sample, matrices with loss modulae, storage modulae and tan delta (see Fig. 4) were stored. From these matrices, complex modulae were computed using equations (*5*) and (*6*).

To compare the MM technique to quasi-static nanoindentation, average values of complex modulae were determined for each sample. This required interpolating the complex modulae with a smooth surface and extrapolating the values to the region representing the whole cross-section of the sample.

We used this technique to study the variations in material properties in the cross-section of the trabecuale. Results were showing similar trend to the findings published by Brennan et al.[1], i.e. the stiffness is highest in the core section of the trabecula and toward its surface it is decreasing. However, for two samples it was not possible to fit smooth surface through the values of complex modulae due to the large size of the samples compared to the relatively small area used for modulus mapping. Average values of the modulae are summarized in Tab. II and compared to the values obtained from micromechanical tests and from static nanoindentation.

In the table, values denoted by E_{mm} represents average values of complex modulae after fitting the smooth surface through the data and integrating the values over the whole cross-section. Values denoted by E_{qs} are average values

Table I
Average values of reduced and elastic modulae obtained by quasi-static indentation

Sample No.	Reduced modulus [GPa]	Young's modulus [GPa]
1	13.26	12.04
2	17.48	15.93
3	17.79	16.22
4	19.52	17.82
5	19.62	17.91
6	13.29	12.07

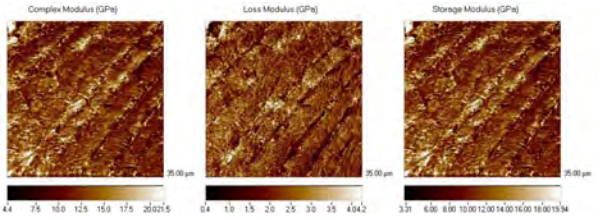

Fig. 4. **Image maps of (a) complex modulus, (b) loss modulus and (c) storage modulus for sample No. 4**

Table II
Young's modulae (in GPa) obtained by modulus mapping (E_{mm}), quasi-static nanoindentation (E_{qs}) and from micromechanical testing ($E_{\mu m}$)

Sample	1	2	3	4	5	6
E_{mm}	--*)	14.17	14.91	16.90	--*)	13.29
E_{qs}	12.04	15.93	16.22	17.82	17.91	12.07
$E_{\mu m}$	10.71	14.61 #)		15.87	9.5**)	11.60

*) For these samples it was not possible to extrapolate a smooth surface over the whole cross-section, #) samples 2 and 3 represents two surfaces prepared for nanoindentation from one sample used in micromechanical testing, **) this value is influenced by overestimation of the cross-sectional area of the sample, see discussion in Jiroušek at al. [9]

obtained by quasi-static nanoindentation and finally $E_{\mu m}$ are elastic modulae measured by micromechanical testing.

4. Conclusions

Comparison of elastic properties obtained from micromechanical testing and modulus mapping technique was determined for each sample. After MM analysis, each sample was also tested using quasi-static nanoindentation.

Local variations in elastic properties were determined in cross-section of each sample using MM technique. Correlation between average elastic properties in cross-section and properties from micromechanical tests was found for all tested samples. Modulus mapping shows the trend of larger stiffness in core, smaller values are measured in superficial areas.

Both quasi-static nanoindentation and MM can be used to measure the elastic properties of extracted trabeculae, however, to identify material constants for more complicated material model (e.g. von Mises plasticity with kinematic hardening) it is necessary to use micromechanical testing.

The research has been supported by the Grant Agency of the Czech Republic (grant No. P105/10/2305), Ministry of Education of the Czech Republic (Transdisciplinary research in Biomedical Engineering II, No. MSM 684077001) and research plan of the Academy of Sciences of the Czech republic AV0Z0710524.

REFERENCES

1. Brennan O., Kennedy O. D., Lee T. C., Rackard S. M., O'Brien F. O.: J. Biomech. *42*, 498 (2009).
2. Asif S. A., Wahl K. J., Colton R. J., Warren O. L.: J. Appl. Phys. *90* (3), (2001).
3. Khanna R., Katti S. K., Katti D. R.: Acta Biomater. *7*, 1173 (2011).
4. Balooch G., Marshall G. W., Marshall S. J., Warren O. L., Asif S. A. S., Balooch M.: J. Biomech. *37*, 1223 (2004).
5. Lucas B. D., Kanade T.: *Proc of Image Understanding Workshop*, 121–130, (1981).
6. Jiroušek O., Jandejsek I., Vavřík D.: J. Instrumentation *6*, C01039, (2011).
7. Dudíková M., Kytýř D., Doktor T., Jiroušek O.: Chem. Listy *105*, s790 (2011).
8. Ladd A. J. C., Kinney J. H.: J. Biomech. *31*, 941 (1998).
9. Jiroušek O., Kytýř D., Kunecký J., Zlámal P., Doktor T., Němeček J.: Chem. Listy *105*, s668 (2011).

O. Jiroušek[a], D. Kytýř[a], P. Zlámal[a], T. Doktor[a], J. Šepitka[b], and J. Lukeš[b] *([a] Academy of Sciences of the Czech Republic, Institute of Theoretical and Applied Mechanics, Prague, [b] Czech Technical University in Prague, Faculty of Mechanical Engineering, Prague, Czech Republic):* **Use of Modulus Mapping Technique to Investigate Cross-Sectional Material Properties of Extracted Single Human Trabeculae**

This study aims to investigate the local variations in material properties of single human trabecula in its cross-section. Thin and straight trabeculae were located in a thin slice of trabecular bone extracted from proximal femur. Tensile and three-point bending tests were performed to determine elastic modulae, yield strains and yield stresses. To determine local variations in elastic properties in trabecula's cross-section, modulus mapping (MM) technique was applied in samples' undamaged parts. Using MM the storage and loss modulae are determined. Correlation between average elastic properties in cross-section and properties from micromechanical tests was found for all tested samples.

INVESTIGATION OF DIAMOND LIKE CARBON COATING DEPOSITED ON PLASMA NITRIDED AUSTENITIC STAINLESS STEEL

ZDENĚK JOSKA, JAROMÍR KADLEC, VOJTĚCH HRUBÝ, QUANG DUNG TRAN, and ZDENĚK POKORNÝ

Department of Mechanical Engineering, University of Defence in Brno, Kounicova 65, 662 10 Brno, Czech Republic
joska.zdenek@email.cz

Keywords: duplex coating, DLC coating, plasma nitriding, microhardness, adhesion

1. Introduction

Austenitic stainless steel AISI 316L is one of the most spread austenitic stainless steel, due to excellent corrosion resistance, superior cryogenic properties, good high-temperature strength, for these properties, it is used in the food and chemical industry and in medicine for surgical instruments[1]. But strong limitation as low wear resistance and poor hardness defend their applications. Duplex surface system was applied to improve surface and subsurface properties. The combination of both plasma nitriding and subsequent deposited thin film Diamond Like Carbon (DLC) were used as duplex treatment. Plasma nitriding is very universal treatment was used for creation of supersaturate austenite layer[2–4]. This layer is non magnetic, it has very high hardness and good corrosion resistance. High hardness, chemical inertness and excellent tribological properties of amorphous carbon coatings often called diamond-like carbon (DLC) coatings, are of great interest for technological applications[5,6]. When these coatings are deposited on soft substrate material due to their very thin thickness, further increase in the wear and especially in the load-bearing resistance is limited by plastic deformation of the substrate, which results in the eventual collapse of the coating. In case of austenitic stainless steel plasma nitrided layer can created very useful transition layer between soft substrate and very hard thin coating[7–9]. The duplex treatment consisted of a plasma nitriding at 510 °C for 6 hours and subsequent coating with DLC layer was applied on AISI 316L stainless steel. The article is concerned to a study of the chemical composition and mechanical properties of duplex system.

2. Experimental material, methods and surface treatment

Samples of an AISI 316L stainless steel in the untreated state had the diameter of 30 mm and a thickness of 7 mm. The substrate had a microhardness of about 230 HV. Before the plasma nitriding process, the samples were wet ground using silicon carbide paper from 120 down to 4000 grit and finally polished with 1 μm diamond paste. Plasma nitriding was carried out in PN 60/60 Rübig equipment with these parameters: temperature of 510 °C, duration 6 h, pressure 320 Pa, gas mixture of H_2 flow 8 l/min and N_2 flow 24 l/min, pulse length 100 μm, voltage 520 V. The pre-nitrided samples were afterwards coated with DLC coatings in PVD industrial equipment HTC 625 Hauser. Depth profiles of plasma nitrided layers and PVD coatings were measured by GDOES/QDP method. GDOES measurements were performed in a LECO SA-2000. Calibration of nitrogen: JK41-1N and NSC4A standards. Confocal laser microscope LEXT OLS 3000 was used for observation of the cross section morphology of duplex coatings and craters after adhesion Rockwell tests. The surface hardness of duplex systems was evaluated by a Vickers microhardness test in a LECO automatic microhardness tester LM 247 AT. Surface microhardness was measured in range of load 0.1 N to 9.81 N. For each load, there were

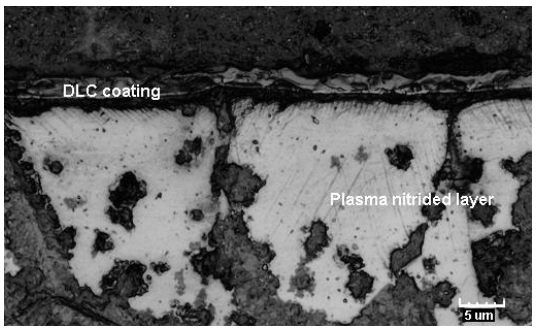

Fig. 1. **The chemically etched (by aqua - regia) cross-section showing the morphology of the duplex coating in a confocal micrograph**

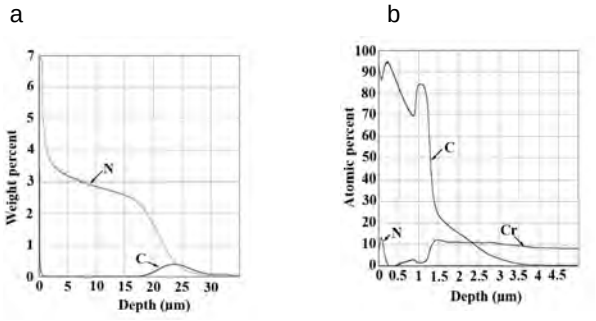

2. **GDOES depth profile of a) plasma nitrided layer b) DLC coating on nitrided surface**

made 5 measurements and the resulting value is the average of these. Adhesion test was performed on the duplex coatings as a standard Rockwell test, while using a load of 1471 N and a diamond Rockwell indenter of 0.2 mm in diameter to assess the vertical adhesion of the coatings.

4. Experimental results

Fig. 1 shows an optical micrograph of a cross-section of the surface of an AISI 316L sample treated by a combination of a plasma nitriding and a PVD coating. The plasma nitriding process created a nitrided layer of 25 μm thickness. The DLC coatings subsequently deposited by PVD have the thickness of 1.5 μm. Depth profiles of the plasma nitrided layer (Fig. 2a) for both carbon and nitrogen are in good agreement with the proposed plasma treatment schedule. Carbon and nitrogen contents decrease along the layer depth (from surface to substrate). For carbon concentration there is a local maximum twenty micrometers from the surface. In the DLC coating on nitrided surface (Fig. 2b) carbon concentration gradually decreases to local maximum in depth 1 μm and decreased to zero value in the substrate. Indentation adhesion tests were performed by Rockwell indentation test (Fig. 4). The sample shows good adhesion in range HF1, without any delamination of coatings. The surface hardness of duplex treated samples (Fig. 3) showed that the highest values 3400 $HV_{0.01}$ were found in the duplex treated sample with the DLC coating. The single coated sample reached only 1700 $HV_{0.01}$.

5. Conclusion

Duplex surface treatment consisted of deposition of a plasma nitrided layer and subsequently deposition of a DLC coating. The analysis carried out by using GDOES/ QDP method was in a good agreement with observation of the metallographic cross-section and microhardness measurement. The thickness of the nitrided layer was 25 μ m and microhardness values were around 1150 $HV_{0.05}$. The surface hardness of duplex coatings reached

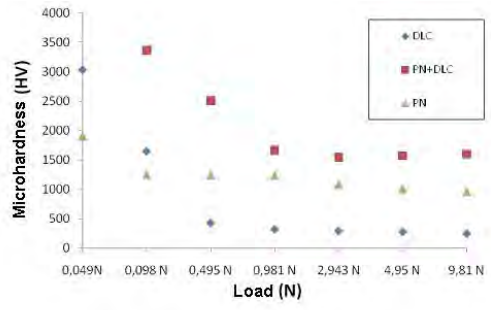

Fig. 3. **Surface microhardness of treated samples**

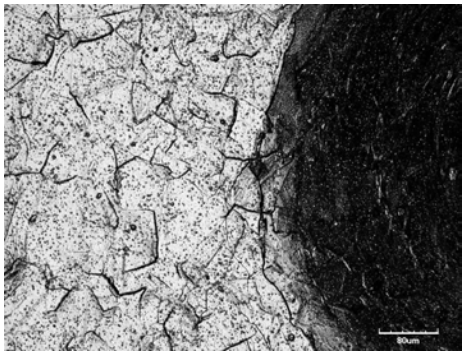

Fig. 4. **Rockwell indentation test of duplex coating**

3400 $HV_{0.01}$. Rockwell adhesion test shows that the plasma nitrided layer contributes to good adhesion of the DLC coating, which has then better adhesion than on a non-nitrided substrate.

The work was supported by the specific research project "Application of Modern Technologies for Components of Special Technology" at the Department of Mechanical Engineering, University of Defence in 2011.

REFERENCES

1. Lo K. H., Shek C. H., Lai J. K. L.: Mater. Sci. Eng. R: Reports. *65*, 4 (2009).
2. Kadlec J., Dvorak M.: Strenght of Materials. *40*, 118 (2008).
3. Czerwiec T., Renevier N., Michel H.: Surf. Coat. Technol. *131*, 267 (2000).
4. Pokorny Z., Kadlec J., Hruby V., et al.: Advances in Military Technology *6*, 1 (2011).
5. Jelinek M., Kocourek T., Kadlec J., Bulir J.: Laser Physics *13*, 10 (2003).
6. Jelinek M., Kocourek T., Bulir J., Novotny M., et al.: Laser Physics *15*, 2 (2005).
7. Joska Z., Kadlec J., Hruby V., et al.: Key Eng. Mater. *465*, (2011).
8. Heras E. De Las, Egidi D. A., Corengiea P., et al: Coat. Technol. *202*, 13 (2008).
9. Joska Z., Pospichal M., Mrazkova T., et al.: Chem. Listy *104*, S (2010).

Z. Joska, J. Kadlec, V. Hrubý, Q. Dung Tran, and Z. Pokorný *(University of Defence Brno):* **Investigation of DLC Coating Deposited on Plasma Nitrided Austenitic Stainless Steel**

In this article a duplex treatment was investigated. Duplex treatment consists of plasma nitriding and deposition of a DLC coating on AISI 316L stainless steel. This study covers the microstructure, chemical composition and mechanical properties of this duplex system. Analysis and discussion of the results showed that combination of these two processes improves considerably the surface hardness.

EVOLUTION OF STRUCTURE DURING LOCAL PLASTIC DEFORMATION IN Fe-Ni-B METALLIC GLASS

ALENA JURÍKOVÁ, KORNEL CSACH, and JOZEF MIŠKUF

Institute of Experimental Physics, Slovak Academy of Sciences, Watsonova 47, 040 01 Košice, Slovakia
akasard@saske.sk

Keywords: local plastic deformation, shear band, structural relaxation, amorphous alloy

1. Introduction

Metallic glasses have an attractive combination of mechanical and other physical properties. These materials can be prepared by rapid cooling of melt with proper composition. In the as-quenched alloy a significant amount of free volume is frozen due to the non-equilibrium processing conditions. As the periodical long-range order is absent in these materials, the creation and propagation the narrow shear bands with the thickness of cca 20 nm is the only micromechanism of the plastic deformation. The shear band creation is carried out under adiabatic conditions, and intensive local heating and subsequent rapid cooling cause the increase of the atomic disordering and the free volume creation[1]. The structure of amorphous alloys is influenced by the free volume amount and the structural relaxation is related to the free volume annihilation. Differential scanning calorimetry (DSC) analysis is the effective method to characterize the structural changes in amorphous materials. In the work we studied the local deformation-induced structural changes in the Fe-Ni-B amorphous ribbon.

2. Experimental

The specimens of the amorphous metallic ribbon $Fe_{40}Ni_{41}B_{19}$ with the thickness of 17.3 μm were annealed inside the tube furnace at the temperature of 200 °C for 2 hours in a flowing nitrogen atmosphere to anneal-out the quenched-in free volume. The structure of the annealed amorphous alloy was modified by the local plastic deformation performed by repeated impactions of a small hammer of 200 g with a tip of 1 mm radius, similar to ref.[2]. The impactions were randomly distributed through the both sides of ribbon samples. The accumulated deformation was characterized by the total number of these impactions per unit area of the sample. In this way the samples with different deformations were obtained (sample 1 – 160 impactions per 1 cm^2, 2 – 240/cm^2, 3 – 320/cm^2 and 4 – 640/cm^2). The enthalpy changes were measured using DSC 8000 calorimeter in two subsequent runs up to the temperature of 350 °C at a heating rate of 20 °C/min in a flowing nitrogen atmosphere. The third run was measured up to 520 °C (above the crystallization temperature). For characterization of structural changes, the differences between the first and the second runs were used.

3. Results and discussion

Fig. 1 shows representative DSC thermograms for the as-quenched sample up to the temperature of 520 °C. The dominant narrow exothermic peak with maximum at 442 °C corresponds to the transition from the amorphous to the crystalline phase. The enlarged portion of the DSC traces depicted by dash-line box for repeated heating up to 350 °C (with saved amorphous structure) can be seen in the insert of Fig. 1. At the temperatures above 140 °C the small enthalpy changes associated with irreversible structural changes occur. This thermal effect is connected with an annihilation of the excess free volume during structural relaxation in the amorphous state.

Repeated tip impactions on the annealed sample surface led to the local plastic deformation of the amorphous ribbon through the creation of narrow shear bands. The typical shear band morphology of a deformed specimen can be seen in Fig. 2. The plastic deformation in complex geometrical conditions occurs via sliding along the shear bands in different directions. Similar morphology of the deformed surface has been observed for other metallic glasses[3,4]. The total deformation energy is stored into the volume of narrow shear bands and into the regions of elastic deformation outside the bands. The structure of the

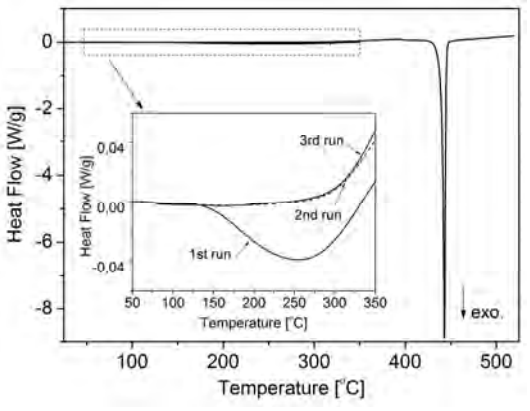

Fig. 1. **DSC scans of Fe-amorphous alloy in the as-quenched state in three subsequent heating runs. The enlarged portion (depicted by dash-line box) in the insert shows the structural relaxation of the amorphous state**

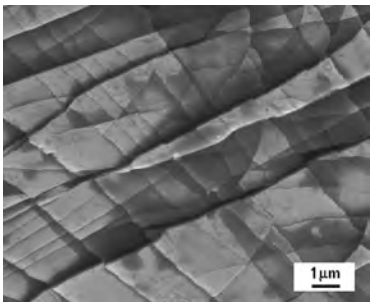

Fig. 2. **The typical morphology of shear bands of the amorphous alloy after repeated impactions**

sample part corresponding to the shear band volume is enhanced with free volume due to the intensive local heating in adiabatic conditions during shear band creation[1].

DSC traces for samples in the state after different plastic deformation as well as in the initial state after annealing are in Fig. 3. All samples exhibit very similar thermal behaviour. The enthalpy change for the as-quenched sample is added for comparison. During annealing at 200 °C for 2 h the sample underwent the structural relaxation and the wide region of enthalpy changes due to free volume annihilation diminished as can be seen on the DSC trace of the annealed sample.

DSC traces of the deformed samples revealed the annihilation of the free volume introduced by plastic deformation. With the increasing the amount of stored deformation energy the larger enthalpy changes are observed. Similar results were obtained in[5,6]. In more deformed sample the amount of shear band regions is higher and so the total free volume increases. In disordered systems the free volume is distributed with activation energy spectrum and therefore the relaxation peak is very wide. At lower temperatures the defects (or free volume) with lower activation energy annihilate[7]. The defects in the as-quenched state begin to anihilate at temperatures above 140 °C. The

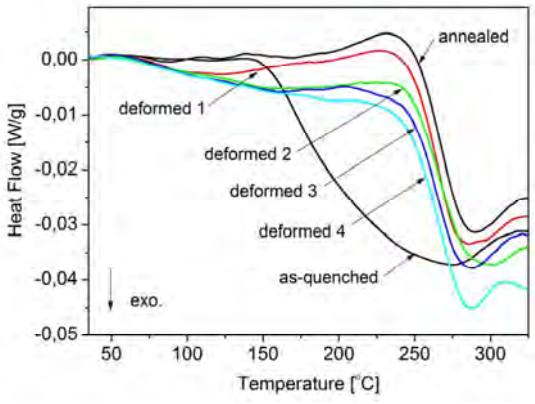

Fig. 3. **DSC scans of the Fe-amorphous ribbon in the as-quenched state, in the state after annealing and in four different deformed states**

defects introduced by the local plastic deformation have lower activation energy and annihilate at lower temperatures. Moreover, higher deformation causes the increasing the amount of defects with higher activation energy and the deformation is then accumulated into the existing shear bands.

Structural changes in the Fe-Ni-B amorphous ribbon at nanoscale level in the narrow shear bands were studied by means of measuring of integral properties like enthalpy changes. Although the plastic deformation is accumulated into 20 nm-narrow shear bands and the part of the sample volume corresponding to the shear band regions is small, the thermal effects connected with the free volume releasing are observable by DSC method. In this way the deformation-introduced free volume was estimated as 1/3–1/2 of the free volume introduced by rapid cooling during metallic glass preparation.

This work was supported by implementation of the project No. 26220120021 provided by the European Regional Development Fund. The authors are grateful to the Centre of Excellence "Nanofluid," VEGA 0185/11 and Slovak Research and Development Agency – contract APVV-0171-10.

REFERENCES

1. Bengus V. Z. et al: Int. J. Rapid Solid. *8*, 21 (1993).
2. Ambriško Ľ., Pešek L., Hlebová S.: Chem. Listy *104*, s287 (2010).
3. Zhang Z., Wu F., He G., Eckert J.: J. Mater. Sci. Technol. *23*, 747 (2007).
4. Yoon K.-S., Lee M., Fleury E., Lee J.-Ch.: Acta Mater. *58*, 5295 (2010).
5. Chen Q., Liu L., Chan K.C.: J. Alloys Comp. *467*, 208 (2009).
6. Pan J., Chen Q., Liu L., Li Y.: Acta Mater. *59*, 5146 (2011).
7. Csach K., Ocelík V., Miškuf J., Bengus V.Z., Duhaj P.: IEEE Trans Magn. *30*, 496 (1994).

A. Juríková, K. Csach, and J. Miškuf *(Institute of Experimental Physics of Slovak Academy of Sciences, Košice):* **Evolution of Structure during Local Plastic Deformation in Fe-Ni-B Metallic Glass**

In metastable amorphous metals the structural relaxation is closely related to the free volume annihilation. In the work we studied the deformation-induced structural changes in the Fe-Ni-B amorphous ribbon. The enthalpy changes connected with structural relaxation of the deformed samples as well as non-deformed samples were measured. With the increasing the amount of stored deformation energy the larger enthalpy changes are observed. The deformation-introduced free volume has lower energy and can achieve ~ 1/3 of the free volume amount introduced by rapid quenching of the melt during metallic glass preparation.

TESTING OF NEW COMPOSITE MATERIALS BASED ON FABRIC FROM USED TIRES

LUCIA KNAPČÍKOVÁ[a], JOZEF HUSÁR[a], MICHAEL HERZOG[b], and LADISLAV PEŠEK[c]

[a] *Department of Manufacturing Management, Faculty of Manufacturing Technologies of TU of Košice with a seat in Prešov, Bayerova 1, 080 01 Prešov, Slovak Republic,* [b] *Technical University of Applied Sciences, Bahnhofstraße 1, 15745 Wildau, Germany,* [c] *Department of Materials Science, Faculty of Metallurgy, TU of Košice, Letná 9, 040 01 Košice, Slovak Republic*
knapcikova.lucia@gmail.com

Keywords: mechanical properties, Shore hardness, fabric, polyvinylbutyral, used tires, composite materials

1. Introduction

Composites are materials formed from a mixture of two or more components to produce a material with properties or characteristics superior to those of the individual materials[1,2]. The matrix is a continuous phase material which is usually less stiff and weaker than the reinforcement. It is used to hold the reinforcement together and distribute the load among the reinforcements. Reinforcements in the form of fibers, fabric, whiskers, or particles are embedded in the matrix to produce the composite[3,4]. These properties depend mainly on the polymers phase state, temperature, time, size and direction of external forces[1,4]. The hardness value is an important value to characterize the mechanical properties of the material[5,6].It is gives an indication of the material resistance against wear, its workability, the heat treatment state, etc. The Shore hardness was determined using standard methods.

2. Material, experiments, results

The investigated composite materials were prepared from recycled components. The matrix was polyvinylbutyral produced by Schirmbeck, Germany, arising from the recycling of car glass. We used the recycled material in the flake´s shape[4], dispersed, spherical, spatially oriented with size of 1–25 mm, Fig. 1.

The fibres were from used tires from passenger cars and trucks, extracted by recycling process (company VODS, Slovakia), then cleaned by separation on vibrating screens, FRITSCH (Germany). Fibres were made of synthetic polymer material, based on polyamide and polyester, Fig. 2, with mean diameter of 30 μm and mean length of 3.55 mm. The properties of investigated materials are presented in Tab. I.

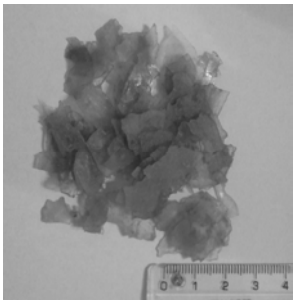

Fig. 1. **Recycled polyvinylbutyral** (Schirmbeck GmbH, Germany)

Fig. 2. **Textiles from used tires** (V.O.D.S., Slovakia)

The homogenization of mixtures was conducted in the temperature range of 80–180 °C (ref.[9]).

The character of the mixing process as well as the emerging nature of the mixture depends on whether the mixed components are completely miscible, partially miscible or completely inmiscible[9,10].

The homogenization began with pre-heating of device at 150 °C, at first adding gradually the thermoplastic material – matrix, polyvinylbutyral, which was thoroughly homogenized for a period of about 30 minutes, then the separated fabrics from used tires were added gradually. On the basis of the previous homogenization of fabrics and PVB, we produced the test boards for 10, 20, 30, 40 and 50 % of fabrics using pressing technology[11,12]. The dependence of tensile strength σ_{max}, Young´s modulus, and tensile strain ε_{max} on percentage ratio of textile in composite materials is presented in Fig. 3. Data were obtained from tensile testing on composite specimens (test board).

Great rubber particles were allways visible on the fracture surface of broken tensile specimens. Young´s

Table I
Mechanical and physical properties of materials

Mechan. and physical properties	PVB Kuraray, GmbH DE[10]	PVB-rec. Schirmbeck GmbH, DE [9]	Fabric from used tires V.O.D.S.,a.s. Slovakia[9]	Kevlar 29 Aramid Fiber DuPont[8]	Comp. material
Young´s modulus [N.mm^{-2}]	3.2	5	-	7.03	5- 62
σ_{max} [N.mm^{-2}]	39.2- 49.2	17.5	-	20.92-3.62	7-18
ε_{max} [%]	205	146	-	3.60	17-146
Shore A/D	70 Shore A	85 Shore A	-	-	36-45 Shore D
T_g [°C]	60-65	50	73	-	46
T_m [°C]	125-200	150	218-255	149-177	259

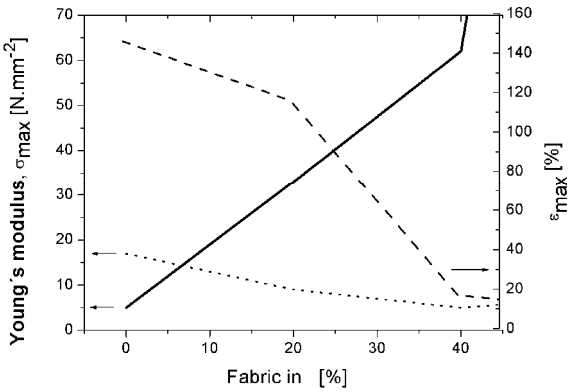

Fig. 3. **Dependence of tensile strength σ_{max}, tensile strain ε_{max} at tensile strength and Young´s modulus E on % ratio of fabrics** (Young´s modulus ——, σ_{max} . . . . , ε_{max} - - - - -)

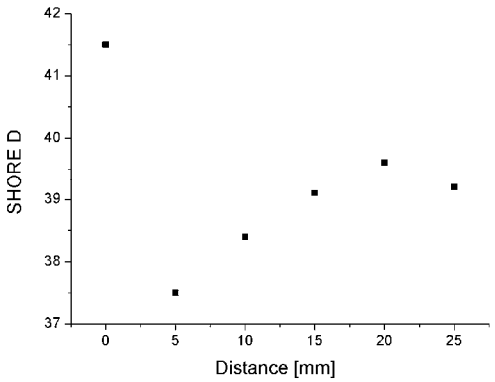

Fig. 5. **SHORE hardness for average value of test boards**

modulus of the material increases with increasing the content of textile fibres in the composite material. However, both the tensile strength σ_{max} and tensile strain ε_{max} decrease.

After pressing the test boards, ineligible rubber particles (1–3 mm in the size) were visible in some areas, Fig. 4. The Shore hardness (durometer hardness[6], DIN 53505-D) was analyzed on the composite material with 50 % textile using a Durometer indenter on test boards, 200×200×6 mm (ref.[14]), by 23 °C and 60 % humidity.

Three boards were tested for each composite on that places where appeared broken rubber particles which were part of the textile and materials remained in spite of separation on vibrating screens[7,13]. The hardness measurement began always starting from the centre of rubber particle (distance = 0, Fig. 5), going away up to 15 mm from the edge of the sample. The distance between the individual indents was 5 mm. The analysed area with one Shore hardness indent[5] was about 1 × 1 mm. The ineligible rubber particles which remained after separation play a significant role and affect negatively fracture properties of the composite. The Shore D hardness in the rubber particle (distance = 0) is higher (41–42), the material around the particles is softer (37–38), Fig. 5.

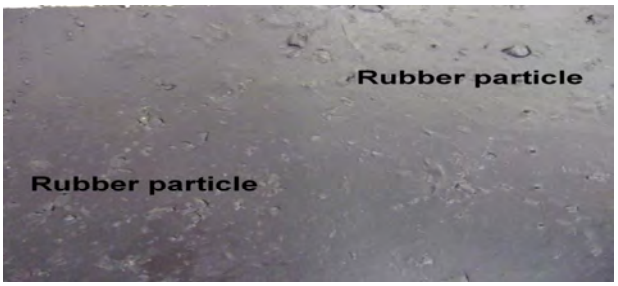

Fig. 4. **Composite material with ineligible rubber particles**

Conclusions

Based on testing of local and global mechanical properties of composites based on fabric from used tires and recycled polyvinylbutyral can be concluded:

– Increasing the fabric volume from 0 up to 40 % the Young´s modulus E is linearly increasing from 5 up to 62 MPa, the tensile strength is linearly decreasing from 17 to 7 MPa, the ε_{max} is sharply decreasing from 146 to 17 %.
– Near the bigger rubber particles was detected an affected zone with lower hardness, which was the cause of fracture.

REFERENCES

1. Eichlerová R. et al.: Chem. Listy *104*, s307 (2010).
2. Zamfirova G. et al.: Chem. Listy *104*, s283 (2010).
3. Vasiliev V. V., Morozov V. E.: *Mechanics and Analysis of Composite Materials*, Elsevier 2001.
4. Nielsen E. L., Landel F. R.: *Mechanics and Analysis of Composite Materials*, Elsevier 2001.
5. Vable M.: Mechanics of materials, Available on internet : <www.me.mtu.edu>, download 20.6.2011.
6. Zaťko M., Eckhardt E.: Methods for measuring of materials hardness and principles by choosing portable devices for measuring, Available on internet : <www. ssndt.sk >, download 20.6. 2011
7. Shore (Durometer) Hardness Testing of Plastics, Available on internet : <www.matweb.com/reference/shore-hardness.aspx> download 17.5.2011.
8. DuPont, Product Kevlar 29Aramid Fiber, Available on internet: <www. matweb.com>, download 10.9.2011.

9. Knapčíková L., Herzog M., Oravec P.: Manuf. Eng. Vol. *4* (2010).
10. Kuraray, Product Mowital B 30 T, Available on internet : <www. kuraray.com>, download10.9.2011.
11. Schuermann H.:*Konstruktieren mit Faser-Kunststoff Verbunden*, Springer Berlin 2001.
12. Švorčík V.: *Structure and Properties of Polymers*, VŠCHT, Praha 2010.
13. Zubko P. et al.: Chem. Listy *104*, s390 (2010).
14. DIN- Taschenbuch, *Kunststoffe- Mechanische und thermomechanische Eigenschaften*, Beuth 1997.

L. Knapčíková[a], J. Husár[a], M. Herzog[b], and L. Pešek[c] *([a]Department of Manufacturing Management, Faculty of Manufacturing Technologies of TU of Košice, [b]TU of Applied Sciences, Wildau, Germany, [c]Department of Materials Science, Faculty of Metallurgy, TU of Košice, Slovak Republic):* **Testing of New Composite Materials Based on Fabric from Used Tires**

The paper deals with testing of new composite materials based on fabric from used tires. The matrix in the composite material is a thermoplastic polyvinylbutyral (PVB), which was obtained after recycling the carglass, where it forms a part of the safety film. The goal of this paper is to present the analysis of mechanical properties of composite materials with various (10–40 %) volume fraction of fabric. Ineligible rubber particles (1–3 mm) were detected in some areas which are remained after separation, they play a significant and detrimental role and affect the mechanical properties of the composite.

PRODUCTION AND TESTING OF THERMOCOUPLES TYPE Cu-CuNi

LADISLAV KOLAŘÍK[a], MARIE VÁLOVÁ[a], PETR VONDROUŠ[a], KAREL KOVANDA[a], and JOSEF ŠEPITKA[b]

[a] *Department of Manufacturing Technology, Faculty of Mechanical Engineering, Czech Technical University, Technická 4, 166 07 Praha 6, Czech Republic,* [b] *Czech Technical University in Prague, Faculty of Mechanical Engineering, Dept. of Mechanics, Biomechanics and Mechatronics, Technicka 4, 166 07 Prague, Czech Republic*
ladislav.kolarik@fs.cvut.cz

Keywords: thermocouple, Cu-CuNi, welding, microplasma, nanoindentation, Young´s modulus, nanohardness

1. Introduction

Purpose of special fast thermocouples is to measure temperature of fast thermal processes with very little time delay (few ms). The response of the thermocouple to the real temperature of the environment depends mainly on heat capacity of the thermocouple and it´s encapsulation. To fasten the response of measurement no encapsulation and the thinnest wire should be used. But such a thermocouple would be damaged in the measurement, so it is only for single usage.

Such a thin thermocouples, with wires of diameter in the scale of 1–100 μm, can be used to measure the real temperatures of the combustion products of explosives, propellants and so on. Interesting application includes temperature measurement of combustion products during airbag ignition in the car[1].

Because the thermocouple needs to have both wires welded, main difficulty producing thin thermocouples is the welding technology giving high quality welds with perfect repeatability of the welding process and results.

2. Experimental

As welding technology we have selected microplasma welding (micro-PAW), because it offers advatages for welding of thin materials (e.g. thermocouples). Plasma arc has very high temperature (up to 25 000 °C), has high energy density, is very stable and well controlable. All these features improve possibility to create sound welds even on very thin materials and wires. Plasma Arc Welding (PAW) has developed from Gas Tungsten Arc Welding (GTAW). In PAW the arc is struck between tungsten electrode and Cu nozzle. By the flow of the plasma gas through the copper nozzle the created plasma is forced to exit the orifice of the nozzle and becomes the heat source, which is very stable and well controlable by setting the current and plasma gas flow. The schematic of the micro-PAW welding method is at the Fig. 1.

For the construction of thermocouples copper, nickel, chromium, platinum alloys are used. Often used thermocouples are e.g. Cu-CuNi, Fe-CuNi, NiCr-Ni, Pt-PtRh. As the basic thermocouple for testing suitability of micro-PAW for welding of thermocouples the Cu-CuNi thermocouple was selected because easy availability of Cu and CuNi (konstantan) wire at the market. Cu-CuNi thermocouple can be used easily in the temperature range from –250 to +400 °C where it´s temperature resistivity is linear.

Cu and CuNi wires, both of diameter 0.1 mm, were used and welded by micro-PAW with very low welding parameters. Set welding current was I = 5 A. Tungsten-thorium electrode (WT) with diameter 1 mm and transferred arc wiring was used. At the Fig. 1 the transferred arc can is done by connecting the switch at the position 11.

Weld quality and fusion of the 2 metals was checked by metallography. Because of the miniature size of the sample the metallography was rather difficult. Special fixing of the sample in the thermoset with very low thermal shrinkage, grinding with SiC emery paper 2500, 4000, polishing with diamond (3 μm) and coloid silica was necessary. For etching (1 part HNO_3 and 9 parts H_2O) was used and photographs are done on metallurgical microscope (Carl Zeiss – AxioObserver D1m) in DIC contrast. Microhardness according to Vickers (load 10 g) of the

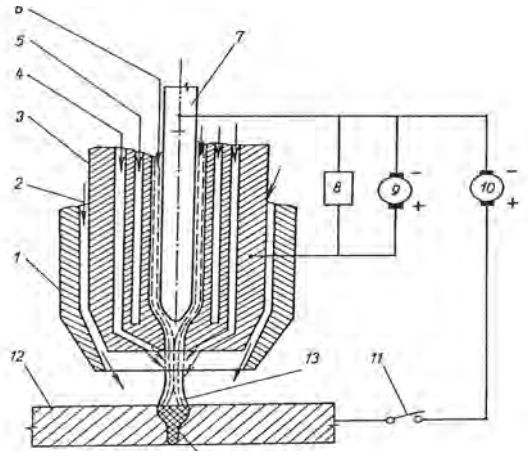

Fig. 1. **Scheme of micro plasma arc welding,** 1 – shielding nozzle, 2 – shielding gas, 3 – water cooled nozzle, tube, nozzle, 4 – focusing gas, 5 – water cooling, 6 – plasma gas, 7 – tungsten electrode, 8 – high frequency ionizator, 9,10 – power source, 11 – switch, 12 – BM, 13 – plasma arc

base metals (wires) and across the joint was measured along the red dashed line shown on Fig. 2. By Hysitron system the nanohardness and Young´s modulus of the BM and WM were measured (load of 1 mN). This measurement was done acoording to Oliver and Pharr[2] using Berkovich indeter, because it is very favourable for small samples (diameter 0.1 mm).

3. Results and discussion

The heterogeneous joint of welded Cu-CuNi thermocouple had a favorable circular shape.

The metallographic cut of the welded thermocouple was done to check penetration, size and quality of joint. The cut is shown at the Fig. 2, where the regular circular shape is visible.

The average results of nanohardness measurement and Young modulus is stated in Table I.

At the Fig. 3 is shown measurement of the Vickers hardness along the red dashed line drawn at the Fig. 2. It is obvious that the joint is ductile without any hard brittle phases, because hardness in HAZ and WM the hardness is quite low, approx. between 70–200 HV0.01, without any hardness peaks.

Hardness measurement by nanoindentation was done. Nanoindentation was made in different parts of the welded part – see Fig. 4. Both measured results are in reciprocal compliance.

Fig. 2. **Welded thermocouple Cu-CuNi, upper wire - Cu, lower wire - CuNi**

Table I
Average values of Young´s modulus and nanohardness

Material	E_{IT} [GPa]	H_{IT} [GPa]
Cu	119.9 ± 5.5	2.29 ± 0.07
CuNi	153.6 ± 6.0	3.43 ± 0.28
weld	148.9 ± 3.8	2.71 ± 0.06

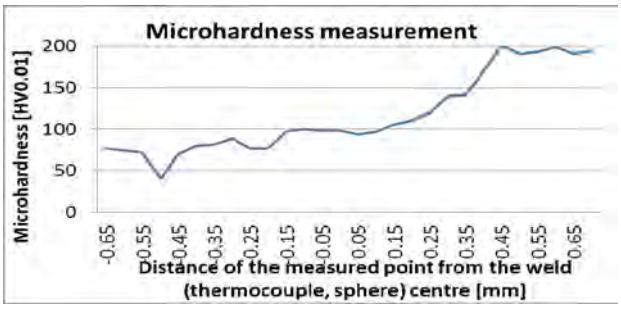

Fig. 3. **Microhardness of the welded thermocouple**

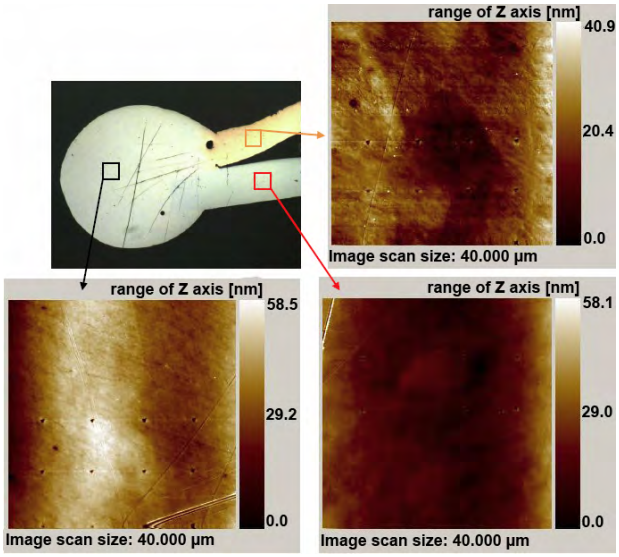

Fig. 4. **Areas of welded sample nano indentation measurement, tested area 40×40 µm, measured results stated in Table I**

4. Conclusion

The creation of the thermocouple Cu-CuNi with favorable circular shape of the weld joint was possible by microplasma welding. No hard brittle phases were found by hardness measurement, so mechanical strength of the joint is satisfactory without any risk of brittle failure. It is possible to say that technology suitable for welding of heterogeneous joints of thin Cu-CuNi thermocouples was found.

The research was financed by the Czech Ministry of Education, Youth and Sport within the frame of project SGS CVUT 2010 – OHK2-038/10.

REFERENCES

1. Lengellé G., Duterque J., Trubert J. F.: RTO-EN-023, Belgium 2002.
2. Oliver W. C., Pharr G. M.: J. Mater. Res. *7*, 1564 (1992).

L. Kolařík[a], M. Válová[a], P. Vondrouš[a], K. Kovanda[a], and J. Šepitka[b] *([a] Dept. of Man. Tech., [b] Dept. of Biomechanics, Faculty of Mech. Eng., CTU in Prague, Prague, Czech Republic)* **Production and Testing of Thermocouples Type Cu-CuNi**

This article focuses on production and testing of thermocouples. Thermocouples Cu-CuNi with fast response for measurement of real thermal cycles during explosions were welded. This work includes details of welding technology and results of testing of the weld by metallography, microhardness and also Hysitron nanoindentation measurement.

TESTING OF DUPLEX COATINGS BY MODULUS MAPPING METHOD

MARIE KOLAŘÍKOVÁ and JAN SUCHÁNEK

Department of Manufacturing Technology, Faculty of Mechanical Engineering, CTU in Prague, Technická, 166 07 Prague, Czech Republic
marie.valova@fs.cvut.cz

Keywords: duplex coating, PVD, nitriding, modulus mapping

1. Introduction

This paper presents results of tribological testing of duplex coatings that have been presented in the previously published paper "The Effect of Duplex Coating on Wear Properties of Tool Steels"[1]. In detail it includes results of testing by Modulus Mapping™ method. Modulus Mapping combines *in-situ* SPM imaging capability of Hysitron's nanomechanical testing instruments with the ability to perform dynamic, or nanoDMA tests.

2. Experiment

The specimens from the low-alloy steel 31CrMoV9 were inert gas quenched and tempered. The duplex treatment had two phases. In the first phase, the specimens were pulse plasma nitrided (depth of nitrided layer is 70 μm). In the second phase, various PVD coatings were deposited: TiN, CrN, TiAlN and a multilayer 3×(TiN-CrN). All coatings were 3 μm thick. Because of the miniature size of the coating, the metallography was rather difficult. There were also problems with the production of sample because plannar surface was required for measurement. The difference in hardness of the substrate, PVD coating and mounting materials cause grinding of sample edge. Therefore, a small steel plate with the same hardness as the base material sample was glued on the coatings. Then the edge gringing was minimalized and the plannarity of the sample was sufficient for nanomechanical tests.

Special mounting of the specimens in thermoset with very low thermal shrinkage, grinding with SiC emery paper with 2500 and 4000 grit and polishing with diamond (3 μm) and coloid silica were necessary. Photographs were taken in a metallurgical microscope (Carl Zeiss – AxioObserver D1m). Treated specimens were tested on Hysitron TI 950 TriboIndenter™ to obtain 3D topography of cross section and a map of complex modulus. The measurement methods are described in details in ref.[1] and ref.[2].

The analysis of the dynamic test is derived from the classical equation for a single degree of freedom harmonic oscillator as given in Eq. (*1*):

$$F_o \sin(\omega t) = mx'' + Cx' + kx \qquad (1)$$

where F_o is the magnitude of the sinusoidal force, ω is the frequency of the applied force, m is the mass, C is the damping coefficient and k is the stiffness of the system. The solution to this differential equation is seen as Eq. (*2*) where a displacement amplitude response (denoted as X_o) is given for a given sinusoidal force F_o, at a frequency ω for a system with a given stiffness, mass and damping.

$$X_o = \frac{F_o}{\sqrt{(k - m\omega^2)^2 + ((C_i + C_s)\omega)^2}} \qquad (2)$$

The phase difference between the force and the displacement is given in Eq. (*3*):

$$\phi = \tan^{-1}\frac{(C_i + C_s)\omega}{k - m\omega^2} \qquad (3)$$

where the total spring stiffness, k, consists of two parts,

$$k = k_s + k_i \qquad (4)$$

The subscripts in Eq. (*1–4*), i and s stand for indenter and sample respectively. From a dynamic calibration m, C_i, and K_i are known, X_o and ϕ are measured, leaving K_s and C_s as the only unknown variables. By assuming a linear viscoelastic response, these equations can be used to calculate the stiffness and damping of a system from the displacement amplitude and phase lag. The stiffness and damping can be used for calculation of the storage modulus and loss modulus using Eq. *5*a and b.

$$E' = \frac{k_s\sqrt{\pi}}{2\sqrt{A_c}} \qquad E'' = \frac{\omega C_s\sqrt{\pi}}{2\sqrt{A_c}} \qquad a = \left(\frac{3FR}{4E_r'}\right)^{\frac{1}{3}} \qquad (5)$$

a) b) c)

where a is the radius of the contact area and R is the radius of curvature of the tip[5].

Eq. (*6*) shows the relationship between complex modulus (denoted as E^*), storage modulus (denoted as E'), and loss modulus (denoted as E''), where i is the imaginary unit.

$$E^* = E' + iE'' \qquad (6)$$

Another theory is presented in ref.[4] and ref [5].

3. Results

Results of Modulus Mapping are shown in Fig. 1 and Fig. 2. Topographic information obtained by *in-situ* SPM is shown in Fig. 3. The tested area was 5×5 μm. We can

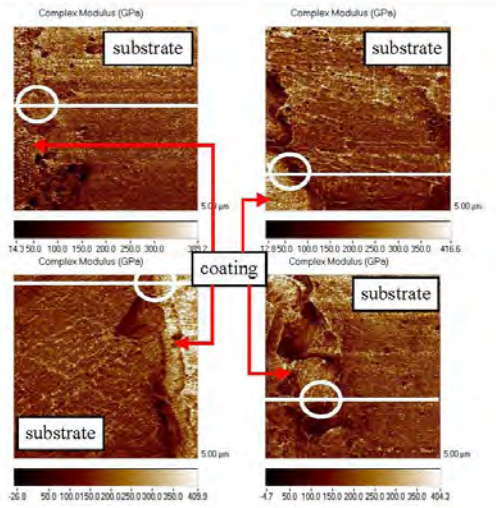

Fig. 1. **Maps of complex modulus for individual coatings: CrN (top left), TiN (top right), TiAlN (bottom left) and multilayer 3×(TiN-CrN) (bottom right). The area in red circle represents a transition zone between substrate and PVD layer**

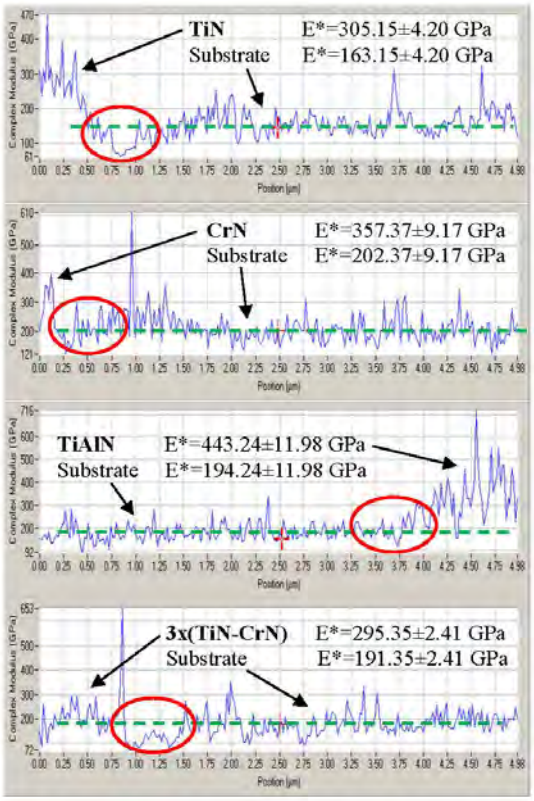

Fig. 2. **Analyses of complex modulus on cross section (The area in red circle represents a transition zone between substrate and PVD layer. The green dashed line shows the average value of complex modulus of substrate)**

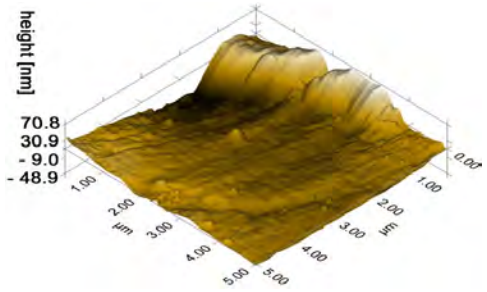

Fig. 3. **Example of topographic information for individual coatings obtained by *in-situ* SPM**

see an increase in values of complex modulus on the area of PVD coating. Measured values of complex modulus are CrN ~ 357 GPa, TiN ~ 305 GPa, TiAlN ~ 443 GPa and 3× (TiN-CrN) ~ 295 GPa.

Complete results of tribological tests are given in ref.[2] and ref.[3].

4. Conclusion

Results for all coatings show that deposited PVD coatings did not affect the properties of nitrided base material. No gradient or transition layer between deposted coating and substrate were observed.

The research was financed by the Czech Ministry of Education, Youth and Sport within the framework of project SGS CVUT 2010 – OHK2-038/10.

REFERENCES

1. Válová M., Suchánek J.: Chem. Listy *105*, s856 (2011).
2. Lukeš J., Šepitka J., Němeček J.: Chem. Listy *104*, s338 (2010).
3. Válová M., Suchánek J., Bláhová O.: Chem. Listy *104*, s378 (2010).
4. Asif S., Wahl K., Warren O.: J. Appl. Phys. *90*, 1192 (2001).
5. Sepitka J., Lukes J., Kuzelka J., Rezníček J.: Chem. Listy *105*, s844 (2011).

M. Kolaříková, and J. Suchánek *(CTU in Prague, Prague, Czech Republic):* **Testing of Duplex Coatings by Modulus Mapping Method**

The paper summarizes partial results of tribological testing of tool steels with duplex coating. Steel samples (31CrMoV9) were nitrided and subsequently treated by PVD process. Different types of coatings (TiN, CrN, TiAlN and a multilayer 3×(CrN-TiN)) with a thickness 3 µm were deposited on samples. The following properties were measured: Results of Modulus Mapping™ are summarized in this paper.

TWO-SCALE MODEL FOR PREDICTION OF MACROSCOPIC ELASTIC PROPERTIES OF ALUMINIUM FOAM

VLASTIMIL KRÁLÍK and JIŘÍ NĚMEČEK

Czech Technical University in Prague, Thákurova 7, 166 29 Prague 6, Czech Republic
vlastimil.kralik@fsv.cvut.cz

Keywords: metal foam, porous system, nanoindentation, micromechanical properties, homogenization

1. Introduction

Aluminium foams belong to the group of modern structural materials with high potential to many engineering applications. It is a highly porous material with cellular inner microstructure. It is also known for attractive mechanical and physical properties. The application of this material is very wide. Some structural and functional applications of aluminium foams for industrial sector which covers mainly automotive, aircraft but also building industries have been reviewed e.g. by Banhart[1].

In this study, commercially available aluminium foam Alporas® (Shinko Wire Co., Ltd) was tested. Alporas is characterized by a closed cell microstructure as shown in Fig. 2. The large inner pores have usually round of polyhedral shape with the mean size ~ 4.5 mm[2]. The very thin cell walls (typically ~ 100 μm thick, Fig. 1) of closed cells create randomly distributed solid metal phase. The overall porosity of this material reaches ~ 90 % (ref.[2]). The manufacturing process of the Alporas is a batch casting process and can be found in details e.g. in Miyoshi et. al.[2].

In this paper, we deal with the assessment of the two-scale microstructural model that takes into account heterogeneity taking place on the cell wall level, as well as at the whole foam level. For this reason, we utilize micromechanical up-scaling procedures that are commonly used in finding effective properties of classical composites. Up-scaling mechanical properties from microscale to the upper level uses so called homogenization techniques[3] in which microscopically heterogeneous material is replaced by a fictitious homogeneous one having equivalent overall behavior.

2. Definition of the model

The Alporas foam is characterized by a hierarchical microstructure. At least two characteristic length scales can be distinguished: the cell wall level and the foam level. Therefore, two-scale microstructural model for the prediction of macroscopic elastic properties on the whole foam level is proposed based on the utilization of nanoindentation data received on cell walls[4]. The model covers:

Level I (the cell wall level).

In this level, characteristic dimension of the cell wall defined by the mean midspan wall thickness is $L \sim 100$ μm. This level consists of prevailing aluminium matrix (Al-rich area) with embedded heterogeneities in the form of Ca/Ti-rich areas (as further discussed in section 3.2). Distinct elastic properties of the microstructural constituents were assesed using nanoindentation at this level.

Level II (the foam level).

At this level, the whole foam containing large pores with an average diameter ~ 2.6 mm (as evaluated for our samples) are considered. Cell walls are considered as homogeneous having the properties that come from the Level I homogenization.

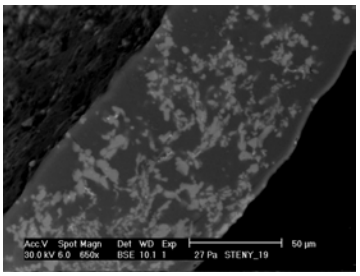

Fig. 1. **Detailed ESEM image of a cell wall showing Ca/Ti-rich area (light zones) – Level I**

Fig. 2. **Overall view on a typical micostructure of aluminium foam – Level II**

3. Experimental part

3.1. Sample preparation

Samples for nanoindentation testing were prepared from small Alporas block 18×18×14 mm which was firstly embedded into cylindrical mould and filled with a low viscosity epoxy resin (Struers®). Then, ~ 5 mm slice was cut

by diamond saw and polished with fine SiC papers with selected technological process[5]. Resulting surface roughness was checked with *in-situ* imaging (surface scanning was performed with the same tip as for nanoindentation). Quadratic deviation from the mean plane (root-mean-square[6]) was found to be $R_q \approx 9$ nm which was more than acceptable compared to the maximum indentation depths 100–300 nm. As a rule of thumb, the surface roughness should be kept within 10 % of the expected maximum depths used in nanoindentation which was fullfilled in our case.

3.2. ESEM and microstructural analysis

The microstructure of the cell wall was studied in electron microscope (ESEM). Two distinct phases, visible as differently colored areas in ESEM images were identified (Fig. 1). The chemical composition of the two phases was checked with EDX element analysis in ESEM. As expected, the majority of the volume (dark zone) was composed of aluminum and aluminium oxide Al_2O_3 (further denoted as Al-rich area). Lighter zones contained significant amount of calcium and titanium (further denoted as Ca/Ti-rich area). The non-uniform distribution of these zones shows on inhomogeneous mixing of the admixtures added during the production process.

3.3. Nanoindentation

The nanoindentation testing was performed using a Hysitron Tribolab system® located at the CTU Prague's laboratory. This system consists of *in-situ* SPM imaging which was used for scanning the sample surface. Berkovich tip was used for all measurements.

Two distant locations were chosen on the sample to capture its heterogeneity. Both locationss were covered by a grid of 10×10 indents with 10 μm spacing. It yields 200 indents in total which was considered to give sufficiently large statistical set of data. Standard load controlled test for an individual indent consisted of three segments: loading, holding at the peak and unloading. Loading and unloading of this trapezoidal loading function lasted for 5 s, the holding part lasted for 10 s. Maximum applied load was 1500 μN.

3.4. Results of the experimental part

Elastic modulus was evaluated for individual indents using standard Oliver and Pharr methodology[7]. The results are depicted in Fig. 3 in which a frequency plot of all elastic moduli merged from two different positions are shown. No significant differences between the positions were found.

Statistical results of elastic moduli have been further analyzed with a deconvolution technique[8–10] which seeks for parameters of individual phases covered in overall results. The deconvolution algorithm searches for n-Gauss distributions in an experimental probability density function (Fig. 3). Random seed and minimizing criteria of the differences between the experimental and theoretical overall PDFs are computed in the algorithm to find the best fit[9]. Two-phase system (one dominant Al-rich phase and one minor Ca/Ti-rich phase) was assumed in the deconvolution. Tab. I contains numerical results from the deconvolution with the estimated volume fractions of the phases.

It can be seen in Fig. 3 that a significant peak appears around 62 GPa appears. This value can be considered as a dominant characteristic of the Al-rich solid phase. This value is in excellent agreement with the value measured by Jeon et al.[11] on melted Al-1.5 wt.% Ca alloy (61.7 GPa).

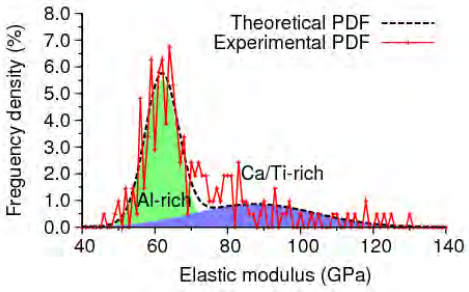

Fig. 3. **Deconvolution of elastic moduli in two phases (Al-rich and Ca/Ti-rich) from two measured positions**

Table I
Elastic moduli and volume fractions from deconvolution

Phase	Mean [GPa]	St. dev. [GPa]	Volume fraction
1 (Al-rich zone)	61.9	4.6	0.638
2 (Ca/Ti-rich zone)	87	17	0.362

4. Numerical part

4.1. Level I homogenization

Continuum micromechanics provides a framework, in which elastic properties of heterogeneous microscale phases are homogenized to give overall effective properties on the upper scale[3]. A significant group of analytical homogenization methods relies on the Eshelby's solution[12] that uses an assumption of the uniform stress field in an ellipsoidal inclusion emnedded in an infinite body. Effective elastic properties are then obtained through averaging over the local contributions[3]. Based on previous experience, we selected two most frequently used analytical schemes and two bounds in the following. At first, rough estimates can be done by computing bounds (limits) based on mixture laws of Voight (parallel configuration of phases with perfect bonding) and Reuss (serial configura-

tion of phases). The disadvantage of using these bounds (or limits) is that they are usually quite far from each other.

Very often, the Mori-Tanaka method[8] can be used for the homogenization of composites with continuous matrix reinforced with discontinuous spherical inclusions. In this method, the effective bulk k_{eff} and shear μ_{eff} moduli of the composite are computed as follows:

$$k_{eff} = \frac{\sum_r f_r k_r (1+\alpha_0(\frac{k_r}{k_0}-1))^{-1}}{\sum_r f_r (1+\alpha_0(\frac{k_r}{k_0}-1))^{-1}} \quad (1)$$

$$\mu_{eff} = \frac{\sum_r f_r \mu_r (1+\beta_0(\frac{\mu_r}{\mu_0}-1))^{-1}}{\sum_r f_r (1+\beta_0(\frac{\mu_r}{\mu_0}-1))^{-1}} \quad (2)$$

$$\alpha_0 = \frac{3k_0}{3k_0+4\mu_0}, \beta_0 = \frac{6k_0+12\mu_0}{15k_0+20\mu_0} \quad (3)$$

where f_r is the volume fraction of the r^{th} phase, k_r its bulk modulus and the coefficients α_0 and β_0 describe bulk and shear properties of the 0^{th} phase, i.e. the reference medium[3]. The bulk and shear moduli can be directly linked with Young's modulus E and Poisson's ratio ν used in engineering computations as:

$$E = \frac{9k\mu}{3k+\mu} \quad (4)$$

$$\nu = \frac{3k-2\mu}{6k+2\mu} \quad (5)$$

At second, the self-consistent scheme[3] was used. It is an implicit scheme, similar to Mori-Tanaka method, in which the reference medium points back to the homogenized medium itself.

The homogenized elastic property for the two considered microscale phases in the cell wall (i.e. Level I) is summarized in Tab. II for individual homogenization techniques. Very close bounds and insignificant differencies in the elastic moduli estimated by the schemes were found.

4.2. Level II homogenization

In this level, cell walls are considered as a homogeneous phase having the properties that come from the Level I homogenization. The walls createa matrix phase and the large air pores can be considered as inclusions in this homogenization.

At first, effective elastic properties of the Level II were estimated with the same analytical schemes used in Level I. The volume of air pores was assessed experimentally by weighing on our samples as 91.4 %. The homogenized elastic modulus for the Level II structure is summarized in Tab. III. It is clear that the analytical methods do not give appropriate results, because the basic assumptions following from Eshelby's solution of an ellipsoidal inclusion in an infinite body and volume fraction restrictions are not fulfilled. Nevertheless, the correct solution should lie between Voight and Reuss bounds that are, in this case, quite distant (Tab. III). The Mori-Tanaka ends up close to the average phase value, whereas the self-consistent scheme tends to reach lower stiffness value (i.e. the air) due to the very large volume fraction of pores.

At second, more appropriate two dimensional microstructural FEM model was applied. The model geometry was generated from high resolution optical images of Al-foam cross-section (Fig. 4a), which was embedded to blackwashed gypsum and than polished with fine SiC papers. Size of this representative area is 36 × 44 mm and represents a higher structural level of the material. At this image, pore centroids were detected, Delaunay triangulation applied and Voronoi cells created. Then, an equivalent 2D-beam structure was generated from cell boundaries (Fig. 4b). As a first estimate, uniform cross-sectional area was prescribed to all beams (~ 8.6 % of the total). Boundary conditions appropriate to the loading (axial tension) are specified in Fig. 4b. The tension test leading to the evalaution of the homogenized elastic modulus was performed using program Oofem software package[13].

In our computations, the homogenized elastic modulus reached $E_{hom} \approx 0.3-0.6$ GPa depending on the stiffness of the contour beams. The higher E_{hom} value appllies for the contour beam stiffness which has the same stiffness as the rest of the beams. The lower E_{hom} value applies if a half

Table II
Effective values of Young's modulus computed by different homogenization schemes

Scheme	Mori-Tanaka	Self-consist. scheme	Voigt bound	Reuss bound
E [GPa]	70.076	70.135	71.118	69.195

Table III
Effective values of Young's modulus by different homogenization schemes

Scheme	Mori-Tanaka	Self-consist. scheme	Voigt bound	Reuss bound
E [GPa]	3.1510	0.0012	6.0200	0.0011

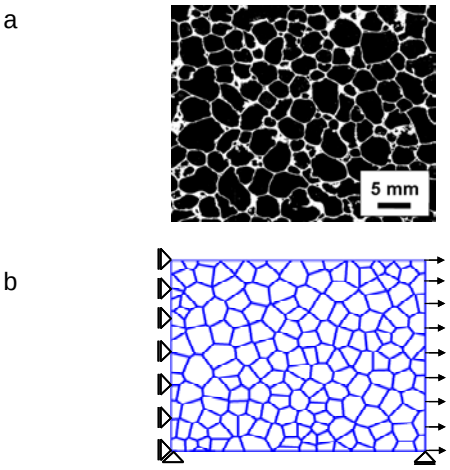

Fig. 4. **(a) High resolution optical image of Al-foam. (b) 2D-beam structure with prescribed boundary conditions**

-stiffness is used for contour beams. Such result is in good agreement with the range of experimental values (0.4−1 GPa) reported for Alporas® e.g. by Ashby et. al.[14]. Our preliminary experiments show on the E_{hom} value 0.27 GPa.

5. Conclusions

Elastic parameters of cell walls were obtained on a statistical set of nanoindentation results from which one dominant and one minor mechanical phase were separated by the deconvolution algorithm. Analytical homogenization schemes showed very similar results of effective cell wall elastic properties ($E_{Level\text{-}I} \approx 70$ GPa). This value together with corresponding volume fraction of cell walls and large pores were used in micromechanical up-scaling to the upper level (Level II). Effective elastic properties of Level II were estimated with the same analytical schemes used in Level I. However, the analytical methods do not give satisfactory results in this case. Therefore more appropriate two dimensional microstructural FEM model was applied. Homogenized elastic modulus reached 0.3−0.6 GPa. These values are in good agreement with the range of experimental values obtained by conventional methods. Further development of the numerical model (influence of boudary conditions, influence of beam stiffness variations, size of RVE, extension to 3D) and extending an experimental program is planned in the future.

Support of the Czech Science Foundation (GAČR 103/09/1748 and GAČR P105/12/0824) is gratefully acknowledged.

REFERENCES

1. Banhart J.: Prog. Mater. Sci. *46*, 559 (2001).
2. Miyoshi T., Itoh M., Akiyama S., Kitahara A.: Mater. Res. Soc. Symp. Proc. *521*, 133 (1998).
3. Zaoui A.: J. Eng. Mechanics *128*, 808 (2002).
4. Němeček J., Králík V., Vondřejc J., Němečková J.: *Proceedings of the Thirteenth International Conference on Civil, Structural and Environmental Engineering Computing*. Edinburgh: Civil-Comp Press (2011).
5. Dudíková M., Kytýř D., Doktor T., Jiroušek O.: Chem. Listy *105*, s790(2010).
6. ISO 4287-1997, "Geometrical Product Specifications (GPS) – Surface texture: Profile method – Terms, definitions and surface texture parameters".
7. Oliver W., Pharr G. M.: J. Mater. Res. *7*, 1564 (1992).
8. Constantinides G., Chandran K. R., Ulm F.-J., Vliet K. V.: Mater. Sci. Eng., A *430*, 189 (2006).
9. Němeček J., Šmilauer V., Kopecký L.: Cem. Concr. Composites *33*, 2 (2011).
10. Tesárek P., Němeček J.: Chem. Listy *105*, 17 (2010).
11. Jeon I. et al.: Mechanics Mater. *41*, 60 (2009).
12. Eshelby J. D.: Proc. Royal Society *241*, 376 (1957).
13. Patzák B., Bittnar Z.: Adv. Eng. Software *32*, 759 (2001).
14. Ashby M. F., Evans A., Fleck N. A., Gibson L. J., Hutchinson J. W., Wadley H. N.: Mater. Design *23*, 1 (2002).

V. Králík and J. Němeček *(Czech Technical University in Prague, Faculty of Civil Engineering):* **Two-scale Model for Prediction of Macroscopic Elastic Properties of Aluminium Foam**

This paper is focused on the prediction of macroscopic elastic properties of highly porous aluminium foam. The material is characterized by a closed pore system with very thin pore walls and large air pores. Intrinsic material properties of cell wall constituents are assessed with nanoindentation whereas analytical homogenizations are employed for the assessment of the cell wall elastic properties. 2D microstructural FEM model was applied to obtain effective elastic properties of the whole foam.

SIZE-DEPENDENT MICROHARDNESS OF TWO-COMPONENT SINTERED MATERIALS

MIRIAM KUPKOVÁ[a] and MARTIN KUPKA[b]

[a] *Institute of Materials Research of SAS, Watsonova 47, Košice,* [b] *Institute of Experimental Physics of SAS, Watsonova 47, Košice, Slovakia*
mkupkova@imr.saske.sk

Keywords: indentation size effect, sintered materials, solid solution, (sub)grain boundaries

1. Introduction

Indentation techniques are widely used in the industry for more than one century. They serve as quality control measurements and as an economical, routine probe for estimating the strength of engineering materials. Indentation tests offer simplicity and speed because they require access only to a flat surface of component rather than, for example, the manufacturing of special specimen for conventional tensile testing. In connection with microdevices, material scientists discovered that they could quickly and conveniently probe the small-scale response of material dimensions by micro- and nanoindentation techniques.

In the Brinell test, a hard ball of diameter D is pressed under a load P into the plane surface to be examined. After removal of the load, the chordal diameter d of a remanent impression left by the indenter is measured. The Meyer hardness H_M is calculated as the load divided by the projected area of the impression.

Tabor[1] demonstrated that for metals with a power-law work-hardening the Meyer hardness is

$$H_M \equiv \frac{4P}{\pi d^2} \approx 3Y_0\left(0.2\frac{d}{D}\right)^n, \qquad (1)$$

and the plot Meyer hardness versus d/D closely reproduces the tensile true stress versus true strain curve. Here Y_0 is a critical tensile stress below which the deformation is elastic, and n is work hardening exponent.

So, by making a series of Brinell tests with indentations of various diameter d the important plastic stress-strain characteristics of the material may be extracted from the observed H_M-d relation.

As regards the conical or pyramidal indenters, Tabor argued that due to the "principle of geometric similarity" the hardness should not depend on the size of the remanent impression left by the indenter or on the indentation load. He demonstrated that for the Vickers indenter

$$H_M \equiv \frac{2P}{d^2} \approx 3(Y \text{ at } 8\% \text{ strain}). \qquad (2)$$

Here d represents the Vickers indent diagonal.

Conical or pyramidal indenters whose sizes exceed tens of microns really produce size-independent hardness values for most metals.

But smaller indenters, in the range from submicrons to about ten microns, often display a significant size effect. That is, the impressions left by such indenters are smaller than expected from the size of impressions left by large indenters. Thus the apparent hardness of a specimen increases as the impression size decreases.

The increase in strength is explained in terms of the local dislocation hardening due to geometrically necessary dislocations (GNDs). These dislocations are required to account for the permanent shape change at the surface. The micron-scale permanent impressions produce the densities of GNDs that are comparable to or exceed the densities of statistically stored dislocations, that is the dislocations present in the material prior to the indentation. The smaller is the size of the non-uniform deformation, the larger is the relative density of the GNDs and the greater is their contribution to the work hardening.

This explanation is suitable for behaviour after plastic deformation has started and the indentation process is "well developed". This theory cannot describe the situation near the initial deviation from the elastic regime at the initiation of the plasticity, as there are no GNDs. So, the hardness data may not follow the theory for very small impression sizes.

2. Theory

The objective of this contribution is to modify the Nix and Gao model to account for the indentation of solid solutions.

Nix and Gao[2] considered the indentation of a pure metal by a rigid cone. Resultant impression is accommodated by circular loops of GNDs with Burgers vectors normal to the plane of sample surface. Assuming that the injected dislocation loops are stored in a hemisphere under the contact perimeter, they found that the density of GNDs is proportional to the reciprocal of indentation depth.

Nix and Gao used the Tabor's finding that the indentation hardness is a measure of the yield stress of the metal, the von Mises yield criterion connecting the yield stress with the critical resolved shear stress, and the Taylor's relation stating that the shear strength is proportional to the square root of the dislocation density.

Expressing the total dislocation density as the sum of densities of statistically stored and geometrically necessary dislocations, Nix and Gao finally found that

$$\frac{H}{H_0} = \sqrt{1+\frac{h^*}{h}}. \qquad (3)$$

Here H_0 is the hardness that would arise from the statistically stored dislocations alone, and h^* is a length that characterizes the depth dependence of the hardness.

As the indenter penetrates the solid solution, it not only produces and emites GNDs, but it also "picks up" the solute atoms from the indent volume. The solute atom either remains "stuck" at the indenter's surface (with probability p^*), or leaves the surface (with probability $p^{**}=1-p^*$) and diffuses into indenter's vicinity. The solute atoms "stuck" at the indenter change its effective shape and size and thus modify the density of GNDs. The solute atoms diffused into indenter's vicinity enhance local concentration of solid solution and thus enhance the solid solution strengthening.

Because two strengthening mechanisms take place, the Taylor's relation for dislocation strengthening is replaced by the expression[3]

$$Y = k_s c^{1/2} + k_d \rho^{1/2}. \qquad (4)$$

Here k_i are particular strengthening coefficients, c is the concentration of solute atoms, and ρ is the total dislocation density (the sum of the statistically stored and geometrically necessary dislocations).

Incorporating the above mentioned into the Nix and Gao model, the following relation for the indentation hardness was found:

$$H = H^* \sqrt{1+\left(1+p^* c\right)\frac{h^*}{h}} + H^{**}\sqrt{c}\sqrt{1+p^{**}\frac{h}{h^{**}}} \qquad (5)$$

Here h^*, h^{**} are two length scale parameters, H^* is the hardness resulting from the statistically stored dislocations alone, H^{**} is the parameter quantifying the contribution of solid solution.

3. Results and discussion

The changes in material's strength as detected by microindentation are explained in terms of local strain and solid solution hardening. The strain hardening decreases and the solid solution hardening increases with the indentation depth. So the former dominates for lower indentation depths, while the latter prevails for higher indentation depths. For a pure metal (c=0) only the strain hardening takes place and the relation (*5*) reduces to that of Nix and Gao (*3*). In this case the indentation hardness monotonously decreases with increasing indentation depth. For a solid solution, the indentation hardness firstly decreases, reaches the minimum, and then slightly increases with increasing indentation depth.

Fig. 1 presents the microhardness of materials made from iron powder coated with 12 wt.% of copper[4]. The data were extracted from the load-displacement curves, measured by the TTX-NHT apparatus with diamond Berkovich tip. The sinusoidal/cyclic mode with the maximum load of 100 mN was chosen. Solid points are for green sample, that is practically for a pure iron. The hardness values monotonously decrease. The empty points are for sintered sample, that is practically for a solid solution. The hardness values firstly decrease and then slightly increase. This qualitatively agrees with the theoretical results.

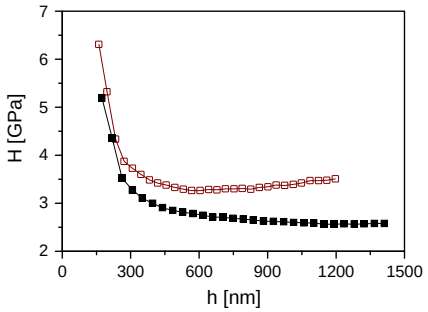

Fig. 1. **Typical curves for indentation hardness as function of penetration depth for samples prepared from 12 wt.%Cu coated iron powders: ■ sample in a "green" state, □ sintered at 1120 °C**

4. Conclusion

The relation for the micro-indentation hardness of solid solutions was obtained theoretically. The results qualitatively agree with the first data obtained for samples from copper-coated iron powders (green as well as sintered).

The applicability of relation (*5*) is now intensively tested on a series of various sintered samples.

This work was supported by VEGA grant 2/0168/12 of the Slovak Grant Agency.

REFERENCES

1. Tabor D.: Philosofical Magazine A *74*, 1207 (1996).
2. Nix W.D., Gao H.: J. Mech. Phys. Solids *46*, 411 (1998).
3. Soboyejo W.: „*Mechanical Properties of Engineered Materials*" (Marcel Dekker, Inc., 2003)
4. Kupková M., Kupka M., Strobl S., Hvizdoš P.: Chem. Listy *105*, s826 (2011).

M. Kupková[a] and M. Kupka[b] (*[a] Institute of Materials Research of SAS, Košice, [b] Institute of Experimental Physics of SAS, Košice, SR*): **Size-Dependent Microhardness of Two-Component Sintered Materials**

Nix and Gao model is modified to account for the micro-indentation of solid solutions. The changes in hardness are explained in terms of local dislocation strengthening due to geometrically necessary dislocations and local solid solution strengthening due to solute atoms transferred from indent volume to its vicinity. There is a qualitative agreement between obtained theoretical relation and first experimental data for sintered iron-copper samples.

LOCAL ANALYSIS OF PLASTIC DEFORMATION IN ECAP AND ECAR PROCESSES

TIBOR KVAČKAJ[a], RÓBERT KOČIŠKO[a], and ANDREA KOVÁČOVÁ[a]

Department of Metals Forming, Faculty of Metallurgy, Technical University of Košice, 042 00 Košice, Slovakia
robert.kocisko@tuke.sk

Keywords: equal channel angular pressing, equal channel angular rolling, finite element method, microhardness

1. Introduction

Ultrafine-grained (UFG) metallic material has received considerable research interest because it exhibits high strength along with good ductility and toughness. Recently, as one of the prominent methods to produce UFG bulk[1-5] and powder[6-8] metallic material, equal channel angular pressing (ECAP) has been studied extensively. The ECAP process (Fig. 1a) is a method that involves large shear plastic deformation in a workpiece by moving through a die containing two intersecting channels of identical cross-sections that meet at a predetermined angle (Φ). The process can be repeated extruding the sample through the same matrix. Several papers evaluated the distribution the effective strain distribution through the cross section of the sample after the ECAP process based on finite element method (FEM) modeling[9,10]. The heterogeneity of non deformation can be reduced by the axial rotation of the sample between passes. Thus the slip planes are activated. ECAP process runs by a discontinuous process, causing a limiting of a maximum lenght of processed sample, which is about 100 mm.

Recently a new continuous shear deformation process, which has several names in the literature as “a continuous ECAP process”, "continuous confined strip shearing (C2S2)"[11] or equal channel angular rolling (ECAR)[12,13] was developed. This process can be applied to strip or profile form of materials. The sample is extruded through a matrix with upper guide roll and lower feeding roll, as shown in Fig. 1b. In this process friction plays a major role, which must provide a frictional force to prevent spin on the material in the feeding roll.

Several authors published the effective strain distribution through the cross section of the strip[14] and sheet[15] after the ECAR process based on FEM modeling. ECAR process is compared to ECAP much more difficult to operate the forming process, therefore this technology is to be reviewed.

This work deals with local comparison of plastic deformation in ECAP and ECAR process after the first pass, on two experimental materials, OFHC copper and alluminium 99.5 %.

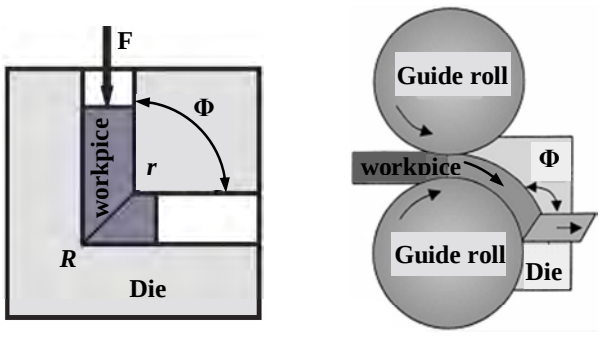

Fig. 1. **Scheme of: a) ECAP and b) ECAR method**

2. Experimental material and methodics

For the experiment two materials with different strain hardening were used. Oxygen-free high conductivity (OFHC) copper and alluminium 99.5 %. Flow stress is characterized by the Hollomans´s equation $\sigma = K \cdot \varepsilon^n$, where: σ - flow stress, ε - strain and n - strain hardening exponent. Flow stress for copper is $\sigma = 460.\varepsilon^{0.38}$ and for alluminium is $\sigma = 108.\varepsilon^{0.22}$. The initial microhardness for the Cu = 117 HV1 and Al= 36 HV1. Both materials were processed by one pass using ECAP and ECAR technology.

The ECAP was realized by hydraulic equipment at room temperature, which makes it possible to produce the maximum force of 1 MN. The die channel angle was Φ = 90° with diameter 10 mm. Extrusion speed was 5 mm min^{-1}. The length of the sample was 100 mm.

The ECAR was carried out on 210 DUO rolling mill at room temperature. The groove of feeding roll has a dimension of 6 x 6 mm. Output channel has dimensions 6 × 6.5 mm. Angle between feeding roll and output channel is Φ = 90°. Angular velocity of rolls were 0.052 rad/s, corresponding to extrusion speed 5 mm s^{-1}.

Stress-strain analysis was performed using the commercial software product Deform 3D. Geometric dimensions and process variables of ECAP and ECAR process were simulated under laboratory conditions listed above. Samples for ECAP and ECAR were defined as a rigid-plastic object. Flow stress was defined according to the above Holloman´s equations. All other components of ECAP and ECAR equipment (die, ram, rolls) were defined as perfectly rigid objects.

Local heterogeneity of plastic deformation in the cross section of smaple after ECAP and ECAR processing was detection by measuring the microhardness as a function of strain hardening. The microhardness measurements

were performed on central planes in steady-state deformation region. The average hardness values and their variation along the length were determined. The Vickers hardness measurements were done with a load of Al = 0.98 N and Cu = 9.8 N for a dwell time of 5 s using a Struers Duramin-5 microhardness tester.

Deformation in the ECAP process was further investigated on the Cu specimen by deformed grids. The sample for this experiment was lengthwise cutting, where one half was applied square grid with a sized 1 × 1 mm.

3. Results and discussion

Fig. 2a shows the effective strain in the deformed Cu sample in the middle of the ECAP process. There shows that the deformation heterogeneity exists in area "head" along X axis (HDZ). After head area the deformation tends to be homogeneous along X axis, indicating that the sample is deformed under steady-state condition. This region is named as the steady-state deformation region herein and most analyses below will be conducted in this region. In the steady-state deformation region but it is possible to observe heterogeneity of effective strain of the sample cross-section (Y axis) between upper and lower surface.

Grid on the Cu sample deformed by one pass ECAP is presented in Fig. 2b. After one pass ECAP of the sample exhibits grid pattern inclined by shear deformation. Is seen that after deformation the elements have been distorted and oriented at shearing angle θ = 62.7° with respect to the X axis. Except the lower part of the sample showing curved grid, which is frequently generated by a geometrical effect of dies or billets[12]. In this area, shearing angle is reduced to θ = 20°, as seen in detail in A. The undistorted region encompasses about 25 % of the billet thickness. In lower surface, as it shows the detail area B, the increased distortion of the network can be observed, which is probably due to the influence of contact friction. Such distortion in the upper surface was not observed.

Fig. 3 shows comparison of effective strain distribution from FEM and microhardness measurement in cross-section of Cu sample after one pass ECAP. Distribution of effective strain can be divided into four areas: I. uniform minimum deformation extending up to 10 % of the thickness of the sample; II. a significant increase in effective strain about 55 %; III. uniform maximum deformation (30 % of the thickness of the sample); IV. slight decrease in effective strain (30 % of the thickness of the sample). The development of microhardness has a similar tendency . The increase in microhardness between the I. and III. area is approximately 55 %.

The increase in hardness can also be attributed to the UFG microstructure and high dislocation density from the ECAP process. Effect of friction on the lower surface is also confirmed by microhardness measurements. FEM simulation of effects of friction didn´t reflect the fiction effect around the upper surface, because the coefficient of

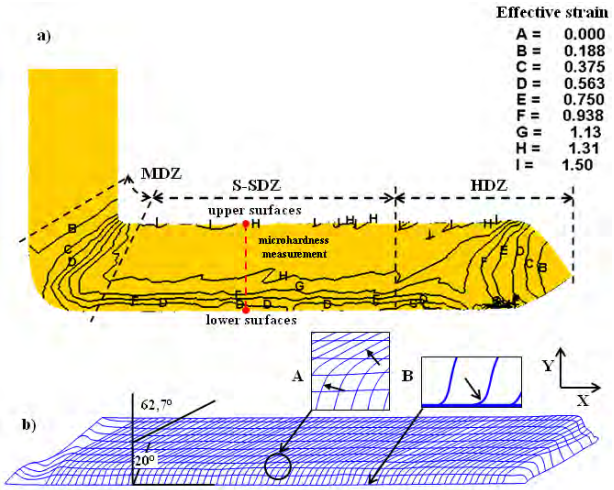

Fig. 2. **Distribution of effective strain and grid in the deformed sample after one ECAP pass: (a) effectiv strain; (b) deformed grid**

friction was defined as a constant value. This investigation indicates that for the FEM simulations, it is appropriate to consider a chase of contact pressure due to friction.

Fig. 4 shows comparison of effective strain distribution from FEM and microhardness measurement in cross-section of Al sample after one pass ECAP. Effective strain and microhardness distribution, can also be divided into four areas, as for copper. Width of the regions is slightly different, due to the higher plasticity of Al. Even in this case the microhardness showed a significant effect of friction on the lower surface of the sample. Simulation did not reflect this effect.

Fig. 5 shows the effective strain distribution in Cu the deformed strip in the ECAR process, where the die channel angle Φ is equal to 90°. The processed strip can be divided into four main zones along the track of ECAR

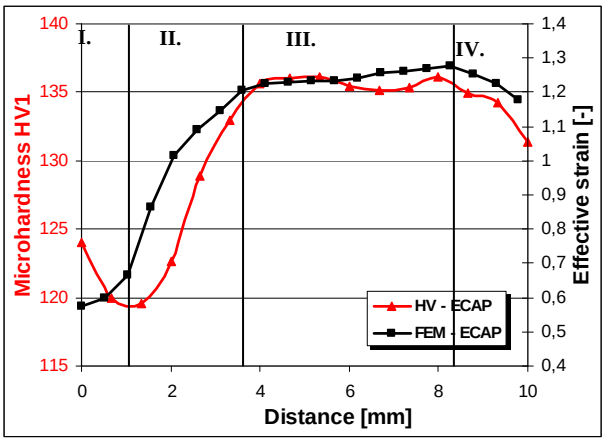

Fig. 3. **Distribution of FEM effective strain and microhardness in cross-section of Cu sample, after one ECAP pass**

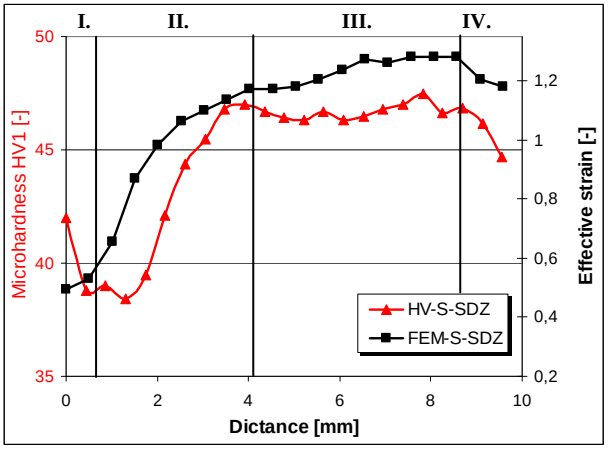

Fig. 4. **Distribution of FEM effective strain and microhardness in cross-section of Al 99.5 % sample, after one ECAP pass**

process: the head of deformation zone (HDZ), the steady-state deformation zone (S-SDZ); the main deformed zone (MDZ) and the groove deformation zone (GDZ). As in the ECAP process, there is heterogeneous strain observed between the lower and upper surface of the sample, which is dependent on the geometry of matrix and contact friction. The HDZ zone has a non-uniform effective strain distribution. The effective strain distribution of the S-SDZ is uniform along the strip metal's (X axis). The MDZ is a shear deformation area which is located at the intersection of the two channels. Input plastic deformation of ECAR process is driven by feeding rolls. It reports the value of $\varphi_{ef} \approx 0.4$ (Fig. 7), which is dependent on groove filling and friction. Therefore, the strains in outlet channel of the S-SDZ in the ECAR are much lower than those in the ECAP.

Fig. 6 shows comparison of to the effective strain distribution from FEM and microhardness measurement in cross-section of sample in groove and after one pass ECAR. There is relatively high φ_{ef} observed in the groove, which linearly increases the thickness of the sample from

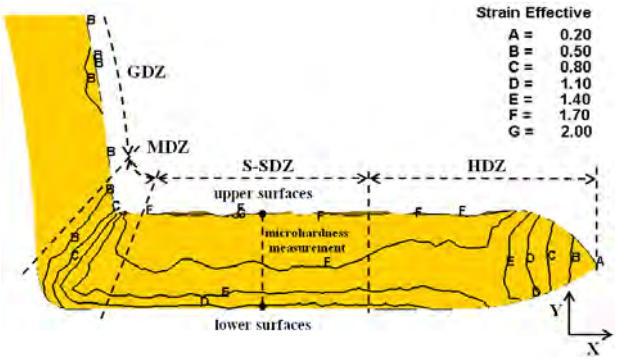

Fig. 5. **Distribution of effestive strain in the deformed sample during one ECAR pass**

the bottom to the top of the sample. Microhardness measured in steady-state of deformation has only two areas: I. a significant increase in the microhardness about 15 HV1; II. Uniform hardness. Distribution of φ_{ef} is in II. area in a slight increase. The same course was also measured on samples of Al, which is shown in Fig. 6. On Al samples was measured microhardness in the groove about 10 mm before entering the MDZ. In the groove, there was the increase in the hardness of about 8 HV from the initial state, the hardening is also dependent on supercharging of channel. In ECAR process levels φ_{ef} are higher and are evenly spaced in cross-section than in the ECAP process.

Fig. 5, 6 from FEM simulations show a net contribution of φ_{ef} of ECAR MDZ, where deformation in groove of feedng roll is not considered. The development of effective strain in the cross section is the same as the deformation in GDZ, their values are lower by $\Delta\varphi_{ef} = 0.3$ [-]. Similar results were published in the article[13], which were based on 2D modeling of ECAR process, in which the deformation

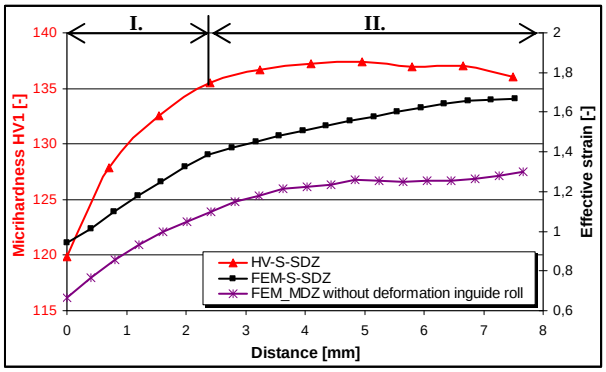

Fig. 6. **Distribution of effective strain and microhardness in cross-section of Cu sample, after one ECAR pass**

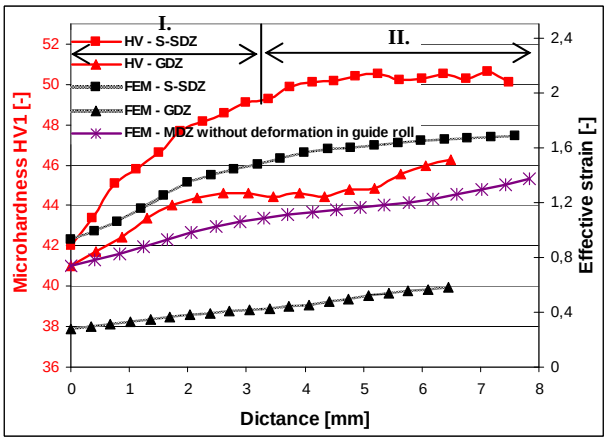

Fig. 7. **Distribution of effective strain and microhardness in cross-section of Al sample, after one ECAR pass**

was not considered in the groove of feeding roll. ECAR process according to the scheme in Fig. 1 uses a high frictional forces in the roll groove, which are able to overcome the deformations in the MDZ. These frictional forces are provide by pressing the material to groove of feeling roll, and therefore deformation must be considered in the FEM simulations in the roll groove.

4. Conclusion

Based on experimental results, it can be concluded that:

- along the sample (X axis) is in the ECAP and ECAR process highest heterogeneity of φ_{ef} at the beginning of the sample, followed by a steady state to the end of the sample.
- greater heterogeneity through the cross-section of samples at steady-state was observed in the ECAP process.
- in the ECAP process was based on the deformed grid and microhardness observed the effect of friction on the bottom of the sample.
- in the ECAR process levels of φ_{ef} are higher, and are evenly distributed in the cross-section compared with the ECAP process.

This work was realized within the frame of the project VEGA 1/0359/11.

REFERENCES

1. Horita Z., Fujinami T.,Nemoto M., Langdom T. G.: J. Mater. Process Technol. *117*, 288 (2001).
2. Kvačkaj T., Bidulská J., Kočiško R., Bidulský R.: *Aluminium Alloys, Theory and Applications*; ISBN 978-953-307-244-9, InTech, Rijeka, p. 3-26 (2011).
3. Chen Z. H., Cheng Y. Q., Xia W. J.: Mater. Manuf. Process. *22*, 51 (2007).
4. Bidulská J., Kočiko R., Kvačkaj T., Bidulský R., Grande M. A.: Chem. Listy *105*, s155 (2011).
5. Kočiško R., Zubko P., Ďurišin J., Molnárová M., Kováčová A., Kvačkaj M., Bacsó J.: Chem. Listy *104*, s330 (2010).
6. Bidulská J., Kvačkaj T., Kočiško, R., Bidulský R., Actis Grande M., Donič T., Martikán M.: Acta Metall. Slovaca *16*, 4 (2010).
7. R. Bidulský, J. Bidulská, M. Actis Grande: High Temp. Mater. Process. *28*, 337 (2009).
8. Hvizdoš P., Besterci: Chem. Listy *105*, s696 (2011).
9. Li S., Bourke M.A.M., Beyerlein I.J., Alexander D.J., Clausen B.: Mater. Sci. Eng. A *382*, 217 (2004).
10. Kvačkaj T., Kováčová A., Bidulská J., Bidulskký R., Kočiško R., Kvačkaj M.: Mater. Sci. Forum, in print.
11. Lee J.C., Seok H.K., Suh J.Y.: Acta Mater. *50*, 4005 (2002).
12. Park J.-W., Kim J.-W., Chung Y.-H.: Scr. Mater. *51*, 181 (2004).
13. Habibi A., Ketabchi M., Eskandarzadeh M.: J. Mater. Process. Technol. *211*, 1085 (2011).
14. Shubo Xu, Guoqun Zhao, Xufang Ren, Yanjin Guan: Mater. Sci. Eng. A *476*, 281 (2008).
15. Wei Wei,Wei Zhang, Kun XiaWei, Yi Zhong, Gang Cheng, Jing Hua: Mater. Sci. Eng. A *516*, 111 (2009).

T. Kvačkaj, R. Kočiško, and A. Kováčová *(Dpt. of Metals Forming, Faculty of Metallurgy, Technical University of Košice, Slovakia):* **Local Analysis of Plastic Deformation in ECAP and ECAR Processes**

The article deals with comparison of two SPD methods: ECAP and ECAR. An angle between the horizontal and vertical channels during ECAP and ECAR pressing was used $\Phi = 90°$. The experiment was focused on the comparison of deformation processes between OFHC copper and Al 99.5 %. Detailed stress-strain analysis of both methods was performed by a finite element method (FEM). The deformation distribution achieved from FEM was made by Vickers microhardness measurement and deformation mesh.

NANOSCRATCH AND NANOWEAR OF DENTAL FILLING COMPOSITES

JAROSLAV LUKEŠ[a], JOSEF ŠEPITKA[a], MARIE VÁLOVÁ[b], and RENATA EICHLEROVÁ[a]

[a] *Department of Mechanics, Biomechanics and Mechatronics, Faculty of Mechanical Engineering, CTU in Prague, Technická 4, 166 07 Prague 6,* [b] *Department of Manufacturing Technology, Faculty of Mechanical Enginnering, CTU in Prague, Czech Republic*
jaroslav.lukes@fs.cvut.cz

Keywords: nanoindentation, dental filling composites, wear, scratch test

1. Introduction

Dental composites and their mechanical behavior have been studied intensively in the last decade. Findings are being used for the dental fillings lifetime improvement in order to prevent fracture of filling, loss of filling and creating of secondary caries on the tooth-filling interface. Next to the aesthetic requirements, there are important mechanical parameters, which are closely watched in a field of restorative dentistry. Dental composites experience internal stresses after polymerization due to the volumetric shrinkage of an epoxy matrix. Polymerization is initiated by the light curing from the outer surface of cavity fillings. Light absorption decreases with depth of cavity and therefore, mechanical properties of dental composite also vary in depth[1]. Finite element analysis of a stress distribution caused by shrinkage with respect to a depth gradient of mechanical properties has been published recently[2]. Finite element models were advantageously based on values of elastic moduli measured by means of nanoindentation.

Wear properties of dental composites are also very important parameters for applicability of materials in modern stomatology. Wear resistivity is one of the qualitative parameters for an estimation of dental filling lifetime. Considering a filling as a nanocomposite material an experimental technique has to be sensitive in micro- and nano level in order to describe wear processes. Existing nanomechanical systems provide wear testing together with some scratch capabilities. Nanomechanical system Hysitron TriboIndenter™, which has been used in this study, provides a scanningWear™ method for a characterization of a wear resistivity of materials. A probe is attached to a three plate capacitive transducer and drawn over a surface with a piezo scanner at certain normal force produced by the transducer. A stage with a sample stays at a fixed position.

Worn area is visualized by *in-situ* Scanning Probe Microscopy (SPM) at low contact force and wear depth is measured from 3D topography image afterwards. Standard nanoindentation tips can be employed in the measurement.

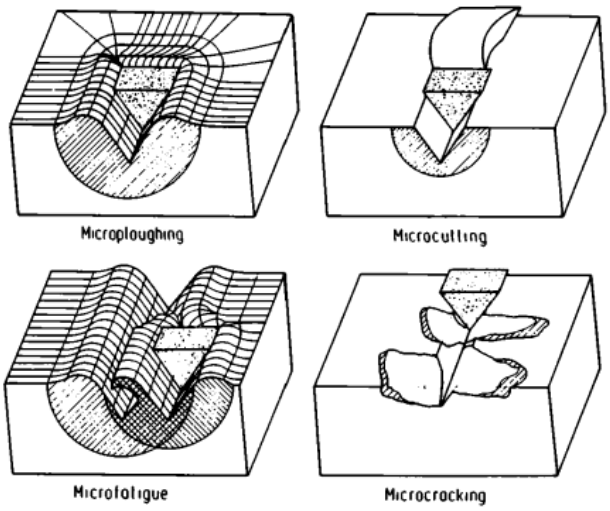

Fig. 1. **Physical interaction between abrasive particle and surface of materials[3] (adopted from Karl-Heinz, 1987)**

There are different mechanisms of material removal distinguished during a sliding wear[3] (Fig. 1). Material properties such as elastic modulus, hardness, fracture toughness or coefficient of friction together with an attack angle (an angle between the surface and cutting face of debris) influence a wear mechanism. Complementary nanoScratch tests and analysis of the *in-situ* SPM scans can provide a close look at the mechanism of removal of dental composite removal for a specific phase. Scratch tests also give values of coefficient of friction, which can explain a wear behavior in more details. This study is focused on wear mechanism of three types of dental composites with respect to their fillings.

2. Materials and methods

2.1. Sample preparation

Cylindrical specimens were made from dental filling composites (Filtek™ Supreme XT, Filtek™ Silorane and Charisma®) with different chemical composition. A single material was pushed into a teflon mould, covered by a transparent plastic film and pressed by a glass slide. Polymerization of the material was activated with a light curing unit (Translux Power BlueTM, Hereaus Kulzer GmbH, Germany) for time period according to the instructions for use. These specimens were removed from teflon

mould and all of them were embedded into EpoFix and polished afterwards. A resulting roughness was approximately RMS = 5 nm at scan size 15 × 15 μm.

2.2. Testing condition

A nanomechanical testing instrument Hysitron TI 950 TriboIndenter™ (Hysitron, Inc., Minneapolis, MN, USA) was used for ScanningWear™ and nanoScratch. ScanningWears of a size of 5 × 5 μm at different contact forces of 40 μN, 50 μN, 60 μN and 70 μN for 10 cycles were applied on each sample. Topography of worn region was acquired by *in-situ* SPM method in order to calculate a wear depth as a difference in a mean height of a surface outside of worn square and a mean height of bottom of worn square. A local tilt of samples was compensated by "average" regression of an image within TriboView software. Complementary three nanoScratch tests were also applied at constant force 800 μN on each sample. Scratch length of 6 μm was reached in 30 s.

3. Results

3.1. Statistical analysis

Statistical analyses for 12 datasets at each normal force for each material were required to determine what force caused a significant material removal. Statistics was carried out using the following methods (STATGRAPHICS Centurion XV, StatPoint, USA). Tests for normality were performed via the Chi-Squared, Shapiro-Wilk test. All data sets were assessed as a normal distribution. Outlier identification was performed via the Grubbs and Dixon tests. No outliers were found in our data sets. Homoscedasticity was checked for the application of ANOVA parametric tests (the Leven, Bartlett and Cochrans tests were used). Variances were found to be different for our data sets; therefore, the statistically significant differences were in most cases checked by nonparametric methods. The Kruskal-Wallis test was used for this purpose. The Mann-Whitney test was used as a post hoc test. The confidence intervals for the mean values were calculated at a significance level of "alfa" = 0.05. The nonparametric analysis of variance was performed at a significance level of "alfa" = 0.05.

Not significant variances of material removal at certain forces are indicated by asterisk in the Fig. 2.

3.2. ScanningWear™

The values of wear depth [nm] were used for demonstration of different wear resistivity to the normal force (Fig. 2). Supreme sample showed the least ability for resistance to wear process at all contact forces. Charisma experienced significant wear depth increase already from the lowest contact force of 40 μN to 50 μN. There was no significant step in wear values between 50 μN and 60 μN contrary to significant step in wear depth from 60 μN to 70 μN of normal force. Siloran was force. A significant increase in the amount of worn material was observed at higher forces. Overall, the highest wear resistivity was measured on Siloran sample.

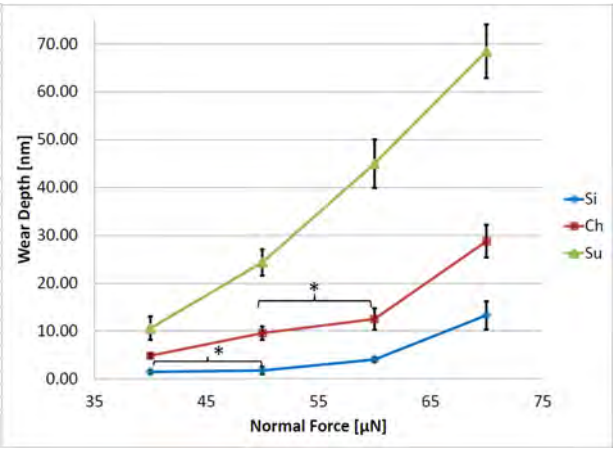

Fig. 2. **Graph shows the wear depth dependence on a contact (normal) force between a tip and sample surface. In this case, stars indicate the statistically NOT significant differences between data sets of measured wear depth at certain contact forces. 'Si' stands for Siloran, 'Ch' for Charisma and 'Su' for Supreme. Error bars indicates the confidential intervals for mean values of wear depths at certain normal force**

3.2. nanoScratch

A coefficient of friction also closely relates to wear behavior. Therefore, six scratch tests were performed on each sample with a standard diamond Berkovich tip of radius ~150 nm. Measured mean coefficients of friction are introduced in Table I. There was no significant difference in friction coefficient among the samples.

In-situ SPM images provide information about mechanism of material removal during scratch tests. There were different mechanisms distinguished for hard particle and softer polymer matrix. Supreme sample contains largest zirkonia/silica particles, which are clearly seen on "post" image of nanoScratch tracks (Fig. 6). In this case, coefficient of friction $f = 0.16 \pm 0.007$ was determined for the particle itself.

Table I
Mean coefficeint of friction f with standard deviation σ measured on dental composits by nanoScratch tests using a dimond Berkovich tip

Charisma	Supreme	Siloran
0.22 ± 0.015	0.2 ± 0.01	0.2 ± 0.023

4. Discussion

Results showed a different wear resistivity of samples of three dental composites. However, the mean values of friction coefficient from the same samples did not show any significant differences. Average coefficients of friction do not predict a wear resistivity of particular dental composite. Therefore, scratch studies needs to be performed at the level of fillers (Fig. 6.)

In-situ SPM images clearly showed the different sizes and distributions of hard particles within composites. Moreover, *in-situ* SPM images of worn squares revealed distinct wear process at composites material phases. Hard and larger particles were less worn than surrounding polymerized matrix already at the lowest normal force of 40 μN (Fig. 3, Fig. 5). This observation was valid for all three samples; however, there were different wear depths measured from the beginning of test cycles. Supreme was the most worn material and kept this lowest wear resistivity for all used normal forces. The wear depth increased with increasing contact force between the diamond tip and the surface.

In case of Charisma and Siloran sample a critical force, which indicates a sudden decrease of wear resistivity, was observed. *In-situ* SPM images revealed that this critical force is associated with a removal of hard particles

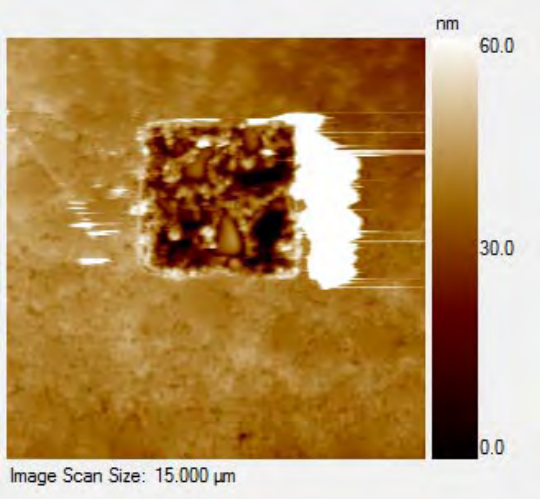

Fig. 3. ***In-situ*** **SPM of a worn location on Charisma at the contact force 60 μN**

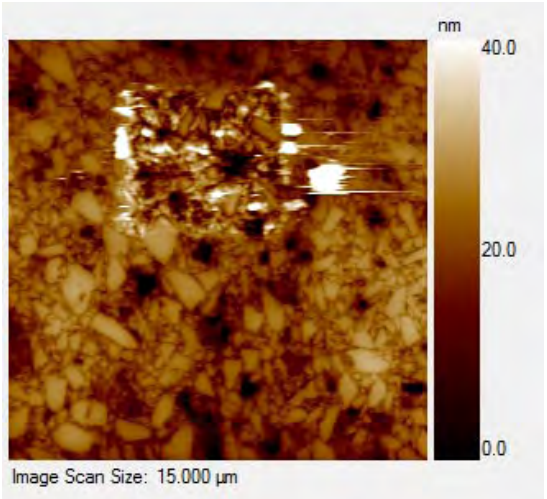

Fig. 5. ***In-situ*** **SPM of a worn location on Siloran at the contact force 50 μN**

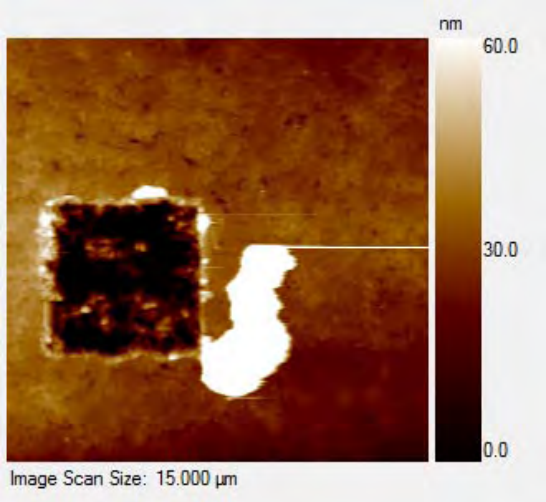

Fig. 4. ***In-situ*** **SPM of a worn location on Charisma at the contact force 70 μN**

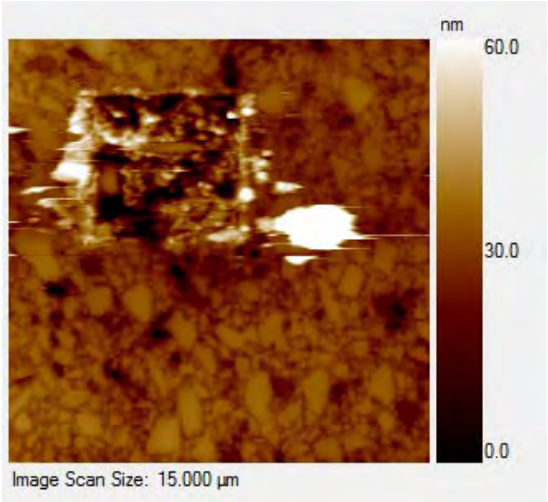

Fig. 6. ***In-situ*** **SPM of a worn location on Siloran at the contact force 70 μN**

on Charisma sample. Large black holes in the Fig. 4 are more likely associated with a particle separation. In case of Siloran sample, there were remaining particles in the worn square even at the highest normal force of 70 μN (Fig. 6). Materials used as filler vary among the composites. Therefore, the wear mechanism of particles also differs. Quantitatively, Siloran particles showed the increased wear and separation resistivity to abrasive loading. A wear mechanism can be observed from scratch tests performed with the same diamond probe as was used for ScanningWear™. Moreover, material removal can be studied at a single particle of filler. Fig. 6 shows two scratch tracks coming over a particle within Supreme sample. It seems that the removal mechanism of material is related to microploughing according to Fig. 1. If we consider no presence of removed material at the end of the scratch tracks (top of the image), the worn material volume present on wear images (Fig. 3–5) can be explained by microfatigue processes during the 10 cycles of ScanningWear™.

5. Conclusions

Nanomechanical system Hysitron TI 950 TriboIndenter™ has successfully quantified a wear resistivity of three dental composites – Filtek™ Siloran, Filtek™ Supreme and Charisma®. Siloran sample showed the highest wear resistivity among the samples. According to producer, Siloran contains quartz and radiopaque yttrium fluoride particles. Quartz surface is modified with a silane layer in order to provide the proper interface of filler to the resin. This could lead to enhanced resistivity of particle separation from the matrix at higher abrasion forces. The critical forces were found at about 60 μN for Siloran and

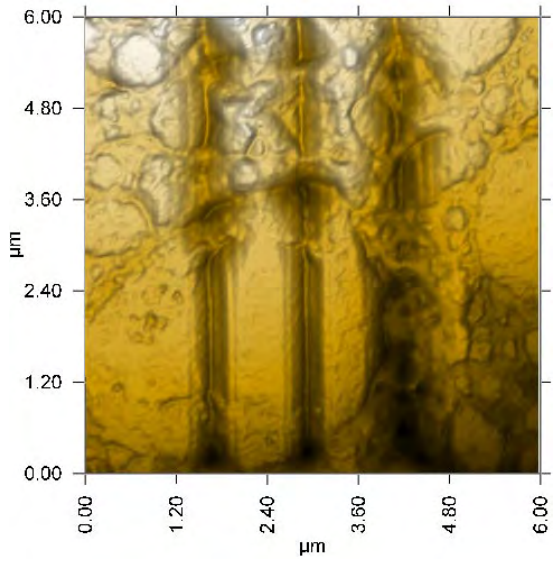

Fig. 7. ***In-situ*** **SPM of scratch tracks on Supreme at the contact force 800 μN**

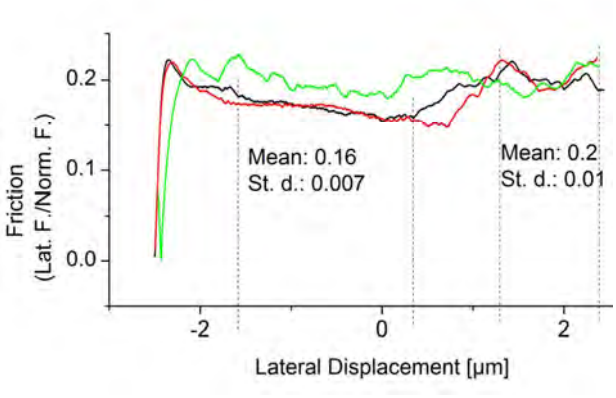

Fig. 8. **Graph shows recorded values of friction coefficients: black and red data correspond to the two left hand scratch tracks in the Fig. 6. Portion of data representing a particle (*f=0.16±0.007*) and matrix (*f=0.2±0.01*) are indicated by dashed lines**

Charisma. These forces indicate a separation or a failure of a particle.

Supreme showed the lowest wear resistivity. According to producer information, Zirconia/Silica nanoclusters shear at a rate similar to the wear of the surrounding resin matrix, therefore, no critical force was observed.

The research has been supported by Transdisciplinary research in Biomedical Engineering II. No. MSM 6840770012.

REFERENCES

1. Eichlerova R., Lukes J., Sepitka J.: Chem. Listy *105*, s794 (2011).
2. Eichlerova R., Lukes J., Sepitka J.: Computer Methods in Biomechanics *14*, 265 (2011).
3. Karl-Heinz Zum Gahr: *Microstructure and Wear of Materials.* Elsevier Science Publishers B. V., Amsterdam 1987.
4. Ryglova S., Sucharda Z., Cerny M., Suchy T., Supova M., Zaloudkova M.: Ceram.-Silik. *54*, 386 (2010).
5. Dudikova M., Kytyr D., Doktor T., Jirousek O.: Chem. Listy *105*, s790 (2011).

J. Lukeš, J. Šepitka, M. Válová, and R. Eichlerová
(Department of Mechanics, Biomechanics and Mechatronics, Faculty of Mechanical Engineering, CTU in Prague, Prague, Czech Republic): **Nanoscratch and Nanowear of Dental Filling Composites**

Three dental composites Filtek™ Siloran, Filtek™ Supreme and Charisma® were submitted to ScanningWear™ tests. Wear resistivity was measured by means of wear depth determined from *in-situ* SPM images. NanoScratch tests with the same diamond Berkovich tip were employed in order to describe the wear mechanisms. Moreover, friction coefficients were determined from scratch data.

MICRO-CRACK BEHAVIOUR IN POLYMER MATRIX OF PARTICULATE COMPOSITE: INFLUENCE OF NON-LINEAR MATRIX

ZDENĚK MAJER[a] and LUBOŠ NÁHLÍK[b]

[a] *Brno University of Technology, Technická 2, 616 69 Brno,* [b] *CEITEC IPM, Institute of Physics of materials AS CR, Žižkova 22, 616 62 Brno, Czech Republic*
majer@fme.vutbr.cz

Keywords: polymer matrix composite, fracture behaviour, non-linear matrix, micro-crack

1. Introduction

Generally speaking, polymer particulate composites are frequently used in many engineering applications. Composites are of great practical importance due to the possibility of modifying the mechanical properties of the resulting composite[1,2]. In this paper polymer particulate composites were modelled as a three-phase continuum (polypropylene matrix, mineral fillers and interphases).

The presence of mineral fillers usually causes a reaction on particle-matrix interfaces and finally results in the formation an interphase. The interphase plays a significant role in the evaluation of micro-crack behaviour[3]. The particles used as filler are usually chemically treated. This treatment positively influences the creation of interphase and contributes to better particle dispersion in the polymer matrix.

It is very difficult to obtain any information about the thickness or material properties of the interphase directly. The interphase thickness can be determined indirectly from the macroscopic composite properties. According to the used method of determination it can result in a huge spectrum of thickness values[2]. In the contribution[4] the interphase thickness was estimated as 0.1 μm. The studied interphase thickness was dependent only on the chemical composition of the particles and the matrix. In addition, the thickness of interphase seems to be independent of particle size.

The numerical model was created with respect to the following general conditions[9]: (*i*) particles should be of small size (less than 5 μm), (*ii*) the aspect ratio must be close to 1 to avoid high stress concentration, (*iii*) the particles must debond prior the polymer matrix reaches the yield strain in order to change the stress state of the matrix material and (*iv*) particles must be dispersed homogeneously in the polymer matrix.

The use of rigid particles[5] leads to an increase of composite Young´s modulus E_{comp}. In the following text the interaction of micro-crack propagation in the matrix filled by rigid particles is analyzed. The influence of further micro-crack propagation α on change of interphase properties is estimated.

2. Experiments

The experiments (tensile tests) focused on determination of macroscopic properties of polymer particulate composite were performed[6].

The measured data of the pure matrix for different temperature values illustrates an increasing of Young's modulus E_m with decreasing temperature (see Fig. 1).

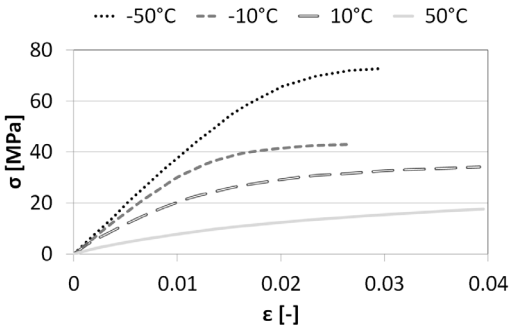

Fig. 1. **σ-ε curves of pure matrix under different temperatures**

The estimation of particle size used for production of the particulate composite was done. From experiments the average size of the particles was determined as 1 μm. The influence of particle size on composite behaviour was formerly studied[7,8].

3. Numerical model

The composite was modelled as a three-phase continuum with homogenously distributed particles by a finite element system ANSYS. Only the particles placed close to the micro-crack tip significantly influence micro-crack behaviour. Geometry of the used model is shown on Fig. 2.

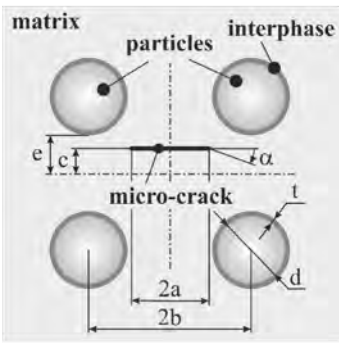

Fig. 2. **Geometry of the model used for micro-crack behaviour estimation in the polymer composite**

The material properties characterizing the composite correspond to rigid particle (H_2MgO_2 or $Mg(OH)_2$) and soft polypropylene matrix. The Young's modulus of the particles E_p was 72 GPa and the value of Poisson's ratio $\nu = 0.29$. Spherical[10] shape of the particles was considered in calculations. The corresponding parameters of neat polymer matrix (at temperature –10 °C) were estimated as 3.3 GPa (see Fig. 1). The thickness of the interphase t was considered here as 0.1 μm (ref.[4]) and a constant value of Young's modulus E_i through the thickness was contemplated. The value of interphase Young's modulus E_i varied from 0.05 GPa to 3.3 GPa (presented configuration without interphase). In this paper the micro-crack placed very close to particle was analyzed (ratio $c/e = 0.95$).

4. Results and discussion

The fracture toughness of the polymeric particulate composite can be influenced by several effects, i.e. material properties of the matrix and interphase.

The micro-crack propagation direction dependence on the micro-crack length was described (see Fig. 3) for matrix material properties measured at –10 °C. For Young's modulus of interphase E_i from 1.0 to 3.3 GPa, the micro-crack propagation direction α was positive for all calculated configurations, meaning that the micro-crack avoids rigid particles and grows only in the matrix. On the other hand, for E_i from 0.05 to 0.1 GPa the micro-crack was attracted by the particle.

In case of very soft interphase the micro-crack is attracted by the particle which is completely shielded (see Fig. 4). Consequently, the micro-crack tip touches the interphase and the particle can be fully debonded[11]. During experiments it was founded that free particles were observed on the fracture surface. Generally, the micro-crack is blunted and singular stress concentration is reduced. For the next micro-crack propagation an additional energy is necessary. This can lead to increase of composite fracture toughness.

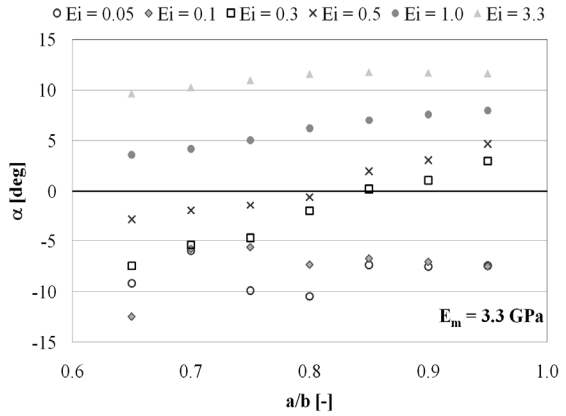

Fig. 3. **Dependence of crack propagation direction on micro-crack length (matrix properties at -10 °C are considered)**

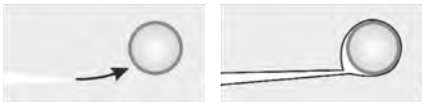

Fig. 4. **Micro-crack approaching particle covered by interphase and the fully debonded particle when micro-crack is blunted**

5. Conclusions

The effect of interphase between matrix and rigid particles on the toughening of composite was studied and one possibility of the basic mechanisms to their increase was described. The presence of the very soft interphase changes the stress field around rigid particles and has significant influence on micro-crack behaviour.

This research was supported by the grants No. P107/10/P503 and 106/08/1409 of the Czech Science Foundation.

REFERENCES

1. Nezbedová E.: Chem. Listy *101*, s28 (2007).
2. Pukánszky B.: Eur. Polym. J. *41*, 645 (2005).
3. Ayyar A., Chawla N.: Compos. Sci. Technol. *66*, 1980 (2006).
4. Moczó J., Fekete E., Pukánszky B.: J. Adhesion *78*, 861 (2002).
5. Veselý P., Nezbedová E., Vlach B.: Chem. Listy *102*, 1276 (2008).
6. Molliková E.: *Ph.D. thesis*, FME Brno UT, pp. 103 (2003) (in Czech).
7. Hutař P., Majer Z., Náhlík L., Šestáková L., Knésl Z.: Mech. Compos. Mater. *45*, 281 (2009).
8. Majer Z., Novotná E.: Chem. Listy *105*, 380 (2011).
9. Zuiderduin W., C., J., Westzaan C., Huétink J., Gaymans R. J.: Polymer *44*, 261 (2003).
10. Majer Z., Hutař P., Knésl Z.: Key Eng. Mater. *465*, 564 (2011).
11. Veselý P.: *Ph.D. thesis*, FME Brno UT, pp. 100 (2008) (in Czech).

Z. Majer[a], L. Náhlík[b] *([a] Brno University of Technology, [b] CEITEC IPM, Institute of Physics of materials AS CR):* **Micro-Crack Behaviour in Polymer Matrix of Particulate Composite: Influence of Non-Linear Matrix**

A numerical study of fracture behaviour of polymer particulate composite with rigid particles is discussed in the paper. The particulate composite was modelled as a three-phase continuum (particles, matrix and interphase). The micro-crack propagation direction using the finite element method was estimated for a variety of matrix and interphase material properties. The non-linear matrix material properties were experimentally determined and used in the numerical calculations.

MICROSTRUCTURE CHARACTERISTICS OF Ni_3Al BASED INTERMETALLIC COMPOUNDS

JITKA MALCHARCZIKOVÁ, MARTIN POHLUDKA, and MIROSLAV KURSA

VŠB-Technical University of Ostrava, 17. listopadu 15/2172, 708 33 Ostrava - Poruba, Czech Republic
jitka.malcharczikova@vsb.cz

Keywords: micro-hardness, micro-structure, Ni_3Al based alloy

1. Introduction

Ni-Al based intermetallic compounds can substitute nickel super-alloys used as high-temperature structural materials. The chemistry of aluminides is much simpler than that of superalloys. Apart from their oxidation and carburization resistances, aluminides possess lower densities, high-melting points, and exhibit interesting mechanical properties due to their ordered crystal structures[1,2]. Main interest is today focused on Ni_3Al based intermetallic compounds with hypo-stoichiometric composition, for which it was established that share of two-phase areas γ/γ' is very significant indicator. These alloys approach by their composition the Ni-based superalloys, where mechanical properties of these materials depend on the volume fraction, distribution, size and morphology of the γ'-precipitates. Their microstructure consists of a high volume fraction of γ'-strengthening precipitates (70 %) coherently merged into a γ matrix[3].

2. Preparations of samples and measurements

Observations were made in orientated state of non-alloyed intermetallic Ni_3Al based compound (22–25 at.% of Al). The samples were solidified by Bridgman's technique. Used rate of directional solidification was 10 and 20 mm/h. The longitudinal sections of samples were used for determination of micro-hardness and for evaluation of structure. It was established that Ni22Al samples containe formations of Ni_3Al (γ´) and solid solution of nickel (γ), Ni25Al samples containe Ni_3Al only. Fig. 1 shows directional microstructure of the sample Ni25Al (only γ´ phase), Fig. 2 shows directional microstructure of the sample Ni22Al (γ´ and γ phase) with indentation. Average microhardness, microhardness for individual occurring phases, and also on grain boundaries, was determined for all types of alloys. Samples of Ni_3Al based alloys with stoichiometric and hypo-stoichiometric composition were used for determination of mechanical characteristics. Composition of samples and obtained results are summarised in Tab. I.

3. Results and discussion

The differences of microhardness were found in the samples 3 and 4 with composition Ni23Al. This is due to

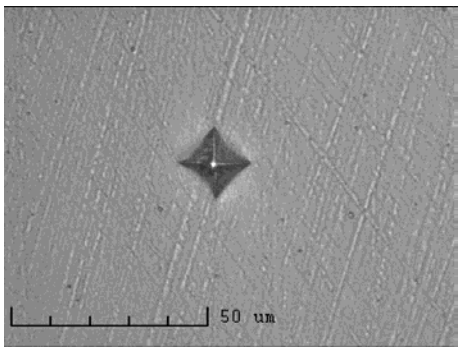

Fig. 1. **Sample Ni25Al, grain of Ni_3Al**

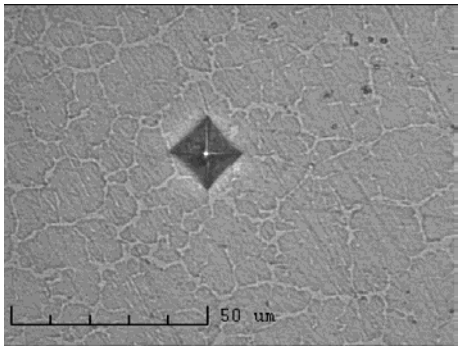

Fig. 2. **Sample Ni22Al, network of Ni_3Al and (Ni)**

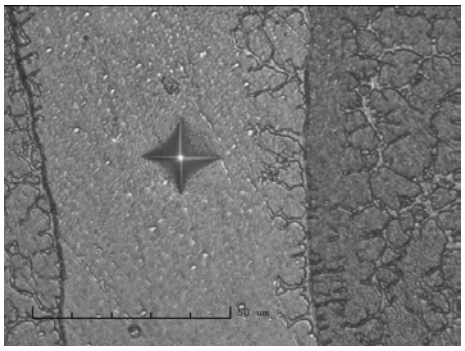

Fig. 3. **Sample Ni22Al, 20 mm/h, network of Ni_3Al and (Ni), grain boundary, grain**

Table I
Microhardness of the samples

Sample No.	Al content	Solidification rate	R_m	A_5*	Microhardness HV 0.05			
	[at. %]	[mm h^{-1}]	[MPa]	[%]	avarage	grain	grain bound.	network
1	25	10	365	18	256 ± 8	223 ± 12	240 ± 30	-
2	25	20	490	13	263 ± 7	232 ± 15	265 ± 20	-
3	23	10	-	-	238 ± 22	206 ± 36	206 ± 13	218 ± 12
4	23	20	790	43	247 ± 15	223 ± 16	223 ± 24	227 ± 14
5	22	10	925	64	247 ± 7	-	-	236 ± 29
6	22	20	735	52	257 ± 14	262 ± 20	255 ± 18	271 ± 17

the fact that the compounds contain grains of Ni_3Al, network structure and grain boundaries. This is evident also in the sample 6 of Ni22Al composition, with higher rates of solidification (Fig. 3), where structure was not perfectly created, as it was in the sample 5. The sample 5 contains only network structure.

The network structure enhances significantly mechanical properties of hypo-stoichiometric alloys based on Ni_3Al. This effect is used also in nickel super-alloys[4,5].

In case of suitable volume of γ' it is possible to influence effectively the creep behaviour and stress rupture properties of Ni and Ni_3Al based alloys[5,6]. High share of network structure in the sample 5 in directed state has influenced significantly the values of strength and ductility determined at tensile tests[7]. Big differences of ductility and strength were found in the samples. For example the sample Ni25Al has strength R_m 490 MPa and ductility A_5* 13 %, the sample Ni22Al has R_m 735 MPa and A_5* 52 % (Tab. I). By contrast to that the sample 1 without network structure shows considerably worse mechanical properties[7]. It is also very interesting that these differences were not manifested at value of avarage microhardness, which is for all the samples approximately within the interval from 240 to 260 HV 0.05 (Tab. I). Microhardness of grain is 206–232 HV 0.05. Only value for sample 6 is greater (262 HV 0.05). Microhardness of grain boundary is 206–265 HV 0.05. Microhardness of network in the sample 6 is greater – 271 HV 0.05. No significant deviations, which would explain the manner of structure strengthening, were found either at determination of microhardness on the grain boundaries and in the areas with network structure.

4. Conclusions

The differences of ductility and strength were found in the samples. It is also very interesting that these differences were not manifested at measurement of microhardness, which is for all the samples approximately within the interval from 240 to 260 HV 0.05. It would be very appropriate to complete the existing measurement also by nanoindentation, which might bring interesting findings.

The presented results were obtained within the frame of solution of the research project MSM 6198910013 „Processes of preparation and properties of high-purity and structurally defined special materials ".

REFERENCES

1. Deevi S. C., Sikka V. K.: Intermetallics *4*, 357 (1996).
2. Westbrook J. H., Fleischer R. L., et al.: *Intermetallic Compounds. Principles and Practice. Volume 2-Practice*. VCH, New York 1995.
3. Cormier J., Villechaise P., Milhet X.: Mater. Sci. Eng. A. *501*, 61 (2009).
4. Reed C. S., Tao T., Warnken N.: Acta Mater. *57*, 5898 (2009).
5. Murakumo T., et al.: Acta Mater. *52*, 3737 (2004).
6. Li P., Li S., Han Y.: Intermetallics *19*, 182 (2011).
7. Malcharcziková J., Kursa M.: *Proceedings of 19th international conference on metallurgy and materials. Metal 2010*, p. 892. Tanger, spol. s.r.o., Ostrava 2010.

J. Malcharcziková, M. Pohludka, and M. Kursa *(VŠB-Technical University of Ostrava):* **Microstructure Characteristics of Ni_3Al Based Intermetallic Compounds**

Observations were made in orientated state of non-alloyed intermetallic Ni_3Al based compound (22–25 at.% of Al). The samples were solidified by Bridgman's technique. It was established that Ni22Al samples contained formations of Ni_3Al (γ′) and solid solution of nickel (γ), Ni25Al samples contained Ni_3Al only. The differences of mechanical properties were not manifested at measurement of micro-hardness, which is for all the samples approximately within the interval from 240 to 260 HV 0.05.

ESTIMATION OF LOCAL MECHANICAL PROPERTIES OF HIGHLY POROUS CERAMIC MATERIALS

PETR MARCIÁN[a], ZDENĚK MAJER[a], IVO DLOUHÝ [a,b], and ZDENĚK FLORIAN[a]

[a] Brno University of Technology, Brno, Czech Republic, Technická 2896/2, 616 69 Brno, [b] Institute of Physics of Materials of the Academy of Sciences of the Czech Republic, Žižkova 22, 616 62 Brno, Czech Republic
majer@fme.vutbr.cz

Keywords: cellular structures, tensile test, microCT, image processing, FEM

1. Introduction

Ceramic foams are a special group of cellular materials with a very advantageous combination of properties, such as low density, huge surface, high thermal insulation abilities, high permeability etc. These material properties predetermine ceramic foams for very broad use in engineering practice.

The tensile test of brittle, highly porous materials is really problematic[1]. In fact, in so complicated structures it is practically impossible to estimate local mechanical properties by experiments. In addition, the fixed specimens are usually damaged and frequently a premature fracture takes place. Because of these difficulties it could be useful to create computational models respecting a porous structure. Data from micro-CT are necessary for creation of computational models.

The aim of the work is to study a response of highly porous ceramic foam material (Vukopor® A – 85 % Al_2O_3 – 14 % SiO_2 – 1 % MgO) to mechanical loading using a computational quantification on micro-level as well as determination of individual struts behaviour and the influence of this behaviour on ceramic foam mechanical performance.

2. Micro-CT

A micro-CT device (ScyScan, Belgium) provides the same information as a conventional CT. It has a much higher resolution of images (from 5 to 20 μm). This has a significant influence for research of highly porous materials[2,3]. Dimensions of struts are approximately 100 × 600 μm (diameter x length).

3. FEM Model

The STL model Creator[4] procedure has been developed in Matlab 2009b for faster image processing and analyzing the micro-CT data (see Fig. 1a). The program loads images in various formats and can create a 3D model in STL format after tresholding[5] (see Fig. 1b). Micro-CT slices were obtained in resolution 700 × 800 pixels (a total of 1000 slices with pixel size 15 × 15 μm^2). On the micro-level the computational model adequately respects the shape of such complicated structure (see Fig. 1c).

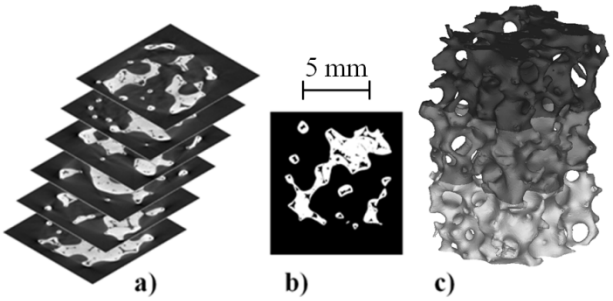

Fig. 1. **Micro-CT slices (a), image created by automatic segmentation (b) and model of reconstructed structure (divided to three parts) (c)**

The computational model was created by a finite element method using the system ANSYS 12. SOLID187 element was used for meshing; it is a10-node element with quadratic displacement behavior. It is necessary to have a very fine and accurate mesh for the analysis of local stresses in such complex microstructure. To create a mesh, the automatic mesh function was used. Consequently, the obtained mesh was checked to avoid error elements. Because of faster calculations the whole reconstructed structure was divided into three parts (length 5 mm), see Fig. 1c. Each of these parts contained approximately 7 million elements; it represented an element size of 7 μm, see Fig. 2.

The computational model was considered as homogeneous isotropic and linear elastic with Young's modulus E = 70 000 MPa and Poisson's ratio ν = 0.3. On the micro-level this ceramic foam can be considered as homogeneous[6]. Von Mises stress was evaluated and compared with the value of yield stress 375 MPa.

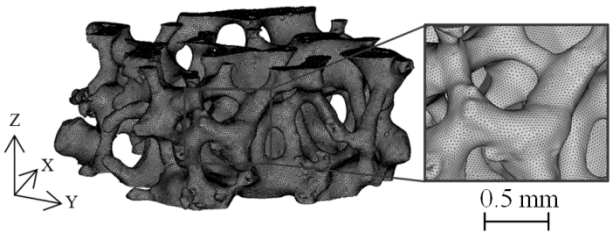

Fig. 2. **Example of finite element meshing**

All three computational models were fixed on one side and was loaded on the opposite side by means of predefined strain (0.1 %).

4. Results and discussion

Forty-five struts were chosen for an analysis. The local stress field (von Mises stress) was determined for each particular strut (see Fig. 3). Maximum local stress values are observed in most cases between the middle and the triple point of strut. This is probably caused by the influence of change in struts geometry and strut stiffness is changed due to the increase in thickness.

Further, the influence of strut rotation on von Mises stress was studied. The orientation related to the loading axis was measured as an angle between the load plane (XY) and the axis of strut. The results are shown in Fig. 4. The graph can be divided into two main parts.

The presented results correspond to the elongation of the computational model 0.1 %. The first set of values was for struts oriented in the range from 0° to 40°; struts in this part were parallel to the load plane. The median of stress values was determined 85.7 MPa. The second set of values was for struts oriented from 40° up. For these struts, the median of stress values was 218.0 MPa, i.e. 2.5 times higher comparing to the first set.

5. Conclusions

Computations using finite element method are suitable for the analysis of local mechanical properties of highly porous ceramic foam. Models of the struts structure can be created using a micro-CT and subsequent image processing.

The results show that the rotation of individual struts is really significant in whole structure. Up to 40°, the struts are not so loaded and the median of local von Mises stress is only about 86 MPa. For the rest of struts, the values of local von Mises stress are about 220 MPa, which is almost

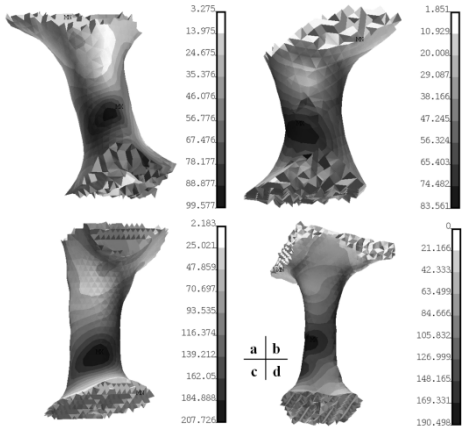

Fig. 3. **Von Mises stress [MPa] on struts samples under angel 4° (a), 9° (b), 62° (c) and 68° (d) relating to loading plane (XY)**

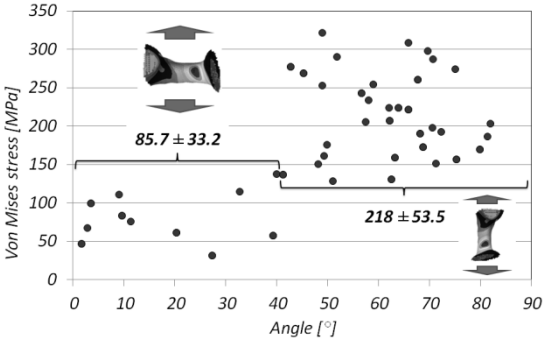

Fig. 4. **Dependence of von Mises stress on struts orientation related to loading plane (XY)**

2.5 times higher comparing to the first set. The maximum values of stress are below the value of yield stress 375 MPa. These conclusions could contribute to the process of designing and creating bone implants.

This work was supported by grant specific research FSI-S-11-12/1225 and project of Czech Science Foundation Nr. 101/09/1821.

REFERENCES

1. Dlouhý I., Řehořek L., Chlup Z.: Key Eng. Mater. *413*, 168 (2009).
2. Cowin S. C., Book: *Bone mechanics handbook, Informa Health Care*, p. 980. S. C. Cowin, 2001.
3. Jiroušek O., Němeček J., Kytýř D., Kunecký J., Zlámal P., Doktor T.: Chem. Listy *105*, s668 (2011).
4. Marcián P., Konečný O., Borák L., Valášek J., Řehák K., Krpalek D., Florián Z.: Mendel J. series 2011, p. 255 (2011).
5. Bankman H. I., Book: *Handbook of Medical Image Processing and Analysis, Elsevier*, p. 1000. I. Bankman, Baltimore, 2009.
6. Marcián P., Majer Z., Florian Z., Dlouhý I.: Adv. Mater. Res. *482-484*, 1330 (2012).

P. Marcián[a], Z. Majer[a], I. Dlouhý[a,b], and Z. Florian[a] *([a] Brno University of Technology, Brno, [b] Institute of Physics of Materials of the Academy of Sciences of the Czech Republic):* **Estimation of Local Mechanical Properties of Highly Porous Ceramic Materials**

In this contribution the ceramic foams are studied. The applications of these materials are extensive due to very advantageous combination of properties. This paper is focused on local mechanical properties of individual struts in a highly porous structure. The computational model is created using a micro-CT by a finite element method in ANSYS 12.0 software. The local equivalent stress (HMH criterion) is analyzed depending on struts rotation.

NANOINDENTATION OF GELATINE/HAP NANOCOMPOSITE

DANIELA MARX[a], JOSEF ŠEPITKA[a], JAROSLAV LUKEŠ[a], and KAREL BALÍK[b]

[a] *Czech Technical University in Prague, Faculty of Mechanical Engineering, Dep. of Mechanics, Biomechanics and Mechatronics, Technicka 4, 166 07 Prague ,* [b] *Institute of Rock Structure and Mechanics ASCR, v.v.i., V Holesovickach 41, 182 09 Prague 8, Czech Republic. hruskova@irsm.cas.cz*

Keywords: nanoindentation, biocomposite, gelatine

1. Introduction

A gelatine is a material consisted of amino acids (as well as collagen), which are very important for human body. It is a biocompatible, bioactive and biodegradable material[1]. Therefore, gelatine is a suitable material for biomedical applications such as bone grafting.

Nanoscale mechanical properities of bioinspired composites are the most important comparative criteria for a fabrication of bone tissue replacements. The aims of this work are the preparation of bioinspired composite material composed of gelatin nanofibers and hydroxyapatite (HA) powder and assess its mechanical properties in nano-scale.

2. Materials and methods

2.1. Samples preparation

Nanofibers (i.e. fibers in scale from 1 nm to 100 nm) can be manufactured by various methods. The most convenient method for tissue engineering applications is the electro-spinning[2,3]. Gelatine nanofibrous matrices produced by the electro-spinning process were found to be very effective as a base for cell increasing.

Nanofibers from porcine gelatine loaded by HA have been provided by ELMARCO s.r.o (basic material-BM) and has been prepared by followed procedure. Porcine gelatin was dissolved in diluted acetic acid. Nanoparticles of hydroxyapatite (20 wt.% to dry matter) were mixed into the solution. In an effort to avoid clumps creation, this mixture was 5 minutes in an ultrasonic bath. Basis weights for gelatine and nHA mixture was approximately 6 gsm. The BM dried up at ambient atmosphere[4].

Special capsule for samples preparation is made from aluminum with polished functional surfaces.

Sixty four layers of BM have been placed into the capsule and pressed at 40 °C by 15 MPa for 15 minutes. The formed surface was already suitable for nanoindentation. The surface of dried BM is shown in Fig. 1.

2.2. Testing conditions

A Hysitron TI 950 TriboIndenter™ nanomechanical test instrument was used for quasistatic indentation of prepared sample. Load-controlled tests were performed on the sample using a diamond Berkovich tip. The standard trapezoidal loading function $5 \times 5 \times 5$ s, maximal load P_{max} = 750 μN was used for all indents. The indents were applied in a grid pattern 10×10 with indents separation 15 μm at two locations on the sample (Area 01 and Area 02).

2.3 Quasistatic nanoindentation

Nanoindentation followed a trapezoidal loading function with 3 segment times for loading, dwell, and unloading, respectively. Recorded force and displacement data were analyzed according to Oliver and Pharr method[5]. A polynomial regression

$$P = \alpha (h - h_f)^m \qquad (1)$$

was applied on data in range 20–95 % of unloading segment of each indentation curve. Here, α, h_f, and m are arbitrary fitting parameters. P is an applied force and h is an indentation depth. A contact stiffness S can be calculated from the derivative of Eq. (*1*), which relates to the reduced elastic modulus E_r by

$$S = \frac{dP}{dh} = \frac{2}{\sqrt{\pi}} E_r \sqrt{A_C} \qquad (2)$$

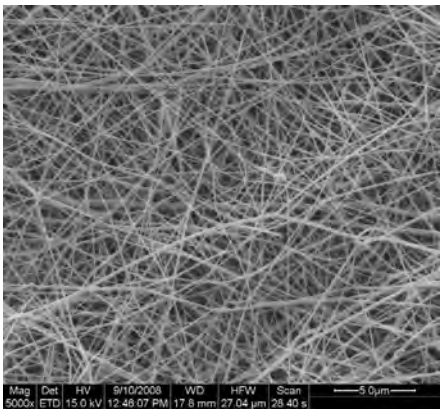

Fig. 1. **SEM image of BM (magnification 5000×)**

where A_C is a projected contact area of the tip, which is known for each contact depth according to a calibrated tip area function.

Indentation hardness is calculated from

$$H = \frac{P_{\max}}{A_C} \qquad (3)$$

at the maximum applied load of $P_{\max}$.

3. Results

Nanomechanical properties of two representative areas of the sample were obtained by nanoindentation. Fig. 2 and 3 show large scattering of local mechanical properties of the analyzed material.

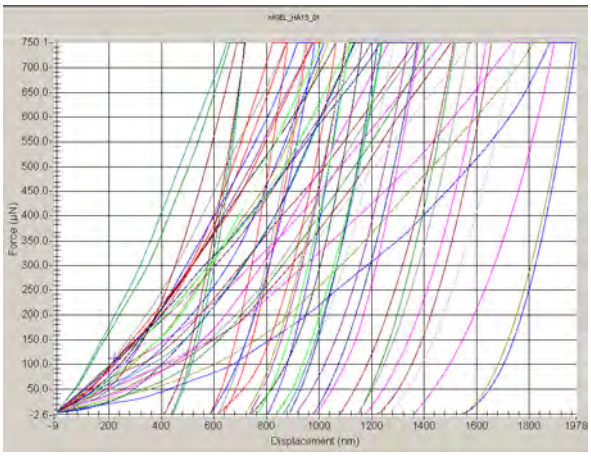

Fig. 2. **Load displacement curves performed at Area 01. There are curves more likely representing locally concentrated hard HAP particles on the very left side of the picture and the opposite side represents a gelatine nanofibers**

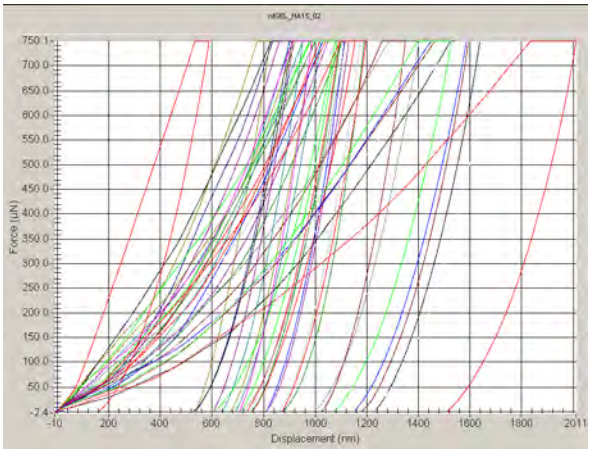

Fig. 3. **Load displacement curves performed at Area 02 also shows scattering of mechanical properties, which confirms inhomegenous distribution of HAP particles within gelatin nanofibers**

Table I
Average values of reduced modulus E_r and indentation hardness H_{IT}

Sample area	E_r [GPa]	H_{IT} [GPa]
Area 01	0.578 ± 0.270	0.032 ± 0.021
Area 02	0.627 ± 0.217	0.036 ± 0.028

4. Conclusion

Complex results of nanomechanical testing of analyzed material showed big non-homogenity, which refered to an porous structure. The attendance of higher local concentration of HA-clumps was eliminated by method of BM preparation. Local HA concentration (distribution) was determined by Raman spectroscopy. Results of those analysis denote to structural, not material non-homogenity (porosity). This non-homogenous structure is not reflected in previous micro(macro)mechanical testing (i.e. tensile testing and consequent analysis of fracture surface-SEM). On the other hand the porosity is better for cell increasing. According to these results, composites based on gelatine nanofibers are suitable rather for low load applications.

This work was supported by the Grant Agency of the Czech Technical University in Prague, under the project No. SGS10/247/OHK2/3T/12 and by grant from Ministry of Industry and Trade of Czech Republic MPO CZ, FT-TA3/131, Ministry of Education of the Czech Republic MSM 6840770003 and MSM 6840770012.

REFERENCES

1. Powell H. M., Supp D. M., Boyce S. T.: Biomaterials *29*, 834 (2008).
2. Lesny P., Pradny M., Jendelova P., Michalek J., Vacık J., Sykova E.: J. Mater. Sci. Mater. Med. *17*, 829 (2006).
3. Šupová M., Hrušková D., Sucharda Z., Svobodová J., In: *Nano for the 3rd millenium-proceedings* (38–43), Elmarco and Technical University of Liberec, 2009.
4. Fuchsová G., Lofaj F., Simkulet V.: Chem. Listy *105*, s796 (2011).
5. Li W. J., Laurencin C. T., Caterson E. J., Tuan R. S., Ko F. K.: J. Biomed. Mater. Res. *60*, 613 (2002).

D. Marx[a], J. Šepitka[a], J. Lukeš[a], and K. Balík[b]
([a] Czech Technical University in Prague, Faculty of Mechanical Engineering, Dep. of Mechanics, Biomechanics and Mechatronics, [b] Institute of Rock Structure and Mechanics ASCR, v.v.i., Prague, Czech Republic):
Nanoindentation of Gelatine/HAP Nanocomposite

There are nowadays available numerous synthetic composites (bone graft materials) that combine the advantages exhibited by each component of the material, with a structure and composition similar to that of natural bone. Gelatine like an aminoacids based material in combination with bioactive nHA could represent suitable composite especially for bone grafting.

Nanoscale mechanical properities of bioinspired composites are the most important comparative criteria for a fabrication of bone tissue replacements.

The aims of this work are the preparation of bioinspired composite material composed of gelatin nanofibers and hydroxyapatite (HA) powder and assess its mechanical properties in nano-scale.

LOW-LOAD NANOINDENTATION: INFLUENCE OF SURFACE FORCES AND ADHESION

JAROSLAV MENČÍK

University of Pardubice, DFJP, Studentská 95, 532 10 Pardubice, Czech Republic
jaroslav.mencik@upce.cz

Keywords: nanoindentation, contact, adhesion, surface roughness, viscoelasticity, elastic modulus

1. Introduction

Atoms of solids attract mutually if their distance is larger than the equilibrium one, and repel if it is smaller. The range of action of attractive forces is very short, about 1 nm. The forces between atoms inside a body are in equilibrium in all directions, but those in a very thin surface layer act also out of the body, onto any other matter close to this surface. This can result in adhesive joining. If the distance between two surfaces drops below a very small value, the bodies sometimes cling spontaneously and remain in close contact even without action of external force, and separate suddenly only after they are pulled apart by certain tensile force (Fig. 1).

In contact of relatively stiff solids, adhesion is usually not observed. Due to surface roughness, both bodies come into contact only at a limited number of matching asperities. The corresponding area of close contacts is minute, and the resultant attractive force is insufficient to compress the hills. If, however, both surfaces are very smooth (roughness of the order of nm!) or if one or both bodies are very compliant, the surfaces adjust one another better and the adhesion is stronger. Examples are gels, soft elastomers, or biological tissues. The adhesion can also be enhanced by the presence of a thin layer of a liquid between both surfaces.

These phenomena can influence nanoindentation measurements as well, especially for compliant materials and very low loads, from μN to mN. Here, surface forces change the character of load-displacement curves and must be considered in the preparation and evaluation of the tests. In this paper, based on literary survey, basic formulae for adhesion are given first. Then, the influence of liquids and humidity is explained, and also that of surface roughness and viscoelasticity of contacting bodies. Finally, a procedure is described for the determination of elastic modulus of compliant materials.

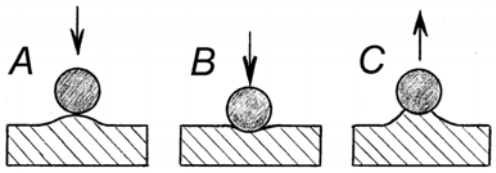

Fig. 1. **Adhesion** (a schematic). A – clinging at approaching, B – penetration, C – separation at unloading

2. Theory of adhesion contact of solids

Two basic theories were developed: by Derjaguin, Muller and Toporov[1], and by Johnson, Kendall and Roberts[2], in both cases for the contact of spherical surfaces. According to the DMT theory, suitable for stiff materials, the force of adhesion equals

$$F_{\mathrm{DMT}} = 2\pi r_{\mathrm{e}} \boldsymbol{W}_{\mathbf{ad}} = 4\pi r_{\mathrm{e}} W_{12} \qquad (1)$$

r_{e} is the equivalent radius of the surfaces in contact ($1/r_{\mathrm{e}} = 1/r_1 + 1/r_2$). For contact of a sphere (radius R) with a plane, $r_{\mathrm{e}} = R$. $\boldsymbol{W}_{\mathbf{ad}}$ is the specific work of adhesion, necessary for separating two bodies. Since in this separation two new surfaces were created, the work of adhesion $\boldsymbol{W}_{\mathbf{ad}}$ (per unit of contact area) is twice of the specific surface energy W (per unit area of surface). This energy depends on the considered material and on the adjacent medium (another solid, liquid, vapour or vacuum), as specified by two subscripts, e.g. W_{12}.

For compliant materials, the Johnson-Kendall-Roberts model[2] is more suitable, which assumes elastic deformations of contacting bodies. It is based on Hertz´ theory, but considers also the adhesive forces. Due to them, the contact deformations differ from those by Hertz (Fig. 2). The actual contact radius a for a sphere (radius R) under load F is larger than Hertzian (given by the first line in Eq. (*2*)), and is obtained[2,3] from

$$a^3 = [3R/(4E_{\mathrm{r}})] \times \{F + 3\pi RW_{12} + [6\pi RW_{12}F + (3\pi RW_{12})^2]^{1/2}\} \qquad (2)$$

E_{r} is the reduced modulus, related to the elastic moduli of both bodies as

$$1/E_{\mathrm{r}} = (1 - \nu_1^2)/E_1 + (1 - \nu_2^2)/E_2 \qquad (3)$$

ν_1, ν_2 is the Poisson´s ratio of material 1 or 2. The expression in curly brackets in (*2*) is the apparent force, consisting of the external load F and the contribution of surface forces (given in the bottom line).

For zero load ($F = 0$), the contact radius is finite,

$$a_0 = [9\pi R^2 W_{12}/(2E_{\mathrm{r}})]^{1/3} \qquad (4)$$

The solids keep together up to a small negative (tensile) force, and suddenly separate at

$$F_{\mathrm{JKR}} = (3/2)\pi RW_{12} = F_{\mathrm{ad}} \qquad (5)$$

with the corresponding contact radius $a_{\mathrm{ad}} = a_0/4^{1/3}$. For

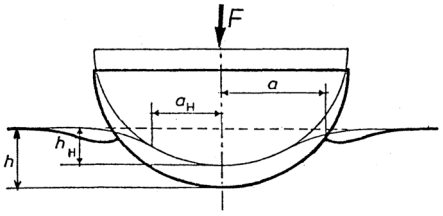

Fig. 2. **Penetration of a stiff sphere into a sample** (a schematic). Bold curves – contact with adhesion, thin curves – Hertzian contact

example, force of adhesion of a spherical ball of R = 100 μm on rubber (W = 62 mJ m^{-2}) is 29 μN.

NOTE: Equation (*5*) also enables the determination of surface energy W from the measured adhesion force F_{ad}.

3. Influence of surface roughness

Due to surface roughness, real (and not very compliant) bodies come into contact only at a limited number of matching asperities, Fig. 3. An idea about the influence of main factors follows from analyses done by Johnson[4] and Tabor[5] for adhesion of rough deformable surface in contact with a smooth rigid flat body. The asperities were assumed to have a spherical shape of radius R and randomly distributed heights. Each asperity adheres until its distance from the flat exceeds δ_c, whereupon the adhesion breaks. The ratio of the standard deviation σ of asperity heights and the distance δ_c at separation can be called elastic adhesion index[4],

$$\alpha = \sigma/\delta_c \qquad (6)$$

This index is related with the ratio of the force $F(\sigma)$, required to compress an asperity by σ, and the force of adhesion for that asperity, F_{ad}. Expressing $F(\sigma)$ via the Hertz´ formula and F_{ad} via the JKR model (*5*) gives:

$$F(\sigma)/F_{ad} = (4/9)(E\sigma^{3/2})/(\pi WR^{1/2}) \qquad (7)$$

E and W are the elastic modulus and surface energy. The right-hand part of Eq. (*7*), multiplied by $9\pi/4$, is called adhesion parameter[5]. Johnson[4] has shown how the apparent adhesion force decreases with increasing roughness. For α = 0, this force is maximum and corres-ponds to the JKR model. For a = 1 it drops to 50 %, and for α = 2 it drops to 10 % and becomes negligible for α larger than 3, see Fig. 4.

If both contacting surfaces are very smooth (roughness of the order of nm), or if one or both bodies are very compliant so that the surfaces can easily adjust one another, the total attractive force (and adhesion) will be

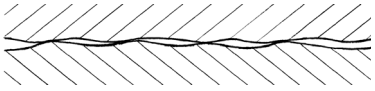

Fig. 3. **Contact of real surfaces** (a schematic)

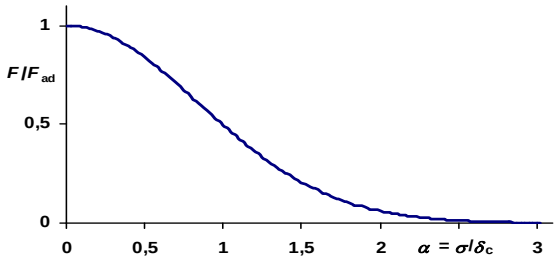

Fig. 4. **Relative decrease of adhesive force** (F/F_{ad}) **with increasing surface roughness** (α). A schematic (after ref.[4])

higher. Examples are gels, some elastomers, or biological tissues. Their response, however, is visco-elastic, which also influences adhesion processes.

4. Influence of viscoelasticity

Viscoelastic deformations depend on the load and its duration[6,7]. As a consequence, the force at which two bodies get adhered during mutual approaching, is lower than the force needed for their separation on unloading[8,9] (Fig. 5). A role is played by varying contact area too. After snapping, the continuing action of the load causes gradual growth of the contact area, also due to gradual decrease of the apparent modulus $E(t)$ with time, so that the force for separation corresponds to a larger area. Moreover, this force also depends on the rate of separation – it is higher for faster separation.

The adhesion of viscoelastic solids was analysed by Greenwood, Johnson and other scientists, who came to the conclusion that during their mutual catching or separation, the surface energy in the JKR model should be modified by the ratio of instantaneous and asymptotic modulus, E_0/E_∞; for details, see ref.[10].

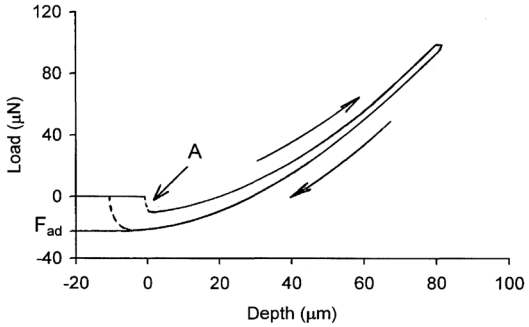

Fig. 5. **Indentation influenced by adhesion and viscoelasticity** (a schematic). F_{ad} – adhesion force at removal, A – adhesion at approach

5. Influence of a liquid or humidity at contact

If a very thin layer of liquid is present between contacting bodies, it contributes to the mutual attraction by its surface tension. The attractive forces between atoms or molecules inside the liquid are in equilibrium in all directions, but the atoms in the thin surface layer (i.e. without counter-atoms) are attracted more inwards. The liquid strives for the minimum surface – as if it were inside a vessel made of a prestretched elastic skin. The tangential force acting per unit length in this „skin" is surface tension γ, whose value corresponds to the surface energy density W. If the surface is curved, surface tension causes capillary pressure in the liquid,

$$p = \gamma (r_1^{-1} + r_2^{-1}) = \gamma / r_m \qquad (8)$$

r_1 and r_2 are radii of surface curvature in two mutually perpendicular directions; r_m is the equivalent (mean) radius of curvature. If both centres of curvature lie in the liquid, the mean curvature is positive and surface tension causes pressure in the liquid. If the mean curvature is negative, the surface tension causes underpressure in the liquid.

The shape of the liquid between two contacting bodies (Fig. 6) depends on their form and on the surface tension for individual interfaces: γ_{L1} for „liquid and body 1", γ_{L2} for „liquid and body 2", and γ_{LV} for „liquid and the adjacent environment" (vacuum, vapour, air or another liquid). In principle, also the surface tension γ_{12} between both bodies could play a role, but this case will not be considered here. If the liquid is in contact with solid „s" (e.g. the specimen or indenter), both surfaces contain contact angle φ, related to the surface tensions of individual phases by the formulae[3]:

$$\cos\varphi = (\gamma_{sV} - \gamma_{sL})/\gamma_{LV} \qquad (9)$$

The liquid can contribute to the adhesion force between both bodies in two ways:

1) Tensile surface stress γ_{LV} acts along the circumference of the liquid ring (with the radius of the contact circle approximately equal a) and attracts the indenter to the specimen by the force $F_\gamma = 2\pi a \gamma_{LV}$.

2) Due to torroidal shape of the free surface at the outer circumference of the contact, surface tension causes underpressure in the liquid, given by Eq. (*8*). Since $r_1 << a$, Eq. (*8*) simplifies to $p = \gamma_{LV}/r_1$. This underpressure attracts the indenter to the specimen by the force

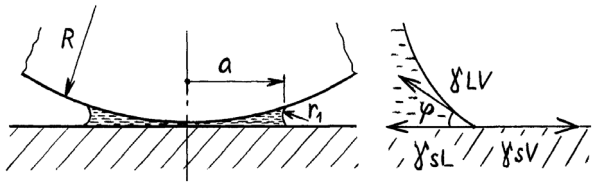

Fig. 6. **Liquid at the contact of two bodies** (a schematic)

$$F_{up} = -\pi a^2 p = \pi a^2 \gamma_{LV}/r_1 \qquad (10)$$

This force, much bigger than F_γ, can also be expressed by the contact angle between the liquid and indenter, φ_{Li} and the liquid and the specimen, φ_{LS}. If both contact angles were the same, equal φ, the attractive force could be expressed (with the simplifications $a^2 \approx 2Rd$ for $r_1 << a$ and $d \approx 2r_1\cos\varphi$ for small angles φ or for $a << R$) as[3]

$$F_{up} \approx 4\pi \gamma_{LV} R \cos\varphi \qquad (11)$$

For example, water (γ_{LV} = 73 mN m^{-1}) between the sample and indenter with R = 100 μm (and φ = 20°) can increase the adhesion force by 86 μN.

An interesting phenomenon must be mentioned. If the liquid wetts the surface well (the contact angle φ is small), its vapours can condense spontaneously in a narrow space between two surfaces, and the corresponding attractive force can appear even without obvious presence of a liquid, just under sufficient concentration of its vapours. This also can happen between a spherical indenter and a specimen. At equilibrium „liquid – vapour", the mean surface radius is given by Kelvin equation[3]

$$r_m = r_K = \gamma_{LV} V / [\mathbf{R}T \ln(p/p_{sat})] \qquad (12)$$

r_K is the Kelvin radius, γ_{LV} is surface tension „liquid-vapour", V is the molar volume, $\mathbf{R}$ is the universal gas constant, T is the absolute temperature, and p/p_{sat} is the relative vapour pressure; p is the actual pressure and p_{sat} is the saturation pressure. For water, p/p_{sat} corresponds to relative humidity, $\gamma V/RT$ = 0.54 nm at 20 °C, and the r_K values are[3]: 10 nm for relative humidity RH = 90 %, 1.6 nm for RH = 50 %, and 0.5 nm for RH = 10 %.

6. Determination of E-modulus by nanoindentation

In the absence of adhesion, E can be calculated from the unloading part of the "indenter load – displacement" curve via the Oliver & Pharr formula[11]:

$$E_{r,OP} = \pi^{1/2} S / (2\beta A^{1/2}) \qquad (13)$$

$S = dF/dh$ is the contact stiffness at nominal load, $A(h_c)$ is the contact area determined from the contact depth h_c, and β is the correction factor for indenter shape. For spherical indenter and elastic deformations, E can be calculated using Hertz formula, $E_{r,H} = (3/4)FR^{-1/2}h^{-3/2}$, but also from its modified version[12]:

$$E_{r,H} = [S^3/(6RF)]^{1/2} \qquad (14)$$

The advantage of Eq. (*14*) is that it is not necessary to know the contact area A nor the instant of first contact, needed for the determination of indenter penetration h. Moreover, if surface forces are not negligible, the relationship between load and displacement is not proportional to $h^{3/2}$, but nearly linear for very low loads (Fig. 7). If the JKR model is used, formula (*14*) must be modified as[12]:

$$E_{r,JKR} = E_{r,H} \times \Phi, \text{ where} \qquad (15)$$
$$\Phi = [(2/3)(1+\psi)^{-1/2} + 1]^{3/2}/\{1 + 2\psi^{-1}[1 + (1+\psi)^{1/2}]\}^{1/2}$$

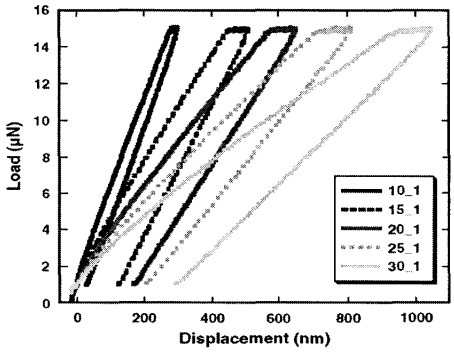

Fig. 7. **Load-displacement curves for various poly-dimethylsiloxane specimens.** Spherical indenter, R = 100 μm. S. Gupta et al.[12]

ψ is the ratio of indenter load and adhesion force, F/F_{ad}, with F_{ad} defined by the JKR model.

Equation (*15*) is based on the expression for contact stiffness, respecting the actual contact radius as a function of the load and work of adhesion, expressed by means of adhesive force F_{ad}, Eq. (*5*). The derivation of the correction factor Φ in Eq. (*15*) proceeded gradually. The first attempt was done in 2005 by Carrillo et al.[13], but in 2006 it was corrected[14] with respect to the earlier work by Pietremont and Troyon[15]. Experimental verification was demonstrated by Gupta et al.[12].

The differences between approaches (*14*) and (*15*) are negligible if the indenter load is many times higher than the force of adhesion, and become significant for loads comparable with F_{ad} or lower. This influence can amount up to several tens of percent.

The procedure for obtaining elastic modulus with the consideration of surface forces consists of the following steps. First, a load-unload test is performed, serving for the determination of adhesion force F_{ad} and contact stiffness S at the nominal load. These values are then – together with the load F and indenter tip radius R – inserted into Eq. (*14*) and (*15*). Elastic modulus of the tested material can be obtained from E_r via Eq. (*3*); if it is much lower than that of the indenter, it can be calculated as $E = E_r(1 - \nu^2)$.

The correction in Eq. (*15*) depends on the ratio of the nominal load and adhesion force. As no analogous procedure for viscoelastic materials exists yet, it is reasonable to assess the elastic modulus using Eq. (*15*) with ψ calculated for the force of adhesion, measured for the instant of: a) clinging and b) separation (Fig. 5). These two values give the probable range of the instantaneous modulus E_0. The higher the nominal load, compared to the adhesive force, the smaller the influence of adhesion and also the difference between both variants of calculation.

This paper was prepared as a part of the project GAČR No. P104/10/1021. The author thanks to the publishing house Elsevier and to S. Gupta and co-authors for the permission to use Fig. 1 from their paper in Materials Letters[12].

REFERENCES

1. Derjaguin B. V., Muller V. M., Toporov Yu. P.: J. Colloid Interface Sci. *53*, 314 (1975).
2. Johnson K. L., Kendall K., Roberts A. D.: Proc. R. Soc. Lond. A *324*, 301 (1971).
3. Israelachvili J. N.: *Intermolecular and surface forces*. 2nd ed. Academic Press, London 1992.
4. Johnson K. L.: Adhesion at the contact of solids, pp. 133–143 in: *Theoretical and Applied Mechanics* (W. T. Koiter, editor) North-Holland Publishing Comp., Amsterdam 1976.
5. Tabor D.: J. Colloid Interface Sci. *58*, 2 (1977).
6. Menčík J.: Chem. Listy *105*, s115 (2011).
7. Menčík J.: Chem. Listy *105*, s143 (2011).
8. Ebenstein D. M., Pruitt L. A.: Nanotoday *1*, 26 (2006).
9. Nohava J., Kempé P., Farine M.: Development of the methodology for testing of extremely soft materials. CSM-webinar, December 2010, http://www.csm-instruments.com/fr/system/files/ doc/ Conference/2010/02_Webinar%20Jiri%20Nohava.pdf
10. Greenwood J. A., Johnson K. L.: Philosophical Magazine A *43*, 697 (1981).
11. Oliver W. C., Pharr G. M.: J. Mater. Res. *7*, 1564 (1992).
12. Gupta S., Carrillo F., Li Ch., Pruitt L., Puttlitz Ch.: Mater. Lett. *61*, 448 (2007).
13. Carrillo F., Gupta S., et al.: J. Mater. Res. *20*, 2820 (2005).
14. Carrillo F., Gupta S., et al.: J. Mater. Res. *21*, 535 (2006).
15. Pietremont O., Troyon M.: J. Colloid Interface Sci. *226*, 166 – 1XX (2000).

J. Menčík *(University of Pardubice, Czech Republic):* **Low-load Nanoindentation: Influence of Surface Forces and Adhesion**

Nanoindentation of very soft materials uses low loads, which are comparable with atomic forces, acting in any surface layer. These forces can also influence the tests. The paper explains the nature of surface forces and adhesion. It presents formulae for these forces according to various models, and corrected formulae for the determination of elastic modulus from a nanoindentation test with a spherical indenter. The paper also discusses the influence of surface tension and capillary forces if a thin layer of a liquid is present at the contact, and the influence of surface roughness and the viscosity of contacting bodies.

MEASUREMENT OF LOCAL TENSILE PROPERTIES OF WELDED JOINT USING DIGITAL IMAGE CORRELATION METHOD

MILOS MILOSEVIC[a], NENAD MITROVIC[b], RADOMIR JOVICIC[a], ALEKSANDAR SEDMAK[b], TASKO MANESKI[b], ALEKSANDAR PETROVIC[b], and TAREK ABURUGA[b]

[a] University of Belgrade, Innovation Center of Faculty of Mechanical Engineering, [b] University of Belgrade, Faculty of Mechanical Engineering, 11120 Belgrade 35, Serbia
mmilosevic@mas.bg.ac.rs

Keywords: welded joint, tensile test, local mechanical properties, digital image correlation, heat affected zone

1. Introduction

One of the important tasks of structure integrity assessment is to determine local mechanical properties of the specimens or structure. In some applications like welding, heterogeneous structure of the tested sample has a different small strain zones. Currently existing mechanical characterization methods often do not allow full characterization of the different local strain areas. In order to solve these kind of problems, there are modern techniques that are able to measure very small areas such as Electronic Speckle Pattern Interferometry (ESPI)[1], Laser Speckle Photography System (LSP) and Digital Image Correlation (DIC). The 3D optical system using DIC technique will be applied in this work to determine local tensile properties of the heat affected zones (HAZ) in the welded specimen. DIC method may be considered as one of the efficient tools to verify the numerical models[2,3]. The main goal of this work is to track the local mechanical properties using DIC method in the both cases – specimens with and without crack in heat affected zone.

2. Materials and methods

Plates (400 × 200 × 10 mm) made of S235JRG2 were butt welded using MAG welding process for specimen preparation. The chemical composition and mechanical properties for the base metal are shown in Tab. I and Tab. II.

In this study, the overmatching welding will be applied to the specimen. Specimen dimensions are shown in Fig. 1.

Type of VAC 60 weld metal was used in order to get overmatching welding. Chemical composition and mechanical properties for the weld metal are shown in Tab. I and Tab. II.

Table I
Chemical composition (%)

Base	C	Si	Mn	P	S
metal	>0.17	<0.4	<1.4	< 0.05	< 0.05
Weld	C	Si	Mn	P	S
metal	0.08	0.90	1.50	< 0.025	< 0.025

Table II
Mechanical properties

Base	$R_{p0.2}$ [MPa]	R_m [MPa]	A_5 [%]
metal	> 235	340-470	> 25
Weld	$R_{p0.2}$ [MPa]	R_m [MPa]	A_5 [%]
metal	> 420	500-640	> 20

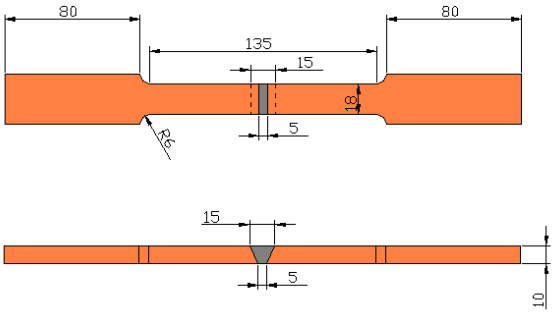

Fig. 1. **Specimens dimensions**

Equipment used in this research for the precise strain/displacement measurement is manufactured by GOM – Optical Measuring Techniques, Braunschweig, Germany. DIC method is computer based process to obtain 3D full strain/displacement field. The preparation of the measuring object starts with the placement of referral points – markers. The referral points, in case of the Aramis system, are placed with black and white spray, in order to create the best possible contrast, and enable the software to track the changes occurring in the object as it undergoes the loading. Mode of calibration is described in several papers[4,5].

Main components of the system using DIC method are:

- stereo cameras and lenses that provide a synchronized stereo view of the specimen or object,
- stand that provide the stability of the sensors,
- trigger box,
- halogen light,
- PC system.

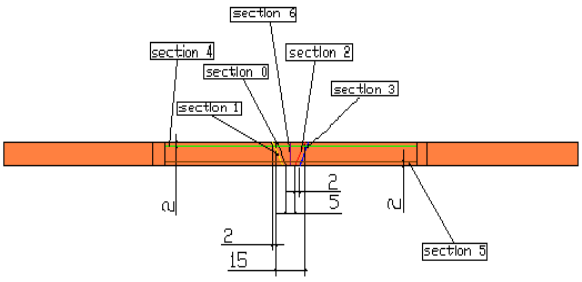

Fig. 2. **Position of the measured sections**

System recognizes the surface structure of the measuring object in digital camera images and allocates coordinates to the image pixels[4]. Computer algorithms compare the images and calculate displacements of characteristic features on the examined surfaces. Aramis is a non-contact and material independent measuring system providing, for static loaded test objects, local 3D surface coordinates displacements and velocities, strain values and strain rates[5,6].

Displacement accuracy of the DIC equipment, and software Aramis 2M used in thus work is 1/100 of a pixel and strain accuracy is 0.01% (ref.[6]).

3. Results and discussion

Results are shown for specimen without cracks No. 1 and the specimen with crack in the heat affected zone No. 2, formed due to overmatching welding. Seven sections on the lateral plane of the specimen surface are followed during the experiment. Sections are located in the fusion line in both sides, vertically located in the weld metal, parallel to the fusion line in the HAZ and horizontally – 2 mm away from the upper and lower surfaces, respectively, as shown in Fig. 2. In this paper the strains were analyzed for stages of maximum load and immediately before fracture. These stages will be studied in order to demonstrate possibility of using DIC technique to track the local mechanical properties of HAZ in the welded structures. Fig. 3 shows the Mises strain field at the maximum load stage of specimen No. 1. The left side curves show the variation of Mises strain values with respect to positions and sections length. The same analysis for the stage before fracture of specimen No. 1 is shown in Fig. 4.

Fig. 5 and Fig. 6 show the equivalent Mises strain field in the both stages for the specimen with crack – No. 2, respectively. In the overmatching welding, the fracture will be in the base metal unless there is a crack in the weld metal or HAZ. Crack that led to fracture was initiated during the welding process and is located approximately in the middle of section 2. Crack was propagated on the fusion line. By comparing these two specimens, the specimen No. 1 has fractured in base metal because of absence of cracks, while in specimen No. 2, the fracture was in the HAZ because of the crack.

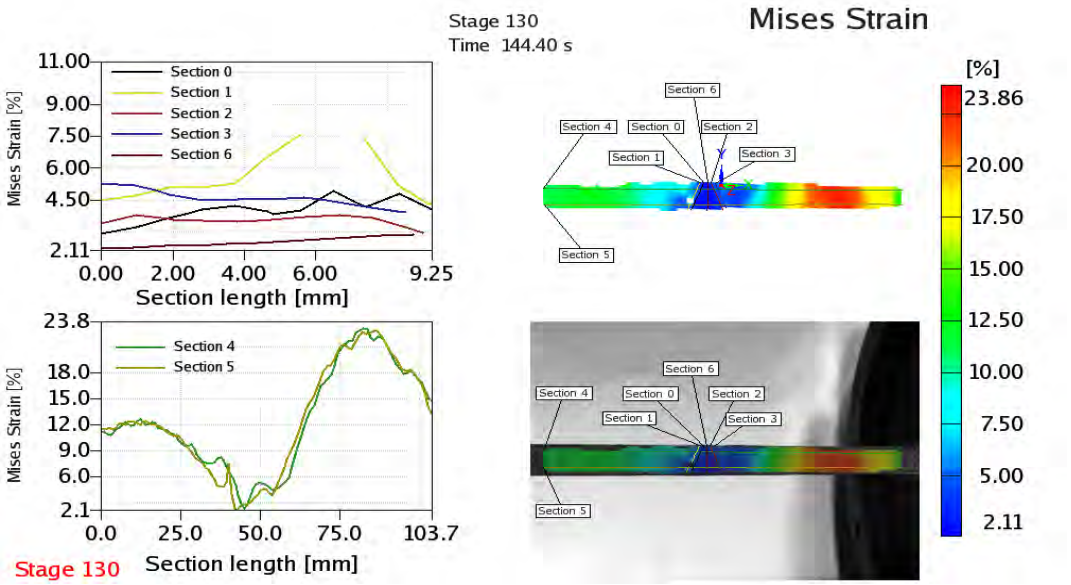

Fig. 3. **Mises strain field at the maximum load stage (F=71 kN) for specimen No. 1**

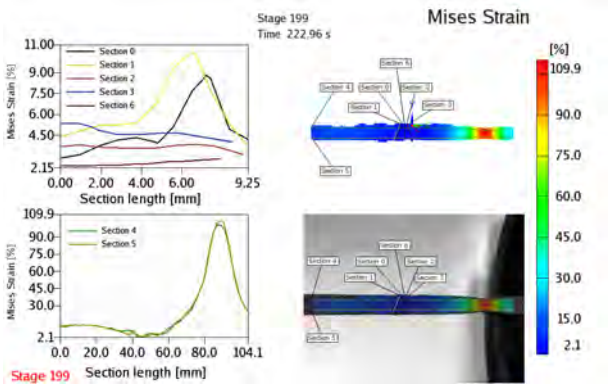

Fig. 4. **Mises strain field at the last stage before failure (F = 54 kN) of specimen No. 1**

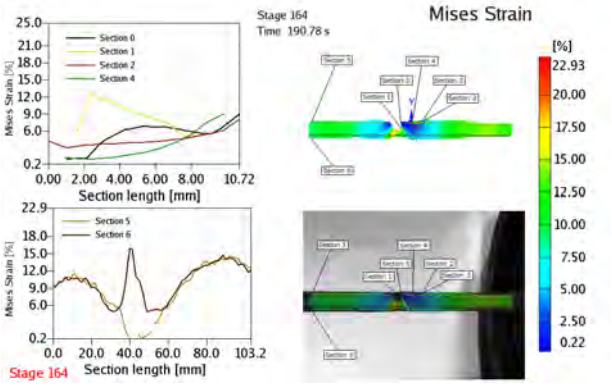

Fig. 5. **Mises strain field at the maximum load stage (F = 68 kN) of specimen No. 2**

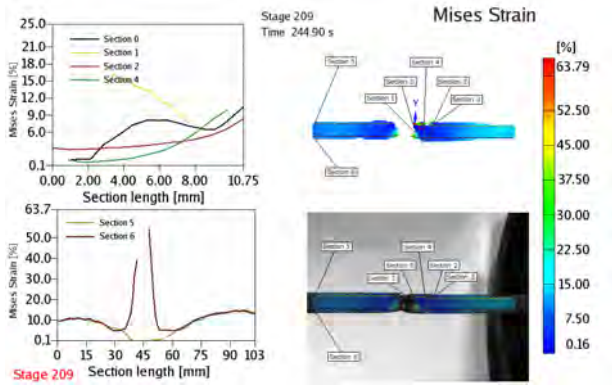

Fig. 6. **Mises strain field at the last stage before failure (F = 3.46 kN) of specimen No. 2**

To clarify the material heterogeneity effect on the behavior of the welded specimen, the five points are taken as a reference in the different local zones as shown in Fig. 7. The values of the Mises strain are shown in the Tab. III and Tab. IV for specimen No. 1 and specimen No. 2. respectively. There are sudden changes in the border of each zone i.e. from 4 % to 23 % in case of maximum load for specimen No. 1, and from 2.5 % to 105 % in last stage for the same specimen. The highest strain values indicate the position of the failure.

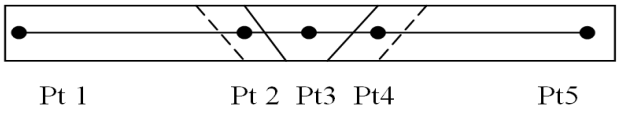

Fig. 7. **Referent points of the local strain fields**

Table III
Max Mises strains % at different areas in specimen No. 1

	Pt 1	Pt 2	Pt 3	Pt 4	Pt 5
	BM_L	HAZ_L	WM	HAZ_R	BM_R
F=71kN	12	4.5	3.0	4.0	23
F=54kN	14	10	3.0	4.5	105

Table IV
Mises strains % at different areas in specimen No. 2

	Pt 1	Pt 2	Pt 3	Pt 4	Pt 5
	BM_L	HAZ_L	WM	HAZ_R	BM_R
F=68kN	11	16	5	5	14
F=3.46kN	11	85	30	5	15

At specific stages, different zones of welded joint can be distinguished. Fig. 8 shows one of these stages where it is possible to characterize the base metal, heat affected zone and weld metal. This can be done either by the contour field where the significant changes in the strain values are located. According to these results, it is clear that for the specimen No. 1 local strain field shows lower values of weld material and HAZ. The higher local strain values are located in base metal. In the case of specimen No. 2, the crack propagation changes the previous local strain fields according to fracture mechanics parameters where the failure will be due to crack propagation.

4. Conclusions

According to the examinations performed the following conclusions can be drawn:

– Optical strain measurements based on DIC method

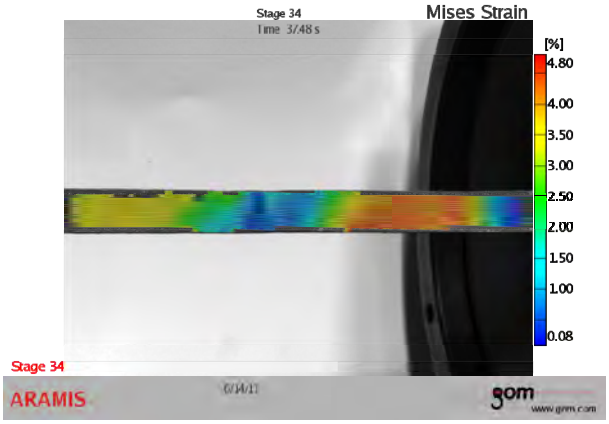

Fig. 8. **Clarity of the different zones**

can be very helpful for local strain measurements during the static tensile test of welded joint.

– Strain values of different local zones of a welded joint can be characterized using DIC technique.
– Analysis is specially shown for measuring local mechanical properties of overmatching welded specimens. It should be emphasized that the method can be used for local mechanical characterization of welded structures in general.

REFERENCES

1. Jacquot P.: Strain *44*, 57 (2008).
2. Rodrigues D., Menezes L., Loureiro A., Fernandes J.: Int. J. Plasticity *20*, 1 (2004).
3. Belhabib S., Haddadi H., Gasperini M., Vacher P Int. J. Mech. Sci. *50*, 14 (2008).
4. Mitrovic N., Milosevic M., Sedmak A., Petrovic A., Prokic-Cvetkovic R.: FME Transactions *39*, 55 (2011).
5. Milosevic M., Miletic V., Mitrovic N., Manojlovic D., Savic Stankovic T., Maneski T.: Chem. Listy *105*, s751 (2011).
6. ARAMIS, User information, Hardware, (2007).

M. Milosevic[a], N. Mitrovic[b], R. Jovicic[a], A. Sedmak[b], T. Maneski[b], A. Petrovic[b], and T. Aburuga[b]
([a] Innovation Center of Faculty of Mechanical Engineering, [b] Faculty of Mechanical Engineering, University of Belgrade): **Measurement of Local Tensile Properties of Welded Joint Using Digital Image Correlation Method**

Welded joints are heterogeneous structures consisted of several zones with different mechanical properties. During the loading, these zones are showing non-uniform mechanical behavior. In the heat affected zones is particularly complicated to monitor mechanical properties due to small dimensions, therefore HAZ mechanical properties were most often estimated through hardness testing, microstructure etc. The aim of the experiment is to assess the possibility of using Digital Image Correlation method in determining local tensile properties of HAZ. Testing was performed using 3D optical measuring system. Plates made of S235 were butt welded using MAG welding process for specimen preparation. Tensile testing of specimen characterized heterogeneous strain field and variable strain values in the monitored HAZ, indicating that DIC method is promising tool for precise local strain analysis of small dimension fields.

LOCAL PLASTICITY AND FAILURE OF NANOCRYSTALLINE Ni-Fe ALLOY AT LOW TEMPERATURES

JOZEF MIŠKUF [a], KORNEL CSACH[a], ALENA JURÍKOVÁ[a], ELENA TABACHNIKOVA[b], VLADIMIR BENGUS[b], ALEKSEIY PODOLSKIY[b], SERGEI SMIRNOV[b], HONGQI LI[c], PETER LIAW[c], and HAHN CHOO[c]

[a] *Institute of Experimental Physics SAS, Watsonova 47, 040 01 Košice, Slovakia,* [b] *B. Verkin Institute for Low Temperature Physics & Eng. UAS, Lenin Ave 47, 61103 Kharkov, Ukraine,* [c] *Department of Materials Science and Engineering, The University of Tennessee, Knoxville, TN 37996, USA*
miskuf@saske.sk

Keywords: nanostructured NiFe alloy, low temperature deformation, activation volume

1. Introduction

Several recent articles[1,2] have been devoted to the identification of mechanisms of low-temperature plastic deformation in the nanocrystalline (NC) face-centered cubic (fcc) metals and alloys with average grain sizes less than 100 nm. It was found[2] that the transition from a polycrystalline coarse-grained (CG) state to an NC state (grain size ~ 22 nm) for the Ni-20%Fe alloy leads to changes in many properties. The calculation of the activation volume for the process of plastic deformation from the strain-rate sensitivity of the applied stress[3] is one of the efficient methods for obtaining information about the mechanisms of thermally activated plastic deformation.

The phenomenon of the local plastic deformation and failure at low temperatures of nanocrystalline Ni-20% Fe alloy were investigated.

2. Experimental

The NC alloys Ni-20%Fe (with average grain size ~ 22 nm) were prepared by the electrodeposition method. The sulfur impurity level in deposits was 74 ppm. The samples were deformed in the compression at the temperatures of 300, 170, 77 and 4.2 K. From the measured strain-rate sensitivity the values of the activation volume (V) of the process of the local plastic deformation of the NC were calculated using Zeeger model with the assumption that the plastic deformation is controlled by thermally activated motion of dislocations. Strain-rate sensitivity was measured during uniaxial compression of $1.5 \times 1.5 \times 3$ mm^3 samples at temperatures of 300, 170 and 77 K. The strain rate was alternated from $3 \cdot 10^{-5}$ to $2.4 \cdot 10^{-4}$ s^{-1} or from $3 \cdot 10^{-4}$ to $2 \cdot 10^{-3}$ s^{-1} in several points of the deformation curves. From these dependencies, the values of the activation volume of a thermally activated plastic deformation were calculated, according to the method described in[3–5].

A part of the samples was deformed up to the fracture at temperatures of 300, 170, 77 and 4.2 K with the aim to study the failure surfaces of the samples. The fractography was carried out by JSM 7000F scanning electron microscope.

3. Results and discussion

The values of the activation volume V of the process of plastic deformation along the deformation curves obtained in the temperature range from 300 to 77 K in compression are in Fig. 1. It was established that the decrease in temperature leads to a decrease of V values from 20 to 8 b^3 (b is Burgers vector). Values of V do not depend on the strain because the dislocation nucleation at grain boundaries does not depend on the achieved strain values. The small activation volume suggests that the nucleation of dislocations from the grain boundaries is associated with a cooperative motion of a small group of atoms within the boundary[4,5].

Increased strength of NC materials is followed by higher localization of the plastic deformation. The fractographic observations revealed the deformation mechanisms of highly localized plastic deformation at last stages of the failure[6,7]. The observed traces of melting are indicated by arrows in Fig. 2. This indicates the intense heating in the catastrophic shear band of the alloy[6]. Two types of the morphology on the fracture surfaces were present: the ductile fracture morphology with elongated dimples as commonly observed in the plastic materials, and the second type of the fracture morphology – the flat clus-

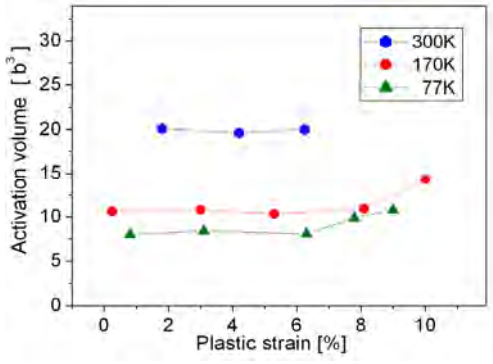

Fig. 1. **The activation volume versus plastic strain for the temperatures of 300, 170 and 77 K**

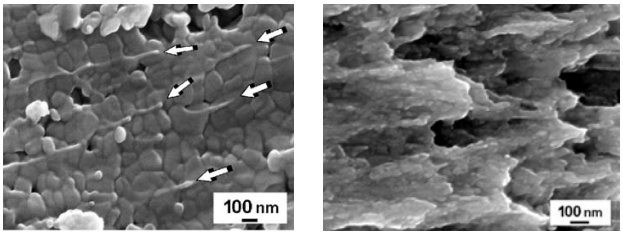

Fig. 2. **Flat clustered shear morphology.** Elongated ridges and drops are indicated by arrows (left). The ductile dimpled shear fracture morphology (right)

tered shear morphology with respect to the separate grains or grain clusters as Fig. 2 demonstrates. When the grain size is sufficiently small and dislocation most likely interact with grain boundaries, the deformation is believed to occur via dislocation activities at grain boundary sliding[2,4,8].

Fig. 3 demonstrates the presence of morphology types at different test conditions (temperature and strain rate). The filled part of a circle symbol represents the portion of dimpled shear morphology, whereas the open one represents the presence of the flat clustered shear morphology.

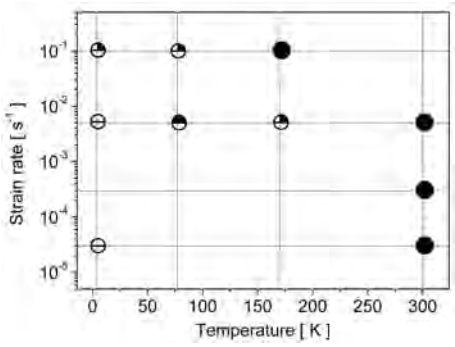

Fig. 3. **The morphology types on the fracture surfaces**

4. Conclusions

It was found that the ductile shear failure occurs at all studied temperatures in uniaxial compression deformation. A temperature dependence of typical patterns at the failure surface was found. A dimpled morphology, observed at 300 K, is gradually replaced with a decrease of the temperature by flat surfaces. At these surfaces, the cavities of various sizes were observed and the separate grains and their conglomerates with size of 200 to 600 nm, which were extracted from their initial places. At the temperatures below 300 K, the traces of melting were revealed, which indicates the intense local heating of the alloy at the moment of the failure. Decreasing of activation volume at lower temperatures tends to more flat fracture surface morphology creation.

This work was supported by implementation of the project No. 26220120021 provided by the European Regional Development Fund. The authors are grateful to the Centre of Excellence "Nanofluid," VEGA 0185/11 and Slovak Research and Development Agency – contract No. APVV-0171-10.

REFERENCES

1. Kim H. S., Estrin Y., Bush M. B.: Acta Mater. *48*, 493 (2000).
2. Tabachnikova E. D., Podolskiy A. V., Bengus V. Z., Smirnov S. N., Bidylo M. I., Li H., Liaw P. K., Choo H., Csach K., Miskuf J.: Mater. Sci. Eng. A *503*, 110 (2009).
3. Evans A. G., Rawlings R. D.: Phys. Status Solidi *34*, 9 (1969).
4. Li H., Ebrahimi F., Choo H., Liaw P. K.: J Mater. Sci. *41*, 7636 (2006).
5. Tribute A. to Nabarro F. R. N. : *Dislocation in Solids* vol. 14, Chapter 82, Ed. J. Hirth, 125 (2008).
6. Bengus V. Z., Tabachnikova E. D., Shumilin S. E., Golovin Y. I., Makarov M. V., Shibkov A. A., Miskuf J., Csach K., Ocelik V.: Int. J. Rapid Solidification *8*, 21 (1993).
7. Tabachnikova E. D., Bengus V. Z., Miskuf J., Csach K., Ocelik V., Johnson W. L., Molokanov V. V.: Mater. Sci. Forum *343–346*, 197 (2000).
8. Tatarko P., Kašiarová M., Dusza J., Šajgalík P.: Chem. Listy *105*, s850 (2010).

J. Miškuf[a], K. Csach[a], A. Juríková, E. Tabachnikova[b], V. Bengus[b], A. Podolskiy[b], S. Smirnov[b], H. Li[c], P. Liaw[c], and H. Choo[c] *([a] Institute of Experimental Physics SAS, Košice, Slovakia, [b] B. Verkin Institute for Low Temperature Physics & Eng. UAS, Kharkov, Ukraine, [c] Department of Materials Science and Engineering, The University of Tennessee, Knoxville, USA):* **Local Plasticity and Failure of Nanocrystalline Ni-Fe Alloy at Low Temperatures**

The local plastic deformation and failure at low temperatures of nanocrystalline Ni-20%Fe were investigated. The samples were deformed in the compression at temperatures from 4.2 to 300 K at different strain rates. The activation volume (V) of the plastic deformation was calculated. It did not depend on the strain and the decreasing in the temperature lead to the decreasing of V from 20 to 8 b^3. Two types of the morphology on the fracture surfaces were present. At higher temperatures and higher V the elongated dimples were observed, whereas the flat clustered shear morphology for lower temperatures and smaller activation volume is typical.

EXPERIMENTAL AND NUMERICAL ANALYSIS OF LOCAL MECHANICAL PROPERTIES OF GLOBE VALVE HOUSING

NENAD MITROVIC[a], MILOS MILOSEVIC[b], NIKOLA MOMCILOVIC[a], ALEKSANDAR PETROVIC[a], ALEKSANDAR SEDMAK[a], TASKO MANESKI[a], and MILORAD ZRILIC[c]

[a] *University of Belgrade, Faculty of Mechanical Engineering, 11120 Belgrade 35,* [b] *University of Belgrade, Innovation Center of Faculty of Mechanical Engineering, 11120 Belgrade 35,* [c] *University of Belgrade, Faculty of Technology and Metallurgy, 11000 Belgrade, Serbia*
nmitrovic@mas.bg.ac.rs

Keywords: globe valve, local mechanical properties, digital image correlation (DIC), finite element

1. Introduction

Globe valves are one of the most widely used industrial valves. During the working life, valves are subjected to various types of loads – static, dynamic, thermal etc, which can cause valve housing failures. Based on previous experiences and research, valve housing failure is expected in the areas of high stress concentration, such as high geometrical discontinuity.

High geometrical discontinuities and complex geometry place a huge challenge to researchers experimentally investigating stress and strain field. Most commonly used equipment for strain/displacement measurement is strain gauge, LVDT, extensometer etc. Problem with this equipment is that it doesn't provide full strain/displacement field, only a result on selected point of the object or specimen. For better understanding of the behavior of complex objects under loading, optical methods are being used in the experiments (videoextensometry, digital image correlation etc.)[1–5].

Digital image correlation (DIC) method is an optical non-contact method that can provide us full 3D strain/displacement field. DIC method is independent from the material tested, as well as from the shape of the object, which enables application of this method in various fields – biomedicine, biomaterials, polymers etc[6–10].

This paper is focused to investigate the possibility to analyze local strain fields of geometrically complex globe valve housing subjected to internal pressure using DIC method.

2. Experiment and experimental object

In this experiment, valve was tested in the installation for pressure testing of industrial valves and subjected to internal pressure using water temperature of 20 °C. One valve flange was clamped to secure that there is no valve translation, and the other flange was free, as shown in Fig. 1.

Experiment was conducted using 3D system Aramis 2M (GOM, Braunschweig, Germany). The system has following characteristics: system type is 2M, camera resolution 1600×1200 pixels and maximum frame rate 12 Hz.

Before the experiment, valve was sprayed with white paint as basic color for spraying stochastic pattern of black dots. As a part of pre-experimental preparations, calibration was also performed. Detailed mode of operation, calibration, preparation of measuring object and measuring procedure is described in several papers[6,11]. Table I shows parameters for basic system setup used for the experiment.

Globe valve used in the experiment is DN 32 and PN 6. Adopted value for experimental pressure is 30 bar, as the pump and installation pressure limit is 30 bar and finite element method (FEM) showed that valve housing is

Table I
Parameters for basic system setup

ARAMIS 2M parameters	
Measuring volume [mm]	100 × 75
Depth of field at aperture 8 [mm]	>100
Base distance [mm]	370
Min. length of camera support [mm]	500
Measuring distance [mm]	800
Camera angle [°]	26
Calibration object (coded)	CP20 90×72

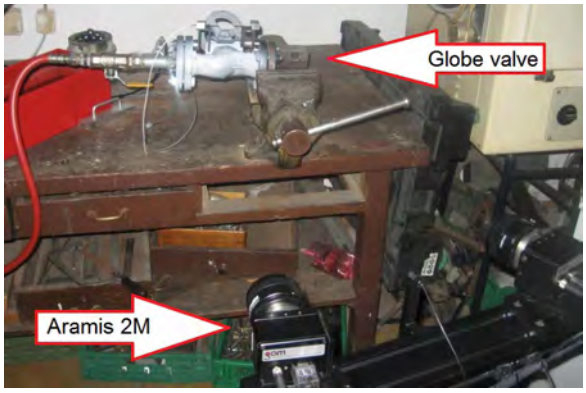

Fig. 1. **Experimental setup**

in the safety zone. Valve was gradually loaded to the highest value of 30 bar, as specified in EN 13445.

Globe valve housing has several local areas with complex geometry. The local area analyzed in this paper is shown on Fig. 2.

Local mechanical properties were determined in the transition area that can be approximated as the sphere to cylinder junction.

3. Numerical model

In this paper, FEM is used for the strain and stress analysis of the globe valve. FEM is respectful method for direct calculation and prediction of behavior of such complex type of structures. This presents even a greater challenge having in mind different geometric transitions within the object. Cross section of the valve parts varies from circle to ellipse and can be compared to cylinder and sphere junction.

FEM software package used in this paper is Abaqus. FE model is based on 6921 tetrahedral element and 1851 node. Mesh has more density where geometric discontinuities occur. FE model of valve is, as well as a real model, subjected to internal pressure, as shown in Fig. 3. Since the object is symmetrical, only one half is analyzed. All the nodes located on the symmetry plane have displacement constrained in transverse direction[12] and rotation constrained in other two directions.

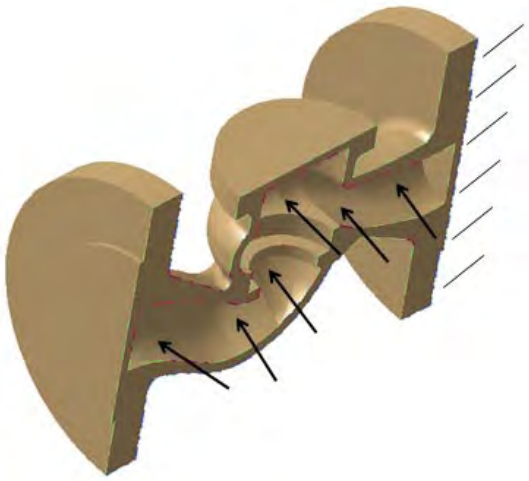

Fig. 3. **3D FE model (constraints and loading)**

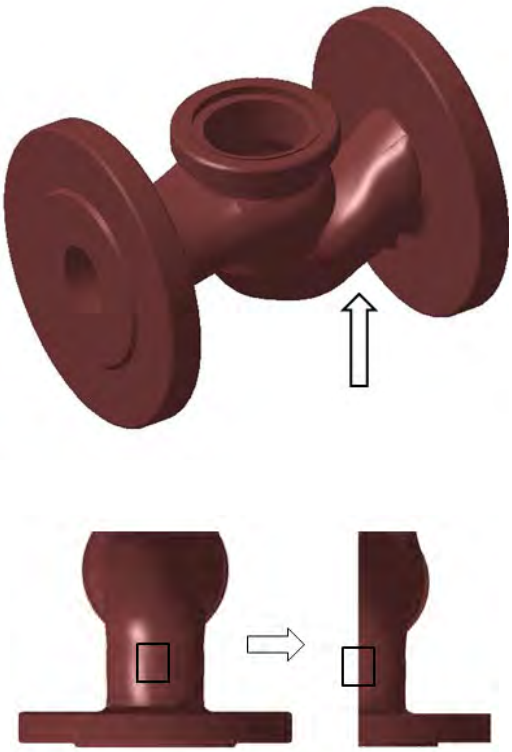

Fig. 2. **3D model of globe valve (rectangle is marking analyzed area)**

4. Results and discussion

For understanding strain and stress conditions of numerous objects in exploitation, numerical and experimental analyses are often used. In this paper, experiment using 3D DIC method was conducted to verify numerical model.

Von Mises strain results obtained from numerical analysis of globe valve subjected to 30 bar are presented in Fig. 4. Results showed strains from nearly $1.46 \cdot 10^{-5}$ up to $1.74 \cdot 10^{-4}$ (0.0015 % to 0.0174 %). Von Mises stresses for this area are in the range of 15 to 25 MPa.

Visualization of the deformation with an image of Strain overlay is shown in Fig. 5. A photograph of a real object is displayed along with the picture processed by the software. The pictures are overlapped, so local zones can be easily spotted. Two sections are defined in Fig. 5. Section 0 is placed transversal to valve housing (blue vertical

Fig. 4. **Von Mises strain results obtained from Abaqus**

Fig. 5. **Local 3D von Mises strain field obtained using Aramis**

line) and Section 1 is placed longitudinally to valve housing (black horizontal line).

Section diagram (Fig. 6) shows one or more sections of the current load stage. This diagram shows the Mises strain with respect to the length of the section per stage. Two sections (0 and 1) are displayed in different colors, showing values for the entire section which can be further examined.

Experimental results presented in Fig. 5 and 6 are confirming that highest strain values are registered in the transition area – sphere to cylinder junction. Mises strain values in this local area are in range from around 0.012 % to 0.025 %. Highest recorded values of 0.025 % are localized at the sphere/cylinder intersection. In comparison to FE model with highest values of 0.0174 % in the intersection area, the result difference is 30.4 %. Recorded experimental values for von Mises strain at spherical and cylindrical part are in range of 0.012 % to 0.015 %. In the same region, FEA showed von Mises strain results in

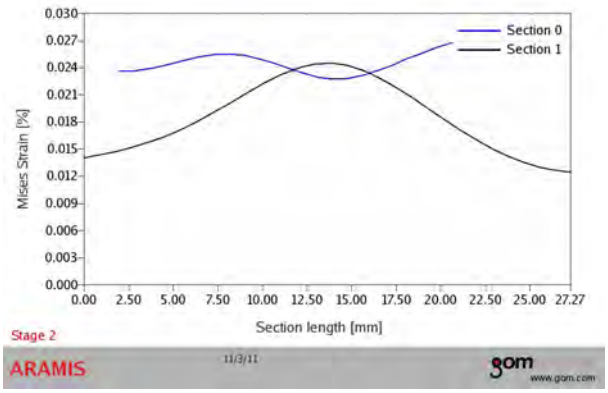

Fig. 6. **Section diagram of local 3D von Mises strain field**

range of 0.009 % to 0.012 %, which is an average result difference of 14.8 % between two methods.

Analyzing experimental and numerical data, there are differences in obtained results, but the trend of strain distribution throughout the analyzed area is highly similar – highest values are recorded in the transition area of sphere/cylinder junction.

5. Conclusions

Local mechanical properties and behavior of valve housing under loading are important basis for further valve analysis and design improvements. DIC method and 3D optical system Aramis are powerful tools enabling mapping of full strain fields in industrial pipeline fittings. Experimental analysis and numerical simulation indicate that local deformation field on globe valve surface has the same nature at cylinder/sphere junction. Analysis shows that the differences between two methods in the area of the highest strain values, in the cylinder sphere intersection, vary 30 % and in the spherical and cylindrical parts result variation is 14.8 %. Obtained results indicate that it is possible to analyze local strain fields of geometrically complex globe valve housing using DIC method.

REFERENCES

1. Ambriško L., Pešek L.: Chem. Listy *105*, s767 (2011).
2. Hlebová S., Pešek L., Kandra T.: Chem. Listy *105*, s577 (2011).
3. Jiroušek O., Němeček J., Kytýř D., Kunecký J., Zlámal P., Doktor T.: Chem. Listy *105*, s668 (2011).
4. Mihaliková M., Ambriško L., Pešek L.: Kovove Mater. *49*, 137 (2011).
5. Pata V., Manas D., Manas M., Stanek M.: Chem. Listy *105*, s290 (2011).
6. Milosevic M., Miletic V., Mitrovic N., Manojlovic D., Savic Stankovic T., Maneski T.: Chem. Listy *105*, s751 (2011).
7. Jerabek M., Major Z., Lang R.W.: Polym. Test. *29*, 407 (2010).
8. Tanasic I., Milic-Lemic A., Tihacek-Sojic L., Stancic I., Mitrovic, N.: Biomech. Model. Mechan., *1* (2011).
9. Tihacek-Sojic L., Milic Lemic A., Tanasic I., Mitrovic N., Milosevic M., Petrovic A.: Gerodontology (2011).
10. Sztefek P., Vanleene M., Olsson R., Collinson R., Pitsillides A., Shefelbine S.: J. Biomech. *43*, 599 (2010).
11. Mitrovic N., Milosevic M., Sedmak A., Petrovic A., Prokic-Cvetkovic R.: FME Transactions *39*, 55 (2011).
12. Galić I., Vučković K., Tonković Z.: Technical Gazette *17*, 71 (2010).

N. Mitrovic[a], M. Milosevic[b], N. Momcilovic[a], A. Petrovic[a], A. Sedmak[a], T. Maneski[a], and M. Zrilic[c]
([a] University of Belgrade, Faculty of Mechanical Engineering, Belgrade, [b] University of Belgrade, Innovation Center of Faculty of Mechanical Engineering, Belgrade, [c] University of Belgrade, Faculty of Technology and Metallurgy, Belgrade, Serbia): **Experimental and Numerical Analysis of Local Mechanical Properties of Globe Valve Housing**

One of the most widely used industrial valves is globe valve. Due to wide industrial application, the valve is subjected to various types of loads – static, dynamic, thermal etc. which causes valve housing failures. Based on previous experiences and research, valve housing failure is expected in the areas of high stress concentration, such as high geometrical discontinuity. This paper is focused to investigate the possibility to analyze local strain fields of geometrically complex globe valve housing subjected to internal pressure using non-contact 3D optical deformation analysis in order to verify numerical model. Experimental system consists of cameras for 3D displacement and strain analysis and software Aramis. Using the Finite Element Method (FEM), numerical model subjected to different loads was analyzed. It is found that the predictions from the model agree well with experimental results as the result differences between two methods in the area of the highest strain values vary 30 % and in the spherical and cylindrical parts result variation is 14.8 %. Experimental and numerical results demonstrate that the experimental method is adequate for solving geometrically complex problems and determining local mechanical properties.

NANOHARDNESS TESTING OF MULTIPHASE C-Mn-Si STEEL

MÁRIA MOLNÁROVÁ[a], PETRA GAVENDOVÁ[a], TIBOR KVAČKAJ[b], and FRANTIŠEK KOVÁČ[a]

[a] Institute of materials research, Slovak academy of sciences, 040 01 Košice, [b] Department of Metals Forming, Faculty of Metallurgy, Technical University of Košice, 042 00 Košice, Slovakia
mariamolnarova@gmail.com

Keywords: nanohardness, transformation induced plasticity, ferrite, austenite, bainite

1. Introduction

TRIP (transformation induced plasticity) steels were introduced by Zackay et al.[1] in austenitic stainless steels in 1967, describing how the transformation supports „high-strength steels toughness improving". After[2–4] the aspect of TRIP steels originates from a phase transformation of metastable austenite into much harder martensite during deformation[5], and must provide ferrite formation and saturation of austenite (RA) solid solution by carbon without possibility of pearlite and cementite formation, which can be suppressed by rapid cooling rate and elements addition like Si, Cr or Mn[6]. After Wu et al.[7] rapid cooling is necessary for preventing the relaxation after deformation, so more dislocations stay retained after several step cooling at room temperature. Tsusaki and Raghavan[8] found that a large dislocation density hinders a growth of martensitic plates. The stability of RA against the martensitic transformation is improved by increasing dislocation density[9]. There are few reports on the mechanical behaviour of different phases in multiphase TRIP steels due to the difficulty of making such small-scale measurements, especially in individual austenite grains[10]. The nanoindentation method, developed by Oliver and Pharr[11], can provide information about the mechanical behaviour when material is being deformed at the sub-micron scale[12].

For this contribution multiphase steel with composition of C 0.18wt.%, Mn 1.47wt.%, Si 1.8wt.%, P 0.015wt.%, S 0.007wt.%, Cu 0.06wt.%, Ni 0.04wt.%, Cr 0.06wt.%, $Al_{tot.}$ 0.028wt.%, Nb 0.005wt.%, Sn 0.007wt.% was investigated for the dependence of nanohardness in different phases on intercritical annealing temperature 540–740 °C and subsequent austempering temperature 350–450 °C.

2. Material and methods

Two groups of steel samples after two step deformation (50 %) were used for investigation of influence of annealing parameters on nanohardness in different structure phases. First group was processed by intercritical annealing (T_{IC} = 540–740 °C) and austempering (T_A = 350–450 °C), where the samples were air-cooled after each processing step down to room temperature (SA). Second group was processed by intercritical annealing (T_{IC} = 540–740 °C) and austempering (T_A = 350–450 °C), where the samples were cooled to T_{IC} by double water jet and air-cooled before and after austempering down to room temperature (QA).

Structure of the samples cooled only in air consisted of ferrite (F), martensite/martnesite+bainite (M+B), pearlite (P) formed at specific isothermal conditions at cca 600 °C and low cooling rates also occurs[13], see Fig. 1. The other group of samples is characterized by the structure F+(M+B) / F+P. Retained austenite was expected in the islands of (M+B) inside original austenite grains bouded by F, see Fig. 2.

Nanohardness testing was performed by Nanoindenter G200 with Berkovich tip indenter using depth control system. Parameters of measurements were as follows: maximum depth h_{max}= 600 nm, the Poisson´s ratio

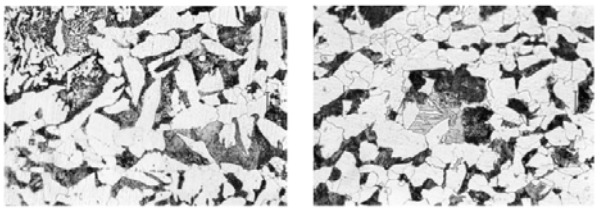

Fig. 1. **Structure of selected samples air-cooled**

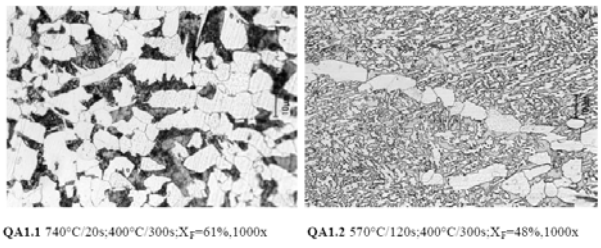

Fig. 2. **Structure of selected samples cooled on air and by double water jet**

s = 0.3, peak holding time 10 s. After reaching the maximum depth the nanohardness was measured in different phases (F, B+M mixture) during the holding time.

3. Results and discussion

Fig. 3 shows indentation curves of average values of different phases. As one can see, there is the difference in hardness values between the phases Fig. 2. Not only due to fraction and morphology of each phase, but also due to different annealing parameters[14] (intercritical annealing and austempering). The indentation hardness reached the values of cca 4 GPa for ferrite and cca 5.5 GPa for mixture of samples cooled by water jet before austempering. Samples cooled only on air reached the values of indentation hardness of cca 3.5 GPa for ferrite and cca 5.5 GPa for mixture.

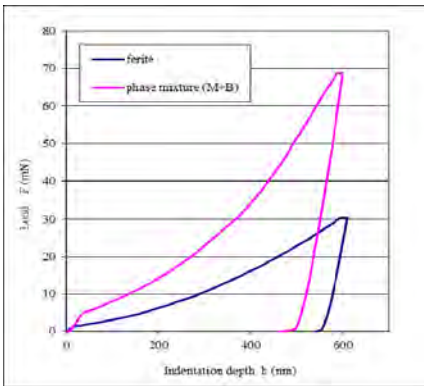

Fig. 3. **Indentation curves of different phases – ferrite (pink), martensite + bainite mixture (blue)**

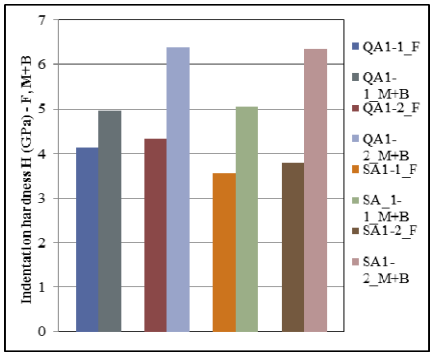

Fig. 4. **Indentation hardness values of selected samples phases influenced by annealing parameters**

4. Conclusions

The local determination of indentation hardness of the investigated multiphase steel revealed differences in the individual phases due to volume fraction and morphology of each phase, and also due to different annealing parameters during controlled rolling.

This work was supported by the Scientific Grant Agency of Slovak republic as a grant project VEGA No. 2 / 0138 / 10. This work was realized within the frame of the project „New Materials and Technologies for Energetics“(ITMS: 26220220061), which is supported by the Operational Program “Research and Development” financed through European Regional Development Fund.

REFERENCES

1. Zackay V. F., Parker E. R., Fahr D.: Trans. ASM *60*, 252 (1967).
2. Olson G. B., Cohen M.: Metall. Trans. A *13*, 1907 (1982).
3. Zaefferer S., Ohlert J., Bleck W.: Acta Mater. *52*, 2765 (2004).
4. Han H. N., Oh C.-S., Kim G., Kwon O.: Mater. Sci. Eng. A-Struct *499*, 462 (2009).
5. Quade H., Prahl U., Bleck W.: Chem. Listy *105*, s705 (2011).
6. Kvackaj T., et al.: Acta Metall. Slovaca *16*, 268 (2010).
7. Wu D., Li Z., Lü H.-S.: J. Iron Steel Res. Int. *15*, 65 (2008).
8. Stephane G., Philippe H., Francis D.: Steel Res. *73*, 280 (2002).
9. Timokhina I. B., Pereloma E. V.: Mater. Sci. Technol. *17*, 135 (2001).
10. Ahn T.-H., et al.: Scripta Mater. *63*, 540 (2010).
11. Oliver W. C., Pharr G. M.: J. Mater. Res. *19*, 3 (2004).
12. Rodríguez R., Gutierrez I.: Mater. Sci. Eng. A-Struct *361*, 377 (2003).
13. Molnárová M., et al.: Chem. Listy *104*, s353 (2010).
14. Némethová L., Kvačkaj T., Mišičko R., Pokorný I., Kovárová I.: Acta Metall. Slovaca *3*, 173 (2009).

M. Molnárová[a], P. Gavendová[a], T. Kvačkaj[b], and F. Kováč[a] *(Institute of materials research, Slovak Academy of Sciences, Košice, [b] Dpt. of Metals Forming, Faculty of Metallurgy, Technical University of Košice, Košice, Slovakia):* **Nanohardness Testing of Multiphase C-Mn-Si Steel**

This paper deals with investigation of the dependence of nanohardness in C-Mn-Si steel different structure phases on intercritical annealing temperature 540–740 °C and subsequent austempering temperature 350–450 °C. There are few reports on the mechanical behaviour of different phases in multiphase TRIP steels due to the difficulty of making such small-scale measurements, especially in individual austenite grains[10]. The nanoindentation method, developed by Oliver and Pharr[11], can provide information about the mechanical behaviour when material is being deformed at the sub-micron scale[12].

UP-SCALING MICROLEVEL ELASTIC PROPERTIES OF HETEROGENEOUS STRUCTURAL MATERIALS

JIŘÍ NĚMEČEK, VLASTIMIL KRÁLÍK, and JAROSLAV VONDŘEJC

Czech Technical University in Prague, Thákurova 7, 166 29 Prague 6, Czech Republic
jiri.nemecek@fsv.cvut.cz

Keywords: micromechanics, nanoindentation, heterogeneous materials, up-scaling, Mori-Tanaka, FFT

1. Introduction

Structural materials such as concrete, gypsum, plastics, wood or metals are characterized by a multiscale heterogeneity at different length scales (nm−m). Their mechanical properties are often assessed from macroscopic tests on large scale samples that can only describe overall (averaged) properties like overall Young's modulus or strength. Nowadays, it is possible to access also lower material levels and small-scale properties of individual material components experimentally e.g. by nanoindentation.

Wide theoretical background has also been laid in the field of micromechanics together with the development of classical composites. Micromechanical approaches are applied for matrix-inclusion problems to search for effective properties of the whole representative volume element – RVE[1–3]. Although, the theoretical development in micromechanics is tremendous the knowledge of the material microstructure and its micromechanical properties is the key factor in obtaining relevant results.

In this paper, we deal with the micromechanical prediction of the effective elastic properties for several structural materials on a scale of several hundreds of micrometers. Simple analytical and more complex numerical approaches are utilized.

2. Methods

Microscale experimental measurements, e.g. nanoindentation, can supply valuable data on mechanical properties of small material volumes or even distinct material phases in multi-phase materials. The size of RVE in a multi-scale material is considered so that it is much larger than the smallest microstructural inhomogeneity but it is small enough to represent the whole material level. Then, the up-scaling methodology can be summarized in the following main steps:

- Definition of scales in the material (i.e. RVE size definition for each scale).
- Nanoindentation on distinct material phases and characterization of their volume fractions within RVE.
- Applying homogenization techniques to assess effective RVE properties.

For heterogeneous structural materials, the task of finding number of mechanically distinct microstructural phases, their mechanical properties and volume fractions, can be solved by nanoindentation. To access distinct phases, the size of individual indents h have to be considerably smaller than the dimension of the studied phase d (i.e. $h<<d$). Such assumption is especially important in multi-phase to avoid phase interactions[4,5]. As a rule of thumb $h<d/10$ is usually used[4]. Also, special approaches like massive grid indentation[4] or statistical deconvolution[4,6,7] can be utilized in solving this task.

3. Homogenization

In general, homogenization methods search for effective composite properties. Analytical schemes often rely on simplified assumptions concerning inclusion geometry, boundary conditions or isotropy. More complex results can be obtained from numerical methods that are based on finite element solution or fast Fourier transformation, for instance.

The classical solution based on constant stress/strain fields in individual microscale components for ellipsoidal inclusion embedded in an infinite body was derived by Eshelby[2]. Effective elastic properties are then obtained through averaging over the local contributions. Various estimates considering different geometrical constraints or special choices of the reference medium known as rule of mixtures, Voight and Reuss bounds, Mori-Tanaka method or self-consistent scheme[1–3] can be used. For the case of a composite material with prevailing matrix and spherical inclusions the Mori-Tanaka method[3] was previously found to be simple but powerful tool to estimate effective composite properties also for structural materials[4] and, therefore, it was used in this paper. In the Mori-Tanaka method, the homogenized isotropic bulk and shear moduli of an r-phase composite are assessed as follows:

$$k_{\mathrm{hom}} = \frac{\sum_r f_r k_r \left(1+\alpha_0\left(\frac{k_r}{k_0}-1\right)\right)^{-1}}{\sum_r f_r \left(1+\alpha_0\left(\frac{k_r}{k_0}-1\right)\right)^{-1}} \qquad (1)$$

$$\mu_{\mathrm{hom}} = \frac{\sum_r f_r \mu_r \left(1+\beta_0\left(\frac{\mu_r}{\mu_0}-1\right)\right)^{-1}}{\sum_r f_r \left(1+\beta_0\left(\frac{\mu_r}{\mu_0}-1\right)\right)^{-1}} \qquad (2)$$

$$\alpha_0 = \frac{3k_0}{3k_0 + 4\mu_0}, \quad \beta_0 = \frac{6k_0 + 12\mu_0}{15k_0 + 20\mu_0} \tag{3}$$

where the subscript 0 corresponds to the reference medium and *r* corresponds to a particulate inclusion. Thus, k_0 and μ_0 are the bulk and shear moduli of the reference medium, while k_r and μ_r refer to the inclusion phases. Further, bulk and shear moduli can be recomputed to engineering values of Young's modulus and Poisson's ratio as:

$$E = \frac{9k\mu}{3k + \mu}, \quad \nu = \frac{3k - 2\mu}{6k + 2\mu} \tag{4}$$

Local strain and stress fields in a RVE can also be found by numerical methods like finite element method or method based on fast Fourier transformation (FFT). The former one was proved to be reliable and computationally inexpensive method which only utilizes mechanical data in the discretization (grid) points. Such a concept perfectly matches with the concept of the grid nanoindentation. Therefore, the FFT method was chosen for our purposes. The numerical scheme used here solves the problem of finding the effective elasticity tensor with a periodically repeating RVE by using discretization of an integral Lippmann–Schwinger equation:

$$\boldsymbol{\varepsilon}(\mathbf{x}) = \mathbf{e}^0 - \int_\Omega \Gamma^0(\mathbf{x}-\mathbf{y}) : (\mathrm{L}(\mathbf{y}) - \mathrm{L}^0) : \boldsymbol{\varepsilon}(\mathbf{y}) d\mathbf{y} \tag{5}$$

in which $\boldsymbol{\varepsilon}$ and L stand for the local (inhomogeneous) strain and stiffness tensor, respectively, and $\mathbf{e}^0$ is the homogenized strain defined as a spatial average over RVE domain Ω as

$$\mathbf{e}^0 = \langle \boldsymbol{\varepsilon} \rangle = \frac{1}{\Omega} \int_\Omega \boldsymbol{\varepsilon}(\mathbf{x}) d\mathbf{x} \tag{6}$$

Γ^0 is the periodic Green operator associated with the reference medium and L^0 in Eq. (5) stands for a reference elasticity tensor, which is a parameter of the method proposed by Moulinec and Suquet[8]. The problem is further discretized in the Fourier space. This leads to the solution of a nonsymmetric linear system of equations, which can be effectively treated by e.g. the conjugate gradient method (Zeman et.al.[9]).

4. Experimental program

Three types of heterogeneous structural materials were selected for this work: cement paste, gypsum and aluminium alloy.

Cement paste samples were prepared from Portland cement CEM-I 42,5 R with water to cement weight ratio equal to 0.5 and stored in water for several years[10]. Therefore, high degree of hydration can be anticipated in the samples. The microstructure of cement paste includes several major chemical phases, namely the hydration products: calcium-silica hydrates (C-S-H), calcium hydroxide $Ca(OH)_2$, residual clinker and the porosity.

Dental gypsum (Interdent®) was chosen as a model system for gypsum based materials[11]. Samples were prepared with water to gypsum ratio 0.2. The Interdent® gypsum is a low-porosity purified α-gypsum ($CaSO_4 \cdot ½H_2O$) used for dental purposes.

Finally, an aluminium alloy used for the production of lightweight aluminium foams Alporas® was studied. The material consists of an aluminium intermixed with 1.5 wt.% of Ca and 1.6 wt.% TiH_2. The microstructures of the selected materials are shown in Fig. 1. Dark areas in the figure can be attributed to the low density components or microporosity in the matrix, whereas lighter areas belong to individual microstructural components mentioned previously. The images show on the heterogeneity of the samples in the tested RVEs whose dimensions are ~100–200 μm.

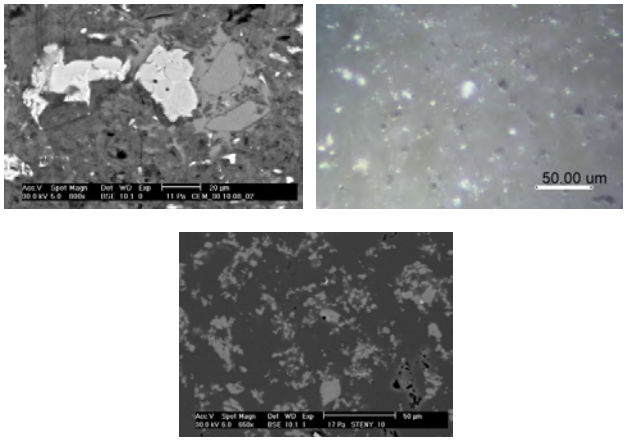

Fig. 1. **Microstructures of cement paste (top left), dental gypsum (top right) and aluminium alloy (bottom)**

5. Results

For cement paste, the microstructural RVE size consisting all the relevant material phases in a representative content is ~200 μm. Grid indentation consisting of approximately 20×20=400 indents with 10 μm spacing was performed. The indents were prescribed as load controlled (to maximum force 2 mN). Final indentation depths arrived at 200−300 nm. Frequency plots of elastic moduli (evaluated with Oliver−Pharr method[12]) were analyzed by statistical deconvolution[6]. Five distinct phases were found as shown in Fig. 2. The peaks were linked with chemically distinct phases denoted as: A=low stiffness phase, B=low density C-S-H, C=high density C-S-H, D=$Ca(OH)_2$, E=clinker. In this case, the notation of mechanically distinct phases matches well with the cement chemistry. Tab. I shows numerical results of the deconvolution and also results from the Mori-Tanaka homogenization.

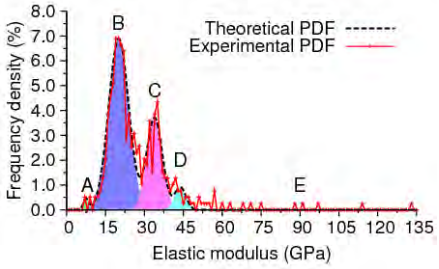

Fig. 2. **Probability density functions of elastic moduli and deconvolution on cement samples**

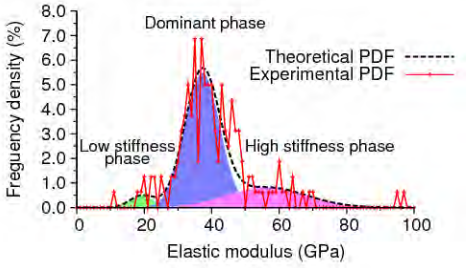

Fig. 3. **Probability density functions of elastic moduli and deconvolution on gypsum samples**

Table I
Data received from statistical deconvolution and homogenized values on cement paste

Phase	*E* [GPa] (mean value)	Poisson's ratio [-]	Volume fraction
Low stiffness (A)	7.45	0.2	0.0105
Low density C-S-H (B)	20.09	0.2	0.6317
High density C-S-H (C)	33.93	0.2	0.2634
$Ca(OH)_2$ (D)	43.88	0.3	0.0461
Clinker (E)	130*	0.3	0.0483
M-T homogenized value	25.3308	0.2067	1.0

*Note: The clinker E-value was adjusted according to ref.[10]

Similar microstructural RVE ~200 μm could be recognized on gypsum samples. Gypsum is characterized with the directionless crystalline microstructure. Indentation matrices containing 15×12=180 indents with 15 μm spacing covered the tested RVE. The same loading as in case of cement was used. Three peaks (low stiffness, dominant and high stiffness phases) were identified in frequency plots of elastic moduli as depicted in Fig. 3. Tab. II shows deconvolution results and Mori-Tanaka homogenization.

Two mechanically distinct phases were found by the statistical deconvolution on Al-alloy sample (Fig. 4). Loading to maximum force 1 mN (final depth ~200 nm) was used. Results from 200 indents (two locations 10×10 indents) with 10 μm spacing were evaluated. The RVE size is ~100 μm in this case. According to the SEM-EDX studies, the dominant phase was denoted as Al-rich zone, whereas the lower stiffness phase as Ca/Ti-rich area. Again, Tab. III shows numerical results and homogenized Mori-Tanaka effective elastic modulus.

Table II
Data received from statistical deconvolution and homogenized values on gypsum

Phase	E (GPa) (mean value)	Poisson's ratio (-)	Volume fraction
Low stiffness	19.357	0.2	0.04375
Dominant	37.234	0.2	0.71250
High stiffness	56.277	0.2	0.24375
M-T homog.	40.000	0.2	1.0

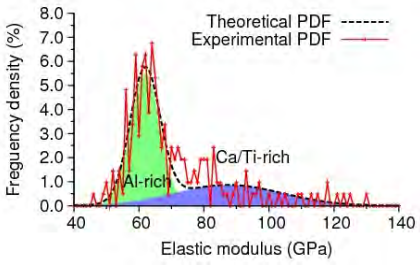

Fig. 4. **Probability density functions of elastic moduli and deconvolution on Al-alloy**

Table III
Data received from statistical deconvolution and homogenized values on Al-alloy

Phase	*E* [GPa] (mean value)	Poisson's ratio [-]	Volume fraction
Al-rich zone	61.882	0.35	0.63768
Ca/Ti-rich zone	87.395	0.35	0.36232
M-T homog.	70.083	0.35	1.0

Results from FFT-based homogenization were received in the form of plane strain stiffness matrices. Generally, anisotropy can be obtained in the numerical compu-

tation. However, it was found that for our materials the anizotropy is very low and related stiffnesses are close to isotropic ones as illustrated for cement in the following equations, in which stiffness matrices computed from analytical solution (Eq. (*7*)) and numerical solution (Eq. (*8*)) are presented.

$$\mathbf{L}_{\mathbf{eff}}^{\mathbf{A}} = \begin{bmatrix} 28.145 & 7.036 & 0 \\ 7.036 & 28.145 & 0 \\ 0 & 0 & 21.109 \end{bmatrix} \qquad (7)$$

$$\mathbf{L}_{\mathbf{eff}}^{\mathbf{FFT}} = \begin{bmatrix} 26.177 & 6.778 & 0.068 \\ 6.778 & 26.224 & 0.014 \\ 0.068 & 0.014 & 19.818 \end{bmatrix} \qquad (8)$$

Note that stiffness matrices in Eq. 7 and 8 are in Mandel's notation. It can be seen that off-axis terms are close to zero which shows on the mentioned very low anizotropy. The difference between the solutions can be characterized with the following matrix error norm:

$$\delta = \sqrt{\frac{\left(\mathbf{L}_{\mathbf{eff}}^{\mathbf{FFT}} - \mathbf{L}_{\mathbf{eff}}^{\mathbf{A}}\right) : \left(\mathbf{L}_{\mathbf{eff}}^{\mathbf{FFT}} - \mathbf{L}_{\mathbf{eff}}^{\mathbf{A}}\right)}{\left(\mathbf{L}_{\mathbf{eff}}^{\mathbf{FFT}} : \mathbf{L}_{\mathbf{eff}}^{\mathbf{FFT}}\right)}} \qquad (9)$$

Respective error norms for cement, gypsum and aluminium alloy are as follows:

$${}^{cem}\delta = 0.071045\ ,\quad {}^{gyps}\delta = 0.075138\ ,\quad {}^{Al}\delta = 0.0393058\ .$$

6. Discussion

The analytically computed effective RVE stiffnesses are in good agreement with those obtained from numerical FFT-based solution. The error is 3.9−7.5 % for the studied materials. Also, the estimated overall elastic moduli are in good agreement with those experimentally measured on larger-scale composite samples for cement[10,13,14], gypsum[15] and Alporas[16].

It was also proved that both simple analytical and numerical FFT-based method give comparable results in our case which is primarily due to the close-to-isotropic nature of the tested materials within the specified RVE.

7. Conclusions

It was shown in this paper that micromechanical homogenization methods can be efficiently used for obtaining effective elastic properties on heterogeneous structural materials. Local mechanical properties were found with the aid of statistical nanoindentation and deconvolution methods that give access to both phase properties as well as their volume fractions. Effective properties of RVEs (100−200 μm) of the three tested materials (cement paste, gypsum and aluminium alloy) were successfully determined with an analytical Mori-Tanaka scheme and numerical FFT-based method. The performance of both approaches was in good agreement for the tested materials as validated against independent macroscopic experimental results. Derived stiffness matrices can be further utilized in standard FEM software, for the development of a multiscale model or for the optimization of the material.

Support the Czech Science Foundation (GAČR P103/09/1748 and P105/12/0824) is gratefully acknowledged.

REFERENCES

1. Zaoui A.: J. Eng. Mech. *128*, 808 (2002).
2. Eshelby J. D.: Proc. Royal Soc. A *241*, 376 (1957).
3. Mori T., Tanaka K.: Acta Metal *21*, 571 (1973).
4. Constantinides G. et al.: Mater. Sci. Eng. A *430*, 189 (2006).
5. Němeček J., Lukeš J.: Chem Listy *104*, s279 (2010).
6. Němeček J., Šmilauer V., Kopecký L.: Cem. Concr. Compos. *33*, 163 (2011).
7. Sorelli L. et al.: Cem. Concr. Res. *38*, 1447 (2008).
8. Michel J.C., Moulinec H., Suquet P.: J. Numer. Met. Eng. *52*, 139 (2001).
9. J. Zeman, J. Vondřejc, J. Novák, I. Marek: J. Comp. Phys. *229*, 8065 (2010).
10. Němeček J.: Mater. Charact. *60*, 1028 (2009).
11. Tesárek P., Němeček J.: Chem Listy *105*, s852 (2011).
12. Oliver W. C., Pharr G. M.: J. Mater. Res. *7*, 1564 (1992).
13. Constantinides G., Ulm F.-J.: J. Mech. Phys. Solids *55*, 64 (2007).
14. Hughes J. J., Trtik P.: Mater. Charact. *53*, 223 (2004)
15. http://ciks.cbt.nist.gov/garbocz/monograph
16. Jeon I. et. al.: Mech. Mater. *41*, 60 (2009).

J. Němeček, V. Králík, and J. Vondřejc *(Czech Technical University in Prague, Faculty of Civil Engineering):* **Up-scaling Microlevel Elastic Properties of Heterogeneous Structural Materials**

The paper shows micromechanical methods used for finding effective elastic properties of selected structural composites (cement, gypsum, aluminium alloy). Phase properties of the composites are received with the use of grid nanoindentation and statistical deconvolution. Elastic moduli for representative volume elements with ~100−200 μm dimensions were assessed with analytical Mori-Tanaka and numerical FFT-based methods with good agreement.

ON THE USE OF DIFFERENT INSTRUMENTED INDENTATION PROCEDURES FOR HVOF SPRAYED COATINGS

JIŘÍ NOHAVA[a], ŠÁRKA HOUDKOVÁ[b], and PETR HAUŠILD[c]

[a] CSM Instruments, Rue de la Gare 4, 2034 Peseux, Switzerland, [b] Research and Testing Institute Plzeň, Tylova 46, 301 00 Plzeň, [c] Czech Technical University in Prague, Faculty of Nuclear Sciences and Physical Engineering, Department of Materials, Trojanova 13, 120 00 Prague, Czech Republic
jiri.nohava@csm-instruments.com

Keywords: nanoindentation, grid indentation, HVOF

1. Introduction

Though the instrumented indentation itself is relatively well-known, it is not yet widely used in the thermal spray community. In the research of thermal spray coatings[1] (TSC), the instrumented indentation has however a great advantage of testing the material at various scales: at the 'nano' or 'micro' levels, where either the individual coatings constituents or the whole blocks of the coating are tested[2,3]. However, as with many novel methods one must be very careful when choosing the testing conditions as errors could easily be introduced in the measurements.

This paper intends to compare two indentation methods for determining the mechanical properties of individual phases in HVOF sprayed cermets: grid indentation and isolated indentation. The grid indentation is based on performing a large matrix of indentations and statistical evaluation of the results[4,5]. The aim of the isolated indentation, on the other hand, is to precisely position the indent so that only properties near the selected area are measured. This paper shows the results on three types of HVOF cermets and discusses the advantages and suitability of each method for this particular type of material.

2. Experimental details

Three types of HVOF sprayed coatings were selected for the experiments: WC-17%Co, Cr_3C_2-25%NiCr and (Ti,Mo)(C,N)-39%NiCo (all wt.%). For simplicity, the samples were labeled as WCCo, CrCNiCr and TiMoCN. The coatings were sprayed using optimized parameters published elsewhere[6]. An example of typical matrix-carbide structure of these coatings is shown in Fig. 1.

The WCCo coatings microstructure consisted of WC grains with size of a few micrometers and smaller. The dimensions of the carbide grains in the CrCNiCr coating were larger than in the WCCo coating.

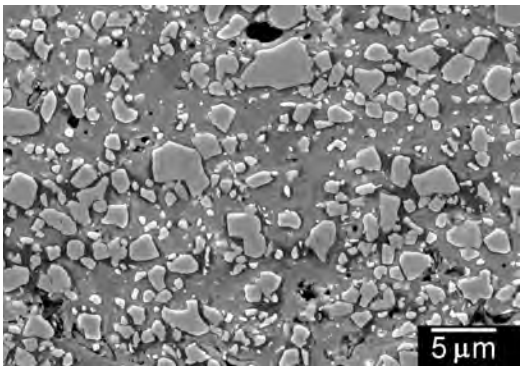

Fig. 1. **SEM images of the microstructure of the WCCo coating**

The dimensions of the hard phase grains in the TiMoCN coating were significantly smaller than those of the other coatings. The core-rim structure of the hard particles is composed of hard TiC centre core surrounded by Mo rich rim. The microstructure and mechanical properties of the (Ti,Mo)(C,N)-NiCo coating are described in more detail in Refs.[7,8].

2.1. Methods

The method of instrumented indentation[9,10] was used in all cases except for micro hardness Vickers measurements where conventional method was used. The isolated nanoindentation consisted in performing 2 mN indentations on each phase separately. At least 10 indentations were performed in several regions on each sample.

The grid indentation method is based on performing several hundreds of indentations and their subsequent statistical evaluation. The grid indentation was performed with the same indentation parameters as the isolated indentation (F_{max} 2 mN). A square matrix of 20×20 indentations spaced by 5 µm was performed in two randomly selected regions on each sample and the results were statistically evaluated using bimodal Gaussian distribution (*1*) where H_{IT} is hardness, p is mixing parameter and μ_1, σ_1, μ_2, σ_2 are the parameters of distribution.

$$f = \frac{1-p}{\sqrt{2\pi}\sigma_1}\exp\left[-\frac{(H_{IT}-\mu_1)^2}{2\sigma_1^2}\right] + \frac{p}{\sqrt{2\pi}\sigma_2}\exp\left[-\frac{(H_{IT}-\mu_2)^2}{2\sigma_2^2}\right] \quad (1)$$

As it will be shown further, several aspects of the grid indentation on this particular type of material caused that also trimodal Gaussian distribution was considered for the statistical analysis of the results. This distribution was used in form of Eq. (*2*):

$$f = \sum_{i=1}^{3} \frac{p_i}{\sqrt{2\pi}\sigma_i} \exp\left[-\frac{(H_{IT} - \mu_i)^2}{2\sigma_i^2} \right] \cdots \sum_{i=1}^{3} p_i = 1 \qquad (2)$$

where μ_1, σ_1, μ_2, σ_2, μ_3, σ_3 are parameters of each distribution corresponding to either hardness or elastic modulus.

Both isolated and grid indentation was done using Table Top Nano Indentation Tester (CSM Instruments, Peseux, Switzerland) with diamond Berkovich indenter. Further, microindentation experiments were performed on each sample with 5 N load using Micro Indentation Tester (CSM Instruments, Peseux, Switzerland) with diamond Vickers indenter. Conventional microhardness measurements were performed on LECO DM-400A hardness tester using load of 300 g. Ten measurements were performed in the center line of each coating. The scanning electron microscopy (SEM) images were acquired using JEOL JSM 5510LV and 6490LV scanning electron microscopes.

3. Results

3.1. Isolated indentation

During the isolated indentation the indentations were placed separately in the matrix and the carbides. It was relatively straightforward to locate and position the indentations in the carbides and matrix on samples WCCo and CrCNiCr, however it was almost impossible on the TiMoCN coating. Although the boundaries between the (Ti,Mo)(C,N) and NiCo phases were clearly visible in SEM images, they did not yield sufficient contrast in optical microscope.

The results of isolated nanoindentation (2 mN) and non-selective microindentation (5 N) results on all three tested samples are compared in Table I. The values of hardness and elastic modulus show good agreement with those of bulk material[11] which confirms the utility of low load nanoindentation for measurements of mechanical properties of individual phases in HVOF coatings.

3.2. Grid indentation

The results of the grid indentation in form of elastic modulus histogram for the three tested samples are shown in Fig. 2. The bar graphs represent the measured data, the dashed lines represent each of the distributions as defined by Eq. (*1*) and the solid line is the sum of two distributions. The parameters of the individual distributions correspond to the average and standard deviation of E_{IT} values of each of the phase present in the coating.

The WCCo and CrCNiCr coatings contained two phases with distinct mechanical properties (see Table I) while the TiMoCN coating contained two phases whose mechanical properties were quite close. Expected two-peak behavior was found only for the E_{IT} histogram of the CrCNiCr coating (Fig. 2b) where the parameters of the two distributions corresponded very well to the isolated indentation results. In the case of the two other coatings, the parameters of the bimodal fit did not reflect exactly the properties of the individual phases as obtained by isolated indentation.

It was mainly the parameter of the second distribution (μ_2) that did not correspond to the results of isolated indentations in carbides. Similar difference was found also for H_{IT} histograms and the isolated indentation values.

Closer observation of the E_{IT} histograms revealed that their shape shall be better described as trimodal rather than bimodal. Considering Fig. 2a one can relatively clearly see three peaks instead of two peaks positioned at ~290 GPa and ~538 GPa, which would correspond to the carbide and metallic matrix values. The histogram therefore seems to reflect not a bimodal Gaussian distribution (Eq. (*1*)) but rather a trimodal Gaussian distribution. Indeed, Fig. 3 shows trimodal Gaussian fit for the E_{IT} histograms of all tested coatings. The third distribution corresponds to indentations done on the carbide-matrix boundary which significantly complicated the statistical analysis.

Table I
Isolated indentation results for all three tested coatings. H_{IT} is indentation hardness, E_{IT} is indentation modulus, h_m is the maximum indentation depth, HV_{IT} is Vickers hardness recalculated from the H_{IT} and HV_{03} is conventional Vickers microhardness measured with 300 g load

Coating	Phase	H_{IT} [GPa]	E_{IT} [GPa]	h_m [nm]	HV_{IT} 5N	HV_{03}
WCCo	Carbides	33.3 ± 2.7	538 ± 25	57 ± 1	1279	1335
	Matrix	16.7 ± 2.2	290 ± 27	79 ± 5		
CrCNiCr	Carbides	26.0 ± 4.0	337 ± 49	68 ± 5	777	700
	Matrix	11.2 ± 3.2	226 ± 44	96 ± 10		
TiMoCN	(Ti,Mo)(CN)-rich	13.1 ± 2.2	208 ± 32	90 ± 7	782	803
	NiCo-rich	12.2 ± 1.0	214 ± 13	92 ± 4		

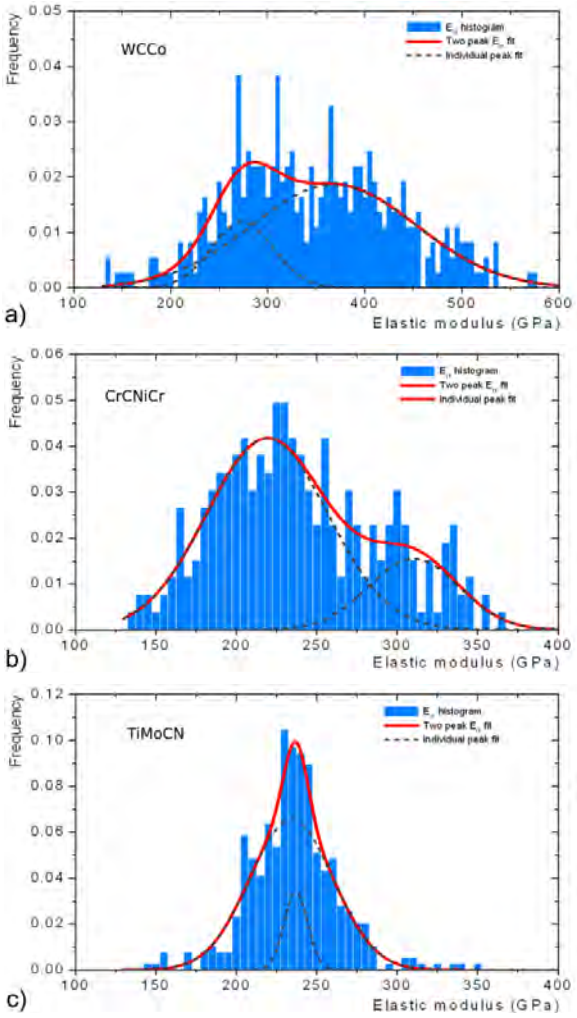

Fig. 2. **Elastic modulus histogram for the WCCo coating (a), CrCNiCr (b) and TiMoCN (c) coatings**

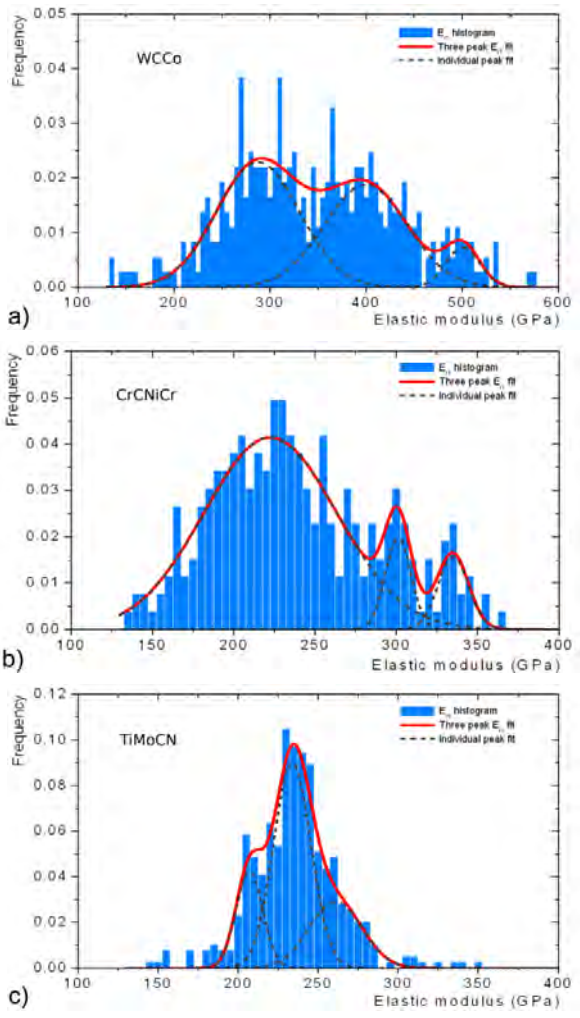

Fig. 3. **Trimodal Gaussian distribution of the E_{IT} histograms for (a) WCCo, (b) CrCNiCr and (c) TiMoCN coatings**

4. Discussion

4.1. Isolated nanoindentation and microindentation

The carbides and metallic matrix in the WCCo and CrCNiCr coatings were easily distinguishable under optical microscope attached to the indentation system. The 2 mN indentations were shallow enough (maximum penetration between ~60 nm and ~130 nm) so that an indentation done on one phase was not significantly influenced by the neighboring phase. In the case of the WCCo and CrCNiCr coatings, the properties of carbides and metallic matrix were obtained while in the case of the TiMoCN coating the properties of TiMoCN-rich and NiCo-rich phases were measured. Very similar results of $\boldsymbol{H_{IT}}$ and $\boldsymbol{E_{IT}}$ from isolated indentation of the (Ti,Mo)(C,N)–rich and NiCo-rich phases pointed out that the visual aspect is not always sufficient for distinguishing between individual phases. To properly characterize the core-rim structure the indentation experiments should be performed on a lightly etched sample where its structure would be revealed.

The high load micro indentation (5 N) was aimed on characterizing the material as a whole, including pores, carbide-matrix interfaces and boundaries, etc[12]. The values of instrumented microhardness and conventional microhardness for 5 N and 3 N loads showed very good agreement. Such agreement between the conventional and instrumented indentation is particularly important as some researchers questioned the reliability of instrumented indentation results.

4.2. Comparison of isolated and grid indentation

As showed in Fig. 2, only the grid indentation results obtained on the CrCNiCr coating showed relatively good agreement with the elastic modulus values obtained via isolated indentation. In other cases, the hardness and/or elastic modulus values obtained from statistical evaluation

of grid indentation results differed considerably from the isolated indentation values. Although the use of a bimodal distribution was expected, the trimodal distribution yielded results in better agreement with the isolated indentation values. The μ_2 parameter, representing the peak between the μ_1 and μ_3 peaks, reflected the indentations done on the carbide-matrix boundary which significantly complicated the statistical analysis. Obviously, the amount of indentations near the carbide-matrix boundary in the grid indentation was not negligible and had to be taken into account during the statistical analysis of the results.

The trimodal Gaussian fit also revealed the existence of hard phase in the TiMoCN coating with hardness of 18.7 GPa (Fig. 4) and elastic modulus of 261 GPa (see Table II). This phase was not detected when performing the isolated indentations and it very likely corresponded to the (Ti,Mo)(C,N) particles, whose hardness is expected to be higher than that of the NiCo matrix.

5. Conclusions

This paper presents the results of two methods of instrumented indentation for determination of mechanical properties of thermal spray coatings. The isolated indentation method yielded very good results with relatively low standard deviation on all three types of tested coatings. The statistical evaluation of the grid indentation was somewhat complicated due to indentations on the carbide-matrix interface. Since the number of such indentations was not negligible, the use of trimodal Gaussian distribution was necessary to extract the properties of individual phases. These properties obtained by the trimodal Gaussian fit were in very good agreement with those obtained by isolated indentation method. The grid indentation also allowed measurement of properties of phases that were difficult to locate under optical microscope.

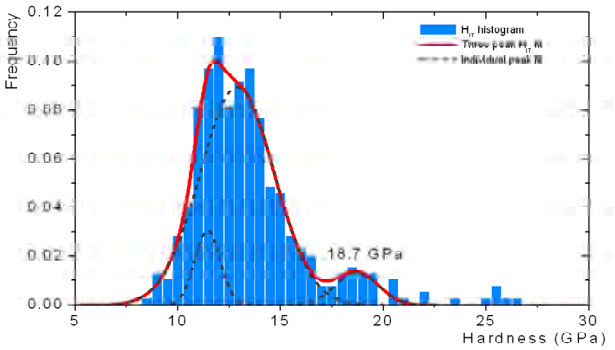

Fig. 4. **Trimodal Gaussian distribution of the H_{IT} histograms for the TiMoCN coatings showing the peak at 18.7 GPa**

Table II
Trimodal Gaussian fit of the grid indentation data compared with isolated indentation results. The standard deviation was omitted for the reasons of clarity

E_{IT} [GPa]	Trimodal			Isolated indentation	
	Soft	Intermediate	Hard	Soft	Hard
WCCo	287	399	500	290	538
CrCNiCr	222	301	335	226	337
TiMoCN	204	234	261	214	208

This work was supported by the SGS10/300/OHK4/3T/14 and VZ/MSM4771868401 projects.

REFERENCES

1. Herman H.: Sci. Am. *259*, 112 (1988).
2. Margadant N., Neuenschwander J., Stauss S., Kaps H., Kulkarni A., Matejicek J., Roessler G.: Surf. Coat. Technol. *200*, 2805 (2006).
3. Racek O., Berndt C. C.: Surf. Coat. Technol. *202*, 362 (2007).
4. Randall N. X., Vandamme M., Ulm F.-J.: Mater. Res. *24*, 679 (2009).
5. Constantinides G., Chandran K. S. R., Ulm F.-J., Van Vliet K. J.: Mater. Sci. Eng. A *430*, 189 (2006).
6. Houdková Š., Zahálka F., Kašparová M., Berger L.-M.: Conf. Proc. ITSC 2008, Maastricht (NL), 1485 (2008).
7. Berger L.-M., Woydt M., Zimmermann S., Keller H., Schwier G., Enžl R., Thiele S.: Conf. Proc. ITSC 2004, Osaka (JP), 10 (2004).
8. Berger L.-M., Zimmermann S., Keller H., Schwier G., Thiele S., Nebelung M., Enžl R.: Conf. Proc. ITSC 2003, 793 (2003).
9. Fischer-Cripps A. C.: Springer, New York 2004.
10. Oliver W. C., Pharr G. M.: J. Mater. Res. *19*, 3 (2004).
11. Lengauer W.: *Handbook of Ceramic Hard Materials*, Wiley, 202 (2000).
12. Nohava J., Bonferroni B., Bolelli G., Lusvarghi L.: Surf. Coat. Technol. *205*, 1127 (2010).

J. Nohava[a], Š. Houdková[b], and P. Haušild[c] *([a] CSM Instruments, Peseux, Switzerland; [b] Research and Testing Institute Plzeň, Czech Republic; [c] Czech Technical University in Prague, Faculty of Nuclear Sciences and Physical Engineering, Department of Materials, Praha, Czech Republic):* **On the Use of Different Instrumented Indentation Procedures for HVOF Sprayed Coatings**

This work compares the isolated nanoindentation with grid indentation on three HVOF coatings. The bimodal and trimodal Gaussian fits are compared with the isolated indentation results and the reasons for the use of trimodal fit are given. The results are completed by comparison of conventional and instrumented micro indentation results.

VISCOELASTIC PROPERTIES OF PORCINE APOPHYSEAL JOINT

MARTIN OTÁHAL[a], JOSEF ŠEPITKA[b], JAROSLAV LUKEŠ[b], and MIROSLAV SOCHOR[b]

[a] *Charles University in Prague, Faculty of Physical Education and Sport, Laboratory of Biomechanics of Extreme Loads, José Martího 31 Prague 190 00,* [b] *Czech Technical University in Prague, Faculty of Mechanical Engineering, Dep. of Mechanics, Biomechanics and Mechatronics, Technicka 4, 166 07 Prague , Czech Republic*
martinotahal@ftvs.cuni.cz

Keywords: spine, apophyseal joint, cartilage, nanoindentation, DMA

1. Introduction

Problem of low back pain is still one of the main problems in a spinal biomechanics. This study is focused on viscoelastic properties of apophyseal joint. Mechanical properties and a shape of apophyseal joints define a small interspaces needed for preserving the principles of the preferred movements, which is defined by the shape of the vertebra and by the viscoelastic behavior of the passive elements of intervertebral joint ligaments, the intervertebral disc, etc. and the tuned movements of intervertebral joint (IVJ) (movements defined by the elements of the active control-muscle system and central nervous system)[1].

Apophyseal joints (Fig. 1) are composed of two neighboring articular processes enclosed in the joint capsule. Facets of both articular processes are covered by thin cartilage layers like in synovial joint[2].

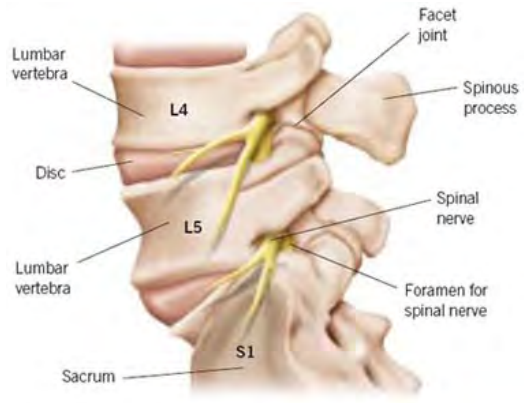

Fig. 1. **Spinal motion segments.** Apophyseal (facet) joints are small joints on each side at the back of the spine which allow movement between adjacent vertebrae while maintaining a spinal stability

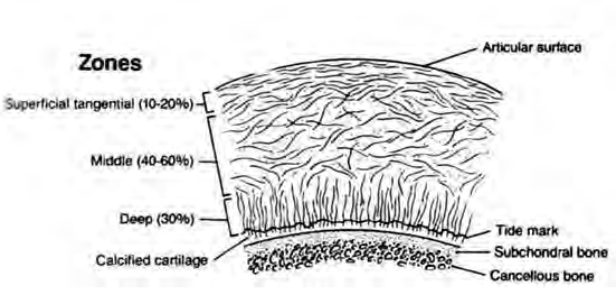

Fig. 2. **Structure of articular cartilage, orientation of collagen fibers.** Arrows show testing directions of the samples

An articulating cartilage is very important part of apophyseal joint from the rheological point of view. Dynamic nanoindentation is one of the possible methods to obtain viscoelastic properties of articular cartilage. Porcine vertebra was used as a biological model of human vertebra in this study.

2. Materials and methods

A porcine apophyseal joint of lumbar spine L4-L5 was used in our study. A specimen of cartilage was cut from fresh porcine vertebra, dissected from 1.5 year old animals. Two specimens were sliced and polished from a single joint. Thus, two surfaces were prepared for nanoindentation in normal and lateral direction to the joint facets. Specimens were submerged into a saline solution immediately after the preparation. Dynamic testing was also carried out within physiological solution.

Each joint was tested in two directions at different locations. Two locations were indented in normal direction and an edge of the cartilage, a central layer of the cartilage and a transition zone between the cartilage and subchondral bone were indented in lateral direction (Fig. 2).

NanoDMA load controlled experiment was performed with Hysitron TriboIndenter™ system with Berkovich diamond tip at the temperature 23.9 °C. Harmonic loading $P_0 = \sin(\omega t)$ with dynamic load amplitude $P_0 = 0.5$ μN was specified for the harmonic frequency range 30–200 Hz. During nanoDMA experiment, static load was applied at maximum force $P_{max} = 200$ μN (ref.[3]). Following amplitude of displacement oscillation X_0, and Φ the phase shift between force and displacement signal are recorded by the nanoindentation system. The machine compliance value C_i and the stiffness value K_i were determined during air indentation calibration. The procedure was adopted from Asif et al. (1999)[4].

The reduced storage modulus (E_r'), the reduce loss modulus (E_r") and $\tan\delta = E_r"/E_r'$ dependent on compliance and stiffness of the sample are given by

$$E'_r = \frac{K_S\sqrt{\pi}}{2\sqrt{A}}, \qquad E''_r = \frac{\omega C_S\sqrt{\pi}}{2\sqrt{A}} \text{ and } \qquad \tan\delta = \frac{C_S\omega}{K_S}$$

where A_c is the contact area based on tip area function related to the contact depth at quasistatic loading[5]

The storage modulus and the loss modulus are related to the complex modulus $E_r^* = E_r' + iE_r''$ and indicate the ability of the material to return energy (E_r') and dissipate energy (E_r''). The ratio of the loss modulus to the storage modulus (i.e., tan δ) reflects the viscoelastic behavior of a material, which is called damping. It is a material parameter independent of a tip-sample contact area[6].

3. Results

Dynamic mechanical characteristics were obtained for the specimens in a range of frequencies 30–200 Hz. Firstly; two locations in normal direction were analyzed. Secondly; the edge of the cartilage, central layer of the cartilage and transition area between the cartilage and subchondral bone were analyzed in lateral direction.

Fig. 3 shows dependence of tan δ on the frequency for both tested directions. There are two noticeable different trends of tan δ. The cartilage analyzed in normal direction shows higher damping capability between 30 and 100 Hz than the cartilage analyzed in lateral direction. There is an intersection of two trends in tan δ at about 100 Hz. There is increasing trend of curves of the edge and middle layer area beyond 100 Hz. Transition area between the cartilage and subchondral bone has decreasing trend from 100 Hz the same as samples tested in normal directions.

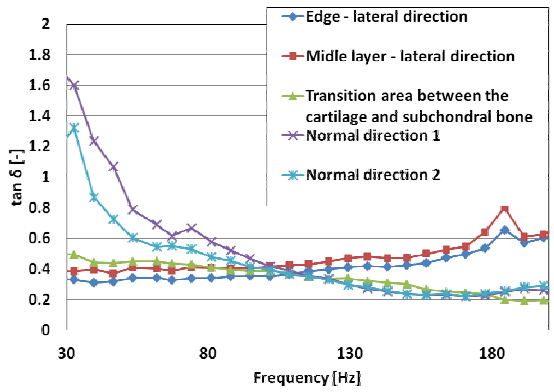

Fig. 3. **Tan δ *vs.* frequency from nanoDMA**

4. Discussion and conclusion

The results show differences of dynamic characteristics for different directions of testing on apophyseal joint. In other words, cartilage has increased ability to damp the dynamic load in normal direction from 30 to 100 Hz contrary to lateral direction. However, damping capabilities decrease within loading rates represented by frequency range. These finding are in an agreement with physiologic behavior of joints in general.

More likely, micromechanical properties reflect inner microstructure of a local region of the cartilage. Structural differences from lateral and normal point of view are clearly seen on Fig. 2. Therefore, mechanical properties vary as well. Nevertheless, structural diversity between the edge and the middle area are not that significant, therefore, mechanical properties follow the same trend. Interestingly, structurally different area close to subchondral bone showed mechanical differences only beyond 100 Hz. Hypothetically, important architectural element, highly oriented collagen fibers are employed when the frequency overcome 100 Hz.

This research was supported by Ministry of Education project: Transdisciplinary research in Biomedical Engineering II. No. MSM 6840770012 and TAČR project: No. TA01010860.

REFERENCES

1. Otahal M., Holub O., Kronek J., Sochor M., Otahal S.: J. Biomech. *41- S1*, 354 – S354 (2008).
2. Adams M., Bogduk N., Burton K., Dolan P.: *The biomechanics of back pain*. Elsevier, Oxford 2006.
3. Sepitka J., Otahal M., Lukes J.: Comput Method Biomech. *14*, 265 (2011).
4. Asif S. A. S., Wahl K. J., Colton R. J.: Rev. Sci. Instrum. *70*, 2408 (1999).
5. Oliver W. C., Pharr G. M.: J. Mater. Res. *7*, 1564 (1992).
6. Menard K. P: *Dynamic mechanical analysis*. Taylor & Francis Group, Boca Raton 2008.

M. Otáhal[a], J. Šepitka[b], J. Lukeš[b], and M. Sochor[b] *([a] Laboratory of Biomechanics of Extreme Loads, Faculty of Physical Education and Sport, Charles University in Prague, [b] Czech Technical University in Prague, Faculty of Mechanical Engineering, Dep. of Mechanics, Biomechanics and Mechatronics, Prague, Czech Republic):* **Viscoelastic Properties of Porcine Apophyseal Joint**

This study is focused on viscoelastic properties of an apophyseal joint. Dynamic nanoindentation was used for a characterization of viscoelastic properties of an articular cartilage. Micromechanical properties reflect inner microstructure of local regions of the cartilage. The results are discussed with respect to the cartilage microstructure in this paper.

IRRADIATED POLYPROPYLENE STUDIED BY MICROHARDNESS AND WAXS

MARTIN OVSIK[a], DAVID MANAS[a], MIROSLAV MANAS[a], MICHAL STANEK[a], MARTINA HRIBOVA[a], KAREL KOCMAN[a], DAVID SAMEK[a], and MARTIN MANAS[b]

[a] *Tomas Bata University in Zlin, Faculty of Technology, Department of Production Engineering, TGM 5555, 760 01 Zlin, Czech Republic,* [b] *MITAS a. s., Švehlova 1900, 106 25 Prague 10, Czech Republic*
dmanas@ft.utb.cz

Keywords: microhardness, irradiation crosslinking, polypropylene, X-ray diffraction

1. Introduction

Isotactic polypropylene is a commodity polymer of a semi-crystalline structure which is very complex and depends strongly on thermal history and processing conditions. Isotactic polypropylene can crystallize into 3 phases: alpha phase is the most stable and the most known. The crystals are monoclinic. Beta phase is metastable and the crystals are hexagonal. β-phase is mainly found in block PP copolymers and can be generated by addition of specific nucleating agents. This phase was discovered by Padden and Keith in 1953 and can be improved by crystallization between 130 and 132 °C or by orientation with high shear or through addition of specific nucleating agents. Presence of β-phase in PP homopolymer generally increase ductility in the finished parts. Maximum effect is observed at 65 % of β-phase. γ-phase – this phase is also metastable with triclinic crystals. This form is not very familiar but appears mainly in low molecular weight polypropylene by crystallization at a very high pressure and a very low cooling rate[1,2].

The irradiation cross-linking of thermoplastic materials via electron beam or cobalt 60 (gamma rays) is proceeding separately after the processing. The cross-linking level can be adjusted by the irradiation dosage and often by means of a cross-linking booster[1,2].

The main diference between β- and γ-rays is in their different abilities of penetrating the irradiated material. γ-rays have a high penetration capacity. The penetration capacity of electron rays depends on the energy of the accelerated electrons.

Due to electron accelerators the required dose can be applied within seconds, whereas several hours are required in the γ-radiation plant.

The electron accelerator operates on the principle of the Braun tube, whereby a hot cathode is heated in vacuum to such a degree that electrons are released.

Simultaneously, high voltage is generated in a pressure vessel filled with insulating gas. The released electrons are accelerated in this vessel and made to fan out by means of a magnetic field, giving rise to a radiation field. The accelerated electrons emerge via a window (Titanium foil which occludes the vacuum) and are projected onto the product.

Cobalt 60 serves as the source of radiation in the gamma radiation plant. Many of these radiation sources are arranged in a frame in such a way that the radiation field is as uniform as possible. The palleted products are conveyed trough the radiation field. The radiation dose is applied gradually, that is to say, in several stages, whereby the palleted products are conveyed around the Co – 60 radiation sources several times. This process also allows the application of different radiation doses from one product type to another. The dimensional stability, strength, chemical resistance and wear of polymers can be improved by irradiation. Irradiation cross-linking normally creates higher strength as well as reduced creep under load if the application temperature is above the glass transition temperature (T_g) and below the former melting point. Irradiation cross-linking leads to a huge improvement in resistance to most of the chemicals and it often leads to the improvement of the wear behaviour.

The thermoplastics which are used for production of various types of products have very different properties. Standard polymers which are easy obtainable with favourable price conditions belong to the main class. The disadvantage of standard polymers is limited both by mechanical and thermal properties. The group of standard polymers is the most considerable one and its share in the production of all polymers is as high as 90 %.

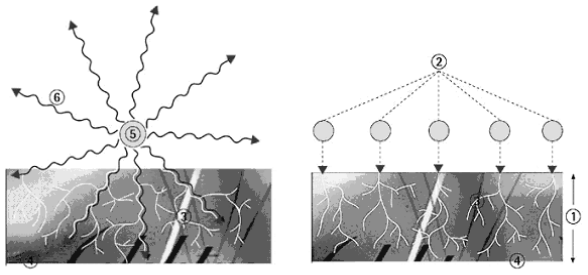

a b

Fig. 1. **Design of Gamma rays (a) and Electron rays (b);** a) 3 – secondary electrons, 4 – irradiated material, 5 – encapsulated Co – 60 radiation source, 6 – Gamma rays; b) 1 – penetration depth of electron, 2 – primary electron, 3 – secondary electron, 4 – irradiated material

The engineering polymers are a very important group of polymers which offer much better properties in comparison to those of standard polymers. Both mechanical and thermal properties are much better than in case of standard polymers. The production of these types of polymers takes less than 1 % of all polymers.

High performance polymers have the best mechanical and thermal properties but the share in production and use of all polymers is less than 1 %.

Common PP, when exposed to the effect of the radiation cross-linking, degrades and its mechanical properties deteriorate. Using cross-linking agent TAIC (triallyl isocyanurate) produces a cross-linking reaction inside the PP structure. The utility properties of PP improve when the noncrystalline part of PP is cross-linked[3–5].

The present work deals with the influence of morphlogy on the microhardness of irradiated crosslinked polypropylene.

2. Experimental

For this experiment polypropylene PP PTS –Crealen EP-2300L1-M800; PTS Plastics Technologie Service, Germany (unfilled, iPP+TAIC, MFR – 230 °C /2.16 kg – 6 g/10 min) was used. The material already contained the special cross-linking agent TAIC – triallyl isocyanurate (5 volume %), which should enable subsequent cross-linking by ionizing β – radiation. The prepared specimens were irradiated with doses of 30, 45, 60 and 90 kGy at BGS Beta-Gamma Service GmbH & Co. KG, Germany[4–6].

The samples were made using the injection molding technology on an injection moulding machine Arburg Allrounder 420C. Processing temperature 210–240 °C, mold temperature 50 °C, injection pressure 80 MPa, injection rate 50 mm s^{-1}.

Instrumented microhardness tests were done using a Micro Combi Tester, CSM Instruments (Switzerland) according to the CSN EN ISO 6507-1. Load and unload speed was 2 N min^{-1}. After a holding time of 90 s at maximum load 1 N the specimens were unloaded. The indentation hardness H_{IT} was calculated as maximum load to the projected area of the hardness impression according to:

$$H_{IT} = \frac{F_{\max}}{A_p} \text{ with } \qquad h_c = h_{\max} - \varepsilon \frac{F_{\max}}{S} \qquad (1)$$

where h_{max} is the indentation depth at F_{max}, h_c is contact depth. In this study the Oliver and Pharr method was used calculate the initial stiffnes (S), contact depth (h_c). The specimens were glued on metallic sample holders[5–7].

Wide angle X-ray diffraction patterns were obtained using a PAN alytical X-pert Prof X-ray diffraction system (Netherlands). The CuK_α radiation was Ni-filtered. The scans (4.5 ° 2Q/min) in the reflection mode were taken in the range 5–30° 2Θ. The sample crystallinity X was calculated from the ratio of the crystal diffraction peaks and the total scattering areas[7–9].

3. Results and discussion

Fig. 2 shows typical X-ray diffraction spectrum of the non-irradiated and irradiated polypropylene. There is an apparent presence of α-phase and β-phase in the non-irradiated specimen. A gradual loss of β-phase can be seen with growing radiation dose, with its maximum loss seen at a radiation dose of 60 kGy (Fig. 2). The greatest loss of α-phase is seen at the radiation dose of 45 kGy (Fig. 2).

The results of the crystal size for non-radiated and irradiated polypropylene are shown in the Fig. 3. The values measured show some heterogeneity of the crystal sizes at individual radiation doses (225–300 Å). When applying β-radiation the structure of polypropylene undergoes a loss of the crystalline phase. It can be assumed that the size of individual crystals will correspond to the loss of crystalline phase (crystalline value X calculated lay in the range 40.8–54 %). Cross-linking occurs in the remaining noncrystalline part which has a significant influence on the micromechanical properties of the surface layer.

The greatest size of crystals was found in the case of the non-irradiated polypropylene (300 Å). On the contrary the smallest size of crystals (Fig. 3) was measured at radiation dose of 90 kGy (225 Å).

The process of irradiation causes physical and chemical changes in the structure of polypropylene. They are mainly changes of crystalline and amorphous phase. The measurement results show clearly that as the irradiation dose increases, the crystallinity reduces and the size of

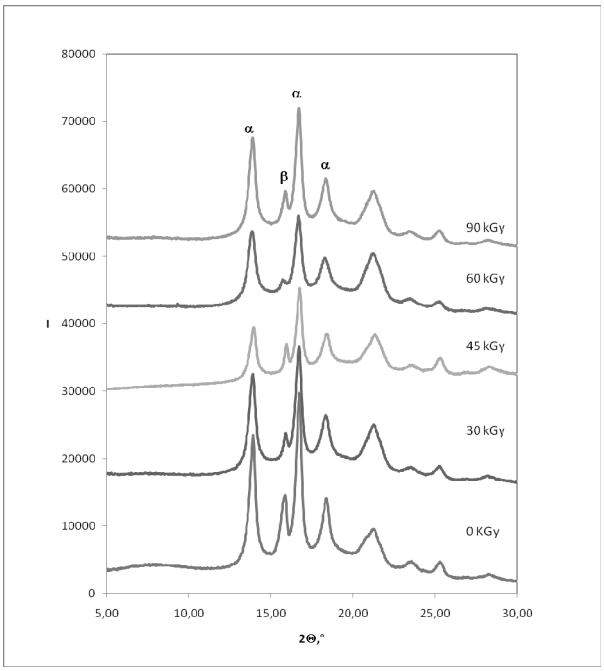

Fig. 2. **Typical X – ray diffractograms of irradiated PP**

crystals diminishes and the structure is finer. During the amorphous phase cross-linking occurs which results in creation of very solid areas as well as considerable growth of microhardness values. Higher irradiation doses do not cause greater cross-linking but rather disruption of links resulting in degradation of the irradiated material.

The values measured during the microhardness test showed that the lowest values of indentation hardness were found for the non-irradiated PP. On the contrary, the highest values of indentation hardness were obtained for PP irradiated by a dose of 45 kGy (by 75 % higher in comparison with the non-irradiated PP), as can be seen at Fig. 4.

Higher radiation dose does not influence significantly the microhardness value. An indentation hardness increase of the surface layer is caused by irradiation cross-linking of the tested specimen. A closer look at the microhardness results reveals that when the highest radiation doses are used, microhardness decreases which can be caused by radiation indusced degradation of the material.

According to the results of measurements of microhardness, it was found that the highest values of indentation modulus of elasticity were achieved at the PP irradiated with dose of 45 kGy (by 95 % higher than compared with non-irradiated PP). On the contrary, the lowest values of the indentation modulus of elasticity were found for non-irradiated PP as is seen at Fig. 5.

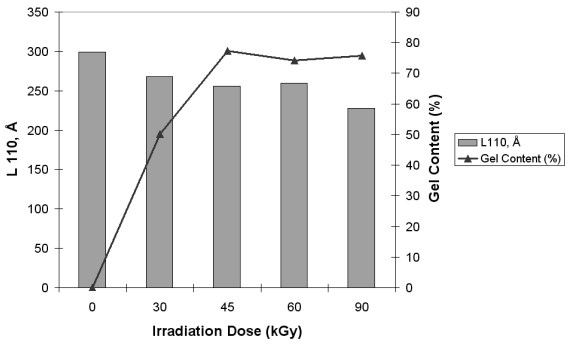

Fig. 3. **Crystals size of polypropylene *vs.* irradiation dose**

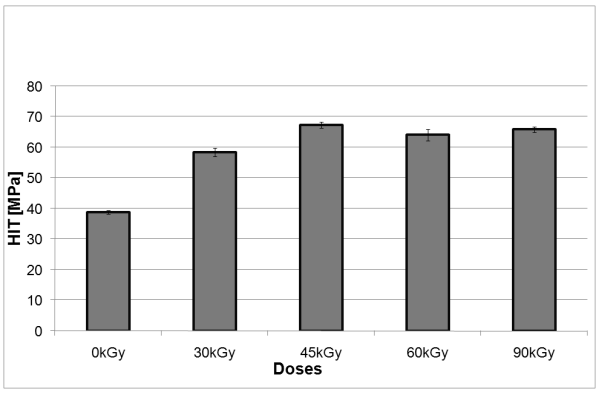

Fig. 4. **Hardness of polypropylene *vs.* irradiation dose**

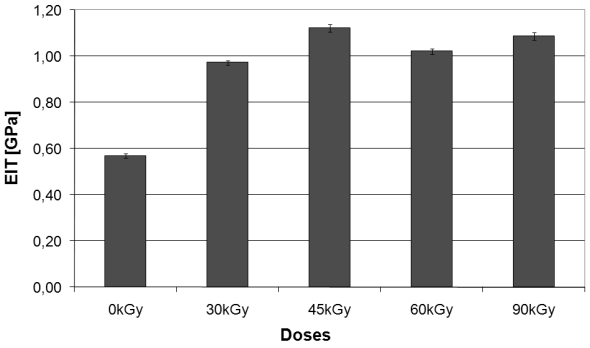

Fig. 5. **Elastic modulus of polypropylene *vs.* irradition dose**

Other important material parameters obtained during the microhardness test were elastic and plastic deformation work. The elastic deformation work W_e determines the reaction of a material to applied (multiaxial) load with reversible deformation. The plastic part of the deformation work W_{pl} defines toughness of the tested material (surface layer) and its resistance to plastic deformation (Fig. 6).

The highest values of plastic and elastic deformation work were obtained for non-irradiated PP. The lowest values of both elastic and plastic deformation work were obtained for PP irradiated with a dose of 45 kGy. Radiation of specimens caused lower values of elastic as well as plastic deformation work which is apparent in Fig. 7. This drop corresponds to the macro tests of impact strength conducted. The non-irradiated specimen did not break during impact test. However, the irradiated specimen broke during the impact test.

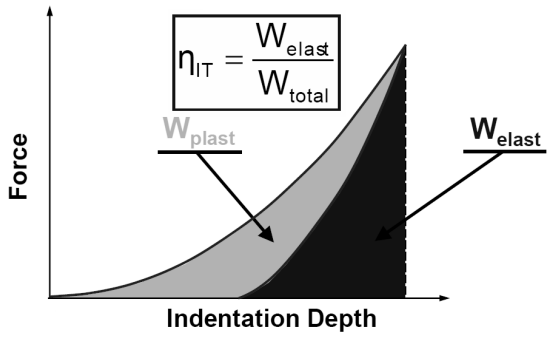

Fig. 6. **Mechanical Work of Indentation**

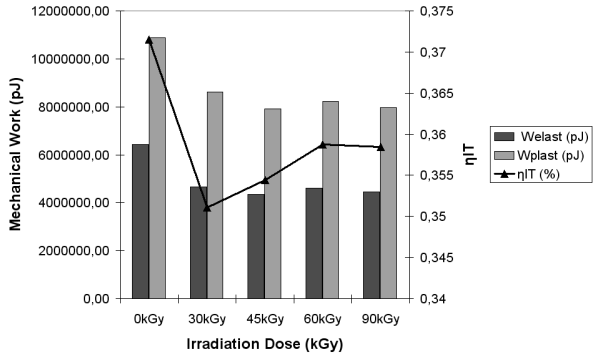

Fig. 7. **Elastic and plastic deformation work of polypropylene *vs.* irradiation dose**

Next to plastic and elastic deformation work, the coefficient of back deformation η_{IT} is especially important for the assessment of the structure of the irradiated polypropylene. The highest values were measured at non-irradiated PP. The smallest values were found at irradiation doses of 33 and 45 kGy.

4. Conclusion

Very interesting results were obtained for irradiation modified PP. When comparing the irradiated and non-irradiated PP it was apparent that the values of indentation hardness, Vickers hardness and the indentation modulus considerably increased, in some cases even by 95 % at the irradiation dose of 45 kGy. Also different depths of indentation in the surface layer of tested specimen were significantly different. It also proved the fact that higher doses of radiation do not have very positive effects on the mechanical properties, on the contrary due to degradation processes the properties deteriorate.

The opposite and deteriorated values were obtained for plastic and elastic work. In both cases the values dropped in the case of irradiated specimen. On the other hand non-irradiated PP showed high values of elastic and plastic deformation work.

This article was written with support of Ministry of Industry of Czech Republic as a part of the project called Development of the system for evaluation of hardness testing with stress on the research of new possibilities of polymer material characteristics analysis and application of the results on the market. FR-TI1/487.

REFERENCES

1. Manas D., Manas M., Stanek M., Danek M.: Arch. Mater. Sci. Eng. *32*, 69 (2008).
2. Uzuna O., Kölemena U., Çelebi S., Güçlü N.: J. Eur. Ceram. Soc. *25*, 969 (2005).
3. Stanek M., Manas M., Manas D.: *Novel Trends in Rheology III*, AIP, New York, USA, p. 75–85 (2009).
4. Oliver W. C., G. M. Pharr.: J. Mater. Res. *7*, 1564 (1992).
5. Chvatalova L., Navratilova J., Cermak R., Raab M., Obadal M.: Macromolecules *42*, 7413 (2009).
6. Stanek M., Manas D., Manas M., Suba O.: J. Mathematics Computers Simulation *5*, 422 (2011).
7. Manas D., Stanek M., Manas M., Pata V., Javorik J.: KGK, Kautsch. Gummi Kunstst. *62*, 240 (2009).
8. Manas M., Stanek M., Manas D., Danek M., Holík Z.: Chem. Listy *103*, s24 (2009).
9. Manas D., Manas M., Stanek M., Zaludek M., Sanda S., Javorik J., Pata V.: Chem. Listy *103*, s72 (2009).

M. Ovsik[a], D. Manas[a], M. Manas[a], M. Stanek[a], M. Hribova[a], K. Kocman[a], D. Samek[a], and Manas M.[b]
([a] Tomas Bata University in Zlin, Faculty of Technology, Department of Production Engineering, Zlin, [b] MITAS a. s., Prague, Czech Republic): **Irradiated Polypropylene Studied by Mircohardness and Waxs**

Hard surface layers of polymer materials, especially polypropylene, can be formed by chemical or physical process. One of the physical methods modifying the surface layer is radiation cross-linking. Radiation doses used were 0, 30, 45, 60 and 90 kGy for unfilled polypropylene with the 5 % cross-linking agent (triallyl isocyanurate). Individual radiation doses caused structural and micromechanical changes which have a significant effect on the final properties of the polypropylene tested. Small radiation doses cause changes in the surface layer which make the values of some material parameters rise. The improvement of micromechanical properties was measured by an instrumented microhardness test. X-ray diffraction was used to study the influence of the structure.

MICROSTRUCTURE AND PROPERTIES OF THE Ni-Al-B ALLOYS AFTER DIRECTIONAL SOLIDIFICATION

MARTIN POHLUDKA, JITKA MALCHARCZIKOVÁ, and MIROSLAV KURSA

VŠB – Technical University of Ostrava, 17. listopadu 15/2172, 708 33 Ostrava Poruba, Czech Republic
martin.pohludka@vsb.cz

Keywords: Ni-Al-B alloys, microstructure, porosity, microhardness

1. Introduction

Ni_3Al intermetallic compound exhibits anomalous deformation behaviour due to the unique structure of $L1_2$. This behaviour is characterised by an increase of deformation stress with temperature up to 800 °C. Then the stress decreases. Therefore Ni_3Al based alloys are used in high temperature applications such as turbine blades[1].

Brittleness of polycrystalline Ni_3Al at room temperature inhibited its usage in industry in past. The brittleness is caused by air moisture which weakens the grain boundaries by accumulation of atomic hydrogen. The brittleness can be reduced by boron alloying of these alloys. Boron protects from a hydrogen placement along grain boundaries and it cohesively strengthens them. Ni-24Al-0.24B alloy (at. %) achieves the best mechanical properties[2].

2. Experiment

Ni-24Al, Ni-24Al-0.1B and Ni-24Al-0.24B alloys (at.%) were prepared by melting in a vacuum induction furnace. After grinding of surface oxide layer, the cast of every alloy was directionally solidified in the super Kanthal resistance furnace used the Bridgman's method at the temperature of 1550 °C and at the rate of 50 mm h^{-1}. The transversal sections were cut from the as-cast (C) and the as-directionally solidified (DS) samples for documentation of microstructure and for evaluation of porosity and microhardness.

3. Results

3.1. Microstructure

Microstructure of the alloys after casting is dendritic (Fig. 1). Dendrite cores are formed by channels of the γ phase which surrounds the fine grains of the γ' phase. These clusters look like a mesh. There is the γ' phase between dendrite core and boundary. The casts alloyed with boron contain many pores.

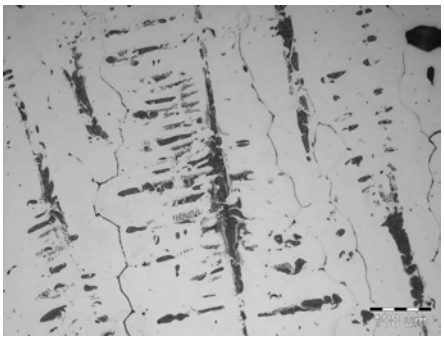

Fig. 1. **Microstructure of Ni-22Al-0.1B alloy (at.%) after cast**

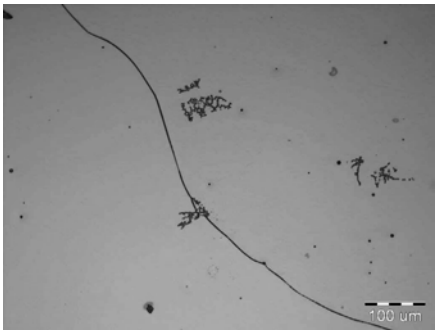

Fig. 2. **Microstructure of Ni-22Al-0.1B alloy (at.%) after directional solidification (V = 50 mm h^{-1})**

After directional solidification, the structure is oriented in a direction of growth (Fig. 2). Grains on the transversal sections are equiaxed and formed by the γ' phase. There are traces of mesh at grain boundaries and also in the centre of grains. Volume fraction of the mesh decreases with increasing boron concentration. Boron does not form individual phases for the used concentrations.

3.2. Porosity

Pore amount in the casts is greater than in the directionally solidified alloys. The alloys contain the pores in sizes from 0.5 to 27.0 μm. For the as-cast and the as-directionally solidified samples, porosity increases together with boron concentration (Tab. I).

The casts contain big and many elliptical pores with rough surface. After directional solidification, amount of big pores decreases. The remaining pores have more circular contour and smoother surface (Fig. 3).

Table I
Porosity of Ni-24Al Alloys without and with Boron

Alloy [at. %]	P_C [%]	P_{DS} [%]
Ni-24Al	0.18 ± 0.10	0.03 ± 0.01
Ni-24Al-0.1B	0.26 ± 0.28	0.12 ± 0.08
Ni-24Al-0.24B	0.33 ± 0.34	0.21 ± 0.21

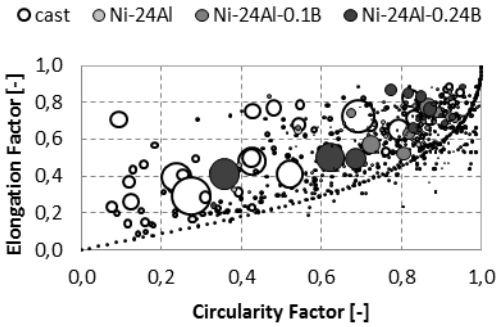

Fig. 3. **Estimation of pore morphology in the samples of Ni-24Al, Ni-24Al-0.1B a Ni-24Al-0.24B alloys (at.%) after cast and after directional solidification**

3.3. Microhardness

Directional solidification process slightly decreases microhardness of the alloys in contrast to cast state. The microhardness of the as-cast and the as-directionally solidified samples increases with increasing boron concentration (Tab. II). The measurement has not confirmed a matrix softening of Ni-24Al alloy by boron alloying.

The presence of boron at grain boundaries has been indirectly confirmed by the microhardness measurement carried out from boundary to the centre of grains (Fig. 4). Alloy microhardness measured by this way always decreases. In this case, the hardest alloy is the one with 0.24 at.% of boron and the weakest alloy is the unalloyed one.

4. Conclusions

The measurements carried out in this paper have confirmed that alloying and process of directional solidification affect microstructure, porosity and microhardness of Ni-24Al, Ni-24Al-0.1B and Ni-24Al-0.24B alloys (at.%).

As-directionally solidified alloys have an oriented microstructure which is formed by elongated grains of the γ' phase parallel to the direction of the growth. They have smaller number of pores with smother surfaces and lower microhardness that the as-cast alloys.

The effect of boron alloying on matrix softening of Ni-24Al alloy has not been confirmed.

Table II
Microhardness of Ni-24Al Alloys without and with Boron (the HV load value is 50 g)

Alloy [at. %]	HV_C 0.05 [-]	HV_{DS} 0.05 [-]
Ni-24Al	244 ± 26	228 ± 20
Ni-24Al-0.1B	254 ± 43	245 ± 12
Ni-24Al-0.24B	273 ± 41	255 ± 11

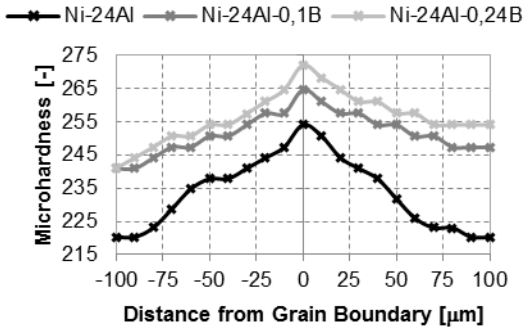

Fig. 4. **Decrease of microhardness in Ni-24Al, Ni-24-0.1B and Ni-24Al-0.24B alloys (at.%) from grain boundary to grain centre**

The presented results were obtained within the frame of solution of the state budget of the Czech Republic and project MSM 6198910013 "Processes of preparation and properties of high-purity and structurally defined special materials".

REFERENCES

1. Stoloff N. S.: Int. Mater. Rev. *153*, 34 (1989).
2. Jiating G., et al.: Mater. Sci. Eng. *120*, A152 (1992).

M. Pohludka, J. Malcharcziková, and M. Kursa *(VŠB – Technical University of Ostrava):* **Microstructure and Properties of the Ni-Al-B Alloys after Directional Solidification**

Ni-24Al, Ni-24Al-0.1B and Ni-24Al-0.24B alloys (at. %) were prepared by vacuum induction melting and by directional solidification at the rate of 50 mm/h and at the 1550 °C. After directional solidification, alloy microstructure consists of elongated grains of the γ' phase. Alloy matrix also contains small amount of the γ phase. There are no boron phases in these alloys. Process of directional solidification decreases an amount of the pores which the alloys contain after cast and modify their morphology. Microhardness of the alloys after directional solidification is lower then microhardness of the alloys after cast. However, there is no matrix softening of Ni-24Al alloy as a result of boron alloying.

LOCAL MICROMECHANICAL PROPERTIES OF DENTAL COMPOSITES

ONDŘEJ PREJZEK, JOSEF ŠEPITKA, JAROSLAV LUKEŠ, and MIROSLAV ŠPANIEL

Czech Technical University in Prague, Faculty of Mechanical Engineering, Dept. of Mechanics, Biomechanics and Mechatronics, Technicka 4, 166 07 Prague, Czech Republic
Ondrej.Prejzek@fs.cvut.cz

Keywords: nanoindentation, dental composites, elastic modulus, reduced modulus

1. Introduction

A detailed knowledge of elastic properties of dental restorative materials is essential for obtaining reliable computational models for an optimization of a mechanical performance. Many works deal with measurement of the elastic modulus of dental composites, but the results vary, depending on the measurement method. In the case of an uniaxial test, moduli measured under tensile load are referred to be significantly higher, than those measured under compressive direction[1–3]. This work has following aim: it maps the elastic moduli of dental composites composed of glass particles and polymer resin, as well as individual constituents. Consecutively, moduli are compared with the moduli previously measured by an uni-axial compressive test. Additionally to each elastic modulus measurement, the value of indentation hardness H_{IT} was determined.

2. Materials and methods

Three commercially available composite materials have been subjected to an experiment. Opticor Flow (SpofaDental a.s., Jičín, Czech Republic), Filtek Z250 (3M ESPE, St.Paul, MN, USA) and Charisma Opal (Heareus Kulzer GmbH, Hanau, Germany). All three materials consist of polymeric resin and glass particles.

2.1. Specimen preparation

The samples are of cylindrical shape (ø 6 × 12 mm), identical to those of samples subjected to compressive experiments. The curing of a specimen has been performed in both radial and axial direction in order to ensure curing of entire volume of the composite. Samples had been cured in a thin plexi tube and thereafter all three samples were put in one mounting cup, embedded in transparent Epofix (Struers GmbH) and polished before the indentation measurement.

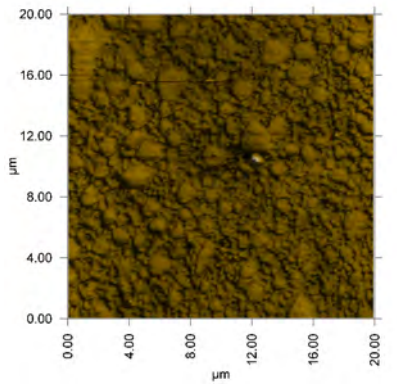

Fig. 1. **Specimen surface (Filtek), obtained by *in-situ* SPM**

2.2. Testing conditions

Quasistatic load controlled experiments were performed with Hysitron TriboIndenter™ system with Berkovich diamond tip.

Time increments of three applied loading steps – increase of loading force, constant loading force, unloading – have been prescribed as 5 × 2 × 5 s. A unique loading force P_{max} has been chosen for each material, in order to meet the indentation depths h_c > 20 nm. For the selected materials, $P_{maxCharisma}$ = 80 μN, $P_{maxFiltek}$ = 120 μN, $P_{maxOpticor}$ = 50 μN. Based on standard tip shape calibration on fused quartz we know, that indentation size effect is present up to contact depth 20 nm.

Two experimental procedures have been employed to determine the location of indents:

1. To measure overall modulus of the composite, indentation of a representative area, selected from an optical microscopic image has been utilized. Indents have been applied in square pattern of 8 by 8 with mutual distance of 2 μm, hence in area of 14 by 14 μm.
2. Indentation by piezo-automation method using an image from *in-situ* scanning probe microscopy (SPM) has been used to measure properties of individual constituents. Sample surface has been scanned with a constant force of 2 μN at a scan size 5 by 5 μm in order to distinguish between phases indented afterwards.

3. Results and discussion

For all examined composite materials, the Poisson's ratio of ν = 0.17 (particle) and ν = 0.35 (resin), respectively, was used for the calculation of elastic moduli[4].

All sets of results refer Filtek Z250 being the material with both highest elastic modulus and indentation hardness. Charisma Opal is, in all cases, the material with medium values and Opticor Flow shows lowest values of both modulus and hardness. The order is equal to that observed by results of the compressive test. Compared to results from compressive test, modulus obtained by nanoindentation reaches significantly higher values. This fact can be attributed to the microstructural irregularity of the composite, that does not allow the standard mixing laws[5,6] to be utilized for calculation of global properties of the composite from known properties of constituents. Plastic microstructural residual stress[7] in certain resin regions can also contribute to the decreased elastic modulus measured in compression.

4. Conclusions

Aforementioned results show locally measured properties of three materials measured by two various nanoindentation approaches. Sequence of results by materials is the same for overall moduli, obtained by the optical microscopy approach as well as the moduli of individual constituents, obtained using the piezo-automation approach. This is also valid for the results of the compressive macroscopic measurement; however those values are distinctively lower. This fact implies careful selection of a method to obtain material properties for each particular case of application. The locally obtained values of moduli can be successfully employed to describe local properties, and their change within one specimen, i.e. gradient. However, to describe overall properties of a composite material with a complex microstructural topography, the locally measured results must be subjected to a homogenization procedure, such as FE analysis of structure's overall performance.

Table I
Indentation of area selected from optical microscopy: averaged values of measured properties

Sample	Charisma	Filtek	Opticor
Contact depth [nm]	39.1± 7.4	39.6±7.8	38.7± 8.7
Reduced modulus [GPa]	15.6±3.0	20.1±2.7	8.4±2.5
Elastic modulus [GPa]	13.9±2.6	17.9±2.4	7.42±2.2
Hardness [GPa]	0.5±0.3	1.4±0.4	0.5±0.2

Table II
Piezo automation method: properties of constituents

Sample	Charisma	Filtek	Opticor
Elastic modulus Filler [GPa]	20.8±2.8	30.1±2.9	9.9± 3.3
Elastic modulus Resin [GPa]	10.4±0.1	14.3±1.4	5.2±0.7
Hardness Filler [GPa]	2.54±0.7	3.2±0.6	0.6±0.3
Hardness Resin [GPa]	0.87±0.06	1.50±0.04	0.45±0.04

Table III
Values of elastic modulus, obtained by compressive test

Sample	Charisma	Filtek	Opticor
Compression [GPa]	3.2±0.5	3.4±0.6	1.8±0.3

This work was supported by the Grant Agency of the Czech Technical University in Prague, grant No. SGS10/247/OHK2/3T/1212 and by the Ministry of Education project: Transdisciplinary research in Biomedical Engineering II, No. MSM 6840770012.

REFERENCES

1. Kleverlaan C.J., et al.: Dent. Mat. *2*, 1150 (2005).
2. Beatty M. W., et al.: Biomaterials *14*, 999 (1993).
3. Pidaparti, R. M. V., et al.: Eng. Fra. Mech. *45*, 51 (1993).
4. Oliver W. C., Pharr G., G.M.: J. Mater. Res. *7*, 1564 (1992).
5. Voigt W.: Ann. Phys. Chem. *274*, 573 (1889), (in German).
6. Reuss A.: ZAMM *9*, 49 (1929) (in German).
7. Harris B.: J. Mater. Sci. *13*, 173 (1977).

O. Prejzek, J. Šepitka, J. Lukeš, and M. Španiel *(Czech Technical University in Prague, Faculty of Mechanical Engineering, Dept. of Mechanics, Biomechanics and Mechatronics, Czech Republic):* **Local Micromechanical Properties of Dental Composites**

The paper deals with nanoindentation measurement of local properties (elastic modulus and indentation hardness) of three dental composite materials. Properties of particular phases of the material, filler particles and resin, respectively, were measured by a piezo-automation approach. To obtain overall properties of the composite, indentation of locations, selected from an optical microscopic image has been performed. Obtained results are compared with data, previously gained by the uni-axial compressive test. Elastic moduli, obtained locally by nanoindentation are higher, when compared with those, measured globally under compressive load. For the elastic modulus, the order of results, measured for particular materials, remains unchanged by various measurement methods and is equal to that of indentation hardness.

EXPERIMENTAL TECHNIQUES FOR THE MICROSTRUCTURAL CHARACTERIZATION OF RETAINED AUSTENITE STABILITY AND SINGLE PHASE PROPERTIES IN LOW-ALLOYED TRIP-STEELS

HENDRIK QUADE[a], ANDRE STEFFEN[b], PETRA GAVENDOVÁ[c], ULRICH PRAHL[a], METIN TOLAN[b], and WOLFGANG BLECK[a]

[a] *Department of Ferrous Metallurgy at RWTH Aachen University, Intzestraße 1, 52072 Aachen, Germany,*
[b] *Fakultät Physik/DELTA, TU Dortmund, Maria-Goeppert-Mayer-Str. 2, 44227 Dortmund, Germany,*
[c] *Institute of Materials Research, SAS, Watsanova 47, 040 01 Košice, Slovakia*
hendrik.quade@iehk.rwth-aachen.de

Keywords: TRIP-steels, synchrotron radiation, high-energy X-ray diffraction, electron backscatter diffraction, nano indentation, phase transformation

1. Introduction

TRIP-steels are subjected to a high attention for the application of automotive parts, because they exhibit a high formability at a given strength level.

It was found that high energy synchrotron X-ray diffraction is excellently suited for the investigation of the austenite stability[12]. To identify the local distribution of the face-centered cubic phase, electron backscatter diffraction can be a usefull technique, especially for the investigation for the local martensite formation[3].

Typically, low-alloyed TRIP-steels consist of a ferrite matrix with embedded islands of retained austenite, bainite and some martensite (Fig. 1).

Two important mechanisms are responsible for the strain-hardening behaviour of a TRIP-steel: the phase transformation of metastable retained austenite to the much harder phase martensite, and the composite effect of the microstructure due to the presents of several single phases[4]. The locations of the austenitic grains in the microstructure are of major importance because they alter the extent of the phase transformation, the microstructural strain localization and therefore the macroscopical formability of the steel[5].

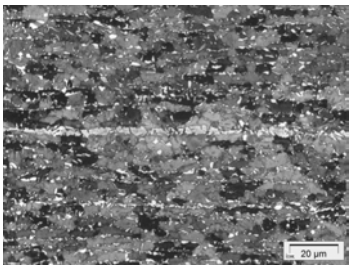

Fig. 1. **Light optical image of a TRIP microstructure after Klemm etching**

2. Materials and methods

The investigations were carried out for three industrial TRIP-steels named TRIP A, B (Rm = 700 N mm^{-2}) and TRIP C (Rm = 800 N mm^{-2}) based on different chemical compositions (Table I). The engineering stress-strain curves can be seen in Fig. 2. TRIP A and B exhibit nearly the same strain hardening and fracture strains were TRIP C has the highest tensile strength due to the highest silicon content, because silicon is a strong ferrite strengthening element.

Synchrotron high energy X-ray diffraction experiments were performed at the beamline BL9 of the Dortmunder Elektronenspeicherring-Anlage (DELTA) in order to study the transformation kinetics in-situ as a function of applied tensile force. The left image of Fig. 3 shows the appeared Debye-Scherrer rings after radiography of a TRIP-steel sample, where each ring belongs to a certain plane of the crystal lattice.

The existence of full Debye-Scherrer rings over the whole 360° indicate that the material exhibits no significant texture in the undeformed state. The disappearance of the peaks corresponding to the {111},{200} and {220} plane of the austenitic phase during straining is a proof for

Table I
Chemical composition of the investigated steel grades

[wt.%]	C	Mn	Si	Al	P
TRIP A	0.165	1.67	0.341	1.10	0.093
TRIP B	0.179	1.77	0.039	1.61	0.014
TRIP C	0.205	1.68	1.63	0.039	0.016

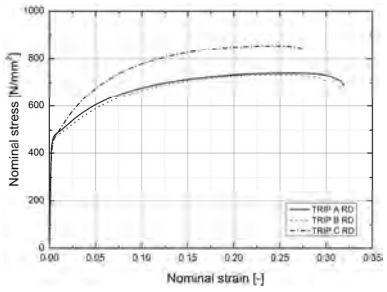

Fig. 2. **Engineering stress strain curves of the investigated TRIP-steels** (gauge length = 80 mm)

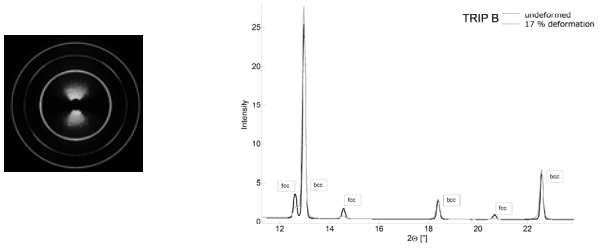

Fig. 3. **Arisen Debye-Scherrer rings after radiography of the sample (left), corresponding diffractogram (right)**

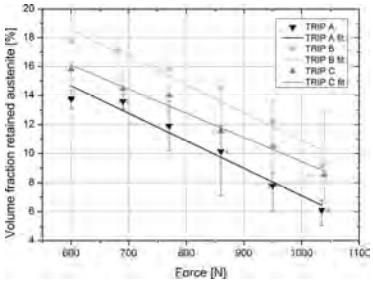

Fig. 5. **Volume fraction of retained austenite as a function of applied tension force determined by synchrotron experiments**

a phase transformation in the sample. The calculation of the volume fraction was carried out by using the evaluation software Maud[6] (Materials Analysis Using Diffraction).

In order to investigate the local, morphological influence on the martensite formation, electron backscatter diffraction was used. Therefore a scanning electron microscope JEOL JSM7000F in combination with an EBSD-detector was applied. A measuring field of 50 μm × 50 μm and a step-size of 60 nm for the readout of the EBSD pattern were chosen. To create a connection with the local plastic deformation on the sample the true strains were measured by the usage of a Vialux Autogrid® system (Fig. 4).

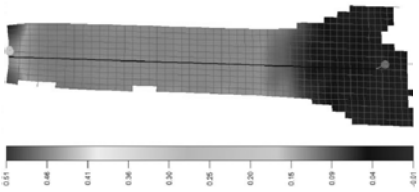

Fig. 4. **Distribution of true equivalent plastic strain on a cracked sample measured by means of Vailux Autogrid® system**

For the determination of the strength of the ferritic phase, nanoindentations were conducted on a Nano Indenter® G 200 by the usage of a pyramidal diamond Berkovich indenter tip. The tests were carried out according to the standard norm[7], where the indentations were done with a maximum force of 5 mN. In order to minimize the measurement error and to achieve representativeness, 50 indentations were performed and for the determination of the hardness modulus a Poissons's ratio of 0.3 was assumed.

3. Results

Fig. 5 shows the austenite volume fractions as a function of applied tension force and nominal strain, determined by the X-ray diffraction experiments. Under consideration of the tensile force it has to be mentioned that all 3 steels show a nearly equal austenite stability, where the highest is presented in TRIP C and the lowest in TRIP B.

Regarding the strains, two regimes were observed, where a massive transformation takes place at the onset of yielding and low states of deformation and a regime at higher strain values were the martensite formation reaches a saturation due to a decrease of availability of possible transformation nucleation sites (Fig. 6). The transformation kinetics stay in close correlation with the development of the strain hardening values over engineering strain. The local transformation kinetic is among other factors influenced by the arrangement of the retained austenite grains in the microstructure which changes over the thickness of the sheet. The phase distribution varies from a nearly homogeneous at one third thickness to an inhomogenous banded dispersion of the second phases at the sheet centre in TRIP steel B. In addition, initial thermal martensite was detected which cannot serve for a TRIP-effect at the beginning of straining of the material (Fig. 7). These martensite bands are a consequence of segregations in the steel sheet, were an enrichment of manganese in these regions was observed.

In order to achieve information about the impact of the local loading condition on the martensite formation the

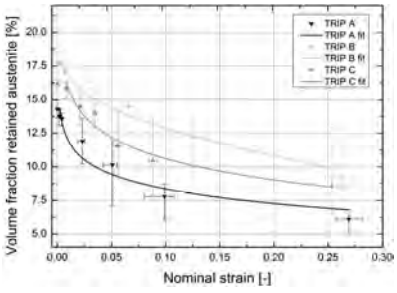

Fig. 6. **Volume fraction of retained austenite as a function of engineering strain determined by synchrotron experiments**

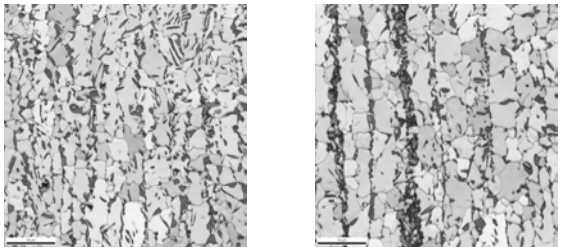

Fig. 7. **Alteration of the morphology over the sheet thickness in TRIP B (left: homogeneous distribution of retained austenite at one third position, right: heterogeneous distribution of the retained austenite in combination with a centred martensite band at sheet centre)**

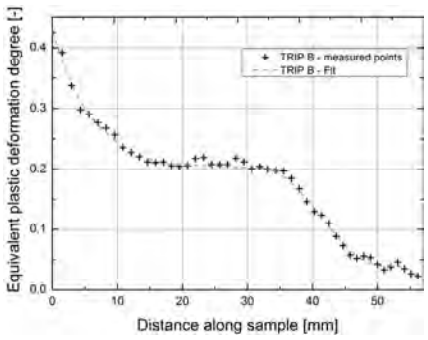

Fig. 8. **True equivalent plastic strain along the tensile sample in TRIP B measured by means of Vialux Autogrid® system**

local stress-strain conditions have to be known. Fig. 8 depicts the magnitude of equivalent plastic strain from the fracture of an investigated tensile sample to the clamping region.

Highest values occur close to the crack due to the strain localization and necking where a plateau is observable in the regions of uniform deformation.

Based on this knowledge the evolution of the phase fractions of retained austenite as a function of the local true equivalent plastic strain with the same trend as acquired by the synchrotron experiments can be seen in Fig. 9. It was found that martensite formation upon deformation of the material takes place only partially within the grains in dependence on the local position in the microstructure and chemical composition.

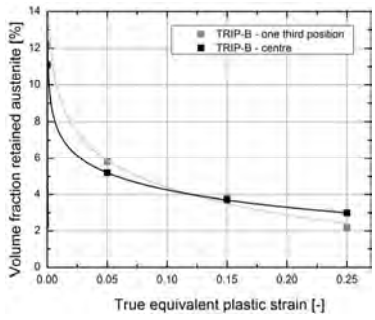

Fig. 9. **Volume fraction of retained austenite determined by electron backscatter diffraction in TRIP B**

The ferritic matrix in the investigated steels has a different strength which itself offers a resistance against the volume dilatation accompanying the martensite formation (Fig. 10). The differences in the hardness values are mainly due to the different contents of silicon. Typically, silicon and aluminium are alloyed for the prevention of carbide precipitation during isothermal holding. But additionally silicon has a strong influence on the ferrite strength were the tensile strength increases by approximately 50 MPa per 0.5 wt.% (ref.[8]).

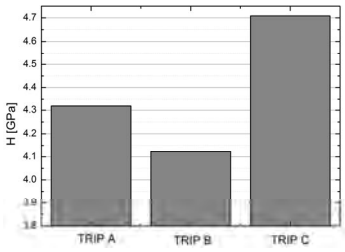

Fig. 10. **Hardness of the ferritic phase determined by nanoindentation**

4. Conclusions

The morphology strongly influences the phase transformation were the martensite formation only partially takes place within austenitic grains. 3 types of local retained austenite morphologies were observed in certain regions of the investigated steel sheets: a homogeneous distribution, an arrangement of austenite particles in bands and retained austenite particles located in a martensitic band.

These different types of microstructural phase distribution leads to an alteration of the local TRIP-effect and therefore mechanical properties.

Not only the retained austenite stability but also the strength of the ferritic matrix plays an important role for the mechanical properties of the entire composite.

This research was carried out under the Project No. MC2.07293 in the framework of the Research Program of the Materials innovation institute M2i (http://www.m2i.nl).

REFERENCES

1. N. Jia, Z. H. Cong, X. Sun, S. Cheng, Z. H. Nie, Y. Ren, P. K. Liaw, Y. D. Wang: Acta Materialia *57*, 3965 (2009).
2. N. H. van Dijk, A. M. Butt, L. Zhao, J. Sietsma, S. E. Offerman, J. P. Wright, S. van der Zwaag: Acta Materialia *53*, 5439 (2005).

3. S. Zafferer, P. Romano, F. Friedel: J. Microscopy *230*, 499 (2008).
4. P. Jacques: *PhD-thesis*, Université catholique de Louvain, Département des sciences des matériaux et des procédés, 1998.
5. H. Quade, U. Prahl, W. Bleck: Chem. Listy *105*, s705 (2011).
6. L. Lutterotti, M. Bortolotti, G. Ischia, I. Lonardelli, H.-R. Wenk: Z. Kristallogr., Suppl. *26*, 125 (2007).
7. DIN-EN ISO 14577-1, Metallic materials – Instrumented indentation test for hardness and materials parameters – Part 1, 2003.
8. F. B. Pickering: *Physical Metallurgy and the Design of Steels*, London, U.K.: Applied Science, 1978.

H. Quade[a], A. Steffen[b], P. Gavendová[c], U. Prahl[a], M. Tolan[b], and W. Bleck[a] *([a] Department of Ferrous Metallurgy at RWTH Aachen University, Aachen, Germany, [b] Fakultät Physik/DELTA, TU Dortmund, Dortmund, Germany, [c] Institute of Materials Research, SAS, Košice, Slovakia):* **Experimental Techniques for the Microstructural Characterization of Retained Austenite Stability and Single Phase Properties in Low-Alloyed TRIP-Steels**

The present work deals with experimental facilities for the characterization of low-alloyed TRIP-steels in terms of the phase transformation and the local mechanical properties of the microstructure. The TRIP-effect is a complex phenomenon which acts locally. An evaluation of the deformation-state in the sheet plane by the usage of a measurement system Vialux Autogrid® gives information about the impact of the local stress-strain condition on the phase transformation. In addition, there exists a further locality effect which becomes noticable over the sheet thickness. Due to industrial boundary conditions, the morphology changes from a homogeneous distribution to a banded arrangement of the second phases. To investigate this local influence, the electron backscatter diffraction technique seems to be a feasible tool. Besides the retained austenite stability, the ferritic phase has a major influence on the behaviour of the overall steel grade. To characterize the strength of the ferrite matrix it was proven that nano indentation is a practical method.

NANOWEAR TESTING OF COMPOSITE MATERIALS

RADEK SEDLÁČEK[a], TOMÁŠ SUCHÝ[a,b], JOSEF ŠEPITKA[a], JAROSLAV LUKEŠ[a], MIROSLAV SOCHOR[a], KAREL BALÍK[b], ZBYNĚK SUCHARDA[b], and JAN BENEŠ[c]

[a] Czech Technical University in Prague, Fac. of Mech. Eng., Technická 4, Prague 6, 166 07, [b] Institute of Rock Structure and Mechanics, ASCR, v.v.i., V Holešovičkách 41, Prague 8, 182 09, [c] Medin, Inc., Vlachovická 619, Nové Město na Moravě, 592 31, Czech Republic
radek.sedlacek@fs.cvut.cz

Keywords: nanoindentation, wear, mechanical properties, polymeric composite, sterilization

1. Introduction

Radiolucent composite materials have properties superior to those of insufficiently radiolucent metal alloys and unreinforced polymers with poor mechanical properties. The steam or dry heat sterilization processes widely employed in medical practice can affect the micromechanical properties of polymeric composites, particularly in the interface region between the matrix and the reinforcing fibers[1]. The structural integrity and the overall performance of fiber-reinforced polymer composites are strongly influenced by the stability of the fiber/polymer interfacial region[2]. It is necessary to investigate both the microscopic and the macroscopic changes in mechanical and structural properties due to the sterilization processes that are employed. The aim of this study was to verify a methodology for assessing the influence of multiple sterilization processes on the inner structure of composites.

2. Materials and methods

Composite materials (C/PPS) based on carbon T300 fibers (plain weave fabrics, Toray, Japan) and polyphenylenesulfide (TenCate, Holland) matrix were prepared. The C/PPS composite was consolidated under a pressure of 1.0 MPa at 310 °C for 10 min (rate of temperature increase and/or decrease: 10 °C/min). In order to assess the influence of multiple sterilization processes on the inner structure of the composites, mechanical and structural analyses were performed before sterilization (**A**), after 1 sterilization process period (**B1**), and after 30 (**B30**) sterilization process periods. An autoclave (Steridент, Prodenta, CZ) for steam sterilization (134 °C, 304 kPa, 10 min) was used for this purpose.

An assessment of the impact of multiple sterilization processes on the inner structure of the composites was carried out at two levels: macroscale and microscale. The macroscopic behaviour was studied by flexural tests. The ultimate strength in bending and the modulus of elasticity in bending in the direction of the fibers were determined with a four-point and three-point bending set-up (Inspekt 100HT, Hagewald & Peschke, Germany), in accordance with ISO 14125.

The microscopic behaviour was studied by nanoindentation tests. The assessment of the impact of multiple sterilization processes on the inner structure of the composites was studied using ScanningWear ™ mode, a nanomechanical instrument option of Hysitron TriboIndenter™ TI 950. A Berkovich diamond tip with apex radius of ~120 nm was employed for the ScanningWear tests. The tip was raster-scanned across a 40×40 μm area of the sample surface (in close proximity to the fibers) in 256 scan lines with 100 μN contact force for 5 passes. Immediately after each wear test had been completed, the worn areas were imaged using a 60×60 μm scan size and a 2 μN contact force (scanning probe microscopy, SPM). The nano wear evaluation was carried out in SPIP 5.1.6. software (ImageMetrology, Denmark). The mean values of each worn area were compared with the mean values of the corresponding unworn areas, and the wear depths were calculated.

A statistical evaluation was carried out using the STATGRAPHICS Centurion XV software (StatPoint, USA): the statistically significant differences were checked by nonparametric methods (the Kruskal-Wallis test, α=0.05); the Mann-Whitney test was used as a post hoc test (α=0.05).

3. Results and discussion

The flexural properties after multiple sterilizations were tested and compared with those of the corresponding unsterilized samples (Fig. 1 and Fig. 2). The results and the statistical analysis show that the modulus of elasticity in bending is not influenced by the multiple sterilizations studied here. The values are in reasonable agreement with earlier results obtained by flexure tests in the direction of the reinforcing fibers[3]. In the case of ultimate strength in bending, a statistically significant increase after 1 sterilization process (app. 6.5 %) and after 30 sterilization processes (app. 7.2 %) can be observed. This increase may be explained by equalization of the residual stress development during the consolidation of the composites. The applied sterilization temperature (134 °C) is above the glass transition temperature (T_g) of the fabric reinforced PPS composites. Depending on the staking sequence, the vol-

ume fraction and the reinforcement material of the laminate, the T_g of the fabric composites is about 83–98 °C (ref.[3,4]). The residual stresses created during the processing of thermoplastic-based composites can probably be optimized by further limited application of temperature above T_g. A further increase in temperature above T_g may soften the matrix behaviour and significantly reduce the mechanical properties[3].

The influence of multiple sterilization processes on the inner structure of the composites was further analysed by an evaluation of the stability of the fiber/matrix interfacial region (see Fig. 3). The wear depths of the worn areas after nano scratching were assessed (Fig. 4). The results provide an assessment of the influence of multiple sterilization processes on the inner structure of the composites. The analysis shows that no structural changes occurred in the region close to the fibers, and the stability of the fiber/matrix region was preserved after 30 sterilization processes. For further analyses in our study, it will be necessary to increase the number of sterilization cycles in a manner that simulates the life cycle of widely-used medical devices, e.g. composite parts of a medical targeting system.

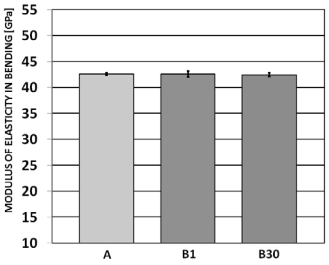

Fig. 1. **Modulus of elasticity in bending before (A), after 1 sterilization process (B1), and after 30 sterilization processes (B30).** There is no statistically significant difference between the values (Mann-Whitney post-hoc test, α=0.05, n=6)

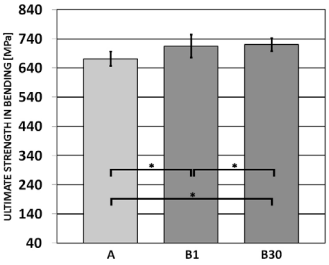

Fig. 2. **Ultimate strength in bending before (A), after 1 sterilization process (B1), and after 30 sterilization processes (B30).** (*denotes statistically significant differences, Mann-Whitney post-hoc test, α=0.05, n=6)

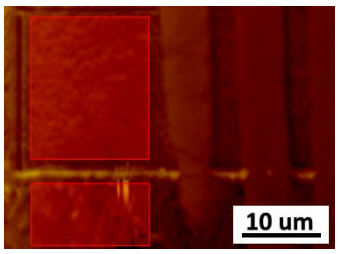

Fig. 3. ***In-situ*** **SPM micrograph of unworn (rectangle below) and worn (at the top) areas after 10 cycles of ScanningWear.** The fibers are situated on the right side of the micrograph

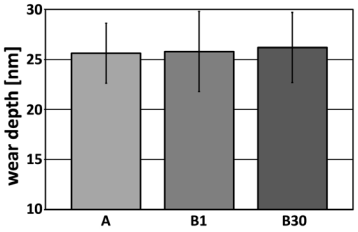

Fig. 4. **Wear depths of worn areas of composites before (A), after 1 sterilization process (B1), and after 30 sterilization processes (B30).** There is no statistically significant difference between the values (Mann-Whitney post-hoc test, α=0.05, n=6)

4. Conclusion

On the basis of our analyses, we can state that the C/PPS composite is a good candidate for application as a radiolucent material providing resistance against steam sterilization decomposition. Before it is presented for application, it will be necessary to apply greater numbers of sterilization cycles.

This research was supported by the Czech Science Foundation (project No. 108/10/1457), and by Ministry of Education project Transdisciplinary Research in Biomedical Engineering II, No. MSM 6840770012.

REFERENCES

1. Zheng Q.: J. Comp. Mater. *27*, 1465 (1993).
2. Godara A., Raabe D., Green S.: Acta Biomater. *3*, 1742 (2007).
3. Vieille B., Aucher J., Taleb L.: Adv. Polym. Tech. *30*, 80 (2011).
4. Rebenfeld L., Desio G.P., Wu J.C.: J. Appl. Polym. Sci. *42*, 801 (1991).

R. Sedláček[a], T. Suchý[a,b], J. Šepitka[a], J. Lukeš[a], M. Sochor[a], K. Balík[b], Z. Sucharda[b], and J. Beneš[c]
([a] CTU in Prague; Fac. of Mech. Eng.; [b] Institute of Rock Structure and Mechanics, ASCR, v.v.i.; [c] Medin, Inc.):
Nanowear Testing of Composite Materials

This study evaluates the resistance against multiple steam sterilization of composite materials based on carbon fibers and polyphenylene sulfide matrix. The influence of multiple sterilization processes on changes in their mechanical and structural properties are determined by flexural and nanoindentation tests.

DYNAMIC MECHANICAL PROPERTIES OF SOFT TISSUES LOCALIZED BY FLUORESCENCE MICROSCOPE OBTAINED USING NANOINDENTATION

JOSEF ŠEPITKA[a], JAROSLAV LUKEŠ[a], LIBOR STANĚK[b], and JAN ŘEZNÍČEK[a]

[a] *Czech Technical University in Prague, Faculty of Mechanical Engineering, Dept. of Mechanics, Biomechanics and Mechatronics, Technicka 4, Prague 166 07,* [b] *Institute of Pathology, General Faculty Hospital, Charles University, Studnickova 2, Prague 2 128 00, Czech Republic*
Josef.Sepitka@fs.cvut.cz

Keywords: nanoindentation, DMA, fluorescence, soft tissue

1. Introduction

Nanoscale dynamic mechanical analysis (nanoDMA) seems to be an effective tool to obtain material characteristics of biological materials; especially for poorly accessible soft tissues[1,2]. However, we have only basic information on particular tissue localization from an optical microscope, which is attached to an indentation instrument and we are not able to localized separate structures or tissue transitions. This problem can be eliminated by an implementation of fluorescence microscope into a nanoDMA instrument.

The aim of this study was to obtain material characteristics of particular substructure of soft tissues their transition boundaries using a fluorescence microscope for their localization as a part of Hysitron TI 950 TriboIndenter™. The experiments, which are carried out with better understanding of material structure, can clear up a variability of data presented in a biomechanics community.

2. Materials and methods

2.1. Samples preparation

A porcine spine was obtained from a sloughterhouse at the day of testing. The lumbar spine motion segments were immediately dissected and ten millimeter thick plates of vertebral body, end plate and annulus fibrosus were cut under running water condition[2].

For histological investigation, the sample was immediately placed into 10 % buffered. Paraffin-embedded samples were cut into 7–10 μm sections in an angle of 45° to transversal plane using a microtome (Leova). Paraffin was removed with ethanol and xylene (Penta, Czech Republic) and the slices were stained with hematoxylin-eosin (Dako, Denmark). Prepared sample is shown in Fig. 1.

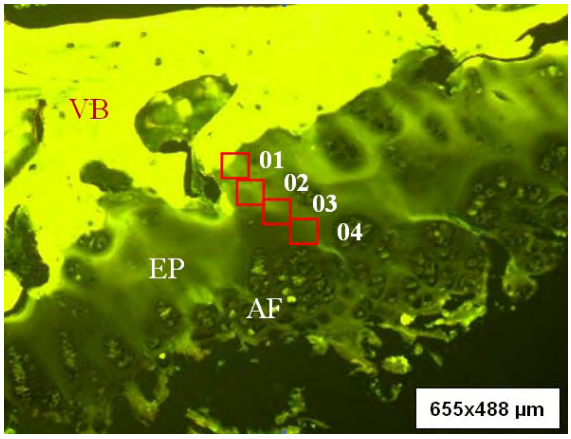

Fig. 1. **Picture obtained by fluorescence microscope shows histological cut which contain vertebral body (VB), endplate (EP) and annulus fibrosus (AF). Red squares denote four indented area**

2.2. Testing conditions

Indents were applied in square pattern of 4 by 4 indents with 15 μm separations. Thus, an area of 45 by 45 μm was characterized by dynamic nanoindentation. Fig. 1 was acquired by built-in flurescence microscope, which clearly shows separate structures and tissue transitions. Red squares 01–04 in the Fig. 1 denote the indented areas. Area 01 represents endplate region close to vertebrae body. Areas 02 and 03 represent central endplate region. Area 04 represents a transition of the endplate and annulus fibrosus.

NanoDMA load controlled experiments were performed with Hysitron TriboIndenter™ system with diamond Berkovich tip. Harmonic loading P_0 = sin (ωt) with dynamic load amplitude P_0 = 30 μN was specified for the harmonic frequency range 5–200 Hz. During nanoDMA experiment, static load was applied at maximum force P_{max} = 2000 μN.

The reduced storage modulus (E_r'), the reduce loss modulus (E_r") and tanδ =E_r"/ E_r' dependent on compliance (C_s) and stiffness (K_s) of the sample are given by

$$E_r' = \frac{K_S\sqrt{\pi}}{2\sqrt{A}}, \quad E_r'' = \frac{\omega C_S\sqrt{\pi}}{2\sqrt{A}} \text{ and } \quad \tan\delta = \frac{C_S\omega}{K_S}$$

where A is a projected contact area. The procedure of dynamic nanoindentation according to Asif et al. (1999)[3] is implemented within TriboScan software as well as a calibration procedures and an analysis.

3. Results

Fig. 2 shows that storage and loss moduli are dependent on the frequency. Both moduli increase in all range of the frequency. Fig. 2 shows that average values of storage and loss moduli slowly increase from vertebral bone to annulus fibrosus region (from area 01 to area 04). Fig. 3 shows increasing trend of tan δ within frequency, which represents increasing damping during the experiment.

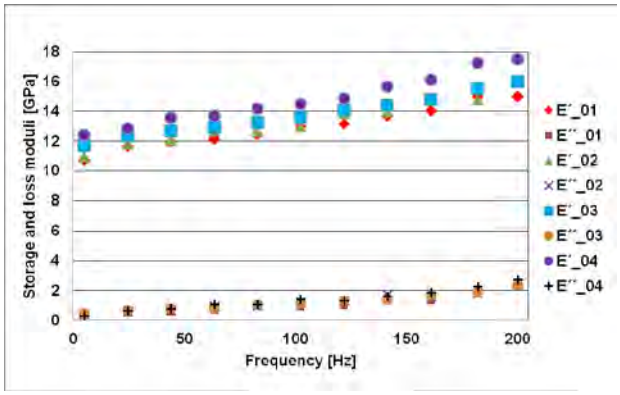

Fig. 2. **Storage (*E´*) and loss (*E´´*) moduli vs. frequency for all tested areas**

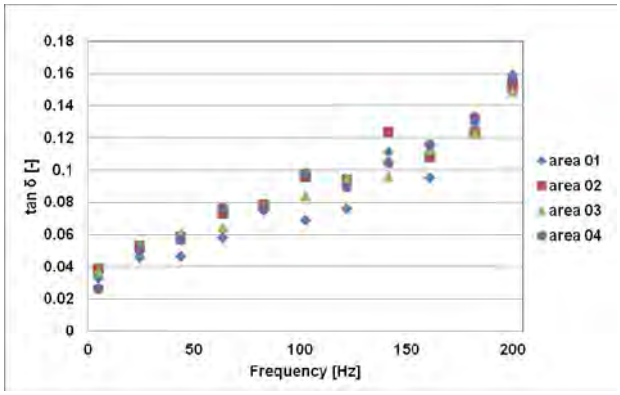

Fig. 3. **Tan δ *vs.* frequency from nanoDMA for all tested areas of the sample**

4. Discussion

Increasing trend of tan δ also indicates increasing amount of dissipation of deformation energy. In other words, viscose element represented by loss moduli increase faster than storage moduli with a strain rate and influences the mechanical behavior of the tissue. We cannot find any slope change in the tan δ trends (Fig. 3) that is usually characterized by an inflection points. Inflection points represent critical values of stiffening (decrease of tan δ) or localized softening (increase of tan δ) of the sample material. It is a question if we can find inflection points in wider range of the frequency as was shown for the cartilage?[1] Analyzed sample seems to be softer with increasing frequency which means that dried endplate has an ability to dissipate more energy at higher frequencies at our frequency range.

5. Conclusions

We obtained local dynamic mechanical properties of a dry porcine intervertebral endplate, which were stained with hematoxylin-eosin, localized by fluorescence microscope using nanoindentation. The combination of both methods shows that we are able to localize and describe particular tissues and their transitions. Damping of the endplate increases during the experiment without critical values of stiffening or localized softening. NanoDMA method is the fastes way of measuring the material characteristics dependent on loading rates. Our end plate sample showed clear dependence on loading rate represented by ramping frequency.

This work was supported by the Grant Agency of the Czech Technical University in Prague, under the project no. SGS10/247/OHK2/3T/12.

REFERENCES

1. Sepitka J., Otahal M., Lukes J.: Comput Method Biomech. *14*, 265 (2011).
2. Sepitka J., Lukes J., Kuzelka J., Rezníček J.: Chem. Listy. *105*, s844 (2011).
3. Asif S. A. S., Wahl K. J., Colton R. J.: Rev. Sci. Inst. *70*, 2408 (1999).

J. Šepitka[a], J. Lukeš[a], L. Staněk[b], and J. Řezníček[a]
([a] Czech Technical University in Prague, Faculty of Mechanical Engineering, Dept. of Mechanics, Biomechanics and Mechatronics, [b] Institute of Pathology, General Faculty Hospital, Charles University, Czech Republic): **Dynamic Mechanical Properties of Soft Tissues Localized by Fluorescence Microscope Obtained Using Nanoindentation**

The paper deals with an assessment of material characteristics of particular substructure of soft tissues their transition by mean of fluorescence nanoindentation.

Ten millimeter thick plates of native lumbar spine motion segments were dissected from sagittaly halved porcine spine. 7–10 μm sections were cut in an angle of 45° to transversal plane using a microtome. They were stained with hematoxylin-eosin afterwards. We obtained dependancies of storage and loss moduli on the frequency range 5–200 Hz. Damping trends and viscosity were discussed in this paper as well.

COMPOSITION, STRUCTURAL AND MATERIAL PROPERTIES OF LEECH TEETH – EXAMPLE OF BIOINSPIRATION IN MATERIALS RESEARCH

JOSEF ŠEPITKA[a], JAROSLAV LUKEŠ[a], ONDŘEJ JIROUŠEK[b], DANIEL KYTÝŘ[b], and JAROSLAV VALACH[b]

[a] *Czech Technical University in Prague, Faculty of Mechanical Engineering, Technická 4, 166 07 Prague 6,* [b] *Institute of Theoretical and Applied Mechanics, Academy of Sciences of the Czech Republic, v.v.i., Prosecká 76, 190 00 Prague 9, Czech Republic*
Josef.Sepitka@fsid.cvut.cz

Keywords: bioinspiration, atomic spectroscopy, nanoindentation

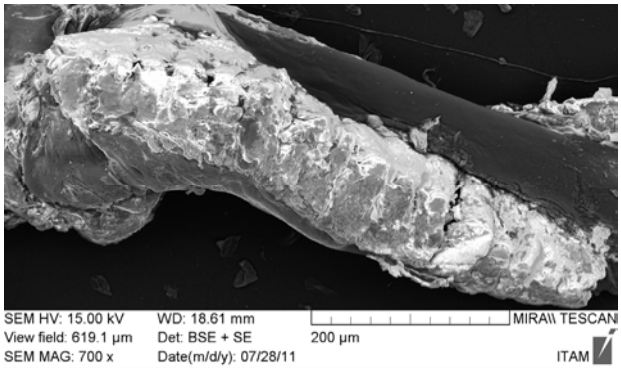

Fig. 1. **Top view on extracted leech's jaw with teeth line obtained by SEM with 700× magnification**

1. Introduction

The leech's sucking apparatus is an amazing instrument – it has 3 jaws and 300 teeth made for easily cut into the skin of the host animal. In ancient India and Greece, leeches have been used in medicine to remove blood from patients. Today, leeching is used rarely and the use of leeches has shifted into reconstructive and plastic surgery. Although there are a number of papers dealing with the leech stretch receptors, body wall muscles[1] or central nervous system CNS[2], there is no paper on the composition or material properties of its teeth. In this study we used nanoindentation and atomic spectroscopy to reveal composition and material properties of leech teeth and to demonstrate the optimization possibilities of nature to manufacture these very sharp and tiny blades which can easily penetrate the host's skin.

2. Experimental details

2.1. Sample extraction and preparation

Five samples of leech's jaws were obtained from adult subjects of *Hemopis sanguisuga*. The subjects were euthanised with ether and sliced in area of sucking apparatus. Individual jaws with length around 500 µm (depicted in Fig. 1) were carefully separated under magnification glass (5×) using a sharp-tip scalpel, microretractores and pair of tweezers. The samples were cleaned from the soft tissues and embedded in low shrinkage epoxy resin.

The surface of the samples was grinded and polished. Diamond grinding discs followed by monocrystalline diamond suspension were used for grinding procedure[3]. The best reached final surface roughness average (R_a) was 16 nm. All samples were prepared with roughness less than 40 nm, which is adequate value for micromechanical testing.

2.2. Mechanical testing

Quasi-static nanoindentation was performed using the nanomechanical instrument Hysitron TI 950 TriboIndenter™. Berkovich diamond tip, (triangular pyramids with angle of 142.3°) was used to obtain elastic properties of the teeth. The test was performed in three segments. Loading, constant force, unloading phase of the test were prescribed. Maximum force was reached at 5 s, then 2 s of dwell and 5 s of unloading followed.

The first set of 5 indents were performed on the sample with roughness approximately R_a = 40 nm. To reduce the influence of roughness on results, a force of P_{max} = 8000–8300 µN was applied resulting in indents depth app. 500 nm. Then the sample was polished again to

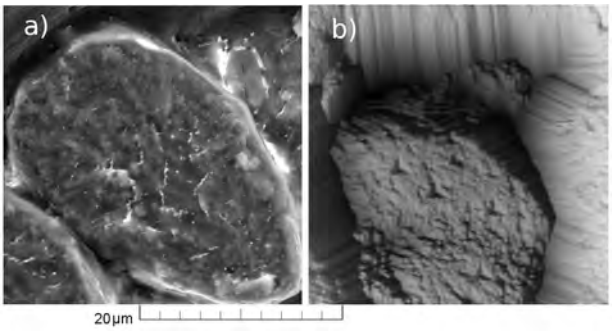

Fig. 2. **Detail of tooth (a) obtained by SEM with 8000x magnification (b) surface reconstruction with indents obtained by scanning probe microscopy (SPM) of image size 40×40 µm**

decrease its roughness down to R_a = 16 nm. The force of P_{max} = 900 μN corresponding to $h_{max} \approx$ 150 nm was used at this time. The force-depth curves were plotted for each indent, and reduced moduli were calculated using the Oliver-Pharr method[4].

2.3. Composition analysis

Morphological investigation of leech's teeth depicting its true size and shape has been accompanied with composition microanalysis. The microanalysis was carried out by Bruker Quantax energy dispersive spectrometer installed in Tescan MIRA II scanning electron microscope (SEM). Concentration of individual elements was determined from the relative intensity of their characteristic X-ray spectra by the Esprit program provided by microanalyser manufacturer. By the nature of elemental microanalysis it is impossible to identify molecular composition of the studied matter, only elemental composition is as the result available. From the composition analysis as the significant elements and their respective concentrations are calcium, oxygen and carbon were identified.

3. Results

In this preliminary analysis, the main constituents of leeche teeth have been identified. The tooth is composed mainly of calcium (41.9 %), oxygen (41.2 %) and carbon (11.4 %), other constituents are present in small quantities (F 2.1 %, Na 1.0 %, P 0.9 %, S 0.6 % and Mg 0.6 %). Therefore, a substance typical for mineral component in bones, hydroxyapatite is likely present in the teeth among other substances.

The mechanical properties of two leech teeth were measured in cross-section (depicted in Fig. 2). The average value of reduced modulus E_r = 29.41±1.10 GPa was obtained from 5 indents of the first test ($h_{max} \approx$ 500 nm, R_a = 40 nm). In the next measurement of 10 indents, the average modulus was E_r = 27.02±4.03 GPa ($h_{max} \approx$ 150 nm, R_a = 16 nm). These values correspond to the values from measurements on cortical bone and tooth dentin[5].

4. Conclusions

From the results of the nanoindentation it could be concluded that the mechanical properties of leech's tooth are independent on indentation depth. High-precision surface preparation allows indenting in small depths with a high accuracy. Another advantage of an achievement of very low roughness can be seen in the possibility for the placement of more indents in the same area. Reduction of indent size is very desirable because of the tiny cross section of the tooth surface, which is smaller than 1000 μm^2.

Mechanical properties and composition microanalysis of the teeth corresponding to biomaterials such as cortical bone or dentin[5] offers the assumption that it is possible that the tooth surface could be composed of enamel, as it is at higher animal species. Therefore, it would be beneficial to prepare longitudinal cuts of leech's teeth, which would enable the indentation of superficial layer and inner part of the teeth. Assessment of mechanical properties from different anatomical parts could help to determine whether the outer layer is created by enamel, and whether the inner part is composed of dentin. Based on this information, an accurate constitutive material model can be created.

The research has been supported by the Grant Agency of the Czech Republic (grant No. P105/10/2305), Ministry of Education of the Czech Republic: Transdisciplinary research in Biomedical Engineering II. No. MSM 6840770012 and research plan of the Academy of Sciences of the Czech Republic AV0Z20710524.

REFERENCES

1. Blackshaw S. E: Comp. Biochem. Phys. A, *105*, 4 (1993).
2. Elliot E. J., Muller K. J.: Brain Res. *218*, 1–2 (1981).
3. Dudíková M., Kytýř D., Doktor T., Jiroušek O.: Chem. Listy *105*, S (2011).
4. Oliver W. C., Pharr G. M.: J. Mater. Res. *7*, 6 (1992).
5. Lewis G., Nyman J. S.: J. Biomed. Mater. Res. B *87B*, 1 (2008).

J. Šepitka[a], J. Lukeš[a], O. Jiroušek[b], D. Kytýř[b], and J. Valach[b] *([a] Czech Technical University in Prague, Faculty of Mechanical Engineering, Prague, [b] Institute of Theoretical and Applied Mechanics, Academy of Sciences of the Czech Republic, v.v.i., Prague, Czech Republic):*
Composition, Structural and Material Properties of Leech Teeth – Example of Bioinspiration in Materials Research

The leech's sucking apparatus is an amazing instrument – it has 3 jaws and 300 teeth made for easily cut into the skin of the host animal. In this study, we used nanoindentation and atomic spectroscopy to reveal composition and material properties of leech teeth. Five samples of leech jaws obtained from adult subjects of *Hemopis sanguisuga* were investigated. Main constituents of leech teeth have been identified. The tooth is composed mainly of calcium (41.9 %), oxygen (41.2 %) and carbon (11.4 %), other constituents are present in small quantities (F, Na, P and S), and therefore, a substance typical for mineral component in bones hydroxyapatite is likely present in the teeth among other substances. Material properties, which are independent on indentation depth, examined by nanoindentation provided average reduced modulus E_r =27.54±3.71 GPa.

NANOINDENTATION BASED MICROANALYSIS OF HENS' BONES

LIBOR SEVERA[a], JIŘÍ NĚMEČEK[b], LADISLAV MÁCHAL[a], JIŘÍ VOTAVA[a], and JAROSLAV BUCHAR[a]

[a] Mendel University in Brno, Faculty of Agronomy, Zemědělská 1, 613 00 Brno, [b] Czech Technical University in Prague, Faculty of Civil Engineering, Thákurova 7, 166 29 Praha 6, Czech Republic
jiri.nemecek@fsv.cvut.cz

Keywords: hen bone, micro-mechanical properties, nanoindentation, elastic constants

1. Introduction

Bone mechanical properties and the presence of fractures in laying hens are both a welfare and an economic concern for the poultry industry. The mechanical properties of the bone have significant importance, especially in understanding fracture behavior as a function of mineralization. If we can obtain an insight into the determinants of the bone strength, then better methods to monitor and select animals with abnormal bones can be identified. The composition of the bone tissue is extremely complex compared to most engineering composites[1]. The organization of the bone within a Haversian system consists of a central canal surrounded by concentric lamella. Lamellae are observed at the level of a light microscope. A number of attempts have been made to describe the biomechanical properties of the bone at this level[1], but this description does not go beyond the histological level. The mechanical properties of cortical bones (including some micromechanical aspects) were described and reviewed in classical work by Reilly and Burstein[2] already in 1974 and more recently by Mammone and Hudson[3]. If one considers the elements that comprise a bone at the molecular level, at which the collagenous matrix and hydroxyapatite crystals appear, then a more fundamental understanding may be achieved. The view that bone may be considered as a two-phase composite to explain its mechanical properties was firstly suggested by Currey[4] back in 1964.

Concerning hens' bones (and similarly eggshells), different aspects such as genetic components[5], diet[6], breeding conditions[7] and/or hen breed[8] were monitored as determining factors. The differences between individual birds in terms of e.g. bone fracture incidence can not be explained by a sole factor. Differences can occur due to calcium metabolism, bone structure, or simply due to the body weight differences. A combination of factors is most likely involved[9]. Micro mechanical properties significantly affect the mechanical behaviour of the whole bone, as it was documented in number of works[10,11] and their detailed determination and interpratation is thus needed. One of the effective, precise and well-proven tools is the nanoindentation.

Nanoindentation has been previously used to compare the bone tissue properties in healthy bones with those of diseased and genetically modified small animal models (including mice, rats, and zebrafish)[12].

In nanoindentation, a small probe with nano-meter dimensions contacts a flat, prepared surface of a material. The resulting force and contact depth (i.e., displacement) data enable the calculation of elastic, plastic, and viscous material properties[13–15] of biological tissues like cortical or trabecular bones[16] or eggshells[17] at a spatial resolution similar to that of the tissue-level structural features in the bone. Nanoindentation can be also used to measure the creep behavior of biological tissues by fitting the depth vs. time data at constant load to rheological models[18]. Viscoelasticity may affect both the elastic and fracture characteristics of the bone[19,20].

In particular, nearly all of the nanoindentation studies on bio-tissues reported to-date employed the Oliver–Pharr method[13] to obtain elastic modulus and hardness values from the nanoindentation data. The basic assumption involved in this method is that the sample behaves purely elastically during unloading, but biological tissues such as bone are well-known to be viscoelastic in both the macroscopic level as well as the microstructural level[21]. Material viscoelastic effects during unloading are well-known to lead to erroneous results in the estimation of contact stiffness and area using the Oliver-Pharr method[13], and in the past, increasing the holding time before unloading and increasing the unloading rate have been suggested as effective procedures to reduce viscoelastic effects during unloading[20,22,23]. An alternative solution is to allow the viscoelastic effects to occur. But then a method that has been well established in monolithic engineering materials to correct for the viscoelastic effects should be used[24].

This study is focused on the use of nanoindentation as a tool for quantification the differences between micro mechanical properties of femoral cortical bone of healthy laying hen and laying hen with defective calcic metabolism.

2. Materials and methods

2.1. Hens' femoral bones

Two bone tissues were compared, both belonging to Rhode Island Red (RIR) laying hen, caged and fed in identical conditions in the breeding station in the Czech Re-

public. The birds were kept in the three-floor cage housing, with 650 cm^2 floor space of individual housing. One of the tissues was extracted from the cortical part of a femoral bone of clinically healthy hen (51 weeks old) with the incidence of cracked eggs lower than 2 % (further denoted as Healthy-series). The second one was extracted from the cortical part of a femoral bone of a hen with calcium metabolism defect (denoted as Ill-series). This defect was shown by a high presence of cracked eggs (more than 20 %).

2.2. Preparation of specimens

The bone specimens were dissected from the femoral diaphysis of a mature hen (RIR) and dried for 48 hours at room temperature. Effect of the bone drying and affecting the values of Young's modulus and hardness was documented for bovine bones[25] but not for hen's bones so far. The samples were milled down to a cylindrical shape of 10 mm in height, their main (cylindrical) axis being aligned with the longitudinal direction of the diaphysis. The specimens geometry and different stages of the testing procedure are shown in Fig. 1. After this preparatory step, the specimens were embedded into metacrylate tablet. The specimens were cold-prepared (the structure was not thermally affected). Commercially available two-component resin was used for metacrylate mixture preparation and the specimens were left to dry and cure for 8 hours. The tablets were polished in order to achieve flat surface with maximum roughness of 10–20 nm.

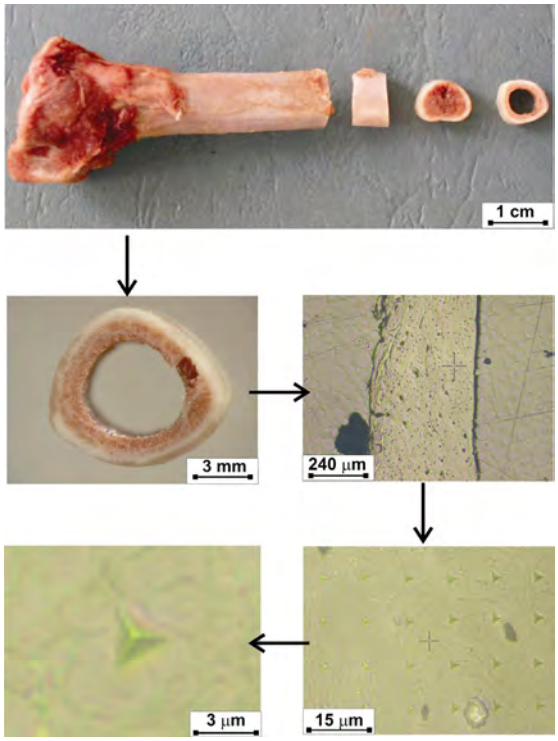

Fig. 1. **Preparation and testing of specimen in different scale levels**

2.3. Experimental set-up and loading conditions

The experiments were performed using nanohardness tester (CSM Instruments, Switzerland). A standard Berkovich tip was brought to the sample surface, producing a series of imprints. Influences of the tip geometry, contact depth, and contact area on nanoindentation properties of the bone were broadly discussed in literature[26], and the results were used for the configuration of presented experiments. The indenter has a nominal tip radius of $R \approx 50$ nm and a half-angle apex of $\theta = 65.27°$. The bone fragments were loaded in directions perpendicular to the cross-sections. Load vs. depth of penetration was measured throughout the whole procedure of loading, holding, and unloading. The load-controlled test was performed using the standard trapezoidal loading diagram as follows: linear loading (60 mN min^{-1}) up to the peak force (5 mN), then a 10 s holding period at the maximum force and linear unloading (60 mN min^{-1}) to zero force level (Fig. 2). Each sample cross-section was covered with a grid of 80 indents with 12 μm spacing. Similar experimental procedure and set-up was used e.g. by Severa et al.[17].

3. Results

Elastic modulus (E) and indentation hardness (H) were evaluated by standard procedure from unloading branches of a loading diagram[13] for each indent. Although, the elastic parameters show high scatter easily distinguishable decrease in both E and H can be observed for Ill-series as depicted in Figs. 3 and 4.

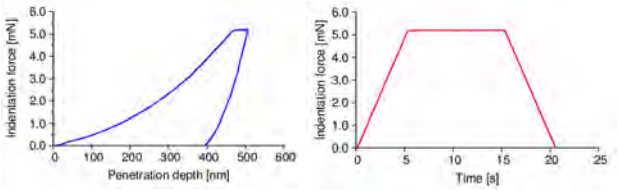

Fig. 2. **Example of a typical nanoindentation loading diagram**

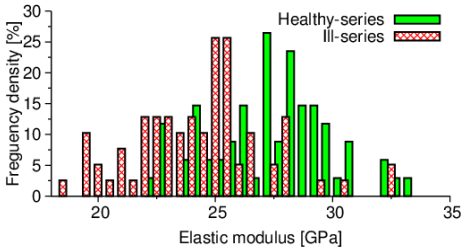

Fig. 3. **Histograms of elastic moduli for Healthy- and Ill-series**

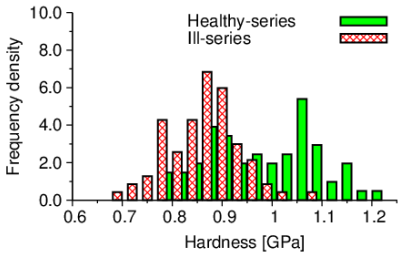

Fig. 4. **Histograms of indentation hardness for Healthy- and Ill-series**

The results of the performed experiments revealed that bone of a clinically healthy hen exhibited higher elastic modulus *E* and indentation hardness values *H*. It points to the fact that both elasticity and strength parameters (that are related to *H*) are afected in Ill-series. In case of non-defective tissue, following values were determined as: *E*=27.5±2.8 GPa, *H*=0.99±0.11 GPa, while in case of defective tissue as: *E*=24.5±3 GPa, *H*=0.88±0.07 GPa. Generally speaking, the values measured on the defective bone are approximately 11 % lower.

Based on optical microscopical observations, the healthy bone tissue contained larger pores in comparison with defective one. Interpretation of this fact needs much deeper investigation.

4. Discussion

This study utilised nanoindentation to investigate the mechanical properties of the microstructure of bone from the mid-femoral diaphyses of healthy and defective laying hen. Unlike the more conventional microhardness techniques, nanoindentation provides both modulus of elasticity and hardness estimates for a material and can be used to target specifically various bone tissue structures at a microscopic level.

A strong motivation behind the use of nanoindentation is the potential to understand the mechanical competence of a whole bone in the light of the properties of its structural units (osteons and trabecular packets) that result from the ongoing remodeling activity. However, given the prohibitively wide range of elastic data measured using bending, buckling, tensile, ultrasound tests or calculated using inverse numerical techniques[27], it still remains unclear how the indentation modulus can be converted into the elastic response of the bone tissue measured at higher levels of its hierarchical organization[28,29].

In general, the variations that have been recorded in the elastic modulus at the bone matrix level are rather high. The elastic modulus ranged between 22 and 38 GPa in osteonal bone of healthy hen and 16 and 32 GPa in osteonal bone of defective hen. The large scatter in *E* (as well as *H*) can be attributed mainly to the naturally varying crystalographic orientations within the cross section of the bone (differently oriented anizotropic lamelas and its fibers)[28,29]. The shape of the *E* and *H* histograms shows also on some kind of bimodality in the case of Healty-series which could be related to the prefferential collagen fiber orientations in the tested area. Despite this fact, presented study was focused on the evaluation of average properties in one direction only to give overall insight into the problem. More detailed research is planned in the future.

5. Conclusions

In the current study the differences between healthy and defect cortical bone tissues were documented and analysed in an average sense. Elastic modulus and hardness droped down by ~11 % for defected series. Similar approaches as used for studying human bones were employed. The data revealed and confirmed the fact that mechanisms described for human tissues can be largely adopted and used for detailed further research of hens' bones as well.

The research has been supported by the Grant Agency of the Czech Academy of Sciences under Contract No. IAA201990701 and Ministry of Education of the Czech Republic (Research Plan MSM 6840770003).

REFERENCES

1. Ascenzi A.: J. Biomech. Eng. *110*, 357 (1988).
2. Reilly D. T, Burstein A. H.: J. Bone and Joint Surgery *56*, 1001 (1974).
3. Mammone J. F., Hudson S. M.: J. Biomech. *26*, 439 (1993).
4. Currey J. D.: Biorheology *2*, l (1964).
5. Bishop S. C., Fleming R. H., McCormack H. A., Flock D. K., Whitehead C. C.: British Poultry Sci. *41*, 33 (2000).
6. Lichovníková M., Zeman L., Jandásek J.: Czech J. Animal Sci. *53*, 7 (2008).
7. Lichovníková M., Zeman L.: Czech J. Animal Sci. *53*, 162 (2008).
8. Máchal L., Jeřábek S., Zatloukal M., Straková E.: Czech J. Animal Sci. *49(2)*, 51 (2004).
9. Clark W. D., Cox W. R., Silversides F. G.: Poultry Sci. *87*, 1964 (2008).
10. Hengsbergera S., Enstroema J., Peyrinb F., Zysset Ph.: J. Biomech. *36*, 1503 (2003).
11. Baranová D., Pešek L., Sály J.: Folia Veterinaria *52*, 168 (2008).
12. Ebenstein D. M., Pruitt L. A.: Nano Today *1*, 26 (2006).
13. Oliver W. C., Pharr G. M.: J. Mater. Res. *7*, 1564 (1992).
14. Oyen, M. L., Cook, R. F.: J. Mater. Res. *18*, 139 (2003).
15. Olesiak S. E., Oyen M. L., Ferguson V. L.: Mechanics of Time-Dependent Mater. *14*, 111 (2010).
16. Jiroušek O. et al.: Chem. Listy *105* (*S*) (2010).
17. Severa L., Němeček J., Nedomová Š., Buchar J.: J.

Food Eng. *101*, 146 (2010).
18. Menčík J., He L. H., Němeček J.: Polymer Testing *30*, 101 (2010).
19. Němeček J.: Mater. Charact *60*, 1028 (2009).
20. Wu Z., Baker T. A, Ovaert T. C, Niebur G. L.: J. Biomech., *in press* (2011).
21. Wang, X. M., Cui F. Z., Ge J., Zhang Y., Ma C.: Biomaterials *23*, 4557 (2002).
22. Cheng Y. T., Ni W. Y., Cheng C. M.: J. Mater. Res. *20*, 3061 (2005).
23. Bushby A. J., Ferguson V. L., Boyde A.: J. Mater. Res. *19*, 249 (2004).
24. Tang B., Ngan A. H. W., Lu W. W.: J. Mater. Sci.: Mater. Medicine *18*, 1875 (2007).
25. Rho J. Y., Pharr G. M.: J. Mater. Sci.: Mater. Medicine *10*, 485 (1999).
26. Paietta R. C., Campbell S. E, Ferguson V. L.: J. Biomech. *44*, 285 (2011).
27. Guo X. E.: *Mechanical properties of cortical bone and cancellous bone tissue*. In: (Cowin S., ed.)), Bone Mechanics Handbook, 2nd Edition. CRC Press, Boca Raton 2000.
28. Hengsberger S., Enstroem J., Peyrin F., Zysset P. K.: J. Biomech. *36*, 1503 (2003).
29. Zysset P. K.: Osteoporosis Int. *20*, 1049 (2009).

L. Severa[a], J. Němeček[b], L. Máchal[a], J. Votava[a], and J. Buchar[a] *([a]MENDELU, Brno, [b]CTU in Prague, Czech Republic):* **Nanoindentation Based Microanalysis of Hens' Bones**

The research is focused on the use of nanoindentation as a tool for quantification of the differences between micro mechanical properties of femoral cortical bone of healthy laying hen and laying hen with defective calcic metabolism. In general, the variations that were recorded in the elastic modulus at the bone matrix level are rather high. The elastic modulus ranged between 22 and 38 GPa in osteonal bone of healthy hen and 16 and 32 GPa in osteonal bone of defective hen. The shape of the *E* and *H* histograms shows also some kind of bimodality, which can be related to prefferential collagen fiber orientations in the tested area.

MICROSTRUCTURE CHARACTERISTICS OF Fe-0.85Mo-3Mn-0.5C SINTERED STEEL IN DEPENDENCE ON SINTERING CONDITIONS

VLADIMÍR SIMKULET, and ĽUDOVÍT PARILÁK

Faculty of Manufacturing Technologies of the Technical University of Kosice with a seat in Presov, Bayerova 1, 080 01 Presov, Slovak Republic
vladimír.simkulet@tuke.sk

Keywords: powder metallurgy, alloying, microhardness measurement

1. Introduction

The development of new alloys, based on composition containing Mn with possible addition of Mo, is an important attempt to increase the application of different sintering processes, especially when special use are required. Moreover, the presence of Mn and Mo as alloying elements is very important; in fact they are helpful to improve hardenability and the mechanical properties[1–7]. However, due to the high dew point, Mn oxides are not reduced during the sintering cycle at atmosphere with dew point approximately –25 °C, accordingly Mn had been avoided, in the past, in ferrous powder metallurgy[8]. The problem of oxide network formation in PM steels with different Mn contents was investigated in ref.[9]. The paper describes local mechanical properties evaluated by microhardness measurement and alloying process after difference sintering conditions. Microhardness was measured in the due zone, in core of iron particles and measured in thick alloyed surface layer. Vickers microhardness test was evaluated on metallographic cross-sections according to STN EN ISO 6507, testing equipment Leco LM 700 with weight 25 g.

2. Experimental procedure

The following powders were used for the preparation of the samples:

- prealloyed Astaloy85Mo powder (Höganäs AB),
- atomized ASC100.29 powder (Höganäs AB),
- Manganese in form of medium carbon ferromanganese (80 % Mn, 1.1 % C, particle size < 45 μm, 0.67 % O, milled in air, EratemElkem),
- Natural graphite CR12 (Grafit Netolice).

The powders were mixed as two systems:
A) Fe – 0.85 % Mo – 3 % Mn – 0.5 % C (referred to as A)
B) Fe – 3 % Mn – 0,5 % C (referred to as B), both were prepared with 0.8 % HW wax as lubricant. The samples (ø 10 × 10 mm) made of the mixed powders compacted at 600 MPa were sintered in dissociated ammonia (dew point –30 °C) at 875 °C, 1120 °C and at 1200 °C for 1, 3, 5, 10, 30 and 60 min in a Mars furnace.

3. Results and discussion

The aim was the comparison of microstructure creation for iron and molybdenum powders independence on manganese addition at chosen sintering conditions, i.e. ferrous matrix alloyed by molybdenum and matrix without molybdenum alloying. Microstructure of samples for both systems A and B was covered after sintering for 1 min with a thin manganese alloying layer as a result of sublimation and condensation of manganese vapors. Centres of the particles remain ferritic. In the case of sintering time at 3 min, Fig. 1a, the matrix was alloyed by manganese along grain boundary – intensive bounders (diffusion to be at grain boundary faster than in a volume). It came to further highlight of grain boundaries and partly to alloying of centers of powder particles after sintering within 5 min. Character of microstructure samples of system B after sintering 30 min corresponds approximately to microstructure samples according to Fig. 1b. In system A sintered at 1120 °C during 1 min we observe more expressive alloying only on particles surface. On the other side system B alloying of core particles by manganese is more intensive at grain boundaries. This shows that the diffusion of manganese from surface was quicker due to higher sintering temperature in molybdenum alloyed matrix. Microstructure of this system was heterogeneous, but evidently different. Alloying of matrix extends in both systems after sintering for 3 min at sintering 1120 °C, but more in molybdenum alloyed.

After sintering at 1200 °C perhaps equal behavior of alloying matrix is observed but only with the difference that a higher homogeneity value of microstructure was achieved. Microstructure of system A evidently consists of bainite and manganese supports bainite formation especially after sintering at 1200 °C for 60 min.

Microhardness values for both systems are described in Fig. 2. Higher microhardness volumes were in samples

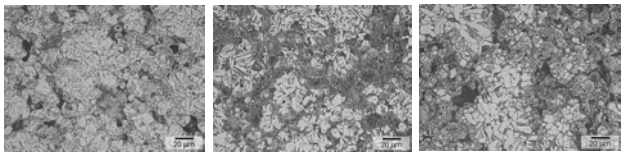

a b c

Fig. 1. **Sintering after 875 °C a) system A during sintering time 3 min, b) system B during sintering time 5 min, c) system B during sintering time 30 min**

prealloyed by molybdenum, Fig. 2a. Microhardness of edges particles at samples of B system after sintering at 875 °C was possible measured during sintering for 30 min only. This also shows the slower diffusion of manganese in iron matrix. It is clear that microhardness values were also affected by carbon in border areas. The microhardness values of microstructure samples sintered at 1120 °C are shown in Fig. 2b. This diagram evidently shows continuous increase of microhardness at borders and small change of microhardness in centre of elements systems. On basis of high microhardness value it can be expected that in border of manganese alloyed areas carbides type of (Fe-, Mo-, Mn-) C were created. The microhardness values of both types of samples after sintering at 1200 °C are shown in Fig. 2c. These microhardness values again show the molybdenum prealloyed matrix as uniform and more hardened, which can be caused as we already mentioned by carbides formation. Microhardness of grain borders corresponds to a martensite after longer sintering time.

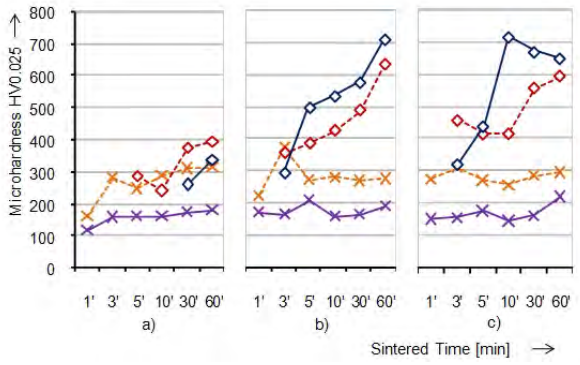

Fig. 2. **Microhardness values (HV0.025) of sintered systems. a) sintered after 875 °C, b) sintered after 1120 °C, c) sintered after 1200 °C.** Legend:

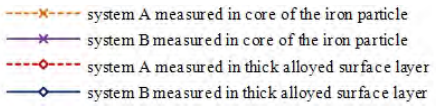

4. Conclusions

Following main results were obtained: Mo alloyed and Fe matrix of compacts samples are alloyed by manganese already at low temperature and apparently during a 3 min. By extension of sintering time and by higher sintering temperature the alloying process of matrix by manganese is reflected by the alloying of powder elements inside and by bigger or smaller homogeneity. We have found out in molybdenum alloyed matrix a more uniform alloying by manganese, which was demonstrated by higher microhardness values. Ferritic grains were located in iron matrix after longest sintering time and at higher sintering temperature. Microstructure of investigation material on bases of prealloyed powder affected by manganese comprised mainly bainite and the grains of ferrite occurred in microstructure of mixed system under all sintering condition.

Authors thank for supporting this research by structural funds of EU grant with ITMS 26220220125 of Agency of Ministry of education of Slovak Republic.

REFERENCES

1. Bidulský R., Grande M. A., Kabatová M.: Chem. Listy *105*, s14 (2008).
2. Šalak A., Vasilko K., Selecká M., Danninger H., Jakubéczyová D., Fáberová M.: Proc. DFPM (2005).
3. Kupková M., Kupka M., Strobl S., Hvizdoš P.: Chem. Listy *105*, s17 (2010).
4. Zubko P., Pešek L., Bláhová O.: Chem. Listy *105*, s17 (2010).
5. Matija R., Vojtko I.: Proc. Progressive Methods of Machining (2011).
6. Novák-Marcinčin J., Barna J., Nováková-Marcinčínová Ľ., Fečová V.: Tehnički Vjesnik *18*, 4 (2011).
7. Duszová A., Horňák P., Stoyka V., Hvizdoš P., Lofaj F., Dusza J.: Chem. Listy *105*, s17 (2011).
8. Castro F., García W., Sainz S.: World Congress on Powder Metallurgy and Particulate Mat. (2008).
9. Selecká M., Keresti R., Šalak A., Bureš R.: Acta Metallurgica Slovaca *7*, 1 (2001).

V. Simkulet, and Ľ. Parilák *(Faculty of Manufacturing Technologies of the Technical University of Košice with a seat in Prešov, Slovakia):* **Microstructures Characteristics of Fe-0.85Mo-3Mn-0.5C Sintered Steel in Dependence on Sintering Conditions**

Manganese in combination with Molybdenum atomized prealloyed powder forms a new group of sintered high strength steels. The final properties of these steels depend on microstructure homogeneity. The aim was to investigate the alloying of molybdenum prealloyed powder with manganese in comparison with plain iron powder. The circular cross section samples were prepared for the investigation from basis water atomized and plain iron powders. The microstructure characteristics of sintered samples were characterized by micro hardness measurement.

COMPARISION OF MECHANICAL PROPERTIES OF NITRIDED CASES AND REMELTED LAYERS OF AUSTENITIC STAINLESS STEEL

ARTUR SITKO, MAREK SZKODO, and BEATA ŚNIEGOCKA

University of Technology in Gdańsk, Faculty of Mechanical Engineering, Department of Materials and Welding Engineering, ul. Gabriela Narutowicza 11/12, 80-233 Gdańsk
asitko@mech.pg.gda.pl

Keywords: remelted layer, nitrided layer, austenitic stainless steel, diffusion layer, termochemical treatment, glow-discharge nitriding process, nanohardness

1. Instroduction

The austenitic stainless steels have very high general corrosion resistance, but they have low hardness and wear resistance. Nowadays, material technologies like laser remelting and low-temperature glow-discharge nitriding process can improve mechanical properties of austentic stainless steel without decrease the corrosion resistance. Laser remelting influence on refinement of microstructure and homogenizing of chemical composition of alloys was studied in ref[1–4]. If the austenitic stainless steels are subjected to glow-discharge nitriding prosess in low temperature, loss of corrosion resistance is not observed. At the temperatures above 450 °C, the precipitation of CrN was observed. The limiting temperature of nitriding process could be about 450 °C, according to the[5–8].

The aim of this article is an analyse of local mechanical properties of nitrided cases and remelted layers after the low temperature glow-discharge nitriding process and laser remelting, respectively.

2. Experimental procedures and results

Every test specimens (diameter of 20 mm and height of 6 mm) were made of austenitic stainless steel type X5CrNi18-10. Young‘s modulus of the steel substrate is approximetely 200±14 GPa and its hardness is about 220±3 HV20. The specimens were subjected to glow-discharge nitriding process at the temperature of 450 °C. Chemical composition of gas mixture during the termochemical treatment was different. Parameters of nitriding process are shown in Tab. I.

The same steel type X5CrNi18-10 was subjected to laser remelting. Laser remelting was done by means of laser MLT 2500 CO_2 (wavelength 10.6 μm) in argon atmosphere. During the laser remelting process no. 5 and 6 the specimens were also immersed in liquid nitrogen. The laser beam dimension 1×20 mm was used. Tab. II presents parametres of laser treatment.

Table I
Parametres of the glow-discharge nitriding process

Number of process	Vacuum pressure [hPa]	Time [h]	Temperature [°C]	Atmospheric composition	
				N_2	H_2
1	4	6	450	10	90
2	4	6	450	50	50

Representative picture of remelted layers is presented in Fig. 1. After laser remelting the surfaces were grinded off through 1200 grit SiC papers. The depth of the remelted layers depended on the laser power. Generally, the increase of the power caused a rise of thickness of the remelted layers.

Investigation of mechanical properties was carried out by using hardness tester with mounted Berkovich indenter. Mechanical properties of the diffusion layers were

Table II
Parametres of the laser remelting

Number of process	Scanning velocity [m min^{-1}]	Power [kW]	Scanning velocity [m min^{-1}]
3	2	2	0,25
4	2	5	0.25
5	2	2	0.25
6	2	5	0.25

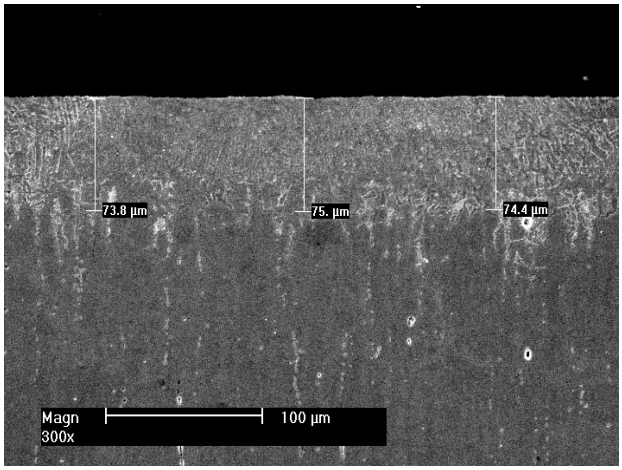

Fig. 1. **Microstructure of remelted layer after process laser remelting**

Table III
Mechanical properties of nitrided and remelted layers

Process	Nano hardness [HV]	Young's modulus [GPa]	Load [mN]
1	614±55	211±28	10
	524±71	201±19	20
	465±44	187±16	30
2	1056±13	232±28	10
	861±98	228±19	20
	737±59	198±18	30
3	352±32	227±17	10
	337±36	213±18	20
	327±22	192±16	30
4	412±42	235±21	10
	411±38	206±18	20
	330±22	192±19	30
5	432±67	227±23	10
	394±42	213±21	20
	377±43	192±17	30
6	432±54	235±26	10
	400±43	206±20	20
	368±32	192±14	30

examined on the surface of specimens using a different loads. Results of surface hardness were obtained by using different loads, respectively: 10, 20, 30 mN. Research was done by means of CSEM NanoHardnessTester (NHT) produced in Switzerland. Oliver-Pharr method was used for calculation of modulus. The value of Poisson's ratio was 0.3. Nanohardness was automatically recalculated between scales and presented in Vickers hardness scale. The results are shown in Tab. III.

3. Conclusion

1. Glow-discharge nitriding process has beneficial influence on nanohardness and Young's modulus.
2. The increase of nitrogen content in gas mixture influence on higher value of Young's modulus.
3. Laser remelting caused the refinement of microstructure in obtained surface layer.
4. Laser remelting process has beneficial influence on nanohardness and Young's modulus.

REFERENCES

1. Pan Q., Huang W., Song R., Zhou Y., Zhang G.: Surf. Coat. Technol. *102*, 245 (1998).
2. Khalfallah I., Rahoma M., Abboud J , Benyounis K.: Optics & Laser Technol. *43*, 806 (2011).
3. Kwok C., Man H., Cheng F.: Surf. Coat. Technol. *99*, 295 (1998).
4. Kwok C., Lo K., Chan W., Cheng F., Man H.: Corros. Sci. *53*, 1581 (2011).
5. F. Borgioli, A. Fossati, G. Matassini, E. Galvanetto, T. Bacci: Surf. Coat. Technol. *204*, 3410 (2010).
6. Köster K., Kaestner P., Bräuer G., Hoche H., Troßmann T., Oechsner M.: Surf. Coat. Technol. doi:10.1016/j.surfcoat.2011.10.059 (2011).
7. Li Y., Wang L., Xu J., Zhang D.: Surf. Coat. Technol. *206*, 2430 (2012).
8. Liang W., Xiaolei X., Zhiwei Y., Zukun H.: Surf. Coat. Technol. *124*, 93 (2000).
9. Liang W., Juncai S., Xiaolei X.: Surf. Coat. Technol. *145*, 31 (2001).

A. Sitko, M. Szkodo, and B. Śniegocka *(University of Technology in Gdańsk, Faculty of Mechanical Engineering, Department of Materials and Welding Engineering, Poland):* **Comparison of Mechanical Properties of Nitrided Cases and Remelted Layers of Austenitic Stainless Steel**

This article presents the results of nanohardness and Young's modulus of nitrided cases and remelted layers. The nitrided cases were obtained by using the glow-discharge nitriding process at the temperature of 450 °C. The termochemical treatment was done by using a different chemical composition of gas mixture (N_2:H_2). The laser remelting was done by using the TRUMPF laser TLF 6000 turbo in Kielce. The laser remelting was done by using different parameters of termochemical treatment. Investigation of mechanical properties was carried out by using hardness tester with mounted Berkovich indenter. Mechanical properties of the diffusion and remelted layers were examined on the surface of specimens using different loads.

NANOINDENTATION TESTING OF LOW-ALLOYED MOLYBDENUM SINGLE CRYSTALS

KATEŘINA SKOTNICOVÁ[a], MICHAL VYLEŽÍK[b], VLASTIMIL MATĚJKA[c], and JAROMÍR DRÁPALA[a]

[a] *Department of Non-ferrous Metals, Refining and Recycling, VŠB – Technical University of Ostrava, Av. 17. listopadu 15, 708 33 Ostrava-Poruba,* [b] *Centre for Advanced Innovation Technology, Av. 17. listopadu 15, 708 33 Ostrava-Poruba,* [c] *CNT – Nanotechnology Centre, Av. 17. listopadu 15, 708 33 Ostrava-Poruba, Czech Republic*
Katerina.Skotnicova@vsb.cz

Keywords: nanoindentation, molybdenum alloy, single crystal, hardness, elastic modulus

1. Introduction

Nanoindentation methods are applied to study nano-scale material deformations and enable accurate measurements of indentation load (*P*) and penetration depth (*h*). Mechanical properties, Young´s modulus and hardness can be obtained from nanoindentation by numerical calculations of the load-displacement curves including loading and unloading process according to Oliver-Pharr method (ref.[1–4]). Recent research has shown that the hardness determined by nanoindentation depends on a test load, i.e. hardness at small depth is much greater than at greater depth. This phenomenon is called the Indentation Size Effect (ISE) (ref.[5,6]). Another method used to measure hardness from load-depth curves is work-of-indentation method. The total mechanical work of indentation can be determined by computing the area under the force increasing portion of the test force vs. indentation depth curve (ref.[7]). The total work includes two components: elastic and plastic. The elastic work can be obtain by the area under the force decreasing portion of the *F* vs. *h* curve, and the plastic work can be determine from the area between the force increasing and force decreasing curve.

Work of indentation method as a means of determining hardness was first proposed by Stillwell and Tabor (ref.[8]). The conventional representation of hardness, maximum applied load *P* divided by the residual area of indent impression A_p, is equivalent to the ratio of plastic work W_{pl} to the plastic deformed volume of the indent V_{pl} (ref.[7, 8]):

$$\frac{F}{A_F} = \frac{W_{pl}}{W_{el}} \qquad (1)$$

The total work W_t can be obtained by integrating loading curve:

$$W_t = \int_0^{h_{\max}} P(h)dh = \int_0^{h_{\max}} Ch^2 = \frac{P_{\max} h_{\max}}{3} \qquad (2)$$

For sharp indentation of elastic-plastic material, the loading response is governed by $P = Ch^2$. The ration h_f/h_{max} is equivalent to that of W_{pl}/W_t. The plastic work W_{pl} can be determined from Eq. (*3*):

$$\frac{W_{el}}{W_{pl}} = 1 - \frac{W_{pl}}{W_t} = 1 - \frac{h_f}{h_{\max}} \qquad (3)$$

where h_f is the final depth of contact impression after unloading and h_{max} the indenter depth at peak load. The hardness concerning total work of indentation, resp. plastic work of indentation can be calculated from Eq. (*4*) (ref.[9]), where κ is a constant equal to 0.0408 for the three sided Berkovich pyramidal indenter:

$$H_{Wt} = \frac{\kappa P_{\max}^3}{9W_t^2} \quad \text{resp.} \quad H_{Wpl} = \frac{\kappa P_{\max}^3}{9W_{pl}^2} \qquad (4)$$

Atomic force microscopy (AFM) can be used for imaging of residual indentations and obtaining accurate dimensional information from an image area of only a few microns.

In this paper, the indentation hardness, Young´s modulus, total and plastic work of pure and low-alloyed molybdenum single crystals are investigated. We compare hardness from the Oliver and Pharr analysis (H_{IT}) and the work-of-indentation method described above. The influence of niobium as an alloying element and crystallographic orientation of single crystals on these nano-scale properties is studied. The effect of the load on pile-up formation is also investigated using AFM imaging.

2. Experimental

Bulk single crystals of Mo-2 wt.% Nb with crystallographic orientation <110> and <100> were used for the experiment. The pure molybdenum single crystal with crystallographic orientation <110> was included in the experiment due to a study of the influence of niobium on the mechanical properties of molybdenum single crystal. All single crystals were prepared by the electron beam zone melting (method of floating zone). The surface of specimens was polished using diamond pastes and *electrolytically in NaOH solution.* The indentation experiments were conducted with the standard three-sided pyramidal Berkovich tip using Triboindenter TI 950 (Hysitron). The tip radius was about 150 nm. For an easier interpretation of mechanical behaviour at various depth, the maximum load

was changed at intervals: 1000, 2000, 3000 and 4000 μN and then unloaded. The dwell time was 2 s. For each material, six indentations were made at each load and the presented results are averages for the group. These indentation loads corresponds to applied depths from 69 to 190 nm for all specimens. The topography of the selected indents was acquired using atomic force microscope SOLVER Next™ (NT-MDT) operated in contact mode. The probes PPP-CONTR (Nanosensors) were used for imaging. The AFM images were processed using software Gwyddion (version 2.25).

3. Results and discussion

The load-depth curves for Mo-2 wt.% Nb <100> single crystal for all applied loads are given in Fig. 1 as an example.

The elastic recovery appears in load-depth curves during unloading processing for all specimens, but the elastic recovery of Mo-2 wt.% Nb with crystallographic orientation <100> is less than other specimens. Fig. 2 shows one of AFM 3D-images of indentations (load 4000 μN) for molybdenum-base single crystals. It is visible that edges of an indentation bend to center because of elastic recovery.

The hardness values H_{IT}, H_{Wt} and H_{Wp} of all specimens are plotted as a function of applied load in Fig. 3 to 5. The results display a strong size effect, i. e. the hardness decreases as the indentation load or indentation depth increases, which is commonly referred to as the indentation size effect (ISE). Numerous investigators have reported studies of ISE using nanoindentation testing for various materials (ref. [6,10,11]). The hardness values calculated using the plastic work of indentation are the highest, especially in smaller depth or for low applied loads. It was found that the hardness of all specimens estimated by the O-P method was significantly (up to 30 %) lower than the hardness calculated using the total work-of-indentation. There are only small differences between the values of hardness for both specimens of Mo-Nb single crystals with different crystallographic orientation. The plastic work must be less than total work, but the plastic hardness H_{Wpl} is larger than H_{Wt}.

The hardness values calculated from the work-of-indentation approach rise more steeply at lower applied load than the hardness values calculated by the O–P method. The reason of this effectcan be explained by the fact that the method of Tuck et al. (ref.[9]) makes no allowance for changes in tip geometry at lower indentation depths, where the tip geometry can significantly influence the calculated values, whereas tip geometry effects are allowed for in the O–P calculations.

At low loading, the indent behaviour of specimens is almost elastic deformation, increasing the Young´s modulus (E_{IT}) – Fig. 6. It was observed that the hardness and Young´s modulus of Mo-2 wt.% Nb single crystal with the

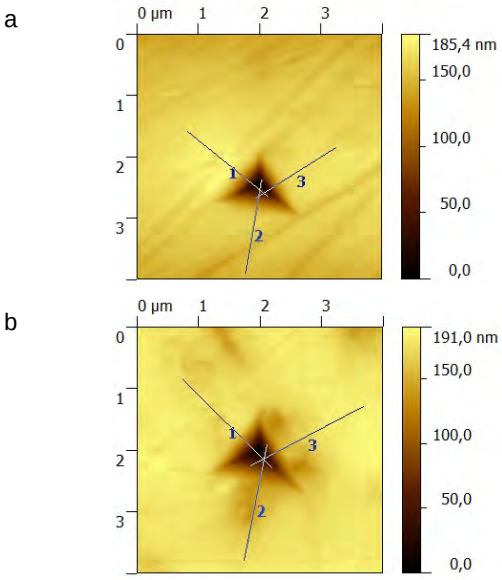

Fig. 2. **AFM images of Mo-Nb <110> (a) and Mo <110> (b) single crystals at load 4000 μm**

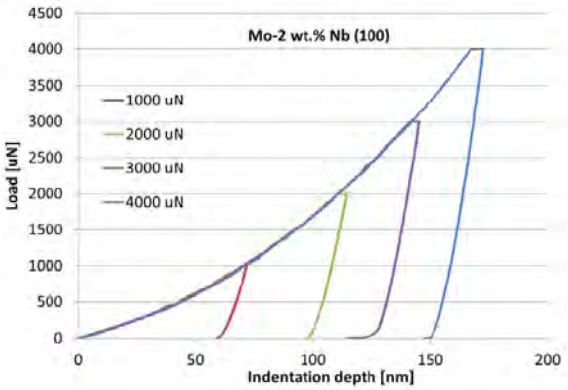

Fig. 1. **Load-depth curves of Mo-2 wt.% Nb <100> single crystal**

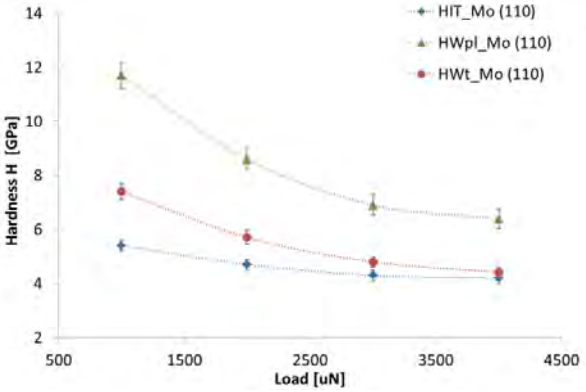

Fig. 3. **Comparison of hardness values obtained by two methods for pure Mo <110> single crystal**

orientation <100> increased at the indentation load 4000 μN probably results of the hardening effect (ref.[6]).

The contribution of the elastic work to total work decreases with increasing maximal load approx. from 21 to 17 % in the case of Mo-2 wt.% Nb and pure Mo single crystals with the orientation <110>. Because of the smaller elastic recovery for indentations into Mo-2 wt.% Nb <100>, there is lower differences between the total work of indentation approach and the plastic work of indentation approach – see Fig. 7.

There is the evident influence of crystallographic orientation of single crystals on mechanical properties. It is known that single crystals of molybdenum and its alloys show the anisotropy of mechanical properties, when the crystals with the crystallographic orientation <110> have much higher plasticity than these crystals with the crystallographic orientation <100> (ref.[12]). The Mo-Nb single crystal with orientation <100> has higher values of Young´s modulus and H_{IT} at most testing loads than adequate alloy with orientation <110>. The similar effect was observed in case of macro-scale testing of mechanical properties of Mo-Nb single crystals (ref.[12]). The alloying of molybdenum single crystal with niobium results in the increase of Young´s modulus and hardness.

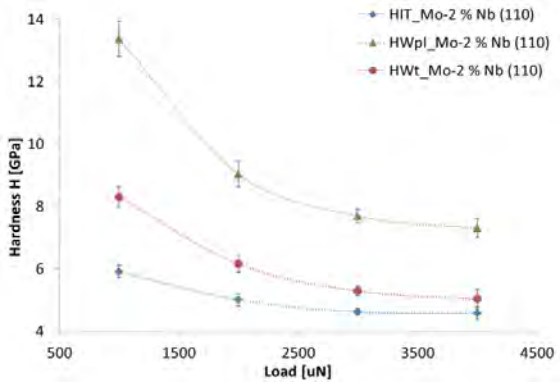

Fig. 4. **Comparison of hardness values obtained by two methods for Mo-2 wt.% Nb <110> single crystal**

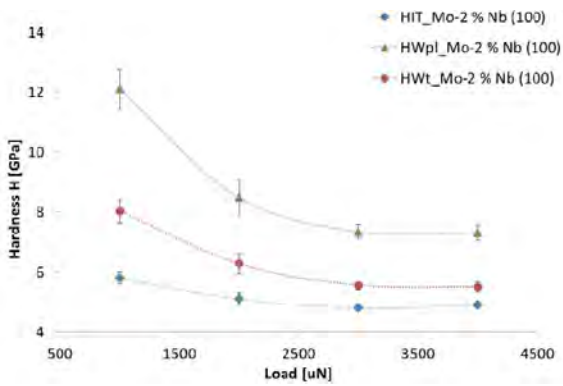

Fig. 5. **Comparison of hardness values obtained by two methods for Mo-2 wt.% Nb <100> single crystal**

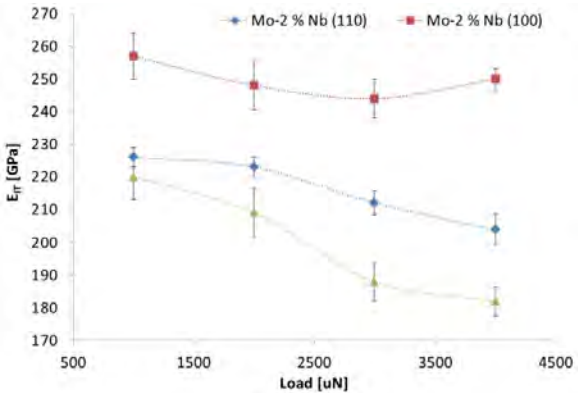

Fig. 6. **The load dependence of Young´s modulus for all single crystals**

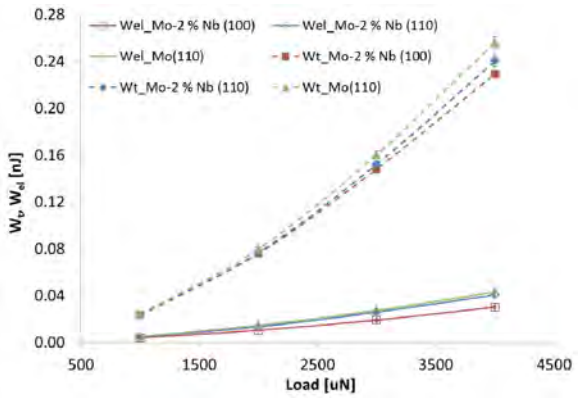

Fig. 7. **Work-depth curves for all single crystals**

The pile-up formation was visible in the AFM images of the indents only for Mo-2 wt.% Nb single crystal with orientation <100> (Fig. 8).

This result corresponds to findings by Stelmashenko et. al. (ref.[13]). In their study, the height of pile-ups on the (110) surface in molybdenum single crystal was very small for each of three different orientations of indenter, and there is no symmetry in the pile-up distribution.

4. Conclusions

The experiments and the above discussion yield the following results:

a) Under the same test condition, the nanohardness and Young´s modulus of all specimen declines as the load increases. The ISE of hardness values was observed.

b) The hardness estimated by the O-P method was significantly lower than the hardness calculated using the total work-of-indentation approach. The main advantage of work-of-indentation method is that there is no need to calculate the area of the indentation, which

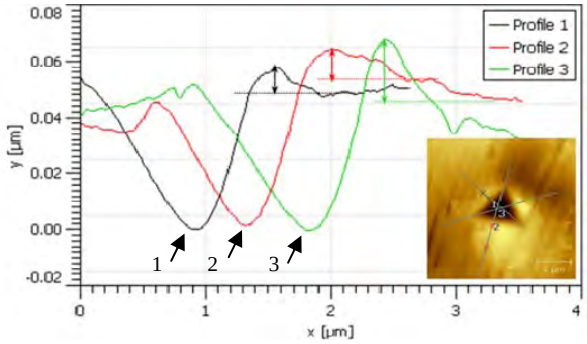

Fig. 8. **Height profile through an indentation (at 4000 mN) showing significant pile-up on the indentation edge in Mo-2 wt.% Nb <100>**

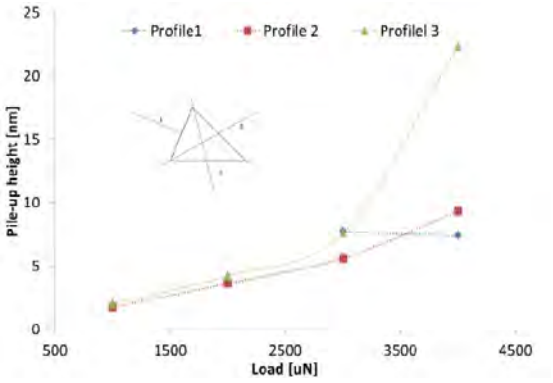

Fig. 9. **Plot of pile-up height with indentation depth in Mo-2 wt.% Nb <100>**

thus eliminates the problems caused by underestimating the contact area.

c) According to literature findings (ref.[12,13]), the hardness values should be higher for molybdenum-base single crystals with crystallographic orientation <100> than for these with crystallographic orientation <110>. The calculated H_{Wt} and H_{Wpl} values for the tested Mo-Nb single crystals don´t correspond to this fact. Thus the discrepancy of these hardness values must be examined.

d) Pile-up formation occurred at the edges of the indentations only in Mo-2 wt.% Nb single crystals with crystallographic orientation <100>. The widely used Oliver-Pharr model does not account for pile-up and consequently can overestimate hardness and elastic modulus.

e) It was confirmed that mechanical properties depend on the crystallographic orientations of single crystals. According to the results, the Mo-Nb single crystal with orientation <100> has higher values of E_{IT} than the same single crystal with orientation <110>. The alloying of molybdenum with niobium led to increasing of values of hardness and $E_{IT.}$

This work was elaborated in the frame of the research project MSM6198910013„Processes of preparation and properties of high purity and structurally defined special materials" and SP2011/170 "The anisotropy of micromechanical properties of selected type of steel".

REFERENCES

1. Oliver W. C., Pharr G. M.: J. Mater. Res. *7*, 1564 (1992).
2. Lucca D. A.: CIRP Ann-Manuf. Techn. *59*, *803* (2010).
3. Tricoteaux A., Duarte G., et al: Mech. Mater. *42*, 166 (2010).
4. Tabor D.: *The Hardness of Metals*. Clarendon Press, Oxford 1951.
5. Menčík J.: Chem. Listy. *105*, s115 (2011).
6. Voyiadjis G. Z., Peters R.: Acta. Mech. *211*, 131 (2010).
7. Beegana D., Chowdhury S., Laugier M. T.: Surf. Coat. Technol. *192*, 57 (2005).
8. Stilwell N. A., Tabor D.: Proc. Phys. Soc. *78*, 169 (1961).
9. Tuck J. R., Korsunsky A. M., et al.: Surf. Coat. Technol. *137*, 217 (2001).
10. Nix W. D. and Gao H.: J. Mech. Phys. Solids. *46*, 411 (1998).
11. Rashid K. Abu Al-Rub: Mech. Mater. 39 (2007).
12. Ljakišev N. P., Burchanov G. S.: *Metallic single crystals* (in Russian). ELIZ, Moskva 2002.
13. Stelmashenko N. A., et. al.: Acta Metal. Mater. *41*, 2856 (1993).

K. Skotnicová[a], M. Vyležík[b], V. Matějka[c], and J. Drápala[a] *([a] Department of Non-ferrous Metals, Refining and Recycling, VŠB – Technical University of Ostrava; [b] Centre for Advanced Innovation Technology, VŠB – Technical University of Ostrava; [c] CNT – Nanotechnology Centre, VŠB – Technical University of Ostrava, Czech Republic*): **Nanoindentation Testing of Low-Alloyed Molybdenum Single Crystals**

The indentation hardness, Young´s modulus, total and plastic work of pure and low-alloyed molybdenum single crystals were investigated. It was found that the hardness of specimens decreases as the indentation load or indentation depth increases due to the indentation size effect (ISE). The same trend was observed for the E_{IT} values of all specimens. The hardness estimated by the O-P method was significantly (up to 30 %) lower than the hardness determined using the total work-of-indentation approach. AFM 3D-images of indentations showed that pile-up formation occurred at the edges of the indentations only in Mo-2 wt.% Nb single crystals with crystallographic orientation <100>. It was confirmed that nanoscale mechanical properties depend on the crystallographic orientations of single crystals. The alloying of molybdenum with niobium led to increasing of values of hardness and $E_{IT.}$

INHOMOGENEOUS PLASTIC DEFORMATION OF TINPLATES UNDER UNIAXIAL STRESS STATE

EMIL SPIŠÁK, JÁN SLOTA, JANA MAJERNÍKOVÁ, ĽUBOŠ KAŠČÁK, and PETER MALEGA

Technical University of Košice, Letná 9, 042 00 Košice, Slovakia
emil.spisak@tuke.sk

Keywords: tinplate, plastic deformation, failure analysis

1. Introduction

Tinplate is essentially low carbon steel, cold reduced between 0.13 and 0.50 mm thick coated with tin produced for packaging industry. Modern tinplate possesses several important advantages, such as excellent drawability combined with good strength, good solderability and corrosion resistance. In many instances, special grades for specific can making techniques have been developed, e.g. for drawing and wall-ironing, redrawing and easy-open ends[1,2]. Their development has required close cooperation between packaging producers and tinplate manufacturers[3].

During the cold rolling on tandem mill the strength and hardness have been increased. On the other hand, the plastic properties of rolled materials have been decreased. To eliminate these negative changes in material, the recrystallization annealing is included in the sheet production process. Some products may be either batch annealed (BA) or continuously annealed (CA). Although the temper of the plate will be the same the mechanical properties may differ as CA plate has a finer grain structure (ref.[9,10]).

A number of materials exhibit discontinuous yielding under monotonic tension. A typical example is annealed mild steel. The monotonic stress–strain curve is not smooth but shows marked irregularities, with negative slopes occurring at or near the initial yield. Elastic deformation is terminated at a stress level known as the upper yield stress. Deformation proceeds at a decreased stress level known as the lower yield stress accompanied with inhomogeneous deformation. The specimen is divided into regions where the strain is relatively high (Lüders strain) and regions which are still elastic. The distinct plateau in the stress–strain curve is characterized by the propagation of Lüders bands. After the whole gage length has been strained by the amount of the Lüders strain, deformation becomes essentially homogeneous again[11].

The formation and propagation of Lüders bands in steels under tension are generally attributed to the strong interactions of interstitial atoms with dislocations, known as Cottrell atmospheres. In Cottrell atmospheres, interstitial atoms segregate to dislocations and pin them in position to lower the lattice distortion energy. At the upper yield stress, dislocations are unpinned from the Cottrell atmosphere and become free dislocations. These free dislocations can move at the lower yield stress and lead to multiplication of new dislocations. Therefore, during the propagation of Lüders bands, the elastic zones are essentially free of dislocations whereas Lüders bands have a high dislocation density. The upper yield stress is regarded as the nucleation stress, and the lower yield stress is the growth stress of the Lüders bands[4].

The macroscopic and microscopic characteristics associated with the propagation of Lüders bands under tension have been studied extensively. They include the angle and the propagation velocity of the Lüders fronts, the in-plane kinking of the strips, the influence of the number of Lüders fronts on the yield stress, and the strain profile at the Lüders fronts. Macroscopic shear bands can be readily observed at the front of the Lüders bands, and very often the band front makes a 45° angle with the loading axis. That is, the band front follows the plane of maximum shear stress. However, this is a first approximation. Some researchers (eg. ref.[7,12]) investigated some differences using specimens with specific cross-section or material, respectively.

The propagation of Lüders bands is influenced by many factors including crystal structure, grain size, composition and microstructure, shape and stiffness of the testing sample, strain rate, and the type of loading[13–15]. Grain size has a great influence on the Lüders strain and the morphology of the Lüders bands, particularly in the case for mild steels (eg. ref.[16]). The Lüders strain decreases significantly as the grain size increases. Zhang and Jiang[6] experimentally studied the local plastic deformation of a carbon steel subjected to monotonic tension. It was found that the strain at the Lüders front was lower than the full Lüders strain (the length of the plateau on the stress–strain curve). During the propagation of Lüders bands, the local deformation is inhomogeneous. The local strain was inhomogeneous even at the work-hardening stage.

In the paper, the BA and the CA double reduced tinplates for can making industry have been analysed. Inhomogeneous plastic deformation of DR tinplates under tension loading was experimentally studied.

2. Experiments

Tinplates are currently produced mainly two ways of rolling. Thicker steel sheets (0.18–0.30 mm) are produced by single reduction, after which the plates are continuous annealed. The sheets of smaller thickness (0.135–0.18 mm) are after the single reduction and annealing a second time rolled (double reduced – DR). Most of the current packaging sheets are further processed by

drawing (drawing two-pieces containers, lids, twist caps, etc.). For this reason, the thin sheets of packaging have to meet certain requirements on the mechanical and plastic properties. Compliance with mechanical properties that are mainly characterized by the yield stress and the tensile strength, it is currently difficult to achieve by the manufacturer within the required limits. Significantly greater problem is the plastic properties of thin metal packaging and method of their evaluation. At present the evaluation of thin sheets for packaging (in terms of standards) mainly the tensile test is used, but on the basis of supplier – customer relations are often used other tests (Springback test, Erichsen cupping test, Bulge test, and others). Based on past experience, the tensile test seems to be problematic for evaluation of thin steel packaging DR sheets[9,10].

In this work, a double reduced tinplates of TH550CA and TS550BA, respectively, with thicknesses of 0.17 mm were used for experiments. To determine an anisotropic properties of tested materials for the uniaxial tensile test samples in rolling direction 0° and perpendicular direction 90° in respect of rolling direction have been taken. From the uniaxial tensile test the following parameters have been evaluated: the yield stress, the ultimate tensile strength and total elongation.

The measured values are shown in Table 1. Typical chemical compositions for the tested materials are given in Table II.

Microstructures of the investigated steels in the direction of 0° and 90° are shown in Fig. 1 and Fig. 2. For both annealing processes of tested thin steel sheets the failure zones are shown in Fig. 3 and 4.

For these sheets that show Lüders band slip at uniaxial tensile test it is problematic to determine the value of maximum uniform deformation[10]. On tested samples it is showed a strain creation in specific sample sections. It

Table I
Mechanical properties of DR tinplates with thickness of 0.17 mm

Sample	Uniaxial test			Biaxial test		
	$Rp_{0,2}$ [MPa]	Rm [MPa]	A_{50} [%]	Re [MPa]	Rm [MPa]	A_B [%]
TS550BA⊥	442	434	3.7	509	598	4.4
TS550BA∥	429	420	5.7			
TH550CA⊥	538	563	4.5	469	609	12.7
TH550CA∥	579	591	10.5			

Table II
Chemical composition of experimental materials

Composition [%]	C	Mn	P	S	Si	Cu	Al	Cr
TS550BA	0.081	0.41	0.018	0.003	0.006	0.041	0.04	0.02
TH550CA	0.055	0.17	0.018	0.002	0.008	0.036	0.05	0.02

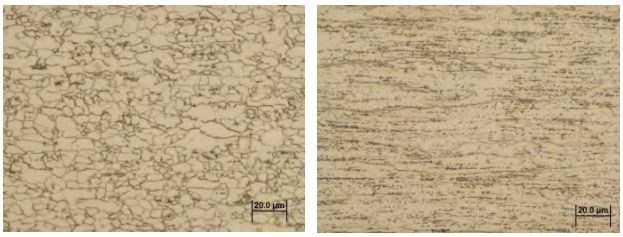

Fig. 1. **Microstructure of TH550CA (left) and TS550BA tinplates (right), direction 0°**

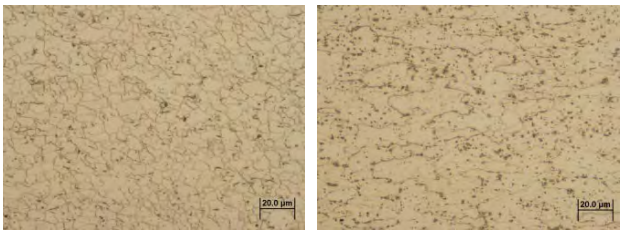

Fig. 2. **Microstructure of TH550CA (left) and TS550BA tinplates (right), direction 90°**

starts in one place, suddenly stops and passes into a completely different sample place (see Fig. 4). During the propagation of Lüders bands, multiple Lüders fronts can be formed. Under tension with a constant axial load, the Lüders front was approximately parallel to the material plane of maximum shear stress[4].

As for batch annealed sheets there have been ruptures in all samples during local sheet strain without any expansion of strain in the whole measured length of tested samples (see Fig. 3 and 4).

In Figs. 5 and 6, the surface failures of tested samples are shown. From Fig. 5a) we can expressly conclude that except primary slip planes where the rupture of tested samples appeared, also the so called secondary slip planes appeared in their proximity.

Local thinning of tested sheet has occurred in these places, as well. In the rest of measured part the tested sample has not been plastically deformed. The rupture surface in Fig. 5a, but also the detail in Fig. 5b and in Fig. 6 show, that in the place of sample rupture a sharp contraction (necking) has occurred. It points at the fact that the materi-

Fig. 3. **Rupture of samples after uniaxial tensile test of TH550CA (left) and TS550BA (right) with several slip planes**

Fig. 4. **Single slip plane of TH550CA tinplate (left) and multiple slip planes of TS550BA (right)**

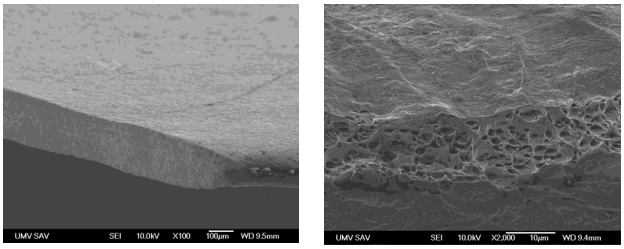

a b

Fig. 5. **Fracture of the TH550CA, a) side view, b) the detail of fracture surface**

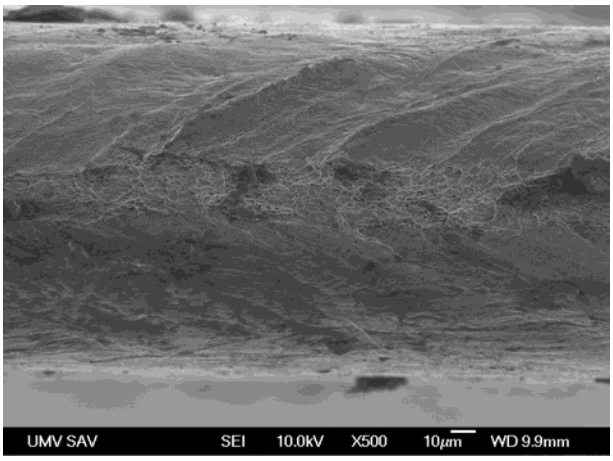

Fig. 6. **Perpendicular view of fracture surface and slip planes of TH550CA tinplate**

al itself has better plastic properties than the plastic properties measured by method of elongation at uniaxial tensile test.

3. Experimental results and discussion

Mean value of elongation of the sheets from 1 to 3 % was measured. Significant differences in mechanical properties were observed in the direction of 0° and 90°. In most cases, the difference of elongation was about 100 %. The results of mechanical tests showed that the uniaxial test of tinplates, especially double reduced, does not provide a true representation of their plastic properties. This fact is fully reflected in cupping test when the cups from packaging steel sheets with an elongation from 1 to 3 % were produced (LDR = 1.67) (ref.[7–9]). Despite very low values of the elongation, it was found that the failure is typical plastic (Fig. 7) and there is a large contraction (Fig. 5). From the details of fracture surface in Fig. 5b, but mainly from Fig. 6, we can clearly see the slip planes which are observed on the surface of the sheet near the fracture as waves. Thus, these tinplates have the local plasticity, but either the plastic strain is inhomogeneous on the whole gage section of the sample or plastic strain propagates only in local band and continue to failure. This cross-section is not able to transfer the strength necessary for the strain of another section of tested sample. The fracture surface shows characteristic signs of plastic intercrystalline fracture expanding along grain boundaries where inclusions can be found.

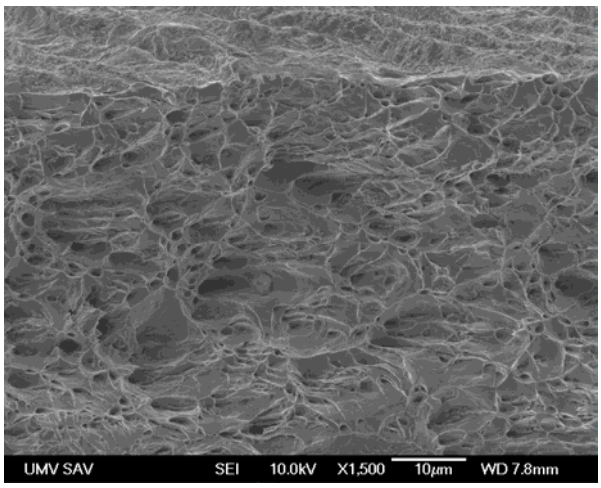

Fig. 7. **A detail view of fracture surface of TH550CA**

A general concept is that the end of the plateau is the starting point of homogeneous deformation in the gage section. However, the results shown that at the end of the plateau, the local deformation was still inhomogeneous. The inhomogeneous deformation persisted in the work-hardening stage. This observation is consistent with that observed by other researchers[4,6]. It was found that the local axial strain increased linearly and rapidly with time, indicating the propagation of the Lüders front over the area. A large amount of ferrite grains within this area experienced plastic deformation. For a mild steel, authors[7] pointed out that the strain rate at the Lüders front was rather high and some dislocations unable to move at the high strain rate can continue to move at a slow velocity after the front has passed them. Some deformed ferrite grains may deform further and some undeformed ferrite grains may experience a delayed plastic deformation. Such actions result in creep deformation. Similar phenomenon was observed in a monotonic tension of a mild steel[6] and an aluminum alloy[8].

Localization of deformation and fracture in a tensile test samples can be explained by the Marciniak theory,

whereby the localization of deformation occurs in areas with material inhomogeneity. Inhomogeneity can be represented by changing the microgeometry of the surface of the material or inhomogeneity (inclusions, cracks caused by one particular reduction of the grain boundaries). Failure of samples is probably initiated by the creation of the local neck in a certain place of the sample. This results in earlier failure and lower ductility. Thus, so narrow region cannot further transmit escalating loading and failure occurs just in this area.

4. Conclusions

In this paper, the causes and diversity of inhomogeneous strain were studied. The failure of tinplates during plastic deformation of simple uniaxial test sample was analysed. Experiments showed that plastic deformation of the samples during loading occurs only in certain places. This means that the plastic deformation do not extend to whole volume of the sample. On the other hand, the analysis of the fracture surface indicates that there is no brittle fracture. From achieved contraction of the sample it is clear that ductile fracture is concerned. This phenomenon can be attributed to inhomogeneity of the material structure, while the way of annealing of the material and structural inclusions, respectively, influence behaviour of the tinplates during loading. One of the conclusions is that there is usually either a one slip plane (TH550CA) with localization of the deformation in the slip plane up to failure or more slip planes (TS550BA) with Lüders bands. More slip planes may be related to the fact that microstructure of the TS550BA tinplate include a larger grains.

This contribution is the result of the projects implementation: Center for research of control of technical, environmental and human risks for permanent development of production and products in mechanical engineering (ITMS:26220120060) supported by the Research & Development Operational Programme funded by the ERDF and VEGA 1/0396/11.

REFERENCES

1. The European Standard EN 10202:2001, Cold Reduced Tin mill Products—Electrolytic Tinplate And Electrolytic chromium/Cr Oxide Coated Steel, The European Standard Publications, Brussels, 2001.
2. Pepelnjak T., Barisic B.: J. Mater. Proc. Technol. *186*, 111 (2007).
3. Barisic B., Pepelnjak T., Kuzman K.: J. Adv. Mater. Res. *6–8*, 329 (2005).
4. Zhang J., Jiang Y.: Int. J. Plasticity *21*, 651 (2005).
5. Yoshida F., Kaneda Y., Yamamoto S.: Int. J. Plasticity *24*, 1792 (2008).
6. Zhang J., Jiang Y.: ASME J. Eng. Mater. Tech. *126*, 164 (2004).
7. Kyriakides S., Miller J. E.: J. Appl. Mech. *67*, 645 (2000).
8. Onodera R., Nonomura M., Aramaki M.: J. Jpn. Inst. Metals *64*, 1162 (2000).
9. Spišák E., Majerníková J.: *Plastic deformation of tin coated steel sheet under different stress-strain states.* In: Progressive technologies and materials. 3-B: Materials, 2009. pp. 25–35.
10. Spišák E, Slota J., Majerníková J: Chem. Listy *105*, s485 (2011).
11. Hall E. O.: *Yield Point Phenomena in Metals and Alloys.* p. 36. Plenum Press, New York 1970.
12. Ananathan V. S., Hall E. O.: Scripta Metall. *23*, 1075 (1989).
13. Ananathan V. S., Hall E. O.: Acta Metall. Mater. *39*, 1353 (1991).
14. Lomer W. M.: J. Mech. Phys. Solids *1952*, 64.
15. Butler J. F.: J. Mech. Phys. Solids *10*, 313 (1962).
16. Morrison W. B., Glenn R. C.: J. Iron Steel Inst. *206*, 611 (1968).

E. Spišák, J. Slota, J. Majerníková, Ľ. Kaščák, and P. Malega *(Faculty of Mechanical Engineering, Technical University of Košice, Košice, Slovak Republic):*
Inhomogeneous Plastic Deformation of Tinplates under Uniaxial Stress State

Tinplates are mainly processed by forming nowadays. It is necessary to know their properties for the evaluation of their suitability for the forming processes. The paper deals with the inhomogeneous plastic deformation during uniaxial loading and the localization of plastic deformation which lead to the early failures of the tinplates. Causes of inhomogeneous strain and local propagation of deformation were analyzed.

JOINING MATERIALS USED IN CAR BODY PRODUCTION BY CLINCHING

EMIL SPIŠÁK[a] , ĽUBOŠ KAŠČÁK[a], and JACEK MUCHA[b]

[a] *Technical University of Košice, Faculty of Mechanical Engineering, Department of Technology and Materials, Mäsiarska 74, 040 01 Košice, Slovakia,* [b] *Rzeszow University of Technology, ul. Wincentego Pola 2, 35-959 Rzeszów, Poland*
lubos.kascak@tuke.sk

Keywords: clinching, car body sheets, evaluation of properties

1. Introduction

The automotive industry is currently working to accommodate the conflicting requirements of both environmental legislation and customer demands for greater performance and more luxury and safety features, by developing a light-weight and therefore essentially, energy-efficient vehicle[1]. One of the possibilities of decreasing the car weight and consequently lowering the fuel consumption is using various combinations of materials, such as combination of conventional deep-drawn steel sheet and high-strength steel sheet. In the areas, where high passive safety is needed, high-strength steels such as TRIP can be used. The usage of such steels can significantly reduce the car weight[2].

The increasing use of coated, lightweight and high-strength materials has led the automotive industry to re-examine traditional methods of component assembly. For example, direct welding of dissimilar sheet metals has proven to be difficult or impossible; thus, alternative joining techniques, such as mechanical fastening systems, have attracted increasing interest and applications in recent years. Mechanical fastening encompasess a broad range of methods, from threaded fasteners to different forms of rivets and mechanical interlocking methods[3].

One of these methods is clinching technology, which has not attracted much attention from researchers as yet, so it has not been studied deliberately so far. Clinching does not use any kind of appending joining components (such as screws, bolts)[4].

Only a die and a punch are used to press the sheet components to finish the whole joining process. The clinching process is a combination of drawing and forming that locks together sheets metal layers. The blanks are plastically deformed and the shape of the tools remains theoretically unchanged during the clinching processes. The punch is movable, whereas the fixture and the die are fixed during the process. The punch force needed for the joining process depends on the thickness and the strength of the materials to be joined, the size of the tools and friction coefficient usually varies from 10 to 100 kN (ref.[5,6]).

The paper evaluates joints made by clinching the following materials: microalloyed steel HSLA H220PD, TRIP steel 40/70+Z100MBO and drawing grade steel DX51D+Z.

Table I
Basic mechanical properties of used materials (*not specified)

	$Rp_{0.2}$ [MPa]	Rm [MPa]	A_{80} [%]	n_{90}
H220PD	238	382	36	0.228
TRIP40/70	450	766	26	0.278
DX51D+Z	≥ 140	270-500	≥ 22	*

2. Materials and methods

The following steel sheets were used for experimets: microalloyed steel HSLA H220PD with the thickness of

Table II
Chemical composition (wt.%) of used materials

Material	Chemical composition in [%] wt.									
	C	Mn	Si	P	S	Al	Cu	Ni	Cr	Ti
H220PD	0.06	0.7	0.5	0.080	0.025	0.020	0.011	0.017	0.310	0.037
TRIP 40/70	0.204	1.683	0.198	0.018	0.003	1.731	0.028	0.018	0.055	0.009
DX51D	0.64	0.178	0.007	0.016	0.002	0.120	0.041	0.02	0.023	0.002
	V	Nb	Mo	Zr						
H220PD	0.002	0.026	0.005	0.001						
TRIP 40/70	0.004	0.004	0.008	0.007						

0.8 mm, TRIP 40/70+Z100MBO with the thickness of 0.77 mm and DX51D+Z with the thickness of 0.9 mm.

Their basic mechanical properties and chemical composition are shown in Tables I and II. Mechanical properties of DX51D steel were specified by producer.

According to the orientation of punch and die to the position of upper and lower joined material, following combinations of steel sheets for press joining were used:

- ***Samples A***:
H220PD (a_0 = 0.80 mm) and TRIP (a_0 = 0.77 mm)*
- ***Samples B***:
TRIP (a_0 = 0.77 mm) and H220PD (a_0 = 0.80 mm)*
- ***Samples C***:
H220PD (a_0 = 0.80 mm) and H220PD (a_0 = 0.80 mm)
- ***Samples D***:
TRIP (a_0 = 0.77 mm) and DX51D (a_0 = 0.90 mm)*
- ***Samples E***:
DX51D (a_0 = 0.90 mm) and TRIP (a_0 = 0.77 mm)*

(*sheet on the die side of press joining tool)

The samples with dimensions of 40 × 90 mm and 30 mm lapping according to STN 05 1122 standard were used for the experiments (Fig. 1). Six samples were prepared for every combination of sheets. It is not necessary to clean the surfaces of samples before clinching[7].

Clinching was performed on the tension machine ZD 40 made by Werkstoffprüfmaschinen Leipzig Company with the loading range of 40 kN. The force needed for joining was 30 kN. The carrying capacities of the clinched joints were evaluated according to standard STN 05 1122 – Tensile test of spot welded joints. This test was used for measuring the maximum carrying capacities Fmax of the clinched joints. The test was carried out on the metal strength testing machine TIRAtest 2300 produced by VEB TIW Rauenstein, with the loading speed of 8 mm min^{-1}.

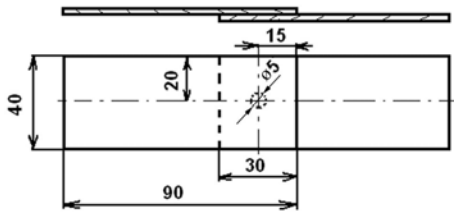

Fig. 1. **Dimensions of samples for the tensile test and principle of clinching**

Further tests for quality evaluation of clinched joints included the metallographical analysis and microhardnesses analysis according to STN EN ISO 6507-1 standard. Microhardness analysis was performed on the sample C with HSLA H220PD sheets.

The results of carrying capacities of clinched joints were compared with the carrying capacities of resistance spot welded joints.

3. Results

The measured values of carrying capacities of clinched joints after tensile test in comparison with the measured values of carrying capacities of resistance spot welded joints are shown in Table III. The resistance spot welded joints were made with the optimized values of welding parameters[2,8]. The resistance spot welds of all observed samples reached higher values of carrying capacities in comparison with clinched joints. On average, the clinched joints reached 13 % (samples A), 18 % (samples C) and 21 % (samples E) of carrying capacities of resistance spot welds.

The carrying capacities of samples B and samples D were not measured, because the joints were not successfully made. The upper sheets of both samples (TRIP 40/70 steel) were cut off in the place of the joint and then pressed to the lower sheet (Fig. 2).

The average value of carrying capacities of samples A was 1008 N. The cracks in the TRIP steel were observed on the die side (Fig. 3), which could possibly have a negative effect, especially during dynamic load. The cracks can even decrease the joints' corrosion resistance. The values

Table III
Measured values of carrying capacities

Number of sample	Carrying capacity Fmax [N]					
	Samples A		Samples C		Samples E	
	CJ	RSW	CJ	RSW	CJ	RSW
1	939	7310	980	5305	1087	7420
2	985	7641	1008	5290	1584	7644
3	1016	7680	956	5072	1334	7710
4	1080	7172	924	5260	1834	7417
5	1093	7417	973	5238	1973	7565
6	937	7581	978	5177	1658	7513

CJ – clinched joints, RSW – resistance spot welded joints

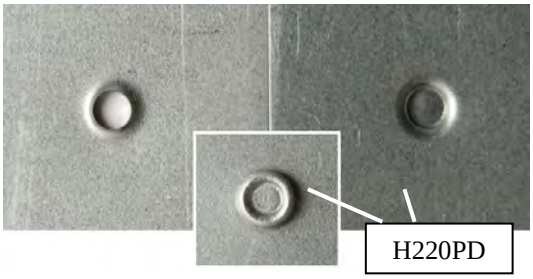

Fig. 2. **Sample B without creating a clinched joint**

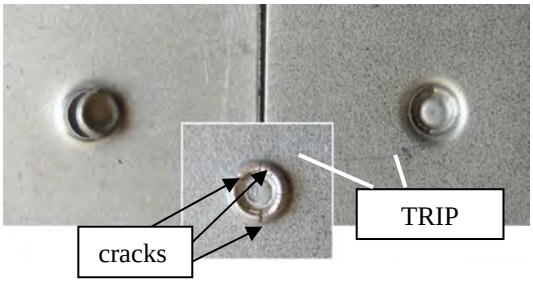

Fig. 3. **Sample A after tensile test with cracks in the CJ joint**

of carrying capacity of samples A are similar to the values measured in clinched joints of the common drawing grade steel sheets, as was published in[6].

The average value of carrying capacity of samples C was 970 N. No cracks occurred in the place of the joint from the side of the die. The carrying capacity values of samples C are similar to the values measured in clinched joints of common drawing grade steel sheets.

The average value of carrying capacity of samples E was 1578 N. Cracks in the TRIP steel on the die side were observed, similar to those in sample A (Fig. 3). The measured values of carrying capacity of samples E are higher than those of samples A and C, which is probably caused by the thicker material of the upper sheet in the joint (DX51D of 0.9 mm).

Figs. 4 and 5 shows the obtained load–displacement curves of clinched joints and spot welded joints os the sample C. The maximum load value of clinched joint is about 1000 N and the maximum load value of spot welded joint is about 5000 N. Fig. 6 shows the obtained load–displacement curves of clinched joints of all successfully made samples A, C, and E. The curve shapes of samples A and C are very similar as well as the values of their carrying capacities.

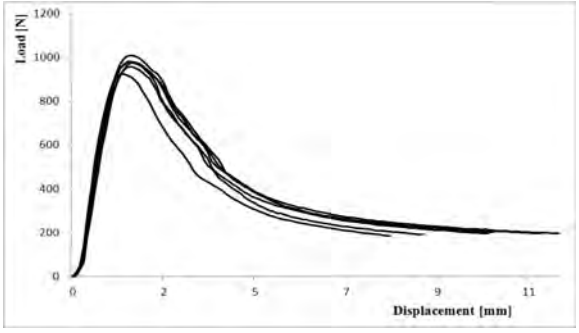

Fig. 4. **Load–displacement curves of clinched joints – sample C**

The metallographical analysis confirmed that the area with the most significant thinning in the joint is its critical area (Fig. 7).

There occured failures in such areas during tensile tests of samples A, C and E, and during the clinching process in samples B and D. The metallographical analysis confirmed the occurrence of cracks in the TRIP steel on the die side of the joints in the round part (Fig. 8).

Fig. 9 presents a sample C with marked areas of microhardness measurements and the measured values. The

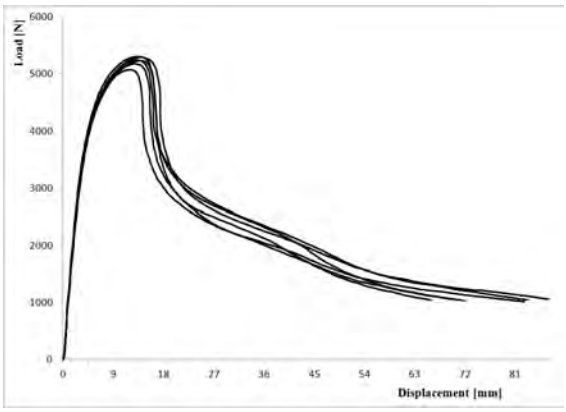

Fig. 5. **Load–displacement curves of spot welded joints–sample C**

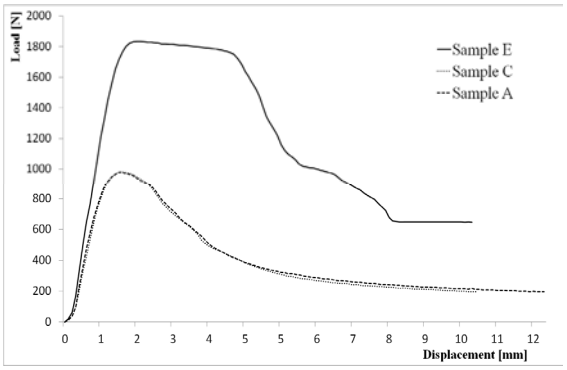

Fig. 6. **Load–displacement curves of clinched joints**

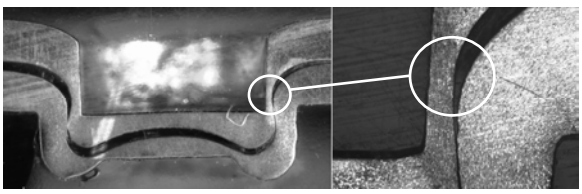

Fig. 7. **The critical area of clinched joint – sample C**

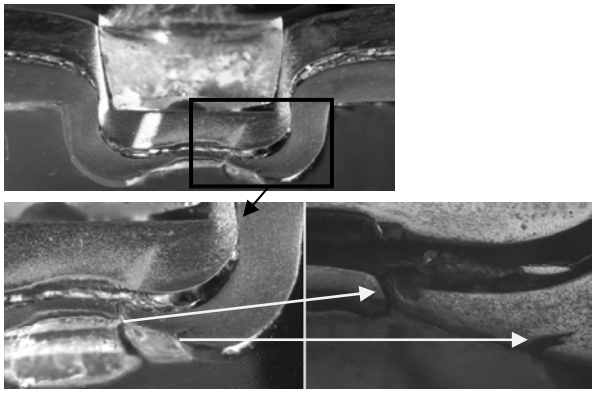

Fig. 8. **The cracks in TRIP steel on the side of die – sample A**

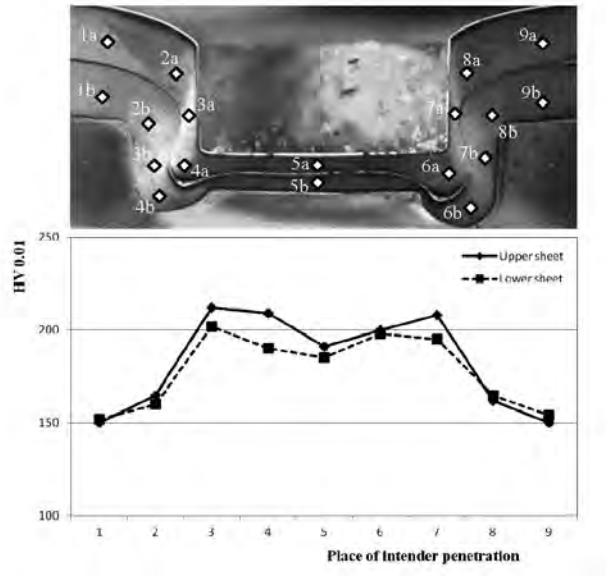

Fig. 9. **Microhardness values of the sample C**

measurements show the changes in the clinched joint, where the highest microhardness vaules were measured in the critical area of the clinched joint.

4. Conclusion

The paper focused on the evaluation of clinched joints of various material combinations. Microalloyed steel HSLA H220PD, TRIP steel 40/70+Z100 MBO and DX51D+Z steel were used for the experiments.

The influence of the orientation of joined materials regarding the position of punch and die of the tool was also observed. The material combinations of TRIP 40/70 with H220PD as well as TRIP 40/70 with DX51D, where TRIP steel is oriented towards the punch, are not suitable for joining by clinching, because the joints were not successfully created. Failures occur during the clinching process in the critical areas of joints. The same material combinations where TRIP steel is oriented towards the die proved to be unsuitable for joining by clinching, even though joints were created, because there occur cracks in TRIP steel, which could negatively affect the joint, especially during dynamic load. The cracks can even decrease the corrosion resistance of the joints.

The only combination that proved to be suitable for joining by clinching was a combination of H220PD materials – sample C. The carrying capacities of these samples were sufficient and the metallographical analysis confirmed no occurrence of cracks or failures in the area of clinched joints. The carrying capacity of these joints reached about 20 % of the carrying capacity of resitance spot welded joints of the same materials.

The paper was elaborated within the project Center for research of control of technical, environmental and human risks for permanent development of production and products in mechanical engineering (ITMS:26220120060).

REFERENCES

1. Barnes T. A., Pashby I. R.: J. Mater. Proc. Technol. *99*, 72 (2000).
2. Spišák E., Kaščák Ľ., Viňáš J.: Chem. Listy *105*, s448 (2011).
3. Sun X., Khaleel M. A.: J. Man. Processes *7*, 83 (2005).
4. Nong N., Keju O., Yu Z., Zhiyuan Q., Changcheng T., Feipeg L.: J. Mater. Proc. Technol. *137*, 159 (2003).
5. Varis J. P.: J. Mater. Proc. Technol. *174*, 275 (2006).
6. Kaščák Ľ., Spišák E.: Scient. Bulletins of Rzeszów University of Technology: Mechanics *73*, 161, (2008).
7. Mucha J., Kaščák Ľ., Spišák E.: Arch. Automot. Eng. *3*, 185 (2010).
8. Kaščák Ľ., Spišák E., Mucha J.: Scient. Bulletins of Rzeszów University of Technology: Mechanics *80*, 121, (2010).

E. Spišák[a], Ľ. Kaščák[a], and J. Mucha[b] *([a] Technical University of Košice, Faculty of Mechanical Engineering, Department of Technology and Materials, [b] Rzeszow University of Technology, Rzeszów, Poland):* **Joining Materials Used in Car Body Production by Clinching**

The paper dealt with the evaluation of properties of joints made by clinching. The microalloyed steel H220PD (a_0 = 0.8 mm), the high strength steel TRIP 40/70+Z100MBO (a_0 = 0.77 mm) and the drawing grade steel DX51D+Z (a_0 = 0.9 mm) were used for the experiments. The orientation of joined materials regarding the position of punch and die of the tool has the significant effect to carrying capacities of the joints. The TRIP steel steel is not suitable material for press joining method, even with both observed combination – with H220PD or DX51D. The carrying capacity of these joints was approximately 20 % of the carrying capacity of resitance spot welded joints.

NANOINDENTATION TESTING OF COMPOSITE BASED ON COLLAGEN AND POLY(DL-LACTIDE) NANOFIBERS

TOMÁŠ SUCHÝ[a,b], ZBYNĚK SUCHARDA[b], MONIKA ŠUPOVÁ[b], KAREL BALÍK[b], JOSEF ŠEPITKA[a], and JAROSLAV LUKEŠ[a]

[a] *Czech Technical University in Prague, Fac. of Mechanical Eng., Dept. of Mechanics, Biomechanics and Mechatronics, Laboratory of Biomechanics, Technická 4, 166 07 Prague 6,* [b] *Institute of Rock Structure and Mechanics, ASCR, v.v.i., Dept. of Composite and Carbon Materials, V Holešovičkách 41, 182 09 Prague 8, Czech Republic*
tomas.suchy@fs.cvut.cz

Keywords: nanoindentation, poly(DL-lactide), collagen, composite, nanofibers

1. Introduction

In bone tissue engineering, there is a great need to engineer multi-phase materials that combine the advantages exhibited by each component of the material, and that have a structure and composition similar to that of natural bone[1]. In our project, we design biomimetic nanocomposite materials that promote the regeneration of defective bone tissue with the required rate of biodegradation. The proposed composition of the material imitates the real bone structure, and combines the advantages of nano fibers, aliphatic polyesters, collagen, and calcium phosphates. This study uses nanoindentation to evaluate the influence of various weight fractions of polymeric nanofibrous phase on the mechanical properties of a composite based on collagen type I matrix and poly(DL-lactide) nanofibers (PDLL). The preparation of composite test samples for nanoindentation and the structure of the samples are discussed.

2. Materials and methods

Composites based on PDLL (PURASORB PDL 05, Purac Biomaterials, the Netherlands; inherent viscosity 0.5 dl g^{-1}) nano fibers and collagen type I matrix were prepared. A poly(DL-lactide) nanofibrous omnidirectional filler (Fig. 1) was prepared by electrospinning (NS 8A 1600, Elmacro Ltd., Czech Republic) from a chloroform solution[2]. Collagen matrix ISC_{40} was isolated from fish skin (carp) under denaturing conditions (40 °C, acetic acid, 30 min) followed by lyophilization according to Pešáková et al.[3] Composite samples were prepared with 6 different weight fractions of nanofibers (0, 60, 70, 73, 80, 87 wt.%) and hardened onto polymethylmethacrylate supporting plates (AZ Plastik, Czech Republic).

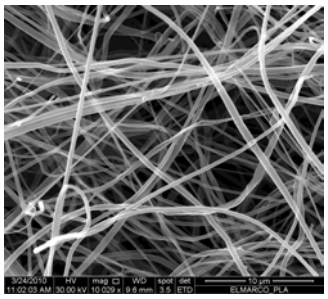

Fig. 1. **SEM micrograph of poly(DL-lactide) omnidirectional nanofibers (mag. x 10,000)**

Briefly, all composite samples were prepared by impregnation of PDLL with collagen/deionized water dispersion. The collagenous dispersion was prepared in the IKA DI18 homogenisator (IKA Werke GmbH, Germany) (at a rotation speed of 20.000 min^{-1} for 2 minutes) by dispersion of 0.5 g of collagen in 100 g of deionized water. The weighed amount of the PDLL nanofibrous layer was placed on to separating foil and impregnated with a weighed amount of collagenous dispersion in order to achieve the chosen weight fraction of the nanofibrous filler after water evaporation (at room temperature). Four layers prepared using this procedure were cut into an appropriate size and laid on a polymethylmethacrylate supporting plate. Finally, the supporting plate and the composite were covered by a separating foil and hardened at 50 °C under a pressure of 4 kPa. A relatively low temperature was chosen to be below the glass-transition temperature of collagen[4] and PDLL[5].

The assessment of various weight fractions of the nanofibrous phase on the mechanical properties (reduced elastic modulus E_r) of the composites was studied using the nanoindentaion mode, which is an option of the Hysitron TriboIndenter™ TI 950 nanomechanical instrument (Hysitron, USA). A Berkovich diamond fluid tip with apex radius ~120 nm was used for the nanoindentation tests. For each tested composite, indents were applied on five 60 × 60 μm areas as a matrix of 5 × 5 indents with 15 μm separation (with 25 μN applied force, lift height 100nm, preload 1 μN).

The prepared composites were also investigated by image analysis, using a QUANTA 450 electron SEM microscope (FEI Company, USA) under a high vacuum, with an Au coating film on the samples.

A statistical evaluation was carried out using the following methods (STATGRAPHICS Centurion XV, StatPoint, USA): the statistically significant differences were checked by nonparametric methods (the Kruskal-

Wallis test, $\alpha = 0.05$); the Mann-Whitney test was used as a post hoc test ($\alpha = 0.05$); and the confidence intervals for the mean values were calculated at a significance level of $\alpha = 0.05$.

3. Results and discussion

The reduced elastic modulus of composites based on collagen matrix and PDLL a nanofibrous phase was measured (Fig. 2).

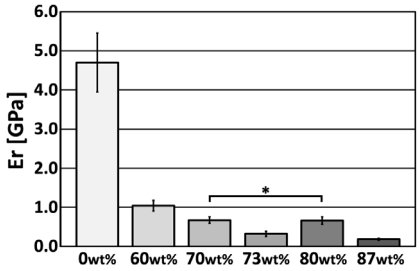

Fig. 2. **The reduced modulus E_r of the tested composites** (* denotes values without statistically significant differences, Mann-Whitney post hoc test, $\alpha = 0.05$)

The obtained value for the modulus of pure collagen matrix (0 wt.%) is in reasonable agreement with earlier results obtained by various methods (2–11.5 GPa)[6,7]. After additions of 60 wt.% of nanofibers, the modulus decreases markedly from 5.45–3.95 GPa to 1.17–0.91 GPa. A further decrease in the reduced modulus (in the case of composites with 70–87 wt.% of PDLL) is less marked.

It can be deduced from the trend of this decrease that the higher the amount of PDLL, the lower the reduced modulus will be. This finding can be explained by the lower elastic modulus of the PDLL precursor used for electrospinning the nanofibers (0.47–0.59 GPa)[2]. The omnidirectional orientation of the nanofibrous phase and mainly the porosity of the composites are probably other important factors that influence the process (Fig. 3). It should be noted that the E_r values can also be partly attributed to the fact that in nanoindentation the Young's modulus represents the lateral elasticity at the surface, rather than the bulk stiffness. For further analyses in our study, it will be necessary to improve the preparation of the composite samples. The improvement will focus on a superior fibrous phase filling with collagenous matrix, and on applying the hardening process under higher pressure. The porosity of the samples will be analysed.

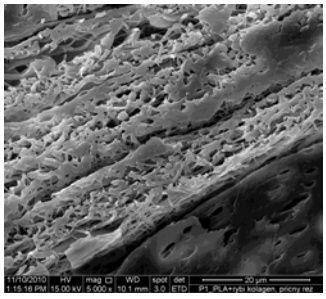

Fig. 3. **SEM micrograph of a cross section of the collagen/ PDLL (60 wt.%) composite illustrates the apparent porosity (mag. x 5 000)**

4. Conclusion

The results provide an assessment of the different weight fraction of the composite reinforcing phase. In general, the PDLL nanofibrous phase decreases the elastic modulus of the composites studied here. The nanoindentation method seems to be a suitable tool for determining the mechanical properties of composite materials variously modified at the nanoscale.

This research was supported by the Czech Science Foundation (project No. 106/09/1000), and by Ministry of Education project Transdisciplinary Research in Biomedical Engineering II., No. MSM 6840770012.

REFERENCES

1. Cancedda R., Giannoni P., Mastrogiacomo M.: Biomaterials *28*, 4240 (2007).
2. Gao Y., Kong L., Zhang L., Gong Y., Chen G., Zhao N., Zhang X.: Eur. Polym. J. *42*, 764 (2006).
3. Pešáková V., Štol M., Gillery P., Maquart F. X., Borel J. P., Adam M.: Biomed. Pharmacother. *48*, 261 (1994).
4. Yan M., Li B., Zhao X., Ren G., Zhuang Y., Hou H., Chen L., Fan Y.: Food Chem. *107*, 1581 (2008).
5. Garlotta D.: J. Polym. Environ. *9*, 63 (2001).
6. Wenger M. P. E., Bozec L., Horton M. A., Mesquida P.: Biophys. J. *93*, 1256 (2007).
7. Meyers M. A., Chen P. Y., Lin A. Y., Seki Y.: Prog. Mater. Sci. *53*, 1 (2008).

T. Suchý[a,b], Z. Sucharda[b], M. Šupová[b], K. Balík[b], J. Šepitka[a], and J. Lukeš[a] *([a] CTU in Prague, Fac. of Mechanical Eng., [b] Institute of Rock Structure and Mechanics, ASCR, v.v.i., Czech Republic):* **Nanoindentation Testing of Composite Based on Collagen and Poly(DL-Lactide) Nanofibers**

The influence of various weight fractions (0, 60, 70, 73, 80 and 87 wt.%) of the poly(DL-lactide) nanofibers on the mechanical properties of the composite based on collagen type I matrix was evaluated by nanoindentation. After addition of 60 wt.% of nanofibers, the reduced elastic modulus decreases markedly (from 5.45–3.95 GPa to 1.17–0.91 GPa) while a further decrease (70–87 wt.%) is less marked.

MICROMECHANICAL PROPERTIES OF DIFFERENT MATERIALS ON GYPSUM BASIS

PAVEL TESÁREK, TOMÁŠ PLACHÝ, PAVLA RYPAROVÁ, and JIŘÍ NĚMEČEK

Czech Technical University in Prague, Thákurova 7, 166 29 Prague, Czech Republic
pavel.tesarek@fsv.cvut.cz

Keywords: nanoindentation, gypsum, micromechanical properties, deconvolution, homogenization

1. Introduction

Gypsum hydration starts right after the mixing of water with gypsum. The process of hydration and setting depends on multiple factors[1]. These effects can be observed on several scales. Usually, two levels (micro- and macro-scale) are considered at least. Material properties of hardened gypsum on macro-level (e.g. thermal and mechanical properties) depend on the material structure (namely porosity) and prevailing matrix properties[2]. As the main factor, water to gypsum ratio determines the value of total porosity which is an effect of over-stoichiometric water. Micro-level material properties depend on microstructural parameters like chemical purity of the used gypsum (plaster); ratio between the three main components of the gypsum binder, i.e. calcium sulfate anhydrite (different phases), calcium sulfate hemihydrate α- or β-gypsum and calcium sulfate dihydrate[3,4]; some impurities and eventually additives; size and ordering of calcium sulfate dihydrate crystals[1,5], etc.

The main objective of this paper was to compare macro- and micro-elastic properties of studied gypsum materials and to find the dependence between macro- and micromechanical properties in connection with porosity.

2. Materials and samples

Three different materials on gypsum basis were selected for the testing. The first one was commercially available dental gypsum Interdent® based on α-calcium sulfate hemihydrate ("Dental gypsum series"). The water to gypsum ratio was 0.2 in this case[6]. The second one was a flue gas desulphurization gypsum (FGD) based on β-calcium sulfate hemihydrate produced at Electric Power Station Počerady (Czech Republic). These samples were denoted as "FGD gypsum series". The water to gypsum ratio was 0.627 in this case. The last series was commercially produced grey gypsum based on β-calcium sulfate hemihydrate (Gypstrend Ltd. – Kobeřice near Opava in Czech Republic) denoted as grey gypsum (after typical color of this gypsum which contained 50 % of natural calcium sulfate dihydrate). The water to gypsum ratio was 0.71. Table I shows the basic material properties as bulk density, total porosity and values of micro-porosity lower then 1 μm. This part of the porosity was assumed to be naturally included in the nanoindentation data since the indentation volume under the tip covered a region of ~1–2 μm^3.

Table I
Basic material properties of the tested samples

Material	Bulk density [kg m^{-3}]	Total open porosity [m^3 m^{-3}]	Open porosity lower then 1 μm [m^3 m^{-3}]
Dental gypsum	2020	0.19	0.12
FGD gypsum	1220	0.51	0.14
Grey gypsum	980	0.61	0.13

3. Experimental methods and results

First, the macroscopic values of dynamic Young's modulus on macro-level were measured by non-destructive impulse excitation method[7] which is based on measuring the fundamental resonant frequencies. The test arrangement was done for longitudinal vibration. The specimen with dimensions of 40×40×160 mm was supported in the midspan, i.e. the fundamental longitudinal nodal position. The acceleration transducer Bruel&Kjaer of Type 4513B was placed at the centre of one sample end face. The opposite end face was hit by the impact hammer Bruel&Kjaer, Type 8206. From the obtained results, the weight of the sample and the dimension of the sample, values of dynamic Young's modulus were calculated[7]. Total open porosity and values of micro-porosity were calculated from results obtained from mercury porosimetry and pycnometric density measurements.

Micromechanical properties of dental gypsum samples were measured by using CSM Nanohardness tester. Quasi-static loading consisted of 10 s of linear loading (rate 30 mN min^{-1}), 10 s of holding period at constant peak force 5 mN and 10 s of unloading (rate 30 mN min^{-1}). The distance between individual indents was set 15 μm to avoid mutual influences[9]. Elastic constants were evaluated for individual indents by standard Oliver and Pharr methodology[8]. Poisson's ratio was estimated to be 0.2 for all cases. Grid nanoindentation and deconvolution techniques were applied[9]. Three phase microstructural system was assumed based on the shape of experimental histograms of elastic moduli[6]. Thus, the anisotropy of gypsum

crystals was replaced by the phase differences at a deconvolution process[6,9]. The dental gypsum composed of one dominant phase (E=37.2 GPa, 71.2 %) and two minor phases (E=19.4 GPa, 4.4 % and E=56.3 GPa, 24.4 %) [6,10].

To compare results from different methods, macroscopic elastic properties were predicted from analytical homogenization scheme, namely Mori-Tanaka method[10], with the assumption of a two-phase composite – matrix (having the properties received from nanoindentation and lower level homogenization[9,10] of the three phase system and air pores larger than 1 μm. The homogenized Young's modulus for the matrix was 34.8 GPa. Results from macroscopic dynamic measurements showed on the value 36 GPa, i.e. the agreement of the macroscopic value and the micromechanically predicted one was within 3.3 % in this case.

Since the direct micromechanical measurements on FGD and grey gypsum samples faced significant obstacles in the form of very high porosity and roughness it was decided to use inverse analysis and predict micromechanical properties of the matrix from the macroscopic ones using the same principles as in case of dental gypsum. The obtained results are summarized in Table II. It can be seen that micro elastic properties of FGD and grey gypsum samples (based on β-gypsum composition) are approximately 2.6–2.8× lower then those for dental gypsum (α-gypsum composition).

Table II
Measured/calculated Young's moduli

Gypsum	Macroscopic Young's modulus [GPa]		Microscopic (homogenized matrix) Young's modulus [GPa]
Dental	36/34.8	←	40.0
FGD	7/-	→	15.2*
Grey	5/-	→	14.2*

Note: *denotes results obtained from inverse analysis. An arrow indicates the analysis direction

4. Conclusions

The paper presents comparison of micro- and macromechanical properties of several types of gypsum materials in dependence on their different chemical origin and porosity. Grid nanoindentation, statistical deconvolution and porosimetry were utilized. Good agreement within 3.3 % was found in case of dental gypsum samples based on α-gypsum composition. The analytical homogenization was used in the prediction of either microscopic matrix properties (for dental gypsum) or for the inverse analysis of microscopic properties from the known macroscopic ones (for FGD and grey gypsum samples). This analysis points on the approximately 2.6–2.8× lower microscopic elastic properties of β-gypsum based samples. Such hypothesis will be subsequently verified using nanoindentation which was beyond the scope of this contribution at present.

Support of the Czech Science Foundation (P105/12/0824) and Ministry of Education of the Czech Republic (MSM 6840770003) is gratefully acknowledged.

REFERENCES

1. Šatava V.: Ceramics–Silikáty *40*, 2 (1996).
2. Singh M.: Constr. Build. Mater. *19* (2005).
3. Garg M., Jain N., Singh M.: Constr. Build. Mater. *23* (2009).
4. Tydlitát V., Tesárek P., Černý R.: J. Therm. Anal. Calorim. 91, *3* (2008).
5. Arslan A. T., Koca M., Aydogmus Y. T., Klapperich H., Yılmaz H. R.: Rock Mech. Rock Engng. *41* (2008).
6. Tesárek P., Němeček J.: Chem. Listy *105*, s17 (2011).
7. Plachý T., Tesárek P., Wilczynska A., Padevět P.: *3rd WSEAS International Conference on Engineering Mechanics, Structures, Engineering Geology/ International Conference on Geography and Geology Location* (2010).
8. Oliver W., Pharr G.: J. Mater. Res. *7* (1992).
9. Němeček J., Šmilauer V., Kopecký L.: Cem. Concr. Compos. *33* (2) (2011).
10. Němeček J., Králík V., Vondřejc J., Němečková J.: *49th International Scientific Conference Experimental stress Analysis* (2011).

P. Tesárek, T. Plachý, P. Ryparová, and J. Němeček *(Czech Technical University in Prague, Faculty of Civil Engineering):* **Micromechanical Properties of Different Materials on Gypsum Basis**

Micro- and macro-level elastic properties of three types of gypsum samples (dental gypsum, flue gas desulphurization gypsum and grey gypsum) were compared. Grid nanoindentation, statistical deconvolution and porosimetry were used on lower composite level and non-destructive impulse method on macro-scale. The transition between the scales was computationally maintained by the Mori-Tanaka homogenization method. Good agreement was achieved between experiments and numerical prediction.

Obtained results also showed that the micro-elastic properties predicted (by inverse analysis) for FGD and grey gypsum samples (β-gypsum composition) are approximately 2.6–2.8× lower then those for dental gypsum (α-gypsum composition).

IMPACT OF BLEACHING GELS ON DENTAL ENAMEL MICROHARDNESS AND 3D SURFACE ROUGHNESS

QUANG DUNG TRAN[a], KAREL MAŇAS[a], EMIL SVOBODA[a], MICHAL BUMBÁLEK [b], and ZDENĚK JOSKA[a]

[a] *Department of Mechanical Engineering, University of Defence in Brno, Kounicova 65, 612 00 Brno,* [b] *Department of Dental Care, Faculty of Medicine, Masaryk University, Kamenice 753/5, 625 00 Brno, Czech Republic*
dungchm@yahoo.com

Keywords: enamel, bleaching, microhardness, 3D surface roughness

1. Introduction

At this time, the popularity of dental bleaching has increased in esthetic dentistry. Tooth bleaching using different oxidizing agents as hydrogen peroxide or carbamide peroxide is one of the most spread procedures[1–4]. The effect of bleaching treatment on dental enamel has long been a concern of many dentists, because bleaching agents react with enamel and cause chemical, structural and mechanical changes on the enamel surfaces. One of the most common methods of evaluation of changes in surface topography[5,6] is electron microscopy, stylus profilometery or atomic force microscopy[7]. The aim of this work is to investigate the effect of two different tooth bleaching gels containing 22 % carbamide peroxide and 38 % hydrogen peroxide on surface microhardness and properties of dental enamel by the 3D surface topography.

2. Materials and experimental methods

Four extracted teeth human third molars were used for experiment. Enamel slabs of 5.0×5.0×1.5 mm were cut from the buccal and lingual surfaces by using a precision slow speed diamond saw with water cooling. Each cut slab was embedded in dentacryl. Enamel surface was wet grounded to achieve flat surface by using 400, 600, 1000 and 2500 grit silicon carbide papers. Then the prepared slabs were placed in an ultrasonic cleaner for 3 min. Samples were stored in distilled water at room temperature prior to the experiment. A total of 8 enamel specimens were prepared for the experiments.

Two different bleaching gels were applied on the prepared specimens. For experiments, „in home“ Yotuel® Patient with 22 % carbamide peroxide (Biocosmetics Laboratories) and „in office“ Opalescence Boost with 38 % hydrogen peroxide (Ultradent products) were used. Yotuel® Patient was applied in 1 cycle for 3 hours and Opalescence Boost was applied in 4 cycles for 15 minutes. After bleaching treatment samples were cleaned in distilled water and Baseline microhardness was measured before treatment with a microhardness Vickers indenter (LECO LM 247 AT) at a 100 g load and 12 s dwell time. The mean Vickers hardness numbers (VHN) were derived from five indentations made across the enamel surface of each specimen.

After microhardness testing, surface topography of the specimens was evaluated on a 3D surface area by the Talysurf CLI 1000 device with non contact confocal gauge. The topography data were visualized and evaluated using commercial software Talymap Platinum. Measured area was 1.25×1.25 mm. The filter cut off which separates the roughness and waviness area λ_c was set to 0.25× 0.25 mm. These roughness parameters were measured: the core roughness depth S_k – the height difference between intersection points of the found least mean square line, the reduced summit height S_{pk} – the height of the upper left triangle and the reduced valley depth S_{vk} – the height of the triangle drawn at 100 %.

3. Results

The confocal microscopy image shows the bleached surface in Fig. 1. The measured values of microhardness of showed enamel before and after treatment remain almost the same (see Fig. 2).

The area measured by the Talysurf CLI 1000 device is shown in Fig. 3. The values of selected parameters before and after bleaching treatment are shown in Tab. I. The results show that bleaching gel Yotuel® Patient has a bigger impact on surface roughness parameters than Opalescence Boost PF. The results from amplitude distribution and material ratio curves (Fig. 4) confirmed that bleaching gels have effects on topography of enamel. After treat-

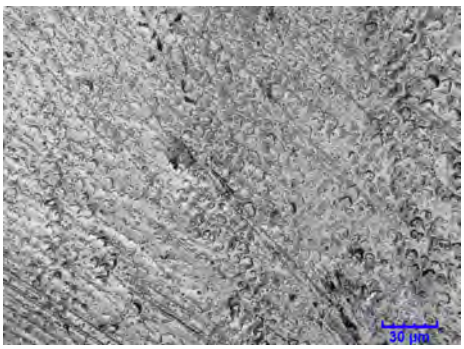

Fig. 1. **The bleached surface of dental enamel in a confocal micrograph**

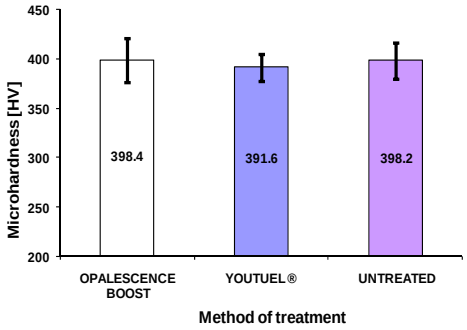

Fig. 2. **Enamel microhardness before and after treatment**

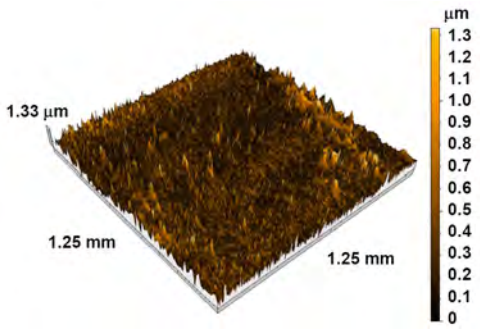

Fig. 3. **The 3D surface roughness of bleached enamel (Opalescence Boost)**

Table I
Values of (3D) surface roughness parameters

[µm]	Yotuel® Patient		Opalescence Boost PF	
	Grounded	Bleached	Grounded	Bleached
S_{pk}	0.416	0.626	0.416	0.565
S_k	0.426	0.213	0.470	0.453
S_{vk}	0.137	0.254	0.165	0.170

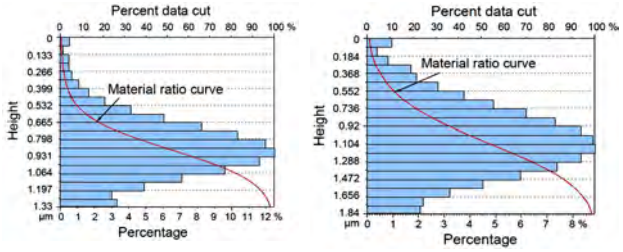

a) Opalescence Boost b) Yotuel Patient ®

Fig. 4. **Amplitude distribution and material ratio curves after treatment**

ment, curves showed different slopes and different ratios of peaks to valleys.

4. Conclusion

The obtained results show that bleaching treatment has only small effects on surface microhardness of dental enamel. The values remained the same. All measured parameters of surface roughness S_k, S_{pk}, S_{vk} after treatment was changed. The biggest change of surface topography was observed for Yotuel® Patient. In this case, the parameter S_k decreased from 0.426 µm to 0.213 µm. The results show that "in home" bleaching gel with 22 % carbamide peroxide has bigger impact on dental enamel roughness than "in office" bleaching gel with 38 % hydrogen peroxide.

The work presented in this paper has been supported by the institutional development project "Support of Education and Research in Mechanical Engineering" and by the specific research project at the Department of Mechanical Engineering, University of Defence.

REFERENCES

1. Ren Y. F., Amin A., Malmstrom H.: J. Dent. *37*, 6 (2009).
2. Hegedüs C., Bistey T., Flóra-Nagy E., Keszthelyi G., Jenei A.: J. Dent. *27*, 7 (1999).
3. Attin T., et al.: Dental Mater. *25*, 143 (2009).
4. Markovic L., Jordan R. A., Nebojsa L., Gaengler P.: J. Endodontics *33*, 5 (2007).
5. ČSN EN ISO 4287 – Geometrical Product Specifications (GPS) – Surface texture: Profile method -Terms, definitions and surface texture parameters.
6. ISO 25178 – Geometrical product specifications (GPS) – Surface texture: Areal – Part 2: Terms, definitions and surface texture parameters.
7. Ctvrtlik R., Morozova J., Zapletalova Z., Ranc V.: Chem. Listy *105*, s785 (2011).

Q. D. Tran[a], K. Maňas[a], E. Svoboda[a], M. Bumbálek[b], and Z. Joska[a] *([a] Department of Mechanical Engineering, University of Defence in Brno, [b] Department of Dental Care, Faculty of Medicine, Masaryk University):*
Impact of Bleaching Gels on Dental Enamel Microhardness and 3D Surface Roughness

The aim of this study was to characterize the effect of two different bleaching gels (with 22 % carbamide peroxide and with 35 % hydrogen peroxide) on the surface roughness and microhardness of enamel. Bleaching gels were applied according to manufacturer´s instructions. For characterization of surface microhardness and 3D surface roughness, non contact 3D profilometer Talysurf CLI 1000 and Vickers microhardness method were used. The results of surface microhardness did not show significant changes from baseline for both gels. 3D surface roughness parameters showed that "in home" gel with 22 % carbamide peroxide caused bigger changes of enamel topography than "in office" gel with 35 % hydrogen peroxide.

DETERMINATION OF LOCAL DISTRIBUTION OF HARDNESS FOR INVESTIGATION OF MATERIAL BEHAVIOR UNDER LOAD APPROACHING ITS STRENGTH

JAROSLAV VALACH [a], MAREK ŽĎÁRSKÝ [b], DANIEL KYTÝŘ [a], TOMÁŠ DOKTOR [a], and MARTIN ŠPERL [a]

[a] *Institute of Theoretical and Applied Mechanics, Academy of Sciences of the Czech Republic, v.v.i., Prosecká 76, 190 00 Prague 9,* [b] *Czech Technical University in Prague, Faculty of Transportation Sciences, Konviktská 20, 110 00 Prague 1, Czech Republic*
valach@itam.cas.cz

Keywords: hardness mapping, crack propagation, image analysis, thermography

1. Introduction

Hardness measurement is one of the most important techniques for assessment of materials' mechanical properties in engineering for more than a century. It allows the non-destructive (or minor destructive if an indent in the surface is considered a damage) quantification of strength as explained in classical text by Tabor[1]. Hardness measurement can be employed as an effective tool for investigation of local distribution of plastic deformation based on strain hardening material model. Homogenous materials subjected to uniform load can be characterized by one hardness value without a significant error, if contributions from individual grain orientation, or detailed phase distribution in structure, or if affected surface layer are "averaged". But when properties vary substantially or when major gradients can be identified in the stress state of the studied object, it is advisable to study distribution of hardness as locally dependent variable. Arrays of indents are used in determination of mechanical properties of materials for many decades. The technique was refined with the introduction of precise recording of depth-force relation and of micro- and nano- indentation and introduction of motorized computer controlled stages holding the specimen[2]. On the other hand, there are situations, where crude information is not only sufficient, but also preferred, especially when it concerns testing on-site and on medium to large scale specimens and constructions. In such a case it is beneficial to use a simple hand powered device (see Fig. 1) capable of operation in any orientation and in any environment, provided it is enhanced by up-to-date technique enabling efficient processing of large quantity of data.

This paper is focused on the presentation of such a technique on a study of large plastic strains in compact tension (CT) specimens and to comparison of the results to that obtained by thermography. This technique is demonstrated on investigation of permanent plastic deformation on surface and in cross-sections of the specimen after loading close to strength limit of the material. This knowledge is important for estimation of the ratio between the energy dissipated into plastic deformation and the energy consumed by crack extension during loading process.

2. Materials and methods

In this paper, the technique for hardness map determination will be presented on investigation of two CT specimens made from the same low carbon pipeline steel of yield strength 235 MPa in as delivered state. One specimen is made from the material in untreated, as delivered state after production, while the second one was annealed at 700 °C for 4 h. It means the two different states of the same material were obtained: one slightly hardened by mechanical process during production, while the other is in the softened state. In this state, major residual stresses attributed to elastic interaction between lattice and other dislocations decreased and the material recovered to the ductile state. Thus, the two same size and same material specimens tested in the same loading conditions offer an interesting insight on the source and manifestation of ductility in metal behavior in loading.

3. Experimental procedure

The specimens were one after another fastened into testing machine. Displacement controlled experiment was carried out under 2 mm min^{-1} crosshead rate. The final displacement was about 7 mm, approximately the same for both specimens. The results were evaluated by two independent methods – one using thermocamera and the second was semiautomatic hardness mapping technique.

3.1. Thermocamera observation

The technique for determination of plastic deformation zone in the vicinity of the specimen's notch from thermograms based on known relations coupling mechanical energy and heat was employed first. Based on this coupling one can analyze stress-strain state of the material indirectly by temperature field measurement[3]. Therefore temperature fields on the specimens' surface were periodically recorded by thermocamera FLIR during the loading. Temperature decrease is associated with thermo-elastic effect accompanying peak of elastic field in the vicinity of notch tip, while the temperature increase indicates energy dissipation due to plasticity.

Fig. 1. **Hand powered portable hardness tester Meopta**

Elastic deformation, e.g. extension of specimen is associated with a decrease of temperature as the material expands in volume when stretched. If the acting stress exceeds the yield strength, the prevailing deformation in a given point is plastic. As plastic deformation is carried out by dislocations movement through a lattice, a substantial part of the mechanical work of the testing machine applied over specimen is converted into friction. The friction is a dissipative process resulting in increased temperature of the specimen. A major part of the external work is converted into the heat and only a small fraction (roughly 10 %) of the work is converted into elastic energy of mutually interlocked dislocations. This energy can be determined by precise calorimetric measurement during annealing that is realized by heating of the specimen to the temperature about 800 °C. One of the earliest observations of such a process is described by Clarebrough et al.[4] Difference in temperature field evolution in response to external load can be seen on Fig. 2. Lower yield stress and lower strain hardening of annealed specimen (left) cause development of plastic hinge localized in narrow strip in the notch front, while specimen in as delivered state hardens simultaneously in large part of the specimen as reflected with a pronounced temperature increase.

3.2. Hardness mapping of plastic zone

Determination of elasto-plastic state of the material by indentation has been given a considerable attention[5]. Hardness measurement of strain hardening of ductile alloy utilizes relation between yield strength and hardness[6,7]. Considering these relations, one can investigate material in state close to its strength limit and determine the distribution of the maximal stresses in great detail over studied area.

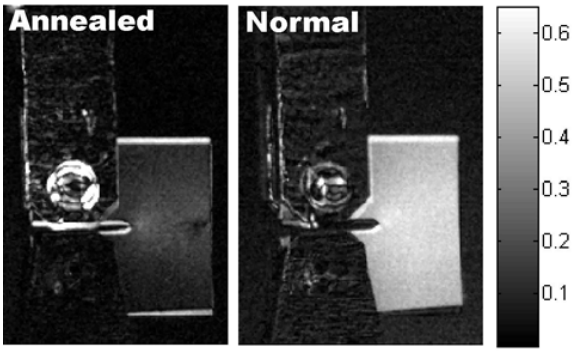

Fig. 2. **Comparison of temperature increase over the same time period (20 s) for specimen in annealed and in as delivered state**

After the test, the plastic deformation zone based on hardness distribution was determined on the carefully milled and polished surface of the specimens. In the vicinity of the notch that coincides with the area of the highest strain and also of the highest strain gradient, the array of indents has been placed by purely mechanical, portable hand powered Vickers hardness tester. The hardness tests were performed using standard loads (981 N and 2743 N) generating indents exceeding dimensions of the affected surface layer produced by the processes of cutting and polishing known as a Beilby layer[5]. Dense grid of indents was imprinted on the surface to obtain a smooth map of hardness distribution on studied surfaces (Fig. 3).

The size of the area of interest was approximately 10 mm. In a subsequent step, the image of studied specimen's surface is acquired by a flatbed scanner allowing simultaneous reading of the data with a reasonable accuracy. The optical resolution of the scanner was 6400 dpi, i.e. one image pixel represents four micrometers on the specimen. Considering that characteristic indent size was about 300 μm on diagonal, the typical uncertainty in indent size determination was 2 to 3 μm of its size. Taking into account that hardness is a function of area, it means of the square of the indents' size, the error due to size measurement is about 2 %, the value far below expected reproducibility of hand tester.

Claimed innovation of this technique is in the improved productivity and comfort of evaluation of indents' size in the studied area by the use of the scanner and by utilization of user-written application simultaneously.

Finally, maps of local hardness distribution in studied areas were produced. A similar approach for determination of macroscopic size and proportions of plastic zone is outlined in the paper[8].

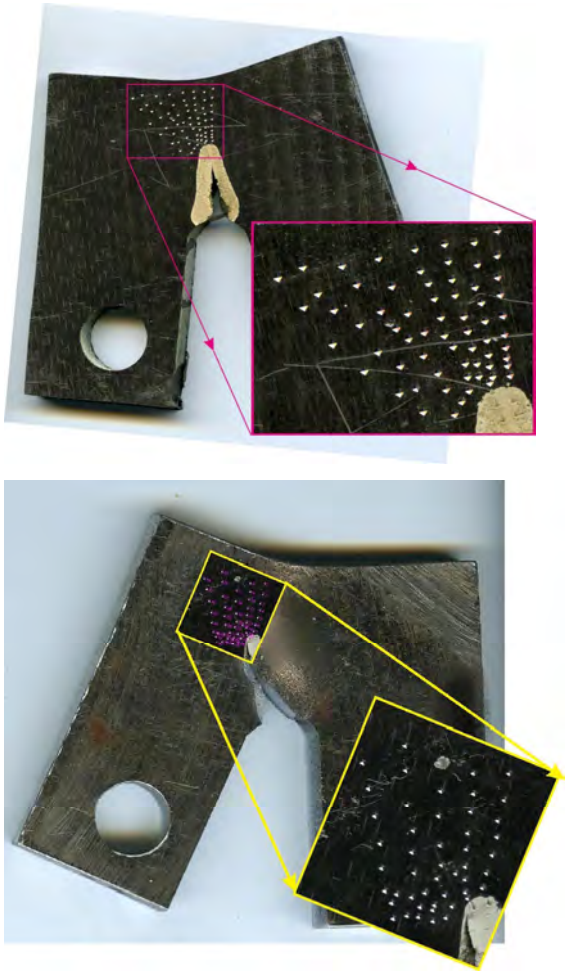

Fig. 3. **Two compared CT specimens and arrays of indents where hardness was determined.** (above – annealed, below – as delivered) Size of the specimen is approx. 60 mm

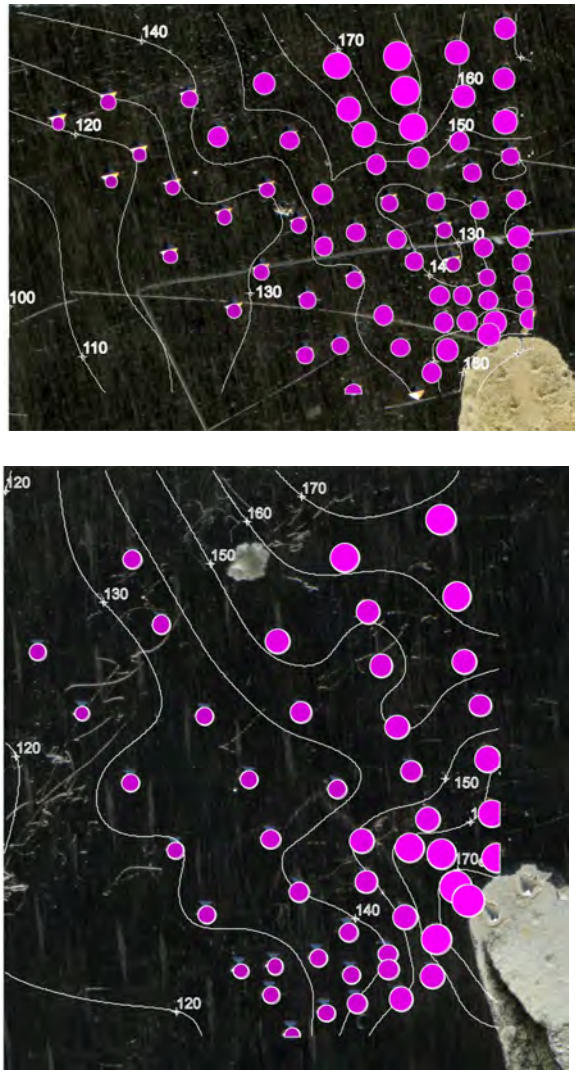

Fig. 4. **Overlay of plot and image depicts lines of equal hardness in front of notch** (in HV, above – annealed, below – as delivered)

4. Results and conclusions

Lines of the equal hardness derived from the interpolated discrete measurements, as well as the indents' original locations with a hardness value "coded" into circle diameter are presented in Fig. 4. It is noticeable that plastic zone in the thermally untreated specimen is more widespread, while the annealed specimen underwent severe plastic deformation localized mainly in the narrowest profile of the specimen. It means that plastic hinge is clearly pronounced in the hardness map of the annealed specimen. The highest values of hardness are not only in front of notch, but also on opposite side of the specimen, as implied by analysis of the stress field calculated from elasto-plastic analysis of the CT specimen during loading[9].

It can be summarized that for both of the specimens, the plastic zone shape and dimensions detected as a result of hardness measurement were confirmed similar to the one deduced from the temperature field. This technique can be successfully applied for complete description of the processes controlling materials' behavior during loading process. In spite of slight variation in relation between hardness, yield stress and plastic strain for a different level of deformation[10], hardness mapping can be used for evaluation of plastic deformation. Combining hardness measurement with data from stress-strain curve of the material, one can also estimate specimens' plastic deformation.

The presented technique is to be applied on investigation of mutual interaction between stress state at the tip of crack and material's hardening. This kind of information can provide useful insight in the elasto-plastic fracture behavior of materials. Utilization of the technique on study of hardness along the path of fatigue crack in cyclically

loaded large elements of steel railway bridges is another possibility. The simplicity of the technique also allows for its application on truly small scale in evaluation of arrays of indents from SEM micrographs.

The research has been supported by Grant Agency of the Czech Technical University (grant No. SGS12/205/ OHK2/3T/16), Czech Science Foundation (103/09/2101), RVO: 68378297 and by research plan of the Ministry of Education, Youth and Sports MSM6840770043.

REFERENCES

1. Tabor D.: *The Hardness of Metals*, Claderon Press, Oxford 1951.
2. Olivier W. C., Pharr G. M.: J. Mater. Res. *7*, 1564 (1992).
3. Žďárský M., Valach J.: In proceedings: *Engineering Mechanics, Praha*, 310, (2009).
4. Clarebrough L. M., Hargreaves M. E., West G. W.: Proc. R. Soc. London, Series A *232*, 252 (1955).
5. Giannakopoulos A. E., Suresh S.: Scr. Mater. *40*, 1191 (1999).
6. Zhang P., Li X. S., Zhang Z. F.: Mater. Sci. Eng., A *529*, 62 (2011).
7. Chaudhri M. M.: Acta Mater. *46*, 3047 (1998).
8. Ambriško L., Pešek L., Hlebová S.: Chem. Listy *104*, s287 (2010).
9. Žďárský M.: *Diploma thesis*. CTU FTS, Prague 2011.
10. Tekkaya A. E., Lange K.: CIRP Annals – Manufacturing technology *49*, 205 (2000).

J. Valach[a], M. Žďárský[b], D. Kytýř[a], T. Doktor[a], and M. Šperl[a] *([a] Institute of Theoretical and Applied Mechanics, Academy of Sciences of the Czech Republic, v.v.i., Prague, [b] Czech Technical University in Prague, Faculty of Transportation Sciences, Prague, Czech Republic):* **Determination of Local Distribution of Hardness for Investigation of Material Behavior Under Load Approaching its Strength**

The paper presents enhanced method for study of severe plastic deformation by hardness mapping utilizing portable hardness tester, flatbed scanner and software processing tool. This technique can be advantageous in situations, where crude information is not only sufficient, but also preferred, especially when it concerns testing on-site and on medium to large scale specimens and construction. Validity of the approach is supported by a comparison of hardness mapping results to the results obtained by an independent method based on evaluation of plastic strains from thermograms. It is shown that both methods determined similar shape and the extent of the plastic zone of the studied specimens.

NEW APPROACH TO EVALUATION OF NANOSCRATCH TEST

MICHAL VYLEŽÍK, JAN BRUMEK, and MARTIN PŘÍKASKÝ

RMTVC, VŠB-TUO, 17. listopadu 15/2172, 708 33 Ostrava, Czech Republic
jan.brumek@vsb.cz

Keywords: nanoscratch, normalized scratch energy NSE, abrasion

1. Introduction

New possibilities of measurements bring increased interest for research in mechanical and tribological properties of surface layers of materials.

Wear behaviour of coatings and materials has usually been described in terms of mechanical properties such as hardness (*H*) and reduced elastic modulus (*E*r). Nanoscratch test is also widely used to determine abrasion resistance of materials.

Tribological tests usually use performed kind of wear process to assess material surface characterization. Typically the wear tests are handled using full scale experimental model and tribological evaluations of the samples are focused on the damage characterization and material wear loss expressed volumetrically.

Tests results parameters can provide complex image of the material behaviour and are usually used for comparison of several types of microstructure. During these approaches is difficult to distinguish which degradation process played major role during wear processes.

This work is focused on quantitative characterization of wear resistivity of the material surface and mathematical modeling of wear process using scratch test[1,2].

2. Normalized scratch energy NSE

Quantification of work can be described by integral of the ratio of acting force and indenter depth over the scratch length:
F_l is lateral force; l is length of nanoscratch test; h is depth

$$NSE = \int_{l_0}^{l_1} \frac{F_l}{h} \cdot dl \qquad (1)$$

of nanoscratch test

In this research a new approach to evaluating the results of nanoscratch test is used. The result of this approach is based on normalized scratch energy NSE.
With the NSE we can accurately numerically quantify the results of the nanoscratch test and also quantify the abrasion resistance of the material.

Materials with higher values of NSE have higher resistance to abrasive violations.

Condition for comparing values of NSE is a standardized load function of nanoscratch test, which must be the same for all compared measurements[3].

3. Experimental procedure

There were performed set of experiments with pure silicon crystal in different crystal orientation planes. In this work is presented energetical approach to evaluation of the scratch test for two crystal orientations and wide range of the condition of the scratch.

This work is focused mainly on mathematical model of the scratch test itsels. Nanoscratch tests were performed on single crystal of silicon with orientation (100) and (111).

Nanoscratch test was performed on the Hysitron Triboindenter TI 950 device. Nanoscratch tests were performed with normal forces 500 μN and 1000 μN in both orientations. Three tests were performed for each force and orientations. Length of nanoscratch test was 10 μm and a velocity of the tip was 0.33 μm s^{-1}. With the higher velocity of the tip the value of NSE will increase, because the resistence of the material and the lateral force will increase.

Nanoscratch tests were performed by Berkovich diamond tip. In this case tip orientation on the track of nanoscratch test is important.

Fig. 1 shows different orientation of the tip. The lateral force will be different in both cases. The lateral force will be lower in Fig. 2a than Fig. 2b. Therefore, the value of NSE will depend on the orientation of indentation tip. Experiment results are only for comparison wich each other, because they were tested in the same orientation of the tip.

The ideal is nanoscratch test performed by spherical

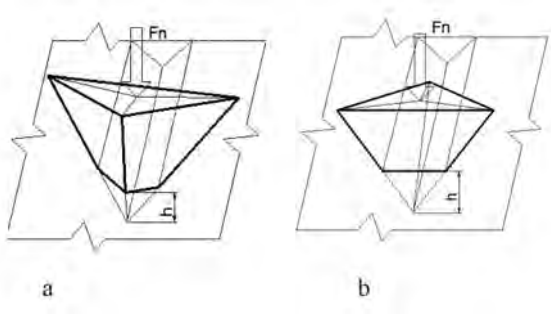

Fig. 1. **a) ideal alignment of the indentation tip b) real alignment of the indentation tip[4]**

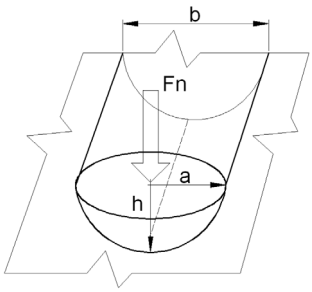

Fig. 2. **Ideal nanoscratch test for measurement NSE**[4]

indentor, which guarantees the same orientation of the tip and the reproducibility of results.

4. Results

Nanoscratch tests were performed on single crystals of silicon with orientations (100) and (111). The resulting values of NSE for normal forces 500 μN and 1000 μN are shown in Tab. I and average values are shown in Tab. II.

Single crystal Si (111) had a higher value of NSE than single crystal Si (100). Higher NSE values of single crystal Si (111) reflect a higher abrasion resistance of this single crystal orientation. Difference of NSE values was very small for both orientations (very small difference of abrasive resistance), but this difference was recognizable by this method. The cause of a small difference in values of NSE was the crystallographic orientation of the test surface.

Table I
Results of NSE

NSE $\times 10^{-3}$ [μNμm/nm]	Si (100)	Si (111)
	12.48	15.39
500 μN	12.34	13.61
	12.57	14.85
	9.67	11.81
1000 μN	9.79	11.79
	9.31	12.03

Table II
Average results of NSE

NSE $\times 10^{-3}$ [μNμm/nm]	Si (100)	Si (111)
500 μN	12.46±0.09	14.62±0.75
1000 μN	9.59±0.20	11.88±0.11

5. Conclusions

This paper demonstrates a new approach to evaluating the abrasion resistance of materials and surface layers. Value of NSE is calculated by quantification of energy consumed during the nanoscratch test. This energy is normalized by depth of nanoscratch test. The value of NSE corresponds to the abrasive resistance of the material. The value of NSE increases with increasing resistance of the material.

The obtained results are dependent on the orientation of the tip and parameters of the nanoscratch test (normal force, speed of lateral displacement).

In the experimental section were compared two single crystal of Si with different orientation (100) and (111). Different values of NSE were measured for both orientations. The NSE value of the single crystal Si (111) was always higher than NSE value of single crystal Si (100). The difference was very small, but recognizable in this new method.

This paper was created in the project of Ministry of Education, Youth and Sports No. SP2011/170 "The anisotropy of micromechanical properties of selected type of steel" and in project No. CZ.1.05/2.1.00/01.0040 "Regional Materials Science and Technology Centre" within the frame of the operation programme "Research and Development for Innovations" financed by Structural Funds and from the state budget of the Czech Republic, their support is gratefully acknowledged.

REFERENCES

1. Fox-Rabinovich G. S., Veldhuis S. C., Scvortsov V. N.: Thin Solid Films *469-470*, 505 (2004).
2. Chatterjee A., Kumar N., Abelson J. R., Bellon P., Polycarpou A. A.: Wear *265*, 921 (2008).
3. Pamuk U., Baydogan M., Nilufer B., Cimenoglu H.: Scr. Mater. 881-885 (2000).
4. Zelenak M., Valiček J., Brumek J.: Chem. Listy *105*, s688 (2011).

M. Vyležík, J. Brumek, and M. Příkaský (*RMTVC, VŠB – Technical University of Ostrava):* **New Approach to Evaluation of Nanoscratch Test**

The paper presents a new perspective on the assessment of abrasive failure of material and surface layers. Wear behaviour of coatings and materials has usually been described in terms of mechanical properties such as hardness (*H*) and reduced elastic modulus (*E*r). Nanoscratch test is also widely used to determine abrasion resistance of materials. This new approach uses to assessment normalized scratch energy NSE. The paper describes the testing methodology and influence of each scratch test parameters on resulting value of NSE. NSE values were experimentally measured and compared on two single crystal of Si.

THE INFLUENCE OF MODIFIED FLY ASH PARTICLES BY HEATING ON THE COMPRESSIVE STRENGTH OF GEOPOLYMER MORTAR

XIEM NGUYEN THANG, PETR LOUDA, DORA KROISOVA, TRUNG NGUYEN DUC, and THIEN NGUYEN

Department of Material Science, Faculty of Mechanical Engineering, Technical University of Liberec, Czech Republic
Thangxiemctm@yahoo.com

Keywords: fly ash particles, water to fly ash ratio, geopolymer mortar, compressive strength

1. Introduction

Every day, the world is generated large quantities of waste materials, such as: water, oils, solvents and solid waste (fly ash, glass, stone powder, mine tailings, etc). Fly ash has emerged as a material with high potential applications in construction because it has a chemical composition similar to Portland cement, cheep material, low density, good dispersion and fluidity[1,2]. However, the scope application of fly ash is very limited due to fly ash is grey or black in color; using only to product where color is not important. For this reason, a heating method was necessary to be developed to increase the whiteness of fly ash.

The purpose of this research is whitening the fly ash to compete with other filler materials. And compared the influence of adding fly ash before and after modified by high temperature in order to obtain the compressive strength and the hardness of geopolymer mortar is investigated. Experimental results show that high temperature is effective method to purify fly ash, high whiteness of the particle which increased with the calcination temperature and slightly reduced the hardness of geopolymer mortar.

2. Experimental

Geopolymer mortar prepared by mixing from calcined shale fly dust from rotary kiln as binder (Si/Al ratio of 2.0) with alkali activator containing NaOH and Na_2SiO_3 with modulus 1.50–1.95. Next the mixture was mixed with fine sand and fly ashes as filler[3]. Compressive strength testing of mortar was performed as per AS 1012.9 using (ø 50 × 100) mm diameter cylindrical moulds.
Fly ashes used in this study came from different sources in Czech Republic. The fly ashes were already classified into 2 names of city and coded such as: OPE (Elna Opatovice), PRT (Pražská Teplárenská).

Fly ashes are heated to improve the whiteness at certain temperature using a furnace. Around 1 kg fly ashes was heated in a furnace to 200 °C, 400 °C, 600 °C, 800 °C and 1000 °C at a heating rate of 5 K/min and with a soak time of 1 hour at the maximum temperature and finally annealed down to room temperature. The exact weight of fly ashes before and after heating was measured by using an analytical balance with a resolution of 0.1 mg. Fig. 1 shows that the weight loss of fly ash samples at temperature below 200 °C is small (less than 0.2 %), it indicates that as-received fly ash samples are relatively dry. When fly ash samples are further heated, the weight loss will be increased and the maximum of weight loss is at around 1000 °C. Fig. 2 shows fly ash particles before and after heating at 1000 °C.

Fly ash particles are generally spherical in shape and range in size from 1 μm to 20 μm. Figs. 3 and 4 show the SEM photographs and corresponding energy spectrum of fly ash OPE, PRT before and after heating at 1000 °C. After heating at high temperature, fly ash particles may suffer sever degradation, pitting, buckling, and breakage, which all can eventually regress the mechanical property of matrix. Tab. I shows the summary chemical composition of fly ashes.

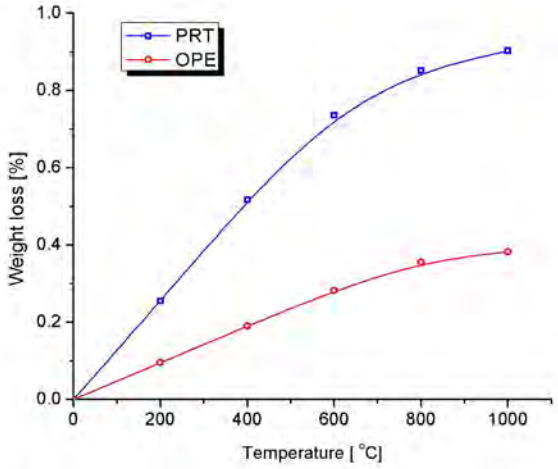

Fig. 1. **The weight loss as a function of heating temperature**

Fig. 2. **The photograph of fly ash OPE, PRT before (grey) and after heating at 1000 °C (brown)**

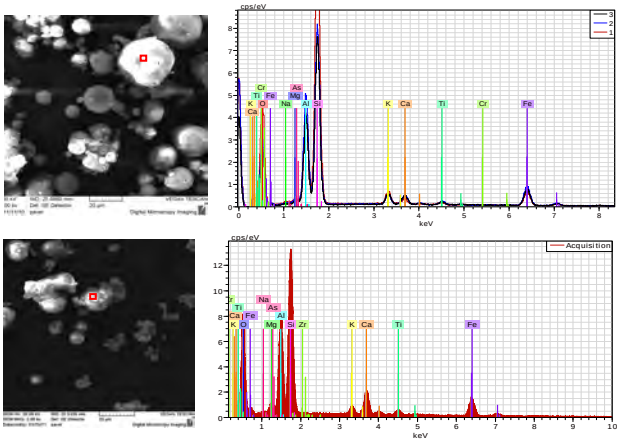

Fig. 3. **SEM photographs and corresponding energy spectrum of fly ash OPE before (above) and after heating at 1000 °C (under)**

Table I
The calcination dependent composition of fly ashes

Atomic [%]	PRT	PRT 1000 °C	OPE	OPE 1000 °C
Na	0.77	0.63	0.47	0.61
Mg	1.17	0.70	0.43	0.53
Al	10.89	4.50	12.64	13.88
Si	25.17	33.56	28.54	22.47
K	1.70	0.83	1.27	1.42
Ca	0.93	1.06	0.97	4.64
Ti	0.53	0.50	0.41	1.06
Fe	3.68	1.76	2.44	8.78
As	0.10	0.03	0.11	1.29
Cr	-	-	0.08	0.08
O	55.06	56.43	52.65	45.24

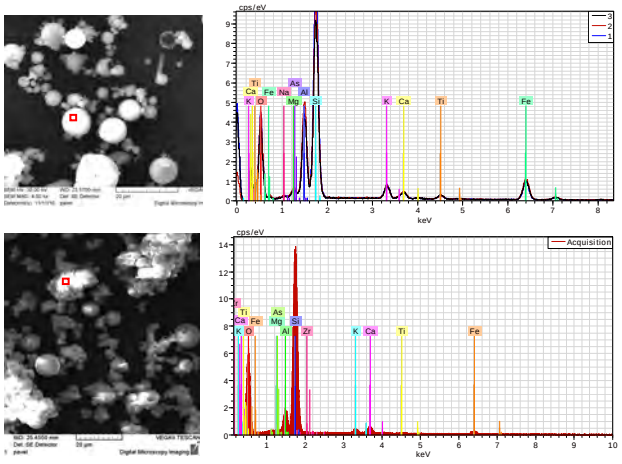

Fig. 4. **SEM photographs and corresponding energy spectrum of fly ash PRT before (above) and after heating at 1000 °C (under)**

3. Results

The obvious color difference can be observed by a naked eye for samples in Figs. 5−7.

This high processing temperature can have significant influence on the final properties of the geopolymer mortar.

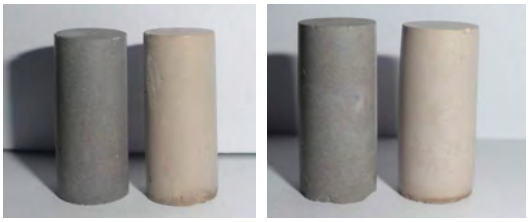

Fig. 5. **The photograph of geopolymer mortar based on fly ash OPE, PRT before (grey) and after heating at 1000 °C (brown)**

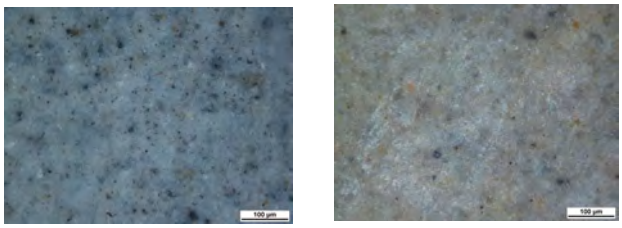

Fig. 6. **SEM photographs geopolymer mortar based on fly ash OPE before (left) and after heating at 1000 °C (right)**

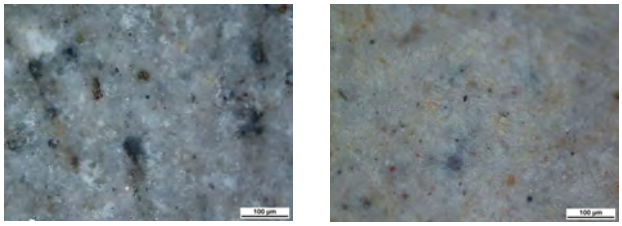

Fig. 7. **SEM photographs geopolymer mortar based on fly ash PRT before (left) and after heating at 1000 °C (right)**

Tabs. II and III present the hardness and density of geopolymer mortar based on fly ashes PRT, OPE before and after modified particles by heating at 1000 °C.

After heating fly ash particles at 1000 °C, the hardness and compressive strength of samples can be reduced slightly but not much in Figs. 8 and 9.

4. Conclusions

The purpose of this research is using the method of calcination temperature to whitening the fly ash to compete with other filler materials. It is evident from the above

Table II
Properties of geopolymer mortar before and after heating PRT fly ash (FA) particles at 1000 °C

Water/fly ash [%]		0.25	0.33	0.37	0.40
Original FA	Density [g/cm^3]	1.75	1.62	1.47	1.53
	Hardness [HV]	353±7	279±5	198±6	146±3
FA at 1000 °C	Density [g/cm^3]	1.73	1.56	1.42	1.46
	Hardness [HV]	346±7	249±7	163±6	132±3

Table III
Properties of geopolymer mortar before and after heating OPE fly ash (FA) particles at 1000 °C

Water/fly ash [%]		0.21	0.33	0.35	0.42
Original FA	Density [g/cm^3]	1.77	1.67	1.53	1.51
	Hardness [HV]	312±9	282±9	231±6	141±6
FA at 1000 °C	Density [g/cm^3]	1.54	1.54	1.36	1.38
	Hardness [HV]	247±4	267±8	189±3	125±4

observations that the high temperature has considerable effect on the surface morphology and pitting of the fly ash particles. The study are used fly ash particles as filler, the particles after heated at high temperature will soften and may have adverse effect on the structural and reduced mechanical properties of the geopolymer mortar. Thus, authors recommend this method use in fine art sculpture, architecture, especially where color is more important than the mechanical properties.

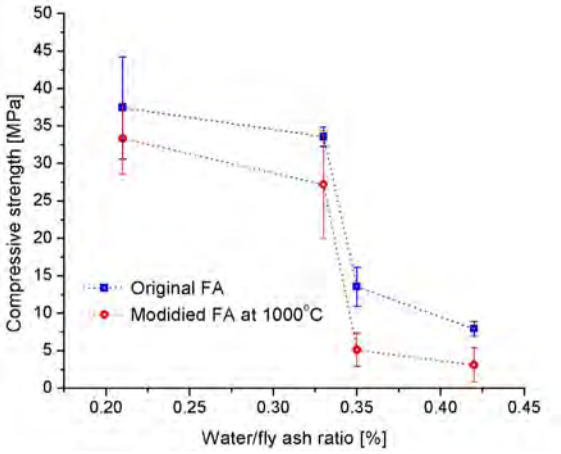

Fig. 8. **Compressive strength of geopolymer mortar based on fly ash PRT**

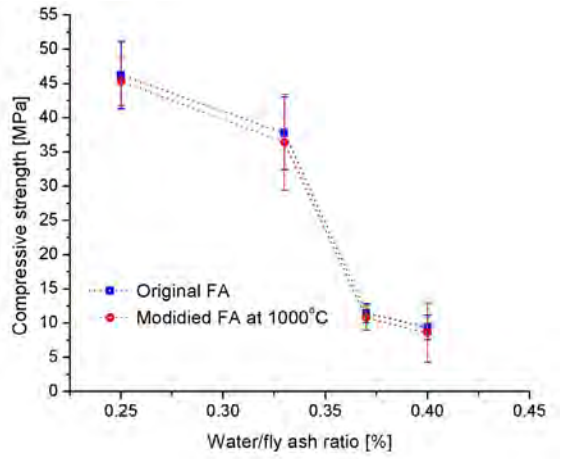

Fig. 9. **Compressive strength of geopolymer mortar based on fly ash OPE**

The authors were supported by Ministry of Education of the European Social Fund (ESF) – Operational Program VaVpI under the project Center for Nanomaterials, advanced technology and innovation", CZ.1.05/2.1.00/01.0005 and by project "Innovation Research in Material Engineering" of PhD student Grant TUL.

REFERENCES

1. Horiuchi S., Kawaguchi M., Yasuhara K.: J. Hazard. Mater. *76*, 301 (2000).
2. Yang H. F., Zhang Q.: Chem. Indus. Press. 165 (2003).
3. Němeček J., Forstová K.: Chem. Listy *105*, s146 (2011).

N. Xiem, P. Louda, D. Kroisová, N. Trung, and N. Thien *(Department of Material Science, Faculty of Mechanical Engineering, Technical University of Liberec, Czech Republic):* **The Influence of Modified Fly Ash Particles by Heating on the Compressive Strength of Geopolymer Mortar**

In this study, 2 types of fly ash from Czech Republic power plants were investigated with respect to composition. Fly ashes particles are heated at high temperature up to 1000 °C to remove the contaminant (unburnt carbon) and the color become brighter can be observed by a naked eye. However, the high processing temperatures can slightly influence on the final properties of the fly ash and geopolymer mortar. After heating fly ash particles at 1000 °C, the compressive strength of samples can be reduced slightly when comparing with original fly ash.

EFFECTS OF COMMERCIAL FIBERS REINFORCED ON THE MECHINCAL PROPERTIES OF GEOPOLYMER MORTAR

XIEM NGUYEN THANG, PETR LOUDA, DORA KROISOVA, VLADIMIR KOVACIC, HIEP LE CHI, and NHUT LUU VU

Department of Material Science, Faculty of Mechanical Engineering, Technical University of Liberec, Czech Republic
Thangxiemctm@yahoo.com

Keywords: basalt fiber, Isover granulate fiber, geopolymer mortar, flexural strength, hardness

1. Introduction

In 1979, geopolymer was first discovered by a French professor Joseph Davidovits, geopolymers have emerged as a promising new material for coatings and adhesives, a new binder for fiber composites, new cement for mortar or concrete and environmentally sustainable properties[1–3]. Geopolymers possess many advantages compared with ordinary Portland cement as the following: high fire resistance (up to 1000 °C), good acid resistance, high compressive strength[4], etc. However, geopolymer mortar and concrete always have flaws and micro-cracks at the interfaces even before an external load was applied[5–8], because the micro-cracks in the matrix (in this case geopolymer resin) are determined as inborn defects of inorganic matrix[4].

Short fibers have been known and used for many decades to reinforce brittle materials like cement[5]. Currently, there are various types of fiber available for commercial use, the basic types being glass[6], carbon[6], polypropylene[7], nylon[8] and some natural fibers[8] (coconut, jute, rice straw, sugar cane, wood, banana, etc.). All previous research has been concerned with short random fibers reinforced concrete and mortar. When combined with short fibers reinforced concrete, the results showed that concrete increases its mechanical and fracture properties compared to unreinforced concrete[6–8].

In this paper, we used basalt and Isover granulate fibers as a filler in geopolymer mortar. These fibers have some advantageous properties including low cost, light weight, good chemical resistance, high-performance insulation materials (thermal and sound), stable in the alkaline environment of concrete and resistant to plastic shrinkage cracking. Especially, the fiberization process is more environmentally safe than other fibers. Further, they have no toxic reaction with air or water, and are noncombustible and explosion proof. Nevertheless, Isover granulate also has some disadvantages including poor fire resistance, a low Young's modulus[10].

At the present time, there are no reports about basalt and Isover granulate reinforced geopolymer mortar. The present paper compares the mechanical properties of geopolymer mortar reinforced with short random commercial fibers and with unreinforced geopolymer mortar. Preliminary, the results showed a significant increase in the flexural strength and the hardness of geopolymer mortar containing different percentages of fibers studied.

2. Experimental

Geopolymer cements were synthesized from shale fly dust burnt in rotary kiln (for 10 hours at 750 °C) with Si/Al and Na/Al molar ratio of 2.0 and 0.8 respectively, that is poly(sialate-siloxo)[4]. Geopolymer resin was prepared by mixing of alkali activator containing NaOH and Na_2SiO_3 with modulus 1.50 ÷ 1.95 with geopolymer cement. The microstructure of pure geopolymer matrix was analyzed by mean of SEM and EDX in Fig. 1.

The fly ash used in this study came from Komořany Látkový Filtr in Czech Republic. Fly ash particles are generally sharp, pointed and range in size from 1 μm to 30 μm, Fig. 2.

All experiments were performed using the same batches of reagents and starting materials. The atomic of fly ash are summarized as following: Na (1.81 %), Mg (0.97 %), Al (14.73 %), Si (23.97 %), S (0.39 %), K (0.41 %), Ca (1.69 %), Ti (0.57 %), Fe (2.57 %), As

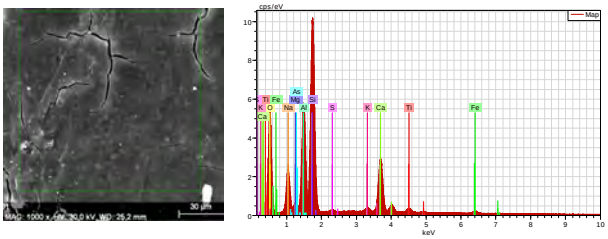

Fig. 1. **SEM and EDX mapping of an individual geopolymer matrix**

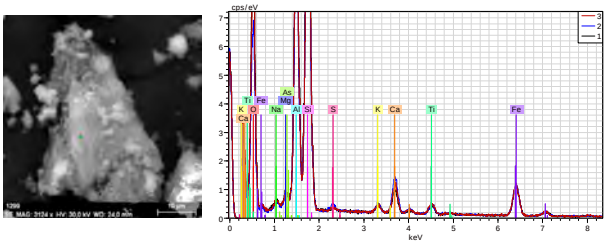

Fig. 2. **SEM and EDX mapping of an individual fly ash**

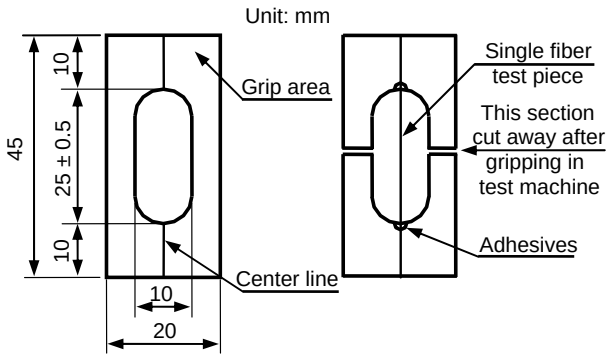

Fig. 3. **Mounting tab for single filament testing**

(0.09 %), O (52.81 %).

Geopolymer mortar mixtures were used to reinforce different volume fractions ranging from 0.2 to 4 % of Isover granulate and basalt fiber from 0.2 to 2 %, respectively. Tensile strength, Young's modulus and elongation of fibers were investigated as following.

A single filament of each kind of fiber was separated with a magnifier and prepared on a punched mounting tab. The single filament test piece was bonded by adhesive so as to let the length specified gauge length under the condition to make the filament straight along the center line of the mounting tab. This was evaluated in accordance with Japanese Industrial Standard (JIS R 7601)[11]. Tensile strength and Young's modulus were calculated from the load-elongation records and the cross-sectional area measurements. The specimen is shown in Fig. 3.

The samples were tested by the machine Instron LaborTech 2.050 (maximum load of sensor: 5 N).

Properties of commercial fibers are illustrated in Tab. I and Fig. 4 displays SEM images of the fibers.

The technology of sample preparation is as follows. At first, the geopolymer resin was prepared by mixing the alkaline activator with the raw materials. The liquid and

Table I
Main properties of short basalt and Isover granulate fiber

Properties	Basalt BCF13-2520tex	Isover granulate
Diameter, μm	13	7
Density, kg m^{-3}	2670	2880
Length, mm	3.2 ± 0.5	1.0 ÷ 5.0
Young's modulus, GPa	64	–
Tensile strength, MPa	2563	0.146
Elongation, %	3.98	2.3
Thermal conductivity, W/(m.K)	0.031÷0.038	0.044

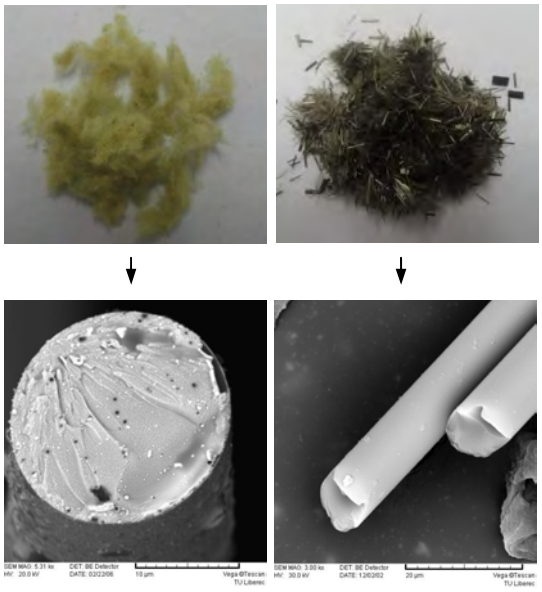

Fig. 4. **The microstructure of commercial fibers, left: Isover granulate, right: basalt**

solid components were mixed for about 3 minutes at room temperature until the solution homogenized, while the mixer was running at 60 rpm. Next, the geopolymer resin mixture was mixed with fly ash and fine sand content[12]. The mixing was done in an air conditioned room at approximately 20 °C until the mixture homogenized (about 5 minutes). The fibers were added, and the mixer was allowed to run for another 5 minutes. Directly after mixing, the fresh mortar was poured into the moulds with dimension (40 × 40 × 160) mm in accordance to ASTM C348 and vibrated for 1 minute on the vibration table to remove air voids. These samples were cured at room temperature for 3 days after casting. Next, the samples were removed from the moulds and left in laboratory ambient conditions until the day of the test. The sample ages for the latter tests were 7, 14, and 28 days. The values are the averages of three separate tests. Data that deviated more than 10 % was eliminated.

The sample dimensions were made and tested under three-point bending in accordance to ASTM C78 standard test method for flexural strength of mortar and concrete. The flexural tests were conducted over a simply supported crosshead speed of 2.0 mm min^{-1} and span length of 120 mm with a center-point load by the testing machine INSTRON Model 4202 (maximum load of the sensor: 10 kN).

3. Results

The initial density of specimens containing Isover granulate and basalt fibers was less than that of mixtures without any fibers. Tab. II shows that the density of specimens was significantly decreased when increasing the per-

Table II
Density ρ [g cm^{-3}] of geopolymer mortar after curing 28 days at room temperature

Percentage of fiber [%]	Isover granulate	Basalt
0.0	1.74	1.74
0.2	1.73	1.69
0.5	1.72	1.68
1.0	1.71	1.58
2.0	1.70	1.57
3.0	1.68	–
4.0	1.57	–

centage of fibers reinforced with geopolymer mortar. The weight change of mortar was mainly due to the dehydration of cement paste.

Figs. 5 and 6 show a flexural strength comparison graph between the commercial fibers studied. According to the results, by increasing the amount of fibers in the matrix the flexural strength of specimens reduced. Also, it is clear that the flexural strength of specimens increased by increasing the curing time at room temperature. When the curing time was increased (particularly from 14 to 28 days) the flexural strength of the geopolymer mortar of the specimens without fibers was significantly reduced by 52 % (5.20 to 2.72 MPa).

The results of geopolymer mortar containing 0 %, 1 % Isover granulate and 2 % basalt fibers are shown in Tab. III. The flexural strength of unreinforced and synthetic reinforced geopolymer mortar is compared to the commercial fiber-reinforced geopolymer mortar. Commercial fibers reinforced geopolymer mortar has higher flexural strength than unreinforced mortar. The test results showed that optimum content of fibers (1 % for Isover and 2 % for short basalt fibers) results in ca the same flexural strength (6.95 and 6.91 MPa) after curing 28 days at room temperature. An increase in the flexural strength of ca 39 % for both fiber reinforcement is observed when compared with unreinforced geopolymer mortar.

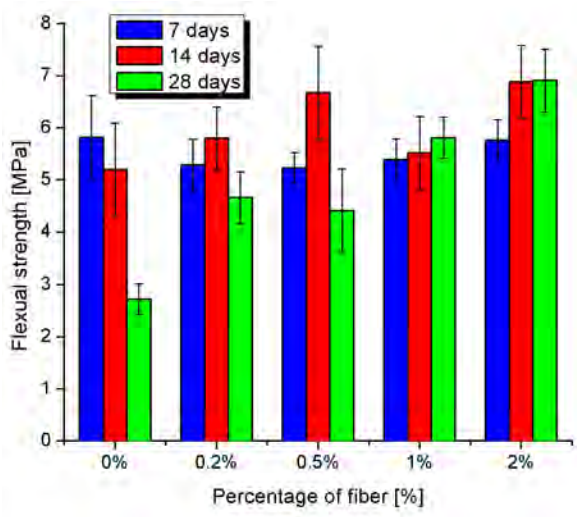

Fig. 5. **The flexural strength of short basalt fiber reinforced geopolymer mortar**

Table III
Flexural properties of geopolymer mortar with 0 %, 1 % Isover granulate and 2 % basalt fiber after curing 28 days

Properties	Flexural strength R_o [MPa]	Flexural modulus E [GPa]	Relative deformation ε [%]
0%	2.72 ± 0.3	1.35	0.66
1% Isover	6.95 ± 0.2	1.15	2.01
2% basalt	6.91 ± 0.6	1.17	1.38

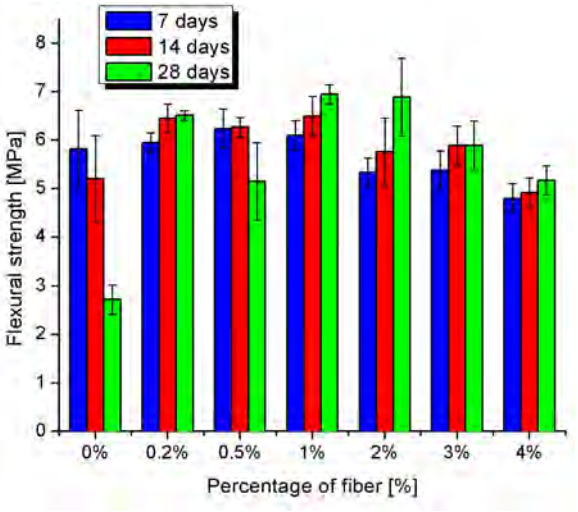

Fig. 6. **The flexural strength of Isover granulate fiber reinforced geopolymer mortar**

Commercial fibers were mixed well homogenized with geopolymer resin.

Fig. 7 shows the variation of Vickers hardness depending on the fibers content and curing time of geopolymer mortar. Isover granulate (1 %) fiber reinforced mortar exhibits the highest hardness of 3.30 GPa compared to 3.08 GPa of the unreinforced sample. Generally the addition of commercial fibers in mortar can lead to the improved hardness.

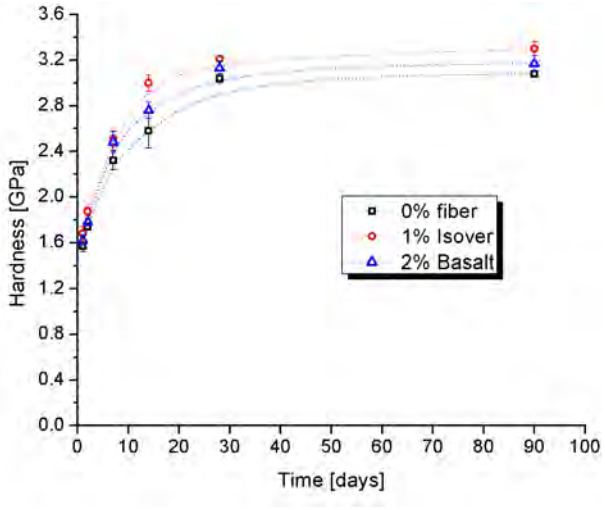

Fig. 7. **The hardness of fibers reinforced geopolymer mortar with function of time and fibers content**

4. Conclusions

Geopolymer mortar and concrete have very promising properties which may place this material in the building and public works market in the near future.

In this study, the effect of commercial fibers content on the mechanical properties of the geopolymer mortar was investigated and the following conclusions were derived:

- The percentage of fibers content in mortar has been optimized.
- Mechanical properties of mortar can be improved by the addition of short basalt and Isover granulate fibers.
- The density of specimens was significantly decreased when increasing the percentage of fibers reinforced with geopolymer mortar.
- Isover granulate fiber displays to be an excellent reinforcement for geopolymer mortar increasing the hardness, flexural strength and can be very easily and homogeneously mixed with geopolymer resin.
- The durability of commercial fibers for reinforcement can be improved by stabilization of micro-cracks and reduced shrinkage.

The authors were supported by the Ministry of Education of the European Social Fund (ESF) – Operational Program VaVpI under the project "Center for Nanomaterials, advanced technology and innovation", CZ.1.05/2.1.00/01.0005 and by project "Innovation Research in Material Engineering" of PhD student Grant TUL.

REFERENCES

1. Palomo A., Grutzeck M. W., Blanco M. T.: Res. *29*, 1323 (1999).
2. Shuzheng Z., Kecheng G., Jianwen L.: Water *58*, 1292 (2004).
3. Duxson P., Provis J. L., Lukey G. C., Van D.: Cem. Conc. Res. *37*, 1590 (2007).
4. Joseph D.: *Geopolymer chemistry & application*, p. 4, Institute Géopolymèr, France (2008).
5. Harun T.: Mater. Des. *30*, 3252 (2009).
6. Reis J. M. L., Ferreira A. J. M.: Cons. & Build. Mater. *18*, 523 (2004).
7. Gonzalo M. B., Fernando U. N., Osman G.: Comp. *42*, 567 (2011).
8. Li Z., Lijing W., Xungai W.: Fib. Poly. *5*, 187 (2004).
9. Saint-Gobain Insulation, http://www.isover.com/, accessed 5.10.2011.
10. Xiem N. T., Kroisová D., Louda P., Hung T. D., Zbynek R., Bortnovsky O.: *16th Strutex*, p. 9 (2009).
11. Kirshenbaum S. L., Barker H. J., Dowell D. W.: Comp. Mater. Test. Des. *8*, 219 (1988).
12. Němeček J., Forstová K.: Chem. Listy 105, s146 (2011).

N. Xiem, P. Louda, D. Kroisová, V. Kovačič, L. Hiep, and L. Nhut *(Department of Material Science, Faculty of Mechanical Engineering, Technical University of Liberec, Czech Republic):* **Effects of Commercial Fibers Reinforced on the Mechanical Properties of Geopolymer Mortar**

The essential objective of this work is to study the mechanical properties and microstructure of geopolymer mortar containing different kinds of fibers. Results show that the use of fibers as reinforcement in geopolymer mortar significantly improves the flexural strength and the hardness of the geopolymer mortar, reduces the amount of cracking and is also more lightweight than before.

APPLICABILITY OF ADDITIVE LAW IN MICROHARDNESS MEASUREMENTS ON POLYMER MATERIALS

GALINA ZAMFIROVA

Transport University "T. Kableshkov", Geo Milev str. 158, 1574 Sofia, Bulgaria
gzamfirova@mail.bg

Keywords: Vickers microhardness, microindentation, additive law

1. Introduction

Additive law known also as a "rule of mixture" could be applied in microindentation measurements when the sample measured is a system consisting of two or more components. Additive law for microhardness could be generally presented by the equation:

$$H = H_1x_1 + H_2x_2 + \ldots + H_ix_i, \quad (x_1 + x_2 + \ldots x_i = 1) \qquad (1)$$

where H_i and x_i are the microhardness and mass fraction, respectively, of each component of the systems.

In the case of polymer materials these components could be: crystal polymers having a crystal and an amorphous phase; copolymers whose molecular structure comprises different incorporated monomers; polymer blends that could be miscible and inmiscible; polymer composites which could be of a greate variety according to the type of matrix and the filler particles size.

The main goal of this work is not to define the limits for validity of additive law, but to describe some cases when the coincidence or the deviation of microhardness values determined experimentally from those predicted by additive law helps to clarify some structural peculiarities of the samples studied.

2. Investigation methods

Two types of microhardness were determined:

– Vickers microhardness (MHV), which is the material resistance against irreversible deformation. This magnitude is determined predominately by the type, quantity and perfectibility of the crystal units (lamellas) and by the mechanism of their deformation during the penetration. It is calculated according to the equation:

$$MHV = kP/d^2 \qquad (2)$$

where P is the applied load, d is the projected diagonal of residual imprint and k is a constant depending on geometry of the pyramid.

– Total microhardness (MHT), which characterizes the overall material response to indenter penetration, including reversible and irreversible components of deformation. It is given by a similar equation:

$$MHT = kP/D^2 \qquad (3)$$

where D is the projected diagonal length of the imprint in the loaded state. For polymers usually the type and structure of the disordered (amorphous) phase is related to reversible deformation.

3. Results and discussion

Some of the experimental work and a good deal of data have already been reported in the literature on these materials. Now we will emphasize and discuss the following multiphase or multicomponent systems with regard to the additive law.

3.1. Semicrystal polymers

It is known that all semycrystal polymers or called only crystal polymers consist of an ordered crystal phase and disordered amorphous one. For them the additive law is expressed as follows:

$$MHV = \alpha MHV_c + (1-\alpha)\, MHV_a \qquad (4)$$

when $MHV_a << MHV_c$ $\qquad MHV = \alpha MHV_c \qquad (5)$

where MHV_c and MHV_a, are Vickers microhardness values of the crystalline and amorphous phases and α is the degree of crystallinity. In accordance with[1] for many polymers $MHV_a << MHV_c$ and could be ignored.

Three types of ultra-high molecular weight polyethylene (UHMWPE) obtained via different catalytic systems and consequently characterised by different molecular weight, M_η, and degree of crystallinity, α were studed[2] (Table I). The difference between catalyst systems 2 and 3 are in the ratio of cocatalyst. The obtained values for MHV and MHT as well as the MHV_c value calculated by equation (5) are also presented in Table I. As seen MHV increases when the degree of crystallinity increases and the molecular weight decreases. It was established that the molecular weight for polyethylene influences linearly MHV only if $M_\eta < 10^5$ (ref.[3]). In this case M_η does not influance directly MHV but influences α and lamelas perfecttions. The too large molecule chaines can take part in more than one lamella. That gives rise to additional entaglements and tie molecules in the amorphous regions between ctystallites. As a result the decrease of the molecule weight leads to increasing of the degree of crystallinity and crystalline perfectuon (MHV_c). On the other hand, it has been established that for samples obtained by titanium catalitic systems the polymerization rate exceeds the crystallization one. That gives rise to many physical entanglements and tie molecules in the amorphous areas which

Table I
UHMWPE obtained via different catalytic systems and their structural (M_η, α) and microhardness characteristics

N°	Catalist system	M_η x10^6	α [%]	MHV [MPa]	MHT [MPa]	MHV_c [MPa]
1	V/SiO_2	5.4	60	32.6	20.7	63.9
2	Ti/SiO_2	2.1	66	37.2	23.1	64.7
3	Ti/SiO_2	1.0	72	41.1	27.6	66.2

contributes to increasing the resistance against elasic deformation. The latter was calculated according to a parallel model[4]: 56.7 MPa, 60.1 MPa, 82.8 MPa, for samples 1, 2 and 3 respectively. In this case microhardness measurements give a possibility to distinguish the efect of crystallinity from the effect of entanglements.

3.2. Copolymers

Norbornen-ethylene copolymers with relatively high norbornene content synthesised using a number of different metallocene catalysts were studied by microindentation methods, PALS (Positron Annihilation Lifetime Spectroscopy) and NMR[5]. The norborene content as well as the prevailing sequences, determined by NMR are listed in Table II.

As seen from Fig. 1 and Fig. 2 the dependences of MHV and MHT as a function of norbornen content are not linear. So, the additive law is not valid. In this case one can expect that Vickers microhardness, could depend both on the rigidity of the polymer chains and on the free volume Fv. MHV is almost the same for the polymers containing meso dyads (C, A, E) and is not sensitive to other sequences included in these samples. So, MHV is not sensitive to block sequences. As distinct from MHV, the alternating groups and blocks influence the resistance against the total deformation (MHT) (Fig. 2). Sample E shows a relatively good resistance against plastic deformation but a very low resistance against total deformation, i.e. it exhibits good elastic properties due the prevailing ethylene blocks. On the other hand, the dependence of the free volume Fv versus norbornene content (Fig. 3) has the same tendency as Fig. 1. That does not mean that MHV depends linearly on Fv, but that MHV and free volume measurements have a similar sensibility to rigidity of the main polymer chain.

Hence, it could be concluded that Vickers microhardness is influenced predominantly by the micromechanical

Table II
Norbornen-ethylene copolymers

Tg [°C]	Norb [%]	The most characteristic norbornene sequences: Alternating ENENENE	Meso dyads ENME	Blocks ENNNE
A	173 55	++	++++	+
C	194 54	+	++++	+
D	148 47	++++ (isotactic)	+	+
E	125 60	++	++	++++
F	156 58	+++ (syndiotactic)	+++ (racemic)	

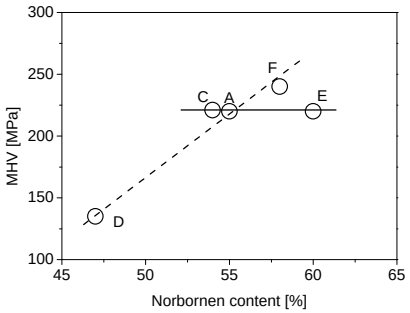

Fig. 1. **Vickers microhardness vs. norbornene content**

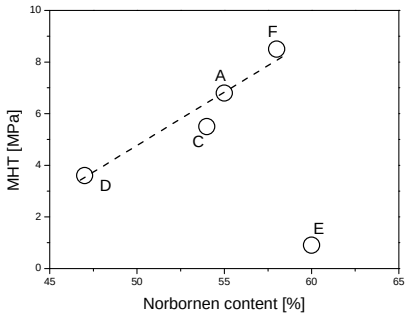

Fig. 2. **Total microhardness vs. norbornene content**

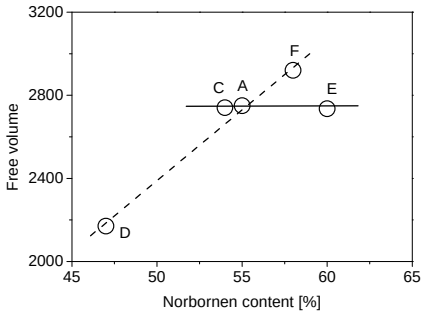

Fig. 3. **Free volume vs. norbornene content**

properties of the polymer chains. This parameter is not sensitive either to dimensions and quantity of the pores or to the free volume.

3.3. Polymer blends

Blends based on a polypropylene/cycloolefin copolymer (COC) with a spontaneously arisen fibrous structure were also studded[6]. Despite of the immiscibility of both components, it was experimentally found that COC fibril has a reinforcing role in the case of blends with small quantity of COC (Fig. 4). Applying the additive law to the blend compositions the inherent values for Vickers microhardness for the ingredients within the blend was estimated (Fig. 5). The unusual trend of the microhardness profiles was explained by the manifestation of the scale factor in the thin COC fibers.

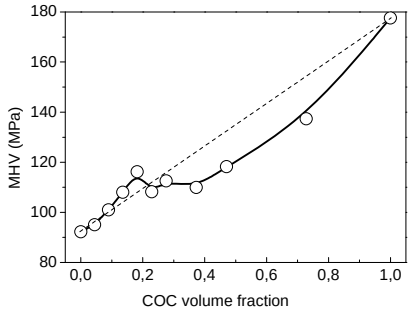

Fig. 4. **Vickers microhardness vs. COC content**

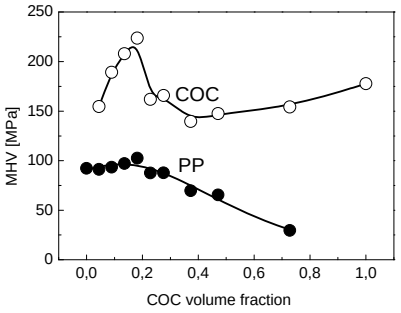

Fig. 5. **Inherent MHV values for PP and COC components for different PP/COC blends**

3.4. Polymer composites

UHMWPE/Fe composites obtained by pressing and sintering were studded[7]. Filler particles were relatively large, in the range 50–200 μm and were extremly porous.

Table III
Vickers microhardness of UHMWPE/Fe composites

Sample	1	2	3	4	5
UHMWPE [wt.%]	100	73	49	24	0
Fe [wt.%]	0	25	49	72	100
Additivves [wt.%]	0	2	2	4	0
MHV [MPa]	41	42	39	40	1700

Small amaunts of the additives (up to 5 %) as carbon, stearates, etc. were also added. Table III presents the relation between composition ingredients in the samples and the obtained mean values of Vickers microhardness.

It is evident that the additive law is absolutely inapplicable and there is no correlation between the microhardness and metal content. When the indenter presses the large iron particle it sinks into the much softer polymer matrix. That is why the overall microhardness of the composites does not vary and is almost equal to that of the pure polymer.

3.5. Polymer nanocomposites

Usually there are deviations from the additive law in the case of nanocomposites. Those are caused by different reasons: changes in the structure of the polymer matrix, agglomeration of the nanofiller particles, etc. Two examples for a crystal and an amorphous polymer nanocomposite are described and discussed below.

PP/multiwall carbon nanotubes composites (MWCNT)[8] which concentration dependence of Vickers microhardness passes through three characteristic zones (Fig. 6). In small weight fractions of MWCNT, MHV rapidely increases (line a) and that is due to the nucleation effect of the MWCNT. Changes in the crystal phase of the polypropylene matrix occur consequently. A further increase in MWCNT content in the composite leads to a smoother increase in microhardness, obeying the additive

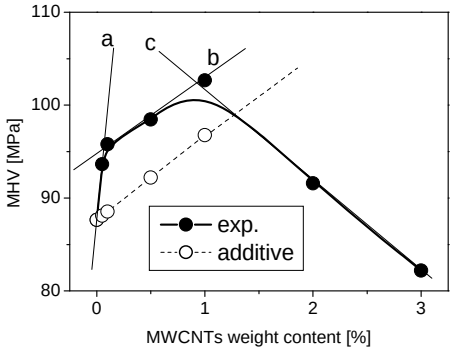

Fig. 6. **Vickers microhardness vs. MWCNT content**

law (line b). After 1 % concentration threshold, percolation processes take place and the effectiveness of the nanofiller decreases drastically (line c). The microhardness even becomes worse than that of the non-filled samples.

Epoxy/multiwall carbon nanotubes composites[9] were prepared by two different processing modes with functionalization and without functionalization of the filler. Polyethylene polyamine was used as a curing agent. The samples without preliminarily functionalized nanoparticles show decreasing of the microhardness parameters (MHV and MHT) at small MWCNT content (about 0.03 wt.%) (Fig. 7), while functionalized ones exhibit an increase in these characteristics due to better exfoliation (Fig. 8). However, an additional portion of MWCNT causes again a diminishing of their hardness which could be attributed to a reached percolation threshold and to the formation of floccules. The hardness increases for composites with filler amount higher than 0.08 % because carbon nanotubes form a spatial network in the entire volume of the composite.

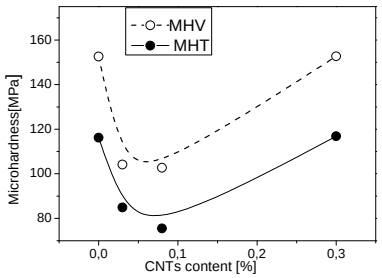

Fig. 7. **MHV and MHT vs. MWCNTcontent for samples without preliminarily functionalized nanoparticles**

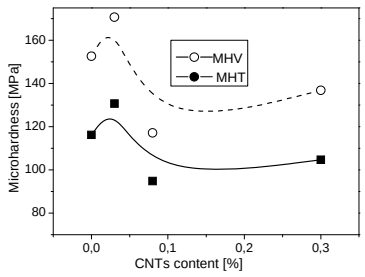

Fig. 8. **MHV and MHT vs. MWCNT content for samples preliminarily functionalized**

4. Conclusions

There are many conditions or limits to the direct applying of the additive law:

– There should be no big difference in the hardness of the components. When solid particles are distributed in a soft matrix during the indentation, they only "float" in the soft medium and do not contribute to the hardness of the system. When soft particles are distributed in a hard matrix, they do not contribute with their inherent small hardness but the system has behavior like that the second component is an empty space.

– For semicrystal polymers not only the degree of crystallinity has to be taken in account but also the inherent hardness of the crystal phase which depends on type of crystal cell, depth of the crystal lamella and their perfectibility. Especially when studying total microhardness, the structure of the amorphous phase and eventually her changes has to be considered because it contributes mainly to the elastic resistance against penetration.

– For copolymers: the relation between the quantity of monomer units is less important than their sequence. The inherent rigidity of the macromolecules is more significant than the magnitude of the free volume.

– For polymer blends and composites the filling agent must not cause structural changes in the polymer matrix. The dimensions of the filler particles must not change with the degree of fillings as in the direction of agglomeration because its effectiveness drastically decreases, as well as in the direction of diminishing because of occurrence of scale factor or orientation reinforcing effect.

– Of course many times the properties of the mezzophase have to be taken into account as an additional component of the system. Hence the miscibility for polymers and wetting of the filler for composite materials are essential factors for the eventual application of the additive law.

Therefore the deviations from the additive law could not be considered as an obstacle for microhardness investigation. Those should be regarded as an indication of some structural peculiarities of the samples and a challenge for structural investigation and characterization of the relatively complicated polymer based materials.

This study has been supported by NSF – Bulgaria, (D002-138/2008-2011).

REFERENCES

1. Baltá Calleja F. J., Fakirov S., *Microhardness of Polymers*, p. 11, Cambridge University Press, Cambrige 2000.
2. Zamfirova G., Pereña J. M., Benavente R., Peréz E., Cerrada M. L.,Nedkov E.: Polym. J. 34, 125 (2002).
3. Baltá-Calleja F. J., Giri L., Ward I. M., Cansfield D. L. M.,: J. Mater. Sci. *30*, 1139, (1995).
4. Zamfirova G.: *Proc. in Int. Conf. "Mech. & Tecnol.of Composite Mat.,"* Varna, Bulgaria, 275 (2009).
5. Zamfirova G., Misheva M., Peréz E., Benavente R., Cerrada M. L., Djourelov N., Kresteva M., Pereña J. M.: Polym. J. *34*, 779 (2002).

6. Zamfirova G., Gaydarov V., Lorenzi D., Fambri L.: *Proc. in 24th ISPAC*, Torino, Italy, 82 (2011).
7. Zamfirova G., Jeliazkov J., Nedkov E.: Coll. Polym. Sci. *260*, 105 (1991).
8. Zamfirova G., Blahova O., Minster J., Gaydarov V.: Chem. Listy *105*, s725 (2011).
9. Zamfirova G., Gaydarov V., Ivanov E., Kotsilkova R.: *Proc. in 24th ISPAC*, Torino, Italy, 89 (2011).

G. Zamfirova *(Transport University "T. Kableshkov", Sofia, Bulgaria):* **Applicability of Additive Law in Microhardness Measurements on Polymer Materials**

This paper deals with some cases when additive law could be applied. It also presents the positive or negative deviations from it exhibited by some semicrystal polymers, copolymers, polymer blends and polymer based materials. The ways how the deviation of experimentally determined microhardness from the one predicted by the additive law could indicate and help to determine some structural peculiarities of polymer based materials with a relatively complicated structure have been described.

INVESTIGATION OF MORPHOLOGY CHANGES ON CARBON THIN FILMS UNDER RECIPROCATING SLIDING TESTS

E. ZDRAVECKÁ[a], V. M. TIAINEN[b], A. SOININEN[b] , Y. T. KONTTINEN[b,c,d], L. FRANTA[e], M. VOJS[f], M. MARTON[f], M. VESELÝ[f], M. KOTLÁR[f] , M. KELEMEN[a], and M. ONDÁČ[a]

[a] Technical university of Košice, Faculty of Mechanical Engineering, Košice, Slovak Republic, [b] ORTON Orthopaedic Hospital, ORTON Foundation, Helsinki, Finland, [c] Department of Medicine, Biomedicum Helsinki, Helsinki University Central Hospital, Finland, [d] COXA Hospital for Joint Replacement, Tampere, Finland, [e] Czech Technical University in Prague, Faculty of Mechanical Engineering, Department Mechanics, Biomechanics and Mechatronics,Prague,Czech Republic, [f] FEI STU Institute of Electronics and photonics in Bratislava, Slovak Republic
eva.zdravecka@tuke.sk

Keywords: diamond like carbon, AFM, ta-C, linear reciprocating sliding

1. Introduction

Diamond-like carbon (DLC) coatings generally have properties such as low friction and high wear resistance[1]. In order to be able to produce reliable DLC coatings for bio-mechanical applications, it is important to understand the tribological behaviour under all operating conditions. This has been studied intensively by numerous scientists e.g.[2–4] during the last years. The wear behaviors of DLC coatings surface can be simulated by various tribological test configurations[5]. Temperature affects wear behavior via thermochemical and thermodynamic mechanisms. For the development of successfully DLC coated implants, it is thus necessary to perform tests under conditions resembling the *in vivo* situation[6]. A unique friction tribometer was designed for this purpose and was used in this study for preliminary screening to analyze the mechanisms of failure of DLC coated samples whose shape corresponds to the knee joint geometry and provides thus a better understading of the tribological processes. Adhesion strength, hardness and elastic modulus are important factors affecting the wear behavior and were also tested[8]. Analyses of the coatings surface changes after testing were done using AFM and SEM techniques.

2. Experimental procedure

The ta-C and a-C:N films were both deposited by FPAD equipments described elsewhere[7,8]. In the designed friction tribometer, shaped metallic samples and flat counterfaces of ultra-high molecular weight polyethylene (UHMWPE) were tested. The radius of the curvature of the knee joint and the geometry of the sample was similar to the geometry of the total knee implants. The parameters used during testing were: normal force 340 N, frequency 1 Hz, environment ± lubrication, temperature 37 °C, trajectory L = 18 mm, mean speed 51.6 mm s^{-1}. Lubrication with bovine serum diluted to 25 % in deionized water, containing penicillin, streptomycin and sodium azice, was used for ta-C coatings. Each test pair received 160 ml of serum. Testing of a-C:N coating was carried out without heating in H_2O+0.9 g l^{-1} NaCl solution. The AFM measurements were made on PARK 100 in non-contact mode.

3. Results and discussion

According to the previous results, the hardness of the ta-C coating was around 46 GPa, and its elastic modulus 352 GPa. The hardness of the a-C:N coating was around 10.4 GPa and elastic modulus 119.1 GPa (ref.[8]). The adhesion behaviour of carbon coatings was characterized using scratch tests. The first failure of the ta-C coating was visible as tensile and cohesive cracks on the scratch path and was detected in the load range from 10 to 33 mN. The first failure of the a-C:N film on the scratch path was detected in the load range from 40 to 57.5 mN. Together with the SEM examination of the scratch, this suggests a good adhesion, when compared to comparable similar coatings[8].

3.1. Wear and friction

The unique friction tribometer was used in a reversible sliding regime mode. The results show that the a-C:N coating on the CoCrMo specimens under lubricated conditions was damaged (Fig. 1). The tests against UHWMPE samples were stopped after $0.3 \cdot 10^6$ cycles. The SEM image shows visible scratches and wear tracks. This could be explained by the influence of the abrasive wear mechanism. Initial results showed that, the substrate material wasn't able to provide adequate support for a-C:N films, adversely affecting their tribological performance and durability. The wear generation of a-C:N coating was thus associated with a failure initiated in the CoCrMo substrate rather than within the a-C:N coating. The occurrence of defects also accelerates the wear mechanism. The coating failure is promoted by lubricant enclosed in the surface microdefects which causes their further connecting and extending. Fig. 2 presents the SEM micrograph of the wear area of CoCrMo/ta-C sample after the test using $1 \cdot 10^6$ cycles. Wear scars on the CoCrMo/ta-C substrate were not observed.

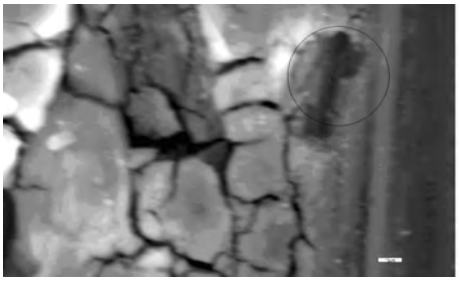

Fig. 1. **SEM of CoCrMo/ a-C:N** (marker 2 μm)

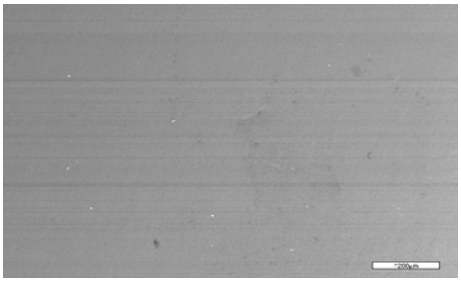

Fig. 2. **SEM of CoCrMo/ta-C** (marker 200 μm)

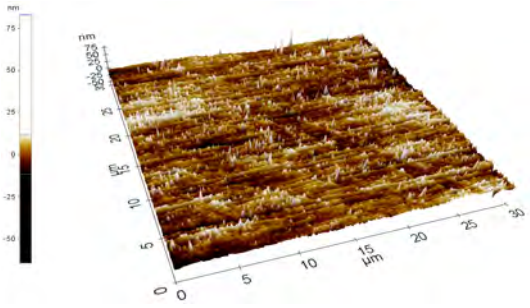

Fig. 3. **AFM of CoCrMo/ta-C before test**

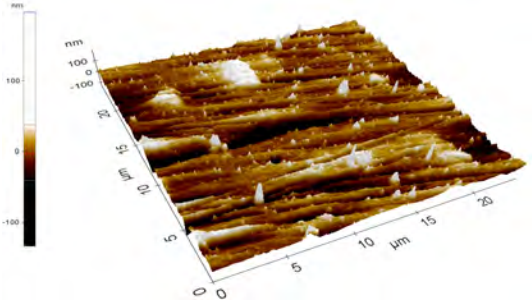

Fig. 4. **AFM of CoCrMo/ta-C after test** ($1 \cdot 10^6$ cycles)

Fig. 3 and Fig. 4 present AFM images of ta-C coated CoCrMo sample before and after $1 \cdot 10^6$ cycles. AFM analysis shows small increase of surface roughness after $1 \cdot 10^6$ cycles (from R_a = 4.104 nm to 17.105 nm).

4. Conclusions

From the ELTC tribometer tests of shaped samples with lubricants, the following conclusions can be made:

– The wear generation of a-C:N coating was associated with a failure initiated in the CoCrMo substrate rather than within the a-C:N coating.
– Studies showed a similar wear mechanism for all test cases of CoCrMo coated with ta-C. The measured values suggest good adhesion properties compared to ta-C coatings produced with other systems[8].
– The application of $1 \cdot 10^6$ sliding cycles increased the roughness of the wear scar (from R_a = 4.104 nm to 17.15 nm), while the weight losses were very low, this may be affected by sticking.

Compared with the plain CoCrMo alloy, the ta-C and a-C:N coated samples showed lower wear rates and high wear resistance under lubricated contact. The adhesive wear was the main mechanism for ta-C coated sample. However, there are a number of important questions, related to key tribological and biomechanical system variables, that cannot be answered by such experiments but which are important in clinical applications. Nevertheless, the application of DLC coatings on CoCrMo substrate has demonstrated a positive effect on reduction of wear and damages.

This work was financially supported by the projects VEGA 1/0264/11, 1/1103/11, 1/1102/11, LPP-0094-09, LPP-0149-09, projects MSM 6840770012, TA01010185 of Ministry of Education, Youth and Sports (CZ), Sigrid Jusélius Foundation, Danish Council for Strategic Research, Helsinki University Central Hospital EVO-grants, ORTON Orthopaedic Hospital of ORTON Foundation, Finska Läkaresällskapet, TBDP National PhD Graduate School of the Academy of Finland and by ELTC company.

REFERENCES

1. Robertson J.: Surf. Coat. Technol. *50*, 185 (1992).
2. Kim D. H., et. al.: Mater. Sci. Eng., C *22*, 9 (2002).
3. Erdemir A.: Tribol. Int. *38*, 249 (2005).
4. Hauert R., Müller U.: Diamond. Relat. Mater. *12*, 171 (2003).
5. Huanga L., et al.: Diamond. Relat. Mater. *10*, 1448 (2001).
6. Thorwarth G., et al.: Acta Biomater. *6*, 2335 (2010).
7. Anttila A., Lappalainen R., Tiainen V. M., Hakovirta M.: Adv. Mater. *9*, 1161 (1997).
8. Zdravecká E., et al.: Vacuum *86*, 675 (2012).

E. Zdravecká[a], V. M. Tiainen[b], A. Soininen[b], Y. T. Konttinen[b,c,d], L. Franta[e], M. Vojs[f], M. Marton[f], M. Veselý[f], M. Kotlár[f], M. Kelemen[a], and M. Ondáč[a]
([a] Technical university of Košice, Faculty of Mechanical Engineering, Košice, Slovak Republic, [b] ORTON Orthopaedic Hospital, ORTON Foundation, Helsinki, Finland, [c] Department of Medicine, Biomedicum Helsinki, Helsinki University Central Hospital, Finland, [d] COXA Hospital for Joint Replacement, Tampere, Finland, [e] Czech Technical University in Prague, Faculty of Mechanical Engineering, Department Mechanics, Biomechanics and Mechatronics, Prague, Czech Republic, [f] FEI STU Institute of Electronics and Photonics in Bratislava, Slovak Republic): **Investigation of Morphology Changes on Carbon Thin Films under Reciprocating Sliding Tests**

In this study ta-C and a-C:N thin films were deposited on medical grade CoCrMo alloy substrates by FPAD method from graphite target using different deposition conditions. The surface morpoholgy changes after use of a friction tribometer testing were investigated by SEM and AFM. The application of $1 \cdot 10^6$ cycles of shaped samples testing increased the roughness of the wear scar, while the weight losses were very low. The measured values suggest good adhesion properties.

PARAMETER ESTIMATION OF MATERIAL MODEL FOR SINGLE TRABECULA FROM MICROMECHANICAL TESTING

PETR ZLÁMAL[a] and ONDŘEJ JIROUŠEK[b]

[a] *Czech Technical University in Prague, Faculty of Transportation Sciences, Konviktská 20, 110 00 Prague 1, Czech Republic,* [b] *Institute of Theoretical and Applied Mechanics, Academy of Sciences of the Czech Republic, v.v.i., Prosecká 76, 190 00 Prague 9, Czech Republic*
xzlamal@fd.cvut.cz

Keywords: finite element method, micromechanical testing, nanoindentation, parameter identification, trabecular bone

1. Introduction

Material properties of trabecular bone at the level of single trabecula are important for understanding of osteoporotic changes, bone remodelling processes[1] and overall deformation behaviour of bone tissue. One of the powerful methods to measure elastic properties of single trabeculae is nanoindentation, however, this method can be reliably used only to get information about elastic properties. Yield properties as well as softening behaviour can not be reliably measured by nanoindentation and have to be obtained by fitting[2]. The purpose of this study is to demonstrate possibilities of micromechanical testing to develop advanced numerical material model for single trabecula and to compare the model to previously developed one which was based on nanoindentation[3].

2. Materials and methods

Samples of trabeculae (n=13) were harvested from human proximal femur of a 70-year old cadaver and cleared off marrow in ultrasonic bath. Clear trabeculae were dipped into a black toner solution to obtain a better contrast of surface for digital image correlation (DIC).

Precision of the experimental setup prior the tests with trabeculae has been evaluated using two groups of specimens of known material properties. BoPET film (Biaxially-oriented polyethylene terephthalate, DuPont, USA) with 72 μm height, Co-Ni wire with 90 μm diameter and 2 mm length were used as the test materials.

For micromechanical testing a novel experimental device has been developed (see Fig. 1). Experimental setup was developed using translational stages and loading is controled by stepper motors (SX16, Microcon, Czech Republic). Design of the setup allows for testing in either tension-compression or three point bending. Applied force is measured with 4.5 N capacity load sensor (FBB350, FUTEK, USA) and the strains are measured optically

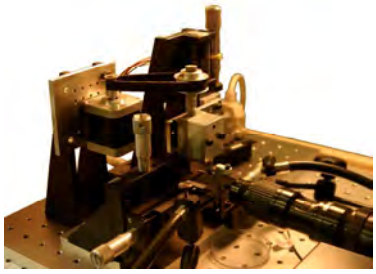

Fig. 1. **Experimental setup for three-point bending tests**

using CCD camera (Vosskuhler CCD-1300F, Germany). From each test the stress-strain curve was established.

Apart from the tension tests, three-point bending with single trabecula (Fig. 2: right) was performed (after verification using three-point bending of BoPET film (Fig. 2: left) and Co-Ni wire).

Groups of markers were selected in the image data captured by the CCD camera. Positions of the markers were tracked using DIC toolkit[4] based on Lucas-Kanade algorithm. From displacements of the markers, strain values were computed. Stresses were calculated using the measured forces and cross-sectional areas. Resulting stress-strain curves were established for each of the sample. Elastic modulus, yield strains and yield stresses were determined using the 0.2 % offset method.

Elasto-plastic material model with von Mises yield criterion and bilinear hardening for trabecular bone was chosen. This material model requires two constants E, μ (Young's modulus and Poisson's ratio) for the elastic part and two constants σ_y, E_{tan} (yield stress, tangent modulus) for the plastic part. Finite element analyses (FEA) used for constants identification of material model were performed for BoPET samples and samples of trabeculae. The geometry of each sample of trabecula was approximated using elliptical cross sections. The lengths of the major and minor axes of the ellipses were obtained from two perpendicular projections captured by CCD camera. These geometric models were meshed and nodes corresponding with places of markers (for DIC) on specimen surface in

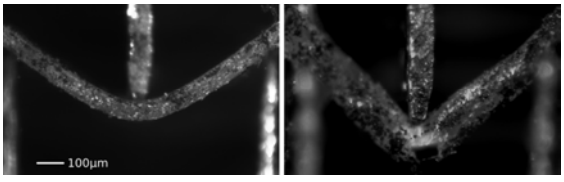

Fig. 2. **BoPET specimen (left), trabecula specimen after breaks (right)**

experiments were selected. The 3D FE models were composed of elements with quadratic shape functions (10,400 brick elements for BoPET, 23,170 tetrahedral elements for trabecula). During the analyses the same boundary conditions and external forces as experimental ones were used a material constants were varied using custom optimization algorithm[5]. Resulting displacements of markers from FEA were fitted to experimentally obtained values and the best constants were found by least square method.

3. Results

Elastic modulus, yield strains and yield stresses were determined using the 0.2 % offset method (usually used for trabecular bone)[6]. Comparison of resulting material constants for BoPET and trabecula from experiments and FEA are shown in Tab. I.

The best fit of identified material constants for marker displacement of the trabecula sample is shown in Fig. 3.

Table I
Resulting material constants

	BoPET		Trabecula	
	exp.	FEA	exp.	FEA
E [MPa]	4615±271	5173±291	10347 ±1162	11835 ±1560
μ [–]	–	0.35 ±0.04	–	0.23 ±0.03
σ_y [MPa]	107 ±7.8	58.1 ±8.6	208 ±23.9	231.8 ±33
E_{tan} [MPa]	–	608 ±200	–	1878 ±310

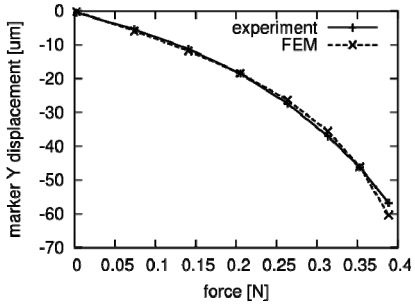

Fig. 3. **Marker displacement of the best fit of material constants**

4. Conclusions

A novel high-precision micromechanical testing system has been developed and used to measure properties of single human trabeculae. Overall precision of measurement was determined (based on experiments with BoPET and Co-Ni wire) as the upper limit of all measurements – elastic modulus 5 %, yield stress 7 % and yield strain 5 %. From comparison of results from FEA and experiments for BoPET material it is apparent that used yield condition is not suitable for polymers however the intention was only to verify the functionality of the proposed identification process (good agreement in the elastic part) and experimental setup (small standard deviation). On the other hand chosen material model and elasto-plastic constants identified using FEA showed good match for trabecular bone. Obtained constants were confirmed by comparison with results from nanoindentation that have been previously published[3,5]. For even better results it is necessary to improve the process of creating model geometry. Cross section of the model has a large influence on the accuracy of determination of material properties from three-point bending.

The research has been supported by the GACR (grant No. P105/10/2305), GA CTU (grant No. SGS11/140/OHK2/2T/16) and research plan of the MEYS CR (Research Plan 6840770043) and Academy of Sciences of the Czech Republic AV0Z20710524.

REFERENCES

1. Busse B., Hahn M., Soltau M., Zustin J., Püschel K., Duda G.: Bone *5*, 1034 (2009).
2. Menčík J., He L. H., Swain M. V.: J. Mech. Behav. Biomed. Mater. *2*, 318 (2009).
3. Jiroušek O., Němeček J., Kytýř D., Kunecký J., Zlámal P., Doktor T.: Chem. Listy *105*, s668 (2011).
4. Jandejsek I., Valach J., Vavřík D.: Exp. Anal. Napětí, *2010*, 121.
5. Zlámal P., Jiroušek O., Kytýř D., Němeček J.: ISB2011 Conference book, 211–212, 2011.
6. Bayraktar H. H., Morgan E. F., Niebur G. L., et al.: J. Biomech. *37*, 27 (2004).

P. Zlámal[a] and O. Jiroušek[b] *([a] Czech Technical University in Prague, Faculty of Transportation Sciences, Prague, [b] Institute of Theoretical and Applied Mechanics, Academy of Sciences of the Czech Republic, v.v.i., Prague, Czech Republic):* **Parameter Estimation of Material Model for Single Trabecula from Micromechanical Testing**

A novel micromechanical device has been developed. Precision of the setup has been evaluated using specimens of known material properties. Applied force was measured with capacity load sensor and the strains were measured optically. Samples of trabeculae were harvested from human proximal femur. A FE model was loaded. From displacements of markers, strain values were computed. Resulting displacements of markers from FEA were fitted to experimentally obtained ones and set of parameters of the material model was determined.

CONTENTS

Invited Papers

Regular Papers

AUTHOR INDEX

//// CSM INSTRUMENTS

Advanced Mechanical Surface Testing

EXCELLENCE IN NANOINDENTATION, SCRATCH AND TRIBOLOGY

//// CSM ULTRA NANOINDENTATION TESTER (UNHT)
the new generation of Nanoindenter with ultra low thermal drift

This new Nanoindenter is based on the principle of using a measurement head (built with drift-free Zerodur© glass material) with one axis for measurement and one axis for reference, each one having its own actuator and its own sensors of depth and force. It is therefore possible to carry out active referencing of the surface of the sample. The true penetration depth is measured with a third capacitive sensor monitoring the direct difference of penetration between the reference and the indenter.

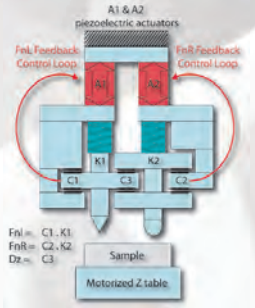

> Extremely soft materials: gels and cells

Experiments performed on gels show the exceptional capabilities of the UNHT in extreme applications: with loads lower than 50 µN, penetration depths can reach 10 to 20 µm!
Great measurement accuracy can be obtained for penetration depths from 10 nm to over 50'000 nm. Thanks to the unmatched thermal stability of the system, adhesion energy can be easily studied on various soft materials.

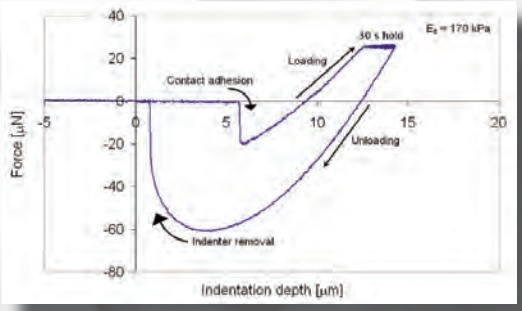

> Ultra low load indentations on low-K films

Low load indentations on low-K films of 200 nm thickness demonstrate the high-resolution capabilities of this unique and patented UNHT instrument. This makes it the ideal instrument for characterization of ultra thin coatings.

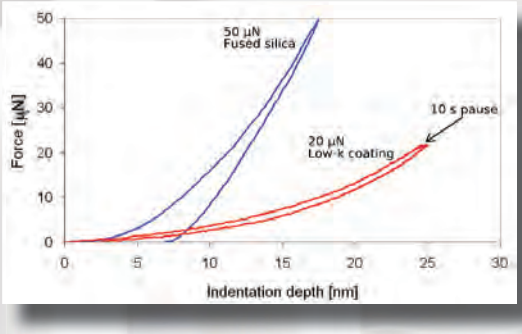

> Creep studies on polymers

Nanomechanical testing of materials exhibiting time-dependent properties requires an instrument with high thermal stability and high resolution. Creep studies on polymers can always be performed without any thermal stabilization period or thermal drift correction!

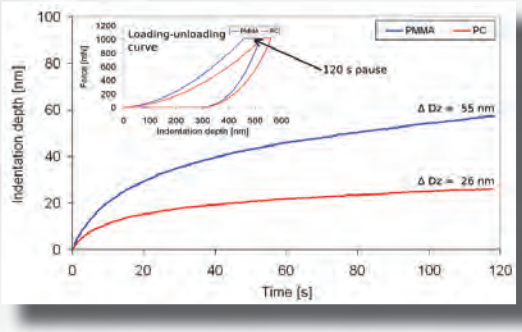

CSM Instruments | Rue de la Gare 4 | CH – 2034 Peseux | www.csm-instruments.com
Phone : +41 32 557 56 00 | Fax : +41 32 557 56 10 | E-mail : info@csm-instruments.com

Výhradní zástupce výrobce elektronových mikroskopů FEI pro Českou republiku a Slovensko

Zařízení a služby pro elektronovou a optickou mikroskopii

Adresa společnosti

EDLIN, s. r. o.
Za Kralupkou 440
277 11 LIBIŠ
www.edlin.cz

tel: +420.313 034 666

fax: +420.313 034 662

AFM, SEM microscopy and nanoindentation
Agilent Technologies

The Agilent 8500 FE-SEM is a compact system that offers researchers a field emission scanning electron microscope (FE-SEM) right in their own laboratory. The innovative 8500 has been optimized for low-voltage imaging, extremely high surface contrast, and resolution typically found only in much larger and more expensive field emission microscopes.

Agilent's highly configurable AFM instruments allow you to expand the system's capabilities as your needs occur. Agilent's industry-leading environmental / temperature systems and fluid handling enable superior control for electrochemistry, polymer and life-science applications.

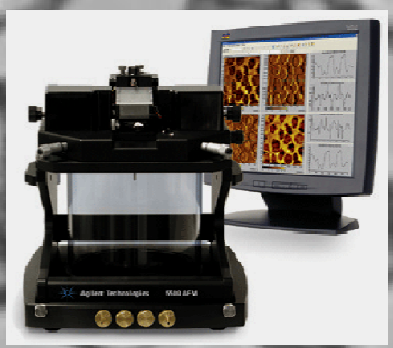

The culmination of decades of research and development, the Agilent Nanoindenter systems are the world's most accurate, flexible, and user-friendly instrument for nanoscale mechanical testing. Electromagnetic actuation technology allows the systems to achieve unparalleled dynamic range in force and displacement.

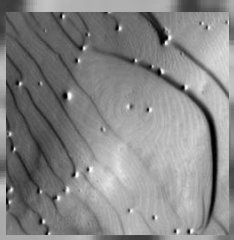
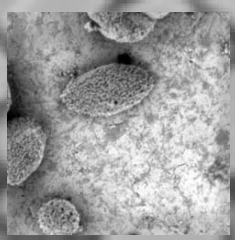
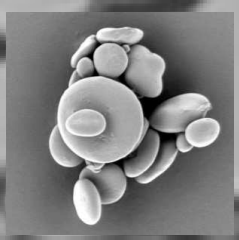
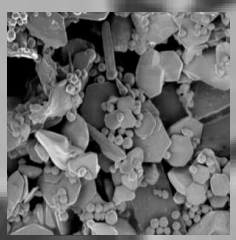
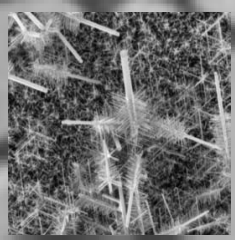

H TEST a.s.
Šafránkova 3
155 00 Praha 5
Tel: 235 365 207
info@htest.cz
www.agilent.com/find/nano

Agilent Technologies
Authorized Distributor

NanoTest™ Vantage

NANOINDENTACE

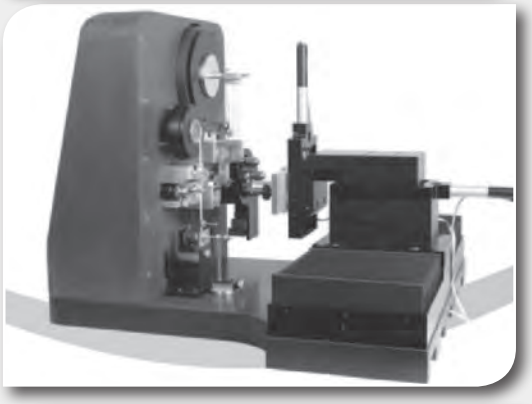

Nízká nebo vysoká zátěž
(10 μN-500 mN) (0.2-20 N)

Řízené prostředí	Dynamické zatížení	Charakterizace
Vysoká teplota (750°C max)	Scratch	3D zobrazení - povrch profiling/ nanopositioner
Nízká teplota (-30°C min)	Wear	Hloubkový profil
Kapalina (H20, Olej) Vlhkost (15-80% RH)	Fretting	3D zobrazení vysoké rozlišení - AFM
Inertní atmosféra (Ar, N2)	Sample impact	Akustická emise Cílená a mapující nanoindentace
Atmosféra s nízkým obsahem kyslíku (0.1% min)	Pendulum impact	

Měřící možnosti systému

Nanoindetace
- Měření tvrdosti, modulu a visko-elastických vlastností pomocí nano a mikro indexačních technik
- Analýza tvrdosti a modulu v závislosti na hloubce
- Mapování mechanických vlastností
- Kvazi-statické a dynamické testování

Nano-impact a fatigue
- Analýza narušení materiálu
- Měření materiálového útlumového koeficientu

Analýza chování při vysoké zátěži
- Nano-scratch a wear
- Analýza kritické zátěže při scratch testu a tření
- Měření počtů cyklů do poruchy pro ochranné vrstvy

Nano-fretting
- Akcelerované reciproké únavové testy
- Nízký kontaktní tlak pro dlouhodobé testování (až 1 milion cyklů)

Kontrolované podmínky testů a rozšíření
Kontrolované podmínky prostředí pro testování za reálných podmínek použití testovaných materiálů

- Vysokoteplotní nanoindentace, nanoscratch a nanoimpact až do 750°C
- Nízkoteplotní nanoindentace a nanoscratch do -30°C
- Testování v kapalinách (vzorek i hrot jsou ponořeny v kapalině)
- Měření při kontrolované atmosféře (bez kyslíku)
- Měření při kontrolované vlhkosti

Naše firma **LAO – průmyslové systémy, s.r.o.** nabízí široké portfolio produktů a služeb v oblasti vědeckých a průmyslových aplikací. Obecně se zabýváme prodejem laserů, vědeckých laserových systémů, optiky a optomechaniky, optoelektronických, detekčních a měřících zařízení, kompletních technologických laserových systémů pro průmyslové aplikace a to včetně servisu, dodávek náhradních dílů a spotřebního materiálu. Na trhu působíme téměř dvacet let a rádi bychom zmínili, že kontinuitu kvalitních služeb vždy zaručovali pracovníci, kteří mají několikaleté zkušenosti s laserovými a optickými aplikacemi. Informace o většině produktů a služeb firmy LAO – průmyslové systémy s.r.o. naleznete na **www.lao.cz**

Snahou firmy **LAO – průmyslové systémy, s.r.o.** je vždy dělat vše pro to, abychom maximálně a efektivně uspokojili Vaše požadavky, potřeby a záměry a zůstali tak ve Vašem povědomí jako schopný a důvěryhodný partner pro dlouhodobou spolupráci. Dokážeme poradit s řešením dané aplikace, navrhnout vhodnou sestavu či pomůžeme s výběrem optimální technologie. Nabízíme kvalitní a prověřené produkty od světových dodavatelů. Zárukou kvality našich služeb je také certifikace ISO 9001-2009, kterou jsme získali v roce 2005.

V případě Vašeho zájmu o naše produkty či o cokoliv dalšího, nás neváhejte prosím kontaktovat. Odpovíme Vám rádi na veškeré dotazy a poradíme se správným výběrem a konfigurací pro Vaše pracoviště, tak aby jste maximálně využili všech možností a schopností, které tyto produkty nabízejí.

Lasery a Optika

SLAVÍME 20. VÝROČÍ

LAO - průmyslové systémy, s.r.o

Na Floře 1328/4, 143 00 Praha 4 • Tel.: (+420) 241 046 800

www.lao.cz

www.tuv.com TÜV TÜV Rheinland Group ID:9105032609

ISO 9001:2011

www.mikroskopy.cz

SURFACE

nanoLab tools

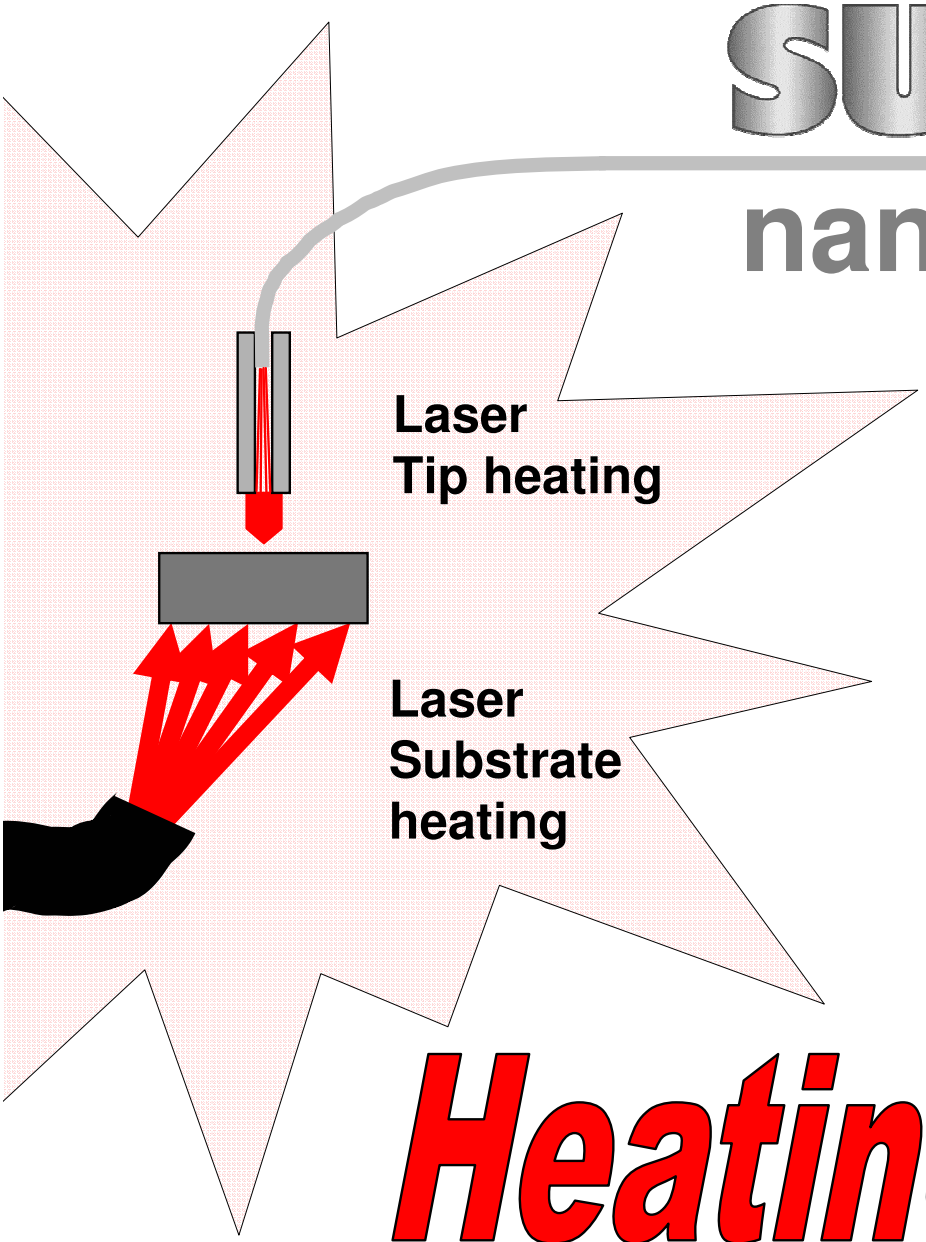

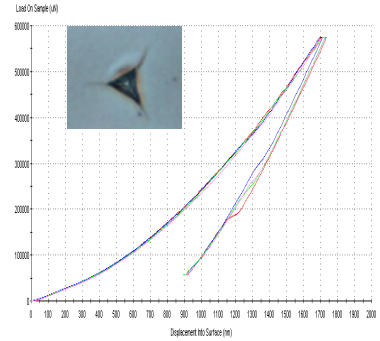

Si at RT (25°C)

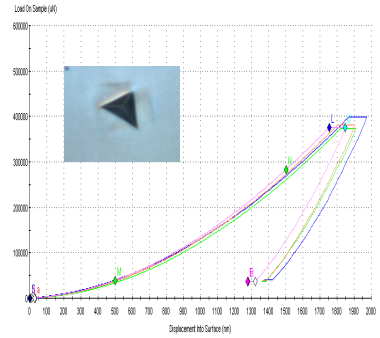

Si at 500 °C

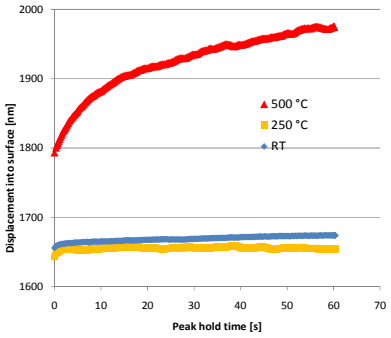

Creep of Si at RT-500°C

Heating & Cooling

for micro/nano mechanical Testing in Nanoindenter and SEM:

Heating: Laser Heater: Rt- 500°C
Cooling: - 80°C to 180°C (250°Cmax)

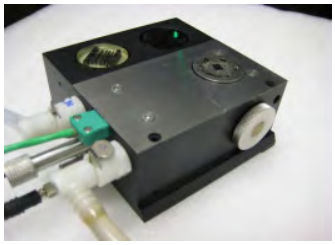

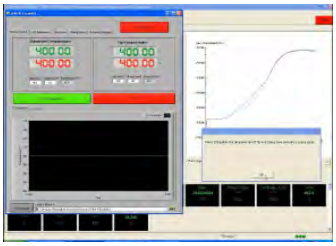

SURFACE Rheinstr.7 D41836 Hückelhoven Tel. +49 2433 970305 info@surface-tec.com www.surface-tec.com

CHEMICKÉ LISTY • ročník/volume 106 (S), čís./no. Symposia • LISTY CHEMICKÉ roč./vol. 136, ČASOPIS PRO PRŮMYSL CHEMICKÝ, roč./vol. 122 • ISSN 0009-2770, ISSN 1213-7103 (e-verze), ISSN 1803-2389 (CD verze) • evidenční číslo MK ČR E 321 • Vydává Česká společnost chemická jako časopis Asociace českých chemických společností ve spolupráci s VŠCHT Praha, s ČSPCH a ÚOCHB AV ČR za finanční podpory Nadace Český literární fond a kolektivních členů ČSCH • IČO 444715 • Published by the Czech Chemical Society • VEDOUCÍ REDAKTOR/EDITOR-IN-CHIEF: P. Chuchvalec • REDAKTOŘI/ EDITORS: J. Barek, Z. Bělohlav, P. Drašar, J. Hetflejš, P. Holý, J. Horák, B. Kratochvíl, J. Podešva, P. Rauch; Bulletin: I. Valterová; Webové stránky: R. Liboska, P. Zámostný • ZAHRANIČNÍ A OBLASTNÍ REDAKTOŘI/FOREIGN AND REGIONAL EDITORS: F. Švec (USA), Z. Kolská (Ústí nad Labem) • KONZULTANT/CONSULTANT: J. Kahovec • TECHNICKÁ REDAKTORKA/EDITORIAL ASSISTANT: R. Řápková • REDAKČNÍ RADA/ADVISORY BOARD: K. Bláha, L. Červený, E. Dibuszová, J. Hanika, Z. Havlas, J. Káš, M. Koman, J. Koubek, T. Míšek, K. Melzoch, V. Pačes, O. Paleta, V. Růžička, I. Stibor, V. Šimánek, R. Zahradník • ADRESA PRO ZASÍLÁNÍ PŘÍSPĚVKŮ/MANUSCRIPTS IN CZECH, SLOVAK OR ENGLISH CAN BE SENT TO: Chemické listy, Novotného lávka 5, 116 68 Praha 1; tel./phone +420 221 082 370, +420 222 220 184, e-mail: chem.listy@csvts.cz • INFORMACE O PŘEDPLATNÉM, OBJEDNÁVKY, PRODEJ JEDNOTLIVÝCH ČÍSEL A INZERCE/ INFORMATION ADS: Sekretariát ČSCH, Novotného lávka 5, 116 68 Praha 1; tel. +420 222 220 184, e-mail: chem.spol@csvts.cz, chem.ekonom@csvts.cz • PLNÁ VERZE NA INTERNETU/FULL VERSION ON URL: http://www.chemicke-listy.cz • TISK: Rodomax s.r.o., Rezecká 1164, 549 01 Nové Město nad Metují • Redakce čísla Symposia (ISSUE EDITOR) R. Čtvrtlík, L. Pešek • SAZBA, ZLOM: ČSCH, Chemické listy • Copyright © 2012 Chemické listy/Česká společnost chemická • Cena výtisku 170 Kč, roční plné předplatné 2012 (12 čísel) 1730 Kč, individuální členské předplatné pro členy ČSCH 865 Kč. Roční předplatné ve Slovenské republice 92 EUR (doručování via SCHS), individuální členské předplatné pro členy ČSCH 70 EUR (doručování via SCHS), 258 EUR (individuální doručování), ceny jsou uvedeny včetně DPH • DISTRIBUTION ABROAD: KUBON & SAGNER, POB 34 01 08, D-80328 Munich, FRG; Annual subscription for 2012 (12 issues) 225 EUR • This journal has been registered with the Copyright Clearance Center, 2322 Rosewood Drive, Danvers, MA 01923, USA, where the consent and conditions can be obtained for copying the articles for personal or internal use • Pokyny pro autory najdete na http://www.chemicke-listy.cz , zkratky časopisů podle Chemical Abstract Service Source Index (viz http://cassi.cas.org/search.jsp) • Chemické listy obsahující Bulletin jsou zasílány zdarma všem individuálním a kolektivním členům ČSCH a ČSPCH v ČR i zahraničí, do všech relevantních knihoven v ČR a významným představitelům české chemie a chemického průmyslu; v rámci dohod o spolupráci i členům dalších odborných společností • Molekulární námět na obálce: P. Drašar • Dáno do tisku 10.8.2012.